



**SIPHT**  
NOVOSIBIRSK 2017

12-th International Conference  
**«Two-Phase Systems for Space and  
Ground Applications»**

2nd International School of Young Scientists  
**«Interfacial Phenomena and Heat  
Transfer»**

**BOOK OF ABSTRACTS**

**Editors:**  
*Sergey V. Alekseenko*  
*Elena F. Bykovskaya*  
*Oleg A. Kabov*  
*Yuriy V. Lyulin*  
*Dmitry V. Zaitsev*

**Kutateladze Institute of Thermophysics SB RAS**  
**Novosibirsk, Russia, 11-16, September 2017**



**N\***NOVOSIBIRSK  
STATE  
UNIVERSITY  
\*The real science

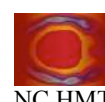


**begell**  
begell house, inc. publishers



**KYUSHU  
UNIVERSITY**

**Aix-Marseille  
université**



12-th International Conference  
**«Two-Phase Systems for Space and Ground  
Applications»**

2<sup>nd</sup> International School of Young Scientists  
**«Interfacial Phenomena and Heat Transfer»**

**BOOK OF ABSTRACTS**

Editors: *Sergey V. Alekseenko, Elena F. Bykovskaya,  
Oleg A. Kabov, Yuriy V. Lyulin and Dmitry V. Zaitsev*

Kutateladze Institute of Thermophysics SB RAS  
Novosibirsk, Russia, 11-16, September 2017

## Welcome

On behalf of the Organizing Committee, it is our pleasure to welcome all participants of the 12-th International Conference «Two-Phase Systems for Space and Ground Applications» and 2nd International School of Young Scientists «Interfacial Phenomena and Heat Transfer» to Novosibirsk. The third largest city in Russia, often referred to as "the capital of Siberia", Novosibirsk is home to a number of research centers and institutes, including the Kutateladze Institute of Thermophysics. The long tradition of research in both fluid mechanics and heat transfer makes this institute a natural venue for the Conference and School, the first of its kind. A wide range of topics in the rapidly developing and highly interdisciplinary field of interfacial phenomena and heat transfer are covered, including boiling, shear-driven films, droplet evaporation, contact line phenomena, thermocapillary flows, two-phase flows in microchannels and minichannels, and effect of gravity on various processes. The Conference and School is made possible by financial support from the Russian Science Foundation. A special issue of the open access Journal of Physics: Conference Series, indexed in Scopus and Web of Science will be published following the conference. Papers for this issue will be subject to the review procedure of the journal. The Organizing Committee wishes all participants a pleasant stay in Novosibirsk and a productive conference.

### Chairs

For more information about the Conference and School please visit the websites

<http://www.itp.nsc.ru/htl/spaceconf-2017/>

<http://www.itp.nsc.ru/htl/school-conference-2017/>



12-th International Conference  
«Two-Phase Systems for Space and Ground Applications»  
Kutateladze Institute of Thermophysics SB RAS  
Novosibirsk, Russia, 11-15, September 2017

**Conference Chairs:**

Sergey V. Alekseenko, Kutateladze Institute of Thermophysics SB RAS, Novosibirsk, Russia  
Oleg A. Kabov, Kutateladze Institute of Thermophysics SB RAS, Novosibirsk, Russia

**Conference Co-Chairs:**

Jungho Kim, University of Maryland, MD, USA  
Haruhiko Ohta, Kyushu University, Fukuoka, Japan  
Lounes Tadrist, Aix Marseille University, Marseille, France  
Jian-Fu Zhao, Institute of Mechanics, Beijing, China

**Conference organizers:**

- Kutateladze Institute of Thermophysics SB RAS, Novosibirsk, Russia
- Novosibirsk State University, Novosibirsk, Russia
- University of Maryland, MD, USA
- Kyushu University, Nishi-ku, Fukuoka, Japan
- Aix Marseille University, Marseille, France
- Institute of Mechanics, Chinese Academy of Sciences, Beijing, China

**Sponsor:**  Russian Science Foundation

**Scientific Secretaries:**

Elena F. Bykovskaya, Kutateladze Institute of Thermophysics SB RAS, Novosibirsk, Russia  
Dmitry V. Zaitsev, Kutateladze Institute of Thermophysics SB RAS, Novosibirsk, Russia

**Conference objective:** The Conference provides researchers the opportunity to present and discuss novel work, while also identifying future needs in this critical area of research. Presentation topics include, but are not limited to:

- Experiments in Microgravity
- Microchannels and Minichannels
- Films, Layers and Interfaces
- Physics of Contact Line and Wetting
- Boiling, Evaporation and Condensation
- Thermocapillary Flow
- Spray, Jets and Two-Phase Flows
- Bubbles, Drops and Foams
- Electronics Cooling
- Properties of Vapor–Liquid–Solid Interfaces

**Scientific Committee:**

Vladimir S. Ajaev, SMU, USA  
Sergey V. Alekseenko, IT, Russia  
Alidad Amirfazli, UA, Canada  
Hitoshi Asano, KoU, Japan  
Avram Bar-Cohen, UM, USA  
Dieter Bothe, TUD, Germany  
Gian Piero Celata, ENEA, Italy  
Catherine Colin, IMFT, France  
Paolo Di Marco, UNIPI, Italy  
Michael Dreyer, ZARM, Germany  
Olga N. Goncharova, ASU, Russia  
Zhenhui He, SYSU, China

Oleg A. Kabov, IT, Russia  
Qusheng Liu, Institute Mechanics, China  
Dmitriy Markovich, IT, Russia  
Olivier Minster, ESA, The Netherlands  
Haruhiko Ohta, KU, Japan  
Eduard E. Son, JIHT, Russia  
Peter Stephan, TUD, Germany  
Lounes Tadrist, IUSTI, France  
John R. Thome, EPFL, Switzerland  
Balazs Toth, ESA, The Netherlands  
Jian-Fu Zhao, IM, China

Website: <http://www.itp.nsc.ru/htl/spaceconf-2017/index.html>



2<sup>nd</sup> International School of Young Scientists  
«**Interfacial Phenomena and Heat Transfer**»  
Kutateladze Institute of Thermophysics SB RAS  
Novosibirsk, Russia, 11-16, September 2017

**School Chair :**

Oleg A. Kabov, Kutateladze Institute of Thermophysics SB RAS, Novosibirsk, Russia

**School Co-Chairs:**

Vladimir S. Ajaev, Southern Methodist University, Department of Mathematics, Dallas, USA

Aleksandr S. Dmitriev, Moscow Power Engineering Institute, Moscow, Russia

Irina Graur, Aix Marseille University, Marseille, France

Tatyana P. Lyubimova, Institute of Continuous Media Mechanics, UB RAS, Perm, Russia

**School organizers:**

- Kutateladze Institute of Thermophysics SB RAS, Novosibirsk, Russia
- Novosibirsk State University, Novosibirsk, Russia
- National committee on Heat and Mass Transfer Moscow, Russia
- Begell House, Inc., Danbury, CT, USA

**Sponsor:**  Russian Science Foundation

**Scientific Secretary:**

Yuriy V. Lyulin, Kutateladze Institute of Thermophysics SB RAS, Novosibirsk, Russia

**School objective:** The School provides researchers the opportunity to present and discuss novel work, while also identifying future needs in this critical area of research. Presentation topics include, but are not limited to:

- Boiling, CHF, Evaporation and Condensation
- Films, Layers and Interfaces
- Physics of Contact Line and Wetting
- Bubbles, Drops, Rivulets and Foams
- Spray, Jets and Two-Phase Flows
- Properties of Vapor–Liquid–Solid Interfaces
- Thermocapillary Flow
- Microchannels and Minichannels
- Electronics Cooling
- Nano and microstructured surfaces
- Drag reduction

**School format:** The School consists of keynote lectures given by experts in selected topics as well as short oral presentations with poster sessions of young scientists.

Website: <http://www.itp.nsc.ru/htl/school-conference-2017/>

## Russian program committee

### Head of the committee

Alekseenko S.V., academician RAS (Kutateladze Institute of Thermophysics, SB RAS, Novosibirsk)

### Deputies

Kabov O.A., professor (Kutateladze Institute of Thermophysics SB RAS, Novosibirsk, Russia)  
Markovich D.M., corresponding member of RAS (Kutateladze Institute of Thermophysics, SB RAS, Novosibirsk)

### Program committee members

Baidakov V.G., professor (Institute of Thermal Physics, UB RAS, Ekaterinburg)  
Berdnikov V.S., professor (Kutateladze Institute of Thermophysics, SB RAS, Novosibirsk)  
Bolshov L.A., academician RAS (The Nuclear Safety Institute of the RAS, Moscow)  
Chinnov E.A., professor (Kutateladze Institute of Thermophysics, SB RAS, Novosibirsk)  
Dedov A.V., corresponding member of RAS (Institute of Thermal and Nuclear Power of the Power Engineering Institute Engineering, Moscow)  
Dragunov Yu.G., corresponding member of RAS (JSC "NIKIET", Moscow)  
Fedoruk M.P., corresponding member of RAS (Novosibirsk State University, Novosibirsk)  
Filippov S.P., academician RAS (The Energy Research Institute RAS, Moscow)  
Golovin S.V., professor (Lavrentyev Institute of Hydrodynamics, SB RAS, Novosibirsk)  
Koroteev A.A., academician RAS (Moscow Aviation Institute, Moscow)  
Koroteev A.S., academician RAS (Keldysh Research Center, Moscow)  
Kuibin P.A., professor (Kutateladze Institute of Thermophysics, SB RAS, Novosibirsk)  
Kupershtokh A.L., professor (Lavrentyev Institute of Hydrodynamics, SB RAS, Novosibirsk)  
Kuznetsov G.V., professor (Tomsk Polytechnic University, Tomsk)  
Kuznetsov V.V., professor (Kutateladze Institute of Thermophysics, SB RAS, Novosibirsk)  
Leontiev A.I., academician RAS (Bauman Moscow State Technical University, Moscow)  
Lyubimova T.P., professor (Perm State University, Perm)  
Maydanik Yu.F., professor (Institute of Thermal Physics, UB RAS, Ekaterinburg)  
Nakoryakov V.E., academician RAS (Kutateladze Institute of Thermophysics, SB RAS, Novosibirsk)  
Nigmatulin R.I., academician RAS (The P.P. Shirshov Institute of Oceanology, RAS, Moscow)  
Novopashin S.A., professor (Kutateladze Institute of Thermophysics, SB RAS, Novosibirsk)  
Pavlenko A.N., corresponding member of RAS (Kutateladze Institute of Thermophysics, SB RAS, Novosibirsk)  
Petrenya Yu.K., corresponding member of RAS (Power Machines, St. Peterburg)  
Petrov O.F., academician RAS (Joint Institute for High Temperatures of the RAS, Moscow)  
Pokusaev B.G., corresponding member of RAS (Moscow Polytechnic University, Moscow)  
Popov G.A., academician RAS (Research Institute of Applied Mechanics and Electrodynamics (RIAME), Moscow)  
Puhnachev V.V., corresponding member of RAS (Lavrentyev Institute of Hydrodynamics, SB RAS, Novosibirsk)  
Rebrov A.K., academician RAS (Kutateladze Institute of Thermophysics, SB RAS, Novosibirsk)  
Sharypov O.V., professor (Kutateladze Institute of Thermophysics, SB RAS, Novosibirsk)  
Shiptyuk A.N., corresponding member of RAS (Khristianovich Institute of Theoretical and Applied Mechanics, SB RAS, Novosibirsk)  
Son E.E., academician RAS (Joint Institute for High Temperatures of the RAS, Moscow)  
Stankus S.V., professor (Kutateladze Institute of Thermophysics, SB RAS, Novosibirsk)  
Stennikov V.A., corresponding member of RAS (Melentiev Energy Systems Institute, SB RAS, Irkutsk)  
Surgikov S.T., academician RAS (A. Ishlinsky Institute for Problems in Mechanics RAS, Moscow)  
Terekhov V.I., professor (Kutateladze Institute of Thermophysics, SB RAS, Novosibirsk)  
Varaksin A.Yu., corresponding member of RAS (Joint Institute for High Temperatures of the RAS, Moscow)

## **Russian organizing committee**

### **Heads of the committee**

Kabov O. A., professor (Kutateladze Institute of Thermophysics SB RAS, Novosibirsk, Russia)

Chinnov E. A., professor (Kutateladze Institute of Thermophysics SB RAS, Novosibirsk, Russia)

### **Deputy**

Marchuk I. V., professor (Novosibirsk State University, Novosibirsk)

### **Scientific secretaries**

Bykovskaya E. F., PhD (Kutateladze Institute of Thermophysics SB RAS, Novosibirsk, Russia)

Zaitsev D. V., PhD (Kutateladze Institute of Thermophysics SB RAS, Novosibirsk, Russia)

Lyulin Yu. V., PhD (Kutateladze Institute of Thermophysics SB RAS, Novosibirsk, Russia)

### **Organizing committee members**

Baranov E. A., PhD (Kutateladze Institute of Thermophysics SB RAS, Novosibirsk, Russia)

Gatapova E. Ya, PhD (Kutateladze Institute of Thermophysics SB RAS, Novosibirsk, Russia)

Grigorieva N. V. (Kutateladze Institute of Thermophysics SB RAS, Novosibirsk, Russia)

Kirichenko D. P. (Novosibirsk State University, Novosibirsk)

Kirichenko E. Ol. (Kutateladze Institute of Thermophysics SB RAS, Novosibirsk, Russia)

Kreta A. S. (Novosibirsk State University, Novosibirsk)

Ronshin F. V. (Kutateladze Institute of Thermophysics SB RAS, Novosibirsk, Russia)

Semenov A. A. (Kutateladze Institute of Thermophysics SB RAS, Novosibirsk, Russia)

Spesivtsev S. E. (Novosibirsk State University, Novosibirsk)

Svetlichnaya O. V. (Novosibirsk State University, Novosibirsk)

Cheverda V. V., PhD (Kutateladze Institute of Thermophysics SB RAS, Novosibirsk, Russia)

Shatskiy E. N. (Kutateladze Institute of Thermophysics SB RAS, Novosibirsk, Russia)

Eloayn K. S. (Kutateladze Institute of Thermophysics SB RAS, Novosibirsk, Russia)

## CONTENTS

### 12-th International Conference on «Two-Phase Systems for Space and Ground Applications»

#### *Session – 1: Experiments in space - 1*

**Eduard Son**

2-phase Interfacial, Droplet, Bubble Turbulence and Combustion in the Normal and Microgravity Conditions ..... 1

**O.A. Kabov, V.V. Cheverda, D.V. Zaitsev and Yu.O. Kabova**

Heat transfer and CHF in a shear-driven liquid film under local heating: preparation of space experiment on ISS ..... 3

**Ke Wu, Peng Liu, Jian-Fu Zhao, Hui-Xiong Li and Kai Li**

Single Bubble Pool Boiling Experiment aboard SJ-10: Bubble Behavior and Local Heat Transfer ..... 5

**Farhat Mohamed, Outi Supponen and Danail Obreschkow**

On cavitation bubble dynamics in variable gravity ..... 7

**E. Trejo, C. Colin, C. Hammer and J. Kim**

Comparison of two similar techniques to study flow boiling in normal and microgravity conditions ..... 9

**Satoshi Okayama, Ren Tianhao, Yasuhisa Shinmoto and Haruhiko Ohta**

Addition of Data for Pool Boiling of Immiscible Mixtures ..... 11

#### **Session – 2: Two phase flows**

**Satoru Miyawaki, Yuma Murata, Ryosuke Ukena and Hitoshi Asano**

Study on the effect of Channel Cross-Sectional Shape on Void Fraction Characteristics of One-Component Vertically Upward Two-Phase Flows ..... 13

**Hang Guo, Xuan Liu, Jian Fu Zhao, Fang Ye and Chong Fang Ma**

Experimental Investigation of Two-phase Flow in Cathodic Flow Field of a Proton Exchange Membrane Fuel Cell in Short-term Microgravity ..... 15

**S.V. Alekseenko, A.V. Cherdantsev, S.V. Isaenkov, M.V. Cherdantsev, D.M. Markovich**

Formation of disturbance waves at the initial area of annular-dispersed flow ..... 17

**E.E. Kitanina, E.L. Kitanin, D.A. Bondarenko, P.A. Kravtsov, M.M. Peganova, S.G. Stepanov, V.L. Zherebzov**

Experimental study and empirical prediction of fuel flow parameters under air evolution conditions ..... 19

**T. Chevalier J. Koivisto, N. Shmakova, M.J. Alava, A. Puisto, C. Raufaste and S. Santucci**

Foam flows in model fracture ..... 21

**Li Liu, Bofeng Bai and Liang Zhao**

A model for gas-liquid swirling separation efficiency and its application ..... 23

#### *Session – 3: Experiments in space – 2*

**Michael Gibbons, Maxime Rouzes, Giacomo Saccone, Seamus O’Shaughnessy, Paolo Di Marco and Anthony Robinson**

Experimental determination of local heat flux during droplet evaporation in microgravity ..... 25

<b>Balázs Tóth, Hans Ranebo, Luciana Montrone, Guan-Lu Zhang, Liesbeth De Smet and Alessandro De Simone</b>	
Future ESA experiments in Two-phase Heat and Mass Transfer Research on-board the International Space Station.....	27
<b>Antoine Philippe, Beghuin Didier, Boussemaere Luc, Ligot Renaud, Roblin Matthieu, Vanhaver Alexandre and Garin Yves</b>	
Real-time measurement of the shape of a 2d liquid surface .....	29
<b>Bin Liu, Yonghai Zhang, Jianfu Zhao, Jinjia Wei, Xin Kong, Zhizhu Cao and Yueping Deng</b>	
Experimental Study of Subcooled Flow Boiling Heat Transfer on Micro-pin-finned Surfaces in Short-Term Microgravity .....	31
<b>Mikhail Ryabov, Oleg Gobysov, Konstantin Inzhevatkin and Artur Bilsky</b>	
Experimental investigation of submillimeter size droplet disruption in supersonic flow .....	33
<b>Dmitry Zaitsev, Dmitry Kirichenko, Vladimir Ajaev and Oleg Kabov</b>	
Levitation and self-organization of liquid microdroplets over dry heated substrates .....	35
<b>Li Zhang, You-Rong Li, Li-Na Liu and Chun-Mei Wu</b>	
Three-dimensional Numerical Simulation of Thermocapillary Convection of Low Prandtl Number Fluid in a Deep Annular Pool with Surface Heat Dissipation.....	36
<b>Evgeniy Baranov, Sergey Khmel, Alexandr Zamchiy and Evgeniy Shatskiy</b>	
Synthesis of silicon oxide micropores on the copper substrate with SiO <sub>2</sub> interlayer .....	38
<b>Ilya Shefer</b>	
Dependence of the critical characteristics of the stability of the evaporating liquid flow on the system geometry .....	40
<b>Boris Pokusaev, Sergey Karlov, Andrey Vyazmin, Dmitry Nekrasov, Nikolay Zakharov, Vyacheslav Reznik, Dmitry Khramtsov and Dmitry Skladnev</b>	
Structure of gels layers with cells.....	42
<b>Natalia Savchenkova and Artem Manukov</b>	
Thermal control system of the heat generating equipment using the two-phase circuit .....	44
<b>Yu.O. Kabova, V.V. Kuznetsov and O.A Kabov</b>	
Cooling of a microchannel with a thin evaporating liquid film sheared by dry gas .....	46
<b>V.V. Zamaschikov and E.A. Chinnov</b>	
Features of liquid fuel burning in a narrow channel .....	48
<b>J. Cook, O. Arjmandy Tash, A. Trybala and V. Starov</b>	
Foam drying under microgravity conditions.....	50
<b><i>Session – 4: Films, thermocapillarity</i></b>	
<b>Luis A. Dávalos-Orozco</b>	
Thermocapillary stability of a thin film coating a cylinder with a thick wall with finite thermal conductivity in the absence of gravity.....	51
<b>Xue Chen, Rong Liu and Zijing Ding</b>	
Thermocapillary effect on the dynamics of an exterior coating film flow down a fibre subject to an axial temperature gradient.....	53
<b>S.P.Aktershev and E.A.Chinnov</b>	
Thermocapillary structures in a heated liquid film .....	55

<b>Andrey Chernyavskiy and Aleksandr Pavlenko</b>	
Numerical simulation of heat transfer at unsteady heat generation in falling wavy liquid films.....	57
<b>Sergey Semenov, Renaud Denoyel, Jean-François Haquet, Pascal Piluso and Mickaël Antoni</b>	
Two-dimensional numerical simulations of the hydrodynamic behaviour of a molten metal-gas-oxide model system.....	59
<b>V.V. Cheverda and O.A. Kabov</b>	
Stable liquid film flow during changeable gravity level .....	61
 <b><i>Session – 5: Boiling, Heat Pipes, mini- and microchannels</i></b>	
<b>Zhenhui He</b>	
Development of Mechanically Pumped Two-Phase Loop for Space Applications .....	62
<b>Igor Kozulin and Vladimir Kuznetsov</b>	
Experimental study dynamics of explosion boiling of liquids on the microheater .....	63
<b>Thibaud Solé-Agostinelli, Vincent Ayel, Florent Vigoureux, Cyril Romestant, Yves Bertin and Marco Marengo</b>	
Thermo-hydraulic characterization of semi-transparent Flat-Plate Pulsating Heat Pipes in variable gravity regimes .....	65
<b>Fedor Ronshin, Vyacheslav Cheverda, Evgeny Chinnov, Yuriy Dementyev and Oleg Kabov</b>	
Experimental characterization of two-phase flow regimes and flow boiling in microchannel.....	67
<b>Nicolas Chauris, Vincent Ayel, Cyril Romestant and Yves Bertin</b>	
Pulsating heat pipe enhancement performance using an electrohydrodynamic pump .....	69
<b>German Bartkus and Vladimir Kuznetsov</b>	
Experimental study of the local characteristics of gas-liquid flow in a rectangular microchannel.....	71
<b>Fang Ye, Xuan Liu, Jian Fu Zhao, Hang Guo and Chong Fang Ma</b>	
Gravitational Effect on Performance of a Polymer Electrolyte Fuel Cell with Vertical Channels.....	73
<b>Dang Minh Nguyen, Fenfang Li and Claus-Dieter Ohl</b>	
Oscillate Boiling with Microheaters.....	75
 <b><i>Session – 6: Condensation, porous media</i></b>	
<b>Leigang Zhang, Juan Shi and Zhenqian Chen</b>	
Condensation of steam on elliptic pin–fin plates .....	77
<b>Yong Li, Jinshi Wang, Kai Xia, Nana Chen and Junjie Yan</b>	
Research on droplets growth of Marangoni condensation during the time-series process .....	79
<b>Igor Marchuk, Yuriy Lyulin and Artem Barskii</b>	
Film Wise Vapor Condensation in Channels and on Curved Surfaces .....	81
<b>Konstantin Goncharov and Vasily Buz</b>	
Modeling of film condensation when the significant influence of surface tension forces.....	82
<b>Alexey Polikarpov and Irina Graur</b>	
Evaporation and condensation of rarefied gas between two parallel condensed phases .....	84
<b>Filippo Pagnoni, Vincent Ayel and Yves Bertin</b>	
Effects of Loop Heat Pipe condenser design on the overall thermal performance .....	86
<b>Kristina Tolmacheva, Sergei Boronin and Andrei Osiptsov</b>	
Multi-fluid modelling of suspension filtration in a porous medium: particle trapping and mobilization, permeability damage and recovery.....	88

<b>Marco Azzolin, Stefano Bortolin and Davide Del Col</b>	
E Experiments and modelling on flow pattern and heat transfer during condensation in a 3 mm channel .....	90
<b>Yury Maydanik, Vladimir Pastukhov and Mariya Chernysheva</b>	
Loop Heat Pipes – Highly Efficient Heat Transfer Devices for Electronics Cooling.....	92
 <i>Session – 7: Invited presentations from Space Agencies</i>	
<b>Rui Ma, Yu-ting Wu, Qiang-yu Wen, Chun-xu Du, Xia Chen, De-lou Zhang and Chong-fang Ma</b>	
Effect of Gravitational Acceleration on the Distribution of Oil Phase .....	93
<b>Ruquan Liang and Song Xiao</b>	
Thermocapillary convection of high Prandtl number fluids .....	95
<b>Tian-Shi Wang, Wan-Yuan Shi, Yi-Wei Jia and Ji-Long Zhu</b>	
Marangoni convection instability induced by evaporation in a sessile droplet of silicone oil on heated substrate.....	97
<b>Zhen-Dong Li, Liang Zhang, Ke Wu, Jian-Fu Zhao, Hui-Xiong Li and Kai Li</b>	
Numerical Simulation of Gravity Influence on Single Bubble Pool Boiling Heat Transfer.....	99
<b>Vladimir Shelukhin</b>	
Two-phase granular fluids.....	101
<b>V.N. Yarygin, Yu.I. Gerasimov, A.N. Krylov, V.G. Prikhodko, A.Yu. Skorovarov and I.V. Yarygin</b>	
Model and on-orbit study of the International space station contamination processes by jets of its orientation thrusters .....	103
<b>E.A. Chinnov, E. N. Shatskiy, S. Ya. Khmel, E. A. Baranov, A.O. Zamchiy, V. V. Semionov and O.A. Kabov</b>	
Enhancement of heat transfer at pool boiling on surfaces with silicon oxide nanowires .....	104
<b>Serafim Spesivtsev, Yuriy Lyulin, Igor Marchuk and Oleg Kabov</b>	
Evolution of the deformation profile of a thin liquid layer when heated from a localized hot spot .....	105
<b>Ekaterina Kirichenko, Alexey Safonov, Veronica Sulyaeva and Nikolay Timoshenko</b>	
The influence of substrate temperature on structure and wettability properties of fluoropolymer coatings by Hot Wire CVD.....	107
<b>Igor Poletaev, Mikhail Timoshevskiy, Konstantin Pervunin and Mikhail Tokarev</b>	
Bubble Identification for Gas-liquid Two-phase Flows Using Artificial Neural Networks .....	109
<b>Varvara Gordeeva and Andrey Lyushnin</b>	
Modelling of thin evaporating film of polar liquid with a surfactant adsorbed on the interfaces.....	111
<b>Vitaly Demin, Alexey Mizev and Maxim Petukhov</b>	
Division of binary metal melts in a thin capillary .....	113
 <i>Session – 8: Drops, wetting, contact line - 1</i>	
<b>Shen Lili, Wu Yuting, Wang Wei and Ma Chongfang</b>	
Numerical study on two-phase flow in leakage path clearance of single screw expanders .....	115
<b>Liang-ming Pan, Run-gang Yan, Hui He and Hao-jie Huang</b>	
Frequency domain analysis of pressure drop characteristics in parallel multiple microchannels.....	117
<b>Benjamin Franz and Peter Stephan</b>	
Numerical Simulation of nucleate boiling in microgravity under the influence of a shear flow .....	119

<b>Oleg Yevdokimov, Shota Piralishvili, Sergey Veretennikov and Alexandr Elkes</b> Cleaning injectors with dual orifice nozzles for aviation gas turbines using vortex ejector: experimental research.....	121
<b>D.S. Klyuev and N.A. Ivanova</b> Laser-induced thermocapillary instabilities in two-layer systems .....	123
<b>Ekaterina Rezanova and Yuriy Lyulin</b> Modeling of the liquid and gas flows with evaporation at interface based on exact solutions .....	125
<b>L.I. Maltsev, Yu.S. Podzharov and O.A. Kabov</b> Modeling dry spots in isothermal liquid films on a horizontal substrate at different gravity .....	127
<b>Ella Barakhovskaia and Igor Marchuk</b> Calculation of the surface tension and its temperature coefficient based on the data on thermocapillary deformations in locally heated horizontal liquid layer.....	129
<b>Ikhtier Umirzakov</b> New correlations between critical parameters of liquid-vapor first-order phase transition .....	131
<b>Oleg Sharypov and Denis Krasinsky</b> Shape of self-sustained evaporation front .....	133
<b>Yu.O. Kabova, V.V. Kuznetsov, V.V. Zamazchshikov, E.A. Chinnov and O.A. Kabov</b> Experimental and theoretical study of the flame propagation mechanism above the surface of the oxidant driven combustible liquid flowing in microchannels .....	134
<b>Konstantin Goncharov</b> Designing and research loop heat pipe for precise thermal control system .....	136
<b>Vladimir Salomatov and Vadim Karelin</b> Study of microwave drying of wet materials based on one-dimensional two-phase model .....	137
 <i>Session – 9: Drops, wetting, contact line – 2</i>	
<b>Chafea Bouchenna, Mebrouk Aitsaada, Salah Chikh and Lounès Tadrist</b> Fluid flow inside and outside an evaporating sessile drop .....	139
<b>Alexey Rednikov, Yannis Tsoumpas, Sam Dehaeck and Pierre Colinet</b> Analysis of contact angles for a perfectly wetting sessile droplet evaporating into air at the evaporation stage .....	141
<b>Nastasia Okulova, Valery Okulov and Rafael Taboryski</b> An interaction of impacting droplets with superhydrophobic coatings .....	143
<b>S. Dehaeck, A.Y. Rednikov, D. Seveno, J.De. Coninck and P. Colinet</b> Spreading dynamics of evaporating and perfectly wetting liquids .....	144
<b>Peter Lebedev-Stepanov, Sergey Efimov and Alexander Kobelev</b> Drying droplet deposited on poor wetting substrate: beyond the lubrication approximation .....	146
<b>Evgeny Ermanyuk and Nikolay Gavrilo</b> Impact of a sphere onto a liquid .....	148
<b>Vladimir Ajaev, Dmitry Zaitsev, Dmitry Kirichenko and Oleg Kabov</b> Investigation of moist air flow near contact line using microdroplets as tracers .....	150
<b>Anton Surtaev, Vladimir Serdyukov, Andrey Chernyavskiy, Denis Kozlov and Dmitry Selishchev</b> Local heat transfer rate in the contact line area beneath vapor bubble at boiling .....	152

<b>Konstantin Kolegov</b> Mathematical modeling of relief glass film formation by evaporative lithography method in combination with IR-heating .....	154
--	-----

***Session – 10: Evaporation, convection, interfaces***

<b>Osamu Kawanami, Shoya Sakoda, Naoto Sasaki, Toshiyuki Furukawa and Kenji Kusunoki</b> Evaporation Local Heat Transfer Coefficients of Refrigerant HFC-245fa in a Plate Heat Exchanger .....	156
<b>Victoria Bekezhanova and Olga Goncharova</b> Exact solution of the 3D problem of evaporative convection .....	158
<b>Elizaveta Gatapova, Ekaterina Korbanova and Oleg Kabov</b> Measurements of the temperature profile near liquid–gas interface during evaporation of different fluids .	160
<b>Li Zhang, You-Rong Li, Ling-Qi Zhou and Chun-Mei Wu</b> Comparision Study on the Calculation Formula of Evaporation Mass Flux through the Plane Vapour-Liquid Interface .....	162
<b>Boris Pokusaev and Dmitry Khrantsov</b> Modelling of liquid evaporation during gel formation.....	164
<b>Yuriy Lyulin, Aleksei Kreta and Oleg Kabov</b> Experimental study of interfacial motion of a horizontal liquid layer evaporating into gas flow .....	166

**2<sup>nd</sup> International School of Young Scientists  
«Interfacial Phenomena and Heat Transfer»**

***Session – 1: Interfacial phenomena in two-phase systems-1***

<b>Varvara Gordeeva and Andrey Lyushnin</b> Modeling of evaporating drop of polar liquid with added surfactant.....	168
<b>Evgeniy N. Shatskiy, Aleksey I. Safonov, and Evgeny A. Chinnov</b> Enhancement of heat transfer at pool boiling on small surfaces with fins and hydrophobic coating .....	169
<b>Maxim Piskunov and Pavel Strizhak</b> An explanation of the mechanism of heterogeneous water droplet boiling and explosive breakup using planar laser-induced fluorescence .....	170
<b>Olga Svetlichnaya and Vyacheslav Cheverda</b> Varieties of the gas driven water rivulet flow regimes in the minichannels .....	171
<b>Xue Chen, Zhiqiang Zhu and Qiusheng Liu</b> The influence of different scale on thermocapillary convection in sessile droplet: experimental study .....	172
<b>E.G. Korbanova and E.Ya. Gatapova</b> Measurements of the evaporation rate upon evaporation of a heated thin layer .....	173
<b>Mikhail Moiseev and Maxim Shugaev</b> Lattice Boltzmann simulation of bubble growth and departure during pool boiling .....	174
<b>Maxim Pryazhnikov, Andrey Minakov, Dmitriy Guzei and Alexander Lobasov</b> Pool boiling of nanofluids on cylindrical surface .....	175
<b>V.P. Fina, F.V. Ronshin and V.V. Cheverda</b> Features of two-phase flow regimes in a horizontal rectangular microchannel.....	176

<b>S.A. Novichkova, Y.V. Panin, M.A. Balykin and K.N. Korzhov</b> Research and development LHP for Chinese spacecrafts .....	177
<b>Karapet Eloyan and Dmitry Zaitsev</b> Thin film evaporative cooling system for high heat flux applications .....	178
<b>Dmitry Khramtsov and Boris Pokusaev</b> Heat and mass transfer of multiphase flow in channels with irregular geometry .....	179
<b>E.O. Kirichenko and E.Ya. Gatapova</b> The interaction of a impinging water drop with a heated surface .....	180
<b>Andrey Bazhenov, Michael Hrebtov and Boris Ilyushin</b> Numerical simulation of turbulent scalar transport in a confined plane jet .....	181
 <i>Session- 3: High-intensity thermal processes</i>	
<b>Alexey Rebrov</b> Gas jet deposition of diamond from high velocity gas flows .....	182
<b>Aleksandr Shilyuk</b> Passive Highspeed Boundary Layer Transition Control Using an Ultrasonically Absorptive Coating	
<b>Lounès Tadríst</b> Keynote lecture	
 <i>Session- 4: High heat flux applications and two-phase flow</i>	
<b>Oleg Kashinsky and Vyacheslav Randin</b> Hydrodynamics and heat transfer in two-phase gas-liquid flows .....	183
 <i>Session- 5: Interfacial phenomena in two- phase systems-2</i>	
<b>Aleksandra Kravtsova and Yury Meshalkin</b> Investigation of Influence of High Frequency External Perturbation on Flow in a T-shape Microchannel by $\mu$ LIF and $\mu$ PIV metods .....	184
<b>Tatyana Ponomarenko and Vyacheslav Cheverda</b> Experimental investigation of heat transfer in the region of contact line of the liquid rivulet .....	185
<b>Dmitriy Guzei, Andrey Minakov, Maxim Pryazhnikov and Konstantin Meshkov</b> Experimental-calculated study of the forced convection magnetic nanofluids .....	186
<b>Dmitry Kochkin and Dmitry Zaitsev</b> Experimental study of the effect of the substrate roughness on the thermocapillary rupture of a horizontal liquid film .....	187
<b>Vitaliy Semionov, Evgeniy Shatskiy and Evgeny Chinnov</b> Rivulets deflection on surface of heated liquid films .....	188
<b>Igor Anufriev, Sergey Arsenyev, Mikhail Agafontsev, Evgeny Kopyev, Egor Loboda, Evgeniy Shadrin, Oleg Sharypov</b> Thermography of flame during diesel fuel combustion with steam gasification .....	189
<b>A.I. Shatekova and D.V. Zaitsev</b> Interdroplet distance in a structured monolayer of levitating liquid microdroplets .....	190
<b>Dmitriy Kirichenko, Dmitriy Zaitsev and Oleg Kabov</b> Experimental investigation of pikoliter liquid drops evaporation on a heated solid surface .....	191
<b>Aleksandr Borisov, Aleksandr Nazarov, Elena Bochkareva and Nikolay Miskiv</b> Suspended nanofluid droplet evaporation .....	192

<b>Egor Tkachenko, Dmitry Zaitsev and Oleg Kabov</b>	
The effect of dry spots on heat transfer in a locally heated liquid film moving under the action of gas flow in a channel.....	193
<b>Andrey Semenov and Dmitry Zaitsev</b>	
The drop evaporation on a heated substrate with single wall nanotubes coating.....	194
<b>Tatiana Korbanova and Oleg Kabov</b>	
Evaporation of a thin liquid film sheared by gas in a mini/microchannel in the presence of an area of intensive heating moving toward the gas flow .....	195
<b>Run-gang Yan, Liang-ming Pan, Hui He and Hao-jie Huang</b>	
Time domain analysis of pressure drop characteristics in parallel multiple microchannels .....	196
 <i>Session- 6: Microstructured Surfaces and nanofluids</i>	
<b>Alexandr Pavlenko</b>	
Heat Transfer Enhancement at Boiling and Evaporation on Microstructured Surfaces .....	197
<b>Jin-Jia Wei</b>	
Boiling Heat Transfer Enhancement by Using Micro-pin-finned Surfaces and Its Application in a Novel Loop Heat Pipe.....	199
 <i>Session- 7: Waves and bubbles</i>	
<b>Bo-Feng Bai</b>	
Huge Wave and Droplet Entrainment in Churn Flow.....	200
 <b>Vladimir Ajaev</b>	
Models of evaporation near contact lines .....	202
<b>Vladimir S. Berdnikov</b>	
Buoyancy and thermocapillary induced convection and its influence on crystal growth.....	203
<b>Evgeniya Orlova, Dmitry Feoktistov and Anastasya Islamova</b>	
Contact line movement over polished and laser processed metal surfaces.....	205
 <b>Author index</b> .....	206



12-th International Conference  
**«Two-Phase Systems for Space and Ground  
Applications»**

**ABSTRACTS**

## 2-phase Interfacial, Droplet, Bubble Turbulence and Combustion in the Normal and Microgravity Conditions

Son Eduard

Moscow Institute of Physics and Technology, School of Airphysics and Space Technologies,  
Physical Mechanics Department, Laboratory of Hypersonic and Plasma Technologies,  
9 Insititsky Lane Dolgoprudny, Moscow Region, Russia, 141700  
E-mail son.eduard@gmail.com

**"Turbulence Theory in spite of very complicated  
mathematics has very limited Physical Concepts"**  
V.M.Ievlev

### Introduction

Turbulence is very common phenomena and in spite of more than 100 years research still has many conundrums. Physical approach and understading phenomena usually based on simple examples and step by step increase the complexity of models until we reach real phenomena. From this point of view the simplest model is incompressible fluid. Studying turbulence better start from the 1D fluid flows, but due to discontinuity equation  $(\partial u_i) / (\partial x_i) = 0$  it follows  $u_i = 0$  for homogeneous flow. We consider developing turbulence in 2D models, of Homogeneous Isotropic then 3D taking into account consequently Gravity, Vibrations, RTI - Kapitza Pendulum and Multiphase Turbulence in Droplets, Bubbles and Interface Turbulence, Reconnections, Coherent Structures, Intermittance are considered in Multiphase Turbulence,

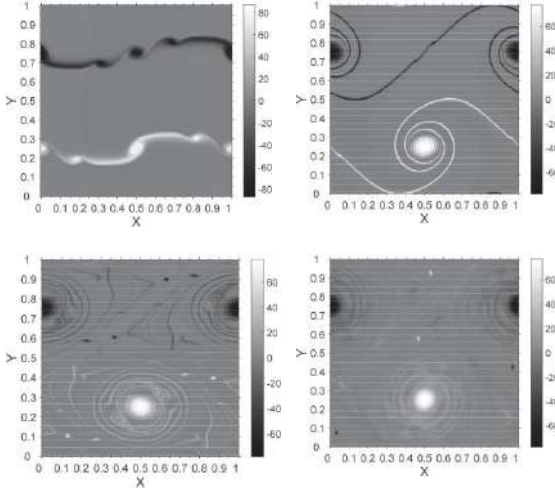


Fig.1. 2D Turbulent Shear Flow Dynamics

### Nature of Hydrodynamics Turbulence

Next simple model is 2D turbulence where the consideration starts from the homogeneous isotropic turbulence and cascade formation from energy to inertial and viscous intervals are considered/ It is found that energy flux in spectral space is forming due to nonlinear terms with essential Obukhov time scales and viscous dissipation play the role of BC for energy spectrum. This result gives the approach to establish specific rotational energy cascade and is generalized to 3D turbulence for different types of

dissipation. As an example we considered the shir

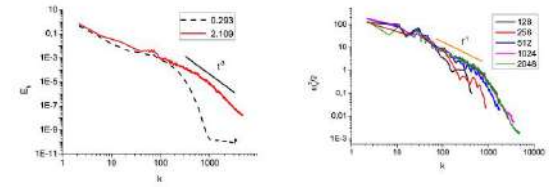


Fig.2. 2D Turbulence Spectra Enstrophy and KE

### General Approach to Multiphase Flows Turbulence

Generalized transport equation with the boundary conditions inserted into the equations

$$\frac{\partial}{\partial t} \varphi_a \rho \xi + \nabla \cdot \varphi_a \rho \xi \mathbf{u} = -\nabla \cdot \varphi_a \mathbf{i}_\xi + \varphi_a Q_{\xi V} + \varphi_a Q_{\xi S} \delta_S + \rho_a \xi (\mathbf{u}_a - \mathbf{D}) \cdot \nabla \varphi_a + \mathbf{i}_\xi \cdot \nabla \varphi_a. \quad (39)$$

For the momentum equation  $\xi = \mathbf{u}$ ,  $\mathbf{i}_\xi = \mathbf{T}$ ,  $Q_{\xi V} = \rho \mathbf{g}$ ,  $Q_{\xi S} = \alpha \kappa \mathbf{n}$  we find out

$$\frac{\partial}{\partial t} \varphi_a \rho \mathbf{u} + \nabla \cdot \varphi_a \rho \mathbf{u} \mathbf{u} = \nabla \cdot \varphi_a \mathbf{T} + \varphi_a \rho \mathbf{g} + \varphi_a \alpha \kappa \mathbf{n} \delta_S + \rho_a \mathbf{u}_a (\mathbf{u}_a - \mathbf{D}) \cdot \nabla \varphi_a - \mathbf{T} \cdot \nabla \varphi_a. \quad (40)$$

For the energy equation  $\xi = e$ ,  $\mathbf{i}_\xi = \mathbf{j}_e$ ,  $Q_{\xi S} = \alpha \kappa \mathbf{D}$ :

$$\frac{\partial}{\partial t} \varphi_a \rho e + \nabla \cdot \varphi_a \rho e \mathbf{u} = -\nabla \cdot \varphi_a \mathbf{j}_e + \varphi_a \alpha \kappa \mathbf{D} \delta_S + \rho_a e_a (\mathbf{u}_a - \mathbf{D}) \cdot \nabla \varphi_a + \mathbf{j}_{ae} \cdot \nabla \varphi_a. \quad (41)$$

### Multiphase Turbulence Moments Equations

In this subsection we will average multi-phase equations (42, 43) with the next averaged variables:

$$\Phi_a = \langle \varphi_a \rangle, \quad \Psi_a = \langle \varphi_a \psi \rangle \quad \text{for any } \psi,$$

$$u_a = \varphi_a v_a, \quad u_a = U_a + u'_a,$$

$$U_a = \langle u_a \rangle = \langle \varphi_a v_a \rangle, \quad u'_a = (\varphi_a v_a)'$$

Below to simplify notations for Stokes stress tensor in some formulas, where evident, we put  $\sigma^S \equiv \sigma$ .

Averaging local phase mass (42) and momentum (43) equations we find out MPRANS (Multi-Phase Reynolds Averaged Navier-Stokes) equations for multi-phase flow.

$$\frac{\partial \Phi_a}{\partial t} + \nabla \cdot U_a = 0, \quad (51)$$

$$\rho_a \left( \frac{\partial U_a}{\partial t} + \nabla \cdot U_a U_a \right) = -\nabla \langle \varphi_a p \rangle + \nabla \cdot \langle \varphi_a \sigma \rangle - \nabla \cdot \rho \langle u' u' \rangle + \varphi_a \rho g + \langle \varphi_a \alpha \kappa \nabla \varphi_a \rangle + \langle p \nabla \varphi_a \rangle - \langle \sigma \cdot \nabla \varphi_a \rangle,$$

Additional terms represents corrections to interfacial pressure and surface tension:

$$\Delta F_a^{pi} = \langle (p - p_a^i) \nabla \varphi_a \rangle \neq 0, \quad (55)$$

$$\Delta F_a^{ci} = \frac{\alpha}{2} \langle (\kappa - \kappa_a^i) \nabla \varphi_a \rangle \neq 0. \quad (56)$$

Reynolds stresses in the used variables are

$$\sigma_a^R = -\rho \langle u' u' \rangle. \quad (57)$$

Rewrite the equation (52) in the form

$$\rho_a \left( \frac{\partial U_a}{\partial t} + \nabla \cdot U_a U_a \right) = -\nabla p_a + \nabla \cdot (\sigma_a^S + \sigma_a^R) + \Phi_a \rho g + m_a,$$

where  $m_a$  is the phase momentum transfer force defined

$$m_a = \left( p_a^i + \frac{\alpha}{2} \kappa_a^i \right) \nabla \Phi_a - \sigma_a^i \cdot \nabla \Phi_a + \Delta F_a^{ci} + \Delta F_a^{pi}, \quad (59)$$

Finally the full set of equations for multi-phase flow consist of mass and momentum equations for each phase (51), (58) and the equation of full mass conservation which follows from the averaging the equation (36)

$$\sum_a \Phi_a = 1. \quad (60)$$

This set of equations slightly different from Drew [26] equations and more convenient for computer simulation.

### Closures

This filtering process generates fewer equations than unknowns, and so further constitutive relations must be provided by  $m_a$  - forces due to a) viscous drag, b) wake and boundary layer formation, c) virtual mass and lift effects.  $S_a$  - subfilter length intraphasic stress terms should include a) dissipation of energy from resolved to unresolved scales (eddy viscosity model), b) back-scatter from unresolved to resolved scales c) Droplet induced turbulence, d) effect of stratification and buoyancy, e) expressions the  $p_a$ ,  $\kappa_a$  and interfacial pressure and curvature  $p_a^i$ ,  $\kappa_a^i$ .

As the first approximation we can use

$$p_a = \Phi_a p, \quad (65)$$

$$m_a = 0 \quad \{ p_a^i = 0, \quad \kappa_a^i = 0, \quad \sigma_a^i = 0, \quad \Delta F_a^{ci} = 0, \quad \Delta F_a^{pi} = 0 \} \quad (66)$$

Below we will discuss the closure for interfacial terms in more details.

We use eddy viscosity ideas to model the stress tensor  $\sigma_a$

$$\sigma_a = 2\rho_a (\Phi_a \nu_a^m + \nu_a^t) S_a, \quad (67)$$

where

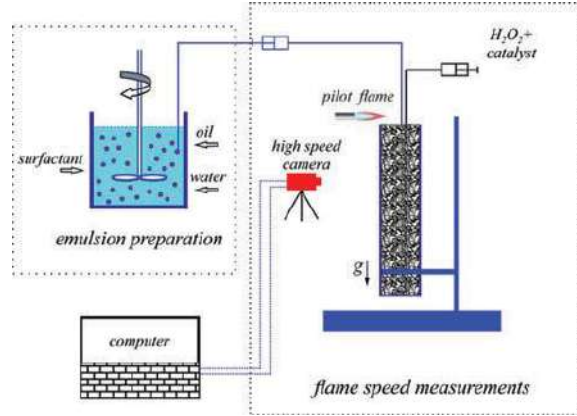
$$S_a = \frac{1}{2} [(\nabla \mathbf{u}_a) + (\nabla \mathbf{u}_a)^T] \quad (68)$$

Here  $\nu_a^m$  and  $\nu_a^t$  are the molecular and turbulent viscosities of phase  $a$ . Smagorinsky type models, see [66] for example, relate  $\nu_a^t$  to the second invariant of  $S_a$ , the spatial filter scale  $L$  and grid-size  $\Delta x$ . With  $L = \Delta x$

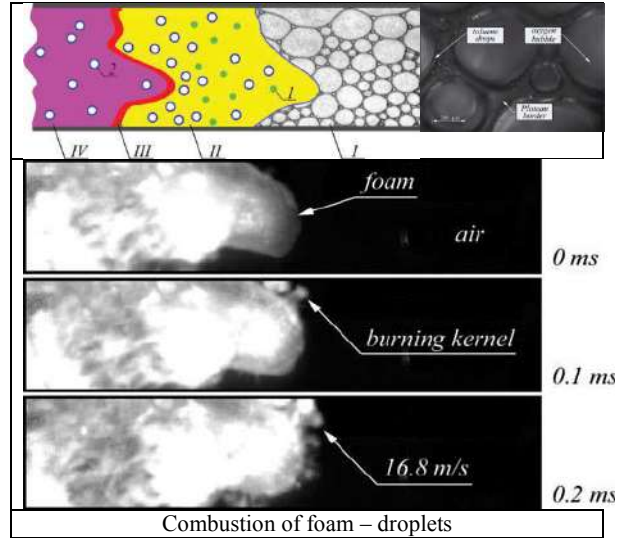
$$\nu_a^t = C_s^2 \Delta x^2 [S_a : S_a]^{1/2} \quad (69)$$

and  $C_s$  is the Smagorinsky constant ( $C_s \approx 0.1 - 0.2$ ).

### Multiphase scales



### Inhomogeneous Interfacial Turbulence



### References

1. Yuri Kulikov, Eduard Son. CABARET scheme implementation for free shear layer modeling. Computer Simulations and Modeling. Vol. 8 No. 1 P. 1-26 (2017)
2. Boris Kichatov, Alexey Korshunov, Konstantin Son, Eduard Son. Combustion and Flame 172. 162-172 (2016)
3. Boris Kichatov, Alexey Korshunov, Alexey Kiverin, and Eduard Son. Methods for Regulation of Flame Speed in the Foamed Emulsion. Combustion Science and Technology <https://doi.org/10.1080/00102202.2017.1361941> (2017).

## Heat transfer and CHF in a shear-driven liquid film under local heating: preparation of space experiment on ISS

O.A. Kabov<sup>1,2</sup>, V.V. Cheverda<sup>1,2</sup>, D.V. Zaitsev<sup>1,2</sup>, Yu.O. Kabova<sup>1</sup>

1 - Kutateladze Institute of Thermophysics SB RAS, Novosibirsk 630090, Russia

2 - Novosibirsk State University, Novosibirsk 630090, Russia

E-mail: kabov@itp.nsc.ru

The fast development in semiconductor technology is leading to ever higher chip power dissipation and heat fluxes. The authors propose a novel method of effective cooling, in which heat removal is due to intensive evaporation of a thin liquid film, moving in a flat micro-/minichannel under the action of gas or vapor flow. This method is a promising solution for on-ground and space applications.

In this talk we report recent results of systematic theoretical and experimental studies which have been carried out in the framework of preparation of the experiments on-board the International Space Station. The goal of the experiments is to study shear driven liquid film flow in a minichannel on the substrate with different boundary conditions during microgravity: 1) Constant substrate temperature - the main goal is to study dynamics and wave formation on liquid film interface; 2) Local small heaters (10x10 mm, 2x2 mm) are designed to study crisis phenomena in liquid film; 3) Local small heater with microgrooves (10x10 mm) will be used to study mechanisms of heat transfer enhancement; 4) Medium heater (20x2 mm) will be used to study thermocapillary deformations on a liquid film. These results will be used to create prototype of highly efficient cooling system for microgravity conditions.

3D nonstationary model of co-current flow of liquid-vapor system, which includes the simulation in both liquid and vapor phases as well as the film thickness, temperature distribution and pressure has been developed. The liquid moving under action of the vapor flow in a microchannel is locally heated from the bottom surface and evaporates at the liquid-vapor interface. For the deformable vapor-liquid interface, it is assumed that the amount of vaporized matter per unit is much less than the flow rate of the forced vapor flows at the same time. Major factors affecting the temperature distribution in the liquid and the vapor phases are as follows: transfer of heat by liquid and vapor flows, heat losses due to evaporation, thermal conductivity in layers, vapor recoil and temperature dependence of surface tension and liquid viscosity. These factors significantly affect each other and, by turn, are heavily dependent on the resulting temperature distribution. The important feature of this problem statement is the fact that in each time moment the vapor pressure must fit the equilibrium pressure, which must correspond to the calculated temperature of the free interface as well. Pressure gradients in the vapor phase will be significant in calculations, that will lead to the changes in the pattern and correspondingly to the changes in the temperature distribution. Marangoni effect is taken into account, but here this effect is less significant than in the works with moving inert gas flow (Kabova et al., 2014). Condition  $T = T_g$  is a

condition of a lack of temperature jump at the free interface, it is equivalent to the fact that we remain in equilibrium thermodynamics.  $T_g$  on the vapor-liquid interface is unknown and it should be determined in the process of solving a problem.

The transport processes in liquid film and in vapor are described by the Navier-Stokes, continuity and energy equations in liquid and vapor phases. The initial film thickness and velocity fields in the liquid and vapor phases are determined from the exact solution of the problem of isothermal laminar co-current flow in the channel with straight streamlines flow (Kabova et al., 2014). The upper wall is assumed to be adiabatic and impermeable. At the bottom wall no slip condition and thermal boundary conditions are posed. At the vapor-liquid interface the condition of continuity of the temperature and the tangential components of the liquid and vapor velocity vectors, the mass conservation condition, the dynamic condition with the term expressing the mechanical effect of the evaporated matter on the liquid, the thermal boundary condition and condition of local thermodynamic equilibrium. We employ the lubrication theory to derive reduced set of equations, so we assume that the characteristic film thickness and the characteristic film thickness variation are much smaller than the characteristic length scale of the film in streamwise and spanwise directions. Numerical solution of the problem is implemented by the finite difference method using the grid approximation. The alternating directions implicit (ADI) method is used to solve the system of grid equations with boundary conditions and to solve the problem on each fractional grid step the Thomas algorithm is used.

The coupled two-phase problem is simulated and the analysis of the liquid film thermocapillary deformations and evaporation versus the main characteristics of the problem has been performed. As an example one can see the ratio of heater length and width affects significantly the intensity of liquid evaporation (Fig. 1). Calculations are performed for water and water vapor, channel height is 250  $\mu\text{m}$ . In all calculations, the heater length in spanwise direction is assumed constant and equal to 0.6 cm. The initial temperature is 40°C and the temperature at the heating surface is equal to 45 °C. The Reynolds numbers of liquid and vapor are, respectively,  $Re = 5$  and  $Re_g = 1$  (here the initial film thickness is  $H_0 = 82.6 \mu\text{m}$ ). The initial average vapor pressure  $p_g = 7376 \text{ Pa}$ , and the average saturated vapor density  $\rho_g = 0.051 \text{ kg/m}^3$  which corresponds to the initial temperature  $T_0=40^\circ\text{C}$ . According to Fig. 1, evaporation is more intensive at relatively low heating for the more extended in streamwise direction heaters. It becomes more intensive due to an increase in the heating area along the liquid flow and significant heat dissipation in direction (y).

This dependence is linear.

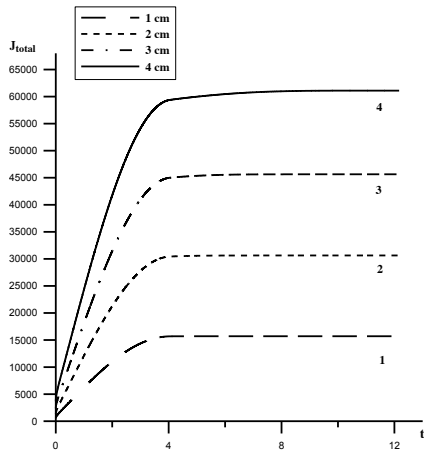


**Figure 1:** Dimensionless total (from the whole area of calculations) evaporation rate  $J_{total}$  vs. time.  $1 \times 0.6$  cm (1),  $2 \times 0.6$  cm (2),  $3 \times 0.6$  cm (3),  $4 \times 0.6$  cm (4).

The flow of liquid rivulet under shear stress of gas in a channel has been investigated under normal, hyper and micro-gravity in the ESA parabolic flight campaign. It was found that under microgravity the rivulet is wavier than during normal and hyper-gravity. The width of rivulet was measured during different level of gravity (Fig. 2). One can see that with gravity level increasing the rivulet width increases.

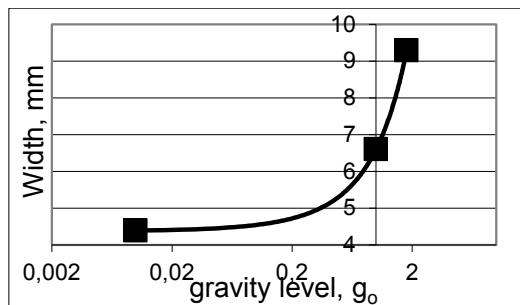


**Figure 2:** The rivulet width versus gravity level,  $Re_g=278$ ,  $Re_l=30.8$ ,  $T_{substrate}=30^\circ$  C.

Systematic experimental studies of the flow and destruction of a water film, shear-driven in the channel, under heating from a local heat source with size of  $1 \times 1$  cm<sup>2</sup> has been performed in terrestrial conditions. The influence of liquid and gas flow rates, the channel height (0.2–2.0 mm) and the angle of channel inclination on heat transfer and critical heat flux have been investigated. With the help of high-speed imaging it was found that the maximum intensity of heat removal from the heater is achieved in the mode, when the film flow continuity is broken, and the heater is covered with small (of about 100 microns) dry spots with the lifetime of about 1/100 – 1/1000 s; at that the number of spots that exist simultaneously on one square centimeter of the surface can reach several hundreds.

Experiments have resulted in the values of heat flux and heat transfer coefficient, which are a record for a thin liquid film ( $1200$  W/cm<sup>2</sup> and  $300\,000$  W/m<sup>2</sup>K, respectively). The values of the critical heat flux are by an order higher than the corresponding values in falling water films. Figure 3 shows comparison of CHF in the locally heated shear-driven liquid film with CHF for channel flow boiling obtained on the same test section. Also shown are data from the literature for flow boiling in minichannels (uniform heating) and microchannels. It is seen that use of shear-driven liquid film allows to reach values of CHF several times higher than CHF for flow boiling in the same channel and an order of magnitude higher than CHF for boiling in mini-/microchannels under uniform heating for the same fluid flow rates, but different length of the heating surface. The CHF values reached are close to the CHF for full evaporation of liquid. This confirms the prospects of using thin liquid films, moving under the influence of the gas flow friction in modern systems of equipment cooling with high local heat release.

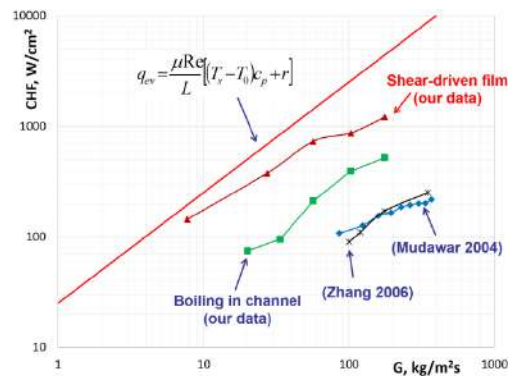


**Figure 3:** Comparison of the dependence of the critical heat flux on the water mass flow rate for: locally heated shear-driven liquid film (our data), flow boiling in a mini-channel under local heating (our data on the same test section), flow boiling in a minichannel under uniform heating (Zhang et al. 2006), boiling in microchannels (Mudawar et al. 2004). Solid line is calculation of CHF for full evaporation of liquid.

### References

Kabova, Yu., Kuznetsov, V.V., Kabov, O., Gravity effect on evaporation and Interfacial deformations in Nonisothermal liquid film moved by a gas flow in a microgap, *Interfacial Phenomena and Heat Transfer*, vol. 2, no. 1, pp. 85-102, 2014.

W. Zhang, T. Hibiki, K. Mishima, Y. Mi. Correlation of critical heat flux for flow boiling of water in mini-channels. *International Journal of Heat and Mass Transfer*, Vol. 49, pp. 1058-1072, 2006.

Issam Mudawar, Weilin Qu. Measurement and correlation of critical heat flux in twophase micro-channel heat sinks. *International Journal of Heat and Mass Transfer*, Vol.47, pp. 2045-2059, 2004.

## Single Bubble Pool Boiling Experiment aboard SJ-10: Bubble Behavior and Local Heat Transfer

Ke Wu<sup>1,2</sup>, Peng Liu<sup>1,2</sup>, Jian-Fu Zhao<sup>1,2,\*</sup>, Hui-Xiong Li<sup>3</sup>, Kai Li<sup>1,2</sup>

<sup>1</sup>CAS Key Laboratory of Microgravity, Institute of Mechanics, Chinese Academy of Sciences. 15 Beisihuan Xilu, Beijing 100190, China

<sup>2</sup>School of Engineering Science, University of Chinese Academy of Sciences. 19A Yuquan Rd, Beijing 100049, China

<sup>3</sup>State Key Laboratory of Multiphase Flow in Power Engineering, Xi'an Jiaotong University. 28 Xianning Xilu, Xi'an 710049, China

\*E-mail address for the corresponding author: jfzhao@imech.ac.cn

SOBER-SJ10 is one of 27 experiments of the program SJ10, proposed to study local convection and heat transfer around an isolated growing vapor bubble during nucleate pool boiling on a well characterized flat surface in microgravity (Hu et al. 2014, Wu et al. 2016). The satellite SJ-10 was successfully launched in April 6, 2016. The result of single bubble pool boiling experiment during space flight will be presented and analyzed in the conference.

The device of SOBER-SJ10 is mainly composed of an air-proof capsule, a boiling chamber, two CCD components, and an electric box. The latter three components are installed inside the air-proof capsule, which is made of aluminium alloy and sealed by a NBR O-ring, in order to obtain a steady pressure condition during the space experiments.

The schematic of the boiling chamber is shown in Fig. 1. Its major components include one liquid chamber, one cover plate with two end caps, a bellows as a pressure regulator, eight film preheaters, one integrated micro heater, one pre-data acquisition board (pre-DAB) and its support, three LED lighting components, two observation components, and one electric connector. The chamber is filled with degassed FC72 as the working fluid. The non-condensable gas concentration is estimated no more than 1300 ppm based on the measured pressure and temperature inside the chamber before launch.

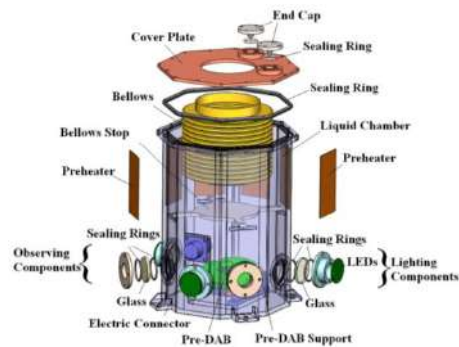


**Figure 1:** Schematic of the boiling chamber

A kind of plastic package, COB (chip on board) encapsulation, is used to encapsulate the integrated micro heater as an independent electronic component. The integrated micro heater is fixed at the center of the pre-DAB, which is installed at the bottom of the liquid chamber with a 15° obliquity angle. Two Keller® PAA-4LD digital absolute pressure sensors are fixed on both sides the integrated micro heater to measure the pressure inside the boiling chamber, as well as the bulk liquid temperature simultaneously.

The integrated micro heater is fabricated by using MEMS technique. The substrate of the integrated micro heater is a 10×10×2 mm<sup>3</sup> quartz glass wafer. The thickness

of 2 mm was determined by a prior numerical study (Zhang et al. 2015, Li et al. 2015). Fig. 2 shows the electro-circuit configurations. The top-side here refers to the one contacting directly with the working fluid.

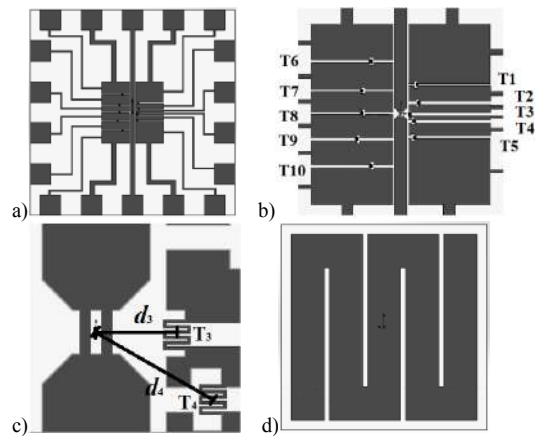


**Figure 2:** Electro-circuit configurations on the top- and back-sides of the substrate of the integrated micro heater

At the center of the top-side, there is a pulse bubble trigger for exciting a bubble nucleus by using the method of local overheating. Around the bubble trigger, there are two groups of four-wire RTDs for local temperature measurements on the heater surface, which are distributed uniformly in the circumferential direction. The distances of these local temperature sensors from the center of the bubble trigger are from 0.15 to 1.0 mm. Each group has 5 series local temperature sensors. The bubble trigger, the sensors and the lead wires are all formed by thin platinum films of about 300 Å in thickness. Furthermore, a 200 Å-thick SiO<sub>2</sub> layer is covered to protect the trigger and the local temperature sensors, as well as to smooth the heating surface. On the back-side of the substrate, a serpentine strip of platinum film of about 5000 Å in thickness acts simultaneously as the main heater to provide the input power for maintaining the boiling process and the temperature sensor to measure the average temperature on the back-side of the substrate.

The in-orbit space experiment lasted for 15 hours, which is divided into 5 stages. The first stage is carried out at ambient temperature without pre-heating process, while the others are carried out at higher temperatures, ranging from 35 °C to 50 °C. In each stage, there are totally 5 runs. The first 4 runs are designed as single bubble boiling mode, in which a bubble nucleus will be excited by the activated pulse bubble trigger and then grow under the action of the main heater on the back-side of the substrate of the integrated micro heater. The heating voltage is kept constant

in each run and increases in successive runs. The last run is designed as normal pool boiling mode, of which the preliminary results obtained from the space flight has been reported by Wu et al. (2016).

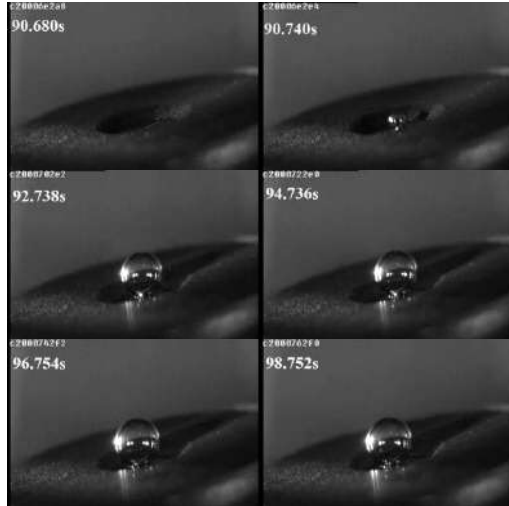


**Figure 4:** Single bubble growth process in SE1/3.2 ( $\Delta T_{sub} = 19.3^\circ\text{C}$ ,  $U_H = 1.5\text{ V}$ )

Fig. 4 shows a typical single bubble growth process in microgravity (SE1/3.2). After the pulse bubble trigger is activated at 90 s, an axisymmetric isolated bubble is observed in the middle of the top surface. The bubble grew both widthwise and lengthwise quickly in the first 2 seconds and then its size remained approximately unchanged in the next 6 seconds. As the bulk liquid was subcooled and the heating surface was superheated, it can be inferred that there might be a balance between the evaporation of the liquid underneath the bubble and condensation of vapor inside the bubble. After 8 s of growth, the bubble started to slide on the surface of the heater, then continually moved and merged with small bubbles appeared on the edge of the heating area.

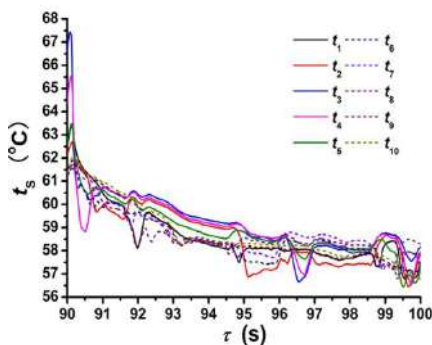


**Figure 5:** Temperature variation on the heating surface underneath the growing bubble in SE1/3.2

Fig.5 shows the temperature variation underneath the growing bubble. The pulse of the bubble trigger generated local overheating at the center of the surface at 90 s, so that the local temperature sensors which were closer to the trigger detected higher temperature raise. Fast and sharp temperature drops were observed from all the 10 local

sensors due to liquid-vapor phase change. Based on these data, the spatiotemporal distribution of local superheat of the heating surface is reconstructed, shown in Fig. 6. After the bubble was excited, the temperature of superheating surface dropped down quickly, about 3 s later it reached to the saturated one outside the bubble base area, while the inner region remained slight superheating. An obvious trajectory with the minimal value of the superheat shows the possible evolution of three-phase contact line. Furthermore, the surface underneath the bubble was re-covered with subcooled liquid film at about 6.5 s after the bubble was excited, which is identical with the observation of bubble sliding on the surface.

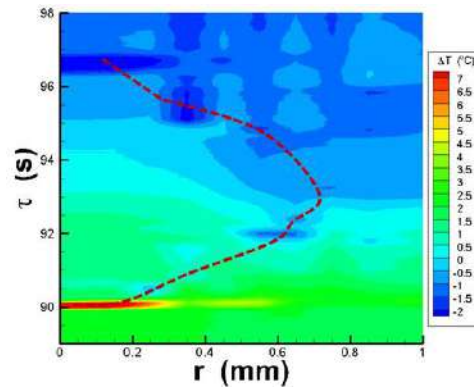


**Figure 6:** Spatiotemporal distribution of local temperature on the heating surface of the integrated micro heater during a single bubble boiling run (SE1/3.2)

**Acknowledgements:** The present study is supported financially by the National Natural Science Foundation of China under the grants of 11372327 and 11402273, and the Strategic Priority Research Program on Space Science/CAS under the grant of XDA04020404.

**References**

Hu W.R., Zhao J.F., Long M. et al., Space program SJ-10 of microgravity research, *Microgravity Sci. Technol.*, Vol. 26 pp. 159–169 (2014)

Li Z.D., Zhang L., Zhao J.F. et al., Numerical simulation of bubble dynamics and heat transfer with transient thermal response of solid wall during pool boiling of FC-72, *Int. J. Heat Mass Transfer*, Vol. 84 pp. 409–418 (2015)

Wu K., Li Z.D., Zhao J.F. et al., Partial nucleate pool boiling at low heat flux: preliminary ground test for SOBER-SJ10, *Microgravity Sci. Technol.*, Vol. 28 pp. 165–178 (2016)

Wu K., Li Z.D., Zhao J.F. et al., Single bubble pool boiling experiment aboard SJ-10: preliminary results, 11<sup>th</sup> Int. Conf. on Two-Phase Sys. For Ground & Space Appl. (ITTW2016), Marseilles, France, Sept. 26-29 (2016)

Zhang L., Li Z.D., Li K. et al., Influence of heater thermal capacity on bubble dynamics and heat transfer in nucleate pool boiling, *Appl. Thermal Eng.*, Vol. 88 pp. 118–126 (2015)

## On cavitation bubble dynamics in variable gravity

Farhat Mohamed<sup>1</sup>, Outi Supponen<sup>1</sup>, Danail Obreschkow<sup>2</sup>

<sup>1</sup>Ecole Polytechnique Fédérale de Lausanne, Laboratory for Hydraulic Machines Avenue de Cour 33 Bis, 1007 Lausanne, Switzerland

<sup>2</sup>University of Western Australia, International Centre for Radio Astronomy Research, 7 Fairway, Crawley, WA 6009, Australia E-mail: mohamed.farhat@epfl.ch

The cavitation phenomenon, which is the formation of vapour cavities within a liquid due to excessive decrease of local pressure, is often associated with efficiency alteration and erosion damage in hydraulic turbines, pumps, marine propellers and space rocket inducers. Nevertheless, owing to the rich physics governing the collapse of individual bubbles, cavitation is nowadays reconsidered for its potential use in a variety of modern applications such as food processing, water treatment, medicine and microfluidics. Since the Rayleigh model (1917), which described the dynamic of an empty spherical bubble implosion, a large amount of research was dedicated to cavitation phenomenon. It is well known that a collapsing bubble may generate strong shockwaves, highspeed micro jetting and luminescence flashes. The magnitude of these processes and the energy released depend on the sphericity of the collapsing bubble, which is mostly conditioned by pressure anisotropy.

We have investigated the dynamics of a single cavitation bubble in still water under different pressure gradients in order to predict key phenomena related to its collapse (Supponen et al. 2017, Supponen et al. 2016, Koukouvinis et al. 2016, Supponen et al. 2015, Obreschkow et al. 2013, Tinguely et al. 2012, Obreschkow\* et al. 2012, Obreschkow et al. 2012, Obreschkow et al. 2011). To this end, we have developed an experimental setup to generate bubbles with a high degree of sphericity, such that gravity is by far the dominant source of symmetry-breaking (Obreschkow et al. 2013). A pulsed laser is focused within still water with the help of a beam expander and an immersed parabolic mirror, which is preferred over the commonly used focusing lens since it produces less aberration and generates a point like hot spot. To eliminate the gravity induced pressure gradient and allow for perfectly spherical bubble growth and collapse, we have conducted our experiments in microgravity conditions in the frame of several ESA (European Space Agency) parabolic flight campaigns. Besides, we have also investigated the influence of neighboring free and solid surfaces on the collapse of cavitation bubbles in normal gravity. In the present paper, we provide an overview of what we have learned from cavitation bubble dynamics in variable gravity.

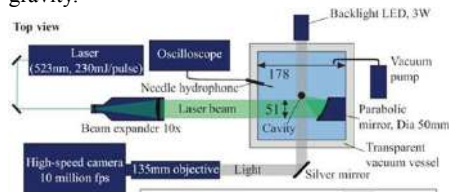


**Figure 1:** Experimental setup for the generation of highly spherical bubbles in microgravity

We have observed the micro-jets induced by collapsing bubbles in various configurations and proposed a unified framework to describe their dynamics with the help of an

anisotropy parameter  $\zeta > 0$ , representing a dimensionless measure of the liquid momentum at the collapse point (Kelvin impulse) (Supponen et al. 2016). This parameter is rigorously defined for various jet drivers, including gravity and nearby boundaries as follows:

$$\begin{aligned} \zeta &= -\rho g R_0 \Delta p^{-1} n && \text{gravitational field,} \\ \zeta &= -0.195 \gamma^2 n && \text{flat rigid surface,} \\ \zeta &= -0.195 \gamma^2 n && \text{flat free surface.} \end{aligned}$$

where  $\gamma$  is the so-called stand-off parameter  $\gamma=h/R_0$ ,  $h$  being the distance from the initial bubble center to the surface and  $R_0$  is the maximum bubble radius.  $\rho$  is the water density and  $\Delta p$  is the driving pressure.

The direct effect of gravity on the collapse and rebound of a ~4 mm maximum radius bubble is illustrated on Figure 2. While in microgravity the bubble collapses and rebounds in almost spherical way, the presence of gravity induces an upward jet, clearly visible during the bubble rebound. We have shown how such a bubble deformation is mainly driven by the gravity induced pressure anisotropy.

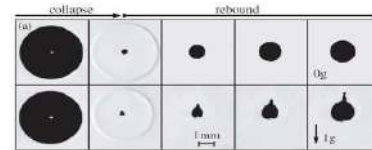


**Figure 2:** Evidence of gravity effects of the collapse of a cavitation bubble ( $R_0 \sim 4$ mm) in 0g (upper) and 1g (lower) (Obreschkow\* et al. 2012)



**Figure 3:** Observations of 3 distinct micro-jet types: (left) weak jet ( $\zeta < 10$ ); (middle) intermediate jet ( $\zeta = 0.01$ ); and (right) strong jet ( $\zeta = 0.64$ ) (Supponen et al. 2016)

We have combined theoretical considerations with hundreds of high-speed visualizations of bubbles collapsing in variable gravity, near a rigid surface and near a free surface and classified the jets into three distinct regimes: weak, intermediate and strong. Weak jets ( $\zeta < 10$ ) remain within the bubble and never pierce it throughout the collapse and rebound. Intermediate jets ( $10 < \zeta < 0.1$ ) pierce the opposite bubble wall at the final stage of the collapse and become visible during the bubble rebound. Strong jets ( $\zeta > 0.1$ ) pierce the bubble early during the collapse. Figure 3 illustrates the 3 types of microjets for a bubble collapsing near a free surface. The dynamics of the jets is analyzed through key observables, such as the jet impact time, jet speed, bubble displacement,

bubble volume at jet impact and vapor-jet volume. We find that, upon normalizing these observables, they all reduce to straightforward functions of  $\zeta$ , which we reproduce numerically using potential flow assumption. An interesting consequence of this result is that a measurement of a single observable, such as the bubble displacement, allows for the estimation of any other parameter, such as the jet speed. Remarkably, the dimensionless parameters of intermediate and weak jets ( $\zeta < 0.1$ ) depend only on  $\zeta$ , not on the jet driver (i.e. gravity or boundaries). In the same regime, the jet parameters are found to be well approximated by power laws of  $\zeta$ , which we explain through analytical arguments (Supponen et al. 2016).

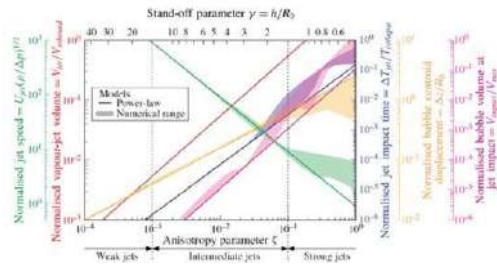


**Figure 4:** Summary of the micro-jet parameters across all regimes. The power laws for the normalised jet impact time, jet speed, bubble centroid displacement, bubble volume at jet impact and vapour-jet volume are plotted vs  $\zeta$  and  $\gamma$ . The shaded areas describe the range spanned by the different jet drivers, calculated numerically (Supponen et al. 2016).

We have observed the structure of shockwaves emitted by a collapsing bubble for various anisotropy parameters in variable gravity and near free and solid surfaces. Interestingly, the same anisotropy parameter,  $\zeta$ , governing the microjets dynamics holds for the shockwaves structure. High speed imaging (up to 10 millions frames/second), reveals how a single shockwave emitted by a spherical collapse ( $\zeta < 10-3$ ) turns into a complex multiple shockwaves system as the bubble is deformed (increasing  $\zeta$ ). In the case of spherical collapse, the shockwave is due to the extreme compression of the non-condensable gas inside the bubble. As the anisotropy parameter is increased beyond 10-3, multiple shockwaves are produced by (i) the jet impact, the collapse of the bubble tip entrained by the jet and the collapse of the torus bubble. Each of these events may generate dominant shockwaves depending on the anisotropy parameter  $\zeta$ .

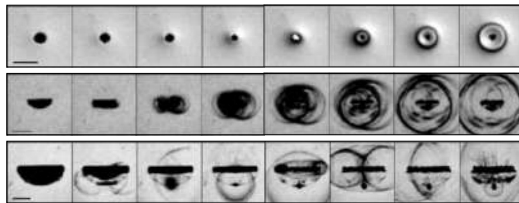


**Figure 5:** Illustration of single and multiple shockwaves emitted by a collapsing bubble at various pressure anisotropies (Supponen et al. 2017)

The research on cavitation bubble dynamics is being pursued with a focus on the luminescence phenomenon, visible on Figure 5 for the spherical collapse ( $\zeta < 10-3$ ). The timeaveraged luminescence spectrum of a single bubble

collapse is detected by a spectrometer (Ocean Optics, exposure 8 ms). The flash emitted by a collapsing bubble is collected using a 1st parabolic mirror inside the reservoir, a UV-window and a 2nd external parabolic mirror, which focuses the light onto the spectrometer (Figure 6). This new setup improves significantly the measurement sensitivity and allows for a

better evaluation of the gas temperature at the final stage of the collapse, assuming black body radiations. We intend to use this improved setup during the upcoming 67th ESA parabolic flight campaign to perform extensive measurements of the luminescence in variable gravity. We will explore a wide parameter space to investigate the relationship between anisotropy parameters and the temperature reached in the bubble center.

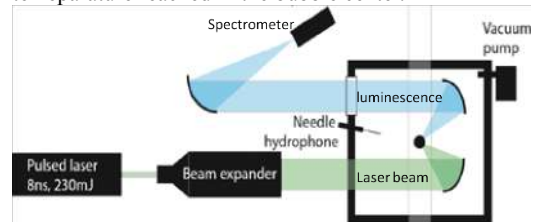


**Figure 6:** Measurement of single cavitation luminescence

**Acknowledgment:** We gratefully acknowledge the support of the Swiss National Science Foundation (Grant No. 513234) and the University of Western Australia Research Collaboration Award. We are also grateful to the European Space Agency (ESA) for hosting our experiment on several parabolic flight campaigns.

## References

- O. Supponen, D. Obreschkow, Ph. Kobel, M. Farhat, under 2nd revision, *Physical Rev. Fluids* (2017)
- O Supponen, D Obreschkow, M Tinguely, P Kobel, N Dorsaz, M Farhat, *Journal of Fluid Mechanics* (2016).
- P. Koukouvinis, M. Gavaises, O. Supponen and M. Farhat., *Physics Of Fluids* (2016).
- O. Supponen, P. Kobel, D. Obreschkow and M. Farhat, *Physics Of Fluids*, Vol. 27, No. 9, p. 091113 (2015).
- D. Obreschkow, M. Tinguely, N. Dorsaz, Ph. Kobel, A. De Bosset, M. Farhat, *Experiments in Fluids* (2013)
- Tinguely M., Obreschkow D., Kobel P., Dorsaz N., De Bosset A., Farhat M, *Physical Review E* (2012)
- Obreschkow D., Bruderer M., Farhat M., *Physical Rev. E*, (2012).
- Obreschkow\* D., Tinguely M., Dorsaz N., Kobel P., De Bosset A., Farhat M., *Physical Review Letters* (2012).
- Obreschkow, D., Dorsaz, N., Kobel, P., De Bosset, A., Tinguely, M., Field, J., Farhat, M., *Physics of Fluids* (2011).

## Comparison of two similar techniques to study flow boiling in normal and microgravity conditions

E. Trejo\*, C. Colin, C. Hammer, J. Kim

Institut de Mécanique des Fluides,  
2 Allée Prof Camille Soula, 31400, Toulouse, France  
University of Maryland, Department of Mechanical Engineering,  
College Park MD 20742, USA  
\*E-mail: etrejope@imft.fr

Applications involving two-phase flows with phase-change, like cooling systems or nuclear reactors, have been the main motivation for the development and understanding of flow boiling. Thermal management is also present in space applications therefore, it is important understand and model two-phase flows in tube in both normal and microgravity conditions. Boiling is a complex phenomenon which combines heat and mass transfers, hydrodynamics and interfacial phenomena. Furthermore, gravity consequently affects the fluid dynamics and may lead to unpredictable performances of thermal management systems.

Microgravity experiments are relevant for industrial applications but also for fundamental research, because these conditions allow putting into light the capillary and viscous effects on the flow dynamics and transfers. The main issue is to be able to characterize and model the flow structure (liquid and vapor phase repartition), the liquid and vapor mean velocities, the pressure drop along the tube and the wall heat transfer coefficient.

This work aims to observe, analyze, and compare data obtained for flow boiling in a circular tube, experimentally in normal and microgravity for an upward flow using the same rig with two different test sections. Both test sections have a 6 mm tubular channel through which liquid refrigerant HFE-7000 or HFE-710 is boiled.

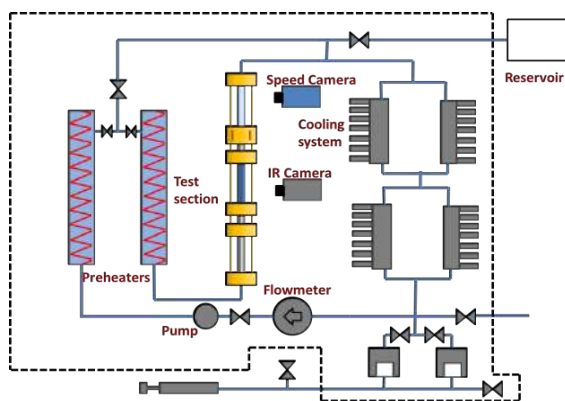


**Figure 1:** Schematic representation of the hydrolique loop.

A two-phase flow loop with a dedicated test section has been designed and built for testing and comparing flow boiling data in normal gravity or under microgravity

conditions. Flow patterns, void fraction, film thickness, wall and interfacial frictions and heat transfer were studied. Figure 2 show the two test sections used for our comparisons, which are the main part of the experiment.

The first measurement technique developed by Narcy et al. (2014), consists of a sapphire tube with an ITO coating of 50  $\mu\text{m}$  allowing the tube to be transparent. The phenomena were observed with a speed camera and the regimes were easily visualized. The tube was heated by joule effect and was tested from 1-4  $\text{W}/\text{cm}^2$  with mass fluxes from 50-400  $\text{kg}/\text{m}^2/\text{s}$ . Temperatures of the liquid at the inlet and outlet of the heated section were measured as well as absolute pressures. Two capacitance probes provide the information to calculate the void fraction. This first technique used HFE-7000 as a working fluid.

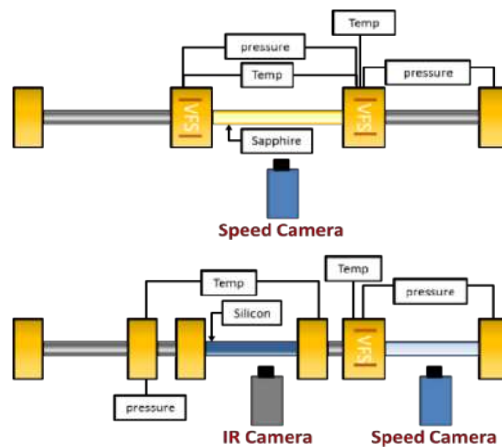


**Figure 2:** Two different test sections used for each technique and its basic elements.

The second method developed by Kim et al. (2012), uses a

doped silicon tube heated by joule effect. The silicon tube is transparent to IR radiations. Its inner wall is covered on its half by a caption tape painted in black. On the outer surface, a black line is painted. The local instantaneous inner and outer wall temperature can be measured thanks to an IR camera and some image/signal processing required to take into account transmittivity, emissivity and reflectivity of the different materials (silicon, tape, glue and black paint). For a better sensitivity of the IR camera HFE-7100 is preferred to HFE-7000 because of its higher boiling temperature

(56°C instead of 34°C at 1 bar). In these experiments, mass fluxes range from 50 to 200 kg/m<sup>2</sup>/s and the heat fluxes from 0.5 to 1.5 W/cm<sup>2</sup>.

Experimental results will be presented for each method for microgravity and normal gravity.

The void fraction  $\alpha$  is measured by a capacitance probe consisting of 2 copper plates of 1 cm<sup>2</sup> located on both sides of the tube. In annular flow, the liquid film thickness  $\delta$  is deduced from the void fraction by geometrical considerations  $\delta = D(1 - \sqrt{\alpha})/2$ , where  $D$  is the tube diameter. The effect of liquid droplet entrainment in the gas core is proved to be negligible and is not considered in the calculation of the liquid film thickness. Figure 3 presents the evolution of the void fraction as a function of the vapor quality for two mass fluxes comparing normal and microgravity conditions. The void fraction is typically smaller in normal gravity than in microgravity conditions, which leads to a higher liquid film thickness in normal gravity.

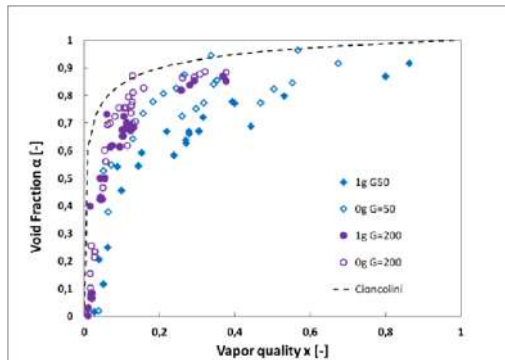


**Figure 3:** Sapphire Tube's void fraction, at the outlet, as a function of the vapor quality during microgravity and normal gravity for two mass fluxes.

Heat transfer coefficients are deduced from the measurements of the mean wall heat flux on the sapphire tube and measurements of the wall temperature at different locations by using PT100 probes. Heat transfer coefficients are plotted versus quality in Figure 4. They increase with quality and with the mass flux. Experimental results are compared with Chen (1966) and Kim and Mudawar (2013) correlations for  $G = 50$  kg/m<sup>2</sup>/s. At low quality smaller than 0.15 in the nucleate boiling regime, HTC is lower than the values predicted by the correlations. It is probably because the surface of the sapphire tube is very smooth and the density of nucleation sites very low compared to classical experiments in metallic tubes. At qualities higher than 0.2, HTC tends to the value predicted by Chen correlation. Heat transfer is controlled by evaporation through the liquid film.

These results will be next compared to microgravity experimental results. Data obtained on the silicon tube with the IR camera are being processed. From previous experiments, HTC is expected to be smaller in microgravity than in normal gravity in the nucleate boiling regime (Ohta & Baba 2013; Baltis *et al.* 2012).

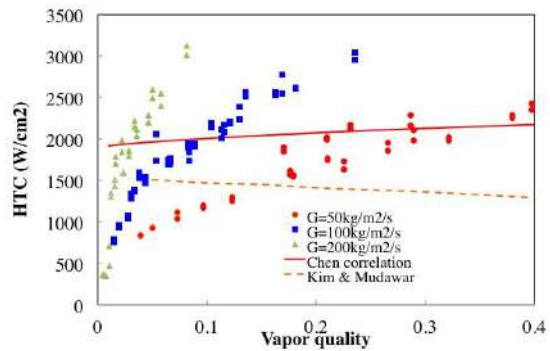


**Figure 4:** Sapphire tube's evolution of HTC with vapor quality for different mass fluxes.

### References

- Narcy M., de Malmazet E., Colin C., Flow boiling in tube under normal gravity and microgravity conditions, *International Journal of Multiphase Flow* Vol. 60, pp. 50-63 (2014)
- Kim T. H., Kommer E., Dessiatoun S., Kim J., Measurements of two-phase flow and heat transfer parameters using infrared thermometry, *International Journal of Multiphase Flow* Vol. 40, pp. 56-67. (2012).
- Chen J., Correlation for boiling heat transfer to saturated fluids in convective flow, *Industrial Engineering Chemistry Process Design and Development*, Vol. 5, pp. 322-339 (1966)
- Kim S.M., Mudawar, I., Universal approach to predicting saturated flow boiling heat transfer in mini/micro-channels – Part II. Two-phase heat transfer coefficient, *International Journal of Heat and Mass Transfer*, Vol. 64, pp. 1239-1256. (2013)
- Ohta, H. and Baba, S., Boiling experiments under microgravity conditions, *Exp. Heat Transfer*, Vol 26, pp. 266–295 (2013).
- Baltis C., Celata G. P., Cumo M., Saraceno L., and Zummo G., Gravity influence on heat transfer rate in flow boiling, *Microgravity Sci. Technol.*, Vol 24, pp. 203–213 (2012).
- Cioncolini A. and Thome J. R. Void fraction prediction in annular two-phase flow, *Int. J. Multiphase Flow*, Vol 43, pp. 72–84, (2012).

## Addition of Data for Pool Boiling of Immiscible Mixtures

Satoshi Okayama, Ren Tianhao, Yasuhisa Shinmoto and Haruhiko Ohta

Dept. Aeronautics and Astronautics, Kyushu University  
744 Motoooka, Nishi-ku, Fukuoka, Japan  
ohta@aero.kyushu-u.ac.jp

Immiscible mixtures have a large potential for high-performance cooling systems applied to semi-conductors with high heat flux density and sometimes with high heat generation area. The increase of CHF is possible simply by the mixing more-volatile component with less volatile one. The decrease of liquid temperature is possible without reduction of system pressure below atmospheric pressure, which eliminates the problem of mechanical toughness and/or thermal contact, and prevents the decrease in CHF. Furthermore, the initiation of boiling is possible at low surface temperature suppressing the overshoot of it, if the boiling system has an appropriate configuration and more-volatile liquid is heated initially. The situation is unavoidable in cooling systems applied to, e.g., automobile inverters. On the other hand, generated bubbles of more-volatile component enhance the heat transfer to less-volatile liquid in the regions of free convection and nucleate boiling by the agitation of temperature field and the formation of liquid film of less-volatile component located between the generated vapor of more-volatile component and the heating surface.

Experiments are performed under pool boiling conditions. The circular flat heating surface is located horizontally in the cylindrical vessel vertically oriented. The heating surface is made of copper with a diameter of 40mm surrounded by a circular thin fin. There is a clearance of annulus between the heating block and the inner wall of the cylindrical boiling vessel which is operated as a reservoir of liquid with higher density. Immiscible liquids are introduced in the boiling vessel, and the height  $H_1$  or  $H_2$  of liquid with higher density before heating is varied as one of important parameters, where more-volatile component is represented by a suffix "1", while less-volatile one is by "2". Figure 1 illustrates the height  $H_1$ . More-volatile liquid could be carried on the heating surface by the disturbance at the liquid-liquid interface even under the condition of  $H_1=0$  after the heating is started.

We already performed the experiments using immiscible mixtures. The mixture of FC72/water (Ohta 2015) is a representative one where the heat transfer characteristics characterized by immiscible mixtures are clearly observed. Also, Novec7100/water (Ohta 2015) and Novec7200/water (Okayama 2016) were tested to change the more-volatile component of FC72. Mixtures of FC72/ethanol (Okayama 2016), FC72/n-propanol (Kita 2014) and FC72/i-propanol (Kita 2014) were tested to change from water to alcohols. In the present experiment, a set of new data for FC72/methanol is clarified for the reduction of surface temperature. In addition, the performance of FC770 and FC3283 is examined by the combinations with water as FC770/water and water/FC3283, where the boiling point of FC3283 is higher than water. Furthermore, the combinations with alcohols as ethanol/FC770, methanol/FC770, ethanol/FC3283, methanol

/FC3283 are tested.

The liquid of one component is compressed excessively by the partial vapor pressure of another component. As a consequence, self-sustained subcooling is imposed to both component liquids. Especially, a large subcooling is expected for the less-volatile liquid as a result of compression by high vapor pressure of more-volatile component. Values of subcooling are listed in Table 1.

Except the case of mixtures using FC770 or FC3283, more-volatile liquids are directly contact the heating surface and/or are accumulated around the heating block at least before heating because of their higher density, while less-volatile liquid contacts the heating surface in the case of mixtures using FC770 or FC3283.

To avoid the superficial underestimation of heat transfer performance by using heat transfer coefficients defined by the subcooled liquid temperature, the method of data plot by heat flux  $q$  versus surface temperature  $T_w$  is adopted here.

Figure 2 shows the result for FC72/methanol, where the reduction of surface temperature is clear by the change of less-volatile component from water [1] to methanol. The value of CHF is increased from  $5.3 \times 10^5 \text{W/m}^2$  for pure methanol to  $8.3 \times 10^5 \text{W/m}^2$  for the mixture  $[H_1/H_2] = [0\text{mm}/100\text{mm}]$ . In the mixtures of FC72 and alcohols, the jump of surface temperature, which does not result in the serious temperature excursion and is referred to as "intermediate heat flux burnout" by the present authors (Ohta 2015), is not observed. The similar results were obtained for FC72/ethanol, FC72/n-propanol and FC72/i-propanol (Okayama 2016, Kita 2014).

Figure 3 shows the data of aqueous mixtures. The heat transfer enhancement is confirmed in these mixtures in the moderate and high heat flux regions. Because data points are located between those of pure more-volatile and pure less-volatile components in all immiscible mixtures tested so far, the effect of thermal properties could influence the enhanced heat transfer. However, as show in Fig. 3(a), the surface temperature for FC770/water [0mm/100mm] is shifted to the left from the levels of surface temperatures for both pure components. The result verifies substantial enhancement of heat transfer to less-volatile liquid by the generation of more-volatile vapor. Two different mechanisms of heat transfer enhancement are possible. One is the agitation of thermal boundary layer by the bubble generation from more-volatile liquid at moderate heat fluxes. The other is the formation of thin liquid layer of less-volatile liquid by the explosive bubble expansion of more-volatile component on the heating surface at high heat fluxes. The situation is clearly explained for water/FC3283, where the data for [100mm/0mm] is located at the left of data for water as shown in Fig. 3(b).

Figure 4 summarizes the results for mixtures of alcohols and FC770 or FC3283. For the mixtures using

FC770, the increment of CHF and the heat transfer enhancement compared to pure FC770 are observed by the addition of alcohols as shown in Figs. 4(a) and (b). It is very interesting that the intermediate heat flux burnout occurs for [100mm/0mm] in ethanol/FC770 and methanol/FC770 resulting in the reduction of surface temperature rather than its increase by the change of liquid contacting the heating surface from FC770 to methanol. In the case of alcohol mixtures using FC3283, CHF values are increased markedly from that of pure FC3283 by the addition of alcohol in a wide range of its concentration except the case of  $H_2=0\text{mm}$  where the surface temperature in addition to CHF almost coincides with that for alcohols.

**Conclusions:**

1. By using alcohol instead of water as a less-volatile component, the surface temperature is reduced increasing the CHF value from pure alcohol (Fig.2).
2. The surface temperature could be reduced from that of more-volatile component in a wide range of heat flux by the addition of less-volatile component (Fig.3).
3. By "intermediate heat flux burnout", the surface temperature could be reduced rather than increased if less-volatile liquid has higher density and its amount is very small (Fig.4(a), (b)).

**References**

Ohta H., Iwata K., Yamamoto D. and Shinmoto Y., "Superior Heat Transfer Characteristics in Boiling of Immiscible Mixtures", *Proc. 26th Int. Symp. Transport Phenomena*, No. 89, (2015)

Okayama S., Iwata K., Shinmoto Y. and Ohta H., "Improvement of Cooling Performance for Electronic Devices by Nucleate Boiling of Immiscible Mixtures ", *J. Physics: Conference Series*, IOP Publishing, Vol. 745, 032073, (2016)

Kita S., Onishi S., Fukuyama Y. and Ohta H., "Improvement of Nucleate Boiling Heat Transfer Characteristics by using Immiscible Mixtures", *Proc. 15th Int. Heat Transfer Conf.*, IHTC15-8941, (2014)

Table 1: Equilibrium temperatures and values of subcooling for immiscible mixtures.

1:More-volatile	2:Less-volatile	$T_c$ [°C]	$\Delta T_{sub,1}$ [K]	$\Delta T_{sub,2}$ [K]
FC72*	Methanol	42.2	13.7	22.5
FC770*	Water	77.7	17.3	22.3
Water	FC3283*	91.0	9.0	37.0
Ethanol	FC770*	66.4	11.9	28.6
Methanol	FC770*	56.8	7.9	38.2
Ethanol	FC3283*	74.5	3.8	53.5
Methanol	FC3283*	62.2	2.5	65.8

\*Higher density

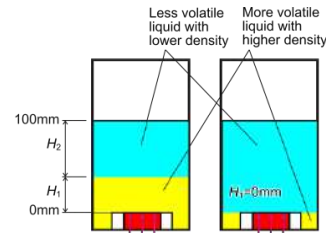


Figure 1: Definition of  $H_1$  in the case of more-volatile liquid with higher density.

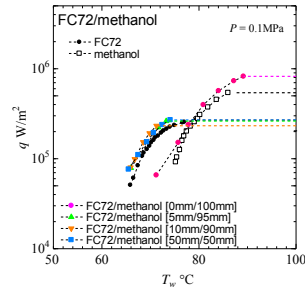


Figure 2: FC72/methanol.

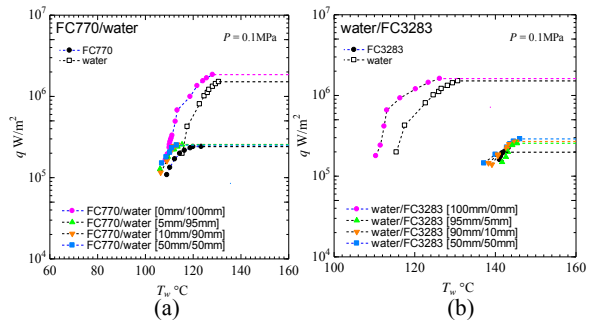


Figure 3: Aqueous mixtures.

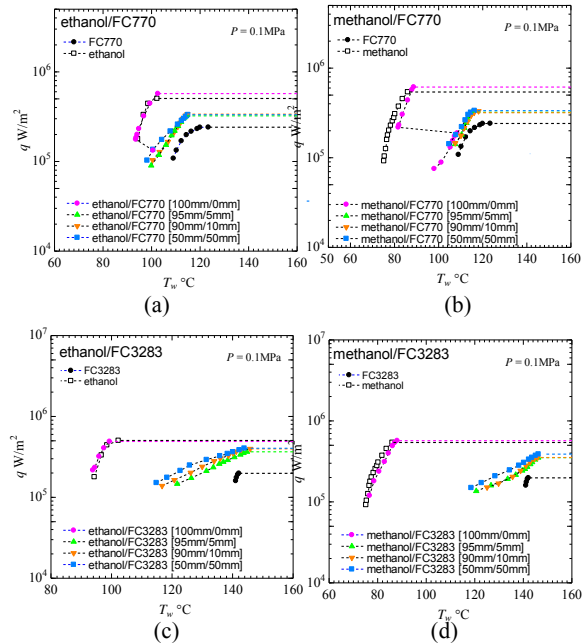


Figure 4: Alcohol and FC770 or FC3283 mixtures.

## Study on the effect of Channel Cross-Sectional Shape on Void Fraction Characteristics of One-Component Vertically Upward Two-Phase Flows

Satoru Miyawaki, Yuma Murata, Ryosuke Ukena, Hitoshi Asano

Department of Mechanical Engineering, Kobe University  
1-1 Rokkodai, Nada, Kobe, 657-8501, Japan  
E-mail: [asano@mech.kobe-u.ac.jp](mailto:asano@mech.kobe-u.ac.jp)

Vapor-liquid two-phase flow dynamics strongly depends on vapor-liquid interface structure. Since gravity, inertia force and surface tension act on vapor-liquid two-phase flows in tubes, the understanding which force is dominant in the flow system is important for system design. Especially, flow characteristics in moderate tube diameters are important for the design of compact heat exchangers and cooling systems, because the effect of surface tension will become larger with decreasing the diameter. When the surface tension effect is large, phase cross-sectional distribution will be strongly affected by surface tension. This means that flow structures in noncircular tube are quite different from those in circular tube.

In this study, experiments on one-component vertically upward two-phase flows in small diameter tube with the hydraulic diameter of 2 mm and various cross-sectional shapes of circular, square, and triangular was conducted. The effect of the channel shape on vapor-liquid interface structure and void fraction was evaluated.

Schematic diagram of experimental setup is shown in Fig. 1. Degassed FC-72 was used as the work fluid. The fluid was supplied to the test section by a gear pump through a volumetric flow meter, pre- and main-heaters. The test section was directly connected to the main-heater of circular stainless steel tube with 2 mm inner diameter, and was vertically placed. The inlet quality was set by the heat input by Joule heating of the main-heater.

The detail of the test section is shown in Fig. 2. Test section is made of transparent acrylic resin. The flow behavior is observed by high speed camera with the frame rate of 1000 fps. Three kinds of cross-sectional shapes were used, circular, square, and triangular. Each channel has the same hydraulic diameter of 2 mm. Void fraction was measured by a capacitance method using a parallel plate-type electrodes. Volumetric average void fraction in the sensing area can be measured from the capacitance,  $C$ , by the following equation.

$$\alpha = (C - C_0) / (C_1 - C_0) \quad (1)$$

where,  $C_0$ ,  $C_1$  is the capacitance for vapor and liquid single phase. The flow structure can be observed from the direction parallel to the electrode plane.

The experiments carried out at the system pressure at about 100 kPa for varied vapor quality with four mass fluxes at 50, 100, 150, 200 kg/(m<sup>2</sup>·s).

Observed flow patterns were classified into bubbly, slug, churn, semi-annular, and annular flows. The churn flow was defined as the flow with intermittent liquid reverse flows. The semi-annular flow was defined as the flow where

gas core formation is imperfect but intermittent liquid reverse flow is not observed.

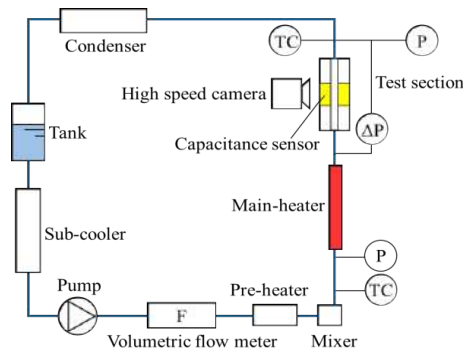


Figure 1: Schematic diagram of experimental setup.

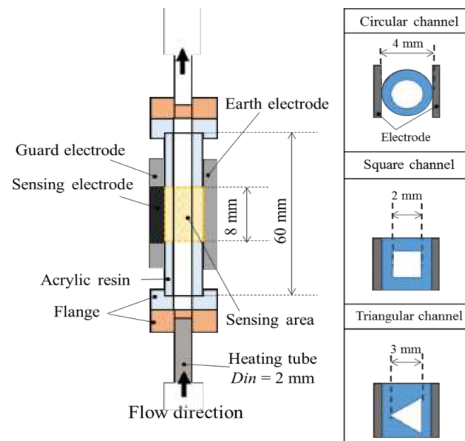
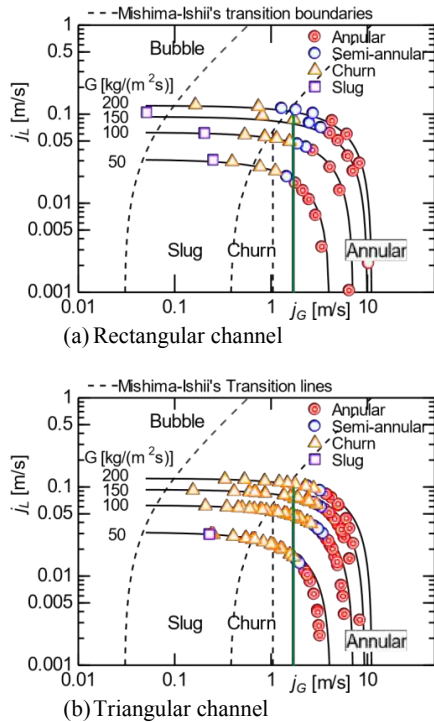


Figure 2: Detail of test section and cross-sectional shapes.

Flow pattern maps for square and triangular channels are shown on gas and liquid volumetric flux diagrams in Fig. 3 (a) and (b). Mishima-Ishii's flow pattern transition boundaries (Mishima 1984) are plotted by dotted lines. Vertical bold solid line shows the flow pattern transition boundary from churn to annular flow for a circular tube with 2 mm diameter given by Gomyo and Asano (2016). They reported that the vapor velocity at the flow pattern transition from churn to annular flow became higher with decreasing tube diameter below 2 mm. Focusing on the transition to annular flow, the value of  $j_G$  for the square channel was almost the same with that for the circular channel. For the triangular channel, the value of  $j_G$  became lower. Since liquid gathered in the corner due to surface tension in the triangular

channel, liquid film thickness became thicker. The thicker liquid film might cause easy formation of intermittent liquid reverse flow due to gravity. On the other hand, for the triangular tube, the area with churn flow spread to the lower  $j_G$ . The reason was on the bubble behavior. Since bubbles in the triangular tube tended to flow along the center axis, void fraction at the center became higher. The behavior might lead to gas core formation. However, under the lower  $j_G$ , interfacial shear stress was not enough to keep the thicker liquid film. Therefore, churn flow was observed in the wider range for the triangular channel.

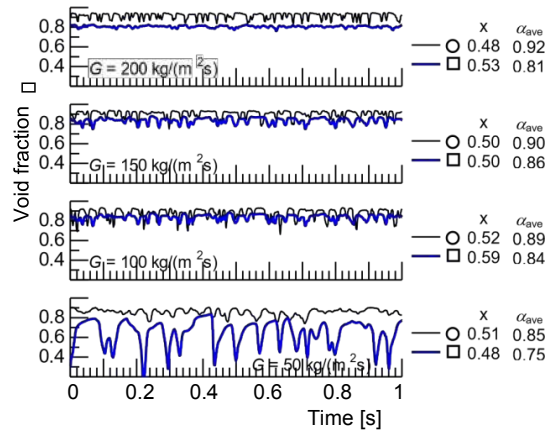


**Figure 3:** Flow pattern map of one-component vertically upward two-phase flows in square and triangular tube.

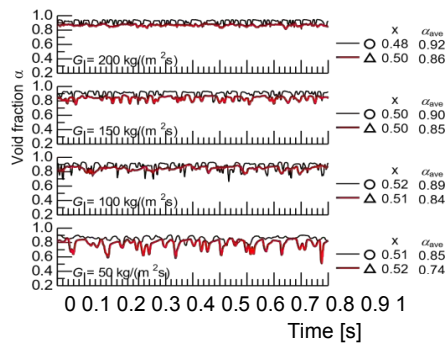
Comparisons in void fraction fluctuations are shown in Fig. 4 (a) and (b). Figure (a) and (b) show the comparison of the square and triangular with the circular channel, respectively. The flow conditions with the vapor quality at about 0.5 were selected. The flow pattern was annular flow. Instantaneous drop of void fraction mean passing of disturbance wave. Different tendency depending on mass flux was observed. For the higher mass flux over  $100 \text{ kg}/(\text{m}^2 \cdot \text{s})$ , average void fraction for noncircular channel became lower, and the passing frequency of disturbance waves became lower. Although lower void fraction means larger velocity difference between gas and liquid, liquid film in the noncircular channels became smoother. The fact might be caused by thicker liquid film thickness in the corners. The interface velocity might be higher in the noncircular channels. So, gas-liquid interface became smoother.

On the other hand, for the lowest mass flux of  $50 \text{ kg}/(\text{m}^2 \cdot \text{s})$ , the magnitude of void fraction fluctuation became

quite larger for the noncircular channel. The thicker liquid film could not be kept by the low gas velocity.



(a) Comparison between the circular and square channel.



(b) Comparison between the circular and triangular channel.

**Figure 4:** Void fraction fluctuation.

Flow pattern transition boundary from churn to annular flow for the square channel was almost the same with the circular tube with the same hydraulic diameter. On the other hand, the gas volumetric flux at the transition for the triangular channel became higher, and the range with churn flow became wider gas volumetric flux. While the void fractions for the noncircular tubes were lower than those for the circular tube, liquid film of annular flow became smoother.

### References

- K. Mishima and M. Ishii, "Flow Regime Transition Criteria for Upward Two-Phase Flow in Vertical Tubes", *Int. J. Heat and Mass Transfer*, Vol. 27, No. 5, pp. 723-737 (1984)
- T. Gomyo and H. Asano, "Void Fraction Characteristics of One-Component Gas-Liquid Two-Phase Flow in Small Diameter Tubes", *Interfacial Phenomena and Heat Transfer*, Vol. 4, No. 1, pp. 1-18 (2016)

## Experimental Investigation of Two-phase Flow in Cathodic Flow Field of a Proton Exchange Membrane Fuel Cell in Short-term Microgravity

Hang Guo<sup>1,\*</sup>, Xuan Liu<sup>1</sup>, Jian Fu Zhao<sup>2,3</sup>, Fang Ye<sup>1</sup>, Chong Fang Ma<sup>1</sup>

<sup>1</sup> MOE Key Laboratory of Enhanced Heat Transfer and Energy Conservation, and Beijing Key Laboratory of Heat Transfer and Energy Conversion, College of Environmental and Energy Engineering, Beijing University of Technology, Beijing 100124, China

<sup>2</sup> Key Laboratory of Microgravity, Institute of Mechanics, Chinese Academy of Sciences, Beijing 100190, China

<sup>3</sup> School of Engineering Science, University of Chinese Academy of Sciences, Beijing 100049, China

\* Corresponding author, E-mail: hangguo@sohu.com, Tel.: +86-10-67391612 ext. 8311

Proton Exchange Membrane Fuel Cells (PEMFCs) are the prospective devices used to supply energy for space engineer with short term mission due to its unique advantages, like high energy conversion efficiency, zero emission, low temperature, regenerative operation and so on. It is well known that most of space devices are working at microgravitational or supergravitational environment; therefore it is necessary to investigate PEMFCs performance at different gravitational levels.

In this paper, different gravitational environment was achieved in a drop tower at a height of 83m, the overall experimental system was installed into a drop capsule, and a recovery string bag was mounted at a height of 22m from the ground to recover the drop capsule. The performance and two phase flow behaviors of PEMFC with horizontal channels at different gravity levels with oxygen volumetric flow rates of 60 ml/min and 120 ml/min respectively were investigated.

values of PEMFC vary with gravity signal are obtained by the data collection and control system. The time  $t=0.000s$  is the transition point from the normal gravity to microgravity, and after the time  $t=3.600s$ , the drop capsule falls into the recovery string bag. The results demonstrate that the microgravity environment has a slight effect on the current density and voltage of PEMFC when the oxygen volumetric flow rate is 60 ml/min, 3.600 seconds later, the current density has an abrupt increase and the voltage has an abrupt decrease when the drop capsule is bounced at the first time, and then the current density and cell voltage revert to initial values in the normal gravity. When the reactant gas flow rate in the cathode is increased to 120 ml/min, same results are showed.

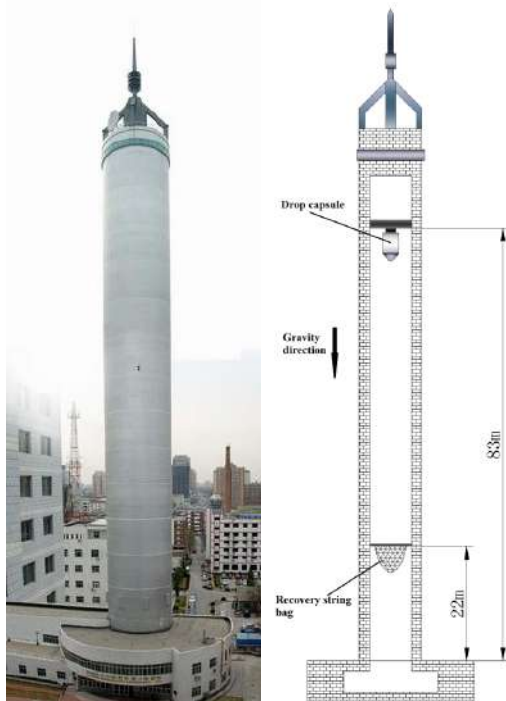


Figure 1: Microgravity drop tower

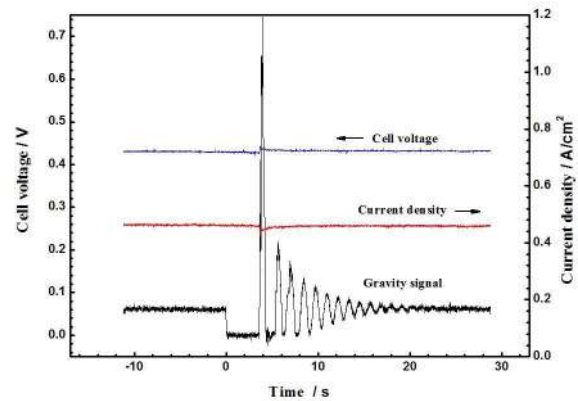


Figure 2: PEMFC behavior varies with gravity level, O<sub>2</sub>: 60ml/min

A transparent PEMFC with horizontal channels is designed to observe the two phase flow behaviors in the cathode flow field. From the time  $t=-1.000s$  to  $t=0.000s$ , the PEMFC is working the normal gravity environment, the first three photographs indicate that PEMFC works in a steady state. And then PEMFC enters the microgravity environment. In horizontal channels of PEMFC, most produced water is swept away by the high flow rate of reactant gas at the first time when it appears on the surface of the gas diffusion layer and little water accumulates on the surface of the flow channels in the normal gravity environment. When the cathode reactant gas flow rate is 60 ml/min, making comparisons of two phase flow behaviors during the time of 0.000s-0.500s, it is easily found that little liquid water aggregation and obstruction occurs in cathode flow channels,

The curves that the cell voltage and current density

however, water stream at the outlet is discharged after the PEMFC enters into the microgravity environment for 1 second, it is lagging behind the condition of the external circuit load  $R=0.01\Omega$  for 0.5 seconds. When the cathode reactant gas flow rate is 120 ml/min, compare with the experiments before, it is easily found that the diameter of liquid water droplet is the minimum and the accumulated liquid water is the least. Therefore the microgravity environment has little impact on the cell performance and gas liquid two phase flow behaviors.

Although the microgravity environment has a almost negligible influence on the cell performance of PEMFC, through the investigation of two phase flow behaviors of cathode flow field in different gravity levels, this research is helpful for further study about how to make the PEMFC performance better in different operating conditions.

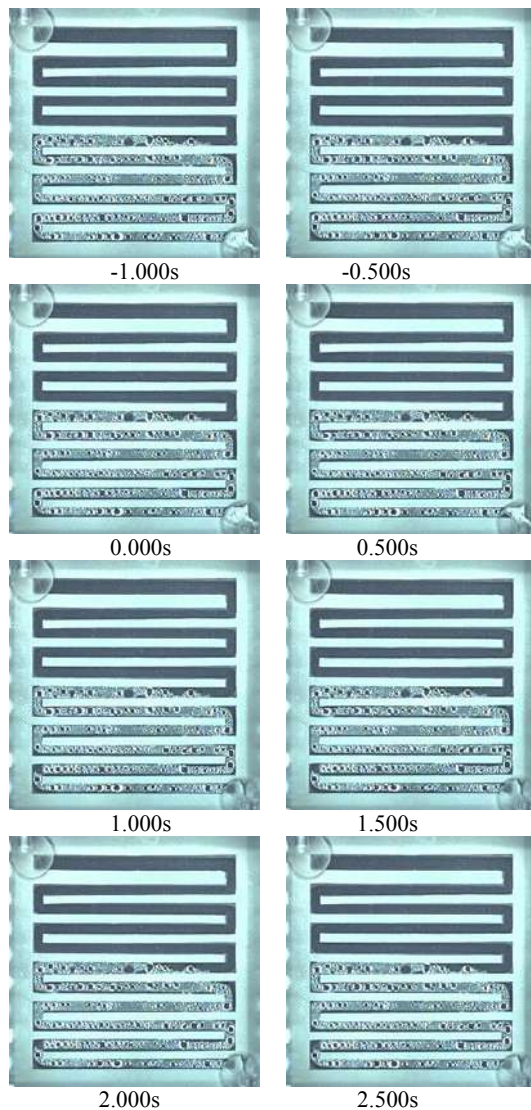


**Figure 3:** The evolutionary process of two phase fluid dynamics in cathode flow channels with time,  $O_2$ : 60ml/min,  $T$ : 65°C

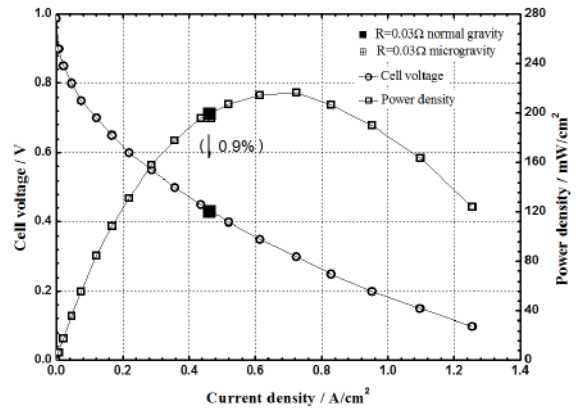


**Figure 4:** PEMFC performance under different gravitational levels,  $O_2$ : 60ml/min,  $T$ : 65°C

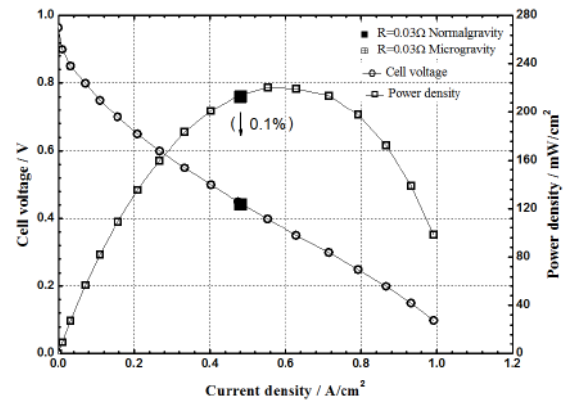


**Figure 5:** PEMFC performance under different gravitational levels,  $O_2$ : 120ml/min,  $T$ : 65°C

The authors appreciate the financial support of the National Natural Science Foundation of China (Grant No. 51476003).

### References

- Guo H., Liu X., Zhao J. F. et al., Effect of low gravity on water removal inside proton exchange membrane fuel cells (PEMFCs) with different flow channel configurations, *Energy*, Vol. 112 pp. 926-934 (2016)
- Liu J. X., Guo H., Ye F. et al., Interfacial phenomena and heat transfer in proton exchange membrane fuel cells, *Interfacial Phenomena and Heat Transfer*, Vol. 3 pp. 259-301 (2015)
- Guo H., Liu X., Zhao J. F. et al., Experimental study of two-phase flow in a proton exchange membrane fuel cell in short-term microgravity condition, *Applied Energy*, Vol. 136 pp. 509-518 (2014)

## Formation of disturbance waves at the initial area of annular-dispersed flow

S.V. Alekseenko, A.V. Cherdantsev, S.V. Isaenkov, M.V. Cherdantsev, D.M. Markovich

Institute of Thermophysics SB RAS (IT SB RAS), 1, Lavrentiev Ave, 630090, Novosibirsk, Russia  
sergei.isaenkov@gmail.com

Annular-dispersed flow regime can be characterized as a flow of a high-speed gas flow surrounded by a liquid film moving along channel walls, as well as the presence of liquid droplets in the core of the gas stream, which are torn from the film surface. The wave pattern under such a flow regime is represented by two types of waves: disturbance waves and ripple waves. Disturbance waves are large-scale waves, presence of which is necessary for liquid entrainment.

In the work (Zhao et al. 2013) the development of disturbance waves in an annular gas-liquid flow was investigated. To measure the local film thickness, the conductance probe method was used. It was found that near the channel inlet the film surface is covered by high-frequency small-scale waves, and the generation of disturbance waves occurs at a distance equal to 5-10 channel diameters. But this method doesn't allow us to study the evolution of an individual wave in time and space. Thus, in the recent paper (Alekseenko et al. 2015) the space-time evolution of the film thickness along one longitudinal section of the channel was studied by using laser-induced fluorescence method. It is revealed that the formation of disturbance waves is due to multiple acts of coalescence of initial high-frequency low-amplitude waves generated at the inlet (Fig. 1a). The local brightness of the image is directly proportional to the local thickness of the film; white color corresponds to a thickness of 1 mm.

To check the results obtained by the two-dimensional approach (Alekseenko et al. 2015), experiments in the three-dimensional approach were carried out using the same method. This approach makes it possible to obtain instantaneous distributions of the thickness of the liquid film along the longitudinal and transverse coordinates with high spatial resolution and the sampling frequency. The upward and downward air-water flows were investigated in the channels of different geometry (cylindrical and rectangular). Average gas velocity varied from 18 to 57 m/s, Reynolds numbers of the liquid  $Re_L$  from 140 to 400.

Figure 1b illustrates the surface of the liquid film at time  $t$ , indicated by the dashed line in Figure 1a. Near the the channel inlet, the film surface (Figure 1b) is covered by two-dimensional waves, usually occupying the entire width of the channel. Further, two-dimensional waves break up into three-dimensional waves with a transverse dimension of the order of several millimeters and propagate with different velocities. Because of the difference in velocity with increasing distance from the inlet, waves merge, which leads to the formation of large quasi 2D-shape disturbance waves. Quantitative assessment of the change in transverse size can be done using cross-correlation analysis.

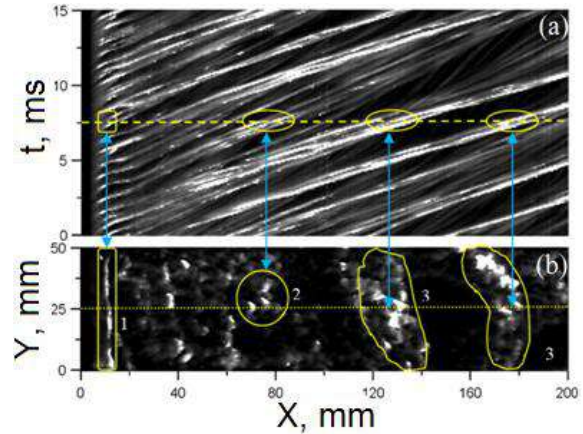


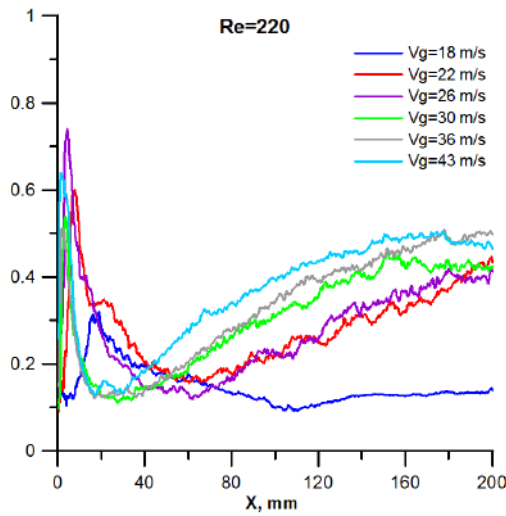
**Figure 1:** Formation of disturbance waves a) 2D approach; b) 3D approach.  $Re_L=300$ ,  $Vg=26$  m/s.

The degree of two-dimensionality is defined as the maximum of the cross-correlation function of temporal records of the film thickness obtained in different longitudinal sections of the channel:

$$b(x_0, y_1, y_2) = \frac{\max(\int H_1(t) * H_2(t - \tau) dt)}{\sum_1^t H_1(t)^2}$$

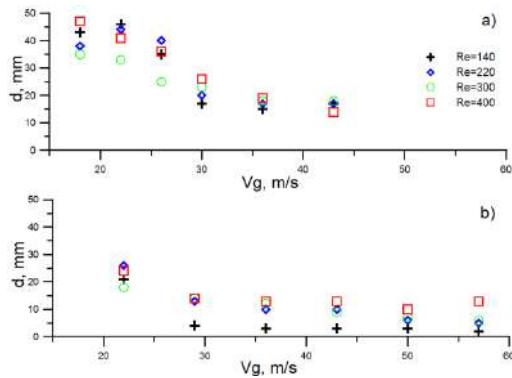
Where  $H_1 = H(x_0, y_1, t)$ ,  $H_2 = H(x_0, y_2, t)$ ,  $x_0$  is a fixed value, varies from 1 to  $X$ ;  $y_1$  and  $y_2$  change from 1 to  $Y$ ,  $X$  and  $Y$  are the longitudinal and transverse dimensions of the working area, and  $\tau$  is the time delay between the compared signals. If signal  $H_1$  equal  $H_2$  and  $\tau = 0$ , then the degree of two-dimensionality is equal to 1.

Figure 2 illustrates changes of the degree of two-dimensionality with increasing distance from the inlet. The peak in the initial region corresponds to the initial two-dimensional waves. The subsequent decrease corresponds to the decay of two-dimensional waves into three-dimensional waves and their domination on the film surface. A further increase in the two-dimensionality corresponds to the merge of small-scale waves into large disturbance waves. At low gas velocities, disturbance waves aren't form in the area of measurements, but with increasing gas velocity, the formation occurs closer to the entrance to the channel.



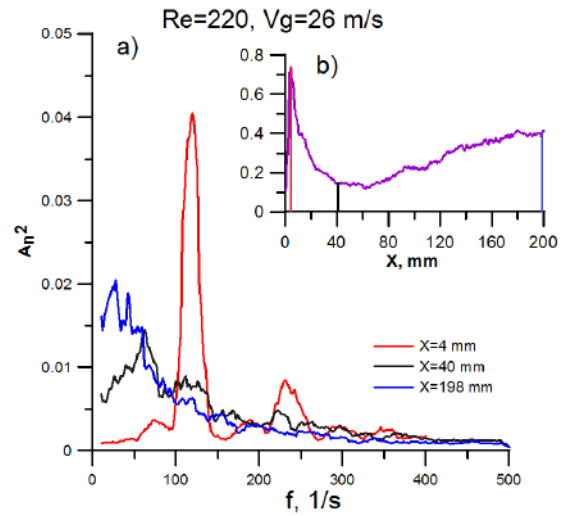
**Figure 2:** The degree of two-dimensionality with increasing distance from the inlet.  $Re_L=220$ . Rectangular duct.

Figure 3 shows the dependence of the length of the initial two-dimensional waves region for two channels with different geometries. With increasing gas flow rate, length of the region in a rectangular channel decreases substantially (Fig. 3a), but decreases weakly in a cylindrical channel (Fig. 3b). The effect of liquid flow rate is stronger in a cylindrical channel. At the highest gas velocities, two-dimensional waves almost immediately break up into three-dimensional waves.



**Figure 3:** Dependence of the length of the initial two-dimensional waves region. a) - rectangular; b) annular duct

A comparison between the results of the two-dimensional analysis and the spectral structure of the waves was made. The initial two-dimensional waves (peak in Fig. 4b) are characterized by high frequency and regularity (Fig. 4a,  $X = 4$  mm). The three-dimensional waves formed as a result of their destruction (minimum in Fig. 4b) are essentially irregular and characterized by lower frequencies (Fig. 4a,  $X = 40$  mm). With the formation of disturbance waves (Figure 4b,  $X = 198$  mm), the role of low-frequency disturbance waves increases (Fig. 4a,  $X = 198$  mm).



**Figure 4:** Spatial evolution of normalized power spectra.  $Re_L=220$ ,  $Vg=26$  m/s.

The process of formation of disturbance waves is multi-stage, nonlinear and essentially three-dimensional. Modeling this process is an extremely difficult task, which is recommended to be solved step by step, starting with the prediction of the characteristics of the initial waves. Information about characteristics of the initial waves and their interaction allows create new theoretical models with their further application in practice.

The work was supported by Russian Scientific Foundation (project 16-19-10449).

## References

- Zhao Y, Markides CN, Matar OK, Hewitt GF, Int J Multiphase Flow, Vol. 55 pp. 111-129 (2013)
- Alekseenko S.V., Cherdantsev A.V., Cherdantsev M.V., Isaenkov S.V., Markovich D.M., Int. J. Multiphase Flow, Vol. 77 pp. 65-75 (2015)

## Experimental study and empirical prediction of fuel flow parameters under air evolution conditions

E.E. Kitanina, E.L. Kitanin, D.A. Bondarenko, P.A. Kravtsov, M.M. Peganova, S.G. Stepanov, V.L. Zherebzo

Peter the Great St.Petersburg Polytechnic University, Institute of Energy and Transport Systems  
Polytechnicheskaya 29, Saint-Petersburg, 195251 Russia, Institute  
kkitanina@mail.ru

Air evolution in kerosene flow may cause issues in aircraft fuel systems. The fuel supplied to the aircraft during fueling is usually saturated with air under atmospheric pressure and ground temperature conditions. In cruise flight the ambient pressure drops, leading to the fuel oversaturation with air. Moreover the over-saturation of the fuel with air is large due to the temperature decrease up to  $-30^{\circ}\text{C}$ . In the case of pump deselection, pressure in the pipeline with pure gravity flow is contingent on the ambient pressure and fuel level in the tank only. Air can evolve from fuel, resulting in a flow rate decrease.

The air flow rate decline can be due to both the flow conditions (pressure, temperature) and the pipeline design. Substantial air evolution may occur as oversaturated fuel passes through the flow limiter (diaphragm) or other local resistance. Experience shows that pressure has a limiting value: above the limit air evolution is virtually imperceptible, whereas below the limit oversaturation drops sharply to provoke intensive air evolution and, consequently, a decline in the fuel flow rate.

The gas phase effect on pressure losses related to friction and the pressure leveling component can be quite reliably handled within the Chisholm model based on the Lockhart and Martinelli approach (Crowe et al. 2005). The much less studied issues are the calculation of the pressure losses at the local resistances under air release conditions and establishing the gas fraction in the flow downstream of the local resistances. There is a definite lack of scientific evidence that would allow researchers to describe the two-phase flow through the diaphragm under air evolution conditions. Moreover, the transition from foamy to stratified flow can occur in a tilted pipeline segment. However, the standard calculation methods mentioned above are devised for the foamy flow mode and do not allow the transition point coordinate determination.

More than 200 experiments were performed to study the dissolved air evolution process and pressure losses in individual pipeline elements. The experiments were conducted using TS-1 jet fuel in several test pipelines. The study was performed at pressure ranging from 0.2 to 1.0 bar and temperature varying between  $-20^{\circ}\text{C}$  and  $+20^{\circ}\text{C}$ . All test rigs included two fuel tanks and a working section of pipeline, isolated by a valve. The volume of each tank was  $3\text{ m}^3$ . In all cases the test rig was prepared for the test following the same steps. First, fuel was saturated by dry air at atmospheric pressure and temperature level in the supply tank. Then air was evacuated from the entire system. As a result the fuel in the supply tank became oversaturated with air. Finally, the valve was opened to let the fuel flow into the experimental pipeline. The test rig control as well as data saving and pre-processing were provided by a specifically designed automatic system.

Fuel temperature and pressure along the pipeline working section and fuel flow rates and pressures at the pipeline inlet were obtained for every experiment. A special technique based on the measurement of the dissolved air concentration,  $C$  [kg/kg], was applied for air evolution calculation. The main idea of the method is illustrated by the following example. Let the dissolved air concentration be measured at the pipeline inlet,  $C_0$ , and in (i) section,  $C_i$ . Then the mass flow quality of evolved air can be calculated as follows:  $X_i = C_0 - C_i$ . To the best of our knowledge, this gas content evaluation technique has never been used before. The dissolved air concentration was measured by chromatographs. A fuel sample was supplied to chromatographs by a specifically designed sampling system. In addition to instrumental measurements, the two-phase flow modes were observed through clear pipeline segments.

Our measurements indicated that air evolution in oversaturated fuel starts as pressure drops abruptly to a certain boundary value. It was shown that this boundary pressure value depends on temperature and fuel velocity. We notice that almost no air evolves downstream of the segments generating a minor pressure drop, e.g. bends, contractions, expansions and branching, whereas the diaphragm provokes intensive air evolution in fuel flow. A large set of experimental data was analyzed to produce empirical correlations for the pressure drop and air evolution after the diaphragm (Kitanin et al. 2013). The correlations provide adequate results in a wide range of diaphragm to pipeline diameters ratios (See an example in Fig. 1). Furthermore, we derived correlations for pressure loss coefficients of the expansion and contraction segments and verified the well-known branching and junctions correlations.

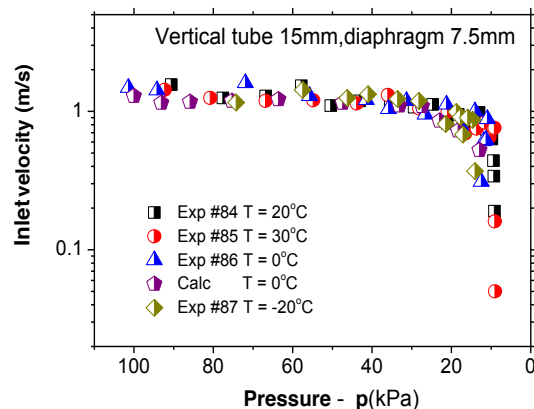


**Figure 1:** Fuel velocity depending on environment pressure value by gravity flow in a pipeline with a diaphragm.

As a result of experimental data analyze a special method of calculating the two-phase flow pressure in a tilted

pipeline segment was developed (Kitanin et al. 2014). Conventional methods prove inefficient under the conditions at hand (very low mass flow quality and fairly high volume flow quality) due to co-existence of two flow modes in different parts of the titled segment. In many experiments we observed stratified flow in the upper part and foamy (bubble) flow in the lower part. Though it is easy enough to calculate the pressure in each individual part, the flow mode transition point proves to be a priori unknown. We built a complete calculation chain including pressure drop equations for both flow modes, an equation taking into account the change in kinetic energy during transition and an empirical equation for calculating the pressure drop in the tilted pipeline segment. This helped estimate the stratified to foamy flow transition point coordinate.

The complete set of empirical correlations obtained by experimental analysis was implemented in the engineering code specifically developed for two-phase gravity flow calculations (Kitanina et al. 2014). The computational algorithm is based on the balance (Bernoulli) equations written for every pipeline segment and for the whole pipeline system. Hence the velocity at the supply tank exit is proportional to the difference in fuel levels in the tanks and inversely proportional to the total pressure loss including two-phase flow acceleration loss, local loss and friction loss that are initially evaluated for each pipeline segment. We notice that the flow parameters (e.g. density, velocity and pressure loss coefficients) strongly depend on the evolved air content in the fuel. Air evolution in its turn depends on pressure, temperature and fuel velocity. Consequently an iterative process was realized for fuel velocity calculations. A postponed recursion technique provided computations of the flow in a pipeline with branching and junctions.

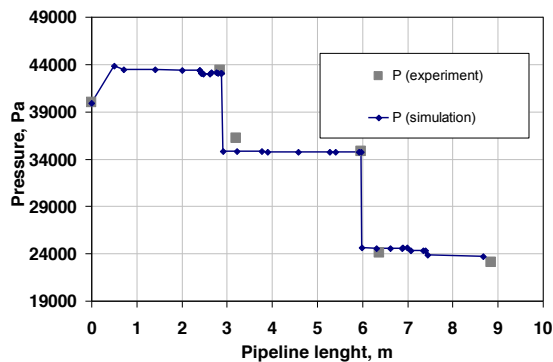


**Figure 2:** Distribution of pressure along the main branch of the horizontal pipeline under air evolution conditions.

The calculation results were verified against both steady and unsteady experimental data obtained by RNC "Applied Chemistry" and by the Airbus team (See Figure 2 and 3 correspondingly). Generally, comparisons display a fairly good match between the simulated and experimental flow parameters in the complex branched pipelines with intensive air evolution. The calculation for Airbus test pipeline with two inclined segments display larger discrepancies. However the simulation results show that the developed method can be applied to more complicated pipelines. On the other hand, these experiments revealed high flow pulsations. Therefore, the uncertainty may result from unsteady phenomena

produced by the flow regime transition and the mutual influences of local resistances in experiments.

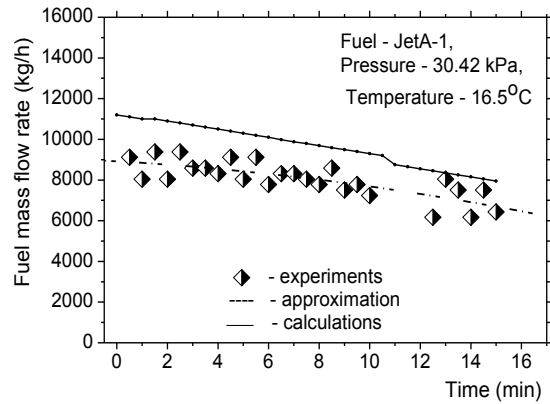


**Figure 3:** Fuel flow rate versus time. Calculations based on our empirical equations and Airbus experimental results.

Several experimental rigs were built to study the effects of different local loss segments on the gravity fuel flow under air evolution conditions. Through these experiments, we established the oversaturation limit beyond which dissolved air starts evolving intensively from the fuel. We also obtained correlations for pressure losses and air evolution on pipeline segments. To predict two-phase flow parameters a special software tool based upon the empirical equations was developed. The simulation results were compared to the experimental studies of steady and unsteady flow in different pipelines of complex geometry. The software tool provides fast and fairly accurate calculations of the fuel flow rate in the fuel system under air evolution conditions.

## References

- C. T. Crowe, Taylor, Francis Multiphase handbook (2005).
- ÉL Kitanin, EÉ Kitanina, VL Zhrebtsov, OA Merkulov, MM Peganova, Influence of Separation of Air Dissolved in Fuel on the Rate of its Gravity Flow in a Pipeline at an Underpressure, *Journal of Engineering Physics and Thermophysics*, Vol. 86, No. 6, pp. 1426-1433 (2013)
- ÉL Kitanin, EÉ Kitanina, PA Kravtsov, DA Bondarenko, D Morrison, Calculation of the Head Loss in a Kerosene–Air Flow Upon Change in the Two-Phase-Flow Structure on an Inclined Portion of a Pipeline, *Journal of Engineering Physics and Thermophysics*, Vol. 87, No. 3, pp. 588-597 (2014)
- EE Kitanina, DA Bondarenko, D Morrison, Air evolution in fuel flow under decreased pressure conditions: experimental studies and engineering code development, *Proc. Int. Council Aeronaut. Sci* (2014)

## Foam flows in model fracture

T. Chevalier<sup>1</sup>, J. Koivisto<sup>1</sup>, N. Shmakova<sup>2</sup>, M.J. Alava<sup>1</sup>, A. Puisto<sup>1</sup>, C. Raufaste<sup>3</sup> and S. Santucci<sup>2,4</sup>

<sup>1</sup>COMP Center of Excellence, Department of Applied Physics, Aalto University, Espoo, Finland

<sup>2</sup>Lavrentyev Institute of Hydrodynamics, Novosibirsk, Russia

<sup>3</sup>Université Nice Sophia Antipolis, CNRS, LPMC, UMR 7336, Nice, France

<sup>4</sup>Laboratoire de Physique, ENS de Lyon, Univ Lyon, CNRS, UMR 5672, Lyon, France  
stephane.santucci@ens-lyon.fr

Liquid foams, such as chocolate mousse and shaving foams are soft materials that we all use in our everyday life. Their multi-scale biphasic structure of gas bubbles within a liquid phase leads to a dual mechanical behaviour: they behave as solids at rest, while they can flow like liquids above a given critical yield stress. Such peculiar rheological properties are at the root of their use in diverse applications, ranging from food, cosmetics and pharmaceutical industries, to oil recovery or soil remediation processes. For those last applications, understanding and controlling the flow of liquid foams in confined heterogeneous media appears of tremendous importance (Weaire and Hutzler 1999, Cantat et al. 2013, Dollet and Raufaste 2014, Stevenson 2012).

We have therefore designed a simple experimental set-up, in order to investigate the flow of a liquid foam, forced to invade a fracture.

Moreover, the cell presents a defect of lateral size  $2 \times 2 \text{ cm}^2$  and height  $H$  (of typically few hundred microns). This bump localized in the center of the cell reduces its gap, and thus acts as a permeable obstacle. To ensure identical surface properties of the top and bottom plates of the cell, both surfaces are covered with a thin stretchable hydrophilic plastic film.

We generate in-situ our liquid foam and forced it to flow in our model fracture, by bubbling filtered pressurized air at a constant flow rate of 40 ml/min (thanks to a mass flow controller) through a needle of inner diameter 0.45 mm in a vertical chamber connected to the cell (via a 10 mm diameter hole drilled in the bottom plate), filled with a soapy solution. This surfactant solution is obtained by mixing 1% of a commercial dishwashing liquid Dawn© with ultra-pure water. In these conditions, the bubbles generated are larger than the cell gap, and therefore, they form a quasi mono-disperse 2-D confined foam, constituted by a mono-layer of millimeters bubbles. Moreover, they invade the cell at a constant rate of around  $v = 15 \text{ mm/s}$ .

We observe directly the steady-state flow of our 2-D liquid foam in the center of the cell around the obstacle (imaging area of  $20 \times 10 \text{ cm}$ ), using a Ximea XiQ digital camera during 400 seconds at 5 Hz. We thus record 2000 frames of  $2088 \times 1048$  pixels. A typical image recorded during an experiment with an obstacle filling 70% of the gap cell is shown on the bottom panel of Figure 1.

Using standard image analysis tools, we can identify all individual bubbles of the flowing foam, for each image recorded during an experiment. Tracking those bubbles, we can measure their velocity (computed as the displacement vector of the bubble centers between the recording of two subsequent images,  $\Delta t = 0.2 \text{ s}$ ). The average velocity field for an experiment with an obstacle filling 70% of the gap is shown on Figure 2.

Far from the obstacle, we clearly observe that the velocity field is uniform corresponding to the flow rate imposed by our experimental procedure. Nevertheless, approaching the permeable obstacle, the amplitude of the velocity field decreases, while it increases when leaving the obstacle. Such flow disturbance caused by the obstacle is clearly revealed when displaying the velocity field in the frame of the flowing foam (shown on the bottom panel of Figure 2). Indeed, a clear recirculation is then observed, characterized by a quadrupolar velocity field around the obstacle. Furthermore, downstream the obstacle, there is a zone where the velocity is larger than the mean velocity (equivalently, in the frame of the flowing foam, the velocity is opposed to the one of the obstacle). Such effect is reminiscent of the observation of a so-called "negative wake" in the flow pattern of rising air bubbles in viscoelastic fluids (Hassager 1979). Our observations and results appear

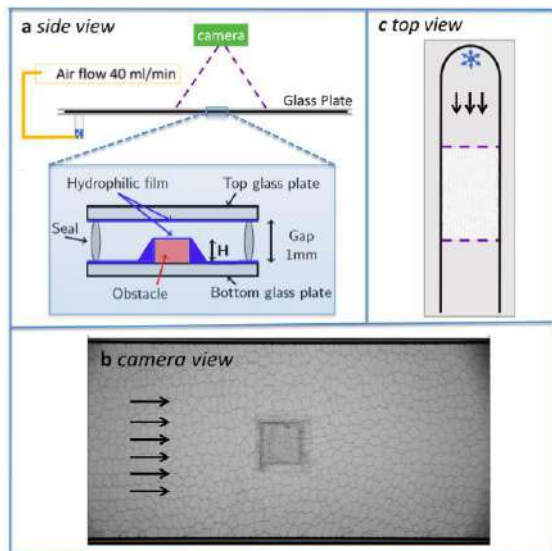


**Figure 1:** Experimental set-up, allowing the direct observation of a 2D liquid foam flowing in a Hele-Shaw cell containing a permeable obstacle (its height  $H$  is smaller than the gap of the cell,  $G = 1 \text{ mm}$ ). The panels (a) and (c) displays respectively side and top views, while the bottom panel shows a typical recorded image (b).

Our set-up allows the direct observation of the motion and deformation of the elementary components of a 2D liquid foam – the bubbles –, when forced to invade a confined heterogeneous medium, that mimicks a simple fracture. Indeed, as shown on Figure 1, our model fracture consists of a Hele-Shaw cell, made of 2 glass plates (15 cm wide, 50 cm long and 1 cm thick), separated by a 1 mm gap.

analogous to the ones obtained for a 2-D foam flow around a full obstacle (using a liquid pool geometry), by Dollet and Graner (2007), Raufaste et al (2007), which were attributed to the visco-elasto-plastic nature of the foam (Cheddadi et al 2011), that cannot be modelled as a simple viscoplastic fluid. Nevertheless, interestingly, in our geometry, modifying the permeability of our obstacle (by simply changing the height of the defect), we can modulate systematically the intensity of the quadrupolar recirculation and specifically the velocity overshoot observed behind the obstacle.

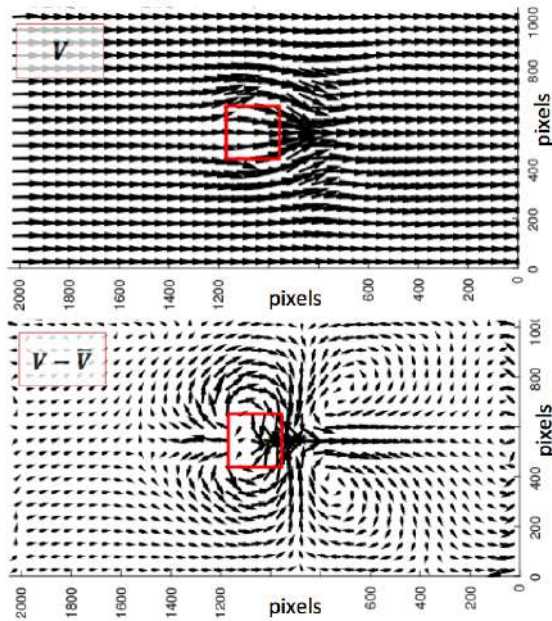


**Figure 2:** Average velocity field for an experiment with an obstacle (red square of  $2 \times 2 \text{ cm}^2$ ) filling 70 % of the cell gap. On the bottom panel, the imposed flow rate at the inlet is subtracted to the velocity field, revealing the strong disturbance induced by the obstacle.

Following the procedure and tools developed by Dollet and Graner (2007), Raufaste et al (2007), Marmottant et al (2008), we are currently investigating in detail the influence of the geometrical properties of such permeable defects (shape, lateral extension and height), as well as other experimental controlling parameters, such as the foam liquid fraction and the imposed flow rate on both the velocity, deformation and the topological rearrangement of the bubbles.

SS and NS have been supported by grant no. 14.W03.31.0002 of the Russian Government.

## References

- O. Hassager, *Nature*, Vol. 279, p. 402 (1979).
- D. Weaire and S. Hutzler, *The Physics of Foams*, Oxford University Press (1999)
- B. Dollet and F. Graner, Two-dimensional flow of foam around a circular obstacle: Local measurements of elasticity,

plasticity and flow, *J. Fluid Mech.*, Vol. 585, p. 181 (2007).

C. Raufaste, B. Dollet, S. Cox, Y. Jiang and F. Graner, Yield drag in a two-dimensional foam flow around a circular obstacle: Effect of liquid fraction, *Eur. Phys. J. E*, Vol. 23, p. 217 (2007).

P. Marmottant, C. Raufaste and F. Graner, Discrete rearranging disordered patterns, Part II: 2D plasticity, elasticity and flow of a foam, *Eur. Phys. J. E*, Vol. 25, p. 371 (2008).

I. Cheddadi, P. Saramito, B. Dollet, C. Raufaste, F. Graner, Understanding and predicting viscous, elastic, plastic flows, *Eur. Phys. J. E*, Vol. 34, p. 1 (2011)

P. Stevenson, *Foam Engineering: Fundamentals and Applications*, Wiley (2012).

I. Cantat I., S. Cohen-Addad, F. Elias, F. Graner, R. Hohler, O. Pitois, F. Rouyer and A. Saint-Jalmes, *Foams, Structure and Dynamics*, Oxford University Press (2013).

## A model for gas-liquid swirling separation efficiency and its application

Li Liu, Bofeng Bai and Liang Zhao\*

State Key Laboratory of Multiphase Flow in Power Engineering,  
Xi'an Jiaotong University, Xi'an 710049, China  
E-mail: [bfbai@mail.xjtu.edu.cn](mailto:bfbai@mail.xjtu.edu.cn)

Swirling separation technique is widely used in two-phase flow systems such as swirl vane separators for gas-liquid separation (Kataoka et al. 2008), vortices tools for liquid drainage in wet-gas wells (Molina et al. 2004) and heat exchangers for flow-boiling heat transfer (Manglik 2004) to remove small droplets from gas stream. A typical swirler as shown in Fig. 1 is generally adopted to induce the fluid swirl and separation. This kind swirler mainly consists of a central hub and several swirl vanes on the hub. The radius of the central hub and cylinder is  $R_i$  and  $R_o$ , and their height is  $h$  and  $H_{sep}$ , respectively. The number of the swirl vanes is  $n$  and the vane angle is fixed to  $\theta$  with respect to the axial direction. The gas-liquid mixture enters the swirler through the inlet pipe and the droplets are driven toward the cylinder wall by the centrifugal force generated by the swirl vanes. When reaching the wall, the droplets deposit on it and form a liquid film which is finally removed from the gas stream.

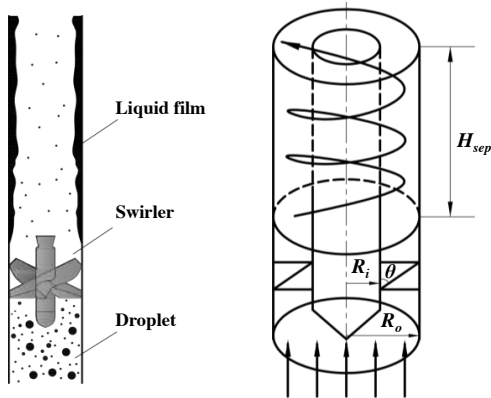


**Figure 1:** A typical swirler and swirling gas-liquid flow induced by swirler.

Laboratory tests on swirling gas-liquid separation efficiency are usually carried out to help establish an experimental database for really separator design and performance improvement. Such model tests are generally performed in the reduced scale and not on the actual working conditions. Though great efficiency is often obtainable in the reduced model, the performance of the full-sized prototype usually cannot be well predicted. To design downscale model tests for swirling gas-liquid separation efficiency and apply the experimental results to predict the prototype, a general relationship to correlate them is required.

In this paper, we first established theoretical models for critical droplet diameter  $d_{pc}$ , grade efficiency  $\eta_{dp}$  and overall separation efficiency  $\eta$  by analyzing the features of

the droplet trajectory in swirling gas flow field. The critical droplet diameter  $d_{pc}$ , defined as 100% separation efficiency for a given droplet, is estimated based on the time-of-flight model (Hoffmann and Stein 2002):

$$d_{pc} = \left\{ B \left[ 1 - (r^0/R_o)^2 \right]^7 \right\}^{1/8} \quad (1)$$

where  $r^0$  is the initial radial position of droplet and  $B$  is defined as separation parameter, which is a function of the geometry parameters and flow parameters:

$$B = 8.498^7 \left( \frac{\rho_g}{\rho_l} \right)^5 \left( \frac{v_g}{j_g R_o} \right)^3 \frac{(R_o + R_i)^{13} (R_o - R_i)^3}{R_o (H_{sep})^7 (\tan \theta)^{10}} \quad (2)$$

where  $j_g$ ,  $\rho_g$  and  $v_g$  are the superficial gas velocity, gas density and gas kinematic viscosity, respectively.

The droplets larger than the critical diameter will be separated. However, Eq. (1) indicates that for different initial radial position  $r^0$ , the corresponding critical droplet diameter  $d_{pc}$  is different. Therefore, there exists a maximum critical droplet diameter  $d_{pc(max)}$  (when  $r^0 = R_i$ ), and the droplets larger than  $d_{pc(max)}$  will be all separated regardless of their initial radial position, whereas the separation efficiency of the droplets smaller than  $d_{pc(max)}$  directly depends on the initial radial position. The separation efficiency of this droplet group is defined as grade efficiency  $\eta_{dp}$ :

$$\eta_{dp} = \frac{1 - \left[ 1 - (d_p^8/B) \right]^{1/7}}{1 - (R_i/R_o)^2} \quad (3)$$

Then the overall separation efficiency  $\eta$  can be calculated as:

$$\eta = \int_{d_{pc(max)}}^{d_{p,max}} f_m(d_p) d(d_p) + \int_0^{d_{pc(max)}} \eta_{dp} f_m(d_p) d(d_p) \quad (4)$$

where  $d_{p,max}$  is the maximum droplet diameter and  $f_m(d_p)$  is the droplet mass percentage probability density function (PDF), can be calculated as:

$$f_m(d_p) = \frac{d_p^3 f_N(d_p)}{\sum d_p^3 f_N(d_p)} \quad (5)$$

where  $f_N(d_p)$  is the droplet diameter PDF.

Since the critical droplet diameter  $d_{pc}$  and droplet separation efficiency ( $\eta_{dp}$  and  $\eta$ ) are directly related to the separation parameter  $B$ , for a scaling consideration,  $B$  can be written with similarity criteria as:

$$B = 13.007^8 C_p^5 (Re_g)^{-3} (1 - Ge_r)^3 (1 + Ge_r)^5 (Ge_h)^{-7} (Sw)^{-10} \left( \frac{R_o + R_i}{2} \right)^8 \quad (6)$$

where  $Re_g = D j_g / \nu_g$  is the gas Reynolds number;  $C_p = \rho_g / \rho_l$  is the density ratio, indicating the dependence on working fluids and pressure conditions;  $Ge_r = R_i / R_o$  and  $Ge_h = H_{sep} / R_o$

are criteria for geometry similarity, charactering the separator design;  $S_w = \tan\theta$  is the swirl number, charactering the swirl intensity;  $(R_i+R_o)/2$  is the characteristic radial position of the swirling flow. When  $B_{\text{model}} = B_{\text{prototype}}$  and the droplet diameter distribution in the model is the same as that in the prototype, we obtain:

$$\eta_{\text{model}} = \eta_{\text{prototype}} \quad (7)$$

The scaling laws for gas-liquid swirling separation efficiency developed above can be served as a basis for downscale model design and also enable us to study the general relationship between the model and prototype.

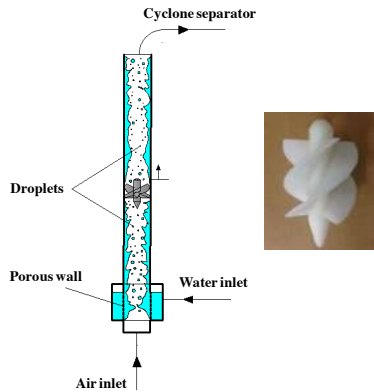


**Figure 2:** Schematic of the downscale model test facilities.

In second part of this work, we carried out laboratory tests on the downscale model to study the swirling separation efficiency (Fig. 2). The air and water are used as the working fluids. The overall separation efficiency under different flow conditions was measured. Based on the experimental results in cooperation with the separation efficiency model (Eqs. (1)-(4)), we first calculated the typical droplet distribution by assuming a normal distribution for the droplet diameter PDF (Fig. 3).

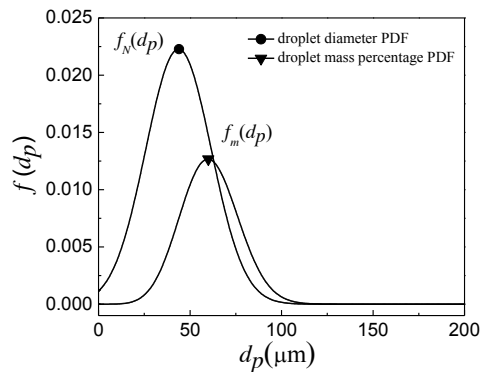


**Figure 3:** Droplet diameter and corresponding mass percentage distribution for a given gas-liquid flow.

When model and prototype is under similar conditions, their droplet distribution is the same. Hence, based on the typical droplet distribution obtained from the downscale model test, we are able to predict the overall separation efficiency of prototype with the theoretical correlations for droplet critical diameter and separation efficiency (Eqs.

(1)-(4)). As a result, the difference of separation efficiency between the downscale model the the full-sized prototype under similar conditions was obtained (Fig. 4).

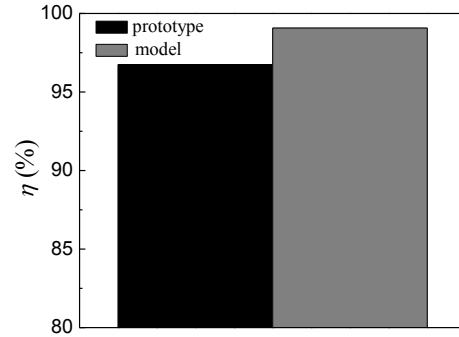


**Figure 4:** A comparison of overall separation efficiency  $\eta$  between model and prototype for a given gs-liquid flow.

The result in Fig. 4 indicates that the model generally has a better separation performance than that of the prototype when similarity holds, but both of them can separate more than 95% of the water from the inlet gas-liquid mixture.

This study was supported by National Natural Science Foundation of China under Grant No. 51276140.

## References

- Kataoka H., Tomiyama A., Hosokawa S., Sou A. and Chaki M., Two-phase swirling flow in a gas-liquid separator, J. Power Energy Syst, Vol. 2 pp. 1120-1131 (2008)
- Molina R., Wang S., Gomez L.E., Mohan R.S., Shoham O. and Kouba G., Wet Gas Separation in gas-liquid cylindrical cyclone separator, J. Energy Resour. Technol, Vol. 130 pp. 1-13 (2008)
- Manglik R.M., Swirl flow heat transfer and pressure drop with twisted-tape inserts, Adv. Heat Transfer, Vol. 36 pp. 183-265 (2004)
- Hoffmann A.C., Stein L.E., Gas cyclones and swirl tubes: principles, design, and operation. Springer-Verlag, Berlin, Germany (2002)

## Experimental determination of local heat flux during droplet evaporation in microgravity

Michael J. Gibbons\*, Maxime Rouzes\*, Giacomo Saccone<sup>o</sup>, Seamus O'Shaughnessy\*,  
Paolo Di Marco<sup>o</sup>, Anthony J. Robinson\*

<sup>o</sup>DESTEC, University of Pisa, Italy; \*Department of Mechanical and Manufacturing Engineering, Trinity College Dublin, Ireland  
[MIGIBBON@tcd.ie](mailto:MIGIBBON@tcd.ie), [g.saccone@ing.unipi.it](mailto:g.saccone@ing.unipi.it), [ROUZESM@tcd.ie](mailto:ROUZESM@tcd.ie), [OSHAUGSE@tcd.ie](mailto:OSHAUGSE@tcd.ie), [p.dimarco@ing.unipi.it](mailto:p.dimarco@ing.unipi.it), [AROBINS@tcd.ie](mailto:AROBINS@tcd.ie)

Evaporation of sessile drops is of significant scientific and engineering interest. It represents a common natural phenomena that is not fully understood while at the same time is used in many industrial fields, ranging from DNA mapping to evaporative spray cooling (Marchuk et al., 2015). Droplet evaporation dynamics depends on many factors, including though not limited to wettability, the evaporation flux at the interface and the triple line, the substrate temperature, external fields and thermocapillarity, and these have been researched extensively over the past decade. From a thermal transport standpoint, the process is a complex interaction of diffusion within the substrate, buoyant convection in the gas and liquid phases, contact line evaporation, vapor diffusion, evaporative cooling at the liquid-gas interface and possible Marangoni effects. The droplet evaporation process is clearly very complex and even though considerable progress has been made with regard to understanding the thermal and fluid transport processes, they are still not fully understood, in particular with regard to the conjugate heat transfer near the triple contact line (Zheng et al., 2016).

Recent works highlighted the dependency of droplet evaporation process on the working fluid, surrounding gas, and heated substrate properties (Brutin, 2015). The highest local heat transfer for an evaporating droplet occurs at the contact line (Marchuk et al., 2015). The contact line or triple line is defined as the region where the gas, liquid and solid phases intersect. It can be broken-up into four distinct regions: Micro-convection region, Intrinsic Meniscus region, Transition region, and Absorbed film region (Stephan and Hammer, 1994, Raghupathi and Kandlikar, 2016). These are depicted in Figure 1.

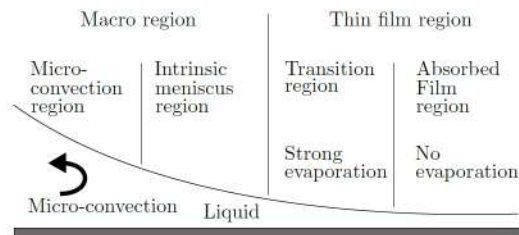


**Figure 1:** Droplet evaporation at the contact line, Adapted from Raghupathi and Kandlikar (2016).

The absorbed film region is characterised by long range intermolecular forces. This disjoining pressure results in a flat liquid-gas interface of a few nanometers thick and prevents evaporation occurring in this region. The transition region is defined by growing film thickness which results in a reduction in the long range intermolecular forces. This region experiences the highest heat fluxes across the droplet as a result of the low thermal resistance due to the small film

thickness. As the film thickness increases further, from the transition region into the intrinsic meniscus and micro-convection regions, so too does the thermal resistance resulting in a decrease in the local heat flux. Both the intrinsic meniscus and micro-convection regions are characterised by surface tension and inertial forces (Stephan and Hammer, 1994). Heat is transferred at the liquid-solid boundary by diffusion and advection.

The underlying physical processes occurring in droplet evaporation are investigated by measuring the local convective-evaporative heat flux beneath an evaporating droplet. Experiments were carried out both on ground under terrestrial conditions and under micro-gravity conditions in the 66<sup>th</sup> esa parabolic flight campaign, held in May 2017. Results will be presented and discussed after the experimental setup presentation.

The experimental apparatus consists of two primary components; the heat transfer section, and the imaging system. These are described below and illustrated in the rig schematic in Fig 2.

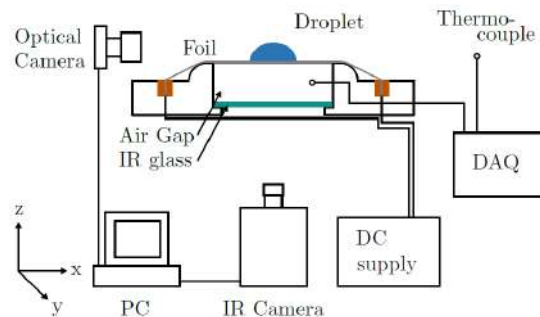


**Figure 2:** Schematic diagram of experimental set-up.

The thermal exchange section consists of a 25  $\mu\text{m}$  thick, 0.072 x 0.035  $\text{mm}^2$  Goodfellow Stainless Steel 316 (Fe/Cr18/Ni10/Mo3) foil. The foil is clamped between two copper bus bars, with both bus bars electrically connected to a DC power supply. The copper bus bars are mounted to a polyetheretherketone (PEEK) housing. A tensioning system is employed in order to counteract foil warping at higher wall heat fluxes. The 25  $\mu\text{m}$  foil is stretched across a 0.70 x 0.40 x 0.15  $\text{m}^3$  central PEEK. The latter serves to house a 0.040 x 0.040 x 0.003  $\text{m}^3$  infrared (IR) transparent Zinc Selenide window. The top of this IR window is positioned 15 mm below the underside of the foil. This configuration establishes a 0.030 x 0.030 x 0.015  $\text{mm}^3$  air cavity. During experimentation this trapped air acts as a thermal barrier, ensuring that the heat transfer by conduction on the underside of the foil is low. An exposed T-type thermocouple is used to measure the air temperature at the

midpoint of the air gap cavity. The underside of the foil is exposed for direct temperature measurement by an infrared camera. It is coated with a thin layer of matt black paint of known emissivity to facilitate accurate temperature measurement. The heat transfer section is mounted on a 3D-printed PLA baseplate. The heater is fed via a DC power supply, 20 A 2 V max, computer-controlled via LabView. The current fed to the heater may be changed during the tests, in order to vary its temperature, in the range 60 °C to 90 °C. The heater power is measured by multiplying the current by the voltage drop, which is measured by means of two sense wires soldered on the two sides of the foil. A washer-shaped electrode is placed above the heater (which is grounded) to generate the required electric field. The center hole allows the insertion of the needle for droplet generation and deposition. A voltage up to 8 kV dc can be applied to it. The electrode is connected to a high voltage, high-impedance DC power supply (Spellman RM18P3000D) controlled by a manual potentiometer.

The imaging system consisted of two parts; an optical camera and a FLIR A655sc thermal imaging camera. Each camera is individually controlled by a dedicated computer. The high resolution and high frame rate InfraRed camera was used to capture the thermal footprint of the evaporating droplet. The IR camera is mounted to the aluminium profile, directly below the thermal exchange surface. The IR camera is fitted with a 50 mm lens. The full camera resolution gives a 640 x 480 pixels<sup>2</sup> field with each pixel corresponding to a width of 157 μm. After a test is completed the acquired raw data is exported in a .seq file extension and is later processed in MATLAB.

The optical images are taken at a resolution of 215 pixel/mm and are used to derive the droplet profile, which is digitized and compared with theoretical and numerical predictions. From the shape of profile it is also possible to evaluate all the forces acting on the droplet.

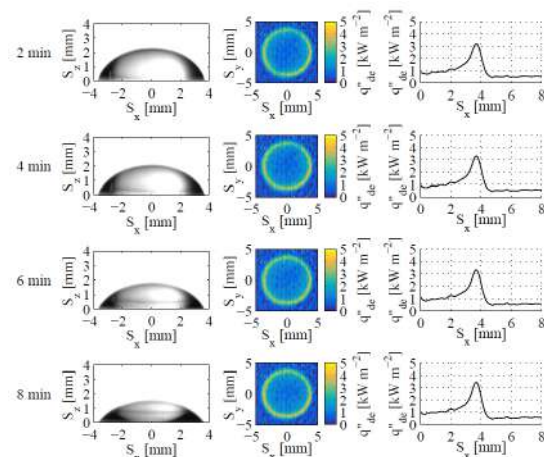


**Figure 3:** Wetting droplet evaporation, shape, heat flux distribution and radial heat flux profile over time in terrestrial gravity conditions.

Figure 3 shows the droplet shapes, heat flux distributions and local convective heat flux distribution over the evaporation pinned regime in terrestrial gravity conditions. From left to right column, it can be seen the

droplet boundary profile, the local convective heat flux distribution and the radial convective heat flux profile. It clearly shows that the droplet follows Constant Contact Radius mode evaporation process. The radial heat flux profile highlights that the peak convective heat transfer is located at the triple line at all times. Despite an obvious droplet morphology change, the local heat flux profile remains basically the same due to pinned contact line. One can therefore conclude that a clear change in the apparent droplet contact angle yields no change in the thin film transition region due to the near constant heat flux distribution.

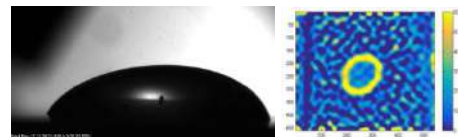


**Figure 4:** optical droplet images (left) and heat flux distribution (right) obtained in the 66<sup>th</sup> ESA parabolic flight campaign under terrestrial conditions.

Figure 4 shows the heat flux distribution of an evaporating droplet and the droplet shape obtained respectively from the IR and optical cameras. Those images are preliminary results from the 66<sup>th</sup> ESA parabolic flight campaign. In the latter, experiments were carried out with and without electric field under both terrestrial and micro-gravity conditions. When a sessile droplet evaporates while an electric field is applied, its shape results from the balance of surface tension, electrostatic and gravitational forces. Its evaporation rate as well as its shape is also intrinsically linked to the contact line motion. This investigation focuses on the impact of force fields (namely, a static electric field and the gravitational one) on triple line dynamics and heat transfer. Their respective contributions to the local convective heat flux in the contact line region and across the entire evaporating droplet will be presented.

## References

- D. Brutin, Droplet Wetting and Evaporation: From Pure to Complex Fluids, Academic Press (2015).
- P. A. Raghupathi, S. G. Kandlikar, Contact line region heat transfer mechanisms for an evaporating interface, International Journal of Heat and Mass Transfer, Vol. 95, pp. 296-306 (2016).
- I. Marchuk, A. Karchevsky, A. Surtaev, O. Kabov, Heat flux at the surface of metal foil heater under evaporating sessile droplets, International Journal of Aerospace Engineering (2015).
- Z. Zheng, L. Zhou, X. Du, Y. Yang, Numerical investigation on conjugate heat transfer of evaporating thin film in a sessile droplet, International Journal of Heat and Mass Transfer, Vol. 101, pp. 10-19 (2016).
- Stephan, P., Hammer, J. A new model for nucleate boiling heat transfer, Wärme - und Stoffübertragung, Vol. 30, No. 2, pp. 119-125 (1994).

## Future ESA experiments in Two-phase Heat and Mass Transfer Research on-board the International Space Station

Balázs Tóth<sup>1)</sup>, Hans Ranebo<sup>2)</sup>, Luciana Montrone<sup>2)</sup>, Guan-Lu Zhang<sup>3)</sup>, Liesbeth De Smet<sup>3)</sup>, Alessandro De Simone<sup>4)</sup>  
on behalf of  
ESA's Science, Payload Development and Operations Teams, Science Teams<sup>5)</sup> and Space Industries<sup>6)</sup>

<sup>1)</sup> HE Space Operations BV for ESA, NL-2200AG Noordwijk, The Netherlands, E-mail: balazs.toth@esa.int

<sup>2)</sup> ESA-ESTEC, NL-2200AG Noordwijk, The Netherlands

<sup>3)</sup> Space Applications Services for ESA, NL-2200AG Noordwijk, The Netherlands

<sup>4)</sup> Vitrociset Belgium Sprl for ESA, NL-2200AG Noordwijk, The Netherlands

<sup>5)</sup> Science Teams: Aavid Thermalloy (IT), Air Liquide (FR), AIST (JP), Airbus Defence and Space (Bremen, DE), Argotec (IT), ATh (GR), CAS (CN), CEA (FR), CCNY (US), CSI (DE), Datec Coating (CA), ENEA (IT), ENSMA (FR), EPFL (CH), Euro Heat Pipes (BE), IITK (IN), IMFT (FR), INSA-LYON (FR), KTH (SE), Kutateladze IT (RU), LAPLACE (FR), Liebherr Aerospace (FR), NLR (NL), P\* (FR), Ónda (IT), Optec (BE), Politecnico di Milano (IT), Promete (IT), Selex ES (IT), SIT (JP), SMU (US), Techno System Developments (IT), Thalès Aliena Space (FR), Trinity College Dublin (IE), TU-Darmstadt (DE), UCLA (US), UFSC (BR), ULB (BE), UNIHEAT (IT), Vangeel Electrical (BE), Wow Technology (BE), ZARM (DE), Universities of Aix-Marseille (FR), Altai State (RU), Bergamo (IT), Brighton (UK), Edinburgh (UK), Hirosaki (JP), Illinois (US), Kyushu (JP), Liège (BE), Ljubliana (SI), Loughborough (UK), Maryland (US), Mons-Hainaut (BE), Naples (IT), Ochanomizu (JP), Padova (IT), Pisa (IT), Purdue (US), Toronto (CA), Tyumen State (RU), Utsunomiya (JP), York (CA)

<sup>6)</sup> Space Industries: Airbus Defence and Space (Friedrichshafen, DE)

Assessing two-phase heat transfer phenomena, where capillary forces play significant role is often challenging on ground. In the majority of the regimes gravity masks certain processes making the representation of the observations difficult. In some particular cases by creating small scale set-ups, the effect of the gravitational field can be minimised. Nevertheless, this solution imposes further challenges to the diagnostic systems, which are mostly optical.

Therefore, researchers often use microgravity condition, where the influence of gravity (i.e. natural convection, buoyancy) can be significantly reduced. To support such studies, in the frame of the *Science in Space Environment* (SciSpacE) programme, the *European Space Agency* (ESA) makes its various microgravity platforms (e.g. drop tower, parabolic flights, sounding rockets, space missions) available for scientific purposes (Tóth 2012).

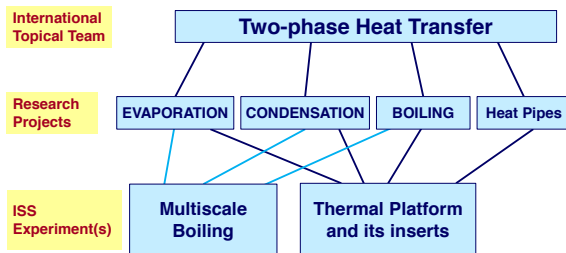


**Figure 1:** Two-phase heat transfer experiments on the International Space Station (ISS) and research projects

The aim of the present contribution is to provide an update of the two-phase heat transfer experiments envisaged by ESA, focusing on gas-liquid phase change and wettability related phenomena within the frameworks of the utilisation of the *International Space Station* (ISS). The context of these experiments is pictured in Figure 1. They serve the objectives of the *EVAPORATION*, *CONDENSATION*, *BOILING* and *Heat Pipes* research projects (further details are given below and in (Tóth 2012)), which are coordinated in the framework of the *Two-phase Heat Transfer*

international topical team. The experiments are planned to be conducted in the *Fluid Science Laboratory* (FSL) and in the second European Drawer Rack (EDR-2) in the Columbus module of the ISS (see Figure 2).



**Figure 2:** Left: The Fluid Science Laboratory (FSL)  
Right: European Drawer Rack (EDR)

### Multiscale Boiling

The *Multiscale Boiling* experiment aims at studying the fundamentals of boiling by analysing the behaviour of a

single vapour bubble with particular attention to the role and behaviour of the three-phase contact line. Furthermore, *Multiscale Boiling* is designed to quantify the effect of external forces on the bubble dynamics, such as a shear flow or an electric field in the regimes not accessible on other platforms. The hardware is being developed by Airbus Defence and Space (in Friedrichshafen) under ESA contract.

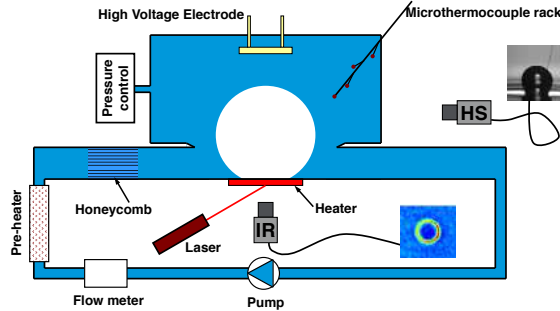


**Figure 3:** Schematic of the boiling cell of the *Multiscale Boiling* experiment

#### Heat Transfer Hosts

To allow a relatively simple implementation of fundamentally similar two-phase flow loops with moderately complicated measurement techniques, the concept of a series of *Heat Transfer Hosts* was proposed and its study was being set up at the time of the preparation of the present abstract.

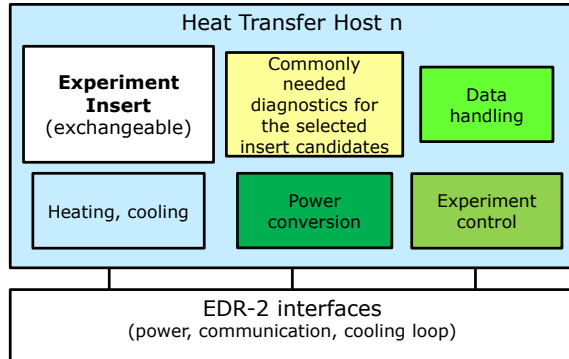


**Figure 4:** Conceptual schematic of the Heat Transfer Hosts

Installed into the EDR-2, one at a time, each Heat Transfer Host will provide for heating and cooling of the test cells of interchangeable flow loops serving the Heat Pipes, EVAPORATION, CONDENSATION and BOILING research projects. The facilities will also host (primarily optical) diagnostics commonly required by the target group of insert candidates. The experiment inserts are associated to the various Heat Transfer Hosts based on commonalities between their requirements. The philosophy is depicted in Figure 4.

At the time of the preparation of the present abstract the below listed 10 experiment candidates were considered as potential users:

- Insert candidates of Heat Transfer Host 1:

- *Enhanced Evaporators* targets global heat transfer performance characterisation of multi-scale evaporator structures. Evaporation regimes, wetted area and consequently the three-phase contact line would be characterised together with the critical heat flux (boiling limit) in a capillary pumped loop.

- *Pulsating Heat Pipes* aims at transient and steady Pulsating Heat Pipe thermal performance studies, flow pattern analysis and local pressure fluctuation with various working fluids and geometries exploring also inertia dominated regimes in large hydraulic diameter tubes.

- *Self-rewetting Fluid* targets the assessment of the heat transfer performances of self-rewetting liquid mixtures, with particular attention to the vapour-liquid interface temperature, the local liquid composition and liquid film thickness distributions as well as film stability and the dry patch formation. The effect of substrate characteristics and different mixtures would be tested in dedicated inserts.

- Insert candidates of Heat Transfer Host 2:

- *Drop Evaporation* would investigate thermocapillary convection and vapour diffusion processes as well as the effect of electric field on a series of volatile sessile drops.

- *Condensation on Fins* targets liquid film thickness distribution characterisation on a single axisymmetric condenser finger for average and local heat transfer coefficient assessment. Surface roughness and the test liquid are among the envisaged experiment parameters.

- *Marangoni in Films* aims to better understand heat transport to a volatile liquid film, through film thickness evolution and dynamics characterisation as well as the vapour concentration distribution. Surfactants are considered as a potential parameter.

- Insert candidates of future Heat Transfer Hosts:

- *Boiling* would assess the effect of confinement, shear flow and electric field on a vapour bubble. Particular mixtures and the investigation of non-condensable gas impact are among the most significant objectives.

- *Shear Driven Film* focuses on determining the heat transfer coefficient, liquid dynamics, film thickness evolution, stability and eventual dry spot formation in liquid films under shear flow influence up-to critical heat flux.

- *In-Tube Condensation* targets void fraction, flow regime and stability characterisation as well as heat transfer coefficient (distribution) measurements and film thickness measurements for annular flow regime in various shapes of tube cross sections.

- *Flow Boiling* aims at resolving the local heat transfer coefficient distribution in various flow regimes and correlate it with time resolved film thickness measurements and other flow characteristics.

Besides these candidates there may be room for other experiments to utilise the capabilities provided with the Heat Transfer Hosts.

#### References

Tóth B., Future Experiments to Measure Liquid-Gas Phase Change and Heat Transfer Phenomena on the International Space Station, *Microgravity Science and Technology*, Vol. 24, No. 3, pp 189-194 (2012)

## Real-time measurement of the shape of a 2d liquid surface

Antoine Philippe, Beghuin Didier, Boussemaere Luc, Ligot Renaud, Roblin Matthieu, Vanhaver Alexandre and  
Garin Yves

Lambda-X, Avenue Robert Schuman, 102, B-1401 Nivelles, Belgium  
pantoine@lambda-x.com

To be able to describe adequately the underlying physics of gas-liquid phase change experiments, the characterisation of the liquid film thickness distribution is essential. This requires measuring the 2D film thickness distribution. Time dependence of the distribution is also necessary to follow film evaporation and condensation.

We have developed a new experimental setup that addresses the multiple challenges corresponding to the real-time thickness measurement for space applications. These are listed hereafter:

- thickness measurement,
- large field of view,
- large angular acceptance,
- real-time measurement,
- simplicity of use,
- robustness to external perturbations,
- long working distance in view of containments
- compactness.

The main issue is the combination of all parameters that makes the instrument very challenging. In particular, all methods that require scanning of single or multiple parameters are incompatible with the real-time requirement. For instance, Fourier-domain optical coherence tomography or confocal chromatic sensor provides the thickness information in real-time but at a single position only. The 2D distribution requires repeating the measurement over the whole field of view. It is possible to integrate multiple sensors but this will only give access to the thickness information at a limited number of positions. In contrast, full-field time-domain optical coherence tomography provides 2D images but at a single depth. Therefore, vertical scanning is necessary to extract the height distribution.

The solution that has been chosen is a trade-off that we believe provides relevant information for scientific experiments. It is proposed to split the 2D height measurement into two simpler measurements: (i) 2D measurement of the shape of the gas-liquid interface, (ii) thickness measurement but at one or two positions only. We propose to measure 2D shape and absolute height with Fourier based deflectometry and with confocal chromatic sensor respectively. The two optical gauges are integrated in a single instrument that is illustrated in Figure 1.

Fourier based deflectometry is well adapted measuring the shape of the interface since it can be extracted from a single image. The proposed configuration is a reflective version of an instrument whose capability was previously demonstrated in transmission (Beghuin et al. 2010). The operating principle is to project a 2D grid close to the sample under test. The grid is imaged on a high resolution camera after reflection on the grid. The image of the grid is distorted when the grid projected at some distance of the

reflecting surface and when the surface is not normal to the optical axis. Distortion magnitudes are proportional to the deviation angles. As a consequence, the gradients of the surface are measured experimentally instead of the surface itself. The surface is then computed numerically from the gradients measured along two perpendicular directions. The principle of the method is illustrated in Figure 2. The sample is a corrugated mirror with local slopes that vary periodically over the mirror. As such deviation angles are position dependent and light rays collected by the imaging system are emitted from positions that depend on the deviation angles because the sample does not coincide with the plane conjugated with the grid. The projection system (MO1&MO3) and the imaging system (MO2&MO3) are made from two custom infinity-corrected objectives. The imaging system is telecentric thanks to the stop placed in the focal plane of the first objective. As such, only light rays that are reflected parallel to the optical axis, are collected by the imaging system. The diameter of the stop defines angular and spatial resolutions. The custom objective has been designed to achieve large angular acceptance (NA=0.15) over a large field of view (20mm). A fast camera achieves 100Hz acquisition speed at full resolution.

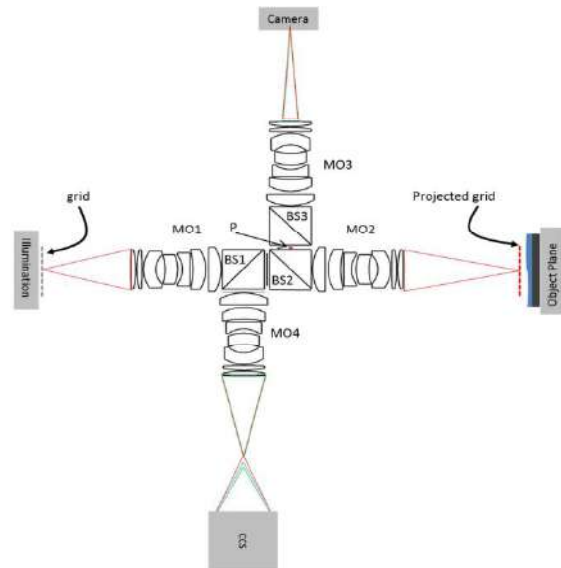


**Figure 1:** Experimental setup. The depicted objectives correspond to the actual custom design. CCS: confocal chromatic sensor, MO: microscope objective, BS, beam splitter, P: pinhole.

A commercial confocal chromatic sensor is integrated into the shape sensor to measure the absolute thickness at a single position. The beam generated by the confocal chromatic sensor is imaged on the sample by means of two infinity-corrected objectives (MO2&MO4). Re-imaging the output of the confocal chromatic sensor also offers a longer working distance required for space applications.

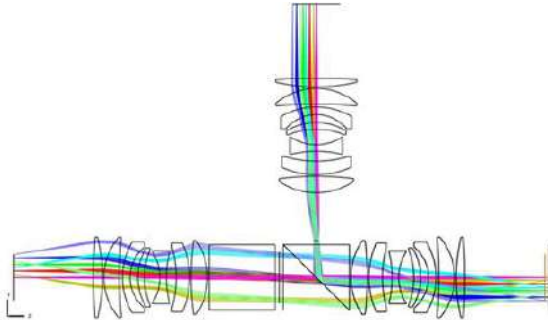


**Figure 2:** Illustration of the Fourier based deflectometry with a corrugated mirror as sample

The optical principles of the proposed instrument and experimental results will be discussed in details during the conference.

This research is supported by the European Space Agency (ESA Contract No. 4000113074/14/NL/KML).

#### References

Didier Beghuin, Xavier Dubois, Luc Joannesc Xavier Hutsebaut, Philippe Antoine, Interferometric precision with Fourier-based deflectometry. Proc. SPIE 7718, Optical Micro- and Nanometrology III, 77180B (2010).

## Experimental Study of Subcooled Flow Boiling Heat Transfer on Micro-pin-finned Surfaces in Short-Term Microgravity

Bin Liu<sup>1</sup>, Yonghai Zhang<sup>1\*</sup>, Jianfu Zhao<sup>3,4</sup>, Jinjia Wei<sup>1,2,\*</sup>, Xin Kong<sup>2</sup>, Zhizhu Cao<sup>1</sup>, Yueping Deng<sup>2</sup>

<sup>1</sup>School of Chemical Engineering and Technology, Xi'an Jiaotong University, Xi'an 710049, China

<sup>2</sup>State Key Laboratory of Multiphase Flow in Power Engineering, Xi'an Jiaotong University, Xi'an 710049, China

<sup>3</sup>Key Laboratory of Microgravity (National Microgravity Laboratory)/CAS, Institute of Mechanics, Chinese Academy of Sciences, Beijing, 100190, China

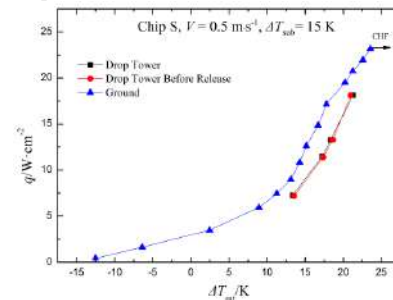
<sup>4</sup>School of Engineering Science, University of Chinese Academy of Sciences, 19A Yuquan Rd, Beijing, 100049, China  
E-mail: zyh002@mail.xjtu.edu.cn; jjwei@mail.xjtu.edu.cn

The flow boiling heat transfer characteristics of subcooled air-dissolved FC-72 on heated micro-pin-finned surfaces were studied in microgravity by utilizing the drop tower facility in Beijing, and the duration of drop tower is about 3.6 s. The dimension of the heater is  $40 \times 10 \times 0.5 \text{ mm}^3$  (length  $\times$  width  $\times$  thickness), which was combined with two silicon chips with the dimension of  $20 \times 10 \times 0.5 \text{ mm}^3$ . The micro-pin-fins with the dimension of  $30 \times 30 \times 60 \text{ }\mu\text{m}^3$  (width  $\times$  thickness  $\times$  height), named PF30-60, were fabricated on silicon chip by using the dry etching technique. The flow boiling heat transfer occurred in a rectangle channel with the across-section dimension of  $12 \times 3 \text{ mm}^2$ . For comparison, experiments of flow boiling heat transfer in terrestrial gravity were also conducted. High-speed visualization was used to supplement trends observed in the heat transfer and vapor-liquid two-phase flow characteristics. The effects of inlet velocity, micro-pin-fins on flow boiling heat transfer as well as the characteristics of vapor-liquid two-phase flow were explored.

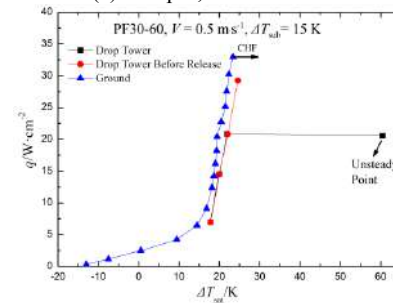
As is well known, flow boiling can provide a practical and effective means to preventing the formation of massive bubbles by relying on liquid inertia to flush discrete bubbles away from the heated wall and sustain liquid replenishment of the wall. But, while the effectiveness of flow boiling might seem quite obvious, supporting experimental evidence is very limited, given that very few studies have been dedicated exclusively to flow boiling CHF in  $\mu\text{g}$  (microgravity). Ohta (1997) obtained limited flow boiling CHF data in  $1\text{g}$  (normal gravity) at high inlet quality, but noted that they could not measure CHF accurately in the absence of local wall temperature measurements along the heated wall. Ma and Chung (2001) investigated subcooled flow boiling of FC-72 across a heated 0.254 mm platinum wire in a 2.1s drop tower. They measured a substantial shift in the  $\mu\text{g}$  boiling curve to lower heat fluxes compared to  $1\text{g}$ , indicating significant reduction in heat transfer effectiveness. CHF was also significantly lower in  $\mu\text{g}$ . However, differences in both heat transfer rate and CHF between  $\mu\text{g}$  and  $1\text{g}$  decreased with increasing flow rate.

Figure 1 shows flow boiling curves of chip S and PF30-60 under different gravity levels at atmosphere pressure. The  $\Delta T_{\text{sat}}$  represents wall superheat which is the difference between  $T_w$  and  $T_{\text{sat}}$ . The heat flux is calculated by the heating voltage  $U$  and heating current  $I$ . As shown in Fig.1 (a)-(b), the CHF of Chip S and PF30-60 with inlet velocity of  $0.5 \text{ m}\cdot\text{s}^{-1}$  are  $23.2 \text{ W}\cdot\text{cm}^{-2}$  and  $33.0 \text{ W}\cdot\text{cm}^{-2}$  under terrestrial gravity, respectively. However, we can not capture the CHF point accurately in microgravity, and for Chip S, the highest heat flux conducted in microgravity is about  $18.1$

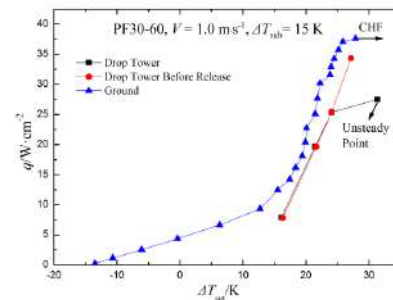
$\text{W}\cdot\text{cm}^{-2}$  at  $V = 0.5 \text{ m}\cdot\text{s}^{-1}$ , which is about 78% of the CHF in normal gravity. For PF30-60, the highest heat flux conducted in microgravity is about  $25.4 \text{ W}\cdot\text{cm}^{-2}$  at  $V = 0.5 \text{ m}\cdot\text{s}^{-1}$ , but it has reached CHF according to experimental results, and thus the CHF point can be inferred between 20.9 and  $25.4 \text{ W}\cdot\text{cm}^{-2}$ , which is 63.2%-76.8% of the CHF in normal gravity. It's obvious that the absence of gravity deteriorates the performance of flow heat transfer in the high heat flux region. Whereas, there is no obvious difference of heat transfer performance between microgravity and terrestrial gravity except for CHF.



(a) Chip S,  $V = 0.5 \text{ m}\cdot\text{s}^{-1}$



(b) PF30-60,  $V = 0.5 \text{ m}\cdot\text{s}^{-1}$



(c) PF30-60,  $V = 1.0 \text{ m}\cdot\text{s}^{-1}$

**Figure 1:** Boiling curves of Chip S and PF30-60

The effects of inlet velocity were also investigated on micro-pin-finned surface. As shown in Fig.1(b)-(c), CHF increases when the inlet velocity increases from  $0.5 \text{ m}\cdot\text{s}^{-1}$  to  $1.0 \text{ m}\cdot\text{s}^{-1}$  in normal gravity. In microgravity, the highest heat flux conducted in microgravity is about  $34.6 \text{ W}\cdot\text{cm}^{-2}$  at  $V = 1.0 \text{ m}\cdot\text{s}^{-1}$ . From the visualization investigation of the experiment with the heat flux  $34.6 \text{ W}\cdot\text{cm}^{-2}$ , it can be inferred that  $34.6 \text{ W}\cdot\text{cm}^{-2}$  is very close to CHF under microgravity environment. Hence, the CHF point can be inferred between  $25.3\text{-}34.6 \text{ W}\cdot\text{cm}^{-2}$ , which is 67.5%-92.0% of the CHF in normal gravity. Consequently, we can conclude that CHF increases with increasing inlet velocity in microgravity, meanwhile, the effects of buoyancy were reduced while the influence of inertia force enhanced. The inertia force becomes the dominant mechanism of flow boiling heat transfer.

Figure 2 shows the transition of the mean heater surface temperature and pressure drop of PF30-60 responding to the variation of gravity level for the heat flux of  $34.6 \text{ W}\cdot\text{cm}^{-2}$  at  $V = 1.0 \text{ m}\cdot\text{s}^{-1}$ . Figure 3 shows the arrangement of four thermocouples. As shown in Fig. 2, from upstream to downstream of the heated surface, the wall temperatures  $T_1\text{-}T_4$  increase gradually after entering the microgravity environment, which means the CHF occurs.

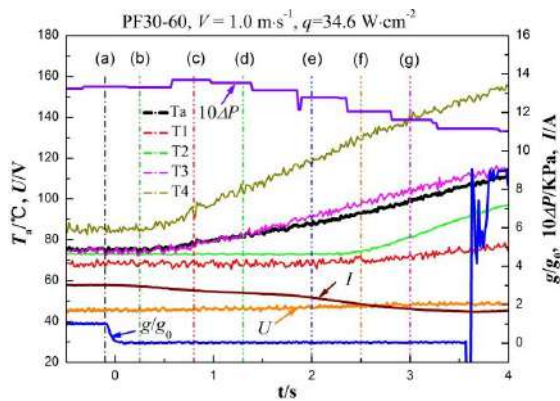


**Figure 2:** Variations of wall temperature, pressure drop and input heat fluxes on PF30-60 at different gravity levels

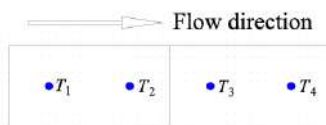


**Figure 3:** Arrangement of thermocouples

Figure 4 shows the evolution progress of two-phase flow characteristics. The positions of Fig. 4(a)–(g) are marked on Fig. 2. It should be noted that the time entering microgravity condition was set to 0s. A remarkable phenomenon is that the pressure drop is very sensitive to the behavior of two-phase flow pattern. The corresponding visual images in Fig. 4 also shows the relationship between pressure drop and the heat transfer performance of flow boiling as shown in Fig.2. The vapor-liquid two-phase flow pattern develops from bubble flow to wavy flow as transition from nucleate boiling to film boiling. As a result, the decrease of pressure drop is attributed to the decrease of friction of the gas-liquid interface caused by void fraction

reduction, and acceleration pressure drop due to the mass quantity decreases as the flow boiling heat transfer performance is deteriorated, while the increase of pressure drop at  $t = 0.6 \text{ s}$  may be attributed to the accumulation of bubbles caused by the transition from terrestrial gravity to microgravity.

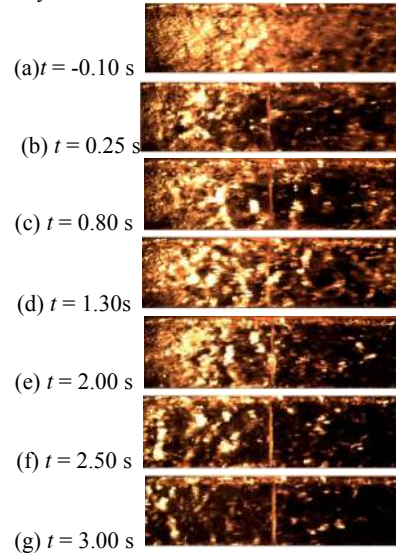


**Figure 4:** Visualization of PF30-60 at  $V = 1.0 \text{ m}\cdot\text{s}^{-1}$  and  $q = 34.6 \text{ W}\cdot\text{cm}^{-2}$

In general, the absence of gravity leads to the flow boiling heat transfer deterioration, but as inlet velocity increases, the influence of gravity on flow boiling heat transfer is weakened. CHF increases with increasing inlet velocity in microgravity. Whereas, there is no obvious heat transfer performance difference between microgravity and terrestrial gravity except CHF. It is found that there is a close relationship among the pressure drop, heat transfer and flow pattern of vapor-liquid two-phase flow in microgravity.

This work is supported by the project of National Natural Science Foundation of China (No.51506169, No.51636006, No.51611130060), and the scientific research program for new lecturer of Xi'an Jiaotong University (No.DW010728K000000B), and China Postdoctoral Science Foundation funded project (No.2015M582653).

## References

- Ohta H., Experiments on microgravity boiling heat transfer by using transparent heaters, Nucl. Eng. Des., Vol. 175 pp. 167–180 (1997)
- Ma Y., Chung J.N., An experimental study of critical heat flux (CHF) in microgravity forced-convection boiling, Int. J. Multiphase Flow, Vol. 27 pp. 1753–1767 (2001)

## Experimental investigation of submillimeter size droplet disruption in supersonic flow

Mikhail Ryabov, Oleg Gobyzov, Konstantin Inzhevatin and Artur Bilsky

Kutateladze Institute of Thermophysics Siberian Branch of Russian Academy of Science  
Lavrentiev st. 1, Novosibirsk, 630090, Russia  
ryabovmn@gmail.com

The process of droplet breakup in gas stream is widely spread in nature and in industrial applications. Nowadays this process is considered as a complex phenomenon that includes surface instability growth caused by aerodynamic impact, stabilization of droplet by surface tension forces, evaporation from droplet surface, boundary layer stripping e.t.c. Therefore, there is no complete theory to describe the process in general. There are a lot of experimental and theoretical investigations of these processes reported in papers. Most of them were conducted for droplet size of 1 mm and larger. Thus, submillimeter size droplet disruption processes still remain uninvestigated in general. This may be caused by complexity of such experiments. At the same time drops with size smaller than 1 mm are more common in practical applications, for example in liquid fuel atomization (Lasheras and Hopfinger 2000), steam turbine blade damage prevention (Ahmad et al. 2009) and cold spray processing (Dykhuizen and Smith 1998). Thus, it is important to reveal similarities and differences for processes with significantly various droplet sizes at similar  $We$ .

To describe the process of aerodynamic breakup two dimensionless criteria are commonly used. These criteria are Weber number ( $We$ ) and Ohnesorge number ( $Oh$ ). Weber number represents a ratio of disruptive aerodynamic forces to stabilizing surface tension forces. Ohnesorge number characterizes relation of viscosity force to surface tension force.

Varying the Weber number one can observe different scenarios of disruption leading to various droplet size distributions. A review on such scenarios was made by Pilch and Erdman (1987). However different papers report slightly varying range of  $We$  for the same scenarios. Such diversity may be caused by more complex correlation of disruption process and Weber number.

In the present work, a process of submillimeter droplet breakup due to gas stream impact are investigated. To provide such investigation a transonic gas stream seeded with liquid droplets was organized. Droplets Weber number in the flow varied from 10 up to 50 To observe a droplet breakup a set of optical diagnostic techniques was used.

Experimental setup is shown in Fig. 1. To provide continuous accelerating supersonic airflow a converging – diverging flat nozzle with Mach number of 1.6 was used. TO observe a disruption processes walls of the flat nozzle were made of transparent acrylic glass. Flat nozzle was operated in underexpanded regime. Spray nozzle (hollow tube) with inner diameter of 0.8 mm was employed to seed the airflow with liquid phase. Primary atomization of liquid jet issued from the tube completed at the distance of  $\sim 11$  mm downstream of the spray nozzle exit which was positioned in a converging area of flat nozzle. Primary jet atomization resulted in droplets with size distribution from 10 to 100  $\mu\text{m}$ . Distilled water was used as working liquid. For these liquid

type and droplet sizes an Ohnesorge number was much lesser than critical value of  $Oh = 0.1$  as stated by Pilch and Erdman. This means that surface tension force dominated over viscosity force in all range of sizes and droplet breakup could be fully described with  $We$ .

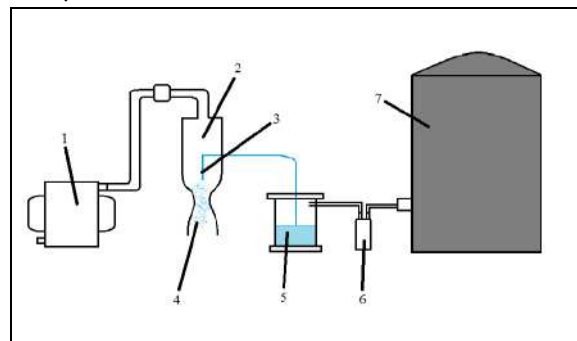


**Figure 1:** Experimental setup. 1 – turboprop engine, 2 – transition area, 3 – spray nozzle, 4 – transonic nozzle, 5 – liquid tank, 6 – flowmeter, 7 – gas tank.

A set of optical diagnostic techniques used in experiments included shadowgraphy (SP) with high spatial resolution for detection of disruption scenarios and droplet size measurements, particle image velocimetry (PIV) for the air and droplets velocity measurements across nozzle and pressure sensitive paint (PSP) technique to detect pressure distribution in flat nozzle.

To fetch images of submillimeter droplet in a supersonic flow a high spatial resolution and short exposure of the recording system were required. This was achieved by using 4 mpix scientific grade CCD – camera and illuminating system based on Nd :YAG pulse laser. Time of pulse was 5 ns. Camera was equipped with an Infinity K2/SC long distance microscope that provided magnification of 4.3 : 1 ( $\sim 1.6 \mu\text{m}/\text{pix}$ ) at distance of  $\sim 200$  mm from measurement area. Same devices were used both in PIV and SP measurements.

Experimental SP images were captured at different frame delays in dual – frame image acquisition mode. A single pair of frames contained a large number of droplet disruption samples. Analysis of experimental images revealed that initially spherical droplets exposed to airflow disrupted through mechanisms in general already mentioned in literature. For example, Fig. 2 demonstrates “bag breakup” regime. Frame delay was 2800 ns. Scale is presented on the image.

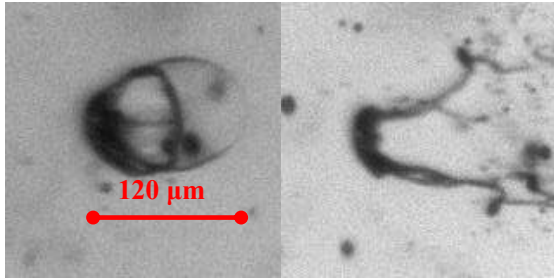


**Figure 2:** "Bag breakup".

However, disruption scenarios had some features not common for larger droplets. Thus, «bag breakup» regime resulted in formation of several liquid ligaments instead of generation of large number of droplets with smaller size after «bag» disruption. These ligaments together with rim formed a fiber that disrupted through a «vibrational breakup» subsequently.

Among already known scenarios two new regimes were also found. The first one was a «multiple bag breakup» regime ( see Fig. 3). In this regime a liquid rim was enveloped within set of «bag» domes one beside another. This might be caused by existence of transversal speed gradient that resulted in initial «bag» separation. The same mechanism at  $We = 34$  was described by Cao et al (2007).

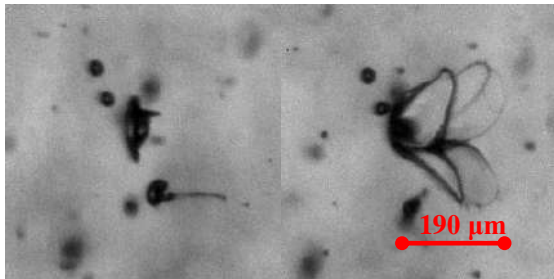


**Figure 3:** "Multiple bag breakup". Frame delay of 2800 ns.

Another mechanism found was a regime with «long fiber» formation that is shown in Fig. 4. This regime can be considered both as elongated «vibrational breakup» or disruption of ligaments formed during «bag breakup» and detached from the liquid rim. This regime resulted in formation of droplets with size compared to several «fiber» diameters.

A critical Weber number below which was no evidences of droplet disruption was of  $\sim 23$ . That value must be associated with droplet size of  $\sim 50 \mu\text{m}$ . At higher  $We$  droplets disrupted mainly through «vibrational breakup» and «bag breakup». Moreover, these regimes occurred for the same Weber numbers. Droplets with size larger than critical presented across the investigation region that means a disruption processes were of statistical nature. In general,  $We$  values of disruption processes for present work were slightly larger than mentioned in papers. This discrepancy can be explained by surface tension force growth on such scale.

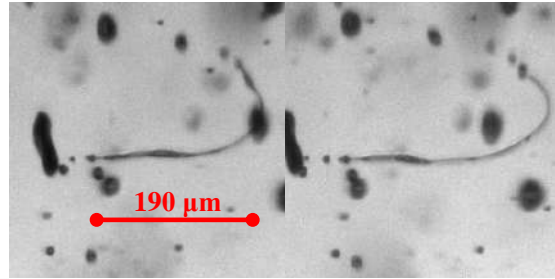


**Figure 4:** "Long fiber". Frame delay of 1500 ns.

## References

Lasheras J.C., Hopfinger E.J. Liquid jet instability and atomization in a coaxial gas stream, *Ann. Rev. Fluid Mech.*, Vol. 32, pp. 275 – 308 (2000).

Joseph D.D., Belanger J., Beavers G.S. Breakup of a liquid drop suddenly exposed to a high-speed airstream, *International Journal of Multiphase Flow*, Vol. 25, pp. 1263–1303 (1999)

Ahmad M., Casey M., Surken N. Experimental assessment of droplet impact erosion resistance of steam turbine blade materials, *Wear*, Vol. 267, pp. 1605 – 1618 (2009)

Dykhuisen R.C., Smith M.F. Gas dynamic principles of cold spray, *Journal of Thermal Spray Technology*, Vol. 7, No. 2, pp. 205-212 (1998).

Pilch M., Erdman C. A. Use of breakup time data and velocity history data to predict the maximum size of stable fragments for acceleration-induced breakup of a liquid drop, *Int. J. Multiphase Flow*, Vol. 13, No. 6, pp. 741-757 (1987).

Xian-Kui Cao, Zhi-Gang Sun, Wei-Feng Li, Hai-Feng Liu, Zun-Hong Yu. A new breakup regime of liquid drops identified in a continuous and uniform air jet flow, *Physics of Fluids*, Vol. 19 (2007).

## Levitation and self-organization of liquid microdroplets over dry heated substrates

Dmitry V. Zaitsev<sup>1</sup>, Dmitry P. Kirichenko<sup>1</sup>, Vladimir S. Ajaev<sup>1,2</sup>, Oleg A. Kabov<sup>1</sup>

<sup>1</sup>Kutateladze Institute of Thermophysics, Novosibirsk 630090, Russia, [zaitsev@itp.nsc.ru](mailto:zaitsev@itp.nsc.ru)

<sup>2</sup>Southern Methodist University, Department of Mathematics, Dallas, Texas 75275, USA

Levitating droplets of liquid condensate are known to organize themselves into ordered arrays over hot liquid-gas interfaces (Fig. 1). The mechanism of levitation is the Stokes force acting onto a drop from the flow originated at the interface, as discussed in Fedorets et al. (2011).

We report experimental observation of levitation and self-organization of liquid microdroplets over a *dry* heated solid surface. The sketch of the experimental set-up is shown in Fig. 2. The substrate is a copper block heated from below. In order to achieve pinning of the contact line at the substrate, the working surface was rough with the root mean square (RMS) roughness of 0.50  $\mu\text{m}$ . The surface temperature of the block  $T_w$  is measured by thermocouples at several points. Degassed ultra-pure water (Merck Millipore) is used as the working liquid. Optical recording is made at 5400 fps using a high-speed CCD camera equipped with a microscope objective of high resolving power (spatial resolution of 0.781  $\mu\text{m}$  per pixel). In experiment, working liquid is deposited with a syringe onto the substrate to form a liquid layer of the initial thickness of 0.40 mm. With a short pulse of air jet a dry spot (about 0.5-1 mm in size) is formed on the copper surface. The heater is then switched on, resulting in evaporation and formation of droplet array over liquid surface, Fig.1. When the array moves to the dry spot, the droplets continue to levitate over the solid dry surface, Fig. 3. Even though the life-time of the array is shorter over the dry surface, its geometric characteristics are remarkably similar to the case of droplets levitating over liquid-gas interface, Fig. 1.

A simple model is developed that explains the levitation over the solid substrate by the reflection of the flow created by the evaporating droplet off the substrate, Zaitsev et al. (2017). Dependence of the relative height of droplet levitation  $\hat{h} \equiv h/R$  on the dimensionless radius of the droplet is shown in Fig. 4 (experiment and theory). It is seen that above  $\hat{h} \sim 2$  the experimental data are in very good quantitative agreement with the model predicting power law  $\hat{h} \sim R^{-3/2}$ . At  $\hat{h} \sim 2$ , a crossover to a different regime is observed. In this regime, the geometry is similar to the one used in studies of Leidenfrost droplets, so the distance between the droplet and the wall is the key parameter; this distance ( $h - R$ ), scaled by  $R$ , is plotted in the inset of Fig. 4 and follows the power law  $\hat{h} - 1 \sim R^{-2}$ .

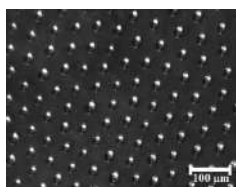


**Figure 1:** Array of levitating droplets over liquid-gas interface viewed from the top,  $T_w = 85^\circ\text{C}$ .

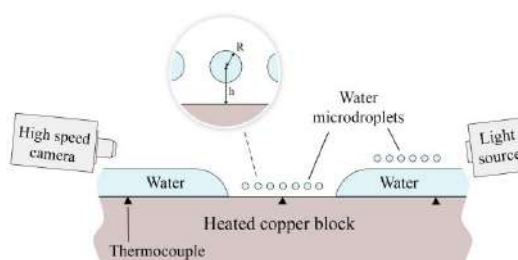


**Figure 2:** Sketch of experiment with definition of  $h$  and  $R$ .

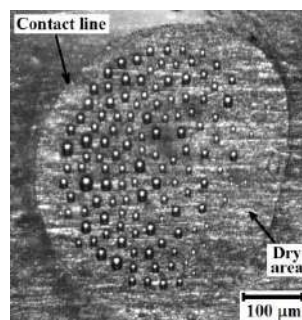


**Figure 3:** Array of levitating droplets over dry surface viewed from the top,  $T_w = 85^\circ\text{C}$ .

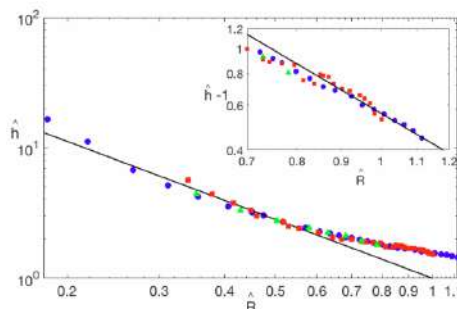


**Figure 4:** Comparison between experiment (three different droplets at  $T_w = 85^\circ\text{C}$ ) and theory (solid line) for droplets levitating over dry substrate; inset illustrates the power law corresponding to Leidenfrost-type situation at lower heights.

### References

- Fedorets A. A., Marchuk I. V. and Kabov O. A., *Technical Physics Letters*, Vol. 37, pp. 116-118 (2011)
- Zaitsev D.V., Kirichenko D.P., Ajaev V.S., Kabov O.A., *Physical Review Letters* (to appear in 2017)

## Three-dimensional Numerical Simulation of Thermocapillary Convection of Low Prandtl Number Fluid in a Deep Annular Pool with Surface Heat Dissipation

Li Zhang, You-Rong Li, Li-Na Liu and Chun-Mei Wu

Key Laboratory of Low-grade Energy Utilization Technologies and Systems of Ministry of Education,  
College of Power Engineering, Chongqing University, Chongqing 400044, China  
E-mail: liyourong@cqu.edu.cn

In the past few decades, thermocapillary convection has received much attention from both fundamental and industrial aspects. Many scholars have been focused on thermocapillary convection of the liquid pool with an adiabatic free surface, and achieved fruitful results (Smith and Davis 1983, Sim et al. 2003, Li et al. 2004). However, as a matter of fact, due to the non-equilibrium effect on the free surface, surface heat dissipation of the liquid layer is inevitable and is also a common thermal process in engineering fields, which has significantly effect on thermocapillary convection of the liquid layer, especially in microgravity-related fluid science and in semiconductor single-crystal growth from melt (Yan et al. 2008, Zhu and Liu 2010). However, thermocapillary convection with surface heat dissipation in an annular pool subjected to a horizontal temperature gradient is few investigated. Surface heat dissipation is bound to change the temperature distribution along the free surface and impacts on the flow patterns and the critical value of the flow bifurcation. There are many kinds of surface heat dissipation, such as convective and radiative heat transfer, and the evaporative cooling etc. This paper presents a series of three-dimensional numerical simulations on thermocapillary convection of the low Prandtl number in a deep annular pool with different specified temperatures at the inner and outer cylinders when surface heat dissipation is taken into account.

A deep annular pool with inner radius  $r_i$ , outer radius  $r_o$ , and depth  $d$  is filled with the low Prandtl number fluid. The radius ratio of the annular pool is defined as  $\eta=r_i/r_o$  and the aspect ratio as  $\varepsilon=d/(r_o-r_i)$ , which are fixed at  $\eta=0.5$  and  $\varepsilon=1.0$ , respectively. The bottom is considered to be thermally adiabatic. On the free surface, the thermocapillary force and the heat dissipation are taken into account. For simplicity, it is reasonable to introduce the following assumptions: (1) fluid is an incompressible Newtonian fluid, whose physical properties are mostly considered as constant except the surface tension; (2) the velocity is small and the flow is laminar; (3) the free surface is flat and non-deformable; (4) the depth of the annular pool is invariable whether there is convective heat transfer or evaporation cooling on the free surface.

When Marangoni number is small, thermocapillary convection is the stable axisymmetric flow, which is called as basic flow. With the increase of Biot number, the radial temperature gradient on the free surface near the inner wall decreases obviously, therefore, the thermocapillary force weakens and the flow of the surface fluid slows down. Furthermore, the thermocapillary flow cell shrinks toward the outer wall.

With the increase of Marangoni number,

thermocapillary convection is enhanced. When Marangoni number exceeds a certain threshold value, three-dimensional disturbances are incubated and their amplitudes increase with time. Finally, the basic flow bifurcates to a three-dimensional stable flow pattern. Figure 1 shows distribution of the temperature fluctuation on the free surface, which is characterized by the straight spoke pattern. With the increase of Marangoni number, the number of the spoke is basically constant, however, the amplitude of the temperature fluctuation on the free surface increase gradually. Furthermore, they all depend on Biot number. With the increase of Biot number, the critical Marangoni number of the basic flow destabilization decreases and the the amplitude of the temperature fluctuation reduces.

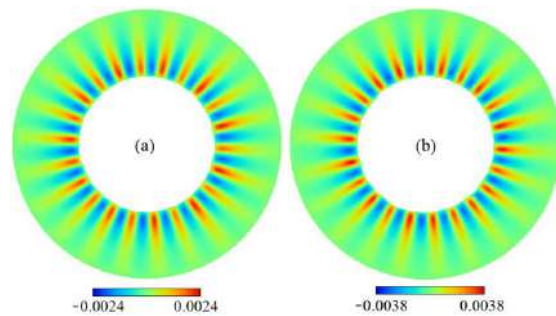


**Figure 1:** Temperature fluctuation on free surface at  $Bi=0$ . (a)  $Ma=300$ ; (b)  $Ma=500$ .

With the increase of Marangoni number, the three-dimensional stable flow bifurcates to a three-dimensional oscillatory flow. Figure 2 shows the distribution of surface temperature fluctuation and a space-time diagram (STD) of surface temperature along a circumference at  $R=1.5$  when  $Ma=600$  and  $Bi=0$ . In this case, the straight spoke pattern decays and emerges periodically, which does not propagate along the azimuthal direction and shows a standing wave type oscillation. This type of oscillatory flow is quite different from the hydrothermal waves appearing in the shallow annular pool (Sim et al., 2003; Li et al., 2004). With the increase of Biot number, the Marangoni number of three-dimensional stable flow destabilization to the oscillatory flow decreases and the oscillatory frequency has only slight variation.

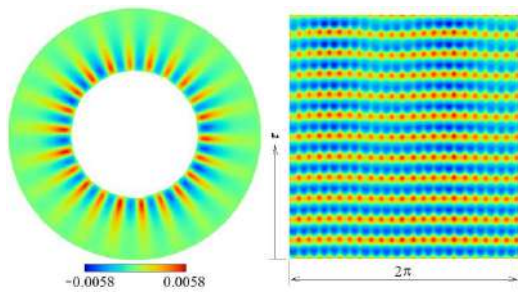


**Figure 2:** Temperature fluctuation (left) and STD (right) at  $R=1.5$  on free surface at  $Ma=600$  and  $Bi=0$ .

This work is supported by National Natural Science Foundation of China (Grant No. 11532015).

### References

- Smith M.K. and Davis S.H., Instabilities of dynamic thermocapillary liquid layer, *Journal of Fluid Mechanics*, Vol. 132 pp. 119-143 (1983)
- Li Y.R., Imaishi N., Azami T. and Hibiya T., Three-dimensional oscillatory flow in a thin annular pool of silicon melt, *Journal of Crystal Growth*, Vol. 260 pp. 28-42 (2004)
- Sim B.C., Zebib A. and Schwabe D., Oscillatory thermocapillary convection in open cylindrical annuli. Part 2. Simulations, *Journal of Fluid Mechanics*, Vol. 491 pp. 259-274 (2003)
- Yan J., Liu Q.S. and Liu R., Coupling of evaporation and thermocapillary convection in a liquid layer with mass and heat exchanging interface, *Chinese Physics Letters*, Vol. 25 pp. 608-611 (2008)
- Zhu Z.Q. and Liu Q.S., Coupling of thermocapillary convection and evaporation effect in a liquid layer when the evaporating interface is open to air, *Chinese Science Bulletin*, Vol. 55 pp. 233-238 (2010)

## Synthesis of silicon oxide micropores on the copper substrate with SiO<sub>2</sub> interlayer

Evgeniy Baranov, Sergey Khmel, Alexandr Zamchiy and Evgeniy Shatskiy

Kutateladze Institute of Thermophysics SB RAS  
Ac. Lavrentiev ave. 1, 630090, Novosibirsk, Russia  
itpbaranov@gmail.com

Nanostructuring of the surface, which is used for the processes of boiling, is a promising technology. Most often, monocrystalline silicon wafers are used for nanostructuring. But copper heaters are may be more promising and these heaters with silicon nanostructures are very interesting system. In addition, one of the important properties of nanomodification is a change of the surface wettability. In this paper, we synthesized array of aligned "micropores" from silicon oxide nanowires on the copper substrate with a silicon oxide (SiO<sub>2</sub>) intermediate layer. The morphology for the synthesis time 2 minutes 30 seconds and 5 minutes was obtained. The contact angle for the nanostructures was measured.

Silicon oxide nanowires were synthesized from mixture monosilane-argon with gas diluent hydrogen by gas-jet electron beam plasma CVD method by Zamchiy and Khmel (2014). Oxygen (3 sccm) was supplied directly into the vacuum chamber. The synthesis was carried out on the copper substrate with tin film mass thickness about 60 nm. The tin film was deposited by thermal vacuum deposition and the SiO<sub>2</sub> film was deposited by magnetron sputtering. The process of nanowire synthesis on the substrate with the catalyst consists of three stages: heating up to operating temperature, treatment of hydrogen plasma and the actual growth of nanowires by vapor-liquid-solid (VLS) mechanism. The synthesis temperature was 330°C.

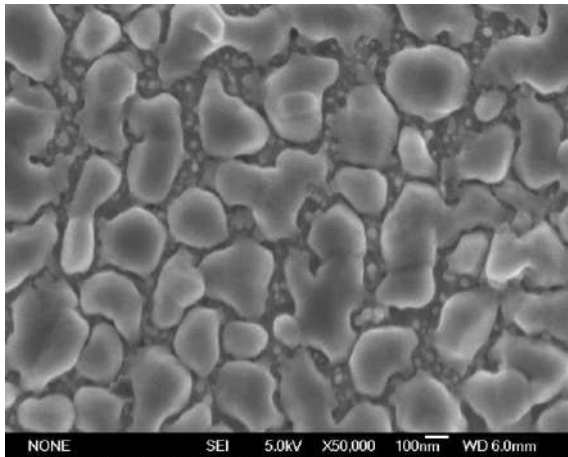


**Figure 1:** SEM image of tin film on the copper substrate without SiO<sub>2</sub> interlayer.

The surface morphology was determined by the methods of scanning electron microscopy (SEM) using the JEOL JSM-6700F microscope. The contact angle of the sample with water was measured by DSA-100 KRUSS

device with high-precision system of liquid supply with a minimal dosing step of 0.1 mcl.

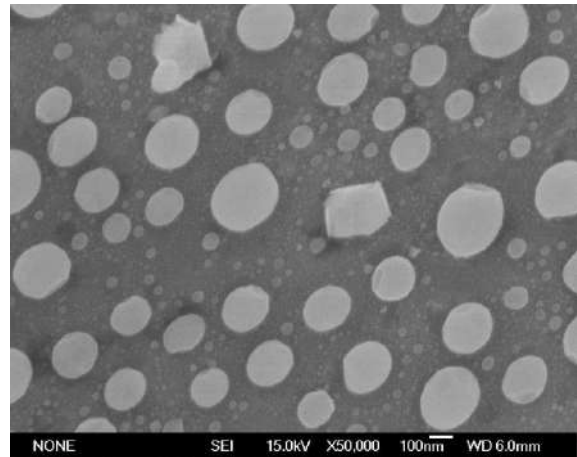


**Figure 2:** SEM image of tin film on the copper substrate with SiO<sub>2</sub> interlayer.

The Fig. 1 shows the SEM image of the tin film on the copper substrate. It is seen that the tin wets the surface. Individual particles with a typical size of 500 nm do not have a fixed shape. Synthesis of the silicon oxide nanowires array does not occur on this catalyst.

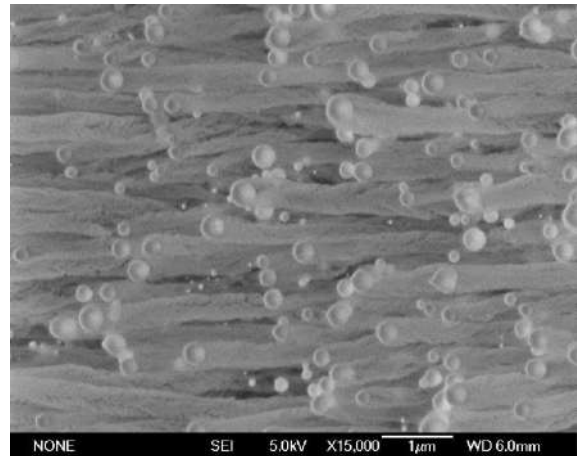


**Figure 3:** SEM image of the silicon oxide nanowires array for deposition time 5 min.

To solve this problem, it was decided to deposit the intermediate layer, which was supposed to have good adhesion with copper, and which is not wetted by tin. This intermediate layer was a silicon oxide with a thickness of 100 nm.

The Fig. 2 shows the SEM image of the Sn film on the SiO<sub>2</sub> interlayer after hydrogen plasma treatment. The treatment promotes reduction of oxide layers on the surface of tin particles. Since the temperature is above the melting point of tin and since the particles are liquid, they become a regular spherical shape. The particle size distribution is about 400–700 nm. X-ray EDS analysis showed the oxygen content in the catalyst particle about 3%.

The SEM image on the Fig. 3 shows of the silicon oxide nanowires array for deposition time 5 min. Each micropipe consists of numerous nanowires with average diameter about 15 nm. Nanowires bunch is on the bottom of the catalyst particle, whereas the nanowires are absent at the top of it. Length of micropipe was about 10 micrometer.

Reducing the time of synthesis to 2 min 30 sec resulted in a decrease in the length of the micropipe and changes in the morphology. As can be seen in the Fig. 4, the length of the micropipe has decreased to 1 micrometer. For single particles, the micropipe is divided into several separate tails.

Most likely, as the length of the micropipe increases, they begin to act on each other forming an ordered array.

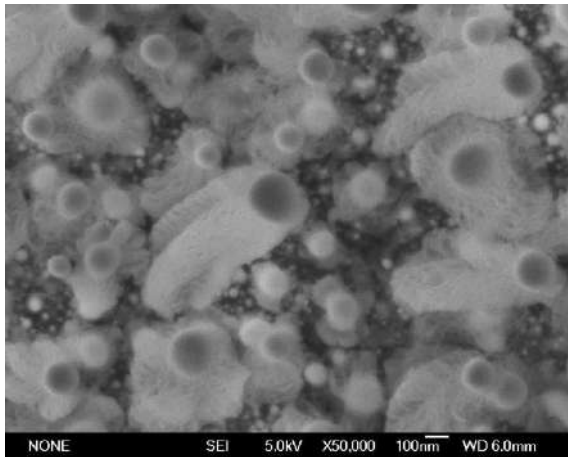


**Figure 4:** SEM image of the silicon oxide nanowires array for deposition time 2 min 30 sec.

Analysis of the photograph of the water droplet on the silicon oxide nanowires grown on the copper substrate with SiO<sub>2</sub> interlayer shows the measured contact angle were for deposition time 5 min - 14° and for deposition time 2 min 30 sec - 10°. This confirms that the surface of the silicon oxide nanowires array, synthesized in this work, is hydrophilic in nature. In addition, it was observed that the droplets on the surface have a very large imbibition layer. We assume that water penetrates easily into grooves constituting the relief in the case of Cassie impregnating wetting.

#### Acknowledgements

The study was carried out by the grant of Russian Science Foundation (agreement no. 15-19-30038).

The authors thank Ekaterina Kirichenko for the contact

angles measurements.

#### References

A. Zamchiy, E. Baranov and S. Khmel, New approach to the growth of SiO<sub>2</sub> nanowires using Sn catalyst on Si substrate, *Physica status solidi (c)*, Vol. 11, p. 1397 (2014)

## Dependence of the critical characteristics of the stability of the evaporating liquid flow on the system geometry

Ilya Shefer

Siberian Federal University, Institute of Mathematics and Computer Science,  
Svobodny 79, Krasnoyarsk, 660041, Russia  
ilya.shefer@gmail.com

At the present time the microsystems of the fluidic thermostabilization are intensively developed. Flows of evaporating liquids within a gas flux are used in these systems. Elaboration of the technologies stimulates special interest to theoretical study of characteristics of two-layer flows of the "liquid-gas" type. Obtained theoretical results are the basis to modifications of the thermostabilization methods.

One way of defining conditions, guaranteeing the stability of the basic state of the working media in the systems is the modeling of the joint flow of an evaporating liquids and gas-vapor phase on the basis of an exact solution of the convection equations. Steady functioning is the one of the main conditions of the correct work of the setups. Solving of the problem stability of the basic flow allows one to specify crisis mechanisms, leading to appearing instabilities and to define manners of the suppression of the most dangerous perturbations.

The aim of the present study is to investigate the evaporative convection regimes, arising in a two-layer system, depending on thicknesses of the liquid and vapor-gas layer. Structure of the characteristic perturbations and influence of the thicknesses of the working media on threshold thermal loads are studied.

Dynamics and heat- and mass transfer processes in a two-layer system of liquid and gas are studied in the full problem statement taking into account evaporation at the interface. The stationary joint flow of liquid and vapor-gas mixture in a plane horizontal channel is described by the Boussinesq approximation of the Navier-Stokes equations:

$$\begin{aligned} u \frac{\partial u}{\partial x} + v \frac{\partial u}{\partial y} &= -\frac{1}{\rho} \frac{\partial p}{\partial x} + \nu \Delta u, \\ u \frac{\partial v}{\partial x} + v \frac{\partial v}{\partial y} &= -\frac{1}{\rho} \frac{\partial p}{\partial y} + \nu \Delta v + g(\beta T + \underline{\gamma C_s}), \\ \nabla \cdot \vec{u} &= 0, \\ \vec{u} \cdot \nabla T &= \chi(\Delta T + \underline{\delta \Delta C_s}), \\ \vec{u} \cdot \nabla C_s &= D \Delta C_s. \end{aligned}$$

Here  $\vec{u} = (u, v)$  is the velocity vector,  $p$  is the pressure,  $\rho$  is the density,  $T$  is the temperature,  $C_s$  is the vapor concentration in the gas phase,  $\vec{g} = (0, -g)$  is the gravity acceleration,  $\nu$  is the kinematic viscosity coefficient,  $\beta$  is the thermal expansion coefficient,  $\gamma$  is the concentration expansion coefficient,  $\chi$  is the coefficient of thermal conductivity,  $D$  is the coefficient of vapor diffusion and  $\delta$  is the coefficient characterizing the Dufour effect. The equations contain underlined terms which are taken into account in modeling the gas-vapor mixture motion. The energy equation includes additional term corresponding to the Dufour effect in the gas phase. The effect is appearance of the temperature gradient due to the concentration

gradient.

On the thermocapillary interface, remaining undeformed, the following conditions are imposed: kinematic and dynamic conditions, the heat transfer condition with a diffusive-type evaporation, continuity conditions for the velocity and temperature fields and the relation for the saturated vapor concentration. On the solid impermeable walls of the channel the no-slip conditions and the linear temperature distribution with respect to the longitudinal coordinate are to be valid. We assume absence of the transversal temperature drop, therefore the longitudinal temperature gradient  $A$  defines a type (heating or cooling) and intensity of the thermal load. Condition of zero vapor flux is imposed for the vapor concentration on the upper channel wall.

Exact solution of the considered conjugate problem were constructed in (Goncharova and Rezanova 2014) and has the following form

$$\begin{aligned} u_i &= u_i(y), \quad v_i = 0, \quad p_i = p_i(x, y), \\ T_i &= (a_1^i + a_2^i y)x + \theta_i(y), \quad C_s = (b_1 + b_2 y)x + \varphi(y). \end{aligned}$$

It allows one to model processes in the two-layer system and to estimate influence of the Dufour effect on characteristics of flows and features of concentration and temperature fields. The investigation of the flows topology was performed depending on longitudinal temperature gradient values on the outer walls of the channel, gravity and thicknesses of the media layers for the "HFE7100-nitrogen" system. Thicknesses of the liquid and gas-vapor layers are  $h_1$  and  $h_2$ , respectively. Conditions of appearance of the reverse flows and dependence of evaporation intensity on the problem parameters were specified.

Stability of the main flow with regard to infinitesimal perturbances were studied by the normal mode method. Influence of the intensity of thermal load, gravity and thicknesses of the media layers on character and a type of the arising perturbations is investigated numerically for the system «HFE7100-nitrogen».

Neutral curves in plane  $(\alpha, A)$  (for instance, see fig. 1) for different values of thicknesses of the media layers and gravity accelerations  $g$  were constructed (here  $\alpha$  is a wavenumber). The minimum of each neutral curve defines the critical thermal load and stability area bound. Maps of the instability regimes were obtained for the considered configurations. Classification of the most dangerous perturbations was performed.

Under the terrestrial conditions thermocapillary effect stabilizes the basic flow. In the system with fixed  $h_1$  with increasing thickness  $h_2$  threshold thermal load rises for the longwave disturbances, and vice versa, critical thermal load decreases for the shortwave ones (fig. 1).

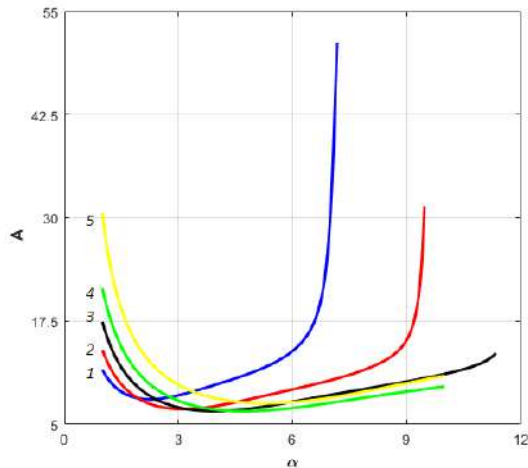


**Figure 1:** Neutral curves for system with  $h_1=3$  mm:  
1 –  $h_2=3$  mm, 2 –  $h_2=4$  mm, 3 –  $h_2=5$  mm,  
4 –  $h_2=6$  mm, 5 –  $h_2=7$  mm.

If  $h_2$  is fixed then increasing thickness  $h_1$  results in essential destabilization of the flow (fig. 2).

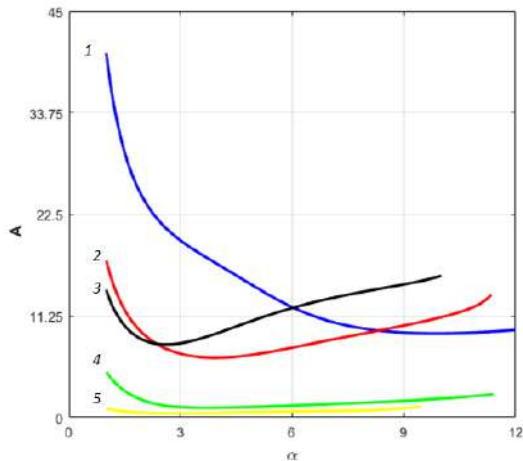


**Figure 2:** Neutral curves for system with  $h_2=5$  mm:  
1 –  $h_1=2$  mm, 2 –  $h_1=3$  mm, 3 –  $h_1=4$  mm,  
4 –  $h_1=5$  mm, 5 –  $h_1=6$  mm.

Conditions of co-existence of the thermocapillary and convective mechanisms of instability were specified. Tables of critical values of the longitudinal temperature gradients and critical wave numbers were obtained for different configurations ( $h_1, h_2$ ).

Typical forms of the most dangerous perturbations for all considered configurations were defined (see, for instance, fig. 3).

Influence of variations of the gas-vapor layer thickness on the characteristics of the basic flow and on critical thermal loads is weaker than changes of the liquid layer thickness. Therefore, we can effectively control suppression of instabilities in a two-layer system with evaporation with help of changes of the liquid layer thickness.

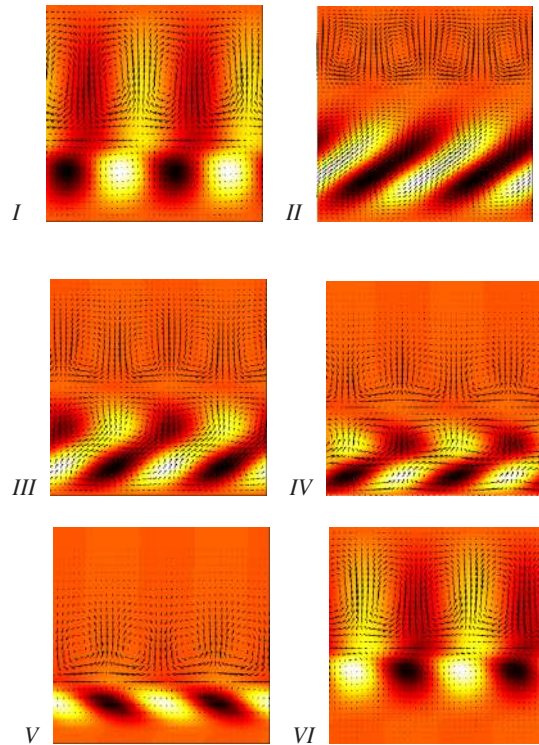


**Figure 3:** Typical patterns of the most dangerous perturbations under the terrestrial conditions: *I* – vortex structures, *II* – deformed convective cells, *III* – two-cell structures, *IV* – chessboard structures, *V* – deformed thermocapillary structures, *VI* – thermocapillary structures.

This work was partially supported by the Russian President Grant MK-4519.2016.1.

## References

Goncharova O.N., Rezanova E.V., Example of an exact solution of the stationary problem of two-layer flows with evaporation at the interface, *J. Applied Mechanics and Technical Phys.*, Vol. 55 pp. 247-257 (2014)

## Structure of gels layers with cells

Boris Pokusaev, Sergey Karlov, Andrey Vyazmin, Dmitry Nekrasov, Nikolay Zakharov, Vyacheslav Reznik,  
Dmitry Khramtsov, Dmitry Skladnev

Moscow Polytechnical University, Department of Chemical Engineering,  
ul. Staraya Basmannaya 21/4, Moscow, 105066, Russia  
pokusaev2005@yandex.ru, av1958@list.ru

The idea of growing tissues and organs in vitro using stem cells is not new. However, in order to implement this idea, it is necessary to create special bioreactors which would be capable of maintaining the required temperature, pH level, osmotic pressure, supplying cells with nutrients and oxygen, removing their metabolic products as well as fulfilling many other requirements, which provides necessary physiological conditions for immobilized cells (Rodrigues et al. 2011). The use of the method of 3D additive manufacturing to create such tissues and organs from stem cells seems to be very promising (Marga et al. 2013). Currently gels are considered a high-potential structure-forming material for formation of artificial tissues from immobilized cells using the method of additive manufacturing.

In the construction of 3D-bioreactors the gels can be used in the capacity of a neutral coat of gels in which biological microscopic objects are cultivated. They allow nutrients and oxygen to penetrate into the growing medium and remove metabolic products and carbon dioxide. Considering that gels have microchannels, for instance, due to the leakage of gas bubbles, it is possible to significantly intensify the processes of nutrition of the cultivated microorganisms.

Agarose gel is a typical gel which is formed from the solution when the temperature is lowered. It is widely used in microbiology for growing of microbiological objects. Such gels have been thoroughly investigated (see, for example, Duckworth and Yaphe 1971), including by the optical methods (Rees et al. 1970). The following aspects has been studied: structure of links which are formed in the disperse phase of gel formation, physical-chemical properties of gels; also, technology of generation for various use has been described by Santos (1990). Nevertheless, many properties of agarose gels which determine whether they may be used for the creation of bioreactors with the help of additive manufacturing require additional studying. The aim here is to carry out an investigation the "thin" structure and adhesion between gel layers applied upon one another in presence of immobilized cells.

For investigation two-layer gels system with immobilized cells the spectroscopic method is used. This method analyses the form of spectrum of transparent or reflected light of the sample.

An agarose-based gel "Chemapol" was used as a main gel during the experiments. It is known that gel properties can vary depending on their manufacturer. The gels used in the experiments were obtained by mixing agarose with distilled water with heating up to 90 °C by convectional and UHF methods. Agarose gels with 0.6–1.5 % of agarose were used in the experiments. In experiments related to immobilization in gels yeast cells *Yarrowia lipolytica* were

used as model eucariot biological object.

One of the objectives of the studies was development of methods and conditions, providing normal physiological state of living cells of a model biological object, immobilized in a volume of agarose gel. In the first phase of a suspension of yeast cells, grown in complete growth medium LB were immobilized in agarose gel with initial concentration of  $5 \times 10^6$  cells/mm<sup>3</sup>. It was important to determine how gel of various thicknesses influences growth of cells in different conditions, practically in conditions of different aeration. Due to formation of layered gels with additive technologies, it is important to know the basic regularities in the behavior of immobilized microorganisms within the gel and in close proximity to border between gel layers, filled only with the dispersion medium. Here is the fundamental answer to the question of whether immobilized gels spontaneously spread through border between gel layers, formed of agarose gels, including different concentrations.

Comparison photos of the two-layer gel system are presented, consisting of both sterile agarose gels with concentration of 0.6%, and the same system, when the upper layer contains encapsulated yeast cells (figure 1). Photos were taken 48 hours after the formation of two-layer systems. It is possible to notice that the gel with cells is much more turbid. Border between gel layers is also filled with the turbid substance and is blurred in the direction of the gel with the cells, whereas for a sterile system, it remains clear.

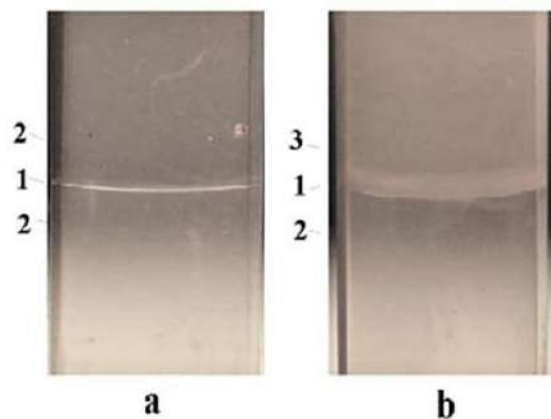


**Figure 1:** Comparison photos of the two-layer agarose gels without and with yeast cells. Notations: 1 – the interface of the gels; 2 - agarose gel with a concentration of 0.6%; 3 – the same gel with yeast cells.

Using a specially developed thin cuvette by visual observation it was found that the density of the yeast growth

remains unchanged in the volume of the agarose gel with a concentration of 0.6 % to a depth of 11-12 mm. The density of yeast growth increased with continued incubation in cuvettes up to 48 hours and its concentration is 10 times more compared with initial concentrations. It should be noted that during the cultivation of yeast in special cuvettes with layered top layer agarose gel with a concentration of 0.3% by weight (during modeling of usage of protection layer of liquid gel) the entire volume of the upper, the source of sterile liquid gel, also gradually filled with yeast cells. This indicates the ability of cells to overcome pre-formed boundary between gel layers in the direction of concentration changes for agarose gel of 0.6% to 0.3% by weight. This circumstance will require additional studies of the movement of specific living cells, designed specifically for 3D-bioprinting in the gels used for their cultivation, variety, and speed changing density.

Figure 2 shows the results of spectral sensing region adjacent to the boundary between gel layers for two-layer gel system formed by the gels with agarose concentration of 0.6% if the top layer of yeast cells (for gel cells distance is measured in the positive region). The measurements were carried out as one hour after the formation of such a system, and in 48 hours, which allows us to trace the spectral changes caused by the condition of the gel and immobilized yeast cells. Intensity values of light transmission were treated to an appropriate amount of sterile gel of the same concentration, measured immediately after its formation. A layer of gel containing the cells has a lower ability for passing light compared with sterile gel, due to the increasing light scattering on yeast cells which size is about 10  $\mu\text{m}$ .

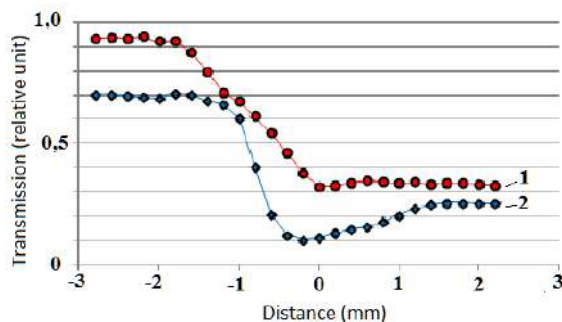


**Figure 2:** The time variation of the relative intensity of light transmittance of the layered gels with agarose concentration of 0.6% in the border areas of the distance to the boundary in the presence of the top layer of yeast cells. Visually observing the interface between the layers of the gels in the beginning of the experiment corresponds to a value of 0, with minus – without yeast (bottom layer), with a plus - with yeast (top layer). Notation of curves: 1 - within one hour after formation. 2 – after 2 days.

We had some differences in the dependency of relative intensity of light transmitted from a distance to border between gel layers. In a two-layer gel system with cells one hour after its formation is practically absent the minimum intensity of transmitted light, which is detected for distinct two-layer sterile system. The reason for this is that space between gel layers is filled by yeast cells in the process of formation. With increasing time of cell cultivation, such a minimum appears and becomes more and more noticeable,

while its width increases significantly in the part of the layer, in which yeast cells were introduced originally. The behavior of curve 2 in figure 2 resembles the change in concentration of a substance in a stationary environment when the diffusive mass transfers through the interface. It can be assumed that the mechanism of migration of cells from one environment to another via boundary between gel layers is presented.

It is important to note that the relative intensity of light transmittance through the layers of the gel after 48 hours it becomes lower than at the beginning of the process, and the gradient of its change from the sterile gel increases. The decrease in the intensity of light transmission explained from the standpoint of the self-seal dispersion medium in the gel when it is aging. This process takes place in both layers of the gel. However, the decrease in relative intensity for sterile gel is significantly more than that of the layer containing cells. This suggests that the observed pattern is caused by the penetration of yeast cells into sterile gel and the beginning of their reproduction and growth in it. Moreover, large gradient of relative intensity of light passing near the boundary shows that, initially, the yeast cells begin their reproduction and growth under sterile gel side boundary between gel layers.

Experimentally for cells of the yeast *Yarrowia lipolytica*, the possibility of their spontaneous transition from one layer agarose gel to another through the surface between gel layers filled dispersive medium was determined. This phenomenon occurs both when gel layers are of the same concentration and when concentration is drastically changes. This mechanism is similar to diffusion. However, it requires detailed examination with reference to a specific type of microorganisms and gels that are intended to use in the technology of bioprinting.

This work was supported by the Russian Science Foundation (project no. 15-19-00177).

## References

- Duckworth M. and Yaphe W. The structure of agar. Part I. Fractionation of a complex mixture of polysaccharides. Carbohydrate Research, Vol. 16, pp. 189–197 (1971).
- Marga F., Jakab K., Khatiwala C., Shepherd B., Dorfman S., Hubbard B., Colbert S. and Gabor F. Toward engineering functional organ modules by additive manufacturing. Biofabrication, Vol. 4. ID 02200 (2012).
- Rees D.A., Scott W.E. and Williamson F.B. Correlation of optical activity with polysaccharide conformation. Nature, Vol. 227, pp. 390-392 (1970).
- Rodrigues C.A.V., Fernandes T.G., Diogo M.M., da Silva C.L. and Cabral J.M.S. Stem cell cultivation in bioreactors, Biotechnol. Advances, Vol. 29, pp. 815–829 (2011).
- Santos G.A. A Manual for the Processing of Agar from Gracilaria. Manila: ASEAN/UNDP/FAO Regional Small-Scale Coastal Fisheries Development Project (1990).

## Thermal control system of the heat generating equipment using the two-phase circuit

Natalia M. Savchenkova, Artem C. Manukov

Department of Heat and Mass Transfer Process and Devices  
National Research University The Moscow Power Engineering Institute  
111250, Moscow, Krasnokazarmennaya str., 14  
Tel/fax.: (495) 362-70-40  
savchenkovanm@mpei.ru

One of the most important technical tasks for today is the development and implementation of highly efficient, reliable and compact thermal control systems. This task is due to the intensive development of space, aviation, electronic and other types of equipment.

Using of a two-phase boiling heat carrier allows a significant intensification of heat transfer in the cooling and thermal control systems of engines and power plants, of aircrafts, ensuring the thermal conditions of spacecrafts, cooling circuits for nuclear and solar power plants. In the contours of the oil system of aircraft engines, two-phase gas-liquid flow is a factor capable of qualitatively changing the nature of the flow and heat transfer, which is necessary for the design and operation of engines. In this connection, there is a need for such pump devices that could simultaneously work with both liquid and vapor phases of the coolant.

Cooling and heat stabilization of various equipment with the use of a two-phase heat carrier can be made as follows:

- using of loop heat pipes (LHP),
- using of two-phase circuits with mechanical pumps.

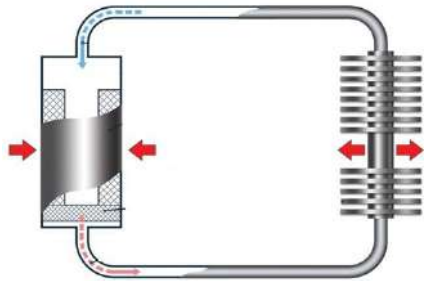


Figure 1: Principal scheme of Loop Heat Pipe

The main advantages of LHP are (Maidanik et al. 2006, Maidanik et al. 1992, Goncharov et al. 2011) the possibility of transferring heat to a distance of several meters for any orientation in the gravity field or more than several tens of meters in a horizontal position or in zero gravity, a maximum reduction in the distance of the fluid in the wick, no using of electricity and moving parts.

Because of the growing size and complexity of satellite platforms and the growing power demand conventional thermal control systems with Heat Pipes (HP) and Loop Heat Pipes (LHP) networks get to their limit. Two-phase Mechanically Pumped Loop is used the circulation of working fluid (van Es et al. 2016, Khalilil 2014). It is possible to distinguish several types of two-phase mechanical pumps the use of which has a number of advantages, in particular, increasing the reliability of the

whole system:

Centrifugal pump is a most common pump used in industries, agriculture, domestic applications, extensively for hydraulic transportation of liquids over short to medium distance through pipelines where the requirements of head and discharge are moderate.

Screw pump can be used as a two-phase pump for a long time, especially for transferring the two-phase flow with high amount of gas and in variable entrance conditions.

Piston pump is one of the simplest forms of the multi-phase pumps that using a big two-phase piston for compacting the mixture of gas-liquid.

Micromechanical piezo pumps of two types: membrane and peristaltic are used for precision pumping of liquid or gas (Križaj 2012, Bar-Cohen 2000).

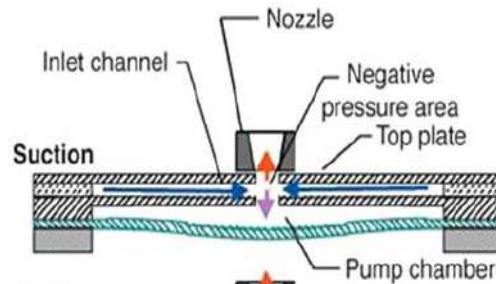


Figure 2: Scheme of membrane piezo pump

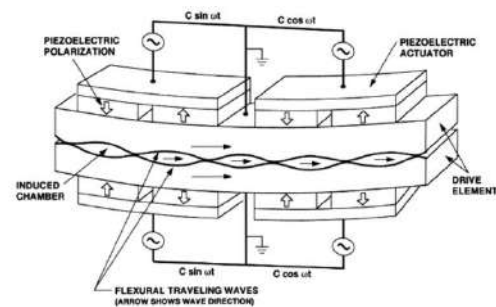


Figure 3: Scheme of peristaltic piezo pump

Advantages of piezo pumps before LHP following:

- The use of a piezoelectric pump will allow circulating the coolant at any orientation of the spacecraft.
- No problems with starting the circulation of the coolant.
- The contour is stable.

- The cost is cheaper
- The reliability of the thermal stabilization system is increased.

### **Conclusion**

It is necessary to consider the following factors to select the system of ensure the thermal regime of an object using different types of two-phase systems:

Reliability and efficiency of the system under given conditions;

The geometry of the object being serviced;

Cost of manufacture and operation.

### **References**

Maidanik Yu.,F. Achievements and prospects of the loop heat pipes, 4th Conference of Heat and Mass Transfer, Moscow, Russia (2006).

Maidanik Yu.,F., Fershtater Yu.G., Pastukhov, V.G., Goncharov, K.A. Zagar, O., and Golovanov, Yu., Thermoregulation of Loops with Capillary Pumping for Space Use, SAE Paper No. 921169 (1992).

Goncharov K., Kochetkov A., Luzhenkov V., Panin Yu. Loop heat pipe application for upper stage "Fregat-SB", International Aerospace Workshop, Los-Angeles, USA, (2011).

van Es J, van Gerner J.H., van Benthem R.C., Lapensée S., Schwaller D., Component Developments in Europe for Mechanically Pumped Loop Systems (MPLs) for Cooling Applications in Space, 46th International Conference on Environmental Systems, Vienna, Austria (2016).

Khalilil M., Shamsabadi A.A., Janaki M.M., Janaki D.M., Examination of Application and Function of Two-phase Pumps, Indian Journal of Science and Technology, Vol 7, No. 8, pp. 1060–1065 (2014).

Križaj D., Pečar B., Vrtačnik D., Resnik D., Možek M., Aljančič U., Dolžan T., Amon S., Analysis of Fluid Pumping with a Throttle Type Piezoelectric Micro Pump, COMSOL Conference, Milan, Italy (2012)

Yoseph Bar-Cohen and Zensheu Chang. Piezoelectrically Actuated Miniature Peristaltic Pump, SPIE's 7th Annual International Symposium on Smart Structures and Materials, CA. Paper No. 3992-103 (2000)

## Cooling of a microchannel with a thin evaporating liquid film sheared by dry gas

Kabova Yu.O.<sup>1</sup>, Kuznetsov V.V.<sup>2</sup>, Kabov O.A.<sup>1</sup>

<sup>1</sup>Institute of Thermophysics, SB RAS, 630090, 1 Lavrentyev prosp., Novosibirsk, Russia, [kabova@itp.nsc.ru](mailto:kabova@itp.nsc.ru)

<sup>2</sup>Lavrentyev Institute of Hydrodynamics, SB RAS, 630090, 15 Lavrentyev prosp., Novosibirsk, Russia  
[kuznetsov@hydro.nsc.ru](mailto:kuznetsov@hydro.nsc.ru)

Investigation of dynamics and evaporation of locally heated thin liquid films sheared by gas flow becomes one of the most important and most complicated problems in thermal physics, since it is concerned with the problem of cooling of microelectronic equipment (Hirokava et al. 2014, Nasr\* et al. 2017, Nasr et al. 2017). Modern microprocessor represents a flat surface consisting of zones with an inhomogeneous heat release (Mahajan et al. 2006). The shape of these zones is often close to rectangular one (Sri-Jayantha et al. 2008), and the size can range from a few hundreds of microns to several millimeters. The thermal-power density in hot zones ("hot spots") can reach 1 kW/cm<sup>2</sup> and differs from the average thermal-power density on the chip by 5-10 times. Such "hot spots" as well as the chip itself might be considered as a local heat sources. Spray cooling, boiling in microchannels, thermoelectric modules are just some examples of methods using to solve the problem of heat removal from small size hot zones. One of the promising solutions allowing to remove high heat fluxes is technology using processes with phase change, for example evaporation of a thin liquid film moving in a flat microchannel under the action of a gas flow, but thin films are subjected to rupture, which drastically reduces the efficiency of the apparatus and can lead to their breakdown. In addition to the thermocapillary effect one of the most important factors affecting the dynamics of the liquid film rupture and the formation of a dry spot in the region of local heating is evaporation (Lyulin et al. 2015). It is worth noting that, as a rule, liquid film is supposed to be sheared by the dry gas flow (Houshmand et al. 2013).

In the present work a joint motion of thin film of incompressible viscous liquid and gas in a microchannel is considered at different values of initial concentration of the liquid vapor in the gas phase taking into account the evaporation process. The microchannel is assumed to be unbounded in streamwise and spanwise directions. A part of wall at the side of liquid film is heated; temperature at the heater is prescribed. The coupled two-phase problem is simulated using a 3D nonstationary model. The transport processes in the liquid and in the gas phases are described by the Navier-Stokes, continuity and energy equations and diffusion equation in the gas phase. For the deformable gas-liquid interface the following boundary conditions are posed: the condition of continuity of the temperature (it is equivalent to the fact that we remain in the equilibrium thermodynamics) and the tangential components of the liquid and gas velocity vectors, the mass conservation condition, the dynamic condition with the term expressing the mechanical effect of the evaporated matter on the liquid, the thermal boundary condition and condition of local thermodynamic equilibrium. The upper wall is adiabatic and impermeable. The dynamic viscosity and surface tension are assumed to depend on temperature. The problem is transformed to specially developed new variables, so that continuity

equations in the liquid and in the gas retain their form in new variables but kinematic condition at the free interface simplifies and become linear. We employ the lubrication theory to derive reduced set of equations.

Major factors affecting the temperature distribution in the liquid and the gas phases are as follows: transfer of heat by liquid and gas flows, heat losses due to evaporation, diffusion heat exchange. These factors significantly affect each other and, by turn, are heavily dependent on the resulting temperature distribution. Previous investigations (Kabova\* et al. 2014, Kabova et al. 2014) have shown that the heat removal from hot spots is mainly determined by evaporation. Therefore, the intensification of the heat dissipation may be achieved by intensifying the evaporation.

An important difference from the previous works is a specification that incoming gas does not contain liquid vapor. Namely, previously (Kabova\* et al. 2014, Kabova et al. 2014) it was posed, so as for many problems with the diffusion evaporation, that the vapor concentration must be equal to the saturated concentration on the free interface (vapor concentration corresponding to the pressure of the saturated vapor).

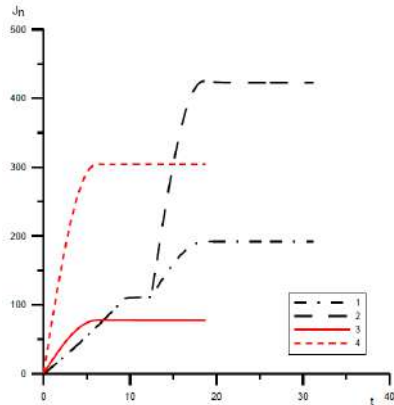
Since a non-stationary problem is solved, for the case of the dry gas, it would be more convenient to calculate the process where, at the beginning of the calculation, the input gas has equilibrium moisture, but for some small time interval the vapor concentration in the input gas flow decreases to zero and remains so (dry gas). Then after a while the heater is turned on, and the heat and mass transfer processes gradually stabilize.

Numerical solution of the problem is implemented by the finite difference method. The alternating directions implicit (ADI) method is used to solve the system of grid equations with boundary conditions. To solve the problem on each fractional grid step the Thomas algorithm is used.

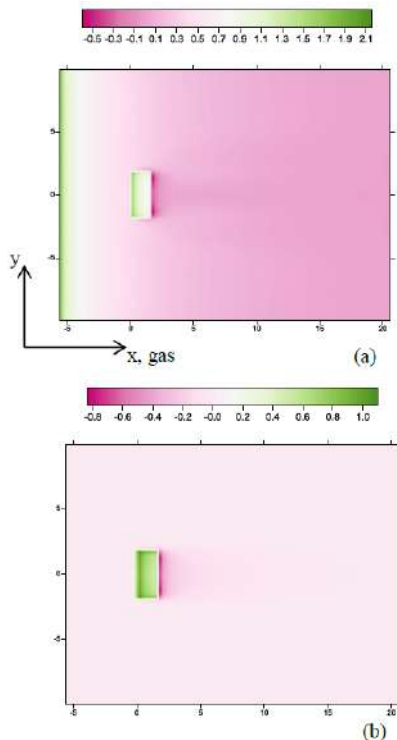
Calculations have been performed for the constant channel height equal to 250 μm. In all calculations the liquid is water and the gas is air. Gas is moving in x-direction and the heater upper edge is located at the origin of coordinate system. The initial temperature is equal to 20°C. The heater size is constant in all calculations and equal to 3 x 6, 4 mm<sup>2</sup> (length x width). Channel has been supposed to be horizontal, so that inclination angle is equal to 0. The gas and the liquid Reynolds numbers have been kept constant in all calculations and equal to  $Re_g=20$  and  $Re_l=8,5$  correspondingly.

Figure 1 shows the total heat transfer from the heater for the cases of dry gas (black lines) and for the case when the vapor concentration in the gas phase at the microchannel inlet is equal to the saturated concentration on the free interface (red lines). It can be seen that the use of the dry gas significantly increases the heat transfer from the heater both at high temperature on the heater and at low temperature prescr

In the case (a) the gas flow entering the channel does not contain liquid vapor, in the case (b) their concentration is equal to equilibrium for the average temperature. It can be noted that the vaporization rate in case (a) is much higher. In addition, it can be seen that in both cases vapor condensation takes place after the heater in streamwise direction and the process of condensation plays an important role in the redistribution of the heat. ibed on the heater.



**Figure 1:** The total heat transfer from the heater vs time. Black lines - dry gas, red lines - equilibrium concentration of vapor in the gas. Lines 1 and 3 correspond to the temperature on the heater equal to 22,5°C, lines 2 and 4 correspond to the temperature on the heater equal to 30°C.



**Figure 2:** Distribution of the evaporation intensity over the gas-liquid interface (or vapor condensation). (a): dry gas, (b): equilibrium concentration of vapor in the gas. Prescribed temperature on the heater is 30°C.

Figure 2 shows the distribution of the evaporation intensity over the gas-liquid interface (or vapor condensation).

As a result, systematic numerical investigations of temperature and concentration profiles evolution in gas and liquid phases were performed. In addition, velocity fields in the liquid and gas phases as well as evolution of free interface deformations and film thickness at constant liquid flow rate and different values of the temperature at the heating element were calculated for the case of the dry gas. A comparison of the numerical results for the case of the dry gas and for the case of equilibrium concentration of vapor in the gas has been carried out.

It is shown numerically that the use of dry gas enhances the heat dissipation from the heater both at high and low temperatures prescribed on the heater. It is found out that not only intense evaporation occurs near the heating areas, but also condensation of vapor. This process plays an important role in the liquid and gas temperature distribution.

The work was supported by the Russian Science Foundation (Agreement no. 14\_19\_01755).

## References

- T. Hirokawaa, M. Murozono, O. Kabov, H. Ohta, *Frontiers in Heat and Mass Transfer*, Vol. 5, No. 17, pp. 1-8 (2014)
- M. H. Nasr\*, C. E. Green, P. A. Kottke, X. Zhang, T. E. Sarvey, Y. K. Joshi, M. S. Bakir, A. G. Fedorov, *Int. Journal of Heat and Mass Transfer*, Vol. 108, pp. 1702–13 (2017)
- M. H. Nasr, C. E. Green, P. A. Kottke, X. Zhang, T. E. Sarvey, Y. K. Joshi, M. S. Bakir, A. G. Fedorov, *Journal of Electronic Packaging*, Vol. 139, p. 011006 (2017)
- Mahajan R., Chin C., Chrysler G., *Proceedings of the IEEE*, Vol. 94, No. 8, pp. 1476-1485 (2006)
- Sri-Jayantha S.M., McVicker G., Bernstein K., Knickerbocker J.U., Vol. 52, No. 6, pp. 623-634 (2008)
- Yu. V. Lyulin, S. E. Spesivtsev, I. V. Marchuk, O. A. Kabov, *Technical Physics Letters*, Vol. 41, No. 11, pp. 1034–1037 (2015)
- Houshmand F., Peles Y., *Int. Journal of Heat and Mass Transfer*, Vol. 64, pp. 42-52 (2013)
- Yu. Kabova\*, V.V. Kuznetsov, O. Kabov, T. Gambaryan-Roisman, P. Stephan, *International Journal of Heat and Mass Transfer*, Vol. 68, pp. 527-541 (2014)
- Yu. Kabova, V.V. Kuznetsov, O. Kabov, *Interfacial Phenomena and Heat Transfer*, Vol. 2, No. 1, pp. 85-102 (2014)

## Features of liquid fuel burning in a narrow channel

V.V. Zamaschikov<sup>1,3</sup>, E.A. Chinnov<sup>2,3</sup>

<sup>1</sup>Voevodsky Institute of Chemical Kinetics and Combustion, SB RAS, 630090, Institutskaya str. 3, Novosibirsk, Russia  
albor@kinetics.nsc.ru

<sup>2</sup> Kutateladze Institute of Thermophysics SB RAS, 630090, Lavrentied ave. 1, Novosibirsk, Russia

<sup>3</sup> Novosibirsk State University, 630090, Pirogov str. 2, Novosibirsk, Russia

Making the miniature power sources, which use the energy released during hydrocarbon combustion, is an urgent task since high intensity of heat transfer in microsystems allows creating the effective heat exchangers that can be useful for development, for example, of thermoelectric converters. The process of flame propagation over the surface of liquid on the bottom of a cylindrical tube was investigated in [1]. At that, liquid heating was observed under the flame front. In more detail, the processes occurring in liquid during flame propagation are studied in [2]. The authors observed the formation of a vortex in liquid that is ahead of the flame front and plays a large role in the mechanism of flame propagation. Experimental studies of liquid combustion in horizontal channels have shown [1, 3] that the flame velocity can vary in a wide range from millimeters per second to several meters per second.

The experiments were carried out in a flat channel with the width of 4 mm and height of 42 mm. In contrast to previous works, in this study, the bottom (lower part) of the channel was not a wide part [3], but a narrow one, and this allowed observing the combustion front and processes occurring in liquid. When air was used as an oxidizer, the flame entered to the channel and quenched. To exclude extinguishing, air was enriched with oxygen. To influence the processes occurring in liquid and combustion, a barrier was mounted on the channel bottom.

In contrast to [3], in this case, the flame velocity did not depend on oxidant flow rate, at least up to the flow rate of 5 liters per minute, which agrees with the data obtained by other investigators at flame propagation over the liquid surface in sufficiently large volumes [2]. This can be explained by the fact that the effect of oxidant flow on combustion should increase with a decrease in the free space above the flame. As expected, the velocity depends on the proportion of oxygen in the oxidant mixture. With an increase in oxygen proportion, the velocity increases almost linearly.

At flame velocities higher than 11 cm/s, there is no visual disturbance of the liquid surface (formation of a roll ahead of the front). However, the region of liquid heating is observed (Fig. 1 a). This region expands with a distance from the combustion front. The fact that in this area the temperature actually increases is shown by thermocouple measurements. A 25- $\mu\text{m}$  chromel-alumel thermocouple was used (it can be seen in Fig. 1). As the flame velocity increases with oxygen enrichment of air, the heating region observed under the front becomes thinner, and eventually it cannot be distinguished (Fig. 1b). To understand the mechanism of flame propagation, it is important to determine where the heating region is relative to the leading point of combustion wave: is it ahead of this point or not.

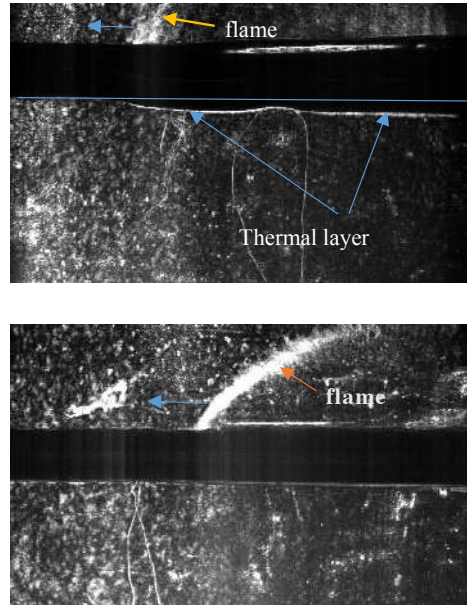


Fig. 1. Photos of flame propagation front a - 20%O<sub>2</sub>+air, b - 100%O<sub>2</sub>

However, thermocouple measurements did not allow this, since, first, when the thermocouple approaches the surface, the latter is bent, and second, the near-surface heated layer can be so thin that the thermocouple does not measure the actual temperature profile near the liquid surface. It should be noted that when measuring the gas temperature, i.e., in the case, when the thermocouple was located above the surface, the temperature profile obtained by the thermocouple was considerably shifted relative to the combustion front because of thermocouple inertia. For the existence of a combustion wave, it is important that a combustible mixture be formed before the front. The combustible mixture is formed at mixing the vapors with an oxidant, if vapor concentration is higher than the limiting value. The authors of [2], in the mechanism of flame propagation proposed by them, have determined the role of thermo-capillary phenomena. Due to the temperature gradient formed along the surface and temperature dependence of surface tension coefficient, a force is generated that moves the heated liquid into the pre-flame region. A thermocapillary wave is formed in liquid, and it moves together with the flame along the liquid surface. As a result, vapors of heated liquid, mixing with an oxidant, form a combustible mixture before the flame.

It is obvious that liquid surface bending affects the processes taking place in liquid and gas, and thus, flame propagation. To study the effect of surface bending on the flame velocity, a cylinder or parallelepiped was placed on the channel bottom. On the one hand, the barrier bent the surface of the liquid, on the other hand, the liquid layer thickness decreased. Both the surface curvature and liquid layer thickness should affect the thermocapillary wave.

When the flame approaches the barrier: a) it slows down; b) its slope relative to the gravity vector changes; c) its position changes, although insignificantly, relative to the liquid surface; d) its length decreases; e) brightness of its image decreases. The shlieren-image brightness should be related to the flame temperature, so it decreases in the flame front. The shape of the flame depends on the vapor flow from the liquid surface and oxidant flow. Since the flame velocity in this case does not depend on the oxidant flow rate, it can be assumed that combustion takes place at low gas velocities, i.e., in almost resting gas. In this case, most likely, there is diffusion mixing of vapors and oxidant with formation of a

determined by the average characteristics, which are not affected by such a change in thickness.

At the place, where the velocity is minimal (Fig. 2), the flame becomes more vertical, it lengthens and its brightness increases. Under some certain conditions (when a parallelepiped is used as a barrier), the flame is stabilized in this place for some time. This behavior can be explained as follows. First, the liquid layer thickness under the flame is small there. Consequently, it is poorly heated due to the heat flux into the solid phase. Second, liquid heating ahead of the front leads to an increase in the vapor flow into the gas phase, but this flow is directed away from the flame by virtue of geometry. Therefore, the flame cannot move forward. The following pattern is observed: behind the flame, there are the combustion products and vapors, and before the flame, there is only an oxidant. The vapors and oxidant diffuse towards each other and react where the combustion front is. While liquid is being heated in the pre-flammable region, the vapor flow becomes so large that the combustible mixture is formed already ahead of the combustion front, and the flame moves forward. In favor of this hypothesis is the fact that the flame, when passing through the place where its velocity is minimal, separates slightly from the liquid surface. Perhaps, more precise description of the flame behavior requires taking into account free convection and oxidant flow, although small, but available on the liquid surface.

Thus, the barrier has an effect on the flame propagation. It affects the processes occurring in the liquid and gas phases. However, the experiments carried out in the presence of a barrier do not give an unambiguous answer about the mechanism of flame propagation.

This work was supported by the grant of Russian Science Foundation (Agreement No. 15-19-30038).

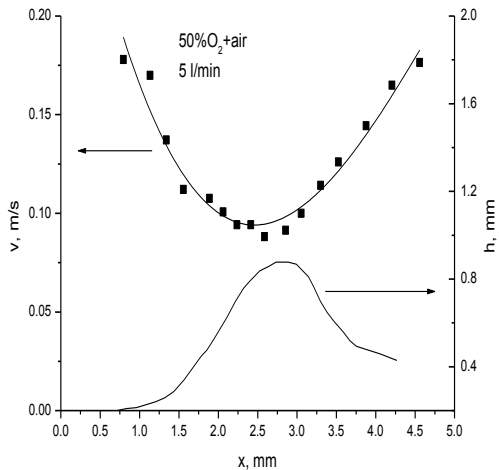


Fig. 2. Flame velocity ( $v$ ) and liquid layer height ( $h$ ) vs. coordinate ( $x$ ).

combustible mixture ahead of the combustion front. The barrier should not have a significant effect on the flame velocity until the flame approaches the barrier. When the flame comes close to the barrier, first, the surface bends, second, the liquid layer thickness changes. Heat transfer through liquid and, hence, the temperature of the near-surface layer depend on these two factors. Diffusion of vapors should also depend on the surface curvature, and the value of this flux should depend on the temperature of the near-surface layer. Dependence of the flame velocity on coordinate and position of the barrier are shown in Fig. 2. The flame spreads from right to left. It can be seen that the velocity decreases, when the flame rises to the barrier. Due to liquid surface curvature, the flame, when moving along the surface, passes the region, where the liquid layer thickness increases first, and then decreases. From the point of view of vapor diffusion and liquid heating ahead of the flame front, the velocity should increase and then decrease, but this is not observed. Perhaps, this relates to the fact that the flame velocity is

## References

1. Zamashchikov V.V. Flame spread across shallow pools in modulated opposed air flow in narrow tube // *Combustion Sci. and Technology*, 2009. Vol. 181, No 1. P. 176-189.
2. Ross H.D., Miller F.J. Detailed experiments of flame spread across deep butanol pools // *Proc. of the Combustion Institute*. 1996. Vol. 26. P. 1327-1334.
3. Zamashchikov V.V., Korzhavin A.A., Chinnov E.A. Combustion of liquid fuel in a flat minichannel // *IJHMT*, 2016 V. 102, P. 470-478.

## Foam drying under microgravity conditions

J. Cook, O. Arjmandy Tash, A. Trybala, V. Starov

Department of Chemical Engineering, Loughborough University  
LE11 3TU, UK

In a number of applications foaming liquids are mixtures of surfactants and polymers. These mixtures frequently show a non-Newtonian power law shear thinning behaviour (Bureiko et al. 2015, Bureiko et al. 2013, Bureiko et al. 2014). Surprisingly drainage of foams built up by non-Newtonian liquids does not attract enough attention in spite of wide use of such foams. In a number of applications foams are deposited on porous substrates: hair, skin, textile, sponges and so on, however even the basics of the interaction of Newtonian and non-Newtonian foams with porous materials have never been thoroughly investigated: there is only one publication in the area where a complex interaction of foams with porous substrates was investigated (Tash et al. 2015). It was found (Tash et al. 2015), that the kinetics of foam drainage on a porous substrate in the case of foam built up by a Newtonian liquid depends on three dimensionless numbers related to the properties of both foam and a porous substrate, and initial liquid volume fraction inside the foam. The result showed that there are three different regimes of the drainage process from foam (Arjmandi-Tash et al. 2015): (a) rate of imbibition into the porous substrate is faster than the rate of drainage from the foam; (b) a comparable rate of drainage and imbibition; (c) rate of imbibition is slower as compared with the rate of drainage. In the latter case, the liquid volume fraction at foam/porous substrate interface reaches maximum limiting value at the moment  $t_m$  and a free liquid layer starts to form on the surface of the porous substrate. However, in the end, the free liquid layer is sucked by a porous substrate and it completely disappears at the particular moment. After that moment again all liquid coming from the foam goes directly into the porous substrate and the liquid volume fraction decreases to its final value.

Foam drying under terrestrial condition proceeds under the combine action of both gravity and capillarity. The gravity forces the liquid to move from the top of the foam to the bottom and it is the only driving force of drainage. Gravitational drainage is the main tool used to dry the foam under terrestrial conditions.

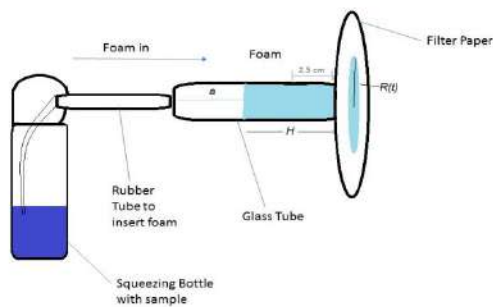


**Figure 1:** The experimental set up to study drainage of foam under simulation of microgravity conditions.

However, the gravity action is negligible under microgravity condition (for example inside a spacecraft). In this case drying the foam is difficult and it is necessary to find a completely new way of arrangement of the drying process. Below new foam drying process is suggested, which is based on a completely new physical phenomenon: capillary suction of the liquid from the foam by a porous body in contact with the foam (Fig. 1)

Let the initial water content inside the foam is  $\varphi_0$  and the average water content inside the foam at the moment  $t$  is  $\varphi(t)$ . It is possible to write the mass conservation law of water at the moment  $t$  in the following form:

$$\pi a^2 H \varphi_0 = \pi a^2 H \varphi(t) + \pi R^2(t) \Delta p \quad (1)$$

where  $\Delta$  and  $p$  are the thickness of the filter paper and the porosity, respectively.

From Eq. (1):

$$\varphi(t) = \varphi_0 - R^2(t) \frac{\Delta p}{a^2 H} \quad (2)$$

According to Eq. (2) the water contents  $\varphi(t)$  decreases over time until a final water content is reached, which is determined by the relation between the capillary pressure inside the foam and the capillary pressure inside the porous substrate (filter paper). If the desired final water content is  $\varphi_f$  then it determines the moment,  $t_f$ . At this moment, the imbibition into the porous substrate should be interrupted (that is, the filter paper should be removed):

$$\varphi_f = \varphi_0 - R^2(t_f) \frac{\Delta p}{a^2 H} \quad (3)$$

The total duration of the drying process can be easily controlled by a proper selection of the thickness, porosity and capillary size of pores inside the filter paper.

The current state of the studies on drainage kinetics will be presented and the experimental study of foam drainage under simulation of microgravity conditions will be discussed.

## References

- A. Bureiko, A. Trybala, N. Kovalchuk, V. Starov, *Adv Colloid Interface Sci*, Vol. 222, pp. 670–677 (2015)
- A. Bureiko, A. Trybala, J. Huang, N. Kovalchuk, V.M. Starov, *Colloids&Surfaces A*, Vol. 434, pp. 268-275 (2013)
- A. Bureiko, A. Trybala, J. Huang, N. Kovalchuk, V.M. Starov, *Colloids &Surfaces A*, Vol. 460, pp. 265-271 (2014)
- O. Arjmandi-Tash, N. Kovalchuk, A. Trybala and V. Starov, *Soft Matter*, Vol. 11, No. 18, pp. 3643-3652 (2015)

## Thermocapillary stability of a thin film coating a cylinder with a thick wall with finite thermal conductivity in the absence of gravity

Luis A. Dávalos-Orozco

Universidad Nacional Autónoma de México, Instituto de Investigaciones en Materiales, Departamento de Polímeros  
Ciudad Universitaria, Circuito Exterior S/N, C.P. 04510, Ciudad de México, México  
ldavalos@unam.mx

The coating of surfaces by thin liquid films is important in industrial applications (Weinstein and Ruschak 2004). As a consequence the study of the stability of thin films has been done since many years ago. In particular, the coating of cylindrical surfaces are of interest due to important applications in the coating of tubes, wires and fibers (Quéré 1999).

The stability of flows down cylinders has been investigated by Shlang and Sivashinsky (1982). They linearized an evolution equation and used normal modes to obtain a formula for the growth rate. They show that the azimuthal modes are able to appear for different magnitudes of the parameters of the problem. They showed that azimuthal modes can be stimulated but they are not the most unstable ones. Only the axial mode is the most important.

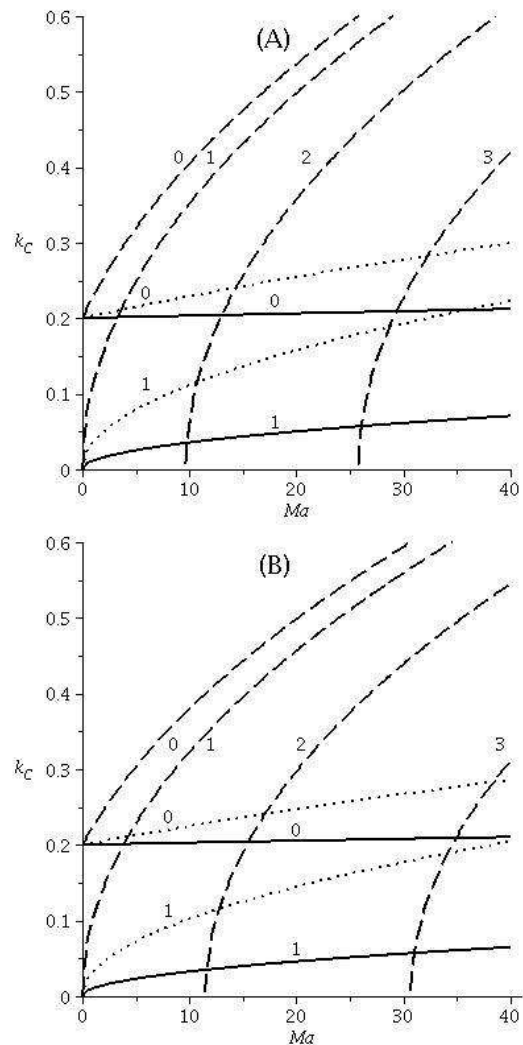
The case of flow down a rotating cylinder was investigated by Dávalos-Orozco and Ruiz-Chavarría (1993), Ruiz-Chavarría and Dávalos-Orozco (1996, 1997). In those papers it was made clear the importance in the stability of the azimuthal mode  $m=1$  when rotation is present.

The linear thermocapillary stability of a thin film flowing down a cylinder was investigated by Dávalos-Orozco and You (2000). A set of equations were calculated which generalize the Orr-Sommerfeld equation for the thermocapillary problem. They were solved numerically to find that the azimuthal modes can be the more unstable when the wavenumber approaches zero. However, for small but larger magnitudes of the wavenumber the axial mode is the most important and presents the largest growth rate. The case when the film is not subjected to the gravity force is also investigated.

An equation of the Benney type for flow down a cylinder was calculated by Frenkel (1993). The evolution equation is obtained under the small wavenumber and large cylinder radius approximation. This approximation was used to calculate the linear stability of a viscoelastic thin film flowing down a vertical cylinder in the isothermal (Moctezuma-Sánchez and Dávalos-Orozco 2008) and thermocapillary problems (Moctezuma-Sánchez and Dávalos-Orozco 2015). In the last paper the film stability was also investigated when the cylinder is in the absence of gravity.

In this lecture, results of the stability of a thin film coating the outside of a hot cylinder which has a thick wall with finite thermal conductivity are presented when the gravity force is zero. The results are calculated under the small wavenumber and large radius of the cylinder approximations. An evolution equation is linearized to calculate by means of normal modes the critical wavenumber and the growth rate of the azimuthal modes of instability.

It is found that the wall/liquid thicknesses ratio  $d$  and the thermal conductivities ratio  $Q_C$  appear as one parameter  $d/Q_C$  under the present approximation. Some plots are presented in Fig. 1 of the critical wavenumber  $k_c$  against the Marangoni number  $Ma$ , for three different magnitudes of the ratio  $d/Q_C$ . Notice that the wall can not be thicker than the radius of the cylinder. Therefore, after fixing the radius, it is possible to limit the magnitude of  $d$  and with the magnitude of the parameter  $d/Q_C$  it is possible to calculate the corresponding values of  $Q_C$ . In the figure it is shown how the increase of  $d/Q_C$  moves the large azimuthal modes outside the region of Marangoni numbers used in the plots.



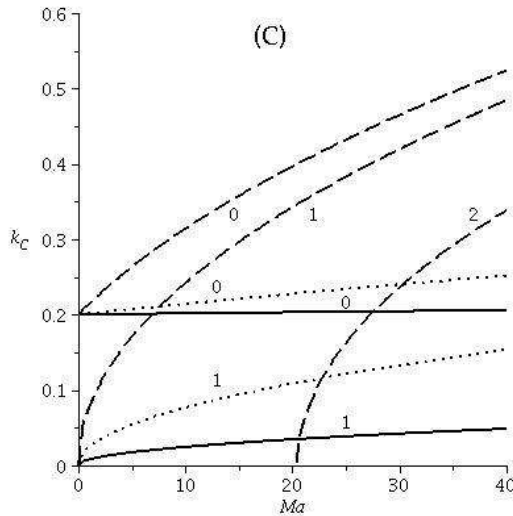


**Figure 1:** Critical wavenumber against the Marangoni number. Radius of the cylinder 5, Three crispation numbers  $Cr=0.001$  (solid),  $Cr=0.01$  (dotted),  $Cr=0.1$  (dashed). Fig 1a ( $d/Q_C=0$ ), Fig 1b ( $d/Q_C=1$ ), Fig 1a ( $d/Q_C=5$ ). The numbers mean the axial mode  $m=0$ , and the azimuthal modes  $m=1, 2, 3$ .

## References

- Weinstein S. J. and Ruschak K. J., Coating flows, *Annu. Rev. Fluid Mech.*, Vol. 36 pp. 29 - 53 (2004)
- Quéré D., "Fluid coating on a fiber", *Annu. Rev. Fluid Mech.*, Vol. 31 pp. 347 – 384 (1999)
- Shlang T. and Sivashinsky G. I., Irregular flow of a liquid film down a vertical column, *J. Physique*, Vol. 43 pp. 459 – 466 (1982)
- Dávalos-Orozco L. A. and Ruiz-Chavarría G., Hydrodynamic instability of a fluid layer flowing down a rotating cylinder *Phys. Fluids A*, Vol. 5 pp. 2390 - 2404 (1993)
- Ruiz-Chavarría G. and Dávalos-Orozco L. A., Stability of a liquid film flowing down a rotating cylinder subject to azimuthal disturbances, *J. Phys. II France*, Vol. 6 pp. 1219 - 1227 (1996)
- Ruiz-Chavarría G. and Dávalos-Orozco L. A., Azimuthal and streamwise disturbances in a fluid layer flowing down a rotating cylinder, *Phys. Fluids*, Vol. 9 pp. 2899 - 2908 (1997)
- Dávalos-Orozco L.A., You X.Y., Three dimensional instability of a liquid layer flowing down a heated vertical cylinder, *Phys. Fluids*, Vol. 12(2198) (2000)
- Frenkel A. L., On evolution equations for thin films down solid surfaces, *Phys. Fluids A*, Vol. 5 pp. 2342 – 2347 (1993)
- Moctezuma - Sánchez M. and Dávalos – Orozco L. A.,

Linear Three dimensional instability of viscoelastic fluid layers flowing down cylindrical walls, *Microgravity Sci. Technol.*, Vol. 20 pp. 161 – 164 (2008)

Moctezuma - Sánchez M. and Dávalos – Orozco L. A., Azimuthal instability modes in a viscoelastic liquid layer flowing down a heated cylinder, *Int. J. Heat Mass Transfer*, Vol. 90 pp. 15 - 25 (2015)

## Thermocapillary effect on the dynamics of an exterior coating film flow down a fibre subject to an axial temperature gradient

Xue Chen<sup>1</sup>, Rong Liu<sup>1,\*</sup>, Zijing Ding<sup>2</sup>

<sup>1</sup> School of Mechanical and Electrical Engineering, Guilin University of Electronic Technology, Guilin, 541004, China

<sup>2</sup> School of Mathematics, University of Bristol, Bristol BS8 1TW, United Kingdom

\*E-mail: rongliu@guet.edu.cn

### 1. Introduction

The dynamics of a film flow down a cylindrical fibre driven by gravity has been much studied due to its technological importance, mainly in the processes of draining, coating of insulation on a wire, and the protection coating of tube walls (D. Quéré. 1999). Lord Rayleigh (1892) was the first to identify the so called Rayleigh-Plateau mechanisms by which droplets form under the action of surface tension in cylindrical fluid threads and jets. For an axisymmetric film flow coating a cylindrical fibre, the Rayleigh-Plateau instability is modified by the presence of flow driven by gravity.

In practical processes, the fibre-coating is often operated in a cooling environment, for example, the glass manufacturing and dry cooling of thermoelectric power plants. In glass manufacturing process, glass fibres are made by drawing molten glass through an array of small diameter bushings. The fibres are sprayed with water from atomizing nozzles to enhance the heat removal from them (M. Sweetland and J. H. Lienhard V. 2000). In the situations where the coating film is cooled by the environment, the Rayleigh-Plateau instability is modified by thermocapillary stress due to surface tension variations produced by temperature disturbances at the interface. The effect of thermocapillarity on the dynamics of thin films on cylinders have given rise to broad scientific interest for its technological importance. Liu and Liu (2014) studied the axisymmetric longwave stability of thin film flowing down a uniformly heated vertical fiber. The results showed that the Marangoni instability and the Rayleigh-Plateau instability reinforce each other. With the increase of the thermocapillary effect, the coating flow has a tendency to break up into smaller droplets. Recently, Liu et al. (2017) studied the Marangoni effect on the absolute and convective instabilities of the coating flow on a fibre. The numerical results showed that for various Marangoni number (Ma), breakup of the film mainly occurs in the absolutely unstable regimes.

The theoretical development of thermocapillary instabilities in thin films on cylinders has been limited so far to films uniformly heated by the cylinders. As a temperature gradient is applied perpendicular to the cylindrical wall, there can be a purely conductive basic state in which the thermocapillarity does not influence the bulk flow. However,

in most common practical situations the imposed temperature gradient will have a component parallel to the free surface so that additional interfacial motions are generated. The thermocapillarity involves a shear flow in the bulk at the basic state. The linear stability of the thermocapillary flow with a temperature gradient along the axial direction has been investigated for plane film flows (M. K. Smith and S. H. Davis. 1983). However, a careful look at previous literatures indicates that the studies on the effect of thermocapillarity with an axial temperature gradient in a coating flow on a fibre are very limited. The main objective of the present paper is to investigate how thermocapillarity induced by axial temperature gradient influences the linear stability and the nonlinear dynamics. The related works to the present problem are the studies on the effect of the thermocapillarity on the capillary instability of liquid jets (J. -J. Xu and S. H. Davis. 1985) which is a fundamental problem found in several applications, for example ink-jet printing, spraying of liquids for cooling, and long liquid bridge (Y. -J. Chen et al. 2003) which is related to experiments on float-zone crystal growth.

### 2. Mathematical formulation

The sketch of the geometry of a coating flow on a fibre subject to an axial temperature gradient is plotted in Fig.1. As shown in Fig.1, a Newtonian fluid, of constant viscosity  $\mu$  and density  $\rho$ , flows down a vertical fibre of radius  $r = a$  under gravity  $g$ . The initial radius of the fluid ring measured from the centre of the fibre is  $r = R$ . We make an assumption that the flow is axisymmetric. A constant temperature gradient  $dT/dz = b$ ,  $b > 0$  is imposed along the axis of the fibre.

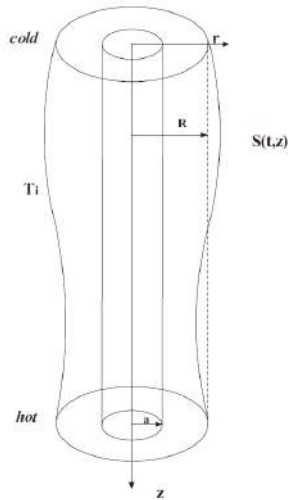


**Figure 1:** Sketch of the geometry of a coating flow on a fibre subject to an axial temperature gradient.

### 3. Results and discussions

The dynamics of the flow are governed by the continuity equation, the Navier-Stokes equations and the energy equation.

For basic state, the velocity is defined by

$$\bar{w} = \left[ \frac{1}{4}(a^2 - r^2) + \frac{1}{2} \ln \frac{r}{a} \right] - \epsilon M a \ln \frac{r}{a},$$

and the flow rate is

$$\bar{Q} = \left[ \frac{(3 - a^2)(a^2 - 1)}{16} + \frac{1}{4} \ln \frac{1}{a} \right] - \epsilon M a \left[ \frac{1}{2} \ln \frac{1}{a} - \frac{1}{4}(1 - a^2) \right].$$

For the linear stability analysis, the yields the dispersion relation

$$\lambda + \left[ \frac{1}{16} k^2 (k^2 \epsilon^2 - 1) (4 \ln \frac{1}{a} - a^4 + 4a^2 - 3) + \frac{ik}{2} (a^2 - 1 - 2 \ln a) \right] - ik \epsilon M a \left[ \frac{1}{4} (a^2 - 1) - \frac{3}{2} \ln a \right] = 0.$$

### 4. Conclusions

The dynamics of a viscous film flowing down a vertical fibre under the action of gravity and the thermocapillarity induced by an axial temperature gradient is analyzed theoretically. This exterior coating flow is driven by a Rayleigh-Plateau mechanism modified by the presence of gravity as well as the thermocapillary flow. A linear stability analysis and a nonlinear simulation are performed to investigate the influence of the thermocapillarity on the dynamics of axisymmetric disturbances. The results of linear stability showed that the thermocapillarity does not influence the growth rate of the disturbance and only affects its frequency. We also examined the effect of thermo

-capillarity on the wavespeed and the characteristics of the structures of travelling wave solutions.

### References

D. Quéré, Fluid coating on a fiber, *Annu. Rev. Fluid Mech.* Vol.31, pp.347-384 (1999).

L. Rayleigh, On the instability of a cylinder of viscous liquid under capillary force, *Phil. Mag.* Vol.34, pp.145-154 (1892).

M. Sweetland and J. H. Lienhard V, Evaporative cooling of continuously drawn glass fibers by water sprays, *Int. J. Heat Mass Tran.* Vol.43(5), pp.777-790 (2000).

R. Liu and Q. S. Liu, Thermocapillary effect on the dynamics of viscous beads on vertical fiber, *Phys. Rev. E.* Vol. 90, pp.033005(1-11) (2014).

R. Liu and Z. Ding and Z. Zhu, Thermocapillary effect on the absolute and convective instabilities of film flows down a fibre, *Int. J. Heat Mass Tran.* Vol.112, pp.918-925 (2017).

M. K. Smith and S. H. Davis, Instabilities of dynamic thermocapillary liquid layers. Part 1. Convective instabilities, *J. Fluid Mech.* Vol.132, pp.119-144 (1983).

J. -J. Xu and S. H. Davis, Instability of capillary jets with thermocapillarity, *J. Fluid Mech.* Vol.161, pp.1-25 (1985).

Y. -J. Chen, R. Abbaschian and P. H. Steen, Thermocapillary suppression of the Plateau-Rayleigh instability: a model for long encapsulated liquid zones, *J. Fluid Mech.* Vol.485, pp. 97-113 (2003).

## Thermocapillary structures in a heated liquid film

S.P.Aktershev, E.A.Chinnov

Kutateladze Institute of Thermophysics, Siberian Branch of the Russian Academy of Science,  
Lavrentiev Ave. 1, Novosibirsk 630090, Russia

E-mail sergey-aktershev@mail.ru

The study of the formation and development of different types of instabilities on the surface of flowing liquid films is an important problem of hydrodynamics and heat transfer not only from a theoretical point of view, but also from practical standpoint, since the falling films are used in many industrial devices. In contrast to the isothermal falling liquid films, film flows on the heated wall in presence thermocapillary effect are poorly understood both in theoretically and experimentally. In addition to hydrodynamic instability, leading to the development of three-dimensional waves, liquid films flowing over a heated surface are characterized also by thermocapillary mechanism of the instability, resulting in the occurrence of the stationary three-dimensional structures on the film surface [1-4].

This paper presents the observations of numerical simulation of stationary three-dimensional capillary structures in a heated liquid film flowing over a "semi-infinite" heater with temperature  $T_w$ . The free surface of a liquid is in contact with a quiescent gas with the temperature  $T_g$ ; the heat exchange between the liquid and gas is described by Newton's law with heat transfer coefficient  $\alpha$ . Density  $\rho$ , kinematic viscosity  $\nu$ , heat conductivity  $\lambda$ , and thermal diffusivity  $a$  of a fluid are considered to be constant, while the surface tension depends on temperature linearly  $\sigma = \sigma_0 - \gamma(T - T_0)$ . The calculations are compared with available experimental data at moderate Reynolds number. Based on the IBL model [5], modified taking into account a shear stress on the film surface, we derive a system of equations for dimensionless required functions  $h(t,x,z)$ ,  $q(t,x,z)$ ,  $m(t,x,z)$ ,  $T(t,x,\eta,z)$ , which describes the unsteady three-dimensional flow of the film involving the thermocapillary effect:

$$\begin{aligned} & \frac{\partial q}{\partial t} + \frac{\partial J_1}{\partial x} + \frac{\partial J_{1,2}}{\partial z} = \\ & = \frac{3}{Re_m} \left( h \left( \sin\theta - \cos\theta \frac{\partial h}{\partial x} \right) - \frac{Ma}{2} \frac{\partial T_s}{\partial x} - \frac{q}{h^2} \right) + Weh \frac{\partial \Delta h}{\partial x}, \\ & \frac{\partial m}{\partial t} + \frac{\partial J_2}{\partial z} + \frac{\partial J_{1,2}}{\partial x} = \\ & = - \frac{3}{Re_m} \left( h \cos\theta \frac{\partial h}{\partial x} + \frac{Ma}{2} \frac{\partial T_s}{\partial z} + \frac{m}{h^2} \right) + Weh \frac{\partial \Delta h}{\partial z}, \\ & \frac{\partial h}{\partial t} + \frac{\partial q}{\partial x} + \frac{\partial m}{\partial z} = 0, \\ & \frac{\partial T}{\partial t} + u \frac{\partial T}{\partial x} + w \frac{\partial T}{\partial z} + \frac{V}{h} \frac{\partial T}{\partial \eta} = \frac{1}{h^2 Re_m Pr} \frac{\partial^2 T}{\partial \eta^2}, \\ & \left( \frac{\partial T}{\partial \eta} + Bi h T \right) \Big|_{\eta=1} = 0, \quad T \Big|_{\eta=0} = 1. \end{aligned} \quad (1)$$

Here  $h(t,x,z)$  is the film thickness,  $T(t,x,\eta,z)$  is the liquid

temperature,  $q(x,z,t) = \int_0^h u dy$  and  $m(x,z,t) = \int_0^h w dy$  are the liquid flow rates per unit width along the  $Ox$  and  $Oz$  axes, respectively,  $\Delta h = \partial^2 h / \partial x^2 + \partial^2 h / \partial z^2$ ,  $T_s$  is the interface temperature,  $\eta = y / h$ ,

$$\begin{aligned} J_1 &= \frac{6q^2}{5h} - Ma \frac{qh}{20} \frac{\partial T_s}{\partial x} + \frac{h^3}{120} \left( Ma \frac{\partial T_s}{\partial x} \right)^2, \\ J_2 &= \frac{6m^2}{5h} - Ma \frac{mh}{20} \frac{\partial T_s}{\partial z} + \frac{h^3}{120} \left( Ma \frac{\partial T_s}{\partial z} \right)^2, \\ J_{1,2} &= \frac{6mq}{5h} - \frac{Ma}{40} h \left( q \frac{\partial T_s}{\partial z} + m \frac{\partial T_s}{\partial x} \right) + \frac{h^3 Ma^2}{120} \frac{\partial T_s}{\partial x} \frac{\partial T_s}{\partial z}, \\ u &= \frac{3q}{h} \left( \eta - \frac{\eta^2}{2} \right) - \frac{Ma}{4} (3\eta^2 - 2\eta) h \frac{\partial T_s}{\partial x}, \\ w &= \frac{3m}{h} \left( \eta - \frac{\eta^2}{2} \right) - \frac{Ma}{4} (3\eta^2 - 2\eta) h \frac{\partial T_s}{\partial z}, \\ V &= \left( \frac{\partial q}{\partial x} + \frac{\partial m}{\partial z} \right) \left( \eta - \frac{3\eta^2}{2} + \frac{\eta^3}{2} \right) - \\ & - \frac{Ma}{4} (\eta^2 - \eta^3) \left( \frac{\partial}{\partial x} \left( h^2 \frac{\partial T_s}{\partial x} \right) + \frac{\partial}{\partial z} \left( h^2 \frac{\partial T_s}{\partial z} \right) \right). \end{aligned}$$

Here, unperturbed film thickness  $h_0$  is used as the distance scale. We also introduced scales for velocity  $u_m = gh_0^2 / 3\nu$ , time  $t_m = h_0 / u_m$ , flow rate  $q_m = h_0 u_m$ , and temperature  $T_m = T_w - T_g$ . Non-isothermal film flow is determined by the following dimensionless criteria: Reynolds number  $Re_m = gh_0^3 / 3\nu^2$ ; Weber number  $We = (3Fi / Re_m^5)^{1/3}$ ; Kapitza number  $Fi = \sigma^3 / \rho^3 g \nu^4$ ; Marangoni number  $Ma = \gamma T_m / \mu u_m$ ; Bio number  $Bi = \alpha h_0 / \lambda$ ; and Prandtl number  $Pr$ . Since  $h_0 \sim Re_m^{1/3}$ ,  $u_m \sim Re_m^{2/3}$ , then  $Bi = Bi^* Re_m^{1/3}$ ,  $Ma = Ma^* / Re_m^{2/3}$ , where the dimensionless complexes of  $Bi^*$  and  $Ma^*$  are not dependent on  $Re_m$  and are determined only by the liquid properties and heating conditions  $Bi^* = \alpha (3\nu^2 / g)^{1/3} / \lambda$ ,  $Ma^* = \gamma (3 / g \nu)^{2/3} (T_w - T_g) / \mu$ .

Modeling of thermocapillary rivulet structure in heated vertical film is carried out by solution of the evolutionary type equations (1) and (2) applying finite difference method. The numerical algorithm is the same used in [6, 7] for the two-dimensional flow.

The formation of rivulets near the edge of the heater was simulated through perturbation of the heater edge, periodic along the coordinate  $z$ , which was imposed on a two-dimensional flow. The equations were solved by the

relaxation method; unperturbed two-dimensional flow of the cold film on "semi-infinite" heater was used as the initial condition. The calculation was ended upon establishing three-dimensional flow with rivulet structure, not changing in time. Periodic rivulet structure was calculated at various values of the parameters  $Re_m$ ,  $Bi^*$ ,  $Ma^*$  and the period  $L_z$ . The calculations were performed for a film section with a width equal to a single period, i.e., the computational domain represented a rectangle  $0 \leq x \leq X_{end}$ ,  $-L_z/2 \leq z \leq L_z/2$ . On the  $x$ -axis where the rivulet crest is arranged, the symmetry condition  $\partial/\partial z = 0$  was provided, while the lateral boundaries of the computational domain (at  $z = \pm L_z/2$ ) were provided by periodicity condition along  $z$ :  $m = 0$ ,  $\partial q/\partial z = 0$ ,  $\partial h/\partial z = 0$ ,  $\partial T/\partial z = 0$ . Unperturbed thickness, flow rate, and temperature were given at the inlet (at  $x = 0$ ).

The calculations have shown that rivulet structure develops according to the following scenario. Film portion flowing over a protuberance of edge of the heater heats up earlier than the film portion flowing over a trough. The temperature gradient on the film surface causes the appearance of shear stress  $\tau_z$  in the transverse direction that pushes the fluid from protuberance edge of the heater to the trough. As a result, the flow rate  $q$  and the film thickness  $h$  in the area of protuberance are smaller than those in the area of the trough. In the trough area, a thicker film is heated more slowly, therefore the surface temperature there is less than that in the area of protuberance. As a consequence, the shear stress  $\tau_z = -\gamma \partial T_s / \partial z$  is directed in such a way as to enhance the perturbation of the film thickness in the transverse direction. This factor is counteracted by the pressure gradient  $p = -\sigma(\partial^2 h / \partial^2 x + \partial^2 h / \partial^2 z)$  caused by curvature of the film surface. Development of disturbances downstream is determined by the interaction of these physical factors and depends on  $Re_m$ ,  $Bi^*$ ,  $Ma^*$  parameters and the period  $L_z$ .

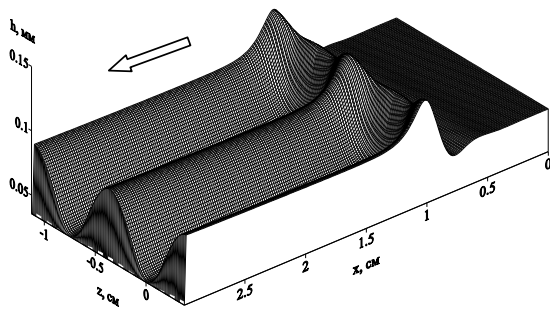


**Figure 1:** Rivulet structure on the surface of the vertical water film at  $L_z = 7.5$  mm,  $Re = 1$ ;  $Bi^* = 0.2$ ;  $Ma^* = 100$ . The arrow shows flow direction.

Figure 1 shows a rivulet structure on the surface of a vertical water film at  $L_z = 7.5$  mm (two periods along  $z$  are shown). It can be seen from the figure that rivulets are branched off from the horizontal bump. The film thickness in the sections between the rivulets is much smaller than the non-perturbed value  $h_0$ . At such a high value of  $Ma^* = 100$ , the rivulets are formed directly behind the horizontal bump, and the amplitude of the rivulets does not change down-

stream. The rivulet structures, similar to those shown in Fig 1, are formed only at a sufficiently large  $Ma^*$  exceeding certain threshold value  $Ma_{cr}$ .

Based on the developed model, we carried out a numerical simulation of thermocapillary three-dimensional structures on the surface of a liquid film flowing over a heater with a constant temperature. In the calculations it is shown that if the Marangoni number exceeds a certain threshold value, the heated film flow is unstable relative to transverse perturbations, which can develop into periodic rivulet structures. At fixed Marangoni and Reynolds numbers the evolution of downstream transverse perturbations significantly depends on the period  $L_z$ . At a given Reynolds number the development of rivulet structure occurs only if the period is within a certain range, which is determined mainly by the Marangoni number. Outside this range the transverse perturbations are damped downstream. The calculation and experimental data are in good agreement.

#### Acknowledgements

The authors acknowledge the support by the Russian Foundation for Basic Research (projects No. 15-01-06702 and No. 15-01-04320).

#### References

1. Kabov O. A. Formation of regular structures in a falling liquid film upon local heating // Thermophys. Aeromech., 1998, V. 5, N. 1. P. 547–551.
2. Kalliadas S., Kiyashko A., Demekhin E.A. Marangoni instability of a thin liquid film heated from below by a local heat source // Journal of Fluid Mechanics, 2003, N 475, P. 377–408.
3. Chinnov E.A., Kabov O.A. Jet formation in gravitational flow of a heated wavy liquid film // Journal of Applied Mechanics and Technical Physics, 2003, N 44, P. 708–715.
4. Chinnov, E.A., Zhukovskaya, O.V. Effect of artificial perturbations on the formation of structures in a nonisothermal liquid film // Technical Physics Letters, 2006, V. 32, N 5, P. 410–413.
5. Demekhin E.A., Shkadov V.Ya. Three-dimensional waves in a liquid flowing down a wall. // Fluid Dynamics 1984, V. 19 N 5, P. 689–695.
6. Aktershev S.P. Stability of the heated liquid film in the presence of the thermocapillary effect. // Thermophys. Aeromech., 2013, V. 20, N. 1. P. 1–16
7. Aktershev S.P. Thermocapillary waves in a liquid film // Journal of Engineering Thermophysics. 2012. Vol. 21. N 1. P. 36-51.

## Numerical simulation of heat transfer at unsteady heat generation in falling wavy liquid films

Andrey Chernyavskiy, Aleksandr Pavlenko

Kutateladze Institute of Thermophysics SB RAS  
Acad. Lavrentiev ave. 1, Novosibirsk, 630090, Russia  
cherny@ngs.ru

The liquid flow over a vertical surface is inevitably accompanied by development of wave perturbations on the free film surface, which bring considerable contribution to the heat transfer processes and development of crisis phenomena.

The area of highly efficient heat transfer at the film flow of liquid is limited by the heat flux and depends significantly on the heat release law.

When the system reaches the critical heat flux, this leads to decay of the film flow, formation of large-scale dry zones, reduction of heat transfer intensity and as a sequence to a drastic increase in temperature of the heat-releasing surface. All these can cause destruction of the heat-releasing element.

The ability to calculate the critical heat fluxes and maximal times of their impact for a given system is required for the design of stably working heat exchangers.

Under the conditions of unsteady heat release, two scenarios of film flow decay are possible depending on heat load and intensity of irrigation: the first is liquid film explosive boiling-up with dispersion of drops and development of large-scaled unwetted areas and the second is total local evaporation of the liquid film.

The time of crisis beginning and scenario of film flow decay are characterized by such parameters as time of boiling expectation ( $\tau_{b,e}$ ) and time of total local evaporation ( $\tau_{t,e}$ ) of the falling liquid film. These values determine maximal times of heat flux influence on the film with certain parameters.  $\tau_{b,e} < \tau_{t,e}$ ,  $\tau_{b,e} < \infty$  is the criterion of explosive boiling-up during the unsteady liquid heating with development of self-sustaining boiling-up fronts. Motion of the self-sustaining boiling-up fronts is followed by liquid dispersion and leads to draining the heating surface in a short time period, which extremely decreases the heat transfer intensity.  $\tau_{t,e} < \tau_{b,e}$ ,  $\tau_{t,e} < \infty$  indicates that the heater draining would be provided by evaporation from the film free surface.

Therefore, the construction of the mathematical model, which allows calculation of boiling expectation time and time of total local evaporation for the heat-exchanging film systems, is an urgent problem applicable for the engineering practice.

Now there are many publications dealing with simulation of wave formation under the conditions of a liquid film flow and investigation of the wave motion influence on development of heat transfer processes and diffusion. However, there were no studies related to simulation of heat transfer processes in the falling wavy films of liquid at unsteady heat release and making it possible to predict the prevailing mechanism of development of the crisis phenomena depending on the regime parameters.

The mathematical model which allows the calculation of the wave surface profile, fields of velocity and

temperature as well as the study of their evolution at a drastic change in heat loads with time has been presented in the current work. This model allows calculations of the wave characteristics and parameters of liquid film decay at different regime parameters. The detailed description of the mathematical model has been presented in (Chernyavskiy, Pavlenko 2017).

The results of numerical simulation performed in the framework of the suggested model have been compared with the experimental data obtained for the liquid nitrogen (Pavlenko et al. 2007).

Boiling expectation times have been calculated as the functions of heat flux density in the falling films of liquid nitrogen upon various input Reynolds numbers (Figure 1). The boiling expectation time has been determined as the minimum time of reaching the given overheat by the heating surface. In the framework of the present work, three threshold values of overheating for the liquid nitrogen under conditions of atmospheric pressure have been used: two theoretically calculated values,  $\Delta T_{b,e} = 26$  K, corresponding to 95% and  $\Delta T_{b,e} = 32$  K, corresponding to 100% of probability of boiling under the conditions of homogeneous nucleation, and one approximation for experimentally retrieved dependency of overheat on heat flux density retrieved for boiling-up under the condition of heterogeneous nucleation:  $\Delta T_{b,e}(q) = 32 - 21.1585 \cdot 0.93^q$ ,  $q$  [W/cm<sup>2</sup>].

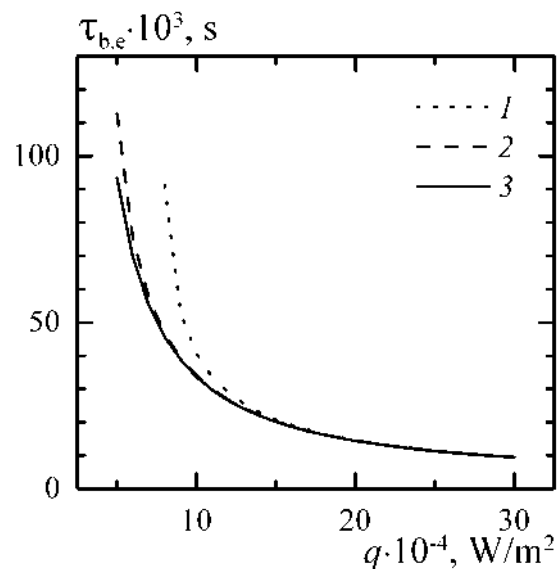
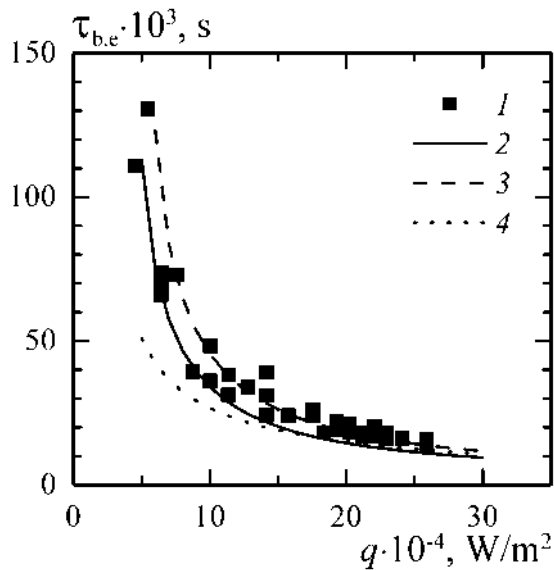


Figure 1: Calculated boiling expectation times,  $\Delta T_{b,e} = 26$  K: 1 —  $Re_{in} = 38$ ; 2 —  $Re_{in} = 230$ ; 3 —  $Re_{in} = 630$ .

For high heat fluxes, the calculated dependences are almost identical for all considered Reynolds numbers. In the region of low heat fluxes, discrepancy between the calculated curves is observed, which can be explained by a considerable contribution of evaporation to heat transfer upon the given parameters of the problem.

The calculated boiling expectation times are in satisfactory agreement with the experimental data (Pavlenko et al. 2007) found under the conditions of evolution of three-dimensional waves on a free surface of the film (Figure 2). The results of numerical simulation agree with experimental data because evolution of three-dimensional waves within the investigated range of Reynolds numbers does not lead to significant variation of the defining wave parameters that determines the contribution of the heat-transfer convective component.



**Figure 2:** Comparison between experimental and calculated boiling expectation times with different  $\Delta T_{b,e}$ ,  $Re_{in} = 230$ : 1 — Experimental data; 2 —  $\Delta T_{b,e} = 26$  K; 3 —  $\Delta T_{b,e} = 32$  K; 4 —  $\Delta T_{b,e} = \Delta T_{b,e}(q)$ .

The regime map, which describes the different mechanisms of decay of the falling wavy film of liquid nitrogen, has been obtained by summing up the results of numerical simulation (Figure 3). Calculated curves 1, 2 and 3 divide the area of the investigated Reynolds numbers and heat flux densities into the set of regions. Region I is characterized by the absence of crisis. Region II describes the set of the problem parameters, where liquid film decay will be performed by total local evaporation without liquid boiling-up. Region III describes the set of parameters where the liquid film decay will be performed by the film boiling-up. Calculated critical heat flux densities of the total local evaporation (curve 3) agree satisfactorily with the values calculated for steady heat release conditions using the formula presented by Pavlenko and Lel' (1997) - curve 4. This is a consequence of the system Fourier number  $Fo > 1$  which means that the time of temperature profile formation is less than the time of total local evaporation and critical heat flux densities in this regime are similar to critical heat

flux densities in the case of steady heat release.

According to the presented regime map, it is possible to make a conclusion that boiling-up becomes the prevailing decay mechanism independently on heat flux density, when the inlet Reynolds number  $Re_{in}$  exceeds 130 – 220 depending on liquid and heater parameters.

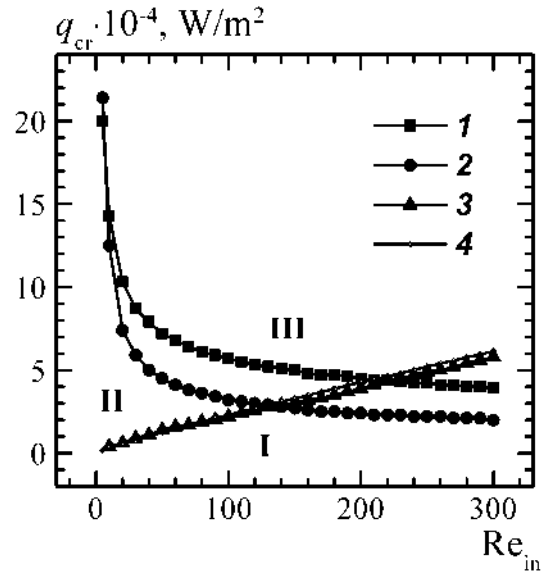


**Figure 3:** Regime map. 1,2 — Film decay on boiling-up,  $\Delta T_{b,e} = 26$  K,  $\Delta T_{b,e} = \Delta T_{b,e}(q)$ , respectively; 3 — Surface draining on unsteady heat release; 4 — Calculation of critical heat flux for evaporation on steady heat release using (Pavlenko, Lel, 1997) model.

The study was performed at Kutateladze Institute of Thermophysics SB RAS and was financially supported by the grant of the Russian Science Foundation (project No. 14-49-00010: blocks of unsteady heat transfer simulation and regime map with different mechanisms of development of the crisis phenomena) and the Russian Foundation for Basic Research grant (project No. 15-08-03221: simulation of wavy film flow hydrodynamics).

## References

- Chernyavskiy A.N., Pavlenko A.N., Numerical simulation of heat transfer and determination of critical heat fluxes at nonsteady heat generation in falling wavy liquid films, *International Journal of Heat and Mass Transfer*, Vol. 105, pp. 648-654 (2017)
- Pavlenko A.N., Surtaev A.S. and A.M. Matsekh, Transient processes in falling films of liquid under conditions of unsteady-state heat release, *High Temperature*, Vol. 45, pp. 826-836 (2007)
- Pavlenko A.N., Lel' V.V., Heat transfer and crisis phenomena in falling films of cryogenic liquid, *Russian Journal of Engineering Thermophysics*, Vol. 7, pp. 177-210 (1997)

## Two-dimensional numerical simulations of the hydrodynamic behaviour of a molten metal-gas-oxide model system

Sergey Semenov<sup>1</sup>, Renaud Denoyel<sup>1</sup>, Jean-François Haquet<sup>2</sup>, Pascal Piluso<sup>2</sup> and Mickaël Antoni<sup>1</sup>

<sup>1</sup> Aix-Marseille University, CNRS, MADIREL, 141 Trav. Charles Susini, 13013 Marseille, France

<sup>2</sup> CEA - Cadarache, DEN/DTN/SMTA/LPMA, Bât. 219B, 13108 Saint-Paul-lez-Durance, France

Nuclear accidents above INES Level 5 imply severe damage of the reactor vessel (2<sup>nd</sup> barrier) and possibly to the containment (3<sup>rd</sup> barrier). One of the consequences is the partial (or total) meltdown of the nuclear fuel due to the loss of the main cooling system. This molten material, called corium, consists of a mixture of the nuclear fuel, zircaloy (material of the 1<sup>st</sup> confinement barrier) and different reactor structural materials such as stainless steel. In case of failure of the vessel, the corium mixture will interact with the concrete containment pit, 3<sup>rd</sup> barrier before soil and ground water contamination. In this context, the configuration of metallic and oxidic phases, two immiscible liquids, will play an important role in Molten Corium Concrete Interaction (MCCI). The spatial distribution of the metallic phase is indeed a key to understand the kinetics of concrete alteration and the resulting ablation process.

Understanding the interaction of corium with a concrete containment pit is the goal of VULCANO-ICB experiments realized at CEA-Cadarache. They are conducted using prototypical materials: bath based on UO<sub>2</sub> and molten steel (Journeau et al. 2009). This experimental system modelled the coexistence of a dispersed phase (metallic droplets and gas bubbles) in a continuous phase (uranium oxide), capillary phenomena, heat exchange and gravity. A stratification by which dense liquids are found beneath lighter ones was expected. However experiments demonstrated separation of the metallic phase in macroscopic proportions (see figure 1). This is demonstrated by post-test analysis that evidence configurations in which the metallic phase is preferably close to the vertical concrete walls of the containment pit. Regarding to the complexity of the VULCANO-ICB experiments, numerical simulation is a straightforward tool to help understanding such unexpected behaviours.

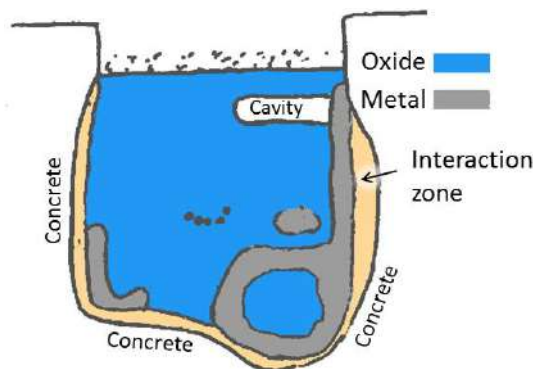


**Figure 1:** Schematic representation of the result of one of the VULCANO-ICB experiments.

The corium has been modelled numerically under isothermal conditions as a two dimensional dispersed medium with multiple metal drops and gas bubbles. For this purpose a home-made multiphase volume of fluid (VOF) code is employed (Lekhlifi et al. 2014, Lekhlifi et al. 2015). It solves the continuity and Navier-Stokes equations for an incompressible medium along with the advection equation for three color functions. In VOF methods, different immiscible fluids are treated as a unique continuous phase but with changing material properties (density and viscosity) according to the local value of color functions. The interfacial stresses are directly included into Navier-Stokes equations in form of equivalent body forces (density-scaled continuous surface forces) according to the Brackbill's approach (Brackbill et al. 1992). Three-phase interactions and wetting phenomena are included in the algorithms. Interfaces are reconstructed using a Piecewise Linear Interface Calculation (PLIC) algorithm. Color functions are advected using the unsplit Eulerian Implicit – Lagrangian Explicit (EI – LE) method (Aulisa et al. 2003). Interfacial curvature is computed with the aid of a height-function (Popinet 2009). The numerical technique is based on 2<sup>nd</sup> order discretization schemes in both time (Backward Differentiation Formula) and space. Pressure is computed with a 2<sup>nd</sup> order (in time) projection scheme. The finite volume method on a staggered (enforcing a balanced-force formulation) uniform computational mesh is used for spatial discretization of all the equations. The resulting system of discretized non-linear equations is solved iteratively with help of effective pentadiagonal solvers: MSIP (Modified Strongly Implicit Procedure) for velocity components and CG-SIP (Conjugate Gradient with Strongly Implicit Procedure preconditioner) for pressure.

The resulting numerical code remains stable for a wide range of involved interfacial tensions, phase viscosities and densities, making it suitable for various multiphase free interface problems, including fluid mixtures under extreme conditions, like in corium. The results of CFD simulations of a metal-gas-oxide model system demonstrate evolving interfaces with complex geometries. Figure 2 shows an example of time evolution of a test system with properties given in table 1, and with all interfacial tensions set to 1.8 N/m. With the mesh size of 300x200 finite volumes, simulation of 10 physical seconds took less than 3 days of computational time on one CPU core.

**Table 1:** Properties used in the numerical simulation presented in figure 2.

	Density, kg/m <sup>3</sup>	Dynamic viscosity, mPa·s
Oxide	6560	5.28
Metal	6850	5.20
Gas	1.2	0.0183

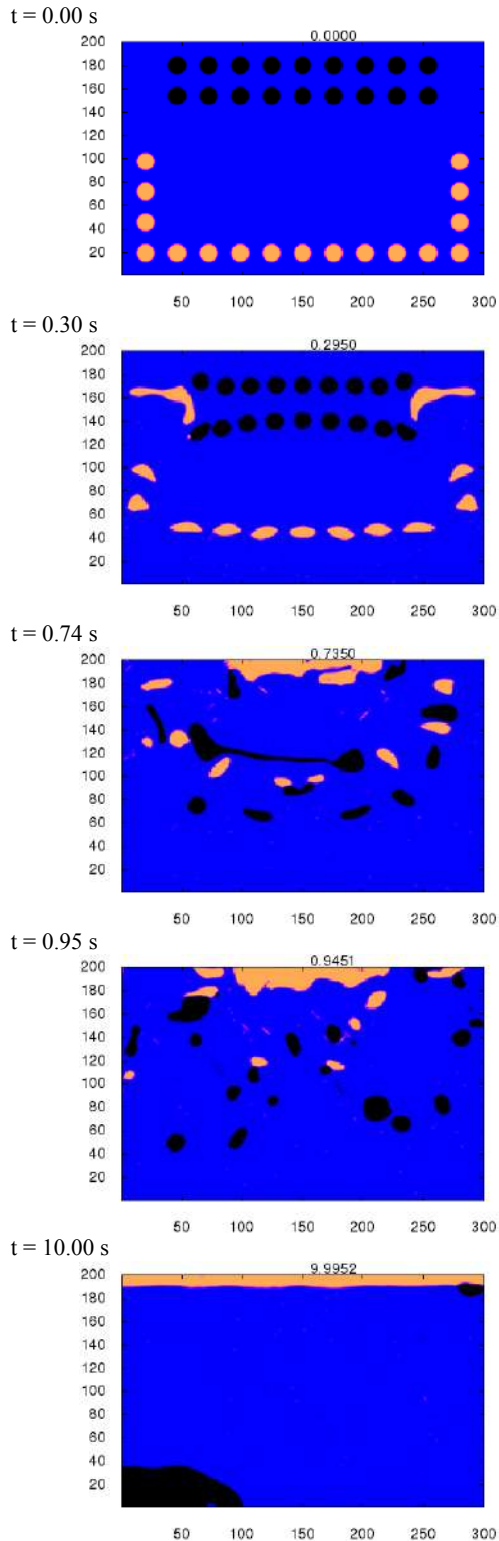


**Figure 2:** Time evolution of a three-phase system of size 300 mm x 200 mm with initial drops and bubbles radius of 7.5 mm. Black, orange and blue colors represent metal, gas and oxide phases, respectively.

Based on the performed numerical studies one can conclude that a suspension of metallic drops (black color in figure 2) in a continuous oxide phase (blue color in figure 2) may result in a primary phase separation as a result of two phenomena: convective flow in the bath due to gravity, and wetting of the concrete walls by the metallic phase. Rising gas bubbles (orange color in figure 2) near the concrete walls of the VULCANO-ICB experiments and possible flotation phenomena can also contribute to the upward motion of the metallic phase, promoting its further segregation.

The values of interfacial tensions and thermophysical properties (Table 1) used for the computation shown in figure 2 have been taken into account to validate the general methodology and the modelling. The values are not strictly the same as for oxidic and metallic melts used in VULCANO facility. In particular, the dynamic viscosity of the oxide phase should be one order of magnitude larger, while the gas density should be one order of magnitude smaller. This will change the typical time scales of the system (and increase drastically CPU time), but we believe the main features of figure 2 to remain. Future simulations will be devoted to this problem. Another future goal is to include in the model heat transfer and action of thermocapillary and solutocapillary stresses at system's interfaces, as well as reactivity to account for metal oxidation.

## References

- Aulisa E., Manservigi S., Scardovelli R., Zaleski S., A geometrical area-preserving Volume-of-Fluid advection method, *J. Comput. Phys.*, Vol. 192 pp. 355-364 (2003)
- Brackbill J.U., Kothe D.B. and Zemach C., A continuum method for modeling surface tension, *J. Comput. Phys.*, Vol. 100 pp. 335-354 (1992)
- Journeau C., Piluso P., Haquet J.-F., Boccaccio E., Saldo V., Bonnet J.-M., Malaval S., Carénini L. and Brissonneau L., Two-dimensional interaction of oxidic corium with concretes: The VULCANO VB test series, *Annals of Nuclear Energy*, Vol. 36 pp. 1597-1613 (2009)
- Lekhlifi A., Ouazzani J. and Antoni M., Drainage of water droplets in a bounded paraffin oil continuous phase: role of temperature, size and boundary walls, *Colloids and Surfaces A*, Vol. 460 pp. 342-350 (2014)
- Lekhlifi A., Fanzar A. and Antoni M., A numerical investigation on the drainage of a surfactant-modified water droplet in paraffin oil, *Adv. Colloid Interface Sci.*, Vol. 222 pp. 446-460 (2015)
- Popinet S., An accurate adaptive solver for surface-tension-driven interfacial flows, *J. Comput. Phys.*, Vol. 228 pp. 5838-5866 (2009)

## Stable liquid film flow during changeable gravity level

V.V. Cheverda<sup>1,2</sup>, O.A. Kabov<sup>1,3</sup>

<sup>1</sup> - Kutateladze Institute of Thermophysics SB RAS, Novosibirsk 630090, Russia

<sup>2</sup> - Novosibirsk State University, Novosibirsk 630090, Russia

<sup>3</sup> - Tomsk Polytechnic University, Tomsk 634050, Russia

Over time, silicon-based technology gains in performance become less expensive to produce, are more plentiful and capable, and become more seamlessly integrated in our daily lives. As result with increasing transistor density of processors, heat dissipations from processors is increasing. Roadmap projections for the high-performance chip category suggest that the maximum chip power dissipation will exceed 500W (Bar-Cohen and Rahim, 2007). A cooling system based on liquid film flow is a promising solution for on-ground and space applications. The heat removal mechanism with the help of a liquid film cooling effect for space applications, has been proposed in (Kim et al., 1994). During the microgravity stable liquid film flow is not investigated.

The experimental setup is specially designed for the parabolic flights. The setup should satisfy for safety technical requirements defined by European Space Agency (ESA) organization. For further detail see (Cheverda, Glushchuk, Queeckers, Chikov, Kabov, 2013). The special test cell is used for the liquid film investigation during variable gravity instead of test for shear driven liquid rivulet flow. The test cell consists of: 1) textolite base plate, 2) stainless steel substrate, 4) liquid film knife, 5) textolite frame and 6) textolite cover with optical window, see Fig. 1. The basic element of the test section is a flat plate of stainless steel. Several calibrated thermistors have been used to manage temperature in several key points. The plate is fixed on the textolite base along with the textolite frame. The frame with the plate is covered by a transparent window forming a rectangular minichannel with dimensions of 67 x 30 x 1.4 mm<sup>3</sup> (length, width and depth respectively). Thermo-electrical module (Peltier elements) is used to stabilize substrate temperature. The liquid is supplied to the buffer chamber of the test cell. The liquid film generated in the nozzle is driven along the channel by the gas flow. The liquid-gas mixture is evacuated to the atmosphere by a vacuum pump.

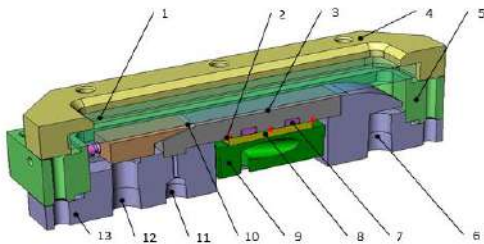


**Figure 1:** Cross-section of the test cell for the liquid film flow with a constant substrate temperature (regulated by Peltier element): 1 – optical window, 2 – thermosensors, 3 – stainless steel plate with silver coating, 4 – textolite cover, 5 – textolite frame, 6 – two-phase mixture outlet, 7 – thermostickers, 8 – Peltier elements, 9 – water heatexchanger, 10 – liquid gap, 11 – liquid inlet, 12 – gas inlet, 13 – textolite base.

In some cases, the expansion of a dilative rivulet is so fast that their boundaries contact the walls of the channel and thus the flow transforms to the film flow. The liquid film flows at different gas and liquid flow rates and levels of gravity are presented in Fig. 2. For any gravity level it is easier to create the liquid film by increasing the flow rate of liquid. It is more difficult to create liquid film at low gravity (Fig. 3). Surface tension became a dominant force strives to minimize the surface. In terms of energy in microgravity rivulets are more efficient then film. That is why the threshold flow rates of liquid necessary to provide the transition from rivulet to the film at microgravity level is several times larger than for normal and hyper gravity.

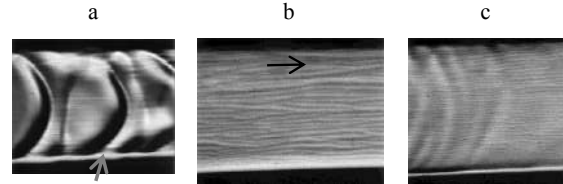


**Figure 2:** The stable shear driven liquid (FC-72) film flow during different level of gravity: a – weightlessness (0.01g), b – normal (1.0g), c – hypergravity (1.8g);  $Re_l=57.2$ ,  $Re_g=370$ ,  $T_s=10^\circ C$

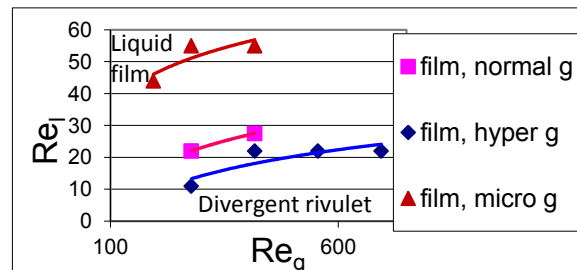


**Figure 3:** Divergent rivulet and liquid film flow for normal, hyper gravity and microgravity for different flow rates

**Acknowledgments.** The authors gratefully acknowledge support ESA Programme.

### References

- Bar-Cohen A. and Rahim E., Proceedings of the 5th International Conference on Nanochannels, Microchannels, and Minichannels ICNMM2007 (2007)
- Kim H., Bankoff S.G., Miksis M.J., J. Heat Transfer, Vol. 116, pp. 986-992 (1994)
- Cheverda, V., Glushchuk, A., Queeckers, P., Chikov, S. B., Kabov, O.A., Microgravity sci. technol., Vol. 25, No. 1, pp. 73-81 (2013).

## **Development of Mechanically Pumped Two-Phase Loop for Space Applications**

Zhenhui He

director of Center for Space Technology, a member of the Chinese Society of Space Research, Development of Mechanically Pumped Two-Phase Loop for Space Applications

Pumped two-phase loops, such as LHPs and CPLs, have been used in space for many years. Because of the coupling between the heat load and the flow rate, the applications are limited, especially for the instability in start-up. A mechanical pump can control the flow rate actively, and thus partially separates the coupling. A large potential of space application is foreseen. In this note, we introduce a few attempts in our group, to develop mechanically pumped two-phase loops for space applications

The first attempt of mechanically pumped two-phase loop, called TTCS, was developed to support the precision measurement of cosmic ray by AMS-02 on the ISS. It has been operating in space for almost six years. The heat load with distributed heat sources is constant, while the environmental temperature varies in a wide range, sometimes, steeply. To keep the AMS-02 tracker in constant, and uniform distributed temperature, CO<sub>2</sub> is used as working fluid. To dissipate heat of about 160W for the transportation distance of more than ten meters, a centrifugal pump is used to circulate the CO<sub>2</sub>. The transportation tubes were designed as small as possible to avoid secondary particle effect, requested by the AMS experiment. Some of the in-orbit performance will be presented.

The second attempt is to support the condensation experiment in the TianZhou cargo one(TZ1). To strength the circulating pump from the cavitation risk, a screw pump was developed, especially, for the two-phase loop. In this case, the heat load can vary from 0 to 90W, depending on the experiment; while the thermal environment is relatively stable, with the setup mounted inside the cargo chamber. R134a is used as the working fluid for this single two-phase loop. In-orbit performance would be observed from May to October, 2017.

To support more two-phase flow experiments in microgravity in the Chinese Space Station, and based on the idea of reusable fluid driving unit, a model of providing low flow-rate liquid with control temperature is proposed and conceptually designed.

## Experimental study dynamics of explosion boiling of liquids on the microheater

Igor Kozulin, Vladimir Kuznetsov

Institute of Thermophysics SB RAS  
pr. Akademika Lavrentjeva, 1, Novosibirsk, 630090, Russia  
[kozulin@itp.nsc.ru](mailto:kozulin@itp.nsc.ru)

In recent years, researches of heat and mass transfer with phase change in microfluidic systems, are rapidly developed. This is related to a growing interest in the MEMS technology (microelectromechanical systems). The MEMS technology makes it possible to obtain extremely high temperatures without the breakdown of the microheater. Experimental investigations of the explosive boiling on the flat microheater in a pulsed heating mode were made by Kuznetsov et al. (2010), Zhao et al. (2000). In this case, the decay of liquid metastable state occurs near the temperature of limit overheating. The aim of this work is an experimental study of the initial stage of explosive boiling of propanol-2 on a microheater using an original optical system.

The experimental setup for studying the dynamics of explosive boiling on the microheater is shown in Fig. 1.

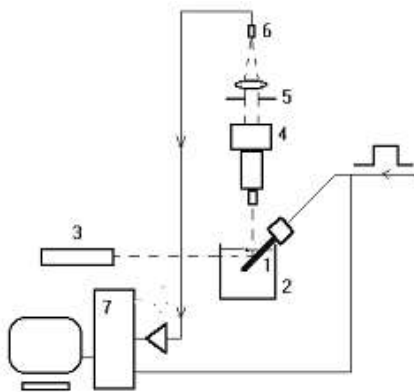


Figure 1: Experimental setup

The multi-layer thin film microheater used in the experiments (1) was described in Allen et al. (2000). The microheater (1) is immersed in the working fluid (2), and its surface is lit by laser (3). The initial temperature of the liquid was determined before the experiment and ranged from 18 to 21°C, the experiments were conducted at atmospheric pressure. The single rectangular current pulse is supplied to microheater from the 214B Hewlett Packard pulse generator. Each pulse has sufficient duration for the explosive boiling of liquid near the surface of the microheater. The initial stage of explosive boiling was studied using the optical registration, based on measuring the intensity of the laser beam (3) reflected from the mirrored surface of the microheater (1). The reflected laser beam from the heater enters to the microscope (4). The diaphragm (5) selects an area with the microheater surface. The intensity of the laser beam is measured by the photodiode (6). The signal from photodiode is registered

with the high-speed ADC (7). The integral coefficient of the reflection of laser light begins to decrease during the appearance of microbubbles on the microheater. The signal from the photodetector provides the information about the history of the heater surface coverage by vapor bubbles.

Figure 2 shows the dynamics of surface coverage by the bubbles during the explosion boiling of isopropanol (propanol-2) on the microheater. The normalized signal from

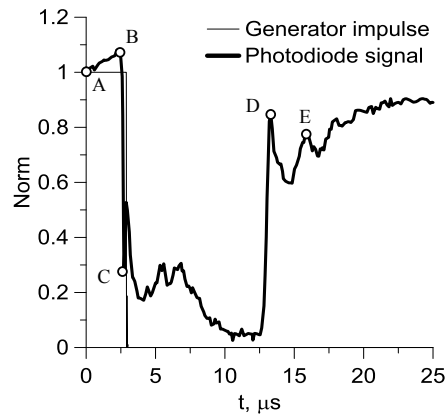
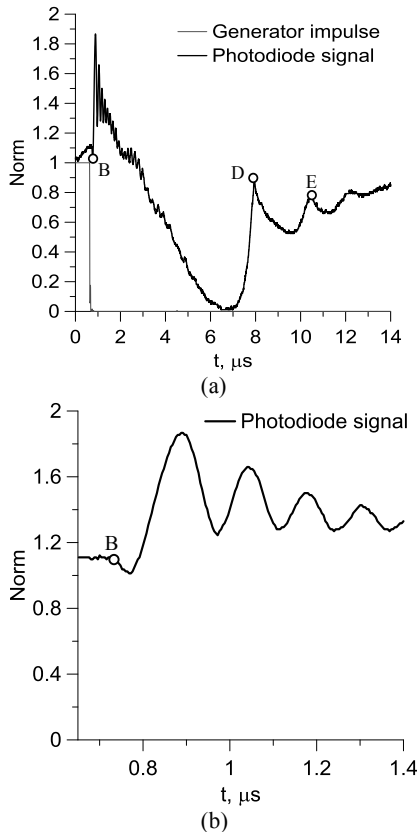


Figure 2: The intensity of the reflected laser beam depending on the time during the explosion boiling of propanol-2  $q_{\text{eff}}=376.7 \text{ MW/m}^2$ ,  $dT/dt=58.41 \text{ MK/s}$ ,  $t=2.912 \text{ μs}$ .

the generator is also shown in Fig. 2 by a thin line. The dark line shows the dependence of reflected light intensity from the microheater according to the time during the explosion boiling of propanol-2 for the effective heat flux  $q_{\text{eff}}=376.7 \text{ MW/m}^2$ , the growth rate of temperature  $dT/dt=58.4 \text{ MK/s}$  and duration of the heating pulse  $t=2.91 \text{ μs}$ . The zero time in Fig. 2 corresponds to a supply of heat pulse from the generator.

Letters A, B, C, D and E in Fig. 2 identify four basic stages of explosive boiling of liquid. The first stage from point A to point B corresponds to the heating of the liquid by heating pulse from the generator. The signal increased in this area because of the change of the optical properties of the microheater surface. The second stage starts from point B which corresponds to the first appearance of bubbles on the surface of microheater and continues to point C. It corresponds to the growth of number of the bubbles on the microheater, which causes a sharp decrease of the reflected laser beam intensity scattering on the bubbles. The exponential growth of the bubbles number is determined by the frequency of homogeneous nucleation (Kuznetsov et al. 2010).

Figure 3 (a) shows the intensity of the reflected laser beam depending on the time during the explosion boiling of propanol-2 for an increased effective heat flux. The normalized signal from the generator is presented by the thin line. The dark line shows the dependence of intensity of reflected light according to the time during the explosion boiling of propanol-2 for the effective density of heat flux  $q_{\text{eff}}=1482.5 \text{ MW/m}^2$ , the growth rate of temperature  $dT/dt=264.4 \text{ MK/s}$  and duration of the heating pulse  $t=0.744 \mu\text{s}$ . The signal detailing from the photodiode is shown in Figure 3 (b). It is seen, for a



**Figure 3:** (a) The intensity of the reflected laser light depending on the time during the explosion boiling of propanol-2  $q_{\text{eff}}=1482.52 \text{ MW/m}^2$ ,  $dT/dt=264.43 \text{ MK/s}$ ,  $t=0.744 \mu\text{s}$ , (b) the signal detailing.

temperature growth rate is higher than 264 MK/s, the nature of the signal changes. There are oscillations in a signal from the photodiode, which may indicate an earlier formation of the vapor cavity due to the unification of the bubbles. A comparison of the reflected light intensity and photographs obtained using a pulsed laser, showed that the cause of this behavior is the appearance of a powerful evaporation wave at the initial stage of explosion and transition to a continuous vapor film that reflects light well.

The dependence of temperature of the explosion boiling initiation from the temperature growth rate for isopropanol, is presented in Fig. 4. Here, the dotted line presents the solution of an equation  $T_{\text{lim}}/T_{\text{cr}}=0.905+0.095 \cdot (T_{\text{sat}}/T_{\text{cr}})^8$  for limiting overheating of liquid based on the data of

Skripov (1974). The solid line shows the spinodal line calculated in the paper Skripov et al. (1988).

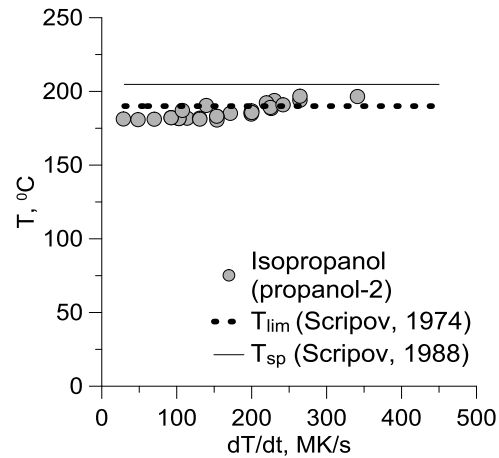


**Figure 4:** The dependence of start temperature of the explosion boiling of propanol-2 from the growth rate of temperature

The analysis of dynamics of the explosive boiling of propanol-2 on the microheater with dimensions of  $100 \times 110 \mu\text{m}$ , is presented in this paper. The dynamics of microheater surface coverage with vapor bubbles depending on effective heat flux and the dependence of temperature of the explosion boiling initiation from the temperature growth rate are determined in this work. The temperature growth rate that corresponds to the change in the mode of vapor phase generation, is determined. It shows a change of the mechanism of the liquid decay in the vicinity of spinodal at a high liquid temperature growth rate.

The research was carried out in the IT SB RAS with the support of the Russian Science Foundation grant (project No. 16-19-10519).

## References

- Kuznetsov V. V., Kozulin I. A. Explosive vaporization of a water layer on a flat microheater, *Journal of Engineering Thermophysics*, Vol. 19, No. 2, pp 102-109 (2010).
- Zhao Z., Glod S. and Poulikakos D. Pressure and power generation during explosive vaporization on a thin-film microheater, *Int. J. Heat Mass Transfer*, Vol. 43, pp. 281-296 (2000).
- Allen R.R., Meyer J.D. and Knight W.R. Thermodynamics and hydrodynamics of thermal ink jets, *Hewlett-Packard J.*, Vol. 36, pp. 21-27 (1985).
- Skripov V.P., *Metastable liquids*. John Wiley & Sons, New York (1974).
- Skripov, V.P.; Sinitsyn, E.N.; Pavlov, P.A.; Ermakov, G.V.; Muratov, G.N.; Bulanov, N.V.; Baidakov, V.G. *Thermophysical properties of liquids in the metastable (superheated) state*; Gordon and Breach Science Publishers: New York (1988).

## Thermo-hydraulic characterization of semi-transparent Flat-Plate Pulsating Heat Pipes in variable gravity regimes

Thibaud Solé-Agostinelli, Vincent Ayel, Florent Vigoureux, Cyril Romestant, Yves Bertin  
and Marco Marengo

Institut Pprime, CNRS – ENSMA - Université de Poitiers, UPR 3346, Département Fluides, Thermique, Combustion, 1  
av. Clément Ader – BP 40109 86961  
Futuroscope - Chasseneuil Cedex, France  
E-mail : thibaud.sole-agostinelli@isae-ensma.fr

An experimental study is reported of a series of six Closed Loop Flat Plate Pulsating Heat Pipe tested under ground, hyper and microgravity conditions. Pulsating Heat Pipes are thermally driven two-phase passive devices mainly based on phase change phenomena (film evaporation, flow boiling, film condensation) and capillary forces, even if also gravity plays an important role. They consist of a meandering capillary tube closed in a loop, evacuated and partially filled with a working fluid at saturation conditions. Once the heat load is applied, the fluid motion starts and an oscillating pattern of alternating vapour bubbles and liquid plugs forms inside the tube.

As it is widely accepted, complex flow patterns, ranging from slug flow to annular flow, occur in the adjacent tubes of pulsating heat pipes (PHP), initiated by local pressure instabilities ((Khandekar et al. 2003) and (Liu et al. 2007). Such flow patterns have obviously effects on the total heat flux transferred from the heated to the cooled ends of the PHP. Many parameters have also a direct influence on their operation (Charoensawan et al. 2003): number of turns, PHP dimensions, filling ratio and physical properties of the working fluid, applied heat power, etc. One of the most important parameter is the channel internal diameter permitting liquid/vapor phase division into liquid slugs and vapor bubbles separated by menisci due to capillary forces. And, more particularly in the context of this study, the inclination with respect to gravity or, generally, the change in the value of acceleration (for example, for tests on board of an aircraft during a parabolic flight campaign and/or under microgravity conditions for space application, (Gu et al. 2005, Ayel et al. 2015 and Mangini et al. 2015). This paper presents some results obtained during the ESA

64<sup>th</sup> Parabolic Flight Campaign during which six similar Flat Plate Pulsating Heat Pipes (FPPHP) have been tested. One example of FPPHP can be seen on Fig. 1. The FPPHP were milled from copper plates (length: 204 mm, with varying widths and thicknesses according to the channel dimension, see below) with a single square shaped groove, forming a series of 11 U-turns in the evaporator (see Fig. 1). Every PHP channels were square shaped, with dimensions  $D$  varying from 1.5 mm to 3 mm. Three condenser lengths (5, 10 and 15 cm) were also tested for the 2.5 mm channel FPPHP. A containment channel link to a reservoir previously emptied has been set in order to avoid introduction of non-condensable gazes in the device (Fig. 1). Thus, considering six devices tested during 3 days of flight, each day 2 separate FPPHP were tested with doubled instrumentation. Two visible cameras (Canon® EOS 100D and 550D, 50 Hz) recorded movies allowing visualizations of fluid flow

motions in the overall channels of both PHP. Ten T-type thermocouples of 0.5 mm ( $\pm 0.5$  K) monitor the temperature of each section in the PHPs: three for each FPPHP evaporator (TEV1-TEV6); two in the water cooling loop and two thermocouples instrument the air temperatures. Two pressure sensors (GE PTX5076-TA-A3-CA-HO-PS, 5 bars absolute,  $\pm 200$  Pa) allow recording of local fluid pressure at the top of the condenser zones. A  $g$ -sensor (DE-ACCM3D,  $\pm 0.1g$ ) is used to measure the gravity level variations during each parabolic flight.

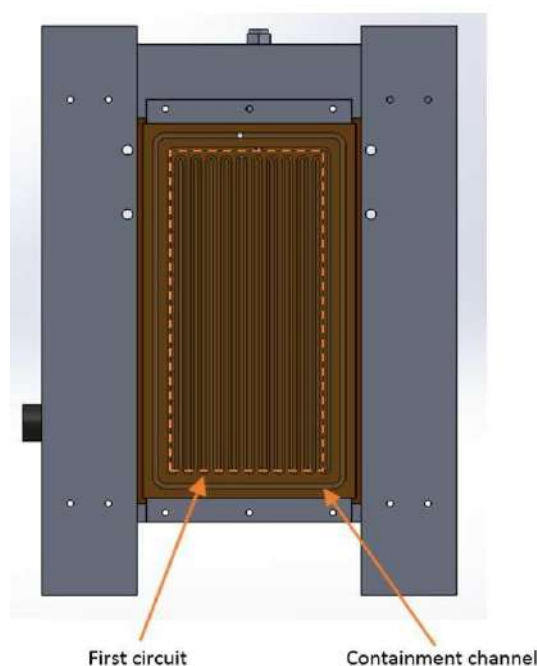


**Figure 1:** Schematic view of one FPPHP tested during the ESA 64<sup>th</sup> parabolic Flight campaign.

The operating conditions were the following ones: Fluid: FC72; filling ratio: 50%; heat power applied: from 20 to 150 W; cold source: plane ambient air; orientation: vertical bottom heated mode (BHM).

Foremost, in Fig. 2 are shown representative temperatures and acceleration profiles for the FPPHP tested with 100 W heat power applied on a set of five successive parabolas (here, only two parabolas are represented). First observation is that temperatures rise in the evaporator zone together with their decrease in the condenser zone during

microgravity phases. Furthermore, the evaporator temperature curves in microgravity are subject to some oscillations that will be explained thanks to visualizations.

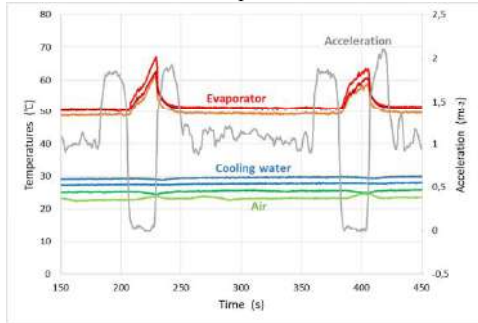


**Figure 2:** Transient temperatures and acceleration responses of the FPPHP to a series of 2 successive parabolas ( $D = 3$  mm,  $Q = 100$  W).

The major findings observed thanks to visualizations during this 64<sup>th</sup> PF campaign are: first, the fluid distribution tends spontaneously to a dry-out at the evaporator zone due to higher and homogenized vapor pressures in the channels; secondly, isolated liquid plugs can easily move under the influence of small pressure instabilities, and that whatever the channel dimensions and the condenser length. An example of visualization of an isolated liquid plug flowing towards the evaporator zone and being subjected to harsh evaporation can be seen on Fig. 3. The pressure increase due to this evaporation will be at the origin of massive mass and heat transfers which spreads throughout the whole PHP channels.

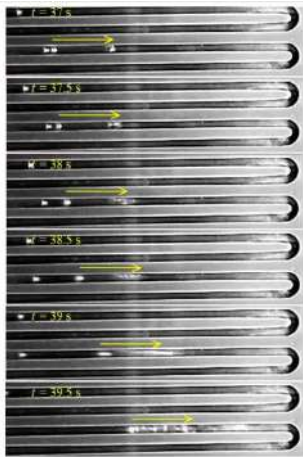


**Figure 3:** Sequence of macro images of isolated liquid plug during microgravity conditions flowing towards the evaporator ( $D = 3$  mm,  $Q = 100$  W).

Another observation was that even with no heat power applied, the liquid plugs began to move as soon as they were in microgravity condition. A video post-processing by image analysis has been done for some visualizations, allowing tracking the menisci positions as functions of time. An example of such displacement can be seen on Fig. 4 during

microgravity conditions, for two menisci situated in adjacent channels, linked by a liquid plug, without heat power applied. The condition of incompressibility of the liquid plug make the displacements symmetrical between both menisci. If the motions were short for the lower channel dimensions (1.5-2 mm), their amplitude was of the order of magnitude of the length of the channels for the bigger diameters (2.5-3 mm). Obviously, the fluid movements were slower and less high amplitude for the lowest channel diameters. This point remains to be clarified.

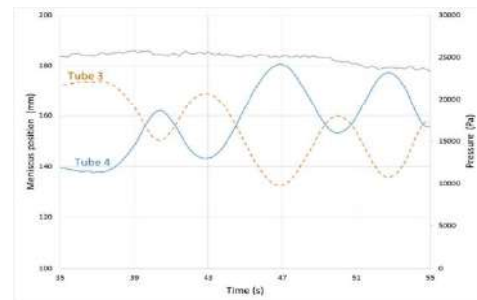


**Figure 4:** Motion of two adjacent menisci during microgravity conditions ( $D = 3$  mm,  $Q = 0$  W).

## References

- Khandekar S., Charoensawan P., Groll M., Terdtoon P., Closed loop pulsating heat pipes, part B: visualization and semi-empirical modeling, *Applied Thermal Engineering*, Vol. 23, pp. 2021-2033 (2003)
- Liu S., Li J., Dong X., Chen H., Experimental study of flow patterns and improved configurations for pulsating heat pipes, *Journal of Thermal Sciences*, Vol. 16, pp. 56-62 (2007)
- Charoensawan P., Khandekar S., Groll M., Terdtoon P., Closed loop pulsating heat pipes, part A: parametric experimental investigations, *Applied Thermal Engineering*, Vol. 23, pp. 2009-2020 (2003)
- Gu J., Kawaji M., Futamata, R., Microgravity performances of micro pulsating heat pipe, *Microgravity Science and Technology*, Vol. 16, pp. 181-185 (2005)
- Ayel V., Araneo L., Scalambra A., Mameli M., Romestant C., Piteau A., Marengo M., Filippeschi S., Bertin Y., Experimental study of a closed loop flat plate pulsating heat pipe under a varying gravity force, *International Journal of Thermal Sciences*, Vol. 96, pp. 23-34 (2015)
- Mangini D., Mameli M., Georgoulas A., Araneo L., Filippeschi S., Marengo, M., A pulsating heat pipe for space applications: Ground and microgravity experiments, *International Journal of Thermal Sciences*, Vol. 95, pp. 53-63 (2015)

## Experimental characterization of two-phase flow regimes and flow boiling in microchannel

Fedor Ronshin, Vyacheslav Cheverda, Evgeny Chinnov, Yuriy Dementyev, Oleg Kabov

Kutateladze Institute of Thermophysics, Siberian Branch, Russian Academy of Sciences 1, Lavrentiev ave., Novosibirsk, 630090, Russia  
Novosibirsk State University  
1, Pirogova str., Novosibirsk, 630090, Russia  
E-mail: f.ronshin@gmail.com

Currently, in microelectronics there is a growth of performance of microprocessors due to an increase in the number of transistors per unit area. This increases the heat flow from the processor in general. Reduction of the sizes of the liquid heat exchanger appear to be an effective solution, since the ratio of heat transfer surface area to volume increases inversely proportionally to its transverse dimensions. This feature causes a high heat transfer rate in such systems. Therefore, the microchannel cooling systems gain a substantial propagation.

Two-phase flow, that is used in various systems in microelectronics, aerospace industry, transport, energy and other industries, has been actively studied in recent years. A significant amount of papers on the two-phase flow in mini- and microchannels has been published. Overview of publications on the two-phase flow in microchannels of various configurations is contained in Chinnov and Kabov (2006), Rebrov et al. (2010), Chinnov et al. (2015). The process is significantly affected by conditions of gas and liquid input in the channel and channel parameters, such as size and shape. Many studies consider circular microchannels, although the rectangular microchannels have a greater prospect for using in systems of thermal stabilization and cooling. In rectangular microchannels, the flow pattern differs substantially from the flow regime in pipes. Chinnov et al. (2016) study the mechanisms influencing the formation of the two-phase flow. Two new types of instability (frontal and lateral) are distinguished; they are responsible for the formation of flow regimes in a microchannel, depending on the channel dimensions and liquid and gas flow rates. The structure of two-phase flows in microchannels is not fully understood and requires detailed study.

Flow boiling in microchannels offers several advantages, such as an extremely high heat transfer rate in a small contact area at low rates of coolant flow, ease of manufacturing process, and little hydraulic resistance compared to single-phase cooling systems. However, the design of microchannel cooling systems requires a deep understanding of the flow structure, of the attendant heat transfer and of pressure drop in the microchannel. Temperature measurement and flow pattern visualization are of utmost importance to the assessments and evaluations necessary for this purpose. Recently, a considerable number of works has been published, devoted to boiling in microchannels (Bar-Cohen and Rahim, 2008; Kabov et al., 2011).

In the present work, the new experimental technique has been devised. The modification of schlieren method that allows one to clearly register the main characteristics of a two-phase flow in horizontal microchannels, such as a thin liquid film on the upper and lower walls of a microchannel (up to several microns), drops, liquid bridges and jets has been developed. The method is used for registration and visualization of surface deformations of a thin liquid film. The light from the source entered the microchannel with the gas-liquid flow through a diffuser, lens, beam splitter and an optical glass. The light reflected from the gas-liquid interface passes through a beam splitter, a lens and a camera lens filter. The schlieren knife-edge shifted by a micro-screw highlights the central part of the light flux. As a result, the camera captures the image in various shades, where each shade corresponds to a certain angle of inclination of the liquid-gas interface. The use of this technique allows us to accurately register the structure of a two-phase flow in channels and clearly define the boundaries between regimes.



**Figure 1:** Characteristic images obtained by a modified schlieren-method. (a) liquid flow in the microchannel; (b) the formation of the film on the lower wall of the microchannel; (c) the formation of the film on the upper wall of the microchannel.

1 – gas input into the microchannel; 2 – the slit in the lower wall of the microchannel for liquid input; 3 – unwetted area on the upper and lower walls of the microchannel; 4 – microchannel area filled by liquid; 5 – film on the lower wall of the microchannel; 6 – film on the upper wall of the microchannel.

White arrow is the direction of gas motion, and black arrows are directions of liquid motion.

Examples of images obtained by the developed modification of the schlieren-method are shown in Fig. 1. Gas is fed into the region (1), liquid is supplied into the region (2) and a flow regime is formed. When the flow rate of liquid is much higher than the gas flow rate, the channel is almost completely filled with liquid, Fig. 1a. In this pattern, there is a clear difference between the microchannel area filled with liquid (4) and the unwetted area on the top and bottom walls of the microchannel (3). This area is located on the edges of the microchannel and is a few millimeters in width. In Fig. 1b, one can observe the motion of a thin liquid film on the bottom wall of the microchannel (5). Movable vertical liquid bridges between the upper and lower walls of the channel (4) and surges of liquid on the upper wall of the microchannel (6) have been also formed. Such regime is observed at high gas flow rates and low liquid flow rates.

At an increase in flow rate of the liquid, the liquid film begins to form on the upper wall of the channel, the gas with the drops of liquid and liquid bridges between the films move. Fig. 1c presents a characteristic photograph of such a regime. Near the liquid nozzle, the film has been formed on the bottom wall of the microchannel (5). The film on the upper wall of the microchannel (6) forms at a distance of several millimeters from the liquid input in the channel. It is also possible to observe the vertical motion of liquid bridges in such regime (4). Thus, the basic types of gas-liquid flows in a microchannel have been distinguished. It should be noted that this method allows registering the main characteristics of the two-phase flow: liquid bridges between the upper and the lower walls of the microchannel and the film on the top and bottom walls of the microchannel.

The obtained images are processed by matlab. Local void fraction, the characteristic areas of the films on the upper and lower walls of the microchannel is established in time. With the help of the obtained numerical characteristics, as well as the measured pressure drop in the microchannel, the boundaries between the regimes of two-phase flow and their main features are precisely established.

Figure 2 shows the mean void fraction of two-phase flow of FC-72 with nitrogen in the microchannel crosssection of  $0.15 \times 20 \text{ mm}^2$ , against the gas superficial velocity at fixed liquid velocities. At very small superficial gas velocities, the jet regime is observed when the gas moves in the central part of the microchannel, and the bulk of the liquid moves at its periphery along side walls and as jets in the center of the microchannel. With the increase in the liquid superficial velocity, it occupies a much larger part of the microchannel, and the gas jet moves along the center and void fraction in the microchannel decreases. This is clearly seen from Figure 2. With the increase in the superficial gas velocity, the liquid is redistributed and moves along the channel in the form of a liquid film, this is the transition to the annular flow regime. In the annular flow regime, the liquid moves along the walls of the microchannel in the form of a film, and in the central part, the gas together with the vertical liquid bridges forms the core of the flow. The gas occupies much larger volume than the liquid. This transition is indicated in Figure 2 by the solid black line. It can be seen that in the transition to the annular flow regime, the void fraction in the microchannel does not increase with the increase in the superficial gas velocity. Most part of the liquid moves along the channel in the form of a film.

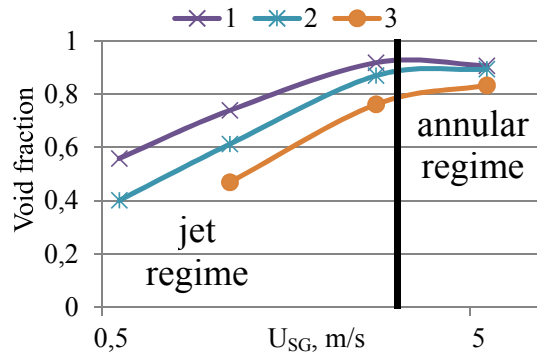


**Figure 2:** Mean void fraction against against the gas superficial velocity at fixed liquid velocities: (1) USL = 0.027 m/s (2) USL = 0.055 m/s (3) USL = 0.11 m/s

The developed experimental technique allows precise determination of the boundaries between the regimes in the microchannel with the help of the quantitative characteristics of the two-phase flow regimes, such as the local void fraction, the characteristic areas of the films on the upper and lower walls of the microchannel, and the measured pressure drop in the microchannel. Understanding the structure of a two-phase flow is extremely important for studying boiling in microchannels.

The study was supported by the Russian Science Foundation (Agreement No. 15-19-30038)

## References

- Bar-Cohen, A., Rahim, E., Modeling and Prediction of TwoPhase Microgap Channel Heat Transfer Characteristics, Heat Transfer Engineering, Vol 30, pp. 601-625 (2008).
- Chinnov E.A., Kabov O.A., Two phase flow in pipes and capillary channels (review), High temperatures, Vol. 44, No. 5, pp. 777-795 (2006)
- Chinnov E.A., Ron'shin F.V., Kabov O.A., Regimes of twophase flow in micro- and minichannels (review), Thermophysics and Aeromechanics, Vol. 22, No. 3, pp. 265-284 (2015)
- Chinnov E.A., Ron'shin F.V., Kabov O.A., Two-Phase Flow Patterns in Short Horizontal Rectangular Microchannels, Int. J. Multiphase Flow, Vol. 80, pp. 57-68 (2016)
- Kabov, O. A., Zaitaev, D. V., Cheverda, V. V., Bar-Cohen, Evaporation and Flow Dynamics of Thin, Shear-driven Liquid Films in Microgap channels, Exp. Thermal Fluid Sci., Vol. 35, pp. 825-831 (2011).
- Rebrov E. V., Two-phase flow regimes in microchannels, Theoretical Foundations of Chemical Engineering, Vol. 44, No. 4 pp. 355-367 (2010)

## Pulsating heat pipe enhancement performance using an electrohydrodynamic pump

Nicolas Chauris, Vincent Ayel, Cyril Romestant, Yves Bertin

Institut Pprime, CNRS – ENSMA - Université de Poitiers, UPR 3346, Département Fluides, Thermique, Combustion, 1  
av. Clément Ader – BP 40109 86961  
Futuroscope - Chasseneuil Cedex, France  
E-mail : Nicolas.chauris@ensma.fr

Pulsating heat pipes (PHP) consist of meanderings formed with a capillary tube between a cold source (condenser) and a hot source (evaporator). These devices were invented by Akachi in 1990 (Akachi 1990) and they have found major research and industrial interests. Indeed, the PHP is relatively simple to manufacture but very complex operational behaviors take place, paving the way for many research investigations both on system and micro-scales approaches.

Many investigations have been carried out on performances of PHP (Charoensawan et al. 2003) and revealed its high heat flux transfer capacity starting from around 15 W (Khandekaret al. 2004) up to more than 4500 W (Ayel et al. 2010). However, performances and behavior of PHP are strongly driven by many different parameters. The high number of first order parameters on PHP behavior makes still difficult its prediction and its sizing. In particular, the effect of gravity has been well studied the last few years especially for spatial application. Ayel et al. (2015) showed that PHP works better with a favorable gravity, meaning condenser above evaporator, than under microgravity (parabolic flight) or horizontal inclination (ground tests). Furthermore, Mameli et al. (2013) highlighted that dry-out limit goes down with the tilt angle ( $0^\circ$  for horizontal and  $90^\circ$  for vertical favorable). Thereby, the gravity pressure difference, which facilitates the liquid to go back from the condenser to the evaporator, has an influence on both thermal resistance and dry-out limit on PHP.

In this present work, a way to improve the dry-out limitation of PHP is investigated, regardless of the gravity, using an electrohydrodynamic (EHD) pump associated with the PHP. The aim of this device is to bring some liquid from condenser to evaporator with the pump as soon as the dry-out of the evaporator occurs. An EHD pump has many advantages compared to a classical mechanical pump. Indeed, the electrical power consumption of an EHD pump is less than 1 W and there are no moving parts inside. The electrohydrodynamic pumping includes interaction of electric field and flow field in dielectric media.

In general, three body forces act on a dielectric liquid volume when an electric field is applied, which is expressed as (Melcher 1981):

$$\mathbf{f}_e = qE - \frac{1}{2}E^2\nabla\epsilon + \frac{1}{2}\nabla\left[E^2\left(\frac{\partial\epsilon}{\partial\rho}\right)_T\rho\right] \quad (1)$$

The first term of Eq. (1) is the force which is acting on the free charges in an electric field, called Coulomb force; the second term is the dielectrophoretic force created by the gradient of permittivity. A change of permittivity occurs, for example, at the interface between liquid and vapor phases or

with a thermal gradient. The third term is the electrostriction force, which is generally negligible.

EHD pumps based on Coulomb force can be divided into three kinds: ion-drag pump, induction pump and conduction pump. For this study, only the conduction pumping is considered. It is the result of the dissociation of the neutral electrolytic species and recombination of the generated ions (Bryan and Yagoobi 1991):



where  $k_d$  is the dissociation rate constant and  $k_r$  the recombination rate, which are constant. The non-equilibrium between dissociation and recombination results to the creation of heterogeneous charge layers closed to the electrodes. Thus, the difference of electrode geometry or ions mobility leads to a dissymmetry of heterocharge layers on electrodes which generates a net flow from Coulomb force as illustrated on figure 1.

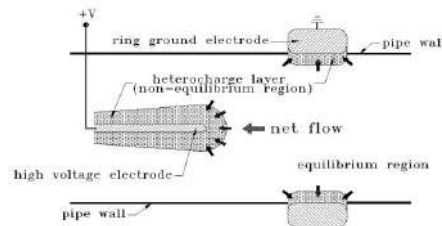


**Figure 1:** Illustration of EHD conduction pumping mechanism (Jeong and Seyed-Yagoobi 2004)

Research about EHD pumping on two-phase heat transfer devices such as heat pipes has already been conducted: Jones and Perry (1974) demonstrated experimentally that EHD pumping is able to bring liquid from condenser to evaporator, but the performances were poor in comparison to capillary driven heat pipes. More recently, Bryan and Yagoobi (1997) carried out a work on a monogroove heat pipe enhancement with an EHD pump. They showed that the EHD pump was able to provide immediate recovery from dry-out. Others researches have been carried out on micro heat pipes (Yu et al. 2002), capillary pump loops (Babin et al. 1993) and capillary loop two-phase thermosyphons (Di Marco and Filippeshi 2013). However, none of these studies considered the interaction between an EHD pump and a pulsating heat pipe (PHP).

For the present work, as evocated earlier, the heat transport capacity enhancement of a pulsating heat pipe with an EHD pump is investigated. The effect of EHD on PHP's performance, in terms of thermal resistance, is also

considered. Finally, the EHD power-consumption is measured.

Firstly, a pulsating heat pipe was designed and test on an experimental set-up. The main characteristics of the pulsating heat pipe are specified in table 1. It is made with copper and have several thermocouples distributed on evaporator, adiabatic and condenser sections. The heat power is supplied by means of two heat cartridge heaters while a water coldplate provides a constant temperature cooling on the condenser.

**Table 1:** Geometric characteristics of designed PHP

Dimensions (length x width x thickness) mm <sup>3</sup>	200 x 80 x 3
U-turns # (channels)	16 (32)
Channel section type	Squared
Evaporator length (mm)	10
Condenser length (mm)	80

Figure 2 depicts the temperature evolution on each section versus time for several heat powers supplied. The PHP is filled with FC72 (filling ratio: 50%) and is set in vertical position. One can notice that the PHP works well until 80 W after which a dry-out occurs. Furthermore, the PHP reach a pretty stable steady-state at each heat power step until the dry-out. This trend is consolidated in figure 3: the lowest thermal resistance is obtained for positive tilt angles of 45° and 90°. It also appears a quite smaller dry-out limit in horizontal orientation that confirms the strong influence of the gravity on PHP. The difference on PHP performance, according to the position, could be a drawback for some ground applications and even more for space applications.

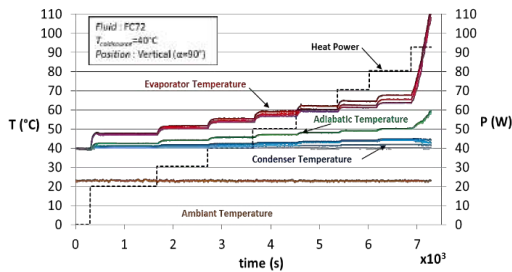


**Figure 2:** Experimental results: temperatures and heat power versus time (vertical position):

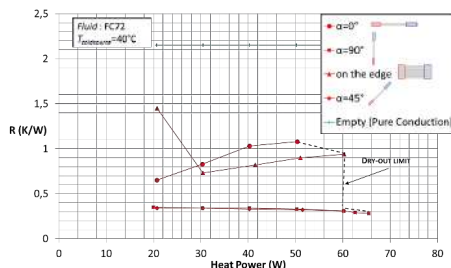


**Figure 3:** Experimental results: Thermal resistance versus heat power

In light of this, an EHD pump added on the PHP presented above has been designed. Several electrode designs will be tested to find the best combination between EHD pumping and PHP in terms of performances. The relevance of such apparatus as EHD pump on both thermal resistance and dry-out limit will be investigated.

## References

- Akachi H., Structure of Heat Pipe, Patent US4921041, (1990).
- Charoensawan P., Khandekar S., Groll M., Terdtoon P., Closed loop pulsating heat pipes, part A: parametric experimental investigations, ATE, Vol. 23, pp. 2009-2020. (2003)
- Khandekar S. Thermo-hydrodynamics of closed loop pulsating heat pipes: Thèse de l'Université - Stuttgart University; 19 juillet (2004).
- Ayel V, Bertin Y, Romestant C, Burban G. Experimental study of pulsating heat pipes tested in horizontal and vertical positions. In 15th International Heat Pipe Conference, Clemson (2010).
- Ayel V, Araneo L., Scalambra A., Mameli M., Romestant C., Piteau A., Marengo M., Filippeschi S., Bertin Y., Experimental study of a closed loop flat plate pulsating heat pipe under a varying gravity force, International Journal of Thermal Sciences, Vol. 96, pp. 23-24 (2015).
- Mameli M., Manno V., Filippeschi S., Marengo M., Multi-parametric investigation on the thermal instability of a closed loop pulsating heat pipe, Proc. 17<sup>th</sup> IHPC, Kanpur (2013).
- Melcher J.R., Continuum Electromechanics, MIT Press, Cambridge (1981).
- J.E. Bryan and J. Seyed-Yagoobi, "Experimental Study of Ion-drag Pumping Using Various Working Fluids", IEEE Transactions on Electrical Insulation, Vol. 26, pp. 647-655 (1991).
- Jeong S.I., Seyed-Yagoobi J., Innovative Designs for Electrodynamic conduction pumping, IEEE Transactions on Industry Applications, Vol. 40 (2004)
- Jones T. B., Perry M.P., Electrohydrodynamic heat pipe experiments, Journal of applied physics, Vol. 45 (1974)
- Bryan J.E., Seyed-Yaggobi J., Heat transport enhancement of monogroove heat pipe with electrohydrodynamic pumping, Journal of thermophysics and heat transfer, Vol. 11 (1997).
- Yu Z., Hallinani K., Bhagat W., Kashani R., Electrohydrodynamically augmented micro heat pipes, Journal of thermophysics and heat transfer, Vol. 16 (2002).
- Babin B.R., Peterson G.P., Seyed-Yagoobi J., Experimental investigation of an ion-drag pump-assisted capillary loop, Journal of thermophysics and heat transfer, Vol.7 (1993).
- Di Marco P., Filippeschi S., Electrical force effect on a capillary loop two-phase thermosyphon, Proc. 17<sup>th</sup> IHPC, Kanpur (2013).

## Experimental study of the local characteristics of gas-liquid flow in a rectangular microchannel

German Bartkus<sup>1,2</sup>, Vladimir Kuznetsov<sup>1,2</sup>

<sup>1</sup> Novosibirsk State University, Department of Physics  
Pirogova, 2, Novosibirsk, 630090, Russia

<sup>2</sup> Kutateladze Institute of Thermophysics  
Academician Lavrentyev Avenue, 1, Novosibirsk, 630090, Russia  
germanbartkus@gmail.com

Great attention is paid in recent times to the study of gas-liquid and the liquid-liquid flows in microchannels. This is caused by the fact that the use of microchannel systems provides an opportunity to control processes in phase transition and chemical reactions with the time resolution of a few milliseconds. Active implementation of the technologies based on microchannels for intensive micro heat exchangers for electronics cooling, chemical reactors and biological chips for rapid analysis of blood have already begun. Examples of application of microchannels presented in detail by Guther (2006), Chinnov et al. (2015), Kuznetsov (2016), Kovalev et al. (2016). The main objective of the present work is experimental studying of the local characteristics and mechanisms of gas-liquid flow in vertical and horizontal microchannels using dual laser scanning method and high-speed video recording for rectangular microchannels with an aspect ratio about 0.7, which is typical in many applications.

The local characteristics of the two-phase gas-liquid flow were measured in the rectangular microchannel with cross section  $269 \times 362 \mu\text{m}$  and inlet T-mixer. The peculiarity of this study is using the set of liquids with different physical properties: ethanol, bidistilled water, 40% ethanol-water solution. In addition, the experiments aimed at studying the effect of microchannel location (horizontal and vertical) on the flow regimes and the area of their existence, were carried out. The visualization of flow regimes and the measurement of its characteristics were obtained using high-speed video camera Optronis CX600x2 and dual laser scanning method.

The experiments on studying the vertical and horizontal gas-liquid flow in a rectangular microchannel were performed using microchannel with a cross-section of  $269 \times 362 \mu\text{m}$ . The nitrogen, which is fed from a tank via the control valve and gas flow meter to the inlet T-mixer, was used as working gas. The bidistilled water also flows from the tank through a flow meter to the inlet T-mixer of the experimental section. Experimental section is the microchannel, assembled from glued glass and aluminum plates with length  $L = 0.3 \text{ m}$ . The hydraulic diameter of the channel is much less than the capillary constant. From the exit of experimental section, the gas-liquid mixture is moved to the liquid tank where the gas escapes to the atmosphere.

The study of gas-liquid flow regimes was conducted using the method of dual laser scanning presented in Figure 1. Two lasers (2) are positioned so that laser beams illuminate one side of the rectangular channel. The lens (3) is used to change the diameter of the laser spot and the aperture is used to reduce the diameter of the laser beam. The intensity of transmitted light is measured by photodiodes (4), arranged at the opposite side of the channel.

The electric voltage from the photodiodes is analyzed using high-speed ADC and processed on the computer over time frame from one to three minutes. Flow regimes are also registered using the high-speed camera (1). The first laser is located at a distance of 6 cm from the inlet, camera – 17.7 cm from the inlet, second laser – 22.4 cm for observing the stable gas-liquid flow.

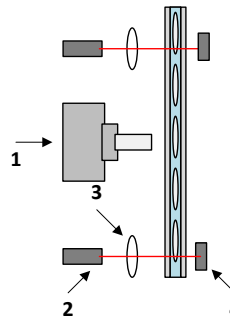


**Figure 1:** Scheme of the dual laser scanning method.

High-speed video shows, that the periodic flow with elongated gas bubbles (Taylor bubbles), the transition flow and annular flow are the main flow patterns for microchannels with the gap substantially less than the capillary constant. Increasing the superficial gas velocity leads to substantial transformation of the flow from periodic elongated bubbles flow to transition flow with the lost of bubbles periodicity and to annular flow without liquid plugs. Figure 2 shows the photos of the flow for the ethanol-nitrogen mixture (a, c) and the corresponding signals from the photodiodes (b, d), in which the existence of the gas phase corresponds to the lowest electric voltage. Based on the signal of laser scanning and video recording, the boundaries of the flow patterns were determined. The Figure 3 (a) presents flow pattern map for the upward flow of bidistilled water-nitrogen mixture. The comparison of the flow pattern maps for horizontal and vertical microchannels shows that influence of the channel location relative to the gravity on flow pattern boundaries is insignificant.

Figure 3 (b) presents flow pattern map for the upward flow of ethanol-nitrogen mixture. It can be seen that the transition between flow patterns occurs at lower superficial gas velocities than for bidistilled water-nitrogen mixture. Similar behavior is observed for the 40% aqueous ethanol solution. It shows that reducing surface tension shifts the boundaries of flow patterns to lower gas velocities.

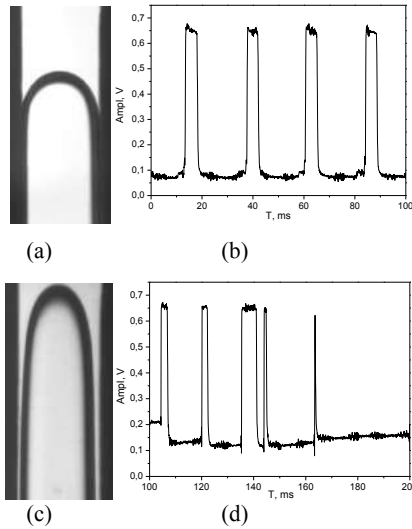


**Figure 2:** Characterization of the flow regime using signal from photodiode for ethanol-nitrogen mixture, (a) –  $J_{liq}=0.042$  m/s  $J_{gas}=0.436$  m/s, (b) -  $J_{liq}=0.042$  m/s  $J_{gas}=2.14$  m/s.

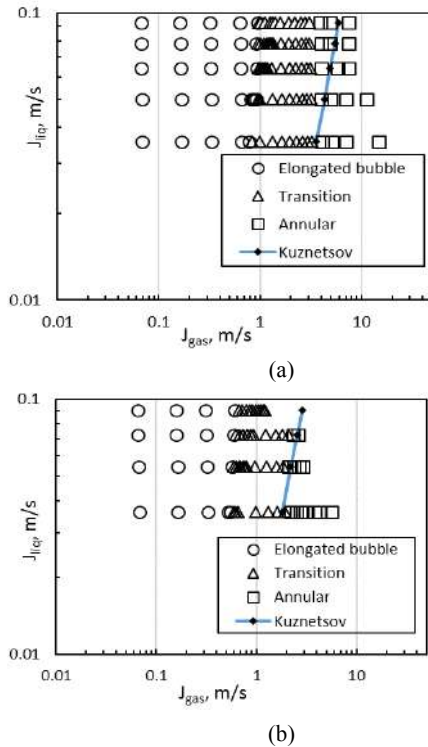


**Figure 3:** Flow pattern map for vertical upward flow in microchannel  $269 \times 362 \mu\text{m}$  for mixtures: a – bidistilled water-nitrogen, b – ethanol-nitrogen.

The solid line in Figure 3 (a), (b) shows the prediction of superficial gas velocity that corresponds to the transformation of the transition flow to annular flow according to Kuznetsov et al. (2012) equivalent film thickness model. In this model, it is assumed that the transition to the annular flow occurs if the film thickness in a

transition flow with liquid plugs equals to the film thickness in an annular flow. This means that the gas velocity becomes sufficiently high to move all liquid in the film under the action of interface shear stress and the formation of liquid plugs does not occur.

To generalize the experimental data for all mixtures, the dimensionless complex suggested by Waelchli (2006) was used. This complex allows us to take into account the physical properties of the liquids used in the experiment. The figure 4 shows that generalized flow pattern map combines the results obtained for liquids with different physical properties and can be used also for prediction of the flow patterns boundaries.

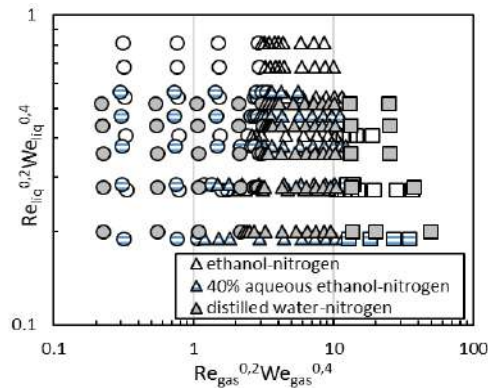


**Figure 4:** Dimensionless map of regimes for horizontal flow in rectangular microchannel  $269 \times 362 \mu\text{m}$  for all mixtures.

This work was performed in the Kutateladze Institute of Thermophysics SB RAS by a grant from the Russian Science Foundation (project No 16-19-10519).

## References

- Günther A. and Jensen K. F., Multiphase microfluidics: from flow characteristics to chemical and materials synthesis, Lab Chip., Vol. 6 pp. 1487–1503 (2006)
- Chinnov E. A., Ronshin F. V., and Kabov O. A., Features of two-phase flow in a rectangular microchannel with the height of  $300 \mu\text{m}$ , Thermophys. Aeromech., Vol. 21 pp.759-762 (2014)
- Kuznetsov V. V. Two-phase microfluidics: thermophysical fundamentals and engineering concepts, J. Phys. Conf. Ser., Vol. 754, 032012 (2016).
- Kovalev A. V., Yagodnitsyna A. A., Bilsky A. V. Experimental study of liquid-liquid plug flow in a T-shaped microchannel, J. Phys. Conf. Ser., Vol. 754, 092001 (2016).
- Kuznetsov V. V., Kozulin I. A. and Shamirzaev A. S., Correlation between Flow Pattern and Refrigerant Flow Boiling Heat Transfer in Microchannel Heat Sinks, J. Phys.: Conf. Ser., Vol. 395, 012093 (2012)
- Waelchli S., Rudolf von Rohr P., Two-phase flow characteristics in gas-liquid microreactors, Int. Jour. of Multiphase Flow, Vol. 32 pp. 791-806 (2006)

## Gravitational Effect on Performance of a Polymer Electrolyte Fuel Cell with Vertical Channels

Fang Ye<sup>1,\*</sup>, Xuan Liu<sup>1</sup>, Jian Fu Zhao<sup>2,3</sup>, Hang Guo<sup>1</sup>, Chong Fang Ma<sup>1</sup>

<sup>1</sup> MOE Key Laboratory of Enhanced Heat Transfer and Energy Conservation, and Beijing Key Laboratory of Heat Transfer and Energy Conversion, College of Environmental and Energy Engineering, Beijing University of Technology, Beijing 100124, China

<sup>2</sup> Key Laboratory of Microgravity, Institute of Mechanics, Chinese Academy of Sciences, Beijing 100190, China

<sup>3</sup> School of Engineering Science, University of Chinese Academy of Sciences, Beijing 100049, China

\* Corresponding author, E-mail: yefang@bjut.edu.cn, Tel.: +86-10-67391985 ext. 8321

It has been about 60 years since polymer electrolyte fuel cells (PEFC) was first applied to space applications, the PEFC as a prospective alternative power source has been researched extensively due to its high efficiency of energy conversion, environmental friendliness, high reliability and flexibility, but few research literatures discuss the gravitational effect on the performance of PEFC.

In this study, a PEFC with single serpentine vertical channels is designed to investigate effect of gravity on the performance of PEFC, gas liquid two-phase flow behaviors at the cathode are also observed by visual windows inside flow channels, and a 3.6 s short-term microgravity environment is achieved by a drop tower at the Key Laboratory of Microgravity, Institute of Mechanics, Chinese Academy of Sciences. Experiments are conducted with oxygen volumetric flow rates of 60 ml/min and 120 ml/min at external circuit load and operating temperature of 65°C; the free drop tower supplied a hermetic microgravity circumstance with a gravity level of 0.01 - 0.001  $g_0$ .

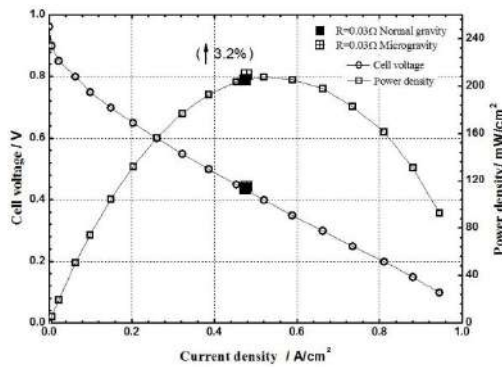


Figure 1: Performance curves of PEFC, O<sub>2</sub>: 60ml/min

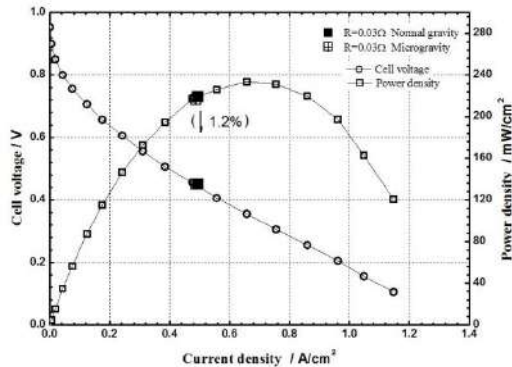


Figure 2: Performance curves of PEFC, O<sub>2</sub>: 120ml/min

Experimental results demonstrate that the PEFC performance and gas liquid two-phase flow behavior show some changes when the PEFC enters the microgravity environment from the normal gravity environment. When the oxygen volumetric flow rate is 60 ml/min, the PEFC shows better performance in the microgravity environment, nevertheless the PEFC performance has a slim decrease when the cathode gas flow rate is increased to 120ml/min.

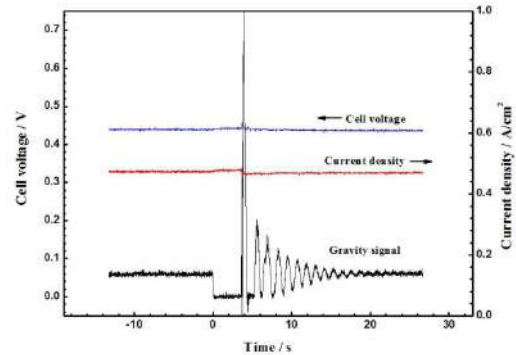


Figure 3: PEFC performances varies with gravity signal, O<sub>2</sub>: 60ml/min

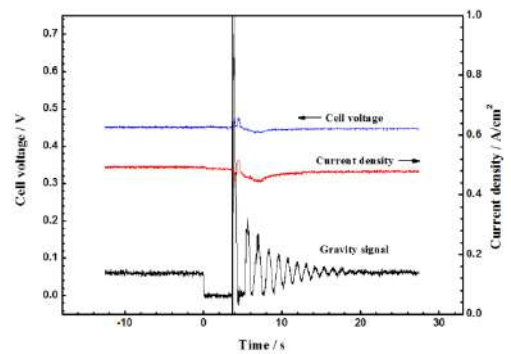
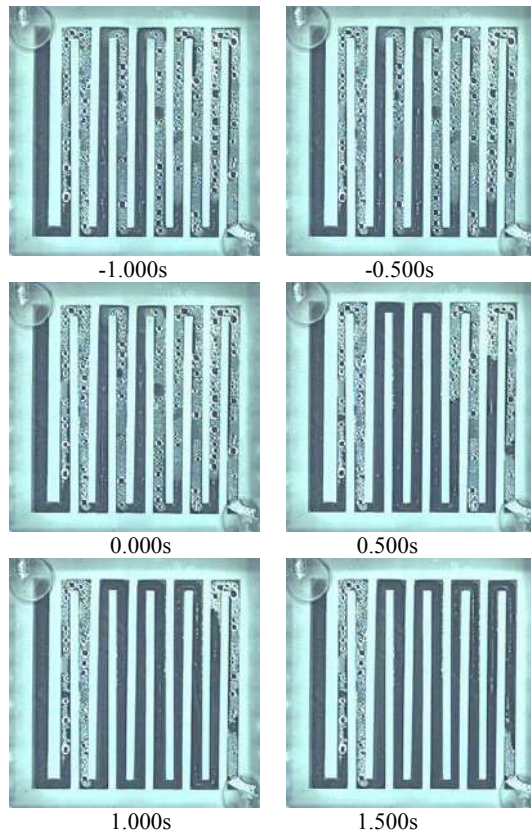


Figure 4: PEFC performances varies with gravity signal, O<sub>2</sub>: 120ml/min

Two phase flow behaviors in the cathode flow field reveal the reasons behind performance changes when the PEFC enters the microgravity environment from the normal gravity environment. Through the comparison of the images of gas liquid two phase flow behaviors in the cathode flow field in the process of free fall of the drop capsule, it is clearly found that the accumulated liquid water in the

bottom of the vertical flow channels is easily removed under the action of reactant gas drag force in the microgravity environment when the gas flow rate is 60 ml/min, which alleviates the cathode flood and makes diffusion of reactant gas easier, therefore the PEFC performance is improved. However, when the oxygen gas flow rate is increased to 120ml/min, on one hand, the microgravity environment leads to the shape change and coalescence of dispersed liquid droplet, on the other hand, the water stream at the outlet of the cathode side is discharged. The high flow rate of reactant gas can effectively avoid the liquid water accumulated in the cathode flow field, however, the bottom of flow field cannot be sufficiently humidified, the polymer electrolyte membrane becomes dry and mass transpotion deteriorates in the microgravity environment, which cause the decrease of performance of PEFC. Simultaneously sudden disappearance of gravity makes the movement of the liquid water droplet easier, and more liquid water droplet gathers at the outlet of the cathode side at the same time, so it can be seen clearly that the water stream is removed.

All the experiments are conducted under the same hydrogen volumetric flow rate, external circuit load and operating temperature. Therefore, microgravity environment have distinct effect on fuel cell performance at the different oxygen volumetric flow rates, which depends to a great extent on the quantity of accumulated fluid water in the cathode flow field before PEFC enters the microgravity environment.



**Figure 5:** The comparison of two phase flow behavior in cathode flow field at different time, O<sub>2</sub>: 60ml/min

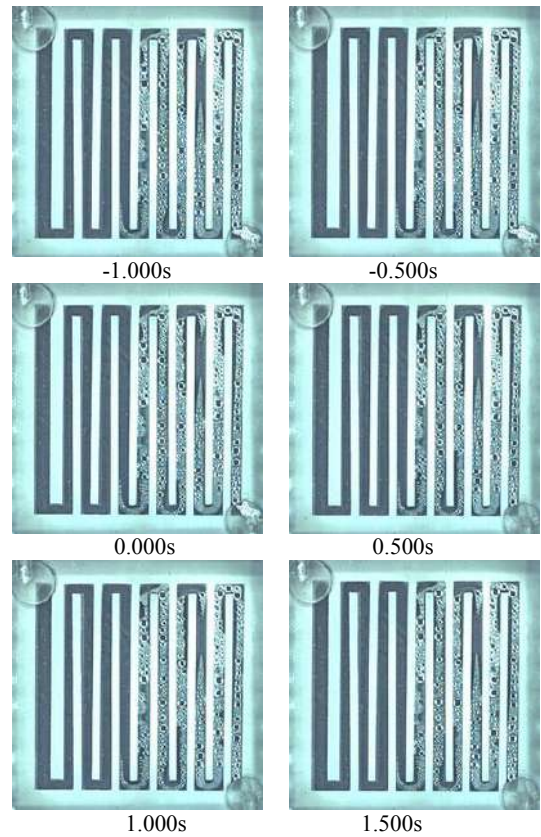


**Figure 6:** The comparison of two phase flow behavior in cathode flow field at different time, O<sub>2</sub>: 120ml/min

We appreciate the financial support from the National Natural Science Foundation of China (Grant No. 51476003).

#### References

- Sone Y., Ueno M., Naito H. et al., One kilowatt-class fuel cell system for the aerospace applications in a micro-gravitational and closed environment, *Journal of power sources*, Vol. 157 pp. 886-892 (2006)
- Yu Y., Tu Z.K., Zhan Z.G. et al., Gravity effect on the performance of PEM fuel cell stack with different gas manifold positions, *International Journal of Energy Research*, Vol. 36 pp.845-855 (2012)

## Oscillate Boiling with Microheaters

Dang Minh Nguyen, Fenfang Li and Claus-Dieter Ohl

School of Physical and Mathematical Sciences, Division of Physics and Applied Physics, Nanyang Technological University 21 Nanyang Link, Singapore 637371  
E-mail: nguyenda001@e.ntu.edu.sg

When a boiler in a subcooled liquid is supplied with too much heat, nucleate boiling bubbles merge and form a thin vapor film layer, separating the liquid and the heating substrate. As a result, the heat transfer coefficient drops and the system's temperature rises significantly, causing a thermal break-down of the device.

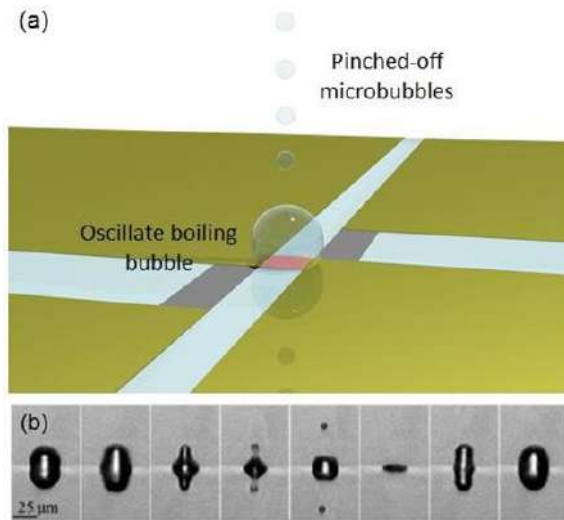


**Figure 1:** (a) Illustration of experimental setup to realize oscillate boiling with electrical microheater (b) Selected images of a cycle of a boiling bubble oscillating at a frequency of 90 kHz

Here we discuss a new boiling regime called oscillate boiling which may help to solve this long-lasting problem of the boiling crisis. This regime is only observed for strongly confined heaters, then the boiling bubble undergoes high frequency oscillations which prevents them to grow and merge into a vapor layer. An important second feature is that the three-phase contact line of the bubble remains pinned and a stream of smaller microbubble is ejected at its top (Fig. 1b). The mechanism resulting in the oscillations and the bubble pinch-off is the presence of a thin liquid jet which impinges onto the heater during each bubble's collapse. Upon its contact with the hot surface, the heat transfer is strongly enhanced, leading to an instant vaporization of the jet and vapor explosion, which drives the re-expansion of the bubble and the emission of the microbubble (Li et al. 2017). Along this process, a large amount of thermal energy flows from the heater to the liquid, which greatly improves the heat transfer efficiency. It thus acts also as a micromechanical cooler of the of miniature heater, preventing its thermal breakdown. The mechanism and

cooling application is supported with bottom-view captures of the bubble as well as thermal readings of the heater during the oscillation process.

The key to achieve oscillate boiling is a confined heat source as small as  $10 \mu\text{m}$ . This heat source can be realized either optically by focusing a continuous laser beam onto a gold substrate, or electrically by connecting two high-conductive gold electrodes with a miniature platinum resistor (Fig. 1a) The electrical microheater is more advantageous in terms of controllability, energy efficiency and large scale implementation. It also allows temperature measurement of the device during the boiling process (Fig. 2)

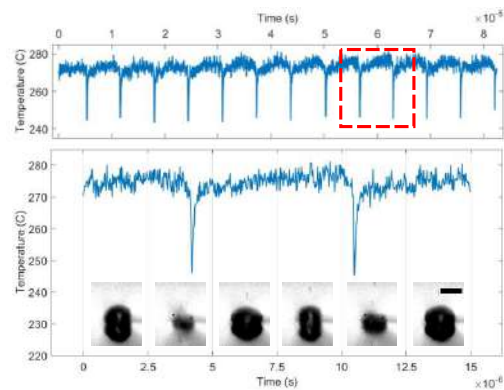


**Figure 2:** (a) Heater's temperature during the oscillate boiling events (b) Zoomed-in temperature of the region marked with a dashed line in figure (a) and the corresponding bubble image. The scale bar is  $20 \mu\text{m}$ .

Although very localized, the oscillate-boiling regime may be exploited in heating and cooling applications. The strong thermal gradient along the bubble's interface induces a thermocapillary flow from the three-phase contact line to the bubble's apex into an upwards-directed jet. Thereby transporting heat from the heater to the subcooled liquid (see Fig. 3). Together with the microstreaming flow, considerably faster heating is found as compared to the conventional nucleate boiling (Fig. 4a). Moreover, unlike convective flow, thermocapillary flow depends only on the temperature gradient making it very suitable for microgravity condition. We have conducted initial experiments by by tilting the heating substrate to alter the effective gravitational acceleration. Figure 4b demonstrates that oscillate boiling regime is only mildly affected by the orientation of the gravity.

The regime also shows potential for large scale implementation. This can be done by aligning multiple microheater close to each other and cover the whole

substrate with oscillate boiling bubbles. When being placed at sufficient distance, these bubbles oscillate independently as shown in Fig. 4c.

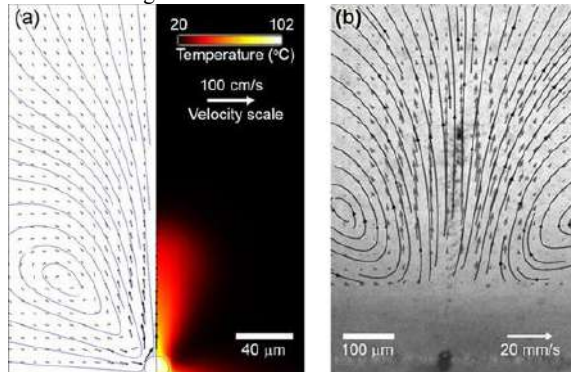


**Figure 3:** Modelling results of the thermocapillary flow and comparison to experiments. (a) Simulation of the heat transfer (right) and the thermocapillary effect induced flow (left) of a steady bubble under laser irradiation of 40 mW for 10 milliseconds. (b) Flow field obtained from particle image velocimetry with 2 μm diameter particles.

Our work will provide characterizations and detailed explanation of oscillate boiling bubbles with both experiments and numerical results. We will also report about potential applications and multi-bubble implementations of this fascinating boiling phenomenon

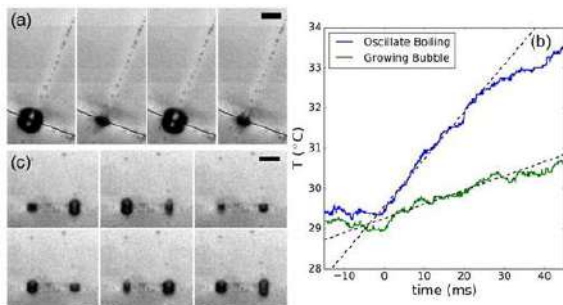


**Figure 4:** (a) Temperature of liquid measured 200 μm above an oscillate boiling and a growing bubble. (b) Oscillate boiling bubble with similar behavior under reduced effective gravitational acceleration when the substrate is tilted by 30°. (c) Independent behavior of two-closely placed oscillate boiling bubble. The scale bar shows 20 μm.

## References

Li, Fenfang, et al., Oscillate boiling from microheaters, Physical Review Fluids, Vol. 2, No. 1, p. 014007 (2017).

## Condensation of steam on elliptic pin-fin plates

Leigang Zhang, Juan Shi, Zhenqian Chen\*

Key Laboratory of Energy Thermal Conversion and Control of Ministry of Education,  
School of Energy and Environment, Southeast University, Nanjing, 210096, China  
\*E-mail address for the corresponding author: zqchen@seu.edu.cn

The condensation process exists widely in energy, chemical industry, electric power, water desalination and other industrial fields. As the energy sources are limited and for their conservation, appropriate design and optimization of condensers is very important. Therefore, different methods have been used by different investigators to increase heat transfer rate in these condensers (Agrawal et al. 2004). There are number of techniques to enhance the heat transfer coefficient (Kumar et al. 1994, Behabadi et al. 2005). One of the passive techniques to enhance heat transfer coefficient is the use of fin tubes.

Steam condensation on the common geometric surface with the presence of air has been widely studied in many researches (Othmer 1929, Dehbi 1990, Liu et al. 2000, Tiejun et al. 2006, Ren et al. 2014, Chanatana 2013). However, compared with the steam-air condensation on common geometric surface, researches are limited on steam-air condensation for enhanced tubes (e.g. finned tube, corrugated pipe), which have been investigated and show an outstanding performance for pure condensation (Ooi et al. 2004, Ouyang et al. 2012). From the reviews above, it can be seen that the scanty investigations are mainly about integral-fin tube, two-dimension enhanced tube. However, there was little experimental investigation of pin-fin plates, especially three-dimension enhanced plates. Taking all these into account, six elliptic pin-fin plates were tested respectively in this study by experiment under steam-air condition.

All tests were done at a little above atmospheric pressure with downward-flowing saturated steam at constant, low approach velocities of approximately 1 m/s. The stainless-steel test apparatus, shown schematically in Fig. 1, consisted of an open loop, with vapor generated in an electrically heated boiler (maximum power 600 W). The saturated vapor was directed vertically down through a superheat section, before flowing over the vertical, electricity-cooled, test condenser plate. Excess vapor passed to atmospheric environment.

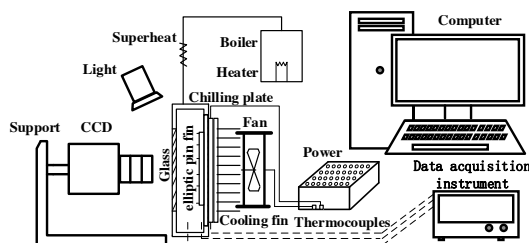


Figure 1: Experimental apparatus.

All the plates had a condensing length of 12 mm, a condensing width of 12 mm, and a thickness from the pin

root to underside of 2 mm. The photograph of elliptic pin-fin plates is shown in Fig. 2. The cross section of pin-fin was an ellipse. Full details of the plates dimensions are given in Table 1. Major axis and minor axis of ellipse were held constant at 1.2 mm, 0.6 mm, respectively. The only geometric parameters varied were pin height and spacing.



Figure 2: Photograph of elliptic pin-fin plates.

Table 1. Geometric parameters of elliptic pin fins

Parameter	P1	P2	P3	P4	P5	P6
$a \times b$ (mm $\times$ mm)	1.2 $\times$ 0.6	1.2 $\times$ 0.6	1.2 $\times$ 0.6	1.2 $\times$ 0.6	1.2 $\times$ 0.6	1.2 $\times$ 0.6
$s_h$ (mm)	1.2	1.6	2.0	1.2	1.6	2.0
$h$ (mm)	1.2	1.2	1.2	2.0	2.0	2.0
$L \times W$ (mm $\times$ mm)	12 $\times$ 12	12 $\times$ 12	12 $\times$ 12	12 $\times$ 12	12 $\times$ 12	12 $\times$ 12
$N$	24	24	24	24	24	24

All temperatures were measured with K-type thermocouples. In order to verify the reliability of the experimental apparatus, condensation experiment of plain plate was carried out. As is shown in Fig. 3, the experimental value of condensation heat transfer coefficient is compared with the theoretical value. It can be seen that the experimental values and the theoretical values are in good agreement, the maximum deviation is less than 5%. It can be concluded that the experimental system is reliable and the experimental principle is correct.

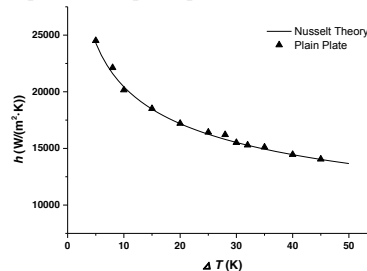
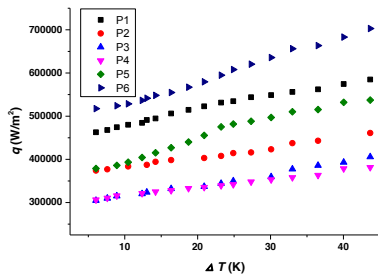


Figure 3: Condensation heat transfer coefficient.

Fig. 4 shows the results for the six elliptic pin-fin plates, plotted as heat flux, against vapor-side temperature difference. For all plates, data were taken on two different days and show good repeatability. The heat flux shows an increasing trend with the vapor-side temperature difference. The enhancing effect of the pins can clearly be seen, with all six pin-fin tubes giving high heat fluxes. It can be seen that the best performing pin-fin plate, P6, gave approximately twice the heat transfer of plate P3 at the same vapor-side temperature difference.



**Figure 4:** Variation of heat flux with vapor-side temperature difference.

In high wall subcooling region, there was plenty of condensate due to a strong driving force of condensation. The pin-fins disturbed the liquid film, contributing to the transition from the laminar to turbulent flow. Furthermore, the pin-fins helped to remove the liquid film, thinning the liquid film. Hence, the pin-fin plates showed an enhancement on the condensation heat transfer compared with the plain tube. However, with a lower wall subcooling, there was less condensate. In this situation, the liquid film was restrained to flow downward by the fins and many droplets would be trapped at the root of the fins or hang on the fins. So, the pin-fin plate showed a poor performance.

It is also found that there are many droplet dropping cycles in the process of condensation, and the period of each cycle is different. As can be seen in Fig 5, the droplet distribution on the plate is very similar before and after each dropping.

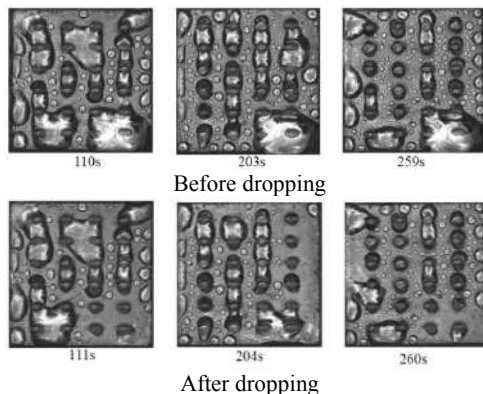


**Figure 5:** Three dropping cycles of plate P1. ( $t_1=110s$ ,  $t_2=93s$ ,  $t_3=56s$ )

The present experimental data provide support for the engineering application and the further optimization design

of pin-fin enhanced condensation structure. It seems likely that more effective pin-fin plates could be designed if more were known about these mechanisms of condensate flow.

**Acknowledgements:** The authors gratefully acknowledge the support provided by the China's Manned Space Program (TZ-1), National Natural Science Foundation of China (51606037) and Natural Science Foundation of Jiangsu Province (BK2016068).

## References

K.N. Agrawal, R. Kumar, S.N. Lal, H.K. Varma, Heat transfer augmentation by segmented tape inserts during condensation of R-22 inside a horizontal tube, *ASHRAE Transact.* Vol. 110, pp. 143–150 (2004).

R. Kumar, K.N. Agrawal, S.N. Lal, H.K. Varma, An experimental study on condensation enhancement of R-22 by the turbulence promoter, *ASHRAE Transact.* 111 (2005) 18–25. Stephan P, Hammer J. A new model for nucleate boiling heat transfer. *Heat Mass Transfer*, Vol. 30, pp. 119–125 (1994).

M.A.A. Behabadi, M.R. Salimpore, R. Kumar, K.N. Agrawal, Augmentation of forced convection condensation heat transfer inside a horizontal tube using spiral spring inserts, *J. Enhanc. Heat Transfer*, Vol. 12, No. 4, pp. 373–384 (2005).

D.F. Othmer, The condensation of steam, *Ind. Eng. Chem.* Vol. 21, pp. 577–583 (1929).

A.A. Dehbi, Analytical and Experimental Investigation of the Effects of Noncondensable Gases on Steam Condensation Under Turbulent Natural Convection Conditions (Doctor Thesis), Massachusetts Institute of Technology, Cambridge (1990).

H. Liu, N.E. Todreas, M.J. Driscoll, An experimental investigation of a passive cooling unit for nuclear plant containment, *Nucl. Eng. Des.* Vol. 199, pp. 243–255 (2000).

Wu Tiejun, Karen Vierow, Local heat transfer measurements of steam/air mixtures in horizontal condenser tubes, *Int. J. Heat Mass Transfer* Vol. 49, pp. 2491–2501 (2006).

Bin Ren, Li Zhang, Xu Hong, et al., Experimental study on condensation of steam/air mixture in a horizontal tube, *Exp. Therm. Fluid Sci.*, Vol. 58, pp. 145–155 (2014).

C. Chantana, S. Kumar, Experimental and theoretical investigation of air–steam condensation in a vertical tube at low inlet steam fractions, *Appl. Therm. Eng.*, Vol. 54, pp. 399–412 (2013).

T.H. Ooi, D.R. Webb, P.J. Heggs, A dataset of steam condensation over a double enhanced tube bundle under vacuum, *Appl. Therm. Eng.*, Vol. 24, pp. 1381–1393 (2004).

Ouyang Xiping, Zhang Tongrong, Experimental study on characteristics of condensation heat transfer of oblique-fin tube, *Refrigeration* 40: Vol. 72, pp. 58–62 (2012).

## Research on droplets growth of Marangoni condensation during the time-series process

Yong Li, Jinshi Wang, Kai Xia, Nana Chen, Junjie Yan

Xi'an Jiaotong University, State Key Laboratory of Multiphase Flow in Power Engineering  
No. 28 Xianning west road, Xi'an, 710049, P.R. China  
[wangjinshi@mail.xjtu.edu.cn](mailto:wangjinshi@mail.xjtu.edu.cn)

Marangoni condensation is caused by the surface tension instability on the condensate film surface of binary mixtures in a positive system, where the surface tension of the mixtures has a negative gradient with the mass fraction of the more volatile component, such as ethanol-water mixtures. The Marangoni force, induced by the surface tension gradient, pulled the condensate with lower surface tension towards the higher part along the liquid surface, which tore the condensate film and resulted in the dropwise mode. It is a new way to achieve dropwise condensation and could maintain for a long time, which depends merely on the physical properties of the mixtures.

The heat transfer coefficient of Marangoni condensation was found to vary non-monotonously with the increase in the vapor-to-surface temperature difference and the ethanol vapor concentration, increase with the increase in the vapor velocity and pressure (Utaka et al. 2004, Yang et al. 2006). Several condensation modes were observed during the experiments and variations of droplet size distribution and maximum diameter were analyzed (Yan et al. 2009).

Previous studies on the Marangoni condensation were mainly on the vertical surfaces, horizontal tubes and vertical tubes, where the gravity effect acted on the condensate with the same direction of the surface tension gradient. However, the essential reason for dropwise modes in the Marangoni condensation was the surface tension gradient. When the gravity effect operated with the same direction of the surface tension gradient, the condensation modes were diversified under the effects of both surface tension gradient and gravity effect. Thus, the condensation modes under the interference of the gravity effect were unrepresentative. Moreover, the interference of the gravity effect could make the condensate droplets leave the condensing surface early and the growth of the droplets was not complete. When the condensing surface was horizontal, the gravity effect was perpendicular with the direction of the surface tension gradient on the condensate. Then the interference of the gravity effect could be neglected and the condensate droplets could grow freely. Then present Marangoni condensation modes were caused merely by the surface tension gradient, which could be regarded as the essential ones. Experimental study was conducted on the horizontal surface for Marangoni condensation of ethanol-water mixtures and droplets growth was analyzed during the time-series process in this paper.

The experimental system consists of four closed loops, which are named as the main vapor loop, the impinging cooling loop, the condenser loop and the auxiliary condenser loop, respectively. The details could be found in the work by Li et al. (2017). As the experiments were conducted horizontally, the condensate film couldn't be removed automatically. For the continuity of the condensation process, a wiper was designed and employed to remove the condensate film on the condensing surface, as shown in Fig.

1. Moreover, two pieces of magnets were adopted to transmit the driving power from a micro-motor for keeping the excellent vacuum condition. The test copper with a condensing surface area of 25.0 mm × 40.0 mm was horizontally installed and fixed with epoxy plates to ensure the heat flux inside transferred vertically.

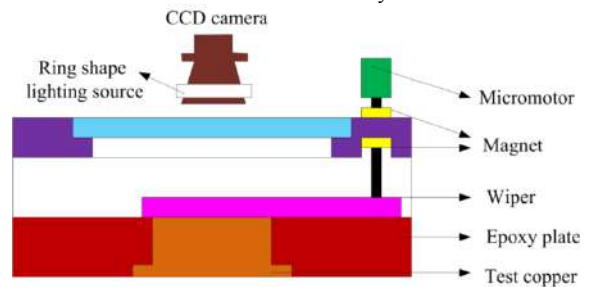


Figure 1: Sketch diagram of the condensing chamber

The image processing method was also one focal point in this study. As the number of condensate droplets formed on the condensing surface was huge, it was difficult to figure out the numbers and sizes of the droplets manually. So the image processing program was written by MATLAB herein and the flow chart was shown in Fig. 2. The ring-shape lighting source was equipped for improving the accuracy of the image processing. The result of the image processing method was shown in Fig. 3. The white parts in the photo were the identified droplets and their numbers and sizes were obtained by the program automatically.

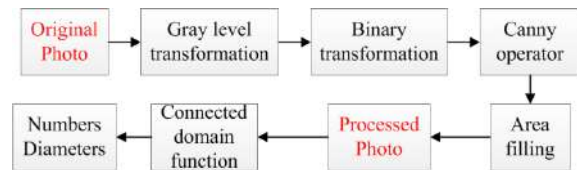


Figure 2: Flow chart image processing program

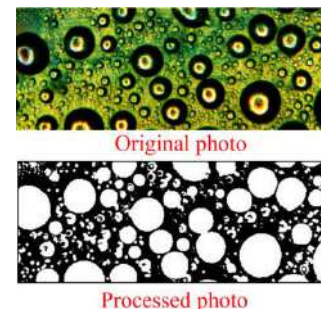


Figure 3: Result of photo processing method

The time-series process expressed the subsequent process after the wiper just brushed over the center of the condensing surface and the condensation process developed freely. The wiper didn't work during this process. Figure 4 showed the visual figures during one time-series process. As the time-series process went on, huge number of small droplets appeared at the beginning and grew up fast mainly by direct condensation. As the time-series process went on, the droplets grew slowly mainly by coalescence.

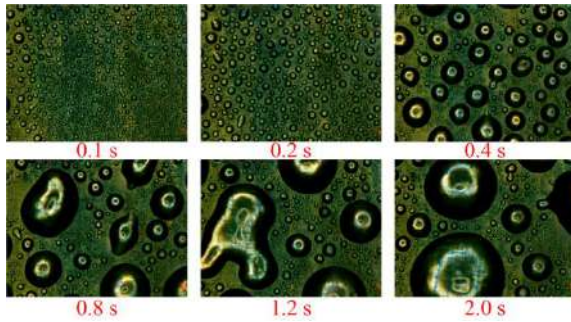


Figure 4: Droplets growth during time-series process

As the primary heat transfer resistances came from the thermal resistances from the condensate droplets and the vapor diffusion layer, which were closely related to condensate droplets coverage ratio and ethanol vapor concentration, respectively. So the condensate droplets coverage ratio was introduced to evaluate the growth of the droplets, which expressed the areas ratio between all the droplets and the condensing surface. The definition equation of condensate droplets coverage ratio was shown in Eq. (1).

$$C(t) = \frac{\sum_1^n A_i(t)}{A_s} \quad (1)$$

where  $C(t)$  expressed the condensate droplets coverage ratio during the time-series process,  $A_i(t)$  expressed the occupied area on the condensing surface of one condensate droplet and  $A_s$  expressed the whole area of the condensing surface. Figure 5 showed the variation of condensate droplets coverage ratio during the time-series process corresponding to the photos in Fig. 4. As the time-series process went on, the condensate droplets coverage ratio increased fast at first, and then increased slowly until reaching a stable state.

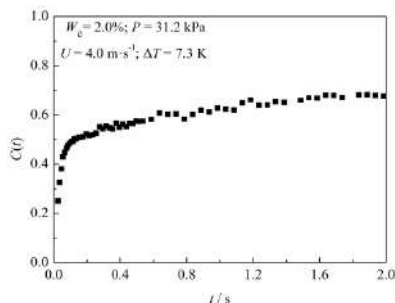


Figure 5: Coverage ratio during the time-series process

Figure 6 showed the effects of vapor-to-surface

temperature difference on the condensate droplets coverage ratio at the ethanol vapor concentrations of 2.0% and 5.0% respectively. The droplets coverage ratio increased obviously with the increase in the vapor-to-surface temperature difference, especially when the time-series reached the stable state. As the vapor-to-surface temperature was the dominant driving force for the Marangoni condensation, when the vapor-to-surface temperature difference increased, the condensate droplets grew up faster and the condensate droplets coverage ratio increased correspondingly.

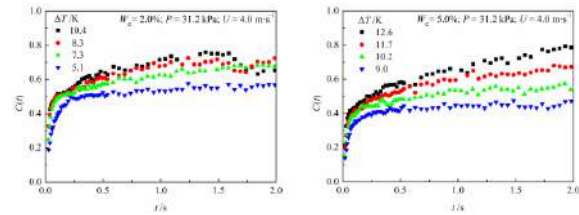


Figure 6: Effects of vapor-to-surface temperature difference

Figure 7 showed the effects of ethanol vapor concentration on the condensate droplets coverage ratio at the impinging cooling water temperatures of 50 °C and 60 °C respectively. The condensate droplets coverage ratio decreased obviously with the increase in the ethanol vapor concentration. The effect of the ethanol vapor concentration mainly came from the thermal resistance in the vapor diffusion layer. As the ethanol vapor concentration increased, the thermal resistance from the vapor diffusion layer increased accordingly, which weakened the heat transfer process and slowed down the growth of the condensate droplets with the smaller coverage ratio. The fluctuation in the data was mainly caused by the movement of condensate droplets.

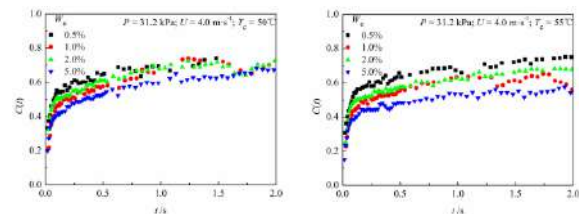


Figure 7: Effects of ethanol vapor concentration

## References

- Utaka Y., Wang, S.X., Int. J. Heat Mass Transfer, Vol. 47, No. 21, pp. 4507-4516 (2004).
- Yang Y.S., Zhen K.J., Yan J.J., Liu J.P., Hu S.H., Journal of Chemical Industry and Engineering (China), Vol. 57, No. 12 pp. 2816-2822 (2006).
- Yan J.J., Wang J.S., Yang Y.S., Hu S.H., Liu J.P., Microgravity Science and Technology, Vol. 21, No. 1, pp. 77-85 (2009).
- Li Y., Wang J.S., Xia K., Chen N.N., Yan J.J., Experimental Thermal and Fluid Science, Vol. 83, pp. 141-156 (2017).

## Film Wise Vapor Condensation in Channels and on Curved Surfaces

Igor Marchuk<sup>1,2</sup>, Yuriy Lyulin<sup>1,2</sup>, Artem Barskii<sup>1,2</sup>

<sup>1</sup> Kutateladze Institute of Thermophysics, Russian Academy of Sciences  
Prosp. Lavrentyev 1, Novosibirsk, 630090, Russia  
<sup>2</sup> Novosibirsk State University  
Pirogova Str. 2, Novosibirsk, 630090, Russia  
marchuk@itp.nsc.ru

Film wise condensation of pure vapor in flattened tubes with flat side walls is studied numerically. Such flattened tubes are used in the manufacture of vapor condensers, in which it is necessary to ensure effective thermal contact with the flat surface of the heat exchanger. The process of unsteady condensation of immobile vapor of Ethanol inside a flattened tube was calculated using the lubrication theory approximation approach (Marchuk and Kabov 2016). The cross section of the tube has the following geometric parameters: length of straight section of section is 3 mm, radius of rounding is 2 mm and perimeter is 18.6 mm, Fig. 1a. In the calculations, the initial thickness of the film was assumed equal to 1  $\mu\text{m}$ , the temperature difference between the pipe wall and the saturation temperature of the vapor is 0.5 K. The minimum thickness of the condensate film and, correspondingly, the highest condensation intensity are observed at the points of conjugation of the flat and round parts of the tube in its upper part, Fig. 1b. The maximum thickness of the condensate film and, accordingly, the place where most of the condensed liquid accumulates, was observed near the lower rounded parts of the tube, where the liquid moves due to gravity and the capillary pressure gradient. The calculated average values of the heat transfer coefficients for the flattened tube turned out to be higher than for a round tube with the same length of the perimeter of the section.

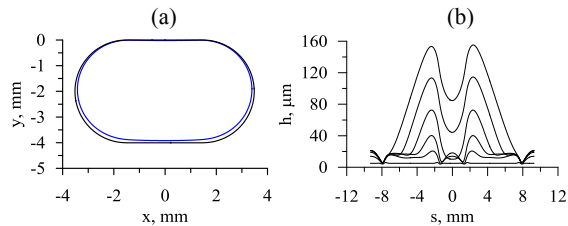


**Figure 1:** Condensate film thickness in the flattened tube. (a) – tube cross section, outer curve is the inner tube wall, inner curve is liquid surface after 10 seconds of condensation, (b) – at different moments after start of condensation: 0.1 s, 0.5 s, 1 s, 2 s, 5 s, 10 s.

Calculation results for the inclined tube are shown in Fig. 2. System loses the symmetry. Minimal condensate thickness is near the upper conjugation point of round and flat part. Maximal condensate film thickness is at the lower round part of the tube

The calculations of the condensation of vapor of HFE7100 on cylindrical fin are performed. The conditions of the variable gravity of the parabolic flight were modeled (Glushchuk et. al. 2017). It is found that under microgravity

conditions the thickness of the condensate layer on the fin top and on the lateral side of the fin is much larger than under the conditions of terrestrial gravity, Fig. 3. After the transition from the microgravity to the normal gravity, the thickness of the condensate layer at the apex of the fin and on its lateral surface decreases again, with a single wave traveling at the surface of the condensate at a speed of about 10 mm/s.

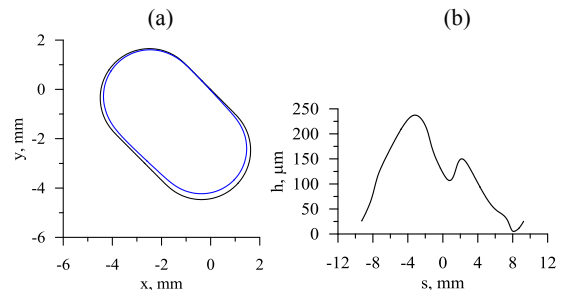


**Figure 2:** Condensate film thickness in the flattened tube rotated on 45°, after 20 seconds of condensation, (a) – cross section, (b) – along the tube cross section.

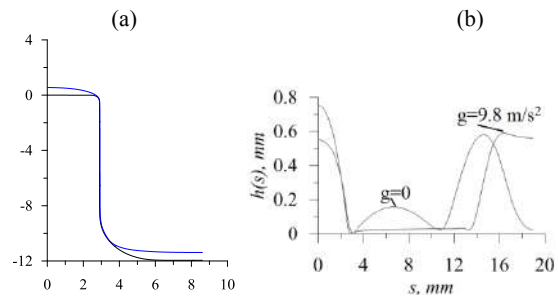


**Figure 2:** Condensate film on cylindrical fin. (a) – cross section of the fin. (b) – condensate film thickness along the fin surface.  $\Delta T=1$  K.

### References

- Marchuk I.V., Kabov O.A., Model of filmwise vapor condensation on curved surfaces Doklady Physics, 61 (1), pp. 19-23 (2016).  
Glushchuk, A., Minetti, C., Machrafi, H., Iorio, C.S. Experimental investigation of force balance at vapour condensation on a cylindrical fin, International Journal of Heat and Mass Transfer, 108, pp. 2130-2142 (2017).

## Modeling of film condensation when the significant influence of surface tension forces

Konstantin Goncharov, Vasily Buz

TAIS Ltd  
Khimky, Moscow region, Russia  
E-mail [tais@heatpipe.ru](mailto:tais@heatpipe.ru)

In microgravity, and also at small dimensions of the condensing surface the important role in the condensation process can provide surface tension forces. The simulation of such processes is important when developing capacitors for the two-phase thermal control systems for space application. Calculation analysis of these devices is based on the model proposed by H. Smirnov, V.Buz and K.Goncharov (1997).

This paper presents a one-dimensional model of film condensation on a randomly oriented flat surface element. The model accounts for the combined effect of the pressure forces, viscous friction, surface tension and gravity. Considered one-dimensional motion of a liquid film to the place of suction, which is located on the boundary of the considered flat element. The equation of momentum conservation along the surface of condensation written in the next form

$$\frac{dp}{dx} = -\frac{3\mu\bar{u}}{\delta^2} + \rho g \sin(\varphi) \quad (1)$$

The first term in this equation represents the pressure force, the second is frictional force, the third force of gravity.

The equilibrium condition of the surface section of phases represents the equality of the current perpendicular to the film surface of the resultant surface tension forces, pressure forces and gravity:

$$\sigma \cdot \left[ 1 + \left( \frac{d\delta}{dx} \right)^2 \right]^{-3/2} \cdot \frac{d^2\delta}{dx^2} = p_s - p_l + \rho g \delta \cos(\varphi - \beta) \quad (2)$$

The combined equation of energy, continuity and heat transfer -

$$\frac{d\bar{u}}{dx} = \frac{\lambda(t_s - t_w)}{\rho r \delta^2} \quad (3)$$

In the case of non-isothermal surface of condensation in the model use the equation of heat conduction wall. To the four differential equations should be written six boundary conditions. These boundary conditions can be of different type and can be specified on different boundaries. The equations in the models for different cases of condensation are identical, and all possible variety of paintings of the condensation is determined by the boundary conditions. In this regard, it is extremely important that the correct assignment of boundary conditions.

Using this model created a computer program that enables to set the different variants of the boundary conditions and to analyze their impact. The example of numerical solution results at different boundary conditions are presented in Figure 1. Film condensing with suction of

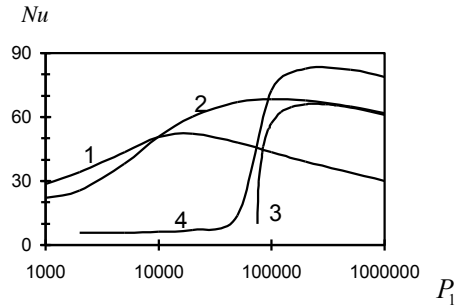


**Figure 1.** Average heat exchange intensity parameter  $Nu$ , versus intensity of liquid suction  $P_1$ , at different boundary conditions.

liquid is characterized by considerable and non-monotonous change of pressure gradient  $P'$  along the liquid film. Assumption that  $P'$  has constant value along  $X$  axis made by some authors is not correct for all cases. Dependence of the average intensity of heat exchange  $Nu$  versus the suction intensity  $P_1$  testifies that there is some maximum of heat transfer intensity (see Figure 1). Considerable difference is also observed in values of integral characteristic of heat ex-change -  $Nu$  number for different boundary conditions.

Figure 2 shows another example of modeling - the condensation on a vertical wall. As we can see, when height of wall is great, the modeling results are corresponded with the Nusselt solution.

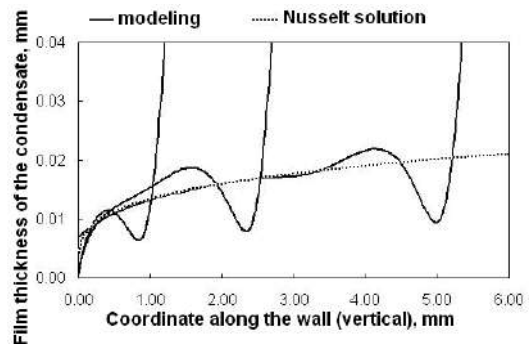


**Figure 2.** An example of the calculations results of film condensation distribution along a vertical surface-condensing, which immersed in the liquid at the different heights.

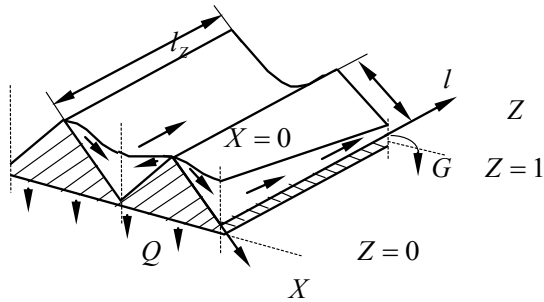


**Figure 3.** Schematic of condensation on ribbed surface in case of liquid removal along grooves between ribs.

External task of condensation on the surface with triangle ribs and liquid suction along grooves between ribs

Schematic of the process is presented in Figure 3. Saturated vapor is condensed over the ribbed surface, heat is rejected from the bottom surface of the wall. Condensed liquid flows along axis  $x$  from the top of rib to its foot. Then liquid moves along the groove between ribs (along axis  $z$ ). Gravity influence is negligible, liquid is moving under the pressure action. Minimum pressure in liquid film is observed in the suction section (at  $z = z_f$ ), maximum pressure is at the top of rib. When liquid moving, pressure in liquid film decreases due to friction. It is assumed that liquid flow along axis  $z$  on the side surface of rib is negligible in comparison with its flow along axis  $x$ . Main liquid stream is observed along  $z$ -axis of the triangle groove.

Task of condensing on rib surface corresponds to one of the tasks described above. For definition of the complete model for considered process, it is necessary to solve this task together with task of liquid flow along triangle groove between ribs (along axis  $Z$ ).

Examples of calculation results for conditions presented in Figure 3 are shown in Figures 4. Difference of curves is conditioned by different  $P_f$  values in each cross section because of hydraulic losses when liquid moving along groove between ribs. These losses (along axis  $Z$ ) have considerably non-linear change. This non-linear characteristic is

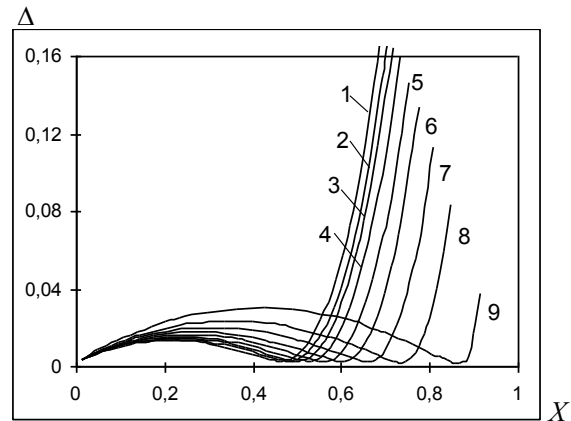


**Figure 4.** Distribution of liquid film thickness along condensing surface for different cross sections  $Z$  :

conditioned, firstly, by increase of liquid mass flow along axis  $Z$  and, secondly, by decrease of cross section area because of surface tension forces action. Average Nusselt number along rib contour changes along axis  $Z$  also. Maximum of heat exchange intensity is observed in case of liquid suction (see Figure 2).

The report presents other examples of simulation of film condensation in two-phase systems for space and ground applications - condensation taking into account the dynamic action of moving vapor on the liquid film, condensation in the axial heat pipes, condensation in loop heat pipes, the dynamics of liquid slugs' formation in the condensers channels and pressure pulsations, and others.

## References

Smirnov H.F., Buz V.N., Goncharov K.A.. Intensification of heat exchange in two-phase loop condensers of space application. Proc. of the 10<sup>th</sup> Int. Heat Pipe Conference. Stuttgart, Germany, (1997).

## Evaporation and condensation of rarefied gas between two parallel condensed phases

Alexey Ph. Polikarpov<sup>1</sup>, Irina A. Graur<sup>2</sup>

<sup>1</sup>Ural Federal University, 620000, str. Lenina 51, Ekaterinbourg, Russia

<sup>2</sup>Aix-Marseille Université, CNRS, IUSTI UMR 7343, 13013 Marseille, France  
Alexey.polikarpov@urfu.ru

Evaporation and condensation phenomena are interesting from the fundamental point of view (Sone 2007), they are also largely present in various industrial applications. The correct and detailed description of these physical processes requires the application of the kinetic theory based approaches (Aoki and Masukawa 1994, Sone 2002). However, the implementation of the kinetic approaches for the practical problems is not so easy. This is why it is interesting to use the classical Navier-Stokes equations with the temperature and pressure jumps boundary conditions (Onishi and Sone 1979) to simulate the evaporation-condensation problems.

The main objective of this study is the development of the mathematical model to simulate the behavior of the vapor phase at the liquid-gas interface.

First the S-model (Shakhov 1968) kinetic approach is used to simulate the evaporation-condensation phenomena appearing between two parallel plates maintained at different temperatures. Then, these kinetic results are compared with that obtained from the Navier-Stokes equations subjected to the special temperature and pressure jumps boundary conditions (Onishi and Sone 1979). These conditions were derived to take into account the non-equilibrium behaviors of a gas during the evaporation and condensation on the vapor-liquid interface. The comparison between two solutions allows us to determine the domain of the applicability of the Navier-Stokes equations with the jump conditions.

We consider two parallel plane gas - liquid interfaces at rest, maintained at temperature  $T_1$  and  $T_2$ , ( $T_2 > T_1$ ) at the bottom ( $y=0$ ) and top ( $y=H$ ) interfaces, respectively. We investigate the behavior of the steady gas flows caused by evaporation and condensation on the condensed phases on the basis of kinetic theory. Let  $p_1$  be the saturation gas pressure at temperature  $T_1$  and  $p_2$  that at temperature  $T_2$ . The problem is characterized by the parameters  $p_2/p_1$  and  $T_2/T_1$  and by the rarefaction parameter  $\delta$ . The saturation gas pressure is a function of the saturation gas temperature given by the Clausius-Clapeyron equation (Landau and Lifshitz 1969).

The S-model kinetic equation is written as

$$\frac{\partial f}{\partial t} + v \frac{\partial f}{\partial r} = Q(f, f), \quad (1)$$

where  $f(t, r, v)$  is the velocity distribution function of gas molecules,  $v$  is the molecular velocity vector,  $r$  is the position vector,  $t$  is a time. In the frame of S-model kinetic equation the collision term  $Q(f, f)$  has the form

$$Q(f, f) = \nu(f^S - f), \quad (2)$$

where  $\nu$  is the collision frequency,  $f^S$  is an equilibrium distribution function defined by

$$f^S(r, v, t) = f^M \left[ 1 + \frac{2m(v-u)q}{15n(r)(kT(r))^2} \left( \frac{m(v-u)^2}{2kT(r)} - \frac{5}{2} \right) \right],$$

here  $f^M$  is the Maxwellian distribution function,  $T(r)$  is a gas temperature,  $n(r)$  is a gas number density,  $u$  is a bulk velocity,  $q$  is a heat flux,  $m$  is a mass of gas molecule,  $k$  is the Boltzmann constant.

The boundary conditions for the plane vapor-liquid interface can be written as

$$f^+ = (\alpha n_i + (1-\alpha)n_{wi})f_w^i, \quad i=1,2, \quad (5)$$

$$f_w^i(v) = \left( \frac{m}{2\pi k T_i} \right)^{3/2} \exp(-mv^2/(2kT_i)), \quad (6)$$

$n_i$  is the number density of the saturated vapor near the plane interface, it can be calculated from the equation of state using the values of the saturated pressure at the saturated temperature as  $n_i = p_i/(kT_i)$ .  $\alpha$  is the evaporation and condensation coefficient, here we supposed that both coefficients are equal.  $\epsilon_c$  is the condensation coefficient. The density  $n_{wi}$  ( $i=1,2$ ) corresponds to the molecules

$$n_{wi} \sqrt{\frac{kT_i}{2\pi m}} = \int_{n_v < 0} v_y f^- dv. \quad i=1,2. \quad (7)$$

If the function  $f$  is known the macroscopic parameters are defined:

$$n(r, t) = \int f(r, v, t) dv,$$

$$T(r, t) = \frac{m}{3kn} \int f(r, v, t) V^2 dv,$$

$$q(r, t) = \frac{m}{2} \int f(r, v, t) V^2 V dv,$$

here  $V = v - u$ . The mass flow rate can be calculated as

$$J_N = \int v_y f(r, v, t) dv \quad (11)$$

The distance  $H$  between the two interfaces is taken as the characteristic dimension of the problem. The Knudsen

number and the rarefaction parameter are defined as following:

$$Kn = \frac{\ell}{H}, \quad \delta = \frac{1}{Kn}, \quad \ell = \frac{\mu_1 \sqrt{2RT_1}}{p_1}, \quad (12)$$

here  $\ell$  is the equivalent mean free path,  $\mu_1$  is the dynamic viscosity of the vapor phase and  $\sqrt{2RT_1}$  is the most probable molecular speed, both at the temperature  $T_1$ ,  $R$  is the specific gas constant.

The for the same two condensed planes configuration the system of the Navier-Stokes equations are solved, completed to the temperature and pressures jumps boundary conditions (Onishi and Sone 1979, Gatapova et al. 2015).

The kinetic S-model equation and the Navier-Stokes equations are solved for several sets of Knudsen number, temperature and pressure ratios. The conditions of the applicability of the Navier-Stokes equations with the jumps boundary conditions are established.

## References

Aoki K. and Masukawa N., Gas flows caused by evaporation and condensation on two parallel condensed phases and the negative temperature gradient: numerical analysis by using a nonlinear kinetic equation, *Phys. Fluids*, Vol. 6 pp. 1379–1395 (1994)

Gatapova E.Y., Graur I., Sharipov F., and Kabov O.A., The temperature and pressure jumps at the vapor-liquid interface: Application to a two-phase cooling system, *Int. J. Heat Mass Transfer*, Vol. 83 pp. 235–243 (2015)

Landau L.D. and Lifshitz E.M., *Statistical physics, volume 5 of Course of theoretical physics*, Pergamon Press (1969)

Onishi Y. and Sone Y., Kinetic theory of slightly strong evaporation and condensation - hydrodynamic equation and slip boundary condition for finite reynolds numberevaporation and condensation - hydrodynamic equation and slip boundary condition, *J. Phys. Soc. Japan*, Vol. 47 pp. 1676–1685 (1979)

Shakhov E.M., Generalization of the Krook kinetic relaxation equation, *Fluid Dyn.*, Vol. 3 pp. 95–96 (1968)

Sone Y., *Kinetic Theory and Fluid Mechanics*, Birkhäuser, Boston (2002)

Sone Y., *Molecular gas dynamics, Theory, techniques and applications*, Birkhäuser, Boston (2007)

## Effects of Loop Heat Pipe condenser design on the overall thermal performance

Filippo Pagnoni, Vincent Ayel and Yves Bertin

Institut Pprime, CNRS – ENSMA - Université de Poitiers, UPR 3346, Département Fluides, Thermique, Combustion, 1  
av. Clément Ader – BP 40109 86961  
Futuroscope - Chasseneuil Cedex, France  
E-mail filippo.pagnoni@etu.isae-ensma.fr

Loop heat pipes are very efficient two-phase thermocapillary driven heat transfer devices, capable to remove and transport several hundreds of Watts for great distances (Maydanik 2005). In addition, their completely passive nature and the resistance to adverse conditions (Fleming et al. 2010) make these devices highly appealing solutions for the thermal control in a wide range of applications: from microelectronic (Khairnasov et al. 2015) to aerospace and terrestrial ones (Gregori et al. 2007), (Hartensine et al. 2008).

The complex phenomena that concern the internal twophase flow of loop heat pipes represent a serious obstacle for their optimal design and modelling. However, some authors proposed a simplified scheme that reduces the problem to analytical expressions derived from the energy and pressure balance of the loop components, an example in (Maydanik et al. 1994). Following this idea, (Launay et al. 2008) derived an analytical closed form of the loop operating temperature based on two independent equations for the variable and fixed, conduction modes, respectively. The simplified analytical approach represents a highly appealing tool in the earliest design phase of a loop heat pipe. However, there is a strong sensitivity of the results with the design parameters. Whilst the evaporator modelling has been extensively debated in literature, the condenser is often relegated to a minor role and it is most of the time subjected to a less careful modelling, based on the attribution of equivalent heat transfer coefficients. Such approach can result as extremely inaccurate whenever there is a lack of experimental data for the given heat sink. The aim of this paper is to show these divergences and to discuss on the role of the condenser on the overall system performances. To do so, a simplified 0D model of the loop heat pipe is firstly presented and used as reference. This model consists of a set of nonlinear equations that has been solved numerically and it has been coupled with two different condenser representations, a 0D and a 2D ones. Results are then compared in terms of loop temperatures.

The development of the 0D loop model starts from the same nodal network introduced by Launay for the analytical development, the idea is to write an energy balance for each component of the loop heat pipe together with a pressure balance between the saturation states of the flow. The heat transfer within the condenser is thus represented by means of two thermal resistances: one for flow condensation and one for liquid subcooling. The importance of the outlet condenser flow temperature becomes apparent from the model validation routine. Indeed, the comparison with the experimental results of (Hodot et al. 2016) has outlined that imposing the real flow temperature at condenser outlet is the only way to achieve a very satisfying convergence of results in terms of LHP temperatures, as shown in figure 1.

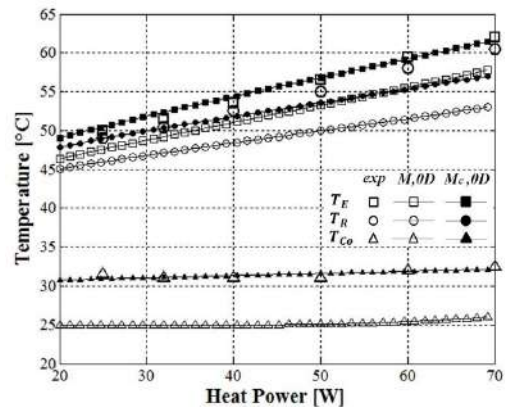


**Figure 1:** Comparison between the LHP evaporator and reservoir temperatures ( $T_E$  and  $T_R$ ) with the experimental values of Hodot (*exp*): computed ( $M, 0D$ ) and imposed ( $M_c, 0D$ ) condenser outlet flow temperature ( $T_{Co}$ ).

To better analyse the influence of condenser geometry on heat transfer, a coupled 1-2D model has been implemented. The model of the condenser consists in a double step iterative procedure where a 1D condensation and subcooling flow problem within the pipe is coupled with the 2D heat conduction on the plate.

As for the pressure drop, the momentum, static and viscous contributions are considered.

The heat sink considered is a flat plate, with a convective boundary condition on one side. The plate has been discretized in a 2D mesh grid and for each element the energy balance equation has been implemented and solved in a forward finite difference scheme.

The coupling of the two sub-problems consists of an iterative procedure where the internal flow evolution that depends on the pipe's wall temperatures, is reduced to an equivalent heat flux distribution on the plate, treated as a boundary condition for those plate elements under the pipe. The pipe is supposed to exchange heat only with the plate (insulated condenser).

The model has been tested with two different condenser geometries, as shown in figure 2:  $HS_1$  and  $HS_2$ , both having the same pipe length and plate extension, with a different  $Y/X$  ratio.

For each geometry of the heat sink two simulations have been run: the fully Loop Heat Pipe 0D model,  $LHP-0D$  and the same coupled with a more refined 2D heat sink representation,  $LHP-0/2D$ .

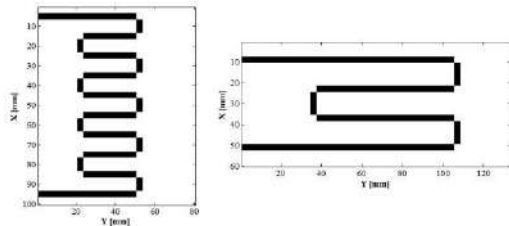


**Figure 2:** Condenser geometries:  $HS_1$ :  $Y/X=0.8$  (left),  $HS_2$ :  $Y/X=2.22$  (right) (pipe's internal diameter: 2mm, external: 2.4mm, plate thickness: 2 mm).

As shown in figure 3, whilst the former model is not affected by the heat sink geometry, the temperature differences between LHP-0/2D with  $HS_1$  and  $HS_2$  prove that a 0D condenser modelling can significantly diverge from the results obtained with a more accurate modelling. This can produce remarkable differences on the whole loop temperatures.

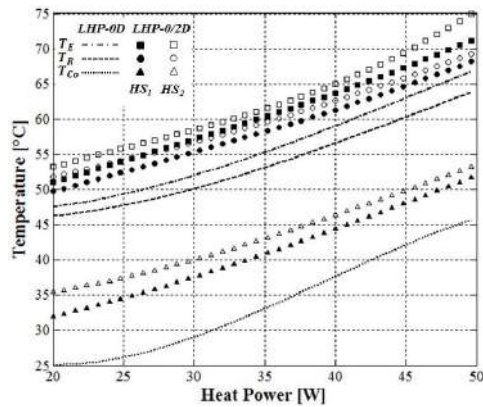


**Figure 3:** Results: main LHP temperatures with both models and heat sink geometries (methanol).

Important differences have been found in the two-phase lengths within the condenser. The total condenser pressure drop seems to not affect the loop temperatures (influence registered always  $< 0.5^\circ\text{C}$  on evaporator and reservoir temperatures). However, the condensation pressure drop was found to be dominant compared to pure liquid one. Furthermore, comparing the both heat sink geometries  $HS_1$  and  $HS_2$  with the LHP-0/2D model at low input heat powers, the proximity of the inlet and outlet pipe branches on  $HS_2$  brings a thermal interaction between them. Thus, the heating of the outlet pipe branch can increase the condenser's outlet flow temperature, as shown in figure 4. This effect is enhanced in case of high conductivity plate, low external heat transfer coefficients and low input heat powers. The results of this paper outline the condenser importance on the entire LHP thermal performance. A 0D model of this component can be unsatisfactory. Furthermore, a careful design of the condenser pipes path on the plate can lead to an optimization of the heat transfer within the subcooling region, depending on the selected pipes and plate materials and on the equivalent heat transfer coefficient of the heat sink.

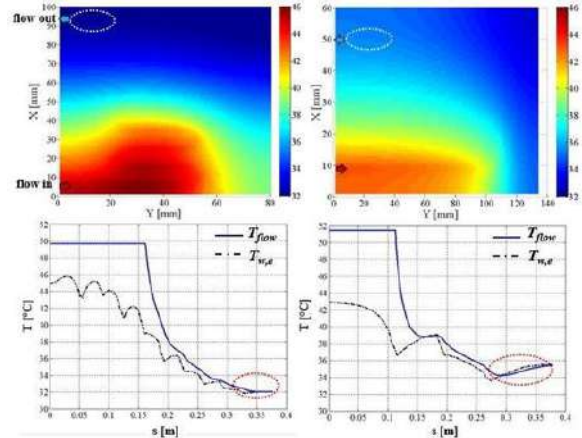


**Figure 4:** 2D effects on the heat sink: simulation results for the LHP-0/2D model with  $HS_1$  (left),  $HS_2$  (right) ( $Q_{in}=20\text{W}$ , methanol).

## References

- Maydanik Yu F., Loop heat pipes, Applied Thermal Engineering, Vol. 25, pp. 635-657 (2005)
- Fleming A. J., Thomas S. K., Yerkes K. L., Titanium-Water Loop Heat Pipe Operating Characteristics Under Standard and Elevated Acceleration Fields, Journal of Thermophysics and Heat Transfer, Vol. 24, No. 1, January-March (2010)
- Khairnasov S., Naumova A., Heat pipes application in electronics thermal control systems, Frontiers in Heat Pipes (FHP), Vol. 6, No. 6 (2015)
- Gregori C., Mishkinis D., Prado P., Torres A., Pérez R., Loop Heat Pipe Technology for Aircraft Anti-Icing Applications, SAE Aircraft & Engine Icing International Conference, Seville, Spain, September 24-27, (2007)
- Hartensine J. R., Anderson W. G., Bonner R., Titanium Loop Heat Pipes for Space Nuclear Power Systems, AIP Conference Proceedings 969, 44 (2008)
- Maydanik Y. F., Fershtater Y. G., Solodovnik N., Loop heat pipes: Design, Investigation, Prospects of Use in Aerospace Technic, Society of Automotive Engineers Paper 941185, (1994)
- Launay S., Sartre V., Bonjour J., Analytical Model for Characterization of Loop Heat Pipes, Journal of Thermophysics and Heat Transfer, Vol. 22, No. 4 (2008)
- Hodot R., Sartre V., Lefèvre F., Modeling and Experimental Tests of a Loop Heat Pipe for Aerospace Application, Journal of Thermophysics and Heat Transfer, Vol. 30, No. 1, JanurayMarch (2016)

## Multi-fluid modelling of suspension filtration in a porous medium: particle trapping and mobilization, permeability damage and recovery

Kristina Tolmacheva, Sergei Boronin and Andrei Osiptsov

Skolkovo Center of Hydrocarbon Recovery, Skolkovo Institute of Science and Technology  
Nobelya st. 3, Moscow, 143026, Russia  
kristina.tolmacheva@skolkovotech.ru

Filtration of suspensions is encountered in a wide range of natural and technological applications, including invasion of mud into the near-wellbore zone during well drilling, conductivity reduction of a hydraulic fracture during cleanup and well testing, and suspension flows in the nearwellbore zone of injection wells. During injection, water adsorbs solids admixtures from wellbore walls and fine particles from the pores in the near-wellbore zone, which results in the flow of suspension in the near-wellbore zone. Suspended particles are trapped in pores, which leads to permeability damage, significant reduction in the fluid injection rate and overall hydrocarbon recovery.

The present study is aimed at constructing a novel model for suspension filtration in porous media with account for the particle trapping and mobilization. The novelty of the model stems from the fact that it accounts for a finite porosity and permeability of a bed formed by the trapped particles inside pores in the matrix.

For suspension filtration in a porous medium, there is a number of models developed earlier and published in open literature. One of the key continuum mechanics models formulated by Gruesbeck and Collins (1982) is a variant of the so-called "deep-bed filtration" model. It is based on splitting of the porous medium into two zones, namely: (i) the zone, where the solid particles can only deposit on a surface of porous matrix, and (ii) the zone, in which the particles can only be trapped in the pores. The trapping process is described using three tuning parameters.

Intensity of particles' mobilization or detachment is proportional to the product of the concentration of trapped particles and the difference between the local filtration velocity and the critical velocity of mobilization, below which particles are immovable (see Herzig, 1970; Gruesbeck and Collins, 1982).

The most frequently used closure relationships for particle trapping and permeability damage were presented, for example, in Zamani and Maini (2009). Intensity of particle trapping is proportional to the product of the fluid filtration velocity and concentration of suspended particles; whereas, the reduction in permeability is determined by the concentration of trapped particles. Most of these formulas involve at least two calibration parameters. Boek (2012) obtained a power-law relation between the reduced permeability and the concentration of trapped non-colloidal particles (4 and 21  $\mu\text{m}$ ) using experimental data for contamination of porous samples.

Existing continuum mechanics models for filtration of suspensions involve free parameters describing particle trapping and mobilization rates, which are required to be tuned against the experimental data. For colloidal (submicron) particles Rajagopalan and Tien (1976) put

forward theoretical formula for filter coefficient describing the initial intensity of particle trapping. For non-colloidal particles only criterium of capturing was proposed by Herzig (1970).

We develop a novel model for filtration of a suspension on the basis of existing models taking into account filtration of the carrier fluid through the pack of trapped fines. Two porosities are introduced:  $\varphi_c$  is the porosity of the medium formed by a porous matrix and the total volume of trapped particles, while  $\varphi_t$  takes into account small channels between trapped particles (Fig. 1):

$$\varphi_c = \varphi_0 - \frac{\sigma}{C_{\max}}, \quad \varphi_t = \varphi_0 - \sigma.$$

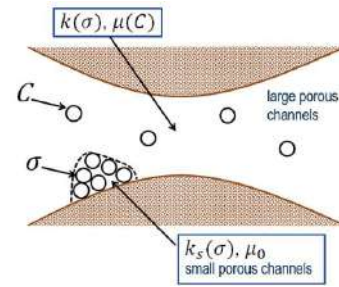


**Figure 1:** Sketch of the suspension filtration in a porous medium.

The particle-laden filtration is described using the three-continua approach, with different phases being a carrier fluid, suspended particles and trapped particles. Continuity equations and Darcy laws for two-phase particle-laden suspension are as follows:

$$\frac{\partial}{\partial t} [\rho_\gamma^f s_\gamma (\varphi_t - C \varphi_c)] + \frac{\partial}{\partial x} [\rho_\gamma^f u_\gamma^f] = 0, \quad \gamma = 1, 2$$

$$\frac{\partial}{\partial t} [\varphi_c s_\gamma C] + \frac{\partial}{\partial x} [u_\gamma^p] = -q_\gamma, \quad \gamma = 1, 2$$

$$\frac{\partial \sigma}{\partial t} = (q_1 + q_2),$$

$$u_\gamma^f = - \left[ (1-C) \frac{k(\sigma) k_\gamma}{\mu_\gamma} + \frac{k_s k_\gamma}{\mu_{\gamma,0}} \right] \frac{\partial p}{\partial x},$$

$$u_\gamma^p = - \left[ C \frac{k(\sigma) k_\gamma (s_\gamma)}{\mu_\gamma} \right] \frac{\partial p}{\partial x}.$$

Here,  $\rho_\gamma^f$  is the fluid density,  $s_\gamma$  is the fluid saturation,  $C$  and  $\sigma$  are the concentrations of suspended and trapped particles, respectively;  $u_\gamma^f$  and  $u_\gamma^p$  are filtration velocities

of the carrier fluid and particles,  $q_y$  is the intensity of trapping and mobilization,  $k$  is the total permeability,  $k_y$  is relative permeability,  $k_s$  is permeability of small porous channels, formed by trapped particles,  $\mu_y$  is the suspension viscosity,  $\mu_{y,0}$  is the fluid viscosity,  $p$  is the pressure.

Intensity of trapping and mobilization takes the following form (Gruesbeck and Collins, 1982):

$$q = \lambda_0 C u - \alpha \sigma (u - u_c) \theta(u - u_c).$$

Here,  $\lambda_0$  is the filter (or trapping) coefficient,  $\alpha$  is mobilization coefficient,  $u_c$  is critical velocity of mobilization.

Permeabilities of small and large porous channels were defined after Boek (2012) and Cozeny-Karman equation (Carman 1956):

$$k_s(\sigma) = k_{s0} \left( \frac{\sigma}{C_{\max} \varphi_0} \right)^3, \quad k(\sigma) = k_0 \left( 1 - \frac{\sigma}{C_{\max} \varphi_0} \right)^3,$$

$$k_{s0} = \frac{(1 - C_{\max})^3 d_p^2}{180 C_{\max}^3}.$$

Validation of the model is carried out by comparison of the simulations against the core-flooding experimental data (Mikhailov et al. 2014) which allowed to determine the values of free parameters  $\lambda_0$  and  $\alpha$ . Results of comparison of the experimental data and numerical simulations are shown in Fig.2. The novel model describes better the particle accumulation zone, which allows a better prediction of the total permeability of a porous medium.

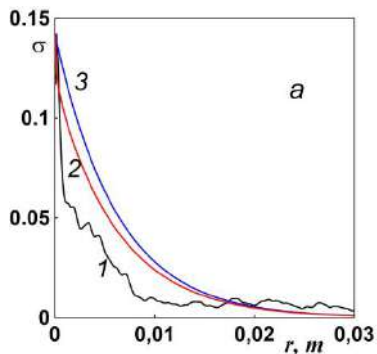


**Figure 2:** Profile of the concentration of trapped particles along Bentheimer sample. Line 1 – experimental data, 2, 3 – numerical simulations based on new and classical models, respectively.

The range of trapping coefficient values was obtained after comparison with experiments with different samples and suspension.  $\lambda_0$  possess values from 100 to 1000  $m^{-1}$ .

Numerical simulations of the contamination of a near-wellbore zone are carried out using the following input parameters: length of porous medium is 1000 m,  $C_0 = 10^{-5}$ ,  $u_0 = 0.1$  m/s,  $k_0 = 10$  mD и  $\lambda_0 = 100 m^{-1}$ . Simulation is stopped, when the porous medium became clogged, i.e.  $\sigma = C_{\max} \varphi_0$ .

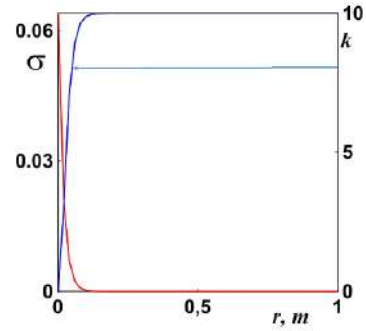


**Figure 3:** Concentration of trapped fines and permeability (in mD) along 1000 m in the near-wellbore zone.

It is shown that the particle trapping may damage the permeability of the near-wellbore zone of injection wells, which can deteriorate the injectivity and resulting production. Various approaches to improving the injectivity of the wells based on transient and cycling injection strategies are proposed.

## References

- Boronin, S. A., Osiptsov, A. A., and Tolmacheva, K. I., Multi-fluid model of suspension filtration in a porous medium, *Fluid Dynamics*, Vol. 50 pp. 759-768 (2015)
- Gruesbeck, C. and Collins, R.E., Entrainment and deposition of fine particles in porous media, *Society of Petroleum Engineers Journal*, Vol. 22 pp. 847-856 (1982)
- Herzig J. P., Leclerc D. M., Goff P. L., Flow of suspensions through porous media—application to deep filtration, *Industrial & Engineering Chemistry*, Vol. 62 pp. 8-35 (1970)
- Zamani A., Maini B., Flow of dispersed particles through porous media—deep bed filtration, *Journal of Petroleum Science and Engineering*, Vol. 69 pp. 71-88 (2009)
- Boek, E.S., Hall, C., Tardy, P.M.J., Deep Bed Filtration Modelling of Formation Damage due to Particulate Invasion from Drilling Fluids, *Transport in Porous Media*, Vol. 91 pp. 479–508 (2012)
- Rajagopalan R., Tien C., Trajectory analysis of deep - bed filtration with the sphere-in-cell porous media model, *AIChE Journal*, V. 22 pp. 523-533 (1976)
- Carman P.C., Flow of gases through porous media, Academic press (1956)
- Mikhailov D., Ryzhikov N., Shako V., & Theuveny, B., An Integrated Experimental Approach to Determining How Invaded Mud Components Modify Near-Wellbore Properties (Russian), *SPE Russian Oil and Gas Exploration & Production Technical Conference and Exhibition* (2014)

## Experiments and modelling on flow pattern and heat transfer during condensation in a 3 mm channel

Marco Azzolin, Stefano Bortolin, Davide Del Col\*

Università degli Studi di Padova - Dipartimento di Ingegneria Industriale  
Via Venezia, 1 – 35131, Padova, Italy

\*Corresponding author: davide.delcol@unipd.it

Two-phase systems are becoming very attractive for the thermal management in both ground and space applications. A correct design of such devices cannot disregard from the understanding of convective condensation mechanisms. Experiments conducted in micro-gravity conditions are essential to achieve a physical knowledge of the phenomenon but unfortunately, they are expensive, have a short duration and sometimes they are limited to certain types of fluids (Azzolin et al. 2016). On the other side, numerical simulations easily allow to change the boundary conditions (e.g. gravity level) or the fluid properties, but often they need to be validated with experimental data. Recently, the Volume of Fluid (VOF) method has been employed by researchers to study two-phase heat transfer during flow boiling (Magnini et al. 2016) and in convective condensation (Da Riva et al. 2012). Despite the rapid increase of computational capacity available nowadays, three-dimensional and unsteady-state simulations of condensation inside channels still remain very challenging. The present work is aimed at the investigation of R134a annular condensation inside a 3.4 mm diameter channel. In the first part, measured heat transfer coefficients in horizontal configuration are presented and compared against three-dimensional steady state simulations. Since experimental flow visualizations at certain mass fluxes emphasizes the presence of waves, axisymmetric unsteady-state simulations have been performed to investigate the condensation process in the same channel but in vertical downflow.

Three-dimensional and steady-state VOF (Volume Of Fluid) numerical simulations of R134a condensation at mass velocity  $G \leq 200 \text{ kg m}^{-2} \text{ s}^{-1}$  inside a 3.4 mm diameter circular minichannel have been performed. The VOF method, implemented in the commercial package Ansys® Fluent is used to track the vapour-liquid interface without using any empirical closure law to model the interaction between the phases.

The numerical results obtained by simulations are reported in Fig. 1. The computed heat transfer coefficients are plotted versus vapor quality for three different values of the mass velocity ( $G = 50 - 100 - 200 \text{ kg m}^{-2} \text{ s}^{-1}$ ) at a saturation temperature of  $40^\circ\text{C}$ . Simulations have been performed with the assumption of laminar liquid film. Numerical results have been compared in the same graph of Fig. 1 with experimental data taken during R134a condensation inside a 3.4 mm diameter circular channel in horizontal configuration; the saturation temperature is  $40^\circ\text{C}$  with a wall-to-saturation temperature difference ranging from 7 K to 15 K. At mass velocity  $G = 50 \text{ kg m}^{-2} \text{ s}^{-1}$  a very good agreement is found between numerical results and experimental data, with a relative error below 2%.

Considering that at such conditions, the vapor-liquid interface is flat without the presence of waves, the good agreement between simulations and experiments is an important validation of the present numerical technique. In fact, since only steady-state numerical simulations are considered in this part, a reliable comparison between numerical results and experimental data can be done only when the flow pattern is annular or annular-stratified. A satisfactory prediction is also found for mass velocity  $G = 100 \text{ kg m}^{-2} \text{ s}^{-1}$  even if in this case the deviation is about -18.1% (it must be mentioned that a stratified-wave flow at  $100 \text{ kg m}^{-2} \text{ s}^{-1}$  was observed). When moving to the highest mass velocity ( $G = 200 \text{ kg m}^{-2} \text{ s}^{-1}$ ) the experimental data are underpredicted by the present simulation by 35%. The underestimation of the heat transfer coefficient can be due to two phenomena occurring for  $G \geq 100 \text{ kg m}^{-2} \text{ s}^{-1}$ :

- the presence of waves at the vapor-liquid interface;
- the transition from laminar to turbulent flow in the liquid film (at  $G = 200 \text{ kg m}^{-2} \text{ s}^{-1}$  the all-liquid Reynolds number is 4220).

Three-dimensional simulations have been used to detect the vapor-liquid interface during R134a condensation at  $G = 100 \text{ kg m}^{-2} \text{ s}^{-1}$  and vapor quality  $x = 0.6$  (Fig. 2). At these operating conditions, the effect of gravity is visible: this force promotes the liquid stratification, thinning the liquid film in the upper side of the tube. Analyzing the distribution of the heat flow rate along the circumference of the tube it results that the 85% of the heat flow rate is transferred in the upper part side of the tube, between the angular positions  $+90^\circ$  and  $-30^\circ$ .

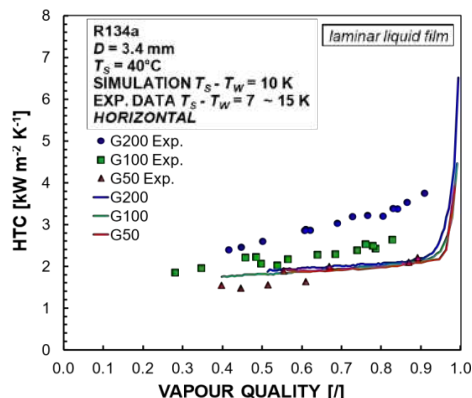
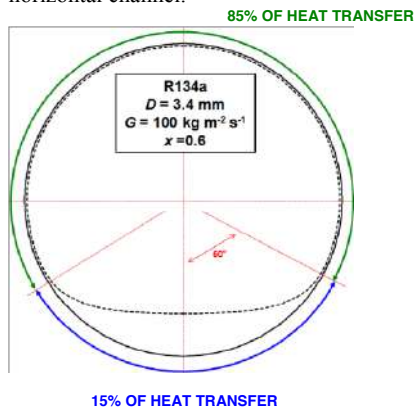


Figure 1: Comparison between heat transfer coefficients obtained by numerical simulations and experimental data

taken during R134a condensation inside the 3.4 mm diameter horizontal channel.

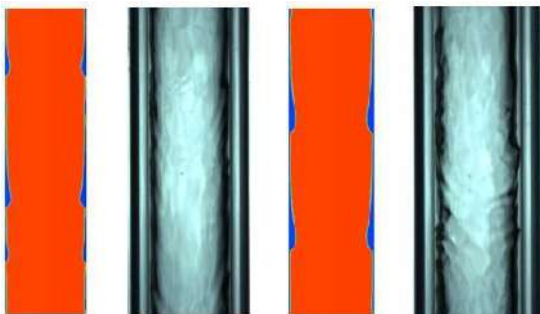


**Figure 2:** Vapor liquid interface and distribution of the heat flow rate inside the 3.4 mm horizontal channel at  $G = 100 \text{ kg m}^{-2} \text{ s}^{-1}$  and vapor quality  $x = 0.6$ .

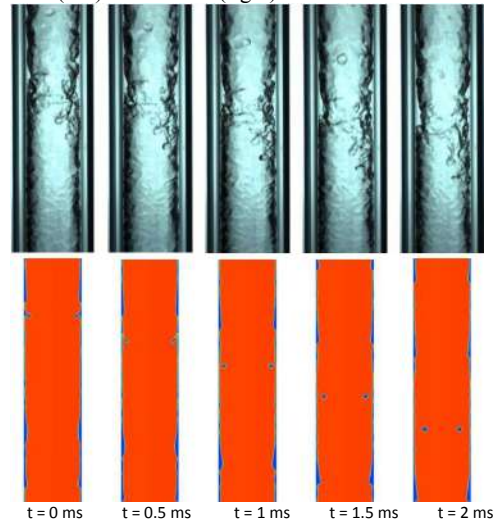
With the aim to study the presence of waves at the vapor-liquid interface, downflow annular condensation has been investigated inside the 3.4 mm vertical channel by transient numerical simulations. In this configuration, the liquid film in the cross section of the channel is uniform and a 2D-axisymmetrical domain can be employed with a reduction of the computation time.

Fig. 3 shows the simulated and experimentally recorded two-phase flow regimes at  $G = 100 \text{ kg m}^{-2} \text{ s}^{-1}$  and at two different values of time-average vapour quality  $x = 0.69$  (left) and  $x = 0.5$  (right). The vapour phase is colored in red, whereas the liquid phase is depicted in blue. It can be observed that the numerical simulations are able to predict the existence of interfacial waves as observed by high-speed visualizations. In particular, at a fixed mass velocity, when the vapour quality decreases, the waves become sharper and their frequency decreases.

Besides the occurring of interfacial waves, when the mass velocity increases, other phenomena can be detected by means of unsteady-state numerical simulations. At  $G = 200 \text{ kg m}^{-2} \text{ s}^{-1}$  and  $x = 0.57$  the vapour-liquid interface becomes more disturbed due to the higher vapour shear stress. The vapour phase can rip some liquid from the annular film, with the formation of liquid entrainment in the vapour phase as can be seen in Fig. 4.



**Figure 3:** Predicted and experimental two-phase flow regimes at  $G = 100 \text{ kg m}^{-2} \text{ s}^{-1}$  and average vapor quality  $x = 0.65$  (left) and  $x=0.50$  (right).



**Figure 4:** Experimental and predicted flow during the formation of liquid entrainment in the vapour phase ( $G = 200 \text{ kg m}^{-2} \text{ s}^{-1}$ , average vapor quality  $x = 0.57$ ).

Three-dimensional and steady-state numerical simulations of R134 condensation inside a horizontal 3.4 mm diameter channel have been performed; results have been validated with experimental data. With the aim to investigate the influence of liquid waves on condensation heat transfer, 2D-axisymmetric and transient numerical simulation of R134a vertical downflow condensation have been run inside the same diameter channel. The VOF method is able to predict the presence of interfacial waves reported by experimental visualizations.

#### Acknowledgements

The authors acknowledge the financial support of the European Space Agency through the MAP Condensation program ENCOM-3 (AO-2004-096).

#### References

- Azzolin M., Bortolin S., Le Nguyen L.P., Lavielle P., Glushchuk A., Queeckers P., Del Col D., Miscevic M., Dutour S., Chikov S., and Iorio C.S., Convective condensation in microgravity conditions: heat transfer coefficient measurements and flow visualizations, Eleventh International Conference on TWO-PHASE SYSTEMS FOR GROUND AND SPACE APPLICATIONS, September 26-29, Marseilles, France (2016)
- Magnini M. and Thome J.R., Computational Study of Saturated Flow Boiling Within a Microchannel in the Slug Flow Regime, *Journal of Heat Transfer*, Vol. 138 (2016).
- Da Riva E., Del Col D., Garimella S.V. and Cavallini A., The importance of turbulence during condensation in a horizontal circular minichannel, *Int. J. Heat Mass Transfer*, Vol. 55, pp. 3470-3481 (2012)

## Loop Heat Pipes – Highly Efficient Heat Transfer Devices for Electronics Cooling

Yury Maydanik, Vladimir Pastukhov and Mariya Chernysheva

Institute of Thermal Physics, Ural Branch of the Russian Academy of Sciences,  
107, Amundsen Street, Yekaterinburg, 620016, Russia  
E-mail: maidanik@etel.ru

Loop heat pipes (LHP) are passive heat-transfer devices, operating in a closed evaporation-condensation cycle and using a "capillary mechanism" for the working fluid transportation (Maydanik 2005). These devices can be successfully used in cooling systems of semiconductor electronics components, LED, computers and other equipment (Pastukhov et al. 2003, Maydanik et al. 2005, and Pastukhov et al. 2009). A schematic diagram of an LHP is shown in the Fig. 1.

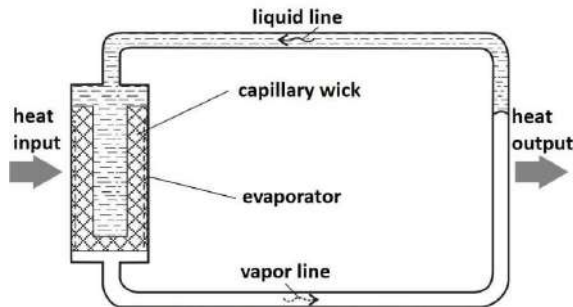


**Figure 1:** Schematic diagram of an LHP

LHP main advantages comprise high heat-transfer capacity at any orientation, good adjustability and flexibility to various location and operation conditions, ability to spread uniformly the removed heat over a big surface (Pastukhov et al. 2007). An external view of some LHPs is presented in the Fig. 2.

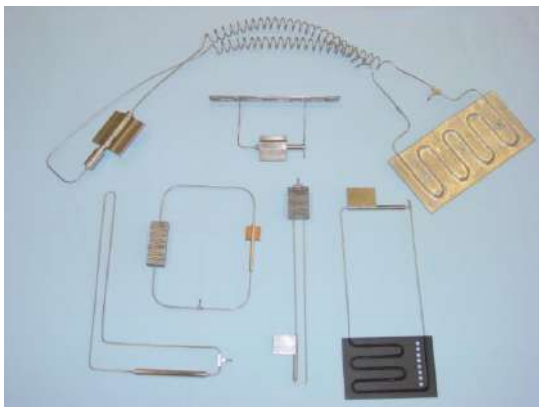


**Figure 2:** External view of an LHP

These devices have a cylindrical evaporator with a diameter from 5 to 10 mm and lines for vapor and liquid,

2-2.5 mm in diameter, which can be easily bended almost in any way. The maximum capacity of these LHPs varies from 50 to 200 W, and heat-transfer distance ranges within 300 to 1500 mm. The nominal working temperatures range for the LHPs is 40-80 °C. The most effectively LHP advantages are demonstrated in cooling systems with a remote heat sink, when the latter is placed far away from a heat source, where more favourable conditions for heat rejection exist (Maydanik et al. 2010).

The paper contains LHP theory basis, various design embodiments of LHPs, test results and application examples for different electronics cooling systems.

### References

- Maydanik Yu. F., Review: Loop Heat Pipes, *Applied Thermal Engineering*, Vol. 25 pp. 635-657 (2005)
- Pastukhov V. G., Maydanik Yu. F., Vershinin C.V., Korukov M.A., Miniature Loop Heat Pipes for Electronics Cooling, *Applied Thermal Engineering*, Vol. 23 pp. 1125-1135 (2003)
- Maydanik Yu.F., Vershinin S.V., Korukov M.A., Ochterbeck J.M., Miniature Loop Heat Pipes – A Promising Means for Cooling Electronics, *IEEE Transactions on Components and Packaging Technologies*, Vol. 28 pp. 290-296 (2005)
- Pastukhov V. G., Maydanik Yu. F., Active Coolers Based on Copper-water LHPs for Desktop PC, *Applied Thermal Engineering*, Vol. 29 pp. 3140-3143 (2009)
- Pastukhov V.G., Yu.F. Maydanik, Low-noise Cooling System for PC on the Base of Loop Heat Pipe, *Applied Thermal Engineering*, Vol. 27 pp. 894-901 (2007)
- Maydanik Yu.F., Vershinin S.V., Pastukhov V.G., Fried S., Loop Heat Pipes for Cooling Systems of Servers, *IEEE Transactions on Components and Packaging Technologies*, Vol. 33 pp. 416-423 (2010)
- Maydanik Yu., Vershinin S., Pastukhov V., Chernysheva M., Sarno C., Tantolin C., Passive Cooling System for an Aircraft Electronic Box, *Heat Pipe Science and Technology, An International Journal*, Vol. 1 pp. 251-260 (2010)

## Effect of Gravitational Acceleration on the Distribution of Oil Phase

Rui Ma, Yu-ting Wu\*, Qiang-yu Wen, Chun-xu Du, Xia Chen, De-lou Zhang, Chong-fang Ma

College of Environmental and Energy Engineering, Beijing University of  
Technology, Beijing, China  
[wuyuting1970@126.com](mailto:wuyuting1970@126.com); [mr12593@126.com](mailto:mr12593@126.com)

The efficient use of energy has a certain effect on the protection of the environment, and the evaporator is ubiquitous in the heat process. So it is very important to simulate two-phase flow in the evaporator. Based on the simulation of the liquid-liquid two-phase flow in microchannels, the mixing mechanism and phenomenon in the droplet in the curved microchannel were investigated (Jianan Wang. 2013). By using the mixture multiphase flow model, the oil-water separation characteristics in the T - channel were studied, and the effects of inlet oil content, outlet split ratio and inlet velocity on the analytical efficiency were analyzed (Kun Hu et al. 2017). By studying influence of gravity on gas-liquid two-phase flow in horizontal pipes, the flow patterns, void fraction distribution and fluctuation in circular pipes under various gravities were all presented (Xiangdong Liu. 2012). But so far the influence of gravity acceleration on the two-phase flow of lubricants and refrigerants in refrigeration systems almost has not been analyzed.

In this paper, the effects of gravity acceleration on the flow of lubricating oil and refrigerant liquid in the evaporator were investigated by Fluent simulation. It was conducted to verify whether the lubricating oil would be deposited on the evaporator without returning to the compressor.

The mixture of lubricating oil and refrigerant flow and heat transfer in the evaporator was studied, assuming that the flow and heat transfer processes were steady-state processes and fluid was incompressible. Figure 1 showed the theoretical model of evaporator based on the vapor compression heat pump experimental system. The evaporator model was built whose length was 81mm, width was 88mm, height was 4mm.

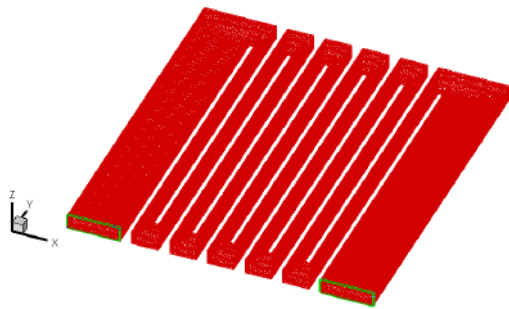


**Figure 1:** Evaporator model

The flow of fluid follows the basic conservation laws, such as conservations of mass, momentum and energy. The governing equations are mathematical descriptions of these conservation equations.

### (1) Continuity equation

The closed space which got in the flow field is called the control body and the surface is known as the control surface. The fluid flows into the control body through the control surface A1, and also flows out of the control body by the control surface A2, during which the fluid quality inside the control body also changes. The difference in the mass of inflow and outflow should be equal to the increment of fluid mass inside the control body. The integral form of fluid flow continuity equation can be derived as Formula (1):

$$\frac{\partial}{\partial t} \iiint_{Vol} \rho dx dy dz + \iint_A \rho \mathbf{v} \cdot \mathbf{n} dA = 0 \quad (1)$$

In the equations, Vol means control body, A means control body. The first term on the left side of the equation represents the increment of internal mass of the control body Vol. The second term represents the net flux flowing through the control surface into the control body.

According to the Gauss formula in mathematics, the above equation can be transformed into the following form (2) in the Cartesian coordinate system :

$$\frac{\partial \rho}{\partial t} + \frac{\partial(\rho u)}{\partial x} + \frac{\partial(\rho v)}{\partial y} + \frac{\partial(\rho w)}{\partial z} = 0 \quad (2)$$

For incompressible fluids, the density is constant and the continuity equation can be simplified as following (3):

$$\frac{\partial u}{\partial x} + \frac{\partial v}{\partial y} + \frac{\partial w}{\partial z} = 0 \quad (3)$$

### (2) Momentum conservation equation

The momentum conservation equation is also called the equation of motion, also known as the Navier-Stokes equations as following (4), (5), (6):

The momentum conservation equation in the x direction:

$$\frac{\partial(\rho u)}{\partial t} + \text{div}(\rho u \mathbf{u}) = \frac{\partial \rho}{\partial y} + \frac{\partial \tau_{xx}}{\partial x} + \frac{\partial \tau_{yx}}{\partial x} + \frac{\partial \tau_{zx}}{\partial x} \quad (4)$$

The momentum conservation equation in the y direction:

$$\frac{\partial(\rho v)}{\partial t} + \text{div}(\rho v \mathbf{u}) = \frac{\partial \rho}{\partial y} + \frac{\partial \tau_{xy}}{\partial x} + \frac{\partial \tau_{yy}}{\partial x} + \frac{\partial \tau_{zy}}{\partial x} \quad (5)$$

The momentum conservation equation in the z direction:

$$\frac{\partial(\rho w)}{\partial t} + \text{div}(\rho w \mathbf{u}) = \frac{\partial \rho}{\partial y} + \frac{\partial \tau_{xz}}{\partial x} + \frac{\partial \tau_{yz}}{\partial x} + \frac{\partial \tau_{zz}}{\partial x} \quad (6)$$

The inlet boundary was set as velocity inlet which inlet velocity and oil content were given. The pressure outlet boundary was set. The influence of gravity acceleration (g) was considered. The mixture model was selected in two-phase flow. The model was calculated using the k-ε model. The oil return of the system in the stable required to be considered. Therefore, the model was calculated with steady state.

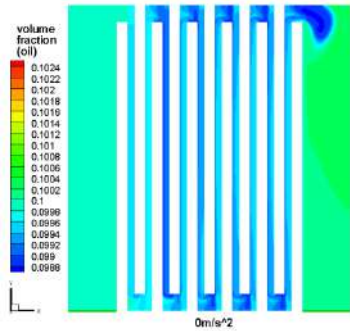


**Figure 2:** Oil phase distribution of 10% lubricating oil without gravity

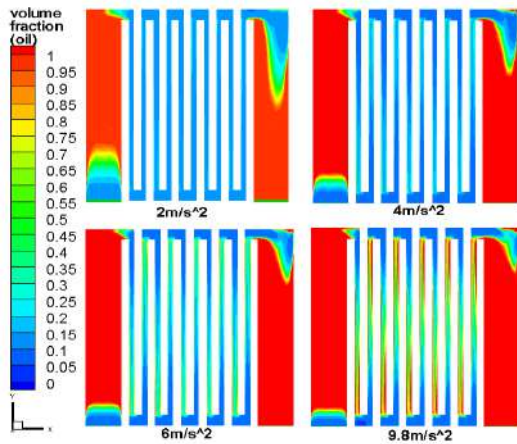


**Figure 3:** Oil phase distribution under variable gravity

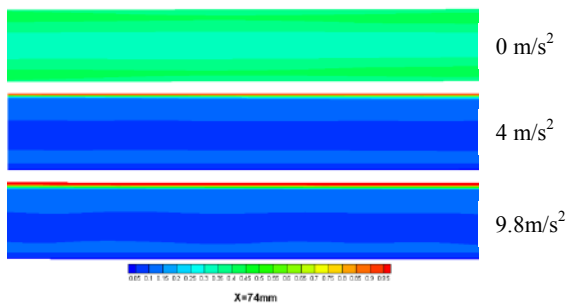


**Figure 4:** Effect of different gravity on phase distribution

It could be seen from Fig. 2 to Fig. 4 that acceleration of gravity decreased from 9.8 to 0 along the z axis and the amount of lubricating oil deposited in the evaporator decreases when lubricating oil amount was 10% and the other conditions were constant.

When the acceleration was 0 m/s<sup>2</sup>, the flow field was almost evenly distributed. This was because under normal gravity the fluid had a tendency of deposition or stratification along the direction of gravity. When the acceleration of gravity decreased, the stratification would be weakened.

When the incompatible liquids mixed under normal gravity, the large density was on the lower layer and the lower density was on the upper layer. The material that had large density in the two-phase flow would precipitate in the

direction of gravity. The media of different densities would no longer precipitate relative to each other and were suspended in space without gravity.

It was great significant to study the distribution of liquid-liquid two-phase fluid at different gravity and the influence of lubricating oil distribution on the heat transfer performance in the evaporator. From the above results we could see that the acceleration of gravity had a significant effect on the two-phase flow of lubricating oil and refrigerant. In this paper only the two-phase flow in the evaporator was simulated. The influence of the acceleration of the two-phase flow on the evaporator in the different placement mode and the heat transfer process will also be studied.

### References

- Jianan Wang, Numerical study on hydrodynamics and mixing process in microchannels for liquid-liquid two-phase flow, Zhejiang University (2013)
- Kun H.U., Zhi-jiu A.I., Bi-wei F.U., Jie L.I., Zhen-bei L.I., Numerical Simulation of Oil-Water Separation Characteristics in Tee Tube, The Chinese Journal of Process Engineering, Vol. 17 pp. 29-34 (2017)
- Xiangdong Liu, Yongping Chen, Mingheng Shi. Influence of gravity on gas-liquid two-phase flow in horizontal pipes, International Journal of Multiphase Flow, Vol. 41 pp. 23-35(2012)

## Thermocapillary convection of high Prandtl number fluids

Ruquan Liang<sup>a,b</sup> and Song Xiao<sup>b</sup>

<sup>a</sup> Northeastern University, Key Laboratory of National Education Ministry for Electromagnetic Process of Materials  
Wenhua Road 3-11, Heping District, Shenyang, 110819, China  
liang@epm.neu.edu.cn

<sup>b</sup> LinYi University, School of Mechanical and Vehicle Engineering  
Shuangling Road, LinYi, 276005, China  
xskmust@163.com

During the floating zone process for single-crystal, thermocapillary convection plays an important role on the quality of crystal material. The oscillatory thermocapillary convection was found in melting zone, and such oscillatory convection brings corresponding oscillatory temperature field, which relates to the growth of striation in the crystal and affects the growth quality of crystal. While in high Pr number range, the experimental and numerical investigations for oscillatory thermocapillary convection are still not enough. It is difficult to find out accurate and stable analyses or numerical simulations on flow structures of high Pr number fluids, and the reason is that the majority studies adopted the simplified model without taking the environment influence and the dynamic surface deformation into account. Meanwhile, there are still major disputes on data veracity (Rupp et al. 1989). In this paper, numerical and experimental researches on thermocapillary convection in liquid bridges for high Pr number fluid under gravity have been conducted to explore the flow pattern in the liquid bridge.

A liquid bridge of 2 cSt silicone oil is used to investigate the thermocapillary convection under gravity. The liquid bridge with radius  $R=2.5$  mm and height  $H=2.5$  mm is suspended between two coaxial disks and surrounded by the air in a rectangular container with height  $H$  and width  $4R_0$ . In Fig. 1, the evolution of thermocapillary convection can be found, which was obtained from a numerical simulation. On the whole, the flow pattern is a symmetric cell flow structure inside the liquid bridge. The bulk returning flow grows up and centers at the axial position of  $y=0.3$ . The scope of thermocapillary convection expands toward the center of liquid bridge, here  $y$  is the distance from the cold disk.

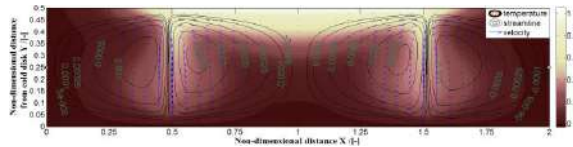


**Figure 1:** Distributions of temperature, streamline and velocity vectors ( $Pr=27.9$ ,  $Ma=73915.6$ ,  $We=268.7$ ,  $Ca=0.1015$ ,  $B=0.03$ ,  $2R=5.0$  mm,  $\Gamma=1.0$ ).

Figure 2 shows the tracer particle images of steady flow patterns in the vertical cross section of a liquid bridge with radius  $R=2.5$  mm and height  $H=2.5$  mm, which was obtained from an experiment. A pair of vortices appear inside the liquid bridge representing two toroidal vortices.

The pair of vortices have the same size constant in time during the steady flow, indicating an axisymmetric flow with the vertical return flow upward along the axis of liquid bridge.

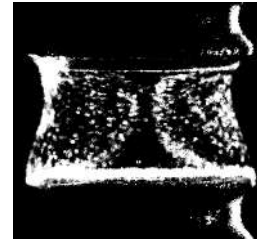


**Figure 2:** Toroidal vortices inside a liquid bridge (tracer particle images in a steady flow).

An investigation on the oscillatory thermocapillary convection in a liquid bridge for high Pr number fluids under gravity was carried out numerically and experimentally, respectively.

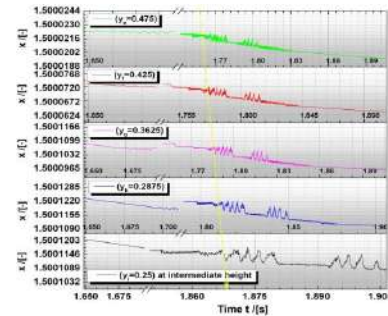


**Figure 3:** Oscillation of free surface on five dynamic monitoring points.

The oscillation originates from the hot corner. Therefore, the surface near the hot corner oscillates firstly and the surface at the lower height begins to oscillate successively. Figure 3 shows the lateral position change of free surface with time at different heights ( $y_e=0.475$ ,  $y_e=0.425$ ,  $y_e=0.3625$ ,  $y_e=0.2875$  and  $y_e=0.25$  (intermediate height)). The oscillation characteristic at lateral position of free surface is similar as that of velocity oscillation near the intermediate height. The difference is that after transition to oscillation the surface oscillation turns into the low frequency with large amplitude and there are also two obvious oscillation bifurcations. The distribution transforms firstly into the steady low frequency oscillation after a long

time, and then the surface oscillation transforms into the high frequency oscillation. The oscillation of free surface is due to the coupling effects of oscillatory temperature and velocity.

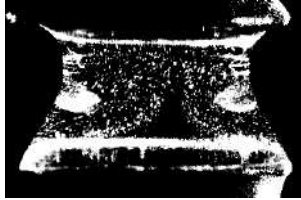


**Figure 4:** Toroidal vortexes inside a liquid bridge (tracer particle images in an oscillatory flow).

Figure 4 shows the tracer particle images of oscillatory flow patterns in the vertical cross section of a liquid bridge. At the onset of oscillatory flow, however, the vortexes start to expand and contract on opposite sides as shown in Fig. 4. The flow then becomes non-axisymmetric and the return flow is no longer vertical along the axis of liquid bridge.

The present study shows that the nature of oscillatory thermocapillary convection is the coupling effects of oscillations for temperature, velocity and surface. The oscillatory thermocapillary convection originates from the hot corner, and the temperature oscillates firstly at the hot corner. The bulk return flow supplements the surface flow and brings the disturbance information of velocity. The velocity oscillation is mainly affected by the interior flow change of liquid bridge, and there is a time lag in space due to this effect. Because the temperature oscillation is directly affected by the thermal disturbance at the hot corner, the velocity oscillation responds slowly to the temperature oscillation. The onset of velocity oscillation lags behind the temperature oscillation at hot corner. In addition, the propagation directions of velocity and temperature oscillations at the corner are opposite, and the difference and complex coupling effects of two kinds of oscillations intensify the disturbance of free surface. Finally, the instability of thermocapillary convection results from the interaction among free surface, velocity and temperature oscillations, and the coupling effects of three kinds of oscillations induce the asymmetric flow of thermocapillary convection.

The present work is supported financially by the National Natural Science Foundation of China under the grants of 51376040, 51676031, and 51568032.

## References

Rupp R., Muller G. and Neumann G., Three-dimensional time dependent modelling of the marangoni convection in zone melting configurations for GaAs, *Journal of Cryst. Growth*, Vol.97 pp. 34-41 (1989)

Yang S., Liang R.Q. and He J.C., Oscillating characteristic of free surface from stability to instability of thermocapillary convection for high Prandtl number fluids, *Int. Journal of Heat and Fluid Flow*, Vol. 61 pp. 298-308(2016)

## Marangoni convection instability induced by evaporation in a sessile droplet of silicone oil on heated substrate

Tian-Shi Wang<sup>1</sup>, Wan-Yuan Shi<sup>1,2</sup>, Yi-Wei Jia<sup>1</sup>, Ji-Long Zhu<sup>1</sup>

<sup>1</sup>College of Power Engineering, Chongqing University, Chongqing 400044, China, CQMr.Wang@cqu.edu.cn

<sup>2</sup>Key Laboratory of Low-grade Energy Utilization Technologies and Systems, Ministry of Education  
Chongqing 400044, China, shiwy@cqu.edu.cn

A sessile droplet on horizontal substrate is a fundamental phenomenon in daily life and in a wide range of practical industrial and scientific applications, such as evaporation cooling of the microelectronic chips, spray cooling technology, inkjet printing of functional materials, manufacturing of DNA chip and medical diagnostics based on stain analyses of bio-fluid samples. In these processes, the internal Marangoni flow induced by non-uniform surface temperature distribution of droplet plays an important role. Both the inhomogeneous evaporation rate and the different length of thermal pathway due to the curved droplet surface would cause non-uniform distributions of temperature and surface tension and then Marangoni convection would occur inside the droplet. The effect of Marangoni stresses on the flow in an evaporating sessile droplet was carried out by Hu and Larson (2005) with lubrication analysis method as well as finite element method. Davis and co-workers (1991) studied stationary and spreading droplets and they took Marangoni stress, evaporation, and moving contact line into consideration. Sefiane et al. (2008) and Carle et al. (2012) observed the hydrothermal waves in evaporating sessile droplet of methanol, ethanol and FC-72. All of them adopted the volatile liquid.

In present work, a low volatility fluid of silicone oil is adopted to observe the Marangoni convection instability induced by evaporation in a sessile droplet on a heated substrate. The effect of the contact angle on the Marangoni convection instability is analyzed. The experimental apparatus is shown in Fig. 1. A droplet of 0.65cSt silicone oil is carefully deposited on the center of a copper substrate coated by FC-3120 by a micro-syringe. The temperature of the substrate is controlled by thermostatic oil inside a cylindrical vessel under the substrate linked with a thermostatic oil bath. The surface thermal pattern of the Marangoni convection in sessile droplet is observed by an Infrared camera (FLIR A655sc, with thermal sensitivity of 30mK and resolution of 640×480) with a microscope lens mounted directly above the droplet. The contact angle of the droplet is measured by a contact angle measurement (JC2000DM from Shanghai Zhongchen Digital Technic Apparatus Co., Ltd) with error of 0.1°.

The thermal patterns of 0.65cSt silicone oil droplet during the evaporation process are observed. The results show that the flower-like Bénard-Marangoni convection cell occurs (see Fig. 2). The Bénard-Marangoni convection cell is sharp and thin at the apex of droplet but circular near the contact line (see Fig. 2a). With evaporating, the cells become short and thickness (see Fig. 2b). It should be noted that the Bénard-Marangoni convection cell only occurs when the contact angle is less than a critical value, because both normal temperature gradient and tangential temperature

gradient exist in the droplet. The Bénard-Marangoni convection caused by normal temperature gradient will be suppressed by the thermocapillary convection. With evaporating, the suppression becomes weak due to the decrease of tangential temperature gradient with the contact angle decreasing so that Bénard-Marangoni convection can appear easily.



**Figure 1:** Schematic of the experimental apparatus.

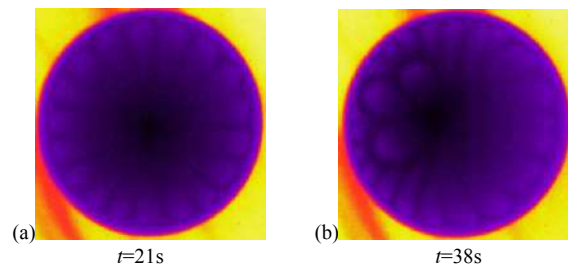


**Figure 2:** The shape of the Bénard-Marangoni convection cell for 0.65cSt silicone oil droplet ( $T_w=305.65\text{K}$ ,  $T_a=300.15\text{K}$ ,  $R=2.73\text{mm}$ ,  $RH=60\%$ ) (a) the flower-like Bénard-Marangoni convection cell is sharp and thin at the apex of droplet but circular near the contact line at  $t=21\text{s}$  (b) the cells become short and thickness at  $t=38\text{s}$ .

The results show that the critical contact angle for the incipience of the Bénard-Marangoni convection increases with increasing  $Ma$  number (see Fig. 3). The  $Ma$  number is increased by increasing the temperature difference between the substrate and the environment which leads to the increase of the normal temperature gradient and Bénard-Marangoni convection will happen easily. The

Bénard-Marangoni convection is therefore dominant, which results in that Bénard Marangoni convection would appear even though the contact angle of the droplet is larger.

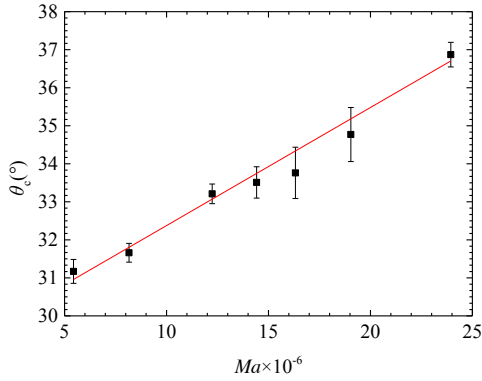


**Figure 3:** Critical contact angle as a function of  $Ma$  number for 0.65cSt silicone oil droplet.

The results show that the cells number of the Bénard-Marangoni convection increases with increasing the wetting radius and the  $Ma$  number.

The authors gratefully acknowledge support from the National Nature Science Foundation of China (Grant No. 51676018).

#### References

Hu H., Larson R. G., Analysis of the effects of Marangoni stresses on the microflow in an evaporating sessile droplet, *Langmuir*, Vol. 21 pp. 3972-3980 (2005).

Davis S. H., Ehrhard P., Non-isothermal spreading of liquid drops on horizontal plates, *J. Fluid Mech.*, Vol. 229 pp. 365-388 (1991).

Sefiane K., Moffat J.R., Matar O.K., Craster R.V., Self-excited hydrothermal waves in evaporating sessile droplet, *Appl. Phys. Lett.*, Vol. 93 pp. 074103 (2008).

Carle F., Sobac B., Brutin D., Hydrothermal waves on ethanol droplets evaporating under terrestrial and reduced gravity levels, *J. Fluid Mech.*, Vol. 712 pp. 614-623 (2012).

## Numerical Simulation of Gravity Influence on Single Bubble Pool Boiling Heat Transfer

Zhen-Dong Li<sup>1</sup>, Liang Zhang<sup>2</sup>, Ke Wu<sup>1,3</sup>, Jian-Fu Zhao<sup>1,3,\*</sup>, Hui-Xiong Li<sup>4</sup>, Kai Li<sup>1,3</sup>

<sup>1</sup>CAS Key Laboratory of Microgravity, Institute of Mechanics, Chinese Academy of Sciences. 15 Beisihuan Xilu, Beijing 100190, China

<sup>2</sup>State Nuclear Power Software Development Center, SPIC. South Park, Beijing Future Sci. & Tech. Park, Beijing 102209, China

<sup>3</sup>School of Engineering Science, University of Chinese Academy of Sciences. 19A Yuquan Rd, Shijingshan District, Beijing 100049, China

<sup>4</sup>State Key Laboratory of Multiphase Flow in Power Engineering, Xi'an Jiaotong University. 28 Xianning Xilu, Xi'an 710049, China

\*E-mail address for the corresponding author: jfzhao@imech.ac.cn

Nucleate boiling is one of the most efficient modes of heat transfer, resulting in its wide applications for high heat flux transfer both on the Earth and in space. It is also a complex and elusive process. Thus, a great amount of empirical correlations and semi-mechanistic models for engineering applications, which are mainly depended upon empirical data obtained from elaborately designed experiments, flood in the literature up to now. Although many empirical correlations and semi-mechanistic models include gravity as a parameter, they usually fail when extended beyond the range of gravity levels they were based on, namely 1g, high-g and low-g.

With quick progress of computer technology and computational science, numerical simulation has been used to reveal the mechanism underlying this phenomenon by more and more researchers. Stephan and Hammer (1994), and Son et al. (1999) are examples among many others. Recently, to reveal the influence of the heater's thermal response on the bubble behaviour and heat transfer, Fuchs et al (2006), Aktinol & Dhir (2012), Zhang et al. (2014, 2015), and Li et al. (2015) numerically studied single bubble nucleate boiling on heaters of finite thickness. It was shown that the heater material properties have a significant effect on local temperature distribution, bubble behaviour, and corresponding heat transfer. These results are helpful to understand the actual nucleation boiling process.

In the present work, an axisymmetric model of single bubble pool boiling, initially proposed by Stephan & Hammer<sup>[1]</sup>, is studied numerically with the Ghost-Fluid method for the sharp interface representation. The model of Son et al.<sup>[2]</sup> is adopted for the micro region, *i.e.* the ultra thin liquid film underneath the growing bubble near the three-phase contact line. For the macro regions occupied by vapor and liquid, and the solid wall underneath the growing bubble, a complete set of conservation equations of mass, momentum, and energy is solved numerically.

The computational domain ( $1L_c, 2\sim 3L_c$ ) is adopted as shown in Fig. 1, where  $L_c$  denotes the Laplace length, *i.e.*

$$L_c = \sqrt{\frac{\sigma}{g(\rho_l - \rho_v)}} \quad (1)$$

Three gravity levels, namely  $1g_0$ ,  $0.1g_0$ , and  $0.01g_0$ , are studied in the present work, and labelled as case 1#, 2#, and 3#, respectively. An extended range, in which the surface temperature and local heat flux from the heater to liquid are the same as those at outer edge of the computational domain, is also applied for computing the averaged wall temperature and heat flux with constant number density of nucleation site at different gravity levels. In contrast, un-corrected data of the numerical simulation at lower gravity may exhibit a smaller number density of nucleation site due to larger Laplace length than that in higher gravity.

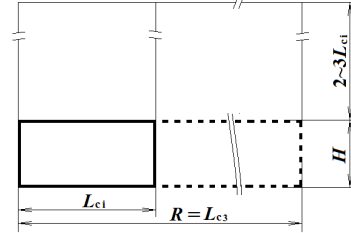


**Figure 1:** Computatuinal domain and the extended range for evaluating averaged heat flux with fixed number density of nucleation site at different gravity levels.

A standard MAC grid ( $100 \times 200$ ) is used for spatial discretization where the velocities are defined at grid surfaces and other variables are defined at grid nodes. The projection method is used to numerically solve the Navier-Stokes equations. The 2<sup>nd</sup> order ENO scheme is used for discretization of the convection term in momentum and energy equations, and central difference for diffusion terms. A small truncated sphere bubble with the initial radius of  $0.05L_c$  is set on the top surface of the solid wall at the beginning of a bubble cycle. Constant nucleating superheat corresponding to a cavity diameter of  $1 \mu\text{m}$  is chosen as the criterion for determining the beginning of the subsequent bubble cycle. More details for the numerical method can be found in Li et al.<sup>[7]</sup>

Bubble dynamics and heat transfer during single bubble pool boiling of saturated FC-72 at different gravity levels are simulated numerically with transient thermal response of the heated  $\text{SiO}_2$  wall with a thickness of 5 mm. A constant and uniform temperature corresponding to a superheat of 10 K is fixed on to the bottom surface of the solid wall in the simulations, and thus, both the spatio-temporal averaged heat flux and superheat on the top surface, which contacts the working fluid directly, are dependent variables instead of controllable ones. Multi-cycle simulations are carried out to eliminate the influence of unreal initial conditions. Quasi-steady periodical processes of single bubble pool boiling can be reached due to the limited simulation time and thus a smaller thermal penetration depth inside the solid wall compared with its thickness. The main results are summarized in Table 1.

**Table 1.** Main results at different gravity levels

	Case 1#	Case 2#	Case 3#
$g/g_0$	1	0.1	0.01
$\tau_c$ (s)	0.0334	0.387	2.72
$D_b$ (mm)	0.619	2.22	6.86
$\Delta T_w$ (K)	6.34/6.65	6.97/7.57	8.53/-
$q$ ( $\text{W}/\text{cm}^2$ )	0.409/0.308	0.146/0.114	0.0650/-

Due to phase change inside the thermal boundary layer, the bubble and its base expand outward rapidly at early stage. With the increase of its volume, the buoyancy force acting on the bubble plays more and more important role which drives the mass centre of the bubble to move upward faster, and thus its base shrinks gradually till its departure from the wall. The thermal boundary layer adjacent to the heating surface is then to recover until the temperature at the nucleation site reaches the nucleating superheat corresponding to the given cavity diameter of the nucleate site. The evolutions of wall temperature at the nucleation site in a bubble circle at different gravity levels are shown in Fig. 2. The bubble departure time  $\tau_d$  and the receding time  $\tau_r$  of its base on the heating surface, as well as impact time  $\tau_n$  of the simplified nucleation method used in the present numerical simulation, are also marked in Fig. 2. At first, it can be observed that the artificial small truncated sphere bubble exhibits the same relative impact period in a bubble circle. Secondly, non-monotonous change of the receding time with gravity is evident, although the period of bubble circle increases, as shown in Table 1, and the waiting time decreases drastically with the decreasing gravity.

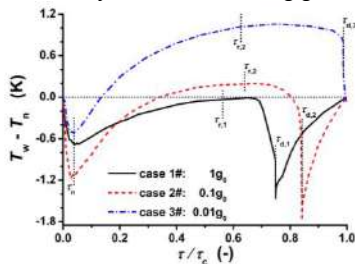


**Figure 2:** The evolution of wall temperature at the nucleation site in a bubble circle at different gravity levels.

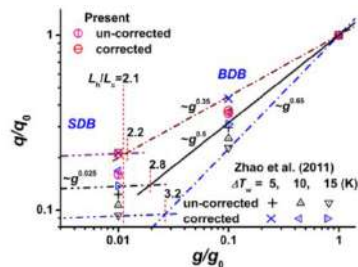


**Figure 3:** Gravity scaling of heat transfer in single bubble pool boiling.

Raj et al. [8, 9] proposed a model for scaling heat flux with gravity and heater size, in which there are two regions for surface tension dominated boiling (SDB) and for buoyancy dominated boiling (BDB), respectively. The transition criterion of  $L_h/L_c=2.1$  was obtained based on the results of variable gravity pool boiling experiments along with corresponding reference earth gravity experiments over a range of heater sizes. According to this model, the case 3# with  $L_h/L_c=2$  in the present study may be located in SDB region, while the other two cases in BDB region. Fig. 3 shows heat flux versus acceleration, ignoring the small differences of the superheat at different gravity levels. The transition boundary proposed by Raj et al. (2012) and data obtained by Zhao et al. (2011) without the influence of the heater's thermal response, as well as their corrected values

by using the present method, are also shown for comparison.

A power law coefficient of  $m$ , ranging from 0.35 at low superheat of 5 K to nearly 0.5 at high superheat of 15 K, can be observed based on the corrected data in BDB region with constant number density of nucleation site at different gravity levels. These values are larger than those obtained by Raj et al. [8, 9], but the trend on the superheat is similar. Furthermore, due to saturated boiling in the present study, there is no jump in heat flux at transition according to the model of Raj et al. [8, 9]. Thus, the intersection point of two curves with different power law coefficients in BDB and SDB regions can provide the corresponding transition criterion, which ranges from 2.2 to 2.8, very close to 2.1 proposed by Raj et al. [8, 9].

The present numerical simulation provides some data supporting partly the model proposed by Raj et al. [8, 9]. However, more studies, both experimental and numerical ones, are needed for thoroughly understanding the gravity scaling law on nucleation pool boiling heat transfer.

The present study is supported financially by the National Natural Science Foundation of China under the grants of 11372327, 11402273 and 51176153.

## References

- Stephan P., Hammer J., A new model for nucleate boiling heat transfer, *Heat Mass Transfer*, Vol. 30 pp. 119–125 (1994)
- Son G., Dhir V.K., Ramanujapu N., Dynamics and heat transfer associated with a single bubble during nucleate boiling on a horizontal surface, *J. Heat Transfer*, Vol. 121 pp. 623–631 (1999)
- Fuchs T., Kern J., Stephan P., A transient nucleate boiling model including microscale effects and wall heat transfer, *J. Heat Transfer*, Vol. 128 pp. 1257–1265 (2006)
- Aktinol E., Dhir V.K., Numerical simulation of nucleate boiling phenomenon coupled with thermal response of the solid, *Microgravity Sci. Tech.*, Vol. 24 pp. 255–265 (2012)
- Zhang L., Li Z.D., Li K., Li H.X., Zhao J.F., Influence of heater thermal capacity on pool boiling heat transfer, *J. Comput. Multiphase Flows*, Vol. 6 pp. 361–375 (2014)
- Zhang L., Li Z.D., Li K., Li H.X., Zhao J.F., Influence of heater thermal capacity on bubble dynamics and heat transfer in nucleate pool boiling, *Appl. Thermal Eng.*, Vol. 88 pp. 118–126 (2015)
- Li Z.D., Zhang L., Zhao J.F., Li H.X., Li K., Wu K., Numerical simulation of bubble dynamics and heat transfer with transient thermal response of solid wall during pool boiling of FC-72, *Int. J. Heat Mass Transfer*, Vol. 84 pp. 409–418 (2015)
- Raj R., Kim J., McQuillen J., On the scaling of pool boiling heat flux with gravity and heater size, *J. Heat Transfer*, Vol. 134, p. 011502 (2012)
- Raj R., Kim J., McQuillen J., Pool Boiling Heat Transfer on the International Space Station: Experimental Results and Model Verification, *J. Heat Transfer*, Vol. 134, p. 011504 (2012)
- Zhao J.F., Li Z.D., Zhang L., Numerical simulation of single bubble pool boiling in different gravity conditions, *New Trends in Fluid Mechanics Research/Proc. 6<sup>th</sup> Int. Conf. Fluid Mech.*, Guangzhou, China, June 30–July 3 (2011)

## Two-phase granular fluids

Vladimir Shelukhin

Lavrentyev Institute of Hydrodynamics and Novosibirsk State University  
Av. Lavrentyev, 15, Novosibirsk, 630090, Russia  
shelukhin@hydro.nsc.ru

Starting from the basic thermodynamic principles, we develop a new mathematical model which governs dynamics of two-phase granular fluids with non-Newtonian rheology. Applications concern suspensions, coal-water slurry fuels, seepage of animal blood with high value of hematocrit, plastic or "fresh" concrete flows etc. The model allows to take into account not only particle-fluid interactions but the particle-particle interactions as well. The first phase is a Newtonian viscous fluid. To tackle the second phase as a granular fluid, we apply the notion of the Cosserat continuum, when each fluid point is treated as a rigid body. Such an approach is known as a theory of micropolar fluids (Eringen 1999). To meet applications, we make generalizations by passing to a non-Newtonian Cosserat-Bingham fluid which is both a micro-polar medium and a visco-plastic material (Shelukhin and Ruzicka 2013). On the one hand, such a fluid exhibits microrotational effects and microrotational inertia; the fluid can support the couple stress, the body couples and the nonsymmetric stress tensor. On the other hand, the fluid stiffens if its local stresses and local couple stresses do not exceed some yield stress  $\tau_*$  and a yield couple-stress  $\tau_n$ , respectively.

In mechanics of the classical Bingham fluid, there is only one yield stress  $\tau_*$  because the local stress state is characterized completely by only one tensor; it is the Cauchy stress tensor  $T$ . To characterize stresses in the micropolar fluid, one should take into account the couple stress tensor  $N$  also; this is why the yield couple-stress  $\tau_n$  was incorporated by Shelukhin and Ruzicka (2013). As for local deformations, they are characterized also by two tensors which allow us to calculate the velocity gradient and the gyration gradient; both these tensors should vanish in a zone of stiffness, the strong plug zone. In contrast to the classical Bingham fluid, the micropolar Bingham fluid may have a weak plug zone where the gyration gradient vanishes, whereas the velocity gradient does not vanish (Shelukhin and Ruzicka 2013, Shelukhin and Neverov 2014). In the present paper, we generalize the model allowing for the variable concentration of polar particles, different phase densities and velocities. To this end, we apply the basic thermodynamic principles and formulate conservation laws and constitutive equations in such a way that they agree with the non-negative sign of entropy production. We emphasize that the concentration flux obeys a generalized Fick law, i.e. it depends not only on gradients of the functions like concentration, temperature, and pressure, but on the particle gyration as well.

To test our model, we address the so-called "tubular pinch effect" of G. Ségre and A. Silberberg (Ségre-Silberberg, 1961) showing that for the laminar flow of neutrally buoyant dilute suspension of rigid spheres through a circular tube, particles tend to migrate towards a concentric annular region with the mean radius  $r_m = 0.6 R$  where  $R$

is the tube radius, Fig.1. (A shift of the maximum concentration point is due to the yield stress.)

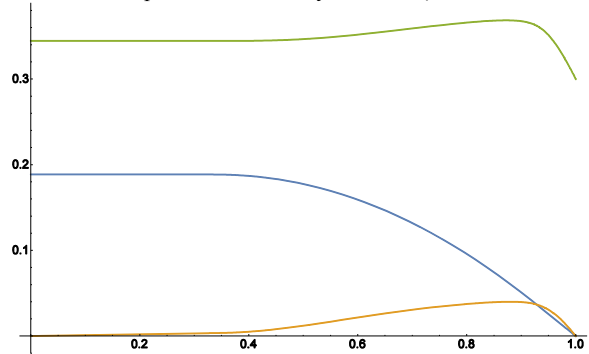


**Figure 1:** The curves from top down correspond to concentration, velocity and gyration; the latter is increased by a factor of 100.

To this end, we apply the equations derived to study one-dimensional steady flows in a channel driven by a pressure gradient for different constitutive parameters and discover that the Ségre-Silberberg effect really occurs for some values of the gyration coefficient in the generalized Fick law provided the yield stresses are small (Shelukhin and Neverov 2016). Our calculations reveal that the apparent viscosity increases as the canal thickness decreases in agreement with the inverse Fahraeus-Lindquist (1931) effect for the blood seepage through a narrow capillary tubes at high values of hematocrit.

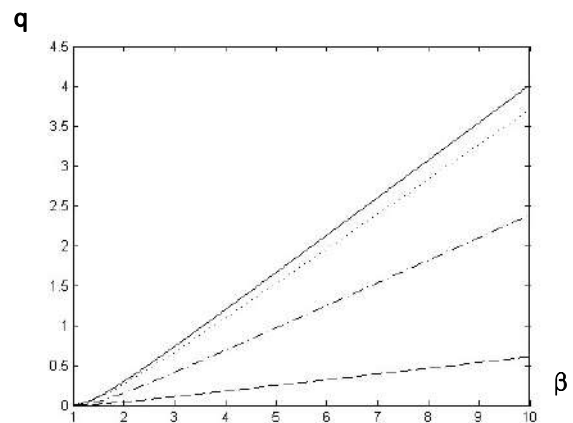


**Figure 2:** Dimensionless volumetric flow rate  $q$  versus dimensionless pressure gradient  $\beta$ . The curves from the bottom upwards correspond to increasing values of the second, "rotation", viscosity. The upper straight line

corresponds to the classical viscous fluid.

As for applications in transport of drilling cuttings, the model developed here predicts that even small increase of the drilling mud discharge may result in a significant pressure growth within the borehole if the cutting concentration and the mud composition are such that the rotation viscosities corresponding to the mud-cutting mixture, are not negligible, Fig.2.

The research is partially supported by Grant of Government of Russian Federation No 14.W03.31.0002.

### References

Shelukhin V.V., Ruzicka V., On Cosserat–Bingham fluids, *Z. Angew. Math. Mech.*, Vol. 93 pp. 57–72 (2013)

Shelukhin V.V., Neverov V.V., Flows of micropolar and viscoplastic fluids within a Hele-Shaw cell, *J. Appl. Mech. Tech. Phys.*, Vol. 55 pp.905–916 (2014)

Shelukhin V.V., Neverov V.V., Thermodynamics of micropolar Bingham fluids. *Journal of Non-Newtonian Fluid Mechanics*. Vol. 236 pp. 83-90 (2016)

## Model and on-orbit study of the International space station contamination processes by jets of its orientation thrusters

V.N. Yarygin<sup>1</sup>, Yu.I. Gerasimov<sup>2</sup>, A.N. Krylov<sup>2</sup>, V.G. Prikhodko<sup>1</sup>, A.Yu. Skorovarov<sup>2</sup>, I.V. Yarygin<sup>1</sup>

<sup>1</sup> Kutateladze Institute of Thermophysics SB RAS,  
Lavrentiev Ave 1, Novosibirsk, 630090, Russia  
yarygin@itp.nsc.ru

<sup>2</sup> Korolev Rocket and Space Corporation ENERGIA,  
Lenin Str. 4a, Korolev, Moscow area, 141070, Russia

Currently liquid-propellant rocket engines of low thrust, employing self-igniting components – dinitrogen tetroxide (amyl) and unsymmetrical dimethylhydrazine (UDMH) are used as orientation thrusters (OT) of the International Space Station (ISS). During operation combustion chamber of the liquid-propellant rocket engine is subjected to high temperatures (about 3000 K) and high pressures (about  $(6-10) \cdot 10^5$  Pa). To protect chamber walls from harmful effect of high temperatures liquid film of one of propellant components is fed on the chamber walls.

Operation of these thrusters is accompanied by ejection of burnt and unburnt propellant fractions (molecular clusters and droplets) into space. Results of both model and on-orbit experiments show that incomplete combustion products (ICP) scatter almost in all the directions: from 0 to 180° relative to the jet axis. This is caused by special character of gas and liquid outflow into vacuum.

The flow of gas at angles over 90° is known as backflow. Such flows lead to contamination of the external surface of the ISS and outside equipment. This in turn poses a risk of toxic ICP penetration into the living space of the ISS.

In this report we study the problem of spacecraft and space station contamination by jets of orientation thrusters. First background of the problem and the concept of the ISS OT jets modeling in vacuum chambers are discussed. Next we justify applicability of integral approach with reproducing integral characteristics – a typical angle of jet divergence defined through the relative jet impulse at nozzle cross-section. This approach is used instead of reproducing full-scale values of Mach number and specific heat ratio in model experiments. Then we describe vacuum gas-dynamic facility VIKING of Institute of Thermophysics SB RAS is given. This facility provides an opportunity to conduct experiments under pulse and continuous modes. Next we pay special attention to measuring technique of wall liquid film parameters under its interaction with co-current gas flow inside supersonic nozzle. Then we consider the process of wall liquid film fragmentation on droplets at the exit edge of the nozzle and formation of gas-droplet flow.

The features of droplets diagnostics in vacuum connected with their fast evaporation are discussed in the report. This difficulty is overcome by addition of the dye, which is not sublimating in vacuum, into model liquid. In this approach the quantity of liquid phase is determined by the amount of remaining dye (the dry residue) on the sensor after liquid evaporation.

The description of visualization and droplet phase spatial distribution measurement techniques are given in the report. Droplet distribution functions in directions of

scattering, sizes and velocities in the peripheral area of the jet are obtained with the help of laser stroboscopic illumination.

Techniques of quartz microbalances, spectrophotometry and deposition on substrates are developed for measurement of droplet phase angular distribution. Experimental studies carried out allowed us to establish the detailed structure of gas-droplet flow which is formed under near-wall liquid film ejection with co-current gas flow from supersonic nozzle into vacuum. Appearance of two typical areas of droplet phase flow behind the nozzle exit – the central one and the peripheral one is shown (Fig. 1). The central area is established by detachment of droplets from the film surface inside the nozzle and their subsequent fragmentation and acceleration by co-current gas flow. The peripheral one is caused by desintegration of near-wall liquid film at the nozzle exit edge. Both model and real thruster experiments show that near-wall liquid film is the main reason for backflow formation.

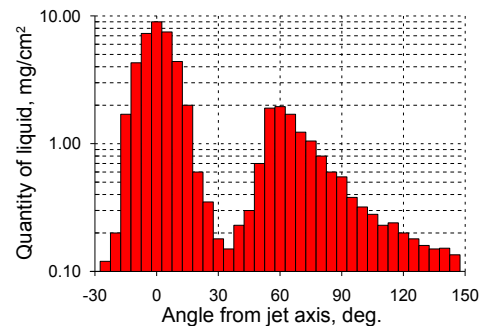


**Figure 1:** Droplet phase angular distribution

The concept of backflows minimization by means of the gasdynamical protecting devices (GPD) installed at the output part of the thruster's nozzle is discussed in this report. We show that the correct choice of GPD is crucially important since incorrect one may cause increase in backflows instead of reduction.

The technique and results of on-orbit experiment on GPD efficiency carried out in 2001-2006 at the Service module of the ISS, their comparison with results of model experiments, and the following stages of on-orbit experiment in 2017-2019 are discussed.

Experimental part of the model study was financially supported by the Russian Foundation for Basic Research, scientific project No.16-08-00436.

## Enhancement of heat transfer at pool boiling on surfaces with silicon oxide nanowires

E.A. Chinnov<sup>1,2</sup>, E. N. Shatskiy<sup>1,2</sup>, S. Ya. Khmel<sup>1</sup>, E. A. Baranov<sup>1</sup>, A.O. Zamchiy<sup>1</sup>, V. V. Semionov<sup>1</sup>, and O.A. Kabov<sup>1,2</sup>

<sup>1</sup> Kutateladze Institute of Thermophysics, SB RAS, 1 Lavrentyev ave., Novosibirsk, 630090, Russia,

<sup>2</sup> Novosibirsk State University, 630090, Pirogov str. 2, Novosibirsk, 630090, Russia

Cooling the heated surfaces in various technologies is an important task, whose solution requires application of such processes as boiling. Today much attention is paid to development of the methods for intensifying the processes of heat and mass transfer at liquid boiling and increasing the critical thermal loads [1]. One of directions is the study of the influence of various nanocoatings on heat transfer intensity. The review of recent studies on the influence of micro/nanomodified surfaces and coatings on heat transfer enhancement and critical heat flux increase at boiling is presented in [2].

In this work, we created an experimental setup for studying heat transfer from a local heat source. The heating element is a cylindrical core made of copper. The upper part of the heater facing the liquid has diametrical dimension  $D = 5$  mm. The heat source is the nichrome ribbon, wound on the lower part of the core. To minimize heat losses, the heating element is carefully insulated. Boiling heat transfer on the local heaters with nanomodified surfaces has been investigated. In this study, we carried out the experiments under the conditions of a large volume of liquid and maintaining the temperature of water at the level of saturation. The copper surfaces coated with a layer of molybdenum or tungsten, where the microropes of silicon oxide nanowires were grown, were used as the nanomodified surfaces. The technology of their production is described in [3].

Experimental data on the heaters with the smooth and nanomodified surfaces are presented in Fig. 1. The boiling curve for the surface with molybdenum coating is shown. On the surface with a molybdenum coating, we failed to grow the silicon oxide nanowires. The contact angle with a water drop on the resulting coating is  $54^\circ$  and it almost coincides with the wetting angle on the polished copper surface.

The best results were obtained on the copper surface with a sublayer of tungsten. On the intermediate layer of tungsten was obtained arrays of microropes and "cocoon", consisting of particles of tin coated with silicon oxide nanowires Fig. 2. The size of the cocoon and the distance between them was up to  $1 \mu\text{m}$ . The contact angle with a water drop on the resulting coating, measured before the experiment, is  $18^\circ$ , and this is significantly less than that on the copper surface or molybdenum, tungsten coating.

According to Fig. 1, the heat transfer coefficient for this coating is substantially higher than for a smooth molybdenum surface. Two series of experiments were performed with limitation of heating. After the first series of experiments, microropes were gone, cocoons were left. During the second series of experiments, the area of nanomodified surface began decreasing, which was reflected in the boiling curve behavior. The coefficient of heat transfer decreased.

It can be concluded that a new type of nanocoatings provides heat transfer enhancement during boiling.

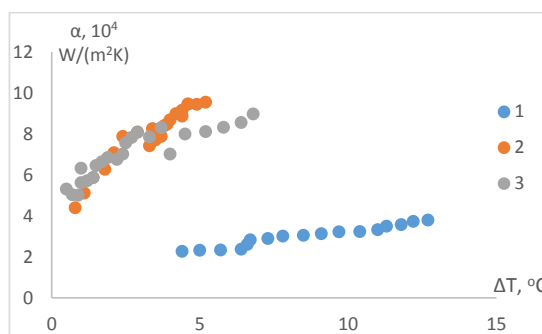


**Figure1:** The dependence of the heat transfer coefficient from the temperature difference for the heater with  $D = 5$  mm. 1– smooth surface with molybdenum coating, 2– silicon oxide nanowires and cocoons on tungsten layer (series 1), 3 – silicon oxide cocoons on tungsten layer (series 2).

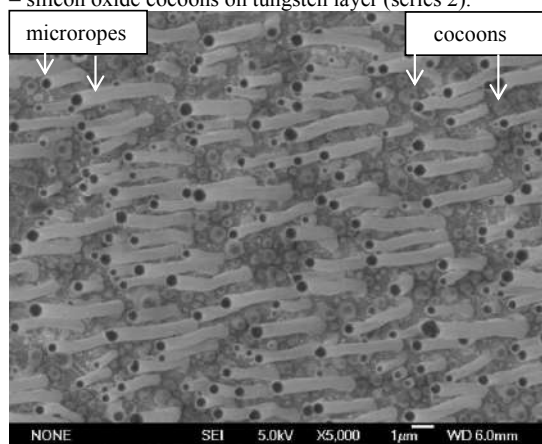


**Figure2:** The nanomodified surfaces with a sublayer of tungsten and arrays of microropes and "cocoon".

This work was supported by the grant of the Russian Science Foundation (Agreement No. 15-19-30038).

### References

- [1] D. Attinger, et al. Surface engineering for phase change heat transfer: A review, *MRS Energy & Sustainability*. V. 1. pp. E4 (2014).
- [2] A.S. Surtaev, V.S. Serdyukov, and A.N. Pavlenko *Nanotechnologies in thermophysics: heat transfer and crisis phenomena at boiling*. Russian Nano-Technologies. V. 11 (11–12), pp. 18-32 (2016).
- [3] S.Ya. Khmel, et al. Influence of substrate temperature on the morphology of silicon oxide nanowires synthesized using a tin catalyst. *Physica Status Solidi A*, V. 213, (7), pp. 1790–1795 (2016).

## Evolution of the deformation profile of a thin liquid layer when heated from a localized hot spot

Serafim Spesivtsev, Yuriy Lyulin, Igor Marchuk and Oleg Kabov

Institute of Thermophysics, 1, Lavrentiev Ave., Novosibirsk, 630090, Russia  
E-mail: simafir94@gmail.com

Study of heat elimination from a pointed heat source becomes one of the most significant problems in thermal physics because of its straight association with the cooling of microelectronics. Permanent development of microelectronic equipment leads to complication of the microchip structure and formation of nonuniform heat flux distribution on the chip surface. Heat flux in some small zones is much greater than the chip regular, of the order of 1 kW/cm<sup>2</sup>. This effect could significantly deteriorate reliability and performance of the device. Nowadays, there are a number of successful methods for cooling of local hot spots, for example spray cooling, thermoelectric coolers, boiling in microchannels. One of the most effective techniques for eliminating such high heat fluxes from a local heat source is technology based on processes with phase change such as evaporation of a thin liquid layer. In this case the main mechanism of heat transfer from the heat source is an intensive evaporation. Dynamics of evaporation and, therefore, the heat elimination from the heat source significantly depend on the conditions in a layer (Fedorets et al. 2013). Especially, the breakdown of liquid layer leads to powerful decreasing of heat transfer from a localized hot spot (Lyulin et al. 2015). Processes of liquid layer breakdown are actively investigated experimentally and theoretically.

The aim of the present work is to study the breakdown dynamics and measure the deformation profile of an evaporating horizontal liquid layer when heated locally.

Experiments were carried out on the setup shown in Fig. 1. The working fluid is supplied to the test cell with the help of the syringe pump and a horizontal liquid layer is created. The thickness of liquid layer is varied from 300 to 700 μm. The layer of liquid is opened to the atmosphere and maintained on the surface of the working area using sharp edge on the substrate perimeter. Spot heating of the horizontal liquid layer takes place in the center of the substrate. The test cell consists of caprolon base, metallic substrate and the heating element. The caprolon base has a special cut on the upper side for installation of the substrate and a central through hole with a diameter of 1.6 mm. The substrate is made of stainless steel and has a diameter of 50 mm and a thickness of 1 mm. In the center of the substrate is a closed hole with a diameter of 1.6 mm and a height of 0.8 mm. The heating element is made of brass and has a round tip with a diameter of 1.6 mm and a height of 3 mm. It is tightly inserted into the closed hole of the substrate through the caprolon base. Thermal paste is used for better thermal contact between the heater tip and the substrate. The distance between the tip and the upper side of substrate is 0.2 mm. The power of heating element is controlled by the power supply. Insulating material is located on the underside of the heater to minimize heat losses. Temperature in the test cell is measured by thermocouples (type K) connected to the measuring system with an accuracy of 0.1°C. Location of

the thermocouples is shown in Fig. 1. Relative humidity and atmosphere temperature are measured using the thermohygrometer Testo 645 with an accuracy of 2% and 0.1°C, respectively.

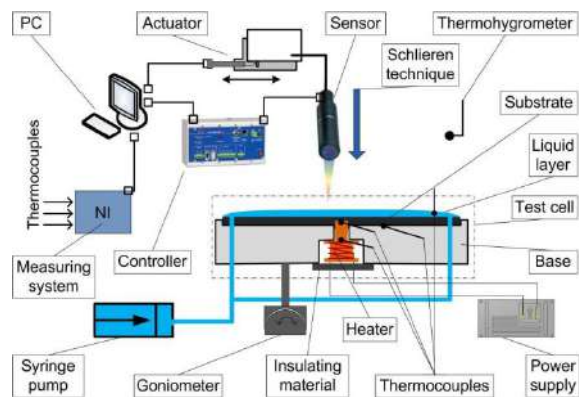
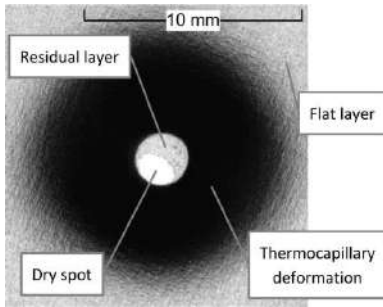


Figure 1: Scheme of the experimental setup.

The heat flux density is determined by measuring the temperature difference between two different sections along the heater tip. The height of the horizontal liquid layer is maintained in constant position during the all experiment. Confocal system Micro-epsilon is used for measuring the layer thickness over the heating element. The system consists of the controller and the sensor. Sensors have the spatial resolution from 10 to 60 nm, the accuracy 0.35 - 0.7 μm, the spot diameter 6 - 16 μm and the measuring range 0.3 - 10 mm. The maximum temporal resolution is 100 μs. The sensor is fixed on the three-dimensional positioning system with high-speed linear actuator on one of the horizontal axes. Linear actuator is controlled from personal computer and by special software. The maximum speed in the axial movement of the confocal sensor provided by linear actuator is 104 mm/s. The sensor moves in range of 50 mm by steps of 1 μm. Also it moves in two other axes with the help of two hand-operated linear stages in range of 50 mm. For visualization the deformations of the gas-liquid interface and recording the layer breakdown dynamics schlieren technique with Photron FASTCAM 675K-M3 high-speed camera was used (5000 fps, 640x640 pixels, 25 μm/pix). The test cell was installed in a horizontal position with the help of two-axis goniometer. Advancing contact angle for ethanol on the substrate surface is defined by Young-Laplace equation at room temperature of 25 ± 2 °C and is equal to  $\theta = 8 \pm 1$  °. Profilometer "Micro Measure 3D station" was used for measuring the roughness of substrate. Average value of the substrate roughness is equal to  $R_a = 37$  nm.

Experiments were conducted at atmospheric pressure, temperature and relative humidity of 28±2°C and 25±3%,

respectively. Layer thickness was ranged from 300 to 700  $\mu\text{m}$ . Ethanol (95%) was used as a working fluid. Heater temperature range was 20 - 105°C. The temperature values were measured at the moment of layer breakdown. Heat flux density was varied from 0 to 95.3  $\text{W}/\text{cm}^2$ . The maximum injection liquid flow rate was 200  $\mu\text{l}/\text{min}$ . During the experiment heat flux is increased up to a critical value at which the liquid layer ruptures. At this moment heating is stopped to prevent the failure of the heating element.



**Figure 2:** Visualization of breakdown dynamics and formation of the dry spots.

It was found that breakdown process consists of several steps. At the beginning, thinning of the liquid layer over the heating area due to the effect of thermocapillary forces (Marchuk 2015) and evaporation is observed. Further thinning leads to the formation of residual liquid layer in the area of the local heating. Then the residual layer evaporates until its thickness reaches the critical and breakdown of the liquid layer occurs, Fig. 2 (Lyulin et al. 2015). After the breakdown the whole area of the local heating rapidly dries and quite symmetrical circular dry spot is formed.

Evolution of the layer thickness in the center of substrate is observed with the help of the confocal system. All detected steps of the breakdown process observed by the schlieren technique were also confirmed using the confocal technique.

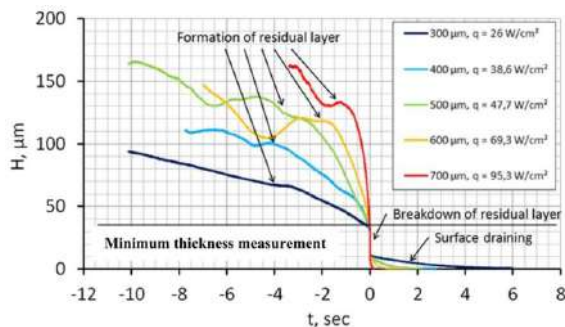


**Figure 3:** Dependence of the layer thickness over the heating area on time for different initial layer depth.

Evolution of the layer thickness before the breakdown was measured for different initial layer depth in range from 300 to 700  $\mu\text{m}$  (Fig. 3). Critical thickness of residual film is less than 30  $\mu\text{m}$ . It is assumed that critical thickness of the residual layer for present substrate mostly depends on the

properties of working liquid. The time of dry spot formation is decreased when the layer thickness and, accordingly, the local heating intensity is increased. The time varies from 6 to 0.67 seconds. Temperature in the center of substrate increases and more intense evaporation of residual layer takes place. The main mechanism of the outflow of the liquid from the heating zone before the residual layer formation is the thermocapillary shear stress, and after it this is the evaporation. At small liquid thickness the viscosity suppresses thermocapillary flows. Evolution of the layer deformation profile is shown in Fig. 4. Pulsations of the layer thickness before formation of the residual layer have been observed. The presence of the thickness pulsations is presumably connected with convective instability, caused by the intense heat and mass transfer in the heating area.

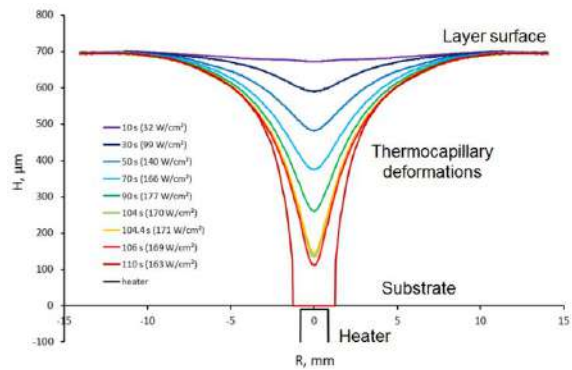


**Figure 4:** Measured thickness of the liquid layer.

Influence of the layer depth on the breakdown dynamics of liquid layer has been studied. Evolution of the layer thickness in the heating point and deformation profile were being monitored using confocal technique. The existence of residual liquid layer over the heating area before the breakdown has been proved. Critical thickness of residual layer is less than 30  $\mu\text{m}$ . Pulsations of layer thickness over the heating area before the formation of residual layer have been found. The main drainage mechanism for the residual layer is evaporation.

The study was financially supported by the Russian Science Foundation (Project 15-19-20049).

## References

- Fedorets A. A., Marchuk I.V. and Kabov O. A., Coalescence of a droplet cluster suspended over a locally heated liquid layer, *Interfacial Phenomena and Heat Transfer*, Vol. 1 pp. 51-62 (2013)
- Marchuk I.V., Thermocapillary deformation of a horizontal liquid layer under flash local surface heating, *Journal Engineering of Thermophysics*, Vol. 24 pp. 381–385 (2015)
- Lyulin Yu.V., Spesivtsev S.E., Marchuk I.V., Kabov O.A., Investigation of disruption dynamics of the horizontal liquid layer with spot heating from the substrate side, *Technical Physics Letters*, Vol. 41 pp. 1034-1037 (2015)

## The influence of substrate temperature on structure and wettability properties of fluoropolymer coatings by Hot Wire CVD

Ekaterina Kirichenko<sup>1</sup>, Alexey Safonov<sup>1</sup>, Veronica Sulyaeva<sup>2</sup> and Nikolay Timoshenko<sup>1</sup>

<sup>1</sup>Kutateladze Institute of Thermophysics SB RAS, Lavrentyev ave. 1, Novosibirsk, 630090, Russia

<sup>2</sup>Nikolaev Institute of Inorganic Chemistry SB RAS, Lavrentyev ave. 3, Novosibirsk, 630090, Russia  
vika@itp.nsc.ru

It is known that the implementation of the next generation of electronic and photonic devices significantly depends on the increase cooling capacity (McCarthy et al. 2014, Garimella et al. 2008, Krishnan et al. 2007). The use of hydrophobic surfaces improves the heat transfer during condensation (Anand et al. 2014, Boreyko et al. 2009, Chen et al. 2011, Miljkovic 2013). This becomes possible due to the use of new methods in the production of micro- and nanoscale surface structures and architectures.

The hydrophobicity is determined by the characteristics of the material (free surface energy) and the structure of near-surface layer, by micro and nanoscale roughness. For example, the fluoropolymers have low surface energy and therefore the contact angle of water with such a surface is more than 100° (Adamson 1976). The fluoropolymer coatings with different morphology were obtained in (Safonov et al. 2015, Rebrov et al. 2009) depending on the deposition conditions. It is shown (Safonov et al. 2015), that depending on the film deposition regime, the wetting angle varies from 120° to 170°.

In work (Safonov et al. 2017) it was discovered that the gold nanoparticles covered thin fluoropolymer film influence on its wettability. The fluoropolymer film a thickness of 20 nm was deposited on the surface of gold nanoparticles. It turned out that the wetting angle of such composites depends on the presence of gold nanoparticles under the covering fluoropolymer film.

It was found (Rogachjov et al. 2010), that after application of the fluoropolymer to the activated surface occurs a significant decrease in the surface energy from 80 to 14 mJ/m<sup>2</sup>. Such a decrease in surface energy is associated primarily with an increase the content of terminal groups of CF<sub>3</sub> having a larger molecular radius than in CF<sub>2</sub> groups. It is established (Rogachjov et al. 2010) that for such conditions the thickness of the layer within which the influence of the activity of the surface (boundary layer) manifests itself, is of the order of 20 nm. In the same place (Rogachjov et al. 2010) IR spectroscopic methods it was shown that the structure of the formed layers essentially depends on the growth rate. Analysis the spectra of the obtained fluoropolymer films with the same effective thickness formed at different rates has shown that these layers have significant differences the supramolecular structure and concentration of end groups.

In this work, the thin fluoropolymer films were deposited by Hot Wire Chemical Vapor Deposition (HWCVD). The gas-precursor – a Hexafluoropropylene oxide (C<sub>3</sub>F<sub>6</sub>O) was activated from the heated nichrome wire and deposited on a silicon substrate in the form of the fluoropolymer coating. The surface morphology of obtained coatings and their thickness were determined by the methods of scanning electron microscopy (SEM) using JEOL JSM-6700F microscope.

The influence of surface substrate temperature during the deposition process on the formation of a fluoropolymer film was investigated. The interest in the study of this process caused by the deposition of the film, in our case, is the reaction of polymerization. The polymerization is an exothermic process, accompanied by release of heat energy that need be transferred away. Thus, if the surface temperature increases, the rate of polymerization is reduced because of the need to transfer away thermal energy. Accordingly, this can have a significant effect on the structure the film formed on the surface the substrate.

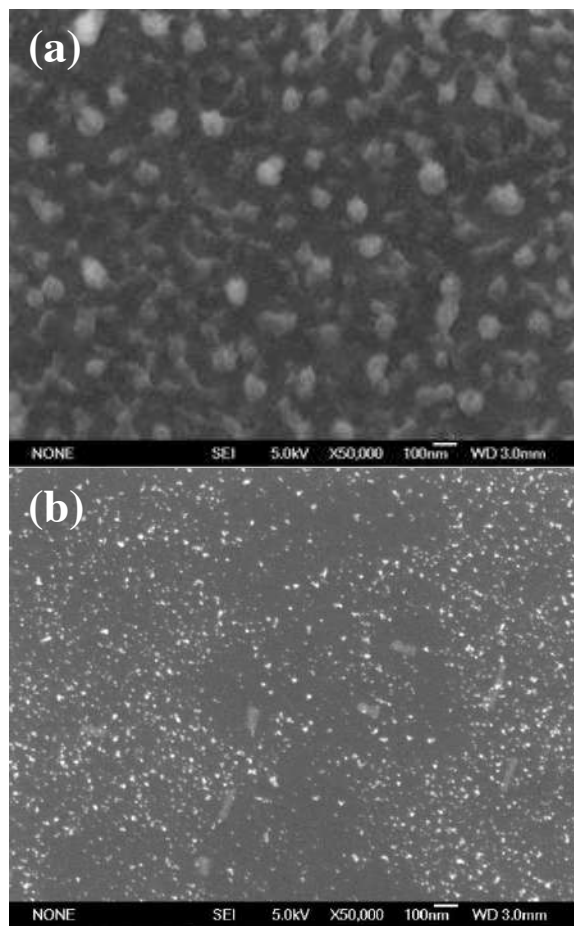


**Figure 1.** The morphology of fluoropolymer films deposited at different substrate surface temperatures: 100 °C (a), 400 °C (b).

The influence of surface substrate temperature on the structure of the deposited fluoropolymer coating was shown. As the substrate temperature increases, the deposition rate decreases from 6 nm/min at a surface temperature  $T_s = 100^\circ\text{C}$  to 0.2 nm/min at  $T_s = 300^\circ\text{C}$ . The structure of coatings changes from a continuous film with globules at 100, 200, 300 $^\circ\text{C}$  (Fig. 1 (a)) to a dendrite-like film at 400 $^\circ\text{C}$  (Fig. 1 (b)).

The hydrophobic properties of fluoropolymer coatings were determined by the measurements of the wetting contact angle (WCA). The contact angles of the coating with water were measured by DSA-100 KRUSS device.

The study showed that the obtained coatings have hydrophobic ( $90^\circ < \text{WCA} < 150^\circ$ ) and superhydrophobic ( $150^\circ < \text{WCA} < 180^\circ$ ) properties. When the thickness of fluoropolymer film is less than a few tens of nanometers, the wetting angle sharply decreases, which indicates the influence of the surface of substrate (silicon or silicon oxide) on the wettability of the deposited fluoropolymer coating. The results of the measurements are shown in the table.

**Table.** The results of measurements.

Substrate temperature at deposition, $^\circ\text{C}$	Wet angle, $^\circ$	Coating thickness, nm	Deposition rate, nm/min
26	136	70	14
109	160	180	6
201	117	13	0,43
300	110	7	0,23
402	119	-	-

The work was supported by the Grant of President of Russian Federation (MK-5052.2016.8) (the deposition of coatings) and Russian Science Foundation (grant number 16-19-10675) (investigation of surface properties). The depositions were performed at a vacuum gas-dynamic complex IT SB RAS.

## References

Adamson Arthur W., Physical chemistry of surfaces, 3 edition, New York, London, Sydney, Toronto (1976)

Anand S., Paxson A.T., Dhiman R., Smith J.D. and K.K. Varanasi, Enhanced Condensation on Lubricant-Impregnated Nanotextured Surfaces, *Acs Nano*, Vol. 6 pp. 10122–10129 (2012)

Boreyko J.B. and Chen C.H., Self-Propelled Dropwise Condensate on Superhydrophobic Surfaces, *Physical Review Letters*, Vol. 103 pp. 184501-1–184501-4, (2009)

Chen X.M., Wu J., Ma R.Y., Hua M., Koratkar N., Yao S.H. and Wang Z.K., Nanograsped Micropyramidal Architectures for Continuous Dropwise Condensation, *Advanced Functional Materials*, Vol. 21 pp. 4617–4623, (2011)

Garimella S.V., Fleischer A.S., Murthy J.Y., Keshavarzi A.,

Prasher R., Patel C., Bhavnani S.H., Venkatasubramanian R., Mahajan R., Joshi Y., Sammakia B., Myers B.A., Chorosinski L., Baelmans M., Sathyamurthy P., and Raad P.E., Thermal Challenges in Next-Generation Electronic Systems, *IEEE Transactions on Components and Packaging Technologies*, Vol. 31 pp. 801–815 (2008)

Krishnan S., Garimella S.V., Chrysler G.M., and Mahajan R.V., Towards a Thermal Moore's Law, *Ieee Transactions on Advanced Packaging*, Vol. 30 pp. 462–474 (2007).

Matthew McCarthy, Konstantinos Gerasopoulos, Shalabh C. Maroo, and A. John Hart, Materials, fabrication, and manufacturing of micro/nanostructured surfaces for phase-change heat transfer enhancement, *Nanoscale and Microscale Thermophysical Engineering*, Vol. 18 pp. 288-310 (2014)

Miljkovic N., Enright R., Nam Y., Lopez K., Dou N., Sack J. and Wang E.N., Jumping-Droplet-Enhanced Condensation on Scalable Superhydrophobic Nanostructured Surfaces, *Nano Letters*, Vol. 13 pp. 179–187 (2013)

Rebrov A.K., Safonov A.I., Timoshenko N.I., Depositing films from a supersonic jet of tetrafluoroethylene activated by interaction with a hot wire obstacle, *Technical Physics Letters*, Vol. 35 pp. 395-396 (2009)

Rogachjov A.A., Luchnikov P.A., Rogachjov A.V., The features of formation of nanoscale films from the gas phase at the initial growth stage, *Nanomaterials and nanostructures*, Vol. 1 pp. 35-44 (2010) (in Russian)

Safonov A.I., Starinskiy S.V., Sulyaeva V.S., Timoshenko N.I., Gatapova E.Ya., The hydrophobic properties of the film of fluoropolymer covering the gold nanoparticles, *Technical Physics Letters*, Vol. 3 pp. 44-49 (2017) (in Russian)

Safonov A., Sulyaeva V., Timoshenko N., Gatapova E., Kabov O., Kirichenko E., Semenov A, Deposition and Investigation of Hydrophobic Coatings, *MATEC Web of Conferences* 37, pp. 01047 (2015)

## Bubble Identification for Gas-liquid Two-phase Flows Using Artificial Neural Networks

Igor Poletaev<sup>1,2</sup>, Mikhail Timoshevskiy<sup>1,2</sup>, Konstantin Pervunin<sup>1,2</sup> and Mikhail Tokarev<sup>1,2</sup>

<sup>1</sup> Novosibirsk State University, Department of Physics, Pirogova St. 1, Novosibirsk, 630090, Russia

<sup>2</sup> Kutateladze Institute of Thermophysics, Siberian Branch of Russian Academy of Sciences, Lavrentyev Ave. 1, Novosibirsk, 630090, Russia  
mtokarev@itp.nsc.ru

Two-phase bubble flows have been used in many technological and energy processes as processing oil, chemical, and nuclear reactors. This explains large interest to experimental and numerical studies of such flows last several decades. Exploiting of optical diagnostics for analysis of the bubble flows allows researchers obtaining instantaneous velocity fields and gaseous phase distribution with the high spatial resolution non-intrusively. Behavior of light rays exhibits an intricate manner when they cross interphase boundaries of gaseous bubbles. Hence the identification of the bubble images is a complicated problem. This work presents a method of bubble images identification based on a modern approach of the Deep Learning, which is called the convolutional neural networks (CNN), see (Le Cun et al. 1998) for details. Neural networks are able to determine overlapping, blurred, and non-spherical bubble images at different backgrounds. CNN can increase accuracy of the bubble image recognition, as well as reduce the number of outliers.

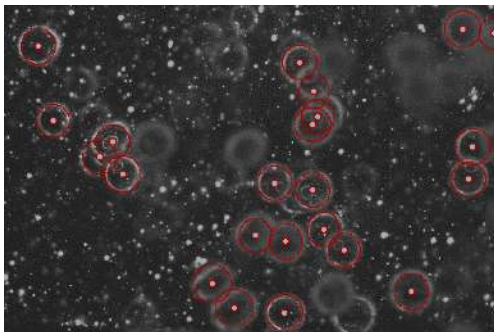
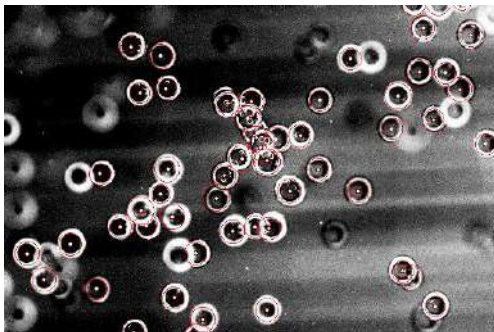


**Figure 1:** Example of bubbles identified by the neural networks (circles with centers) in flows with (top) and without (bottom) tracer particles.

Furthermore, CNN significantly decrease the number of settings for the identification task and boost processing time

of high resolution images in several times in comparison with the standard recognition methods developed before (Lindken and Merzkirch 2002, Honkanen et al. 2005, Akhmetbekov et al. 2010). In addition, usage of GPUs speeds up the learning process of CNN owing to the modern adaptive gradient optimization techniques.

The originality of the proposed method consists in training of a neural network model using synthetically generated images that mimic real registration conditions during LIF experiment (Akhmetbekov et al. 2010, Poletaev et al. 2016): bubbles size, their shape, intensity profile, background, degree of overlapping. This allows us to automatically create a required set with several thousand examples for training at specific registration conditions in a reasonable time. The ability to resolve the overlapping bubbles lets us get reliable characteristics of two-phase flows both with tracers and without them respectively (Figure 1).

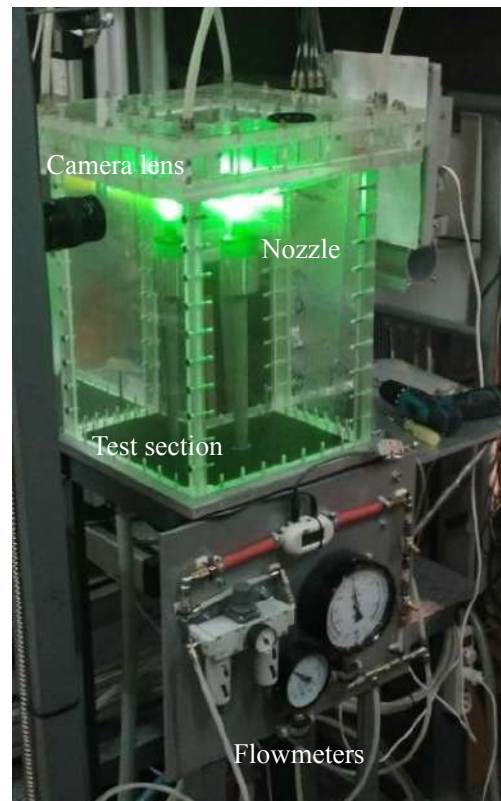


**Figure 2:** Photograph of the experimental test section.

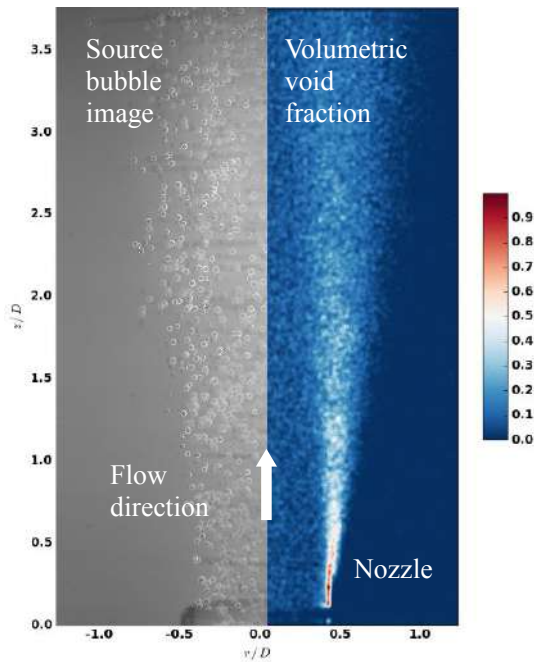


**Figure 3:** Example of the left half of a source image and the right half of the mean planar distribution of volumetric gas share (right) processed via the neural networks.

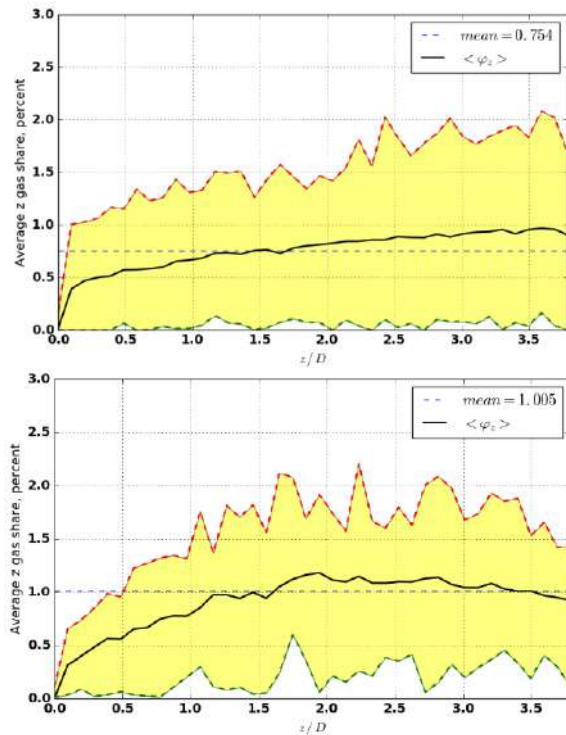


**Figure 4:** Profile of the mean gas share along the jet axis averaged in time and in the crossflow direction obtained by the correlation method (Akhmetbekov et al. 2010) (top) and the neural networks (bottom).

In order to validate the approach an experiment was carried out with the submerged air-water two-phase jet at  $Re = 12\,500$ , and gas share of 1, 2 and 3 %, which was controlled with flowmeters (Figure 2). After processing 300 pairs of PIV images for the first case (Figure 3) the correlation method (Akhmetbekov et al. 2010) gave the average gas share approximately equal to 0.75%, while the CNN approach gave the gas share value 1.01%. Figure 4 illustrates obtained minimum, maximum and mean volumetric gas share distribution measured in a plane along the jet axis averaged in the crossflow direction. Further post processing allows obtaining gas and liquid phase velocity distributions as well as their joint correlations.

### References

Y. Le Cun, L. Bottou, Y. Bengio, and P. Haffner. Gradient-based learning applied to document recognition, Proceedings of the IEEE (1998)

Lindken R, Merzkirch W A novel PIV technique for measurements in multiphase flows and its application to two-phase bubbly flows, Exp. Fluids, Vol. 33, pp. 814–825 (2002)

Markus Honkanen et al. Recognition of highly overlapping ellipse-like bubble images, Meas. Sci. Technol., Vol. 16, p. 1760 (2005)

Akhmetbekov Ye.K., Alekseenko S.V., Dulin V.M., Markovich D.M., Pervunin K.S. Planar fluorescence for round bubble imaging and its application for the study of an axisymmetric two-phase jet, Exp. Fluids., Vol. 48, No. 4, pp. 615–629 (2010)

I.E. Poletaev, K.S. Pervunin, M.P. Tokarev Artificial neural network for bubbles pattern recognition on the images, Journal of Physics: Conference Series, Vol. 754, p. 072002 (2016)

## Modelling of thin evaporating film of polar liquid with a surfactant adsorbed on the interfaces

Varvara Gordeeva<sup>1</sup> and Andrey Lyushnin<sup>2</sup>

<sup>1</sup> Perm National Research Polytechnic University, Lysva branch

2, Lenina, Lysva, Perm territory, 618900, Russia

[yanma@mail.ru](mailto:yanma@mail.ru)

<sup>2</sup> Perm State Humanitarian Pedagogical University,

In last few decades, technology developed in direction of miniaturization. Super-slim smartphones, laptops, monitors etc. are old hat already. Production of such thin microchips and screens faces a problem born by behavior of materials in nanoscales. Even more thin films are used for durability and response of screens, solar cells, fuel cells, etc., as it was described in critical review of Zhang et al. (2005). Deposition of these films is made by two general ways: either evaporation of liquid film with dry matter production, or deposition of suspended dust.

Another area using the thin films is medicine investigations where evaporating biological fluids can help in early detection of many diseases. Tarasevich (2007) showed that slowly evaporating thin film of a biological fluid is able to self-organize and bring proteins to contact line. The mechanism of such self-organization is not clearly understood yet. In this work we will made one more step to prove or contest the hypothesis that the proteins as surfactants can cause the self-organization of thin liquid films.

In very thin liquid films with thickness of nanoscale, disjoining pressure begins to play significant role. In polar liquids like water the disjoining pressure is composed from intermolecular forces and electrostatic forces. If the liquid is not very clear, the impurities also can give some contribution into the disjoining pressure, as it was shown in book of Deryagin (1974).

The impurities can also change surface tension of the liquid and thus destroy (or stabilize) the liquid film. Move of the film surface at surface tension gradient is called as Marangoni effect, and it was shown earlier in paper of Lyushnin and Pismen (2015) that the effect can destabilize the film of polar liquid. It should be noted that the Marangoni effect is not the only effect which should be considered in the impured liquid films: solubility and diffusion of the surfactant in the liquid, slipping of the liquid along the substrate, adsorption of the surfactant on the interfaces can also play significant role in stabilization or destabilization of the liquid film. It is reported in paper of Gordeeva and Lyushnin (2016) how the Marangoni effect interact with the listed above effects in the thin films of polar liquids but the authors did not simulated evolution of such systems.

In this paper, we would like to present simulations of the thin film of polar liquid with free deformable gas-liquid interface and added surfactant which can adsorb on the substrate and on the gas-liquid interface. Evolution equations were deduced for film thickness and for surface concentrations on free gas-liquid interface and on solid-liquid interface. Gokhale and Plawsky (2005) made an experiment with evaporation and condensation of water thin films and showed that in presence of surfactant the liquid

drop spinned to the substrate and change its volume in account of thickness. But it known that the liquid film takes an energetically favourable thickness determined by the disjoining pressure. The disjoining pressure depends, among other matters, on surface concentration of surfactant on the substrate:

$$\varphi = \frac{A}{6\pi h^3} - \frac{S^p}{l_0} \exp \frac{d_0 - h}{l_0} + \frac{RT}{V_w} \ln[\alpha(1 - \Gamma_s)] \quad (1)$$

where  $A$  is Hamaker constant,  $S^p$  is parameter of ion adsorption from the substrate,  $d_0$  is distance of molecular interaction,  $l_0$  is distance of dipole interaction,  $R$  is universal gas constant,  $T$  is temperature,  $V_w$  is molar volume of the liquid,  $\alpha$  is chemical activity of the liquid,  $\Gamma_s$  is the surface concentration on the substrate (Eijkel, van der Berg, 2005).

Introducing the disjoining pressure (1) in evolution equations for liquid and surface concentrations, and using a semi-implicit Crank-Nikolson scheme, we made a few simulations of quick evaporation of the thin film of water with added surfactant:

- 1) with little initial concentration on the substrate, and well-soluted surfactant;
- 2) with high initial concentration on the substrate, and well-soluted surfactant;
- 3) with little initial concentration on the substrate, and bad-soluted surfactant which is settled to the substrate at the end;
- 4) and with high initial concentration on the substrate, and bad-soluted surfactant.

First of all, we should present how the clear liquid evaporates without any surfactant (Fig. 1). In this and following figures, dashed line shows initial profile of the film.

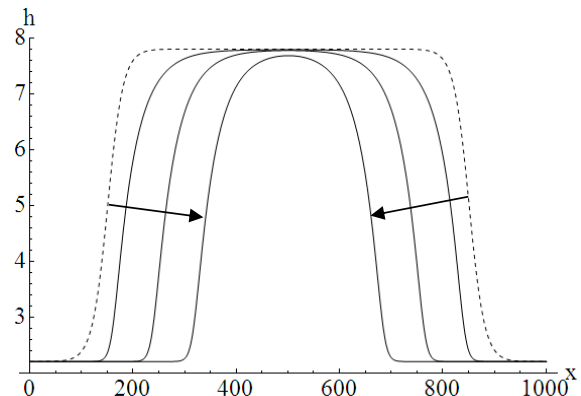


**Figure 1:** Evaporation of polar liquid without surfactant.

In Figure 1 we can see that thickness of the film doesn't change, and volume reduces in account of area of

thicker part. This is explained by the fact that the present thicknesses (2.2 and 7.8 in dimensionless units) are the stable value for this film (water on mica substrate). The layer is infinite, so the liquid could flow in from an area outside of visual field if the thickness would not be of stable value. Let's look now, how the film will behavior with added surfactant:

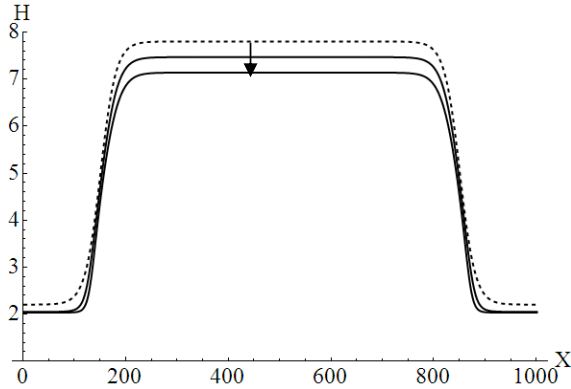


**Figure 2:** Evaporation of thin film of polar liquid with little initial concentration of a well-solved surfactant on the substrate.

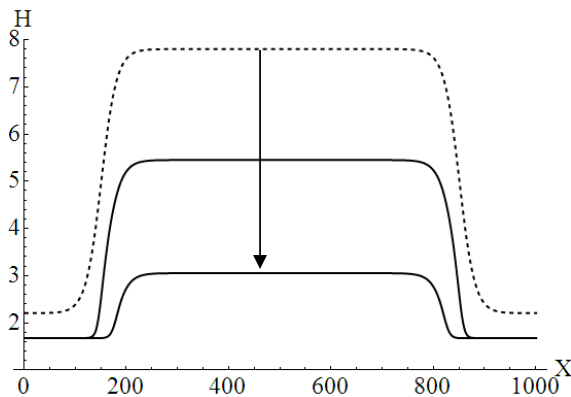


**Figure 3:** Evaporation of thin film of polar liquid with high initial concentration of a well-solved surfactant on the substrate.

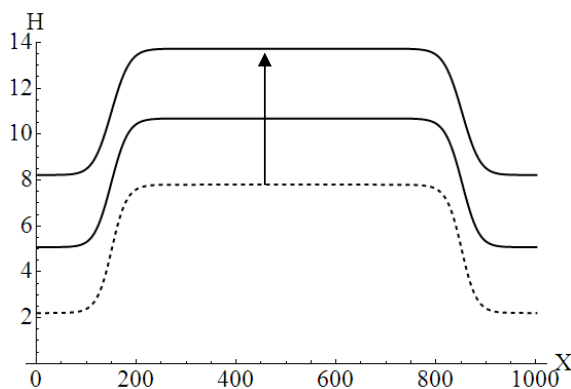


**Figure 4:** Evaporation of thin film of polar liquid with little initial concentration of a bad-solved surfactant on the substrate.

As one can see from Figures 2 and 3, the well-solved surfactant precipitates thinning of the liquid. It can not be said that the liquid evaporates quicker, it just flow out to the area outside of visual field.

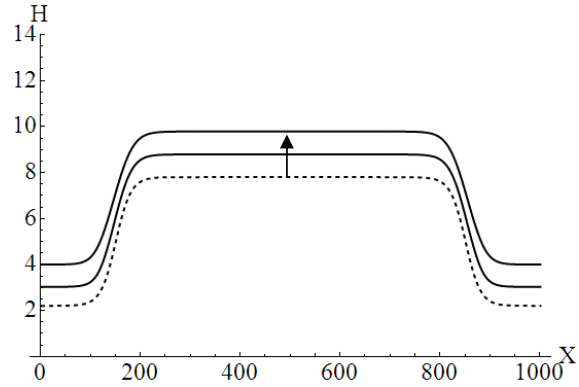


**Figure 5:** Evaporation of thin film of polar liquid with high initial concentration of a bad-solved surfactant on the substrate.

Figures 4 and 5 show how the film becomes thicker in account of liquid flowing in from the area outside of visual field. The bad-solved surfactant is adsorbed on the substrate and changes the disjoining pressure of the film, thus it changes the stable values of film thickness.

#### References

Zhang S., Sun D., Fu Y., and Du H. Toughening of hard nanostructural thin films: a critical review, *Surface and Coatings Technology*, Vol. 198 pp. 2-8 (2005)

Tarasevich Y. Y. and Pravoslavnova D. M., Segregation in desiccated sessile drops of biological fluids, *The European Physical Journal E*, Vol. 22 pp. 311-314 (2007)

Derjaguin B. V. and Churaev N. V., Structural component of disjoining pressure, *Journal of Colloid and Interface Science*, Vol. 49 pp. 249-255 (1974)

Lyushnin A. V. and Pismen L., Analysis of stability of a thin evaporating water film in the presence of a solvable surfactant on the free surface, *Technical Physics*, Vol. 60 pp. 782-784 (2015)

Gordeeva V. Y. and Lyushnin A. V., Dynamics of an evaporating thin film of polar liquid with solutocapillary Marangoni effect and capillary osmosis, *Surface and Coatings Technology*, in press (2016)

Gokhale S. J., Plawsky J. L. and Wayner, P. C., Spreading, evaporation, and contact line dynamics of surfactant-laden microdrops, *Langmuir*, Vol. 21 pp. 8188-8197 (2005)

Eijkel J. C. and Van Den Berg A., Water in micro-and nanofluidics systems described using the water potential, *Lab on a Chip*, Vol. 5 pp. 1202-1209 (2005)

## Division of binary metal melts in a thin capillary

Vitaly Demin<sup>1</sup>, Alexey Mizev<sup>2</sup> and Maxim Petukhov<sup>1</sup>

<sup>1</sup>Perm State National Research University, Physics Faculty, Theoretical Physics Department  
Bukirev str. 15, Perm, 614990, Russia  
demin@psu.ru

<sup>2</sup>Institute of Continuous Media Mechanics, Laboratory of Hydrodynamic Stability  
Korolev str. 1, Perm, 614013, Russia  
alex\_mizev@icmm.ru

Theoretical research has been devoted to the study of binary fusible metal melts behaviour in a thin capillary. Earlier it was found experimentally that unusually significant and quick redistribution of melts components took place along capillary after the instant cooling. The character difference of metals concentrations was approximately equal to 5 – 10 %. Therefore numerical simulation of concentration-induced convection was carried out to explain experimental data.

Two-component melt of both liquid metals filling vertical thin capillary with non-uniform temperature distribution on the boundaries has been considered. It is assumed for simplicity that the condition of absolute nonwetting takes place because of the alundum sidewalls of the capillary. As a result of this effect there is a free surface on vertical boundaries where thermocapillary force is appeared due to the external longitudinal temperature gradient and nonuniformity of surface concentration which makes to move liquid elements at a big distance, compared with axial size of capillary.

The classical equations of interfacial hydrodynamics were used to model convective processes in the thin channels (Slavtchev et al. 1998, Birikh et al. 2003). The system of non-dimensional equations and boundary conditions is written in the following form

$$\begin{aligned} \frac{\partial \vec{v}}{\partial t} + \frac{1}{Pr} (\vec{v} \nabla) \vec{v} &= \nabla p + \Delta \vec{v} + Ra(T - C) \vec{y}, \\ Pr \frac{\partial T}{\partial t} + (\vec{v} \nabla) T &= \Delta T, \quad \text{div } \vec{v} = 0, \\ \frac{\partial C}{\partial t} + \frac{1}{Pr} (\vec{v} \nabla) C &= \frac{1}{Sc} \Delta C, \\ \frac{\partial \Gamma}{\partial t} + \frac{1}{Pr} \nabla^s (\vec{v} \Gamma) &= \frac{1}{Sc_s} \Delta^s \Gamma + k_+ C - k_- \Gamma, \\ x = 0: -\frac{1}{Sc} \frac{\partial C}{\partial x} &= -k_+ C + k_- \Gamma, \\ x = 1: -\frac{1}{Sc} \frac{\partial C}{\partial x} &= k_+ C - k_- \Gamma, \\ z = 0, z = H: \quad \partial C / \partial z &= 0, \\ x = 0: \quad \varphi &= -Ma_T \frac{\partial T}{\partial y} - Ma_\Gamma \frac{\partial \Gamma}{\partial y}, \\ x = 1: \quad \varphi &= Ma_T \frac{\partial T}{\partial y} + Ma_\Gamma \frac{\partial \Gamma}{\partial y}. \end{aligned}$$

Here  $\vec{v}$ ,  $T$ ,  $p$  and  $C$  are the fields of the velocity, temperature, pressure and volume concentration of the heavy admixture, respectively;  $\Gamma$  is the surface concentration of the heavy component,  $\varphi$  – is the vorticity. The set of non-dimensional governing parameters has the form

$$\begin{aligned} Ra &= \frac{g \beta_T \Theta L^3}{\nu \chi}, \quad Pr = \frac{\nu}{\chi}, \quad Sc = \frac{\nu}{D}, \quad Sc_s = \frac{\nu}{D_s}, \\ k_+ &= \frac{k_A L}{\nu}, \quad k_- = \frac{k_D L^2}{\nu}. \end{aligned}$$

where  $Ra$ ,  $Pr$ ,  $Sc$  are the Rayleigh, Prandtl and Schmidt numbers correspondingly;  $Sc_s$  is the surface analogue of the Schmidt number,  $L$  and  $H$  are the width and height of the capillary,  $\Theta$  is the character temperature difference along the channel. Parameters  $k_+$  and  $k_-$  are the non-dimensional coefficients of adsorption and desorption.

Additional important non-dimensional parameters are the Marangoni numbers:

$$Ma_T = \sigma_T \frac{\Theta L}{\eta \chi}, \quad Ma_\Gamma = \sigma_\Gamma \frac{\Theta \beta_T L^2}{\beta_c \eta \chi}$$

These parameters characterize the tangential force on the free surface and include the dependence of surface tension coefficient on temperature and concentration inhomogeneity respectively.

The following values have been chosen as units to measure the distance, volume and surface concentrations, time, velocity, temperature and pressure:  $L$ ,  $\Theta \beta_T / \beta_c$ ,  $\Theta \beta_T L / \beta_c$ ,  $L^2 / \nu$ ,  $\chi / L$ ,  $\Theta$ ,  $\rho \nu \chi / L^2$ .

The numerical calculations have been performed on the "PGU-Tesla" supercomputer of the Research Academic Center "Parallel and Distributed Calculations" at the Perm State National Research University. The method of finite differences in combination with the explicit scheme was applied. Numerical code was written in programming language Fortran-90. The working mesh contained the  $21 \times 311$  grid nodes. It was assumed that the capillary was narrow. Thus, the non-dimensional thickness of the channel was equal to  $H = 30$ . The values of other parameters were fixed and were taken equal to  $Ra = 0.01$ ,  $Pr = 0.05$ ,  $Sc = 300$ ,  $Sc_s = 200$ ,  $k_+ = 0.0001$ ,  $k_- = 0.054$ .

When the dependence of the surface tension coefficient on concentration is negligible, it means that  $Ma_\Gamma = 0$ . This limiting case was considered by Demin and Petukhov (2016). Let us present now the calculation results for nonzero values of  $Ma_\Gamma$ . The isolines of the stream function, concentration of heavy component and temperature are shown in Fig. 1 for  $Ma_\Gamma = 8$  and  $Ma_\Gamma = 7$ .

Processes of adsorption and desorption on the surface, thermocapillary force, convective motion in a volume and diffusion are characterized by essentially different times. These mechanisms generate a large-scale process of circulation which includes the carrying-out of admixture on the surface in the hot higher part of capillary, its following transfer down along the boundary due to the thermocapillary force and its subsequent return in the volume over the

desorption in the lower part of capillary. The numerical calculations demonstrate that the lifting speed of returning motion in the volume is less, than on the surface, that's why heavy admixture in the stage of saturation can be accumulated nearby the lower part of capillary (Fig. 1a).

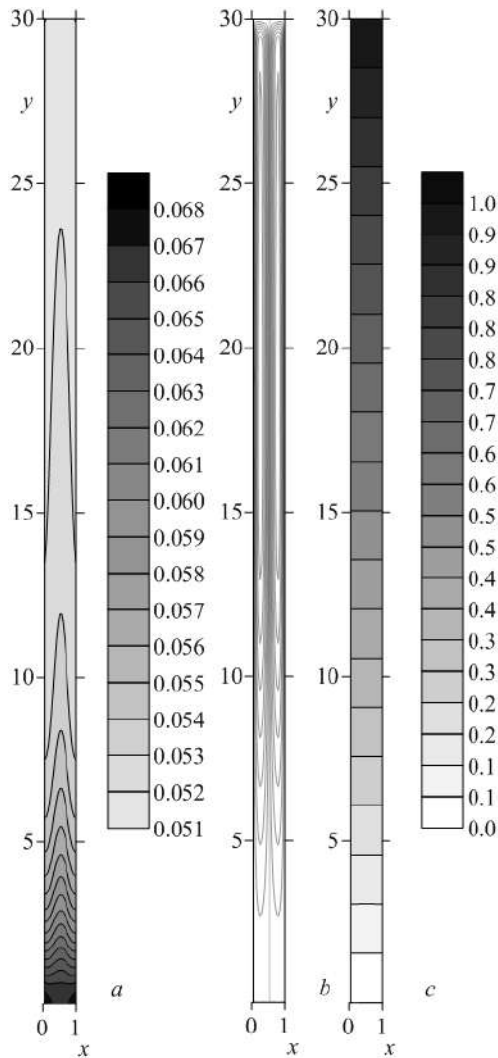


**Figure 1:** The fields of heavy admixture concentration (a), stream function (b) and temperature (c) in the channel for  $t = 800$ .

After the fast establishing the flow becomes stationary and has the form of two elongated vortices. Its magnitude on the surface and, as a result, in the volume is determined by the Marangony numbers  $Ma_T$  and  $Ma_r$ . Intensity of motion and processes of adsorption-desorption on the free boundary have the decisive influence upon the formation of surface and volume concentration fields and the speed of redistribution of components in a molten mixture.

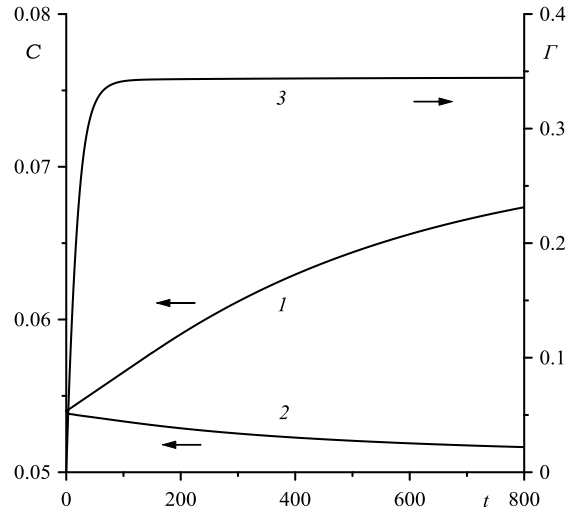


**Figure 2:** Maximum and minimum values of the heavy component concentration in the volume (lines 1, 2); Line 3 is the maximum of surface concentration in dependence on time.

The kinetics of the mixture division on components as a function of time is presented in Fig. 2. It can be seen that the significant stratification occurs for reasonable values of governing parameters. Thus, one of the possible mechanisms of longitudinal separation on components in thin channels has been demonstrated for the liquid binary mixtures. This theoretical investigation can explain the results of certain experiments with fusible metals on segregation of molten metal mixtures.

This work is supported by Russian Foundation of Basic Research, grant № 16-01-00662 a.

### References

Slavtchev S., Hennenberg M., Legros J.-C., Lebon G., Stationary solutal Marangony instability in a two-layer system, *Journal of Colloid and Interface Science*, Vol. 203 pp. 354–368 (1998)

Birikh R.V., Briskman V.A., Velarde M., Legros J.-C., *Liquid Interfacial Systems: Oscillations and Instability*, CRC Press, 392 p. (2003)

Demin V.A., Petukhov M.I., On Mechanism of Large-Scale Transfer of Molten Metal Components in Non-uniformly Heated Thin Capillaries, *Bulletin of Perm University. Physics*, Vol. 3 pp. 65-71 (2016)

## Numerical study on two-phase flow in leakage path clearance of single screw expanders

Shen Lili, Wu Yuting, Wang Wei, Ma Chongfang

Key Laboratory of Enhanced Heat Transfer and Energy Conservation, Ministry of Education and Key Laboratory of Heat Transfer and Energy Conversion, Beijing municipality, College of Environmental and Energy Engineering, Beijing University of Technology, Beijing 100124, China  
shenlili@emails.bjut.edu.cn

As one of the rotary type expanders, single screw expanders can be widely used in converting thermal energy into work., because they have advantages such as high-pressure ratio, low rotational speed, smooth operation, high efficiency, and tolerance of the two-phase flow (Bao et al. 2013, Ziviani et al. 2014).

However, internal leakage loss has great influence on the performances of single screw expanders because there broadly exists the clearance between moveable components in the single screw expanders. Wang et al. (2011) studied the performance of a single screw expander prototype by using compressed air as the working fluid. The results showed a maximum isentropic efficiency of 59% at a rotational speed of 2,850rpm and maximum power output of 5kw. Wang et al. (2013) also analyzed the influence of the gap size on the performance of single screw expanders. The experimental results indicated that the prototype of medium size gap had the best overall performance with a maximum volumetric efficiency of 66%, gas consumption rate of about 65kg/kWh and the shaft efficiency of 60%. Lu et al. (2013) tested an SSE with a 175mm diameter rotor by using a compressed air refrigeration system and obtained an adiabatic efficiency above 65%. Ziviani et al. (2014) established a comprehensive simulation model for an SSE, and their model was proved by experimental results obtained from an ORC set-up that employed SES36 as the working fluid. The model agreed with the experimental results within 10% and 15% for the mass flow rate and power output, respectively. Desideri et al. (2014) presented an experimental characterization of SSE utilizing SES36 as the working fluid. The results showed that a maximum expander isentropic efficiency of 64.78% and maximum generated power of 7.8kW. Although some present researches of single screw expanders have been carried out, few can directly reflect the effect of internal leakage on the performance of expanders. Therefore, it is necessary to research the internal leakage characteristics of the single screw expanders.

Research on the leakage characteristics of other rotary compressors and expanders have been investigated systematically in both theoretical and experimental. Xing et al. (2010) established the two-phase leakage model to calculate the leakage flow rate of contact line in the screw compressors which decrease the volumetric efficiency by about 8%. Wang et al. (2015) built a two phase leakage mathematical model for gas-oil flow to predict the gas leakage flow rate of the single screw compressor with multicolumn envelope meshing pair. Costa et al. (1990) carried out a visualization experiment on the leakage through the radial clearance in rotary compressor. They observed a strong formation of bubbles just after the minimal clearance, which can be explained that the refrigerant dissolved in the oil separates with the pressure

drop in the two phase leakage flow. Mitsuhiro et al. (1996) also found that the radial clearance between the cylinder and the rotor was normally sealed by the oil in visualization experiment. Because of the separation of refrigerant from the oil, a comb-shaped oil film was observed on the cylinder wall by Costa et al. (1990) and Mitsuhiro et al. (1996).

According to the above discussion, the reasonable model to calculate the gas leakage flow rate through the leakage path clearance in single screw expanders should consider the two-phase flow of the oil-gas mixture. Moreover, the influence of the clearance geometry on the leakage must be considered in order to improve the accuracy of the model. The height of leakage path clearance in single screw expander are normally in the range from 0.02 to 0.12mm, which are regarded as micro-channel by Laplace constant (Akbar et al. 2003).

A numerical study of a single screw expander with compressed air as the working fluid was carried out to analyze its internal leakage flow characteristics. Based on the theory of engineering thermodynamics and hydrodynamics, a one-dimensional two-phase leakage low models was presented to calculate the leakage flow rate and volumetric efficiency of a single screw expander. The mathematical model of working process was calculated by classical fourth-order Runge-Kutta method using MATLAB programming. And the numerical model was verified by experimental results as shown in Figure 1.

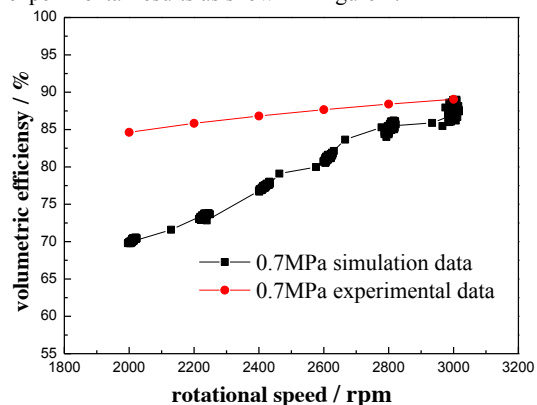


Figure 1: Comparison of the experimental with the simulation results at the suction pressure of 0.7MPa.

It is difficult to measure the leakage rate through each clearance during the single screw expander operation. Therefore, the calculation results of volumetric efficiency were compared with the available experimental data to validate the two phase leakage model in this paper. The suction pressure values are 0.7MPa, whereas the intake air

temperature is 20°C. Figure 1 compare the theoretical and experimental volumetric efficiency values of the two SSE prototypes for the different rotational speeds. The average absolute error between the experimental and the simulation results are approximately 7.5%. The minimum absolute error of simulation model is approximately 1.14% when the rotation speed is 3,000rpm. This model has suitable applicability for single screw expanders at a high rotational speed. Figure 1 also shows that the volumetric efficiency increases with the increase of the rotation speed. Setting a higher rotational speed is an effective way to decrease leakage. However, the above analysis does not consider the influence of mechanical performance on the leakage.

According to the spatial geometry of the gap and the movement of the wall surface, gas-oil two phase flow in the leakage path could be treated as flat plate flow model. The clearance height and rotation speed are set at 0.1mm and 3,000rpm, respectively. There are nine leakage paths in single screw expander. The average gas leakage rate of the different channels in the working process is shown in Figure 2. The said figure shows that the sequence of the leakage rate from large to small is  $Q_8 > Q_7 > Q_9 > Q_{2+4} > Q_1 > Q_6 > Q_{3+5}$ . Most of the leakage occurred through the fit clearances. The distribution changed when we adjusted the clearance gap values. The results show that the main gas leakage flow through the clearances between the edge of the screw and inside surface of the shell. Hence, the decreased fitting clearances height is effective to reduce the gas leakage flow rate and improve volumetric efficiency.

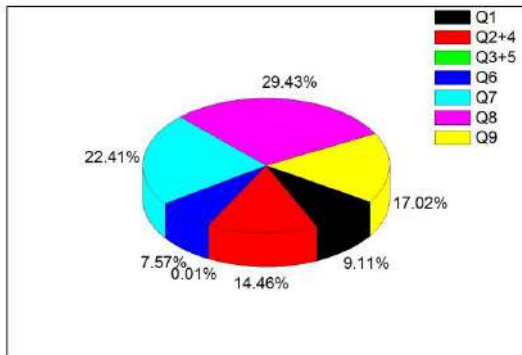


Figure 2: Diagram of the average gas leakage rate of the different channels.

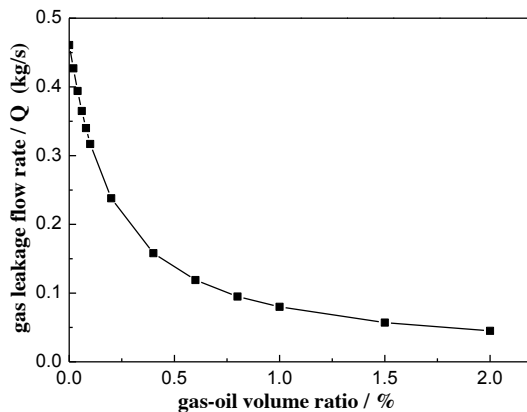


Figure 3: Variation of the gas leakage flow rate with the

gas-oil volume ratio.

Figure 3 shows gas leakage flow rate varies with the gas-oil volume ratio. The clearance height and rotation speed are set at 0.1mm and 3000rpm, respectively. Gas leakage flow rate decrease first quickly then slowly with the increase of the gas-oil volume ratio. Gas leakage can be reduced by 81.26%, when the gas-oil volume ratio from 0 to 1.0%. Therefore, too much injection of lubricant oil will aggravate mechanical friction loss and the suitable injection of oil can effectively reduce the gas leakage.

## References

- Akbar M.K, Plummer D.A, Ghiaasiaan S.M., On gas-liquid two-phase flow regimes in microchannels, *International Journal of Multiphase Flow*, Vol. 29(5) pp. 855-865 (2003)
- Bao J., Zhao L., A review of working fluid and expander selections for organic Rankine cycle. *Renew Sustain Energy, Rev Vol.* 24 pp. 325-42 (2013)
- Costa, C.M.F.N., Ferreira, R.T.S., Prata, A.T., Considerations about the leakage through the minimal clearance in a rolling piston compressor, *Proc. Purdue Compressor Technology Conference*, pp. 853-863. (1990)
- Desideri A., Martijn V.D.B., Gusev S., et al, Experimental campaign and modeling of a low-capacity waste heat recovery system based on a single screw expander, *22nd International Compressor Engineering Conference at Purdue*, pp. 14-17 (2014)
- Lu Y.W, He W., Wu Y.T., et al, Performance study on compressed air refrigeration system based on single screw expander, *Energy*, Vol. 55 pp. 762-768 (2013)
- Mitsuhiro, F., Tadashi, Y., Takashi, S., Toru, M., Observation of oil film condition in a cylinder of rotary compressor, *Proc. Purdue Compressor Technology Conference*, pp. 401-406 (1996)
- Wang W., Wu Y.T., Ma C.F., et al, Preliminary experimental study of single screw expander prototype, *Applied Thermal Engineering*, Vol. 31 pp. 3684-3688 (2011)
- Wang W., Wu Y.T., Ma C.F., et al, Experimental study on the performance of single screw expanders by gap adjustment, *Energy*, Vol. 62 pp. 379-384 (2013)
- Wang Z.L., Liu Z., Wu W.F., et al, Research of leakage characteristics of single screw refrigeration compressors with the Multicolumn Envelope Meshing Pair, *International Journal of Refrigeration*, Vol.49 pp. 1-10 (2015)
- Xing Z.W., Peng X.Y., Shu P.C., Study of leakage characteristics in twin screw compressor with refrigerant R134a, *Journal of Refrigeration*, Vol. 4 pp. 23-28 (2010)
- Ziviani D., Bell I.H., Broek M.V.D., et al, Comprehensive model of a single screw expander for ORC-systems, *22nd International Compressor Engineering Conference at Purdue*, pp. 14-17 (2014)

## Frequency domain analysis of pressure drop characteristics in parallel multiple microchannels

Liang-ming Pan<sup>1,\*</sup>, Run-gang Yan<sup>1,2</sup>, Hui He<sup>1</sup>, Hao-jie Huang<sup>1</sup>

1. School of Power Engineering of Chongqing University, Chongqing, 400044, China

2. Factory 7304, China Aerospace Science and Technology Corporation, Chengdu, 610100, China

\*Corresponding Author: Liang-ming Pan, +86-23-65102280, cneng@cqu.edu.cn

With the increasing application of Microelectro Mechanical Systems (MEMS) in aerospace field etc., As the large ratio of surface area to volume in micro/minichannels, a higher heat transfer performance is expected comparing to the conventional ones (Wu and Sundén. 2014).

The state-of-art study on the pressure drop characteristics of parallel multiple microchannels are mainly focused on the total pressure drop characteristics (Qu and Mudawar. 2004, Wang et al. 2008, Law and Lee. 2015). With the exception of that Mosyak et al. (2012) measured the upstream and downstream pressure of few individual channels of the parallel multiple microchannels which were connected through needle tips. However, they did not clarify the relationship between total pressure drop variation characteristics and pressure drop characteristics of single-channels. As a consequence, both of total pressure drop between plenum of the test section and that of individual single-channel are studied based on the experimental loop system shown as Fig. 1. The electrical conductivity of the working fluid is 1  $\mu\text{S}/\text{cm}$ . The thermostatic bath was used to provide a desired inlet temperature when the deionized water flows successively to test section, viz., the heated microchannel block. Finally, the working fluid flows through the test section, and it is condensed by the coagulation device and water-cooled condenser and then returns to the reservoir.

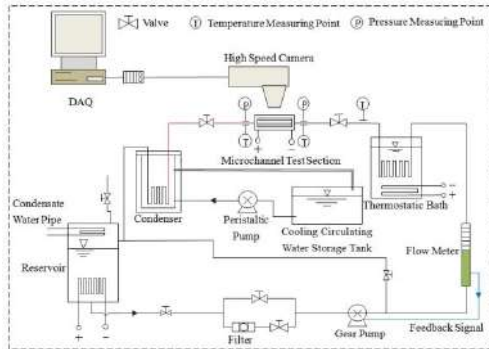


Figure 1: Schematic diagram of the flow loop.

There are 6 parallel rectangular channels in the test section. The distance between the upstream and downstream two pressure measuring points inside the second and fourth single-channels are 42 mm. In this paper, the pressure drop between two measuring points inside the second and fourth single-channels are expressed as  $\Delta p_2$  and  $\Delta p_4$ , respectively. And the pressure drop between mainfolds of the test section is expressed as  $\Delta p_{exp}$ . The flow boiling experiment is carried out by using high purity deionized water as the working fluid. And the main results in terms of frequency domain analysis of pressure drop are shown in Fig. 2-7.

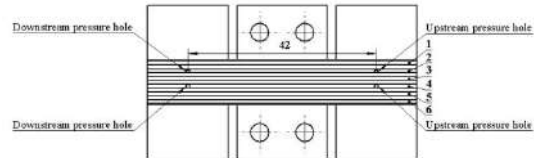


Figure 2. Schematic diagram of the local pressure measuring point and distribution

Figure 3-4 show the frequency domain variation characteristics of the total pressure drop. The stability of single phase flow does not change with the change of heat flux when the mass flux and inlet temperature are constant. However, for the case of two-phase flow, the amplitude of the total pressure drop increases and the frequency decreases with the increase of heat flux when keeping the mass flux and inlet temperature constant, and the total pressure drop amplitude decreases and the frequency increases with the increase of mass flux at constant heat flux and inlet temperature conditions.

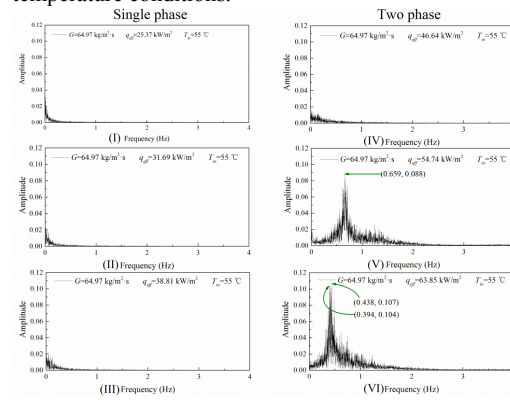


Figure 3. Frequency domain characteristics of the total pressure drop under different heat flux.

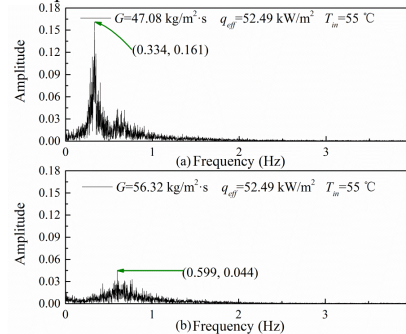
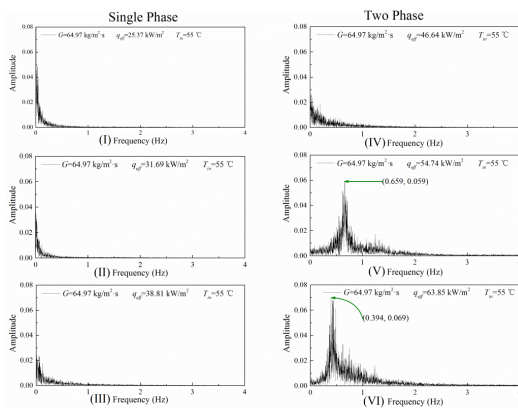
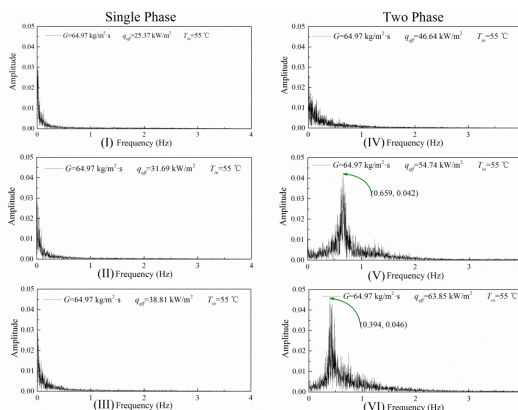


Figure 4: Frequency domain characteristics of the total pressure drop under different mass flux.

Additionally, it can be found that the frequency variation of pressure drop oscillation inside two individual single-channels is similar to that of the total pressure drop with the increase of heat flux by comparing Fig. 5(V~VI), Fig. 6(V~VI) and Fig. 3(V~VI) respectively. It should be noted that the amplitude of the pressure drop oscillation in two individual single-channels is much lower than that of the total pressure drop oscillation amplitude, and the amplitudes of the pressure drop oscillation in two individual single-channels have shown to differ slightly, i.e. the amplitude of the pressure drop oscillation in the second single-channel is slightly higher than that of fourth single-channel. It is interested that the frequency corresponding to pressure drop maximum amplitude of the total pressure drop between plenum of the test section coincides with the frequency referencing to the maximum amplitude of the pressure drop inside the two individual single-channels when the heat flux reaches 54.74 kW/m<sup>2</sup>. Besides, the frequencies corresponding to pressure drop maximum amplitude inside two individual single-channels are completely the same and consistent with the frequency corresponding to total pressure drop of the second largest amplitude when the heat flux is 63.85 kW/m<sup>2</sup>.



**Figure 5.** Frequency domain characteristics of the pressure drop inside the second channel under different heat flux.



**Figure 6.** Frequency domain characteristics of the pressure drop inside the fourth channel under different heat flux.

A similar phenomenon can be found by comparing Fig. 6(a, b), Fig. 7(a, b) and Fig. 3(a, b) respectively, i.e. the frequency corresponding to pressure drop maximum

amplitude of the total pressure drop between plenum of the test section coincides with the frequency referencing to the maximum amplitude of the pressure drop inside the two individual single-channels. However, the main reason for these pressure drop severe oscillation is that the phenomena of bubble growth, confinement, reversal flow and cleared away process alternately occur in each subchannel, leading to the occurrence of system instability. Therefore, according to the above analysis, it can be found that, in a certain extent, the flow instability in parallel multiple microchannels experiment can be analyzed by the frequency domain characteristics of the total pressure drop oscillations.

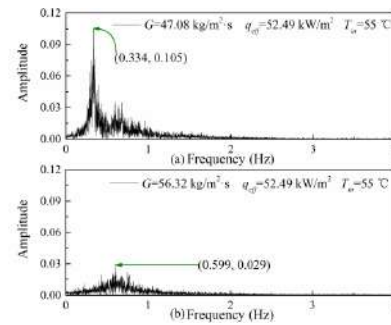


**Figure 7.** Frequency domain characteristics of the pressure drop inside the second channel under different mass flux.

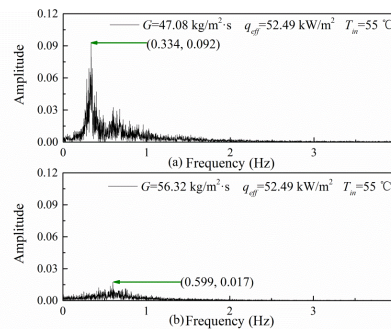


**Figure 8.** Frequency domain characteristics of the pressure drop inside the fourth channel under different mass flux.

## References

- Z. Wu, B. Sundén, *Renewable and Sustainable Energy Reviews*, Vol. 40 pp. 11-27 (2014).
- W. Qu, I. Mudawar, *Int. J. Heat Mass Transfer*, Vol. 47, No. 10-11, pp. 2045-2059 (2004).
- G. Wang, P. Cheng, A.E. Bergles, *Int. J. Heat Mass Transfer*, Vol. 51, No. 9-10, pp. 2267-2281 (2008).
- M. Law, P.-S. Lee, *Int. J. Heat Mass Transfer*, Vol. 85, pp. 797-810 (2015).
- A. Mosyak, L. Rodes, G. Hetsroni, *Int. J. Multiphase Flow*, Vol. 47, pp. 150-159 (2012).

## Numerical Simulation of nucleate boiling in microgravity under the influence of a shear flow

Benjamin Franz, Peter Stephan

TU Darmstadt, Department of Mechanical Engineering, Institute for Technical Thermodynamics  
Alarich-Weiß-Straße 10, Darmstadt, 64287, Germany  
franz@ttd.tu-darmstadt.de

Nucleate Boiling is a promising process for the cooling of electronic devices in space applications, which are continuously dissipating heat. It is not possible to employ correlations for the design of heat exchangers, which have been obtained in experiments under normal gravity conditions. The influence of gravity on local transport phenomena has to be understood in more detail. For that purpose an experimental setup called RUBI (Reference mUlti-scale Boiling Investigation) is planned and designed for operation aboard ISS in order to investigate nucleate boiling in a shear flow. Prior to and accompanying the ISS experiments, numerical and experimental studies are performed on ground in order to gain a better understanding of phenomena occurring during the RUBI experiments.

The aim of the simulations presented here is to investigate the influence of system parameters on a single bubble boiling process and on the thermal boundary layer above the heated wall. A parametre study is performed varying flow velocity, heater power, system pressure, subcooling and superheating, respectively, during single bubble nucleate boiling at different gravity levels. The time, which the thermal boundary layer needs to fully recover after bubble detachment, is analyzed depending on the above mentioned parameters, in order to determine the maximum bubble frequency for which stable nucleate boiling of a single bubble event is possible.

According to Siegel (Siegel 1967) bubble detachment is independent of gravity if the heat supplied to the boiling process is high enough to let the bubble grow explosively and let it detach in an early phase of the growth process. This will be analyzed numerically, too. Additionally, the boiling process in the presence of a shear flow, is investigated.

Full 3-D-simulations of the two-phase flow are performed using the topology of the RUBI experimental setup. The simulation setup consists of two domains, a fluid and a solid domain, representing the centerpiece of the RUBI experimental framework. (Fig. 1, 2). The fluid domain is a cutout of the RUBI nucleate boiling test cell. It represents the actual flow channel between the inlet and the outlet of the test cell with a constant flow area. In order to save mesh cells and thus simulation time, the symmetry of the flow channel is taken into account.

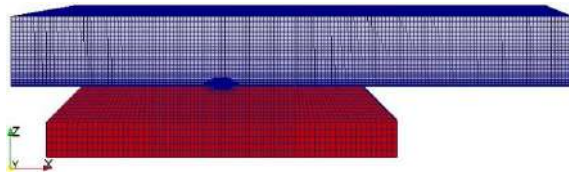


**Figure 1:** Fluid domain (upper part) with flow in positive  $x$ -direction and solid domain (lower part)

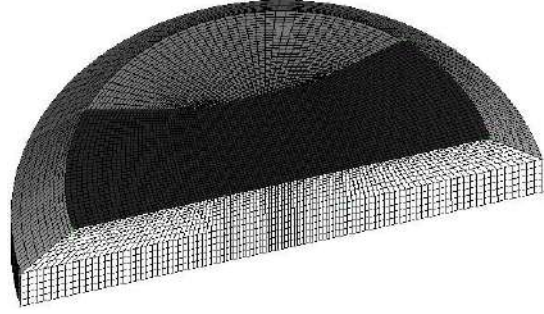


**Figure 2:** Half model of the heater (solid domain)

The solver for the evaporating two-phase flow combines a finite volume method with a Volume-of-Fluid method that is used for interface capturing at the liquid-vapor interface in the fluid domain. The conservation equations for mass, momentum, energy, and volume fraction (eqs. 1-4) are solved. The source terms on the right hand side of eqs. 1, 3 and 4 account for phase change; the force vectors on the right hand side of eq. 2 account for surface tension at the interface and gravity, respectively.

$$\nabla \cdot (\rho \vec{u}) = \dot{\rho} \quad (1)$$

$$\frac{\partial \rho \vec{u}}{\partial t} + \nabla \cdot (\vec{u} \cdot \rho \vec{u}) = -\nabla p + \nabla \cdot (\mu \cdot \nabla \vec{u}) + \vec{f}_{ST} + \vec{f}_g \quad (2)$$

$$\frac{\partial \rho c T}{\partial t} + \nabla \cdot (\vec{u} \cdot \rho c T) = \nabla \cdot (\lambda \cdot \nabla T) + \dot{h} \quad (3)$$

$$\frac{\partial F}{\partial t} + \nabla \cdot (\vec{u} \cdot F) = \frac{\dot{\rho}}{\rho} F \quad (4)$$

The simulations are performed with the open source CFD toolbox OpenFOAM. Its native interFoam solver has been complemented by methods to account for phase change (based on an evaporation model by Hardt and Wondra 2008), evaporation at the three-phase contact line (based on the theoretical model of Stephan and Busse, 1992) and for the transient heat conduction between the solid heater and the fluid. Adaptive mesh refinement is used to increase the grid resolution in the vicinity of the liquid-vapor interface. For a detailed description of the numerical model please refer to the thesis of Batzdorf (Batzdorf 2015).

The velocity profile of a Poiseuille flow given in Eq. (5) (with flow velocity  $u_x$  in  $x$ -direction, the maximum velocity  $u_{x,max}$  at half the channel height, the channel height  $H$  and the height coordinate  $z$ ) is set as boundary condition at the inlet and as start condition throughout the whole channel. The flow is assumed to be fully laminar.

$$u_x(z) = 4u_{x,max} \left(1 - \frac{z}{H}\right) \frac{z}{H} \quad (5)$$

The dark part of the surface of the heater in Fig. 2 represents the heater coating, the heat supply is modeled as a power per area source since the heater coating is extremely thin. The interaction between the liquid and the surface of the solid heater which it is in contact with is simulated using a custom boundary condition which takes the transient heat conduction between solid and liquid as well as contact line evaporation and its effect on contact line speed and contact angle into account. Furthermore, prior to the actual nucleate boiling simulations, a single phase simulation is conducted in order to determine the thermal boundary layer at the bottom of the flow channel in dependence of flow velocity and heater power. These transient simulations are performed until a steady state of the temperature distribution in the whole numerical domain is reached. This temperature distribution is then used as starting condition for the boiling simulations.

For the simulation of nucleate boiling the volume fraction field is altered in a way that a vapor bubble with a very small radius pops up at the nucleation site.

Fig. 3 shows the temperature distribution at the symmetry plane of the flow channel for one of the calculations after a simulation time of 0.04 s. It can be seen that above the nucleation site the thermal boundary layer is still thinner than upstream of the nucleation site. This is caused by the vapor bubble that has grown at the nucleation site and has then moved downstream because of the shear flow. The evolution of the thickness of the thermal boundary layer above the nucleation site over time with regard to its thickness before nucleation is evaluated in order to determine how much time is needed for a full recovery. This evolution is shown in Fig. 4. Values greater than 1 for the start phase can be explained by the bubble still being situated above the nucleation site, because for the determination of the thickness of the boundary layer the first z-wise cell with saturation temperature is searched.

For this configuration the thermal boundary layer has fully recovered after appr. 0.05 s, this is when a second bubble could nucleate and a stable boiling process is still ensured.

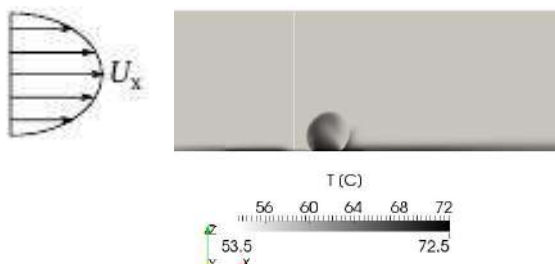


**Figure 3:** Temperature distribution at a simulation time of 0.04 s after nucleation during saturated boiling with  $p = 0.9$  bar,  $u_{x,max} = 0.15$  ms<sup>-1</sup>,  $\dot{q} = 2e4$  Wm<sup>-2</sup>

The presented results show that the used method is suitable to examine the influence of the boiling process on the thermal boundary layer above the heater. In a next step the recovery times for different sets of flow velocity and

heat distribution are determined and compared. Furthermore, the influence of system pressure and subcooling on the overall boiling process will be investigated in parameter studies.

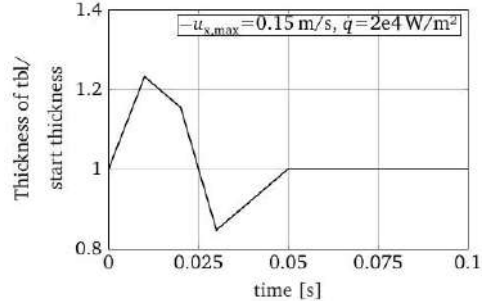


**Figure 4:** Evolution of the normalized thermal boundary layer thickness during saturated boiling with  $p = 0.9$  bar,  $u_{x,max} = 0.15$  ms<sup>-1</sup>,  $\dot{q} = 2e4$  Wm<sup>-2</sup>

## References

Batzdorf, S., Heat Transfer and Evaporation during Single Drop Impingement onto a Superheated Wall, PhD Thesis, Technische Universität Darmstadt (2015)

Hardt, S., Wondra, F., Evaporation Model for Interfacial Flows Based on a Continuum-Field Representation of the Source Terms, Journal of Computational Physics, Vol. 227, pp. 5871-5895 (2008)

Siegel R., Effects of Reduced Gravity in Heat Transfer, Advances in Heat Transfer, Vol. 4, pp. 143-228 (1967)

Stephan, P., Busse, C., Analysis of the Heat Transfer Coefficient of Grooved Heat Pipe Evaporator Walls, International Journal of Heat and Mass Transfer, Vol. 35, pp. 383-391 (1992)

## Cleaning injectors with dual orifice nozzles for aviation gas turbines using vortex ejector: experimental research.

Oleg A. Yevdokimov<sup>1</sup>, Shota A. Piralishvili<sup>1</sup>, Sergey V. Veretennikov<sup>1</sup> and Alexandr A. Elkes<sup>2</sup>

<sup>1</sup>P.A. Soloviev Rybinsk State Aviation Technical University University, Faculty of Aircraft Engines, Department of General and Technical Physics

Pushkina st., 173a, Rybinsk, 152934, Russian Federation

<sup>2</sup>PAO «NPO «Saturn», D-30KP/KU Department

Lenina av., 163, Rybinsk, 152903, Russian Federation

E-mail: yevdokimov\_oleg@mail.ru

A high-quality fuel atomization is connected with cleanliness conditions of the injectors' nozzles. Contamination of nozzles can lead to atomization uniformity reducing, NOx and CO emission increasing, burn-out of the combustion chamber.

Modern methods of fuel injectors cleaning based on its removing from engine, subsequent mechanical, chemical or/and ultrasonic cleaning and reinstalling the injectors. Such a procedure is rather expensive and time-consuming and requires temporary engine decommissioning.

One of the possible solutions of the problem described could be implemented for injectors with dual orifice nozzles mounted on fuel collector having two circuits for introducing fuel. The first (primary) circuit is usually associated with axial spray nozzles and the second circuit is connected with peripheral centrifugal nozzles. A special heated washing liquid is supplied to the inlet of the first circuit of the fuel collector, reaches nozzles and after that it turns to the second circuit of the fuel collector. Such a circulation of the washing liquid can be achieved through providing an evacuation at the inlet of the second circuit of the fuel collector. The design of the fuel injector is shown in the figure 1. The scheme of the circulation is shown in the figure 2.

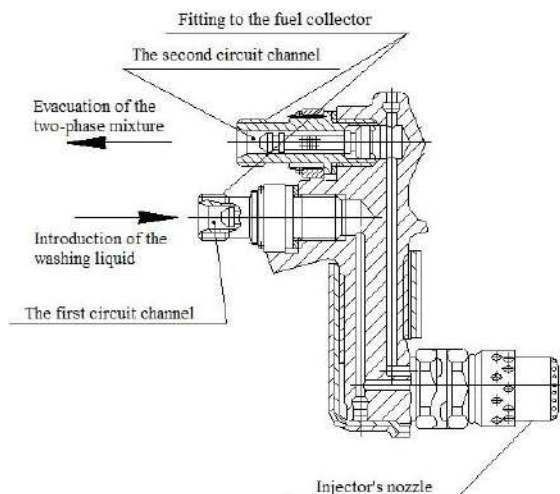


Figure 1: Design of the fuel injector

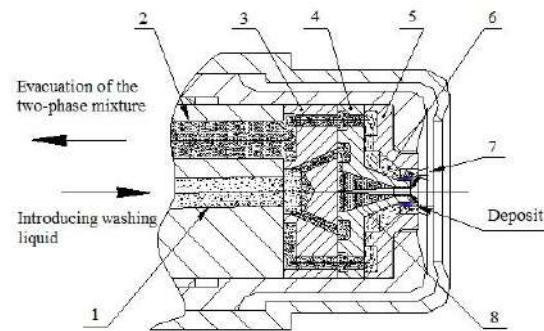


Figure 2: Scheme of the circulation of the washing liquid: 1) the first circuit channel; 2) the second circuit channel; 3) adapter; 4) atomizer of the first circuit; 5) atomizer of the second circuit; 6) two-phase mixture; 7) intaking washing liquid and air; 8) washing liquid.

Evacuation process is accompanied by two-phase flow of air and washing liquid that defines specific requirements for vacuum device. Many authors note (Suslov et al. 1985, Piralishvili et al. 2012, Biruk et al. 2014) that deep vacuum particularly in multiphase flows could be achieved using vortex ejectors. Ejectors are used in such sectors of industry, energy and construction where there is a necessity of low pressure, separation and mixing.

Experimental research was carried out for some sets of 12 injectors mounted on fuel collector of D-30KU aviation gas turbine (produced by NPO «Saturn», Russian Federation). Evacuation of air-liquid mixture was provided using vortex coflow ejector connected with the inlet of the second circuit of the fuel collector.

At the first stage it was defined an influence of the manometric pressure of washing liquid  $p_{wl}$  and evacuation pressure  $p_{vac}$  on circulation process. Experimental research has shown that circulation process is unsteady and pulsating. It leads to evacuation of air-liquid mixture by small portions and the dependence of evacuation pressure on time shown in the figure 3. Average pulsations frequency is equal to 1.15 Hz and defines value of mass fraction of washing liquid returned to the operation of 52%.

It is caused by unsteady choking effect when washing liquid enters the ejector: in this moment incompressible fluid close the ejector's inlet that leads to evacuation decreasing. Then washing liquid gets inside the ejector, evacuation starts anew and after that the process repeats itself.

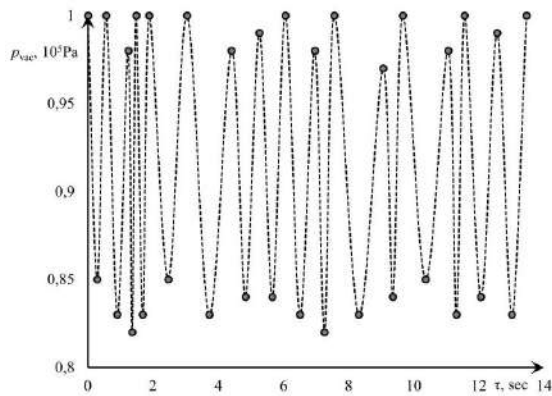


**Figure 3:** Dependence of absolute evacuation pressure  $p_{vac}$  on time  $\tau$ : pressure of washing liquid  $p_{wl} = 0.5 \cdot 10^5$  Pa

The problem of low return of washing liquid to the circulation process was solved by using damping capacity mounted between the vortex ejector and the inlet of the second circuit of the fuel collector. It has made it possible to exclude the choking effect and unsteady pulsations of evacuation pressure and to provide ejector operating on only air: washing liquid was accumulated in the damping capacity. The dependence of mass fraction of washing liquid returned to the operation  $g_{return}$  on absolute evacuation pressure  $p_{vac}$  for some values of manometric pressure of washing liquid  $p_{wl}$  is shown in figure 4.

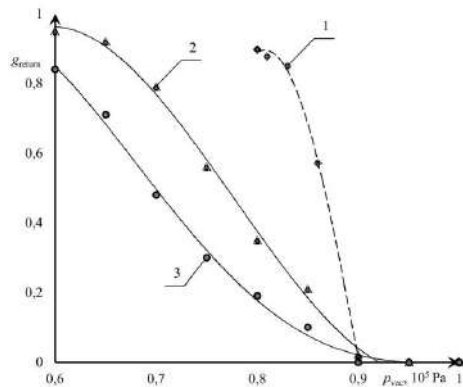


**Figure 4:** mass fraction of washing liquid returned to the operation  $g_{return}$  on absolute evacuation pressure  $p_{vac}$ : 1) pressure of washing liquid  $p_{wl} = 0.55 \cdot 10^5$  Pa; 2)  $p_{wl} = 1.0 \cdot 10^5$  Pa; 3)  $p_{wl} = 1.9 \cdot 10^5$  Pa

It was determined a significant effect of adhesion force on washing liquid flow near the injector's nozzle and liquid's surface-tension. It allows to formation of quasi-steady fluid film limited by nozzle's sidewalls and air flow ejected. This process is visualized in figure 5.

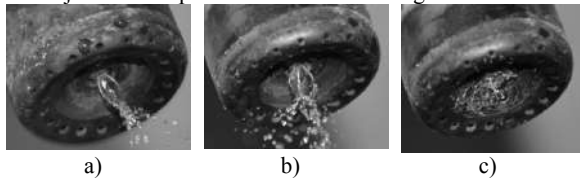


**Figure 5:** Visualisation of washing liquid's evacuation  $p_{wl} = 0.55 \cdot 10^5$  Pa: a)  $p_{vac} = 0.95 \cdot 10^5$  Pa; b)  $p_{vac} = 0.9 \cdot 10^5$  Pa; c)  $p_{vac} = 0.8 \cdot 10^5$  Pa

Experimental results of the research of cleaning quality for two freely selectable injectors are shown in figure 6. It is seen that cleaning injector's nozzle without washing liquid circulation does not provide required visual quality and total deletion of lacquer and soot deposit.

Check experiments for definition of cleaning quality using aviation kerosene and parameters of atomization have shown that the required cleanness of nozzles can be reached by means of 90 minutes circulation of washing liquid through the fuel collector. Such a procedure provides a compliance with the requirements of injectors' maintenance

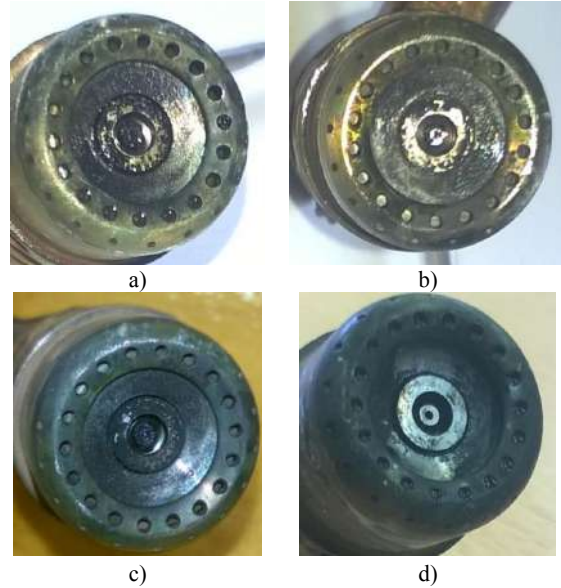


**Figure 6:** Photos of injectors' nozzles: a) injector №1 before cleaning; b) injector №1 after cleaning without circulation of washing liquid; c) injector №2 before cleaning; d) injector №2 after cleaning with circulation of washing liquid

The research is carried out at financial support of Russian Foundation for Basic Research, the Agreement on grant №16-08-00974 from 29.02.2016.

## References

- Suslov A.D., Ivanov S.V., Murashkin A.V., Chizhikov Yu. V., Vortex devices, Mashinostroenie, 256 p (1985)
- Piralishvili Sh.A., Ivanov R.I. Calculation and experimental investigation of mixture formation in a vortex mixer, Russian Aeronautics (Iz VUZ), Vol. 55, No. 2 pp. 179–183 (2012)
- Biruk V.V., Veretennikov S.V., Guryanov A.I., Piralishvili Sh.A., Vortex effect. Technical applications. Vol. 2 Part 2, Nauchteclitizdat, 288 p. (2014)

## Laser-induced thermocapillary instabilities in two-layer systems

D. S. Klyuev and N. A. Ivanova

Photonics and Microfluidics Laboratory, Tyumen State University, Volodarskogo 6, 625003, Tyumen, Russia,  
n.ivanova@utmn.ru

Thermocapillary convective instabilities in two-layer systems is of great importance in natural processes and industrial applications (Nepomnyashchy et al. 2012). Most of works are devoted to the case of interfacial instabilities in two-layer liquid systems confined two rigid walls where heating is applied to either the bottom or the upper wall (Nepomnyashchy et al. 2012, Juel et al. 2000) or alternatively to the interface (Chraïbi and Delville 2014). Depending the direction of the temperature gradient different types of instabilities can arise in the liquid-liquid systems due to competition between thermocapillary of buoyancy mechanisms.

The liquid-liquid systems with an unbounded upper layer - a free surface of the upper layer are studied in molten material in microgravity experiments (Doi and Koster 1993). In a few works, such configuration was studied as a prototype of a sensitive IR visible image converter (Loulergue et al. 1981). In this situation, a patterned deformation of the upper liquid layer is induced by heating the liquid-liquid interface with a spatially modulated IR laser beam.

In the present work, we demonstrate a new kind of oscillatory instability arising in the two-layer systems under a local heating of the light-absorbing liquid-liquid interface with the laser beam.

The experimental method is shown in Fig. 1. Two-layer system (L1 – a bottom layer, L2 – an upper layer) was created in Petri dish 60 mm in diameter. The thickness of the L1 layer was fixed at 2.2 mm, while the thickness of the L2 layer was varied from 0.3 to 1 mm. The L1 liquid was colored with Brilliant Green to enable the absorption of the irradiation of the He-Ne laser (20 mW, 632.8 nm), and the L2 liquid was transparent. When the laser irradiation is absorbed by the L1 liquid temperature at the L1-L2 interface increases and after a lag time  $\tau_d = h_{L2}^2 / 4\kappa_{L2}$  required for the diffusion across the L2 liquid, temperature at the free surface of the L2 locally increases as well. Here  $h_{L2}$  and  $\kappa_{L2}$  are the thickness and the thermal diffusivity of the L2 liquid. The local heating produces a thermally dependent surface tension gradient along the free interface resulting in a thermocapillary depression of the L1, Fig. 1. The laser beam, partially reflected from the thermocapillary depression forms on a remote screen a circular interference pattern called as the photothermocapillary (PTC) signal), Fig. 1. The diameter of the PTC signal is changed in accordance with the size of the thermocapillary depression. Further, the time evolution of the diameter of the PTC signal was measured to obtain a quantity information about the processes in the systems studied. Several pairs of immiscible liquids listed in Table were investigated.

**Table:** Liquid combinations used the experiments.

L1 liquid (bottom)	L2 liquid (upper)
Glycerol (60 mN/m, 1300 cS @ 20°C)	20 cS Silicon oil
Ethylene Glycol (48 mN/m, 20 cS @ 20°C)	20 cS Silicon oil
Benzyl Alcohol (37 mN/m, 5.8 cS @ 20°C)	5 cS Silicon oil 10 cS Silicon oil 20 cS Silicon oil

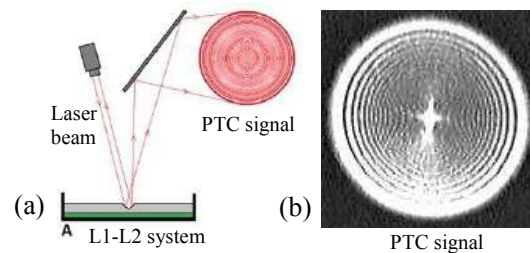


**Figure 1:** (a) Schematic view of the experimental method. (b) An image of the typical photothermocapillary (PTC) signal.

In the course of experiments, three modes of the thermocapillary convection were identified:

(i) The steady state *thermocapillary rupture* of the L2 - during the laser irradiation, an increase of the PTC signal changes to a degeneracy of the fringe pattern, which corresponds to the reflection of the laser beam from a flat layer, Fig. 2a;

(ii) The steady state *thermocapillary depression* - the PTC signal increases until reaching the constant size;

(iii) A transient mode - *the decaying oscillations* of PTC signal are observed, Fig. 2b. In this case, the thermocapillary rupture of the L2 and its consequent recovering is repeated periodically with the decaying amplitude until the L2 layer become the flat.

It was found that for the pairs of Glycerol/Silicon oils and Ethylene Glycol/Silicon Oils only (i) and (ii) modes take place depending on the thickness of the L2. Such behavior is similar to that of the laser induced thermocapillary convection in a single layer on a solid surface. That similarity allows for concluding that the L1 may serve as a rigid substrate. However, in case of the Glycerol/Silicon oil pair a convex deformation of the L1 in the area of the laser spot

was observed, Fig. 3, hence the vortex flows in the L1 take place.

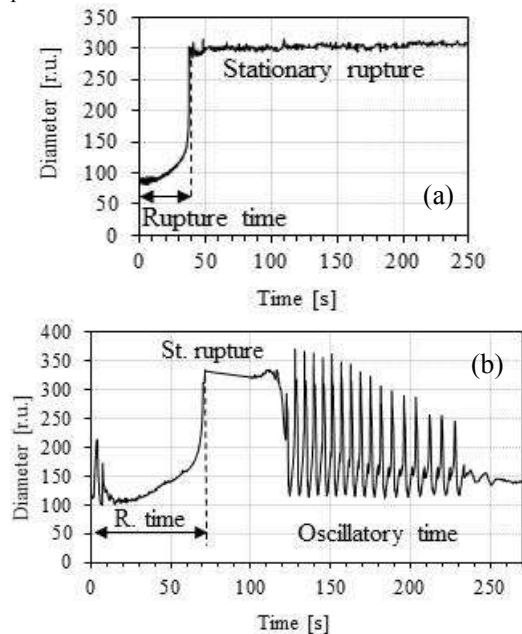


**Figure 2:** The diameter of the PTC signal vs. time: (a) the thermocapillary rupture mode, (b) the decaying oscillations mode.



**Figure 3:** A side-view image of the thermocapillary rupture in the Glycerol/Silicon oil pair.

The Benzyl alcohol/Silicon oil systems demonstrate all three modes depending on the thickness ratio -  $\varepsilon = h_{L2}/h_{L1}$ : (i) the thermocapillary rupture of the L2 layer is observed at  $\varepsilon < 0.3$ , (ii) the thermocapillary depression of the L2 layer takes place at  $\varepsilon > 0.4$ , and (iii) the decaying oscillations of the diameter of the PTC signal is observed at  $\varepsilon$  laying in between 0.3 to 0.4.

We have determined that a decrease of the thickness of the L2 ( $\varepsilon$  decreases) leads to the increase of the oscillation time, and to the decrease in the PTC signal amplitude and the period of oscillations. For example, the increase of  $\varepsilon$  from 0.3 to 0.4 the oscillation time increases from around 200 to 400 sec, and the period of the oscillations decreases from 7 to 3 sec. Meanwhile, the viscosity of the L2 liquid affects only the rupture time.

We have surmise that the mechanism behind the oscillations itself is due to the competition between thermocapillary and solutocapillary forces, which act in opposite directions. When the thermocapillary rupture of the L2 liquid occurred, the L1 liquid becomes free, which in turn

causes opposite surface tension gradient due to the difference in surface tension between two liquids.

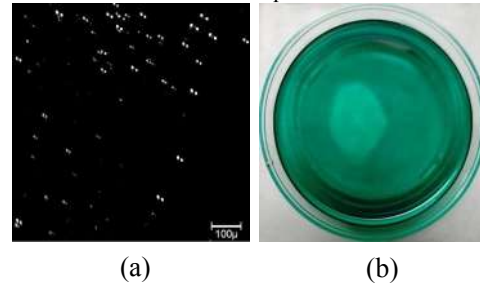


**Figure 4:** (a) The micrograph of bubbles. (b) A top view image of the two-layer system with the bubble cluster.

The decaying of oscillations is caused by an appearance of smallest bubbles ( $\sim 50 \mu\text{m}$  in diameter) at the L1-L2 interface in the laser spot area, Fig. 4(a). The population of bubbles grows with time irradiation resulting in a formation of dense bubble cluster, which is observed as a white spot, Fig. 4(b). The bubble cluster scatter the laser radiation and, therefore, prevent the absorption of the light energy. This fact cases to the decrease of the temperature gradient require to generation of the thermocapillary flows, as a result the oscillations decay.

To clarify the bubbles formation mechanism more experimental investigations to be done.

**Acknowledgments:** The research was supported by the RFBR (Grant no. 17-08-00291) and the Ministry of Education and Science of the Russian Federation (Grant no. 1019).

## References

- Nepomnyashchy A., Simanovskii I., Legros J.C., *Interfacial Convection in Multilayer Systems*, Springer Science (2012).
- Juel A., Burgess J.M., McCormick W.D., Swift J.B., Swinney H.L., Surface tension-driven convection patterns in two liquid layers, *Physica D*, Vol. 143, pp. 169–186 (2000).
- Chraïbi H., Delville J-P., Thermocapillary flows and interface deformations produced by localized laser heating in confined environment, *Phys. Fluids*, Vol. 24, pp. 032102 (2012).
- Doi T., Koster J.N., Thermocapillary convection in two immiscible liquid layers with free surface, *Phys Fluid A*, Vol. 5, pp. 1914-1927 (1993).
- Loulergue J. C., Manneville P., Pomeau Y., Interface deflections induced by the Marangoni effect: an application to infrared visible image conversion, *J. Phys. D*, Vol. 14, pp. 1967 (1981).

## Modeling of the liquid and gas flows with evaporation at interface based on exact solutions

Ekaterina Rezanova<sup>1</sup> and Yuriy Lyulin<sup>2,3</sup>

<sup>1</sup>Altai State University, Faculty of Mathematics and Information Technologies, pr. Lenina, 61, Barnaul, 656049, Russia

<sup>2</sup>Kutateladze Institute of Thermophysics SB RAS, 1, Ac. Lavrentyieva ave., Novosibirsk, 630090, Russia

<sup>3</sup>Novosibirsk State University, 2, Pirogov Ave., 630090, Novosibirsk, Russia

katerezanova@mail.ru

The nonisothermal fluid flows, complicated by the evaporation processes under action of a gas flow are actively studied experimentally and analytically nowadays. The development of mathematical models of convective motions taking into account the processes of heat and mass transfer at the interface are devoted the works by Goncharova et al. The problem of studying solutions of a special type for description of the two-layered or multilayered flows of liquids attracts a particular interest. The liquid flows in the infinite layers accompanied by a co-current gas flux and with evaporation at a thermocapillary interface are investigated theoretically and experimentally. The system of differential equations based on the Oberbeck-Boussinesq approximation of the Navier-Stokes equations (Andreev et al. 2012) is used to model the two-layer flows. Concentration of the vapor in the gas layer is determined with the help of the diffusion equation. The Soret and Dufour effects are taken into account by modelling of the gas-vapor mixture flows.

The objective of the work is analytical study of the gas-liquid flows with account for evaporation at interface, as well as validation of theoretical model based on exact solution using experimental data.

Let the solution of the equations have a special type (see Birikh 1969 and Gonchrova et al. 2013, 2014). The unknown functions are characterized by the following polynomial dependencies:

$$\begin{aligned}
 u_i &= \frac{y^4}{24} L_4^i + \frac{y^3}{6} L_3^i + \frac{y^2}{2} c_1^i + y c_2^i + c_3^i, \\
 T_i &= (a_1^i + a_2^i y)x + \frac{y^7}{1008} N_7^i + \frac{y^6}{720} N_6^i + \frac{y^5}{120} N_5^i + \frac{y^4}{24} N_4^i + \\
 &\quad + \frac{y^3}{6} N_3^i + \frac{y^2}{2} N_2^i + y c_4^i + c_5^i, \\
 C &= (b_1 + b_2 y)x + \frac{y^7}{1008} S_7 + \frac{y^6}{720} S_6 + \frac{y^5}{120} S_5 + \frac{y^4}{24} S_4 + \\
 &\quad + \frac{y^3}{6} S_3 + \frac{y^2}{2} S_2 + y c_6^i + c_7^i, \\
 p'_i &= \left[ d_3^i \frac{y^2}{2} + d_2^i y + d_1^i \right] x + \frac{y^8}{8} K_8^i + \frac{y^7}{7} K_7^i + \\
 &\quad + \frac{y^6}{6} K_6^i + \frac{y^5}{5} K_5^i + \frac{y^4}{4} K_4^i + \frac{y^3}{3} K_3^i + \frac{y^2}{2} K_2^i + y K_1^i + c_8^i.
 \end{aligned}$$

Here the index  $i$  is responsible for belonging to the liquid layer if  $i = 1$  or to the gas layer if  $i = 2$ ,  $u_i$  is the longitudinal velocity function,  $T_i$  is the temperature,  $C$  is the vapor concentration,  $p'_i$  is the deviation from the hydrostatic pressure. The coefficients  $L_4^i, L_3^i, N_j^i, S_j, K_m^i$  are expressed in terms of physical parameters of the problem.

The coefficients of integration  $c_j^i$  ( $i=1, 2; j=1, \dots, 8$ ) are determined with the help of the boundary conditions.

On the upper and lower fixed boundaries, the temperature is distributed linearly with respect to the longitudinal coordinate  $x$  and the no-slip conditions for the velocity are imposed. The vapor concentration on the upper boundary is equal to zero.

On the thermocapillary interface the conditions of the velocity and temperature continuity are set, the kinematic condition is fulfilled automatically. Projections of the dynamic condition can be written as follows:  $\rho_1 v_1 u_{1y} = \rho_2 v_2 u_{2y} + \sigma_T T_{1x}$ ,  $p_1 = p_2$  ( $\rho_i$  are the densities,  $v_i$  are the kinematic viscosities of liquid and gas,  $\sigma_T$  is the temperature coefficient of the surface tension  $\sigma$ ,  $\sigma = \sigma_0 + \sigma_T(T - T_0)$ ). The heat transfer condition has the form:  $\kappa_1 T_{1y} - \kappa_2 T_{2y} - \delta \kappa_2 C_y = -\lambda M$  (here  $\kappa_i$  are the thermal conductivity coefficients,  $\delta$  characterizes the Dufour effect,  $\lambda$  is the latent heat of evaporation,  $M$  is the evaporation mass flow rate supposed here being constant). A mass balance equation at the interface can be written as follows:  $M = -D \rho_2 (C_y - a T_{2y})$ , where  $D$  is the coefficient of vapor diffusion,  $a$  characterizes the Soret effect. The saturated vapor concentration is determined with the help of the relation  $C = C_* [1 + \varepsilon(T_{2y} - T_0)]$  as the result of the Clapeyron-Clausius equation and Mendeleev-Clapeyron equation for the ideal gas ( $C_*$  is the saturated vapor concentration at  $T_2 = T_0$ ,  $T_0$  is a some initial temperature,  $\varepsilon = \lambda \mu / R T_0^2$ ,  $\mu$  is the molar mass of the evaporating liquid,  $R$  is the universal gas constant). The gas flow rate  $Q$  in the upper layer is given.

The exact solutions allow us to study the dependence of flow structure, distribution of temperature and vapor concentration and the intensity of evaporation of liquid on such parameters as the gas flow rate, longitudinal temperature gradients, liquid layer thickness, intensity of the gravitational fields (Goncharova et al. 2013-2015).

The two-layer system, where the lower and upper layers are filled by HFE7100 (liquid) and nitrogen (gas) respectively is considered. In the course of experimental studies the formulas were obtained, which determine the dependence of the evaporation rate on the gas flow velocity and temperature of the liquid and gas (Lyulin, Kabov 2013, 2014). The linear approximation of the experimental data is used for comparison of the experimental and analytical results.

The results of investigation of the mass flow rate  $M$  as a function on the gas flow rate  $Q$  have been obtained experimentally and with help of the analytical formulas. They are presented in Fig. 1 and 2. Fig. 1 shows the dependence of the evaporation intensity on the gas flow rate for the liquid layer thickness of  $0.5 \cdot 10^{-2}$  m and the

longitudinal temperature gradient  $A_1$  ranges from -15 K/m to -80 K/m. Fig. 2 presents the case of the liquid layer thickness of  $0.3 \cdot 10^{-2}$  m and the temperature gradient  $A_1$  has the values -90 K/m and -100 K/m. The intensity of the liquid evaporation increases with increasing of the gas flow rate. This effect occurs by extension of the vapor concentration gradient in the gas phase. The mass flow rate of evaporation increases with the increase of the temperature in the channel, that agrees with the experiments well enough. Analytical calculations are performed for two-dimensional case and did not take into account all the factors that are presented in the experiment. However, both figures illustrate qualitative agreement between the experimental and analytical results of investigations of dependence of the evaporating mass flow rate  $M$  on the gas flow rate.

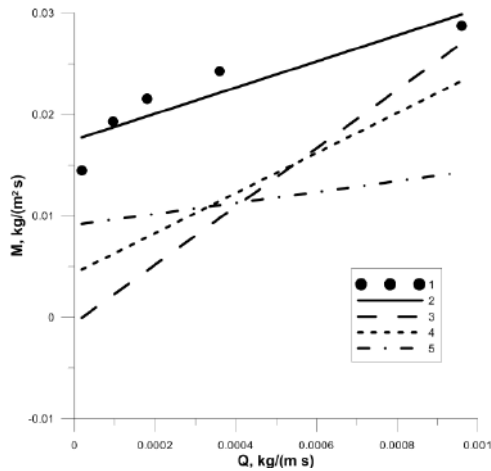


**Figure 1:** Dependence of the evaporation intensity on the gas flow rate.  $h = 0.5 \cdot 10^{-2}$  m,  $l = 0.5 \cdot 10^{-2}$  m (1 – experimental data; 2 – trend line of the experimental data; 3 – calculations at  $A_1 = -80$  K/m; 4 – calculations at  $A_1 = -55$  K/m; 5 – calculations at  $A_1 = -15$  K/m).

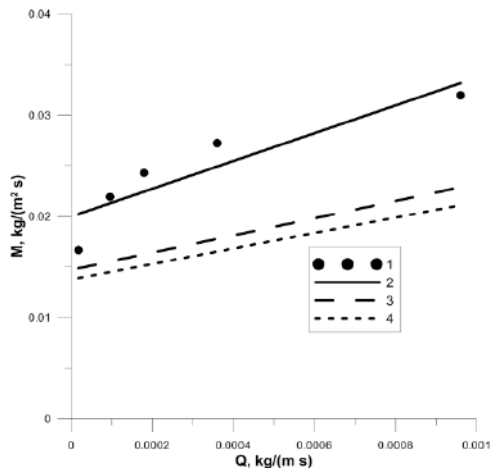


**Figure 2:** Dependence of the evaporation intensity on the gas flow rate.  $h = 0.5 \cdot 10^{-2}$  m,  $l = 0.3 \cdot 10^{-2}$  m (1 – experimental data; 2 – trend line of the experimental data; 3 – calculations at  $A_1 = -100$  K/m; 4 – calculations at  $A_1 = -90$  K/m).

**Acknowledgments.** The study was financially supported by the Russian Science Foundation (Project 15-19-20049).

### References

Andreev V.K., Gaponenko Yu.A., Goncharova O.N., Pukhnachov V.V. Mathematical models of convection (de Gruyter Studies in Mathematical Physics), Berlin/Boston: De Gruyter (2012).

Birikh R.V., Thermocapillary convection in a horizontal layer of liquid, J. Appl. Mech. Tech. Phys. №3 pp 43-45 (1969).

Goncharova O.N., Hennenberg M., Rezanova E.V., Kabov O.A. Modeling of the convective fluid flows with evaporation in the two-layer systems, Interfacial phenomena and heat transfer, Vol. 1. № 4 pp 317-338 (2013).

Goncharova O.N., Rezanova E.V. Example of an exact solution of the stationary problem of two-layer flows with evaporation at the interface, Journal of Applied Mechanics and Technical Physics №55(2) pp 247-257 (2014).

Goncharova O.N., Rezanova E.V., Lyulin Yu.V., Kabov O.A. Modeling of two-layer liquid-gas flow with account for evaporation, Thermophysics and Aeromechanics, № 5 pp. 631-637 (2015).

Lyulin Yu.V., Kabov O.A., Measurement of a mass velocity of evaporation in a horizontal partially open liquid layer into a moving gas, Technical Physics Letters № 39(17) pp 88-94 (2013).

Lyulin Yu.V., Kabov O.A. Evaporative convection in a horizontal liquid layer under shear-stress, Int. Journal of Heat and Mass Transfer, Vol. 70 pp 599-609 (2014).

## Modeling dry spots in isothermal liquid films on a horizontal substrate at different gravity

L.I. Maltsev, Yu.S. Podzharov, and O.A. Kabov

Kutateladze Institute of Thermophysics SB RAS, 1 Lavrentyev Ave.  
Novosibirsk, 630090, Russian Federation,  
Maltzev@itp.nsc.ru

Processes in liquid films are widely used in industry, in particular, for heat and mass transfer intensification. At that, the decrease in film thickness allows substantially increasing the efficiency of the method. Submicron liquid film formed on the boundary of dry spots due to intensive evaporation can make a major contribution to the total heat and mass transfer (Ajaev and Kabov 2017). Zaitsev et al. (2009) in the film flow regimes with small-scale washed out dry spots obtained the heat flux by an order exceeding the one, realized in the continuous film flow under the same fluid flow rate. However, thin films are subject to break-off, which drastically reduces the efficiency of devices and can lead to their malfunctioning (Ajaev et al. 2016, Ajaev 2013). Analysis of mechanisms of dry spots forming in the films and their modeling are covered in numerous experimental and theoretical works (Bankoff 1971, Chung and Bankoff 1980, Podgorsky et al. 1999, Maltsev and Zavarzin 2012, El-Genk and Saber 2001, Kadoura and Chandra 2013, El-Genk and Saber 2002, Kabov 2000, Zaitsev et al. 2004, Maltsev and Kabov 2016). In theoretical works on film break-off modeling, the cross-section of the free boundary of the rim, surrounding the spot, as a rule, is approximated by circular arcs. This paper proposes a criterion for dry spots development in isothermal liquid films on a horizontal substrate, Fig.1. It is based on a strict solution of the problem about the form of free boundary of the rim around the stationary dry spot, formed under gravity and surface tension at a given value of the wetting angle.

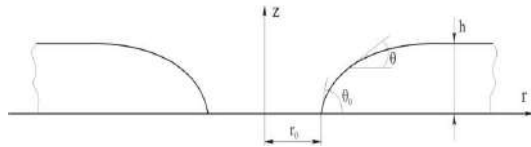


**Figure 1:** Cross section of liquid film with a round dry spot.

The equations for determining the shape of the free film boundary in the vicinity to the dry spot have the form:

$$\begin{aligned} \frac{d\theta}{d\tilde{S}} &= Bo(\tilde{z} - 1) - \frac{\sin \theta}{\tilde{r}} \\ \frac{d\tilde{z}}{d\tilde{S}} &= \sin \theta \\ \frac{d\tilde{r}}{d\tilde{S}} &= \cos \theta \end{aligned} \quad (1)$$

with initial conditions:

$$\theta(0) = \theta_0, \quad \tilde{r}(0) = \tilde{r}_0, \quad \tilde{z}(0) = 0,$$

where  $\tilde{z} = \frac{z}{h}$ ,  $\tilde{r} = \frac{r}{h}$ ,  $\tilde{S} = \frac{S}{h}$ ,  $S$  is the angular

coordinate of free boundary points starting from the point of contact with the substrate,  $\theta_0$  is the wetting angle,

$\tilde{r}_0$  is the dimensionless radius of the dry spot,

$Bo = \frac{\rho g h^2}{\sigma}$  is the Bond number.

The system of equations is solved by variational method relative to  $\tilde{r}_0$ . The criterion of solution is the condition of free boundary smoothness at the point of transition of the curved surface of liquid-gas interface into the linear one ( $\tilde{z} = 1$ ). The variation is convenient to make by bisecting.

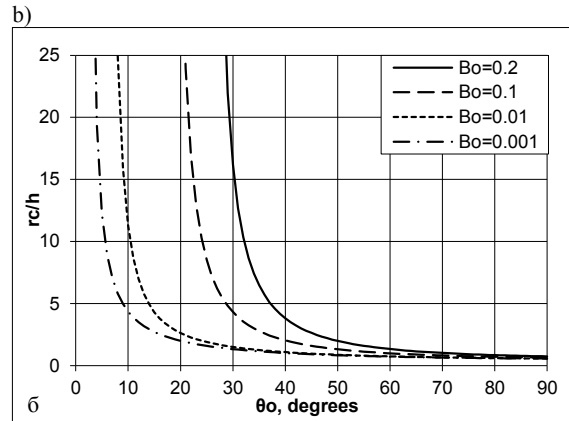
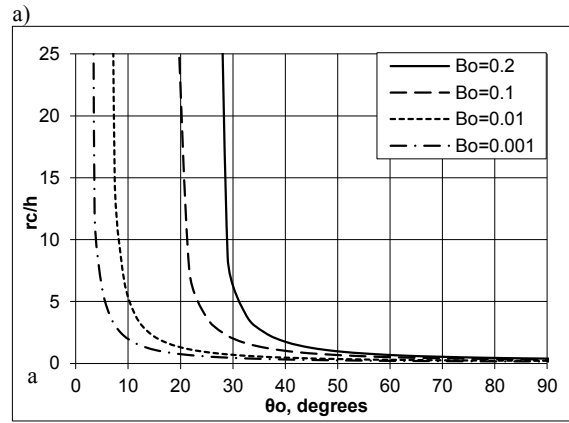


**Figure 2:** Critical radius of the dry spot, depending on the wetting angle at various Bo numbers, obtained by solving system (1) (a) and in the variant of approximation of the free boundary of the cylinder cross section by the circular arc (b).

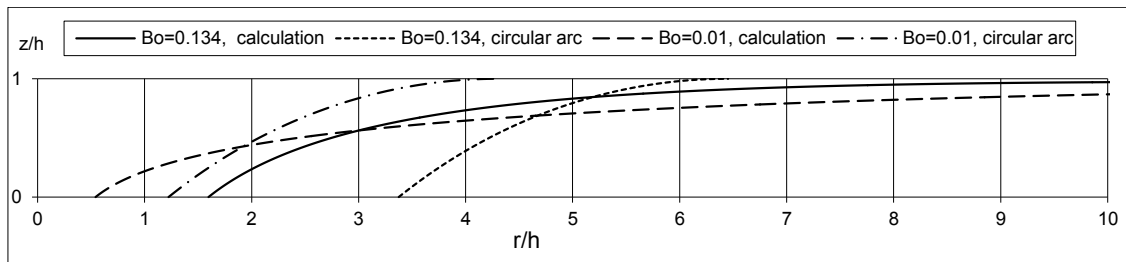


**Figure 3:** Comparison of the equilibrium shape of the free boundary of a rim, built by proposed method, and the shape, obtained by approximating the free boundary by the circular arc, when  $\theta_0=36^\circ$ , for two values of Bo number.

Thus, the solution of the system of equations (1) at specified Bo number and wetting angle allows for precise (with no additional simplifications) determination of the form of the free film surface in the immediate vicinity of the equilibrium dry spot and, in particular, determining the critical size of dry spots  $r_c$ . As mentioned above, the film thickness in the vicinity of the dry spot has great effect on the intensity of heat and mass transfer processes. Therefore, the accuracy of determining the geometry of the film in the area of the dry spot is extremely important to analyze the operation of heat exchange devices.

Comparison of the results of calculating the exact shape of the free surface with the ones from approximation by a circular arc shows that the use of approximation leads to a 2-3 times increase in the critical radius of the dry spot (Fig.2). Figure 3 shows the form of the free boundary of the rim, built as a result of solving the problem in exact statement and approximating free boundaries by circular arcs. Obviously, the form of the free film boundary in the vicinity of dry spots varies significantly as a result of the usage of two approaches.

It is known (Maltsev and Kabov 2016) that with decreasing Bond number (for example, due to reduced acceleration of free fall or, in other words, changes in the overload value) the impact of this parameter on the development of dry spots is reduced. Calculations show that the error in determining the critical radius of the dry spot due to approximation also decreases at Bo number decrease.

The study was financially supported by the grant of Russian Science Foundation (project 14\_19\_01755).

## References

Vladimir S. Ajaev, Oleg A. Kabov, Heat and mass transfer near contact lines on heated surfaces, *Int. J. of Heat and Mass Transfer*, Vol. 108 pp. 918 – 932 (2017)

Zaitsev D.V., Rodionov D.A., Kabov O.A., *Technical Physics Letters*, Vol. 35 pp. 680 – 682 (2009)

Vladimir S. Ajaev, Elizaveta Ya. Gatapova, Oleg A. Kabov, Stability and break-up of thin liquid films on patterned and structured surfaces, *Advances in Colloid and Interface Science*, Vol. 228 pp. 92-104 (2016)

Ajaev V.S., *Instability and Rupture of Thin Liquid Films on Solid Substrates, Interfacial Phenomena and Heat Transfer*,

Vol.1 pp. 81 – 92 (2013)

Bankoff S.G., Minimum thickness of a draining film, *Int. J. Heat Mass Transf.*, Vol.14. pp. 2143-2145 (1971)

Chung J.C. and Bankoff S.G., Initial Breakdown of a Heated Liquid Film in Cocurrent Two-component Annular Flow: II. Rivulet and dry patch models, *Chemical Eng. Comm.*, Vol. 4(455) (1980)

Podgorsky T., Flesseles J.-M., Limat L. Dry arches within flowing films, *Phys. of Fluids*, Vol. 11 pp. 845-852 (1999)  
Maltsev L.I. and Zavarzin D.S., *Thermophysics and Aeromechanics*, Vol. 19 pp. 607–614 (2012)

El-Genk M.S., Saber H.H., *International Journal of Heat and Mass Transfer*, Vol. 44. pp. 2809–2825 (2001)

Kadoura M., Chandra S., *Experiments in Fluids*, Vol. 54 p. 1465 (2013)

El-Genk M.S., Saber H.H., *J. Heat Transfer*, Vol. 124 pp. 39–50 (2002)

Kabov O.A., *Thermophysics and Aeromechanics*, Vol. 7 pp. 513–520 (2000)

Zaitsev D.V., Kabov O.A. Cheverda V.V. and Bufetov N.S., *High Temperature*, Vol. 42 pp. 449 – 455 (2004)

Leonid Maltsev and Oleg Kabov, Criterion for dry spot development in isothermal liquid film on a horizontal substrate, *MATEC Web of Conferences* Vol. 84(000) (2016)

## Calculation of the surface tension and its temperature coefficient based on the data on thermocapillary deformations in locally heated horizontal liquid layer

Ella Barakhovskaia and Igor Marchuk

Novosibirsk State University  
2 Pirogova Str, Novosibirsk, 630090, Russia  
Kutateladze Institute of Thermophysics  
1 Pr. Lavrentyeva, Novosibirsk, 630090, Russia  
ella94@bk.ru

At the present time there is an actual problem of using thermocapillary effect in identifying of liquids properties. In horizontal layers of investigated liquids it can be made a liquid identification based on the individual characteristics of thermocapillary flows and deformations. Thermocapillary effect is a basic idea in a range of methods for studying the chemical composition and properties of different liquids. To a great extent the thermocapillary effect occurs while thin liquid layers are locally heated. It is perspective to use the thermocapillary effect to determine the properties and the thickness of the thin liquid locally heated layer (Bezuglyi and Fedorets 2001).

This paper presents a method for calculating the surface tension coefficient  $\sigma$  and surface tension temperature coefficient  $\sigma_T$  based on the data on deformation dynamics in the locally heated horizontal liquid layer.

Direct problem about thermocapillary deformation in horizontal liquid layer with local heating in the centre of circle cuvette and inverse problem of determining the coefficients  $\sigma$  and  $\sigma_T$  are solved numerically in approximation lubrication theory for two-dimensional axisymmetric non-stationary case (Oron et al. 1997, Marchuk 2015). The model takes into account gravity, surface tension, thermocapillary effect, viscosity, heat transfer in the substrate and in the liquid. Evaporation rate is neglected. Initially the liquid surface is flat; the temperature of liquid is uniform. There is produced pulse heating by the substrate side with given power during 1 second. Liquid surface deformations are determined by the properties of the liquid, the substrate and the heater. Stationary solutions obtained by the establishment method. System scheme is shown in Fig. 1.

The essence of inverse problem is to identify properties of liquid:  $\sigma$  and  $\sigma_T$ . As additional information for solving inverse problem is used a function of thermocapillary response. This is a special experimentally measured function of laser beam diameter, reflected from the liquid surface and projected on a screen, dependence on the time, Fig. 1.

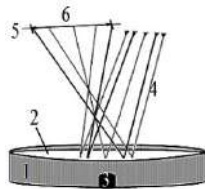


**Figure 1:** System scheme. 1 – fluoroplast cuvette  $d=36$  mm, 2 – liquid PMS-5 initial thickness is  $238 \mu\text{m}$ , 3 – heater  $d=1.6$  mm, 4 – laser beam, 5 – screen, 6 – diameter of the light spot.

A function of thermocapillary response is defined as:

$$dSp(t) = \max_{r \in [0, d_i/2]} \left| 2 \cdot |r - (d - h(i)) \cdot \text{tg}(2 \arctg(h'(i, dr)))| \right|,$$

where  $d_i$  – diameter of a laser beam,  $dr$  – step in direction  $r$ ,  $r = (i+1/2) \cdot dr$ ,  $h(i)$  – film thickness in node  $(i+1/2)$ ,  $h'(i, dr)$  – first derivative of thickness in  $(i+1/2)$  node,  $d$  – distance to the screen.

Liquid motion and deformations of its surface and, as a result, thermocapillary response are determined by the properties of the liquid, as well as the properties of the cuvette material, heater and heating characteristics. For different liquids, ceteris paribus, the kind of thermocapillary response is significantly different.

Numerical modeling is based on algorithms that had been developed for solving the direct problem of thermocapillary convection (Marchuk 2015, Barakhovskaia et al. 2016). Results obtaining by the solution of the direct problem about thermocapillary deformation in locally heated liquid layer provide the basis for solving the inverse problem of thermocapillary convection (Marchuk and Kabov 2015, Barakhovskaia et al. 2016).

The algorithm for solving inverse problem is based on solving problem of minimizing the residual function, that expresses the integral deviation of the measured response and calculated for certain values of the unknown coefficients. Using Newton's method minimum is solving numerically.

Residual function is shown in Fig.3 and is given as

$$J(\sigma^k) = \frac{1}{t_1} \int_0^{t_1} [dSp(\sigma^*) - dSp(\sigma^k, t)]^2 dt \geq 0,$$

where  $dSp$  – function of thermocapillary response,  $\sigma^*$  or  $\sigma_T^*$  – the exact value of the surface tension,  $t_1 = 5$  seconds measurement time.

It has been made numerical calculations for silicone oil (dimethylpolysiloxane) type PMS-5. Silicone oil PMS-5 is weakly evaporating liquid, so evaporation rate is neglected in the model.

In Fig.2 there are shown calculated thermocapillary responses for different values of the coefficients  $\sigma$  and  $\sigma_T$ . It can be seen that for different  $\sigma$  or  $\sigma_T$  the diameters of thermocapillary responses are significantly different. For the same heating power if initial thickness is increasing then variation of thermocapillary response values is significantly less. This is due to the strong dependence of the dynamics of the depth of thermocapillary deformation on initial thickness.

Ceteris paribus, the thinner layer the greater maximum amount of deformation is (Barakhovskaia et al. 2016).

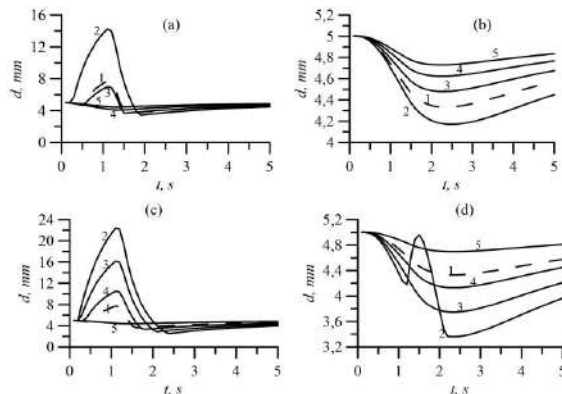


**Figure 2:** Thermocapillary response depending on different  $\sigma$  and  $\sigma_T$  for PMS-5, heating power  $Q=0,00165$  W, for different initial layer thickness: (a) –  $\sigma$ , 238  $\mu\text{m}$ ; (b) –  $\sigma$ , 538  $\mu\text{m}$ ; 1 – exact solution  $\sigma^*=0,01827$  N/m, 2 –  $\sigma=0,01$  N/m, 3 –  $\sigma=0,02$  N/m, 4 –  $\sigma=0,04$  N/m; 5 –  $\sigma=0,08$  N/m. (c)  $\sigma_T$ , 238  $\mu\text{m}$ ; (d)  $\sigma_T$ , 538  $\mu\text{m}$ ; 1 – exact solution  $\sigma_T^*=-0,000066$  N/m, 2 –  $\sigma_T=-1,6 \cdot 10^{-3}$  N/m, 3 –  $\sigma_T=-1,41 \cdot 10^{-3}$  N/m, 4 –  $\sigma_T=-1,04 \cdot 10^{-3}$  N/m; 5 –  $\sigma_T=-0,3 \cdot 10^{-3}$  N/m.

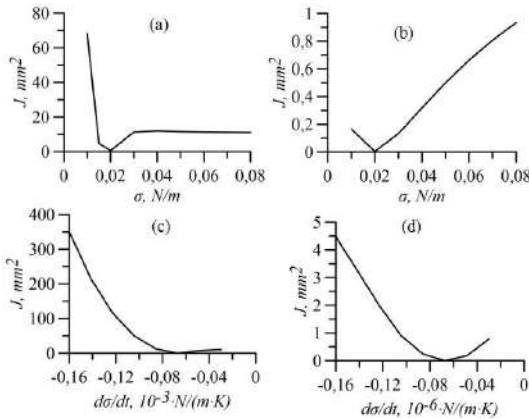


**Figure 3:** Residual function for  $\sigma$  and  $\sigma_T$  for layer of PMS-5 for different initial layer thickness: (a), (c) – 238  $\mu\text{m}$ ; (b), (d) – 538  $\mu\text{m}$ .

The results of the calculated functions  $J(\sigma)$  and  $J(\sigma_T)$  for different initial thicknesses of layer PMS-5 is shown in Fig.3. It can be seen that the functions are "good" in terms of solving the inverse problem: the forms of functions are convex and have unique minimum. This allows finding the minimum functions by Newton method for several iterations with a sufficiently high accuracy.

For a layer of silicone oil with an initial thickness of 538  $\mu\text{m}$  residual function has a better view than the initial layer with a thickness of 238  $\mu\text{m}$ , when all other things being equal. Note that for solving the problem of minimizing with the Newton method, in the case of the function  $J(\sigma)$  in Fig. 3a, it is necessary to follow the choice of the initial approximation close to the solution.

It has been developed algorithms and created calculating code for solving inverse problems for identifying

properties of liquid: surface tension and surface tension temperature coefficient. As additional information for solving inverse problem it is used function of thermocapillary response. This dependence is caused by thermocapillary deformations of liquid surface, which in its turn are determined by local heating of liquid. The developed algorithms have been tested on synthetic data, which has been obtained from the solution of direct problems. A good convergence and efficiency of the developed algorithms has been showed.

The study was financially supported by the Russian Science Foundation (Project 15-19-20049).

## References

- Bezuglyi B.A., Fedorets, A.A., Measuring the thickness of thin liquid films on solid surfaces using the laser-induced thermocapillary response, *Technical Physics Letters*, Vol. 27 pp. 359-361 (2001)
- Marchuk I.V. and Kabov O.A., Model of filmwise vapor condensation on curved surfaces // *Doklady Physics*, Vol. 61 pp. 19-23 (2016)
- Barakhovskaia E.V., Marchuk I.V., Fedorets A.A., Thermocapillary deformation in a locally heated layer of silicone oil, *Journal of Physics: Conference Series*, Vol. 754 pp. 1-6 (2016)
- Kabov O.A., Interfacial thermal fluid phenomena in thin liquid films, *International Journal of Emerging Multidisciplinary Fluid Sciences*, Vol. 2 pp. 87-121 (2010)
- Oron A., Davis S.H., Bankoff S.G., Long-scale evolution of thin liquid films, *Reviews of Modern Physics*, Vol. 69 pp. 931-980 (1997)
- Marchuk I.V., Thermocapillary deformation of a horizontal liquid layer under flash local surface heating, *Journal of Engineering Thermophysics*, Vol. 24 pp. 381-385 (2015)

## New correlations between critical parameters of liquid-vapor first-order phase transition

Ikhtier H. Umirzakov

Kutateladze Institute of Thermophysics  
Lavrenteva prospect, 1, Novosibirsk, 630090, Russia  
E-mail: umirzakov@itp.nsc.ru

The values of temperature, density and pressure at critical point of liquid-vapor first-order phase transition of most of substances, including metals and their compounds, are unknown because their critical points are unreachable for experimental methods. The equations of state of them which can help define critical parameters are also usually unknown. Therefore it is necessary to search correlations between known critical parameters of real substances to define unknown critical parameters of substances with unreachable critical point.

The following correlation:

$$T_c / T_B + \rho_c / \rho_B = 0.67, \quad (1)$$

where  $T_c$  and  $\rho_c$  are critical temperature and density,  $T_B$  and  $\rho_B$  are Boyle temperature and density, was established, and it was widely used to define critical density of metals by Apfelbaum and Vorob'ev (2016). Its inaccuracy is mainly defined by inaccuracy of defining of density, because the inaccuracy of defining of temperature is by two orders of magnitude less than that of density. We have established that for 11 substances (Ar, CH<sub>4</sub>, O<sub>2</sub>, N<sub>2</sub>, F<sub>2</sub>, C<sub>2</sub>H<sub>4</sub>, H<sub>2</sub>S, C<sub>2</sub>H<sub>6</sub>, C<sub>3</sub>H<sub>8</sub>, C<sub>4</sub>H<sub>10</sub>, CO<sub>2</sub>) with known parameters  $T_c$ ,  $\rho_B$ ,  $\rho_c$  and  $T_B$  (Magalinski, Sidorenko 1996), Eq. (1) has inaccuracy 2.3%, while the inaccuracy of density is by many times smaller. Therefore one needs the correlation which is much more accurate than Eq. (1). The compressibility factor

$$z(\rho, T) \equiv p(\rho, T) / \rho k T,$$

where  $p(\rho, T)$  is the pressure, for many pure substances obeys

$$z(\rho_1(T), T) = 1,$$

if (Nedostup and Galkevich 1970)

$$\rho_1(T) = \rho_B \cdot (1 - T / T_B).$$

From two latter equations one can obtain the relation

$$\frac{p(\rho_1(T), T)}{\rho_B k T_B} = \frac{T}{T_B} \cdot \left(1 - \frac{T}{T_B}\right) = \frac{\rho}{\rho_B} \cdot \left(1 - \frac{\rho}{\rho_B}\right).$$

We study this relation and establish correlation

$$\frac{T_c}{T_B} \cdot \left(1 - \frac{T_c}{T_B}\right) + \frac{\rho_c}{\rho_B} \cdot \left(1 - \frac{\rho_c}{\rho_B}\right) = 0.4377, \quad (2)$$

which has inaccuracy 0.3% (see Fig. 1). One can define critical density from (2) using known  $T_c$ ,  $T_B$  and  $\rho_B$ .

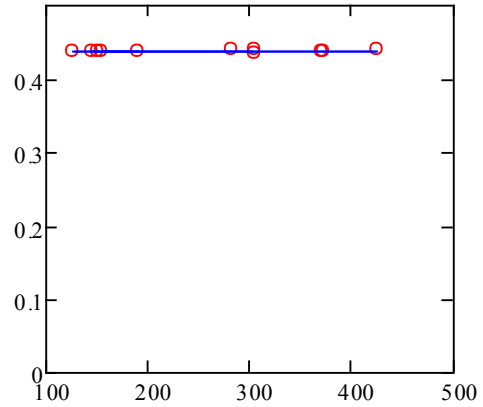


**Figure 1:** Dependences of of left (open circles) and right (solid line) hand sides of correlation (2) on critical temperature.

Using correlation (2) and Thimtermann's correlation (1950):

$$\frac{p_c m}{\rho_c k T_c} = \frac{\rho_c}{\rho_B}$$

the following correlations:

$$\frac{T_c}{T_B} \cdot \left(1 - \frac{T_c}{T_B}\right) + \frac{p_c m}{\rho_c k T_c} \cdot \left(1 - \frac{p_c m}{\rho_c k T_c}\right) = 0.4377 \quad (3)$$

$$\frac{p_c m}{\rho_B k T_B} = \frac{T_c}{4 T_B} \cdot \left(1 - \sqrt{4 \cdot \frac{T_c}{T_B} \cdot \left(1 - \frac{T_c}{T_B}\right) - 0.7508}\right)^2 \quad (4)$$

$$\frac{p_c m}{\rho_B k T_B} = \frac{\rho_c^2}{2 \rho_B^2} \cdot \left(1 - \sqrt{4 \cdot \frac{\rho_c}{\rho_B} \cdot \left(1 - \frac{\rho_c}{\rho_B}\right) - 0.7508}\right) \quad (5)$$

where  $p_c$  is critical pressure,  $k$  is Boltzmann's constant,  $m$  is mass of molecule or atom, are also

established. It is shown that using the correlations (2) and (3) one can define two of three critical parameters ( $T_c, p_c, \rho_c$ ) from one of them known, if  $T_B$  and  $\rho_B$  are known.

Timmermann's correlation and relation (1) give

$$\frac{p_c m}{\rho_B k T_B} = \frac{T_c}{T_B} \cdot \left( 0.67 - \frac{T_c}{T_B} \right)^2, \quad (6)$$

$$\frac{p_c m}{\rho_B k T_B} = \left( \frac{\rho_c}{\rho_B} \right)^2 \cdot \left( 0.67 - \frac{\rho_c}{\rho_B} \right), \quad (7)$$

Comparison of values of  $p_c / \rho_B k T_B$ , calculated from relations (4) and (6), with that of for 11 substances, is presented on Fig. 2. The same from relations (5) and (7) are presented on Fig. 3. The inaccuracies of (4) and (6) are equal to 4.4% and 12.3%, respectively. The inaccuracies of (5) and (7) are equal to 4.5% and 6.3%, respectively. As one can see, the correlations (4) and (5) are more accurate than the correlations (6) and (7).

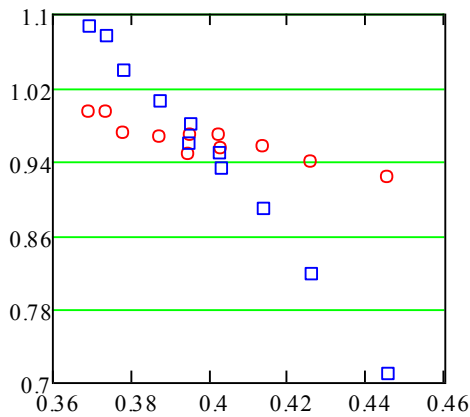


**Figure 2:** Comparison of dependence of ratio of  $p_c / \rho_B k T_B$  on  $T_c / T_B$ , calculated from correlations (4) (open circles) and (6) (squares), to that of for 11 substances.

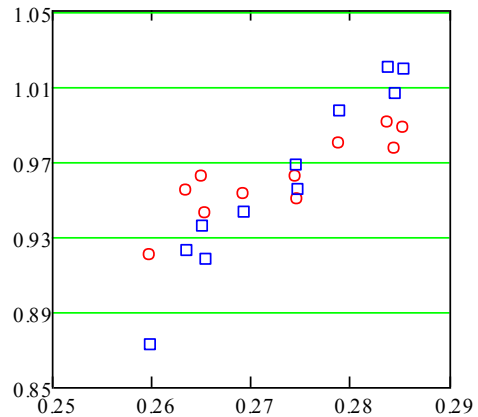


**Figure 3:** Comparison of dependence of ratio of  $p_c / \rho_B k T_B$  on  $\rho_c / \rho_B$ , calculated from correlations (5) (open circles) and (7) (squares), with that of for 11 substances.

## References

Vorob'ev V.S., Apfelbaum E.M., The generalized scaling laws based on some deductions from the van der Waals equation. High Temperature. Vol. 54, pp. 175-185 (2016).

Apfelbaum E.M., Vorob'ev V.S. The application of Zeno line similarities to alkaline earth metals. Journal of Molecular Liquids (2016).

Magalinski V.B., Sidorenko S.N. Statistical and thermodynamic methods in approached theory of condensed condition of matter. Moscow, Nauka, (1996).

Nedostup, V.I. and Gal'kevich, E.P., Raschet teplofizicheskikh svoystv gazov i zhidkosti metodom ideal'nykh krivykh (Calculation of the Thermodynamical Properties of Gases and Liquids by the Method of Ideal Curves), Kiev: Naukova Dumka (1986)

Timmermans, J., Physico-Chemical Constants of Pure Organic Compounds, Amsterdam: Elsevier (1950)

## Shape of self-sustained evaporation front

Oleg Sharypov, Denis Krasinsky

Kutateladze Institute of Thermophysics SB RAS  
Lavrentyev av., 1, Novosibirsk, 630090, Russia  
sharypov@itp.nsc.ru

The regime interesting from a scientific and technical point of view is observed in the experiments on the heat exchange during the boiling, with which occurs the propagation of steam layer along the cylindrical heater under the overheated conditions of the liquid higher than the boiling point at the assigned pressure. Known models don't describe the form of interphase surface.

The self-sustained front of evaporation in the overheated liquid along the flat heater is analytically investigated in the work. The shape of stationary interphase surface is analyzed in the framework approximate physical-mathematical model. The analytical dependence of the thickness  $y=f(x)$  of the steam layer on the coordinate and the physical parameters is obtained. It contains an integrable singularity at  $x=0$ . The solution is represented in the dimensionless invariant form in the variables  $\varphi = mx$ ,  $g = mf$ :

$$\varphi = (1 + g/2)\sqrt{g + g^2/4} - 2 \operatorname{Arsh}(\sqrt{g}/2),$$

here  $m$  is the governing parameter of the model, depending on the velocity of the evaporation front propagation, overheating, thermal conductivity and heat capacity of liquid, density of vapor and liquid, latent heat of evaporation.

In the figures 1-3 the comparison of the analytical solution with the experimental data for different physical conditions is represented.

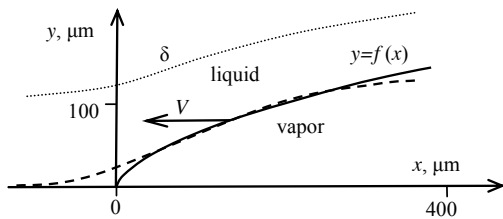


**Figure 1:** Analytical solution at  $m^{-1} = 20 \mu\text{m}$  (solid line) and experimental data (Pavlenko et al. 2014) for Freon-21: interphase surface (broken line) and thermal layer ( $\delta$ ).

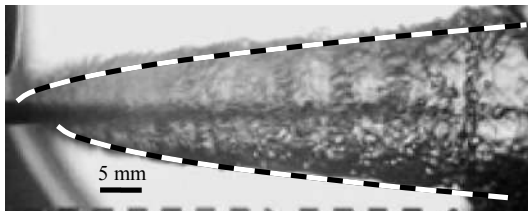


**Figure 2:** Analytical solution at  $m^{-1} = 400 \mu\text{m}$  (broken line) and photo of vapor cavity in acetone (Avksentyuk et al. 2008).

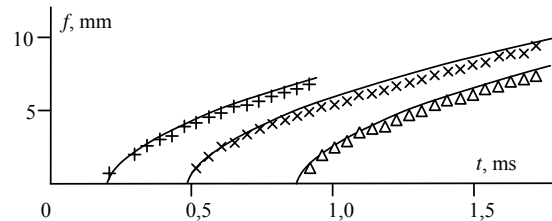


**Figure 3:** Analytical solution (solid line) and experimental data (Avksentyuk et al. 2004) for vapor cavity thickness in benzene.

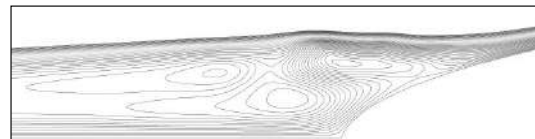


**Figure 4:** The flow lines in the stagnation zone near the forward section of the surface, streamlined with liquid (numerical simulation), the hydrodynamic parameters correspond to the conditions for the experiment (Pavlenko et al. 2014).

The numerical simulation of the flow pattern in liquid, which flows around about the impenetrable nondeformable surface, is carried out for the obtained analytical dependence. The distributions of the velocity and pressure in liquid are obtained. It is shown that near the forward section of the evaporation front the stagnation zone with the closed flow lines is formed in the liquid (see the figure 4).

The work is carried out with the financial support from Russian Foundation for Basic Research, grant No. 15-08-01359-a.

### References

- Avksentyuk B.P., Ovchinnikov V.V., The shape of a vapor cavity at explosive heterogeneous boiling, *Thermophysics and Aeromechanics*, Vol. 11, No. 4, pp. 609-616 (2004)
- Avksentyuk B.P., Ovchinnikov V.V., Third heat transfer crisis at subcooling, *Thermophysics and Aeromechanics*, Vol. 15, No. 2, pp. 267-274 (2008)
- Pavlenko A.N., Tairov E.A., Zhukov V.E., Levin A.A., Moiseev M.I., Dynamics of transient process at liquid boiling-up in the conditions of free convection and forced flow in a channel under nonstationary heat release, *Journal of Engineering Thermophys.*, Vol. 23, No. 3, pp. 173-193 (2014)

## Experimental and theoretical study of the flame propagation mechanism above the surface of the oxidant driven combustible liquid flowing in microchannels

Yu.O. Kabova<sup>1</sup>, V.V. Kuznetsov<sup>2</sup>, V.V. Zamazchshikov<sup>3</sup>, E.A. Chinnov<sup>1</sup>, O.A. Kabov<sup>1</sup>

<sup>1</sup>Kutateladze Institute of Thermophysics, SB RAS, 1 Lavrentyev prosp., Novosibirsk 630090, Russia,  
kabova@itp.nsc.ru

<sup>2</sup>Lavrentyev Institute of Hydrodynamics, SB RAS, 15 Lavrentyev prosp., Novosibirsk 630090, Russia  
kuznetsov@hydro.nsc.ru

<sup>3</sup>Voevodsky Institute of Chemical Kinetics and Combustion, SB RAS, 3 Institutskaya, Novosibirsk 630090, Russia  
albor@kinetics.nsc.ru

The tendency to reduce the characteristic dimensions of devices in various fields of technology determines the development of research on hydrodynamics and heat transfer in mini- and microchannels. Many papers dealing with the gaseous fuels combustion in narrow channels of various configurations have appeared recently. This is due to the great practical interest in miniature power sources, as well as heat and mechanical energy sources [1] that is due to the high energy density of hydrocarbon fuels relative to traditional electric power storage batteries.

When reducing the height of flat channels, the ratio of the channel surface to its volume increases inversely to its minimum transverse dimension that increases heat transfer coefficient in the microsystems. In terms of the processes occurring in reacting systems, such as for example, combustion of combustible liquids in small size channels, an increase in the heat transfer coefficient leads, as a rule, to a decrease in the mass burning rate. Ultimately, at a certain channel size, flame propagation reaches its limit [2]. On the other hand, high heat transfer coefficient in microsystems allows designing efficient heat exchangers, which can be useful also in terms of, for example, thermoelectric converters. In addition, under certain conditions, high heat transfer coefficient with the walls of the microsystem leads to the return of noticeable amount of heat, released due to chemical transformation, into the original mixture, that makes possible the combustion even where the characteristic size of the system is less than the critical value. Therefore, the study of combustion processes in microsystems is important to develop new applications and enhance existing technical solutions.

Most of the works devoted to the study diffusion combustion of liquid, whose vapor pressure at an initial temperature is less than the extreme pressure, were carried out in large volumes [3]. Diffusion combustion in a confined volume is characterized by an important feature, which is the inability of the flame spread over the surface of the liquid without flow of oxidant [4-6]. Experiments [5, 6] have shown that the flame propagation in such systems depends on the flow of oxidant. In a cylindrical channel, when using air as an oxidant, the flame propagates with pulsations [5]. In a rectangular channel with a height less than 4 mm, the flame can spread only in case where the air is enriched with oxygen. It was shown in [5, 6] that the flame velocity can vary within a wide range from millimeters per second to several meters per second. The flame propagation velocities obtained under

such conditions are comparable to the normal velocities for carbon-oxygen gas mixtures. These facts set us thinking about the flame propagation mechanism over the liquid surface. The currently accepted thermocapillary mechanism is reasonably criticized in [6]. The authors indicate that the flow of heated fluid from the region containing the combustion products to the pre-flame zone due to capillary forces requires quite a lot of time. This process is lacking when flame spreads in a premixed gas mixture. Therefore, to reach the velocities close to the normal values characteristic of the carbon-oxygen gas flames, the combustible mixture formation process in pre-flame region needs to be significantly accelerated. Currently, there are no theoretical studies of liquid combustion processes in flat rectangular channels.

In order to understand the flame spreading mechanism over the liquid surface, in the present work, an attempt is made to simulate the processes occurring in the film of combustible liquid. To simplify the task, we consider small rates of oxidation in the channel, whose height is chosen to be much less than its width that corresponds to the parameters of a flat compact heat exchangers. This was done also in order to possibly create a two-dimensional flow structure and the flame front that facilitates the simulation process. As a first step we carried out theoretical study of "heat wave" propagation in the horizontal rectangular channel during flow of a gas driven liquid film, taking into account the evaporation process. The model is built based on the previously developed model of thermocapillary flow of the gas driven heated liquid film in the channel, taking into account the dynamic effects of gas flow on the liquid, as well as the diffusion and convective heat and mass transfer mechanisms in liquid, gas and through the deformable gas-liquid interface [7,8]. In this paper, it is assumed that the gas flow consists of oxygen-enriched air, while liquid is n-butanol. The problem is solved in a two-dimensional formulation under the conditions of the thin layer approximation, taking into account the specific heat release and the radiation and absorption processes in the gas and at the interface, as well as in the emerging zone of intense heating over the surface of the liquid film. The conducted calculations have shown that the combustion of oxygen-enriched air leads to the formation of "heat wave", moving quickly toward the gas flow with the velocity close to constant. Figure 1 shows an example calculation of the temperature field in the liquid film and the gas phase for

different points in time. The zone of intense heating in gas phase, moving upstream, can be identified with the combustion wave. In this case the front velocity is equal to 2.7 m/s.

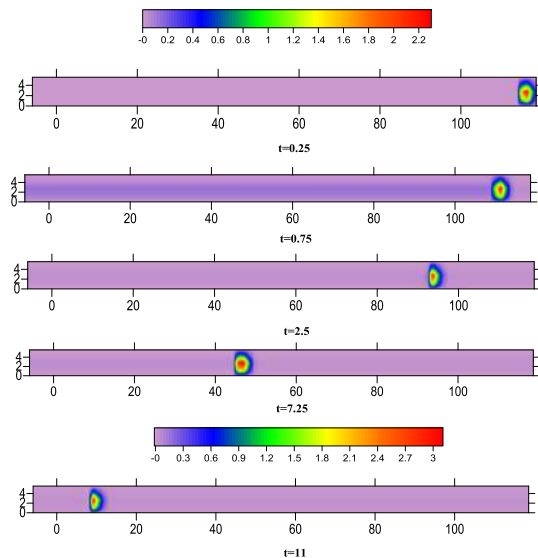


**Figure 1:** The combustion front propagation in the channel (on the symmetry axis at  $y=0$ ) over time. The temperature in the channel at different points in time (all values are given in dimensionless form). Channel height - 500 mm, length - 30 cm, Reynolds number in the gas -  $Re_g=10$ , and thickness of the liquid film - 90 microns. The ignition temperature  $T^*=340^\circ\text{C}$ , initial temperature  $T_0=20^\circ\text{C}$ .

We carried out experimental investigations of flame propagation under the conditions of changed composition of the oxidant. It is shown that the average flame propagation velocity increases with increasing concentration of oxygen in oxygen-nitrogen mixture. Therefore, pure oxygen was selected as the oxidizing agent for low height channels. The experimental data for pure oxygen were obtained for channels of 0.3 and 0.5 mm in height. The comparisons have shown that the increase in the average velocity of oxygen, similarly to that in the channel with the height of 0.5 mm, leads to a reduction in flame velocity. However, decrease in the channel height from 1 to 0.5 mm leads to significant change in flame velocity, while when reducing the height of channel from 0.5 to 0.3 mm it varies only slightly at moderate oxidant velocities, manifesting the trend of increasing difference in velocity with increasing velocity of the oxidant.

In consequence of conducted experimental and theoretical studies we have obtained new experimental results for flames spreading over the surface of the n-butanol in mini and microchannels. It was revealed that when using oxygen as the oxidant, a critical channel size falls within the range of 0.23 - 0.3 mm that corresponds to the estimated critical size for pre-mixed homogeneous gas mixture. We conducted a theoretical study of a problem of "heat wave" propagation in the horizontal rectangular channel during flow of the gas driven liquid film at high oxygen concentration and low oxidant velocities. When building the model we have taken into account the evaporation, the specific heat release, and the radiation and absorption

processes in the gas and at the interface, as well as zones of intense heating above the surface of the liquid film.

In addition, we can conclude that at high oxygen concentration and low velocities of the oxidant, the experimental and calculated values of the velocity coincide quite well.

This work was supported by the grant of the Russian Science Foundation (Agreement No. 15-19-30038).

## References

- 1 Maruta K. Micro and mesoscale combustion // Proc. of the Combustion Institute. 2011. Vol. 33, No. 1. P. 125–150.
2. The Mathematical Theory of Combustion and Explosions Ya.B. Zeldovich, G.I. Barenblatt, V.B. Librovich, G.M. Makhviladze; New York, 1985. p.118.
3. Ross H.D., Miller F.J. Detailed experiments of flame spread across deep butanol pools // Proc. of the Combustion Institute. 1996. Vol. 26. P. 1327–1334.
4. Bieri J.A., Kurdyumov V.N., Matalon M. The effect of gas expansion on edge flames stabilized in narrow channels // Proc. of the Combustion Institute. 2011. Vol. 33. P. 1227–1234.
5. Zamashchikov V.V. Flame spread across shallow pools in modulated opposed air flow in narrow tube // Combustion Sci. and Technology. 2009. Vol. 181, No 1. P. 176–189.
6. Zamashchikov V.V., Korzhavin A.A., Chinnov E.A. Combustion of liquid fuel in a flat minichannel // IJHMT, 2016 V. 102, P. 470–478.
7. Yu. Kabova, V.V. Kuznetsov, O. Kabov, T. Gambaryan-Roisman, P. Stephan, Evaporation of a thin viscous liquid film sheared by gas in a microchannel // IJHMT **68** (2014)
8. Yu. Kabova, V.V. Kuznetsov, O. Kabov, Gravity effect on evaporation and interfacial deformations in nonisothermal liquid film moved by a gas flow in a microgap // Interfacial Phenomena and Heat Transfer **2**,1 (2014)

## Designing and research loop heat pipe for precise thermal control system

Konstantin A. Goncharov

Chief designer, Head of Heat Pipe Center, The Heat Pipe Centre of Lavochkin Association,  
24 Leningradskaya street, Moscow region, Khimky, 141400 Russia, Tel/Fax: 495 5736374;  
heatpipe@laspace.ru

Controlled loop heat pipes (LHP) are being successfully used on board space crafts developed by Lavochkin Association and other Russian space companies. Controlled LHP were integrated into thermal control systems (TCS) of the following space rafts: "Obzor", "Yamal-200", "MIM-1", "Electro-L", "Spectrum-R", "EgyptSat", "Condor" and others. Application of LHP with high-precision thermal control performance is considered in this paper.

Thermal control system (TCS) of so called "hydrogen frequency standard" (H-maser) developed on base of LHP with high control accuracy.

"Spectrum-R" spacecraft (figure 1) was developed by Lavochkin Association and was put into elliptical orbit with apogee of 200 000 km in July 2011. Radio telescope with 10 m diameter contained two hydrogen frequency standards. Controlled LHP contains pressure regulator and bypass line. When changing ambient conditions on LHP evaporator and condenser, TCS shall assure the temperature of the equipment with accuracy better than 0.1°C from the average value of the equipment temperature. Average temperature of the unit in the time interval of up to 2400 seconds shall not differ for more than 0.003 degrees in comparison with the unit temperature in the adjacent time interval.



Figure 1: "Spectrum-R" spacecraft

To ensure this requirement different design solutions were suggested for increasing control accuracy.

Dynamic model of LHP and TCS that was developed for calculation of LHP and TCS parameters (figure 2). It presented in the paper. Calculation results allowed to specify and optimize LHP parameters and prove the possibility of meeting set requirements. Calculation results are presented in the paper.

For carrying out ground tests, special installation was developed for high-accuracy measuring of numerous temperature parameters. Predicted control accuracy of equipment temperature was proved experimentally when carrying out LHP qualification tests.

In the paper presented critical cases of LHP operating (start up, freezing of fluids and other) and it analyze. For example, at the stage of telescope antenna opening working fluid (ammonia) froze in LHP condenser. Ammonia was melted by the sun heat flux reflected from the Earth surface and LHP started up without actuation of reserve systems. After Ammonia melting LHP saved its leak tightness and performance.

Despite the fact that measuring accuracy of telemetry system is much worse than expected control accuracy we can conclude that thermostating accuracy meets requirements.

According to telemetric data received from board the "Spectrum-R" spacecraft in the period 5 year, the temperature of LHP evaporator is in the strict set range.

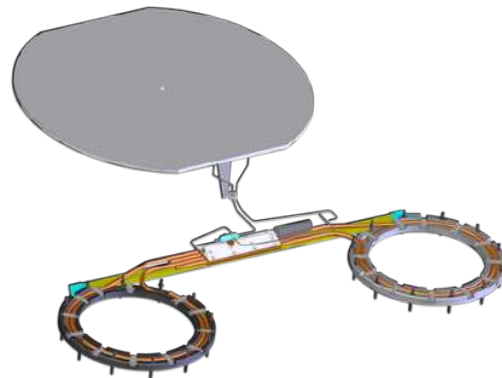


Figure 2. Layout of H-maser TCS

### References

Fershtater Yu.G., Analytical study and the fundamentals of the engineering calculation of LHP6 Heat Pipes: Theory and Practice: Proceedings6 Proceedings of the International School-Seminar, Minsk, Paper 1, pp. 87-94 (1190).

V. Buz, K. Goncharov, Modeling of LHP Performances by Means of Specialized EASY Package Program, IHPC 12, May 19-24, Moscow, Russia (2002)

Goncharov K., Kotarov E., Tulin D., Serov G., Loop heat pipe: Patent RU № 2473035, 11 p.

## Study of microwave drying of wet materials based on one-dimensional two-phase model

Vladimir Salomatov, Vadim Karelin

Kutateladze Institute of Thermophysics SB RAS  
Kutateladze 2, Novosibirsk, 630090, Russia  
[salomatov.vv@mail.ru](mailto:salomatov.vv@mail.ru), [vad2hen@mail.ru](mailto:vad2hen@mail.ru)

Wet material drying processes are among the most energy-intensive. At the present stage is a theoretical and practical interest of heat transfer techniques to dried product, based, in particular, to microwave exposure. Important advantage of microwave energy is electromagnetic radiation ability to penetrate into the material to a considerable depth and creating in it the volume distribution of the heat sources without requiring the presence of a heat transfer medium. Microwave exposure is controlled and almost inertialess process that enables instantly change flow of heat. Energy consumption for evaporation during traditional drying types are up to 3.0 kWh / kg. With microwave drying, they are reduced to 1.6-1.8 kWh / kg. The drying time is between 8-20 hours, and under microwave drying under otherwise equal conditions is reduced to 4 hours.

Most large-scale processes are drying coal fuel. Applying electromagnetic microwave radiation will increase the heat of combustion, to reduce the moisture content, ash content and also lower levels of mercury, chlorine, sulfur and other harmful constituents.

The combustion of fuel in the presence of the microwave field increases the rate of combustion, combustion becomes self sustainable, improved ignition mode, increase environmental performance and others.

To wide dissemination of microwave technology in coal energy, which in the world today there is a strong interest, interferes mainly developed of weak scientific foundations interconnected, rather complex electro and thermal processes. Use the full benefits of microwave effects on quality of coal preparation and drying as well as eco-friendly combustion is possible only in the presence of advanced mathematical modeling and analysis tools. The study of these problems is the subject of this work.

In the article analytically solved the problem of wet coal drying under the influence of a plane electromagnetic wave of the microwave range. The phase transition at the border is formulated in the form of Stefan conditions characterizing the consumption of heat for evaporation and drying, which determines the dynamics of the movement of the front. A mathematical model of microwave drying is considered in two stages.

Stage 1 - the task of microwave warming. At the first stage we study of microwave warm of wet coal regime, when the absorption of microwave radiation is subject of Bouguer's law. By the time the first phase ends when the maximum temperature within the coal reaches the phase transition temperature "water - steam".

The mathematical formulation of the first phase includes the following key assumptions, which give the possibility of obtaining an analytical solution:

1. Internal power microwave heat absorption follows an exponential function of the coordinate -

$$q_1(x) = q_{v0} \exp(-\psi_2 x).$$

2. Electrophysical and thermal characteristics of the coal substance conditionally constant.

3. The initial conditions are assumed to be zero.

4. Heat flows on the boundary surfaces in a first approximation, there are no.

The system of differential equations solved on step 1 with double Laplace transform and cos-Fourier. As a result, we found as the temperature field of the first stage, and the time to achieve the temperature of phase transition "liquid-vapor". Driving the problem is shown in fig. 1

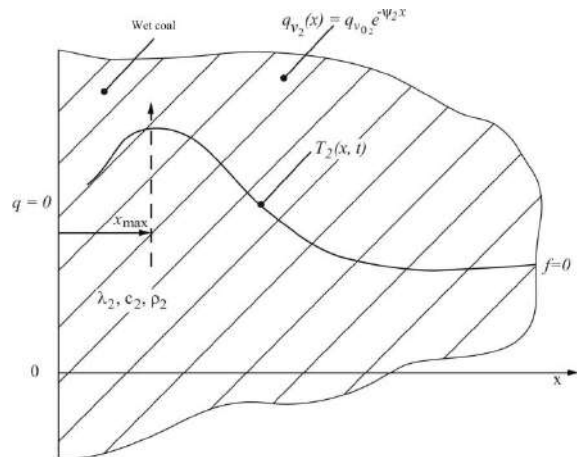
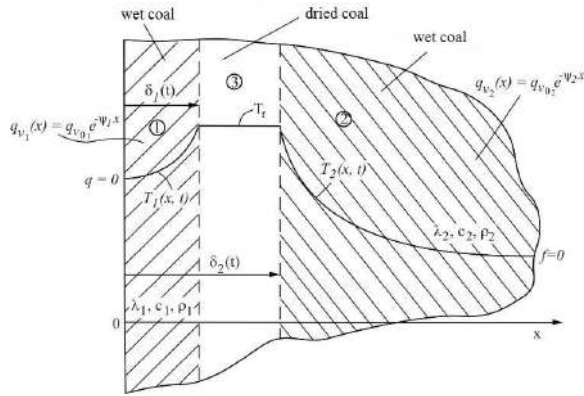


Figure 1: Scheme of the first stage of the task.

Stage 2 - the problem of microwave drying. The drying process in this article studied as heat transfer medium in the phase-change - known Stefan problem. In our case, we propose a new approach to the of microwave drying of coal array of the problem, which is based on a method developed by us heat quasistationary approximation. It is based on the concept that the movement of the phase transformation front controls part of the quasi-stationary temperature field.

For calculation formulas and the further search for the basic laws of the microwave drying process itself develops as follows. Due to internal heat sources from the microwave absorption of coal mass after reaching the phase transition temperature dries, forming three different areas in their properties (fig. 2).

Zones 1 and 2 are partially dried. Zone 2 is taken fully dried. In the future, the heat from the microwave absorption is spent on evaporation of residual moisture and making the phase transition "liquid - vapor" on moving the borders. It is required to determine the dynamics of the reduction of humidity, temperature distribution in zones 1 and 2, the dynamics of the reduction of humidity.



**Figure 2:** Temperature zones in coal layer.

In addition to the basic assumptions of the first stage is taken as follows:

- Diffusion of moisture are neglected;
- Heat of vaporization and the phase transition temperature assumed to be constant;
- Dielectric constant and dielectric loss tangent in the humid zones 1 and 2 several times more than similar characteristics zone 3. Therefore, the internal heat source in the zone 3 can be neglected in a first approximation.

In the microwave drying step the problem is solved analytically approximated using effective asymptotic procedures. Dynamics of the phase boundary is found within the framework of the quasi-stationary approximation. This approach is based on the following physical principle. Due to lack of comparability of the transfer rate of the heat pulse and movement of the phase boundary, the evaporation front movement is controlled by the limit on part-time temperature field. The fundamental role given to the quasi-stationary asymptotic behavior for large times. Calculations on the derived dependencies found such important characteristics of the studied processes as a warm-up time, drying speed, drying time and other popular options practices.

## Fluid flow inside and outside an evaporating sessile drop

Chafea Bouchenna<sup>1a</sup>, Mebrouk Aitsaada<sup>1b</sup>, Salah Chikh<sup>1c</sup>, Lounès Tadriss<sup>2d</sup>

<sup>1</sup>USTHB, Faculty of Mechanical and Process Engineering, LTPMP, Alger 16111, Algeria

<sup>2</sup>Aix-Marseille Université, CNRS, Laboratoire IUSTI, UMR 7343, Marseille 13453, France

<sup>a</sup>bouchennachafea@hotmail.fr, <sup>b</sup>m\_aitsaada@yahoo.fr, <sup>c</sup>salahchikh@yahoo.fr, <sup>d</sup>lounes.tadriss@univ-amu.fr

Sessile drop evaporation is a process, which has extensive applications in biochemical assays, thin film coating, spray cooling, microelectronics, nano-devices and others. It is a complex physical problem which involves fluid flow, heat and mass transfer as well as interactions between the solid substrate, the liquid droplet and the surrounding gas throughout moving interfaces and a pinned or receding contact line (Yang et al., 2014). Recently Larson (2014) summarized analytical, numerical and experimental literature works on drying sessile droplets and deposition of suspended materials. He presented a list of useful dimensionless groups governing mass, momentum, and heat transfer effects in the droplet, the surrounding gas and the substrate.

One of the most important applications of the sessile drop evaporation in thin film technology is the final pattern of the solid particles deposits on substrates. The particle deposition is strongly affected by the flow inside the drop. The competition of the flow induced by the privileged evaporation near the contact line, the thermo-capillarity and the buoyancy effects, is strong during drop evaporation, and the prevalence of one or two effects rules the flow direction inside the drop. Several works were conducted to study the influencing parameters, which define flow patterns in the evaporating sessile drops (Lu et al., 2011).

The present work is a numerical study of the convective internal and external flow of an evaporating water sessile drop. Understanding the fluid dynamics during the evaporation allows handling and controlling the strains of particle deposits near the contact lines on substrates of different natures and in heated or non-heated cases. In this framework, a numerical model is developed by taking into account (1) the flow induced by the strong liquid loss at the contact line, (2) the thermo-capillary flow resulting from the surface tension gradient due to temperature variation at the drop surface, and (3) the flow induced by the buoyancy in the liquid or the gas. The objective is to analyze the internal and external flow intensity and the flow pattern resulting from the competition of the driving effects as well as its impact on the evaporation rate.

We consider a small water drop on a substrate of high thermal conductivity. The surrounding air is at ambient temperature  $T_\infty = 25^\circ\text{C}$  and relative humidity  $Ha = 40\%$ . The lower face of the substrate is maintained at a temperature  $T_w \geq T_\infty$ . The drop evaporation is assumed to occur with pinned contact line. Buoyancy effect is included in the model with the Boussinesq approximation. Convective flow in both liquid and gas phases is governed by the equations of conservation of mass, momentum and energy coupled with the vapor transport equation in the surrounding air and heat conduction equation in the substrate. Mass conservation, momentum and energy balance at the liquid-gas interface are expressed in dimensionless forms as follows:

i) mass conservation,

$$(\vec{W}_\ell - \vec{W}_I) \cdot \vec{n} = R_\rho (\vec{W}_g - \vec{W}_I) \cdot \vec{n} = \frac{R_{\alpha_T} (\Delta C / \rho_\ell)}{Le Ma} \vec{J}^* \cdot \vec{n} \quad (1)$$

$\vec{n}$  is a normal unit vector,  $\vec{W}_I$  is the velocity of the moving interface,  $\vec{W}_{\ell,g}$  is the velocity of a liquid (gas)

particle,  $\vec{J}^*$  is evaporation flux,  $\rho_\ell$  is the liquid density and  $\Delta C$  is equal to  $(C_v(T_w) - Ha C_v(T_\infty))$  where  $C_v(T)$  is the saturated vapor concentration. Different dimensionless numbers appear in Eq. (1): Marangoni number (Ma), Lewis number (Le), ratio of gas/liquid density ( $R_\rho$ ), ratio of gas/liquid thermal diffusivity ( $R_{\alpha_T}$ ).

ii) Shear-stress balance,

$$\left[ (\vec{n} \vec{\tau}_\ell) - (\vec{n} \vec{\tau}_g) \right] \cdot \vec{t} = \vec{\nabla} T^* \cdot \vec{t} \quad (2)$$

$\vec{t}$  is a tangential unit vector and  $\vec{\tau}$  is the dimensionless stress tensor. The temperature gradient ( $\vec{\nabla} T^*$ ) in Eq. (2) represents the term of thermo-capillary effect.

iii) Energy balance,

$$\frac{Ja}{Le} \left( \frac{\Delta C}{\rho_\ell} \right) \vec{J}^* + \left( R_k^g \nabla T_g^* - \nabla T_\ell^* \right) \cdot \vec{n} = 0 \quad (3)$$

$R_k^g = k_g / k_\ell$  is the ratio of gas/liquid thermal conductivity,

$Ja = h_{\ell g} / (c_{p\ell} \Delta T)$  is the Jacob number,  $\Delta T$  is equal to  $(T_w - T_\infty)$ ,  $h_{\ell g}$  is the latent heat of vaporization and  $c_{p\ell}$  is the liquid specific heat.

The governing equations in a quasi-steady state with the associated boundary conditions and interfaces conditions are solved numerically by a procedure based on finite volume method. The concentration gradients at the drop surface are then used to evaluate the evaporation rate and deduce the drop lifetime.

Results are presented for a water drop of  $10 \text{ mm}^3$  initial volume deposited on a substrate with high thermal conductivity. Velocity and temperature fields are plotted in Fig. 1 for a contact angle  $\theta = 20^\circ$  and wall temperature  $T_w = 50^\circ\text{C}$ . A tri-cellular flow appears in the drop due to the thermo-capillary effect in heating conditions and confined geometry of the drop at  $\theta = 20^\circ$ . The external flow near the drop surface is driven by the internal flow, whether the buoyancy in the gas is included or not. This is due to the viscosity of the liquid which is much greater than that of the gas.

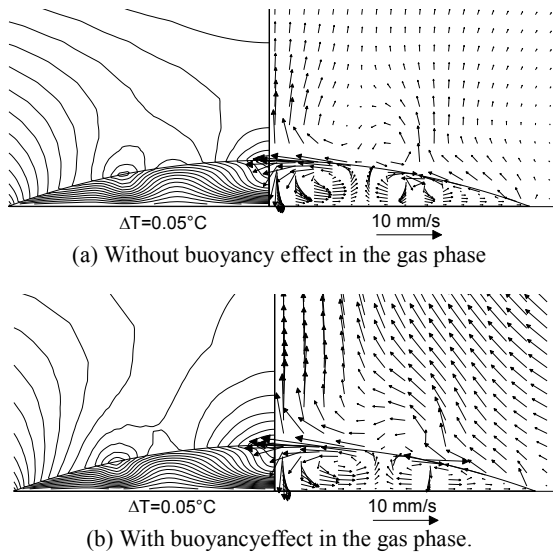


**Figure 1:** Velocity and temperature fields for a contact angle  $\theta$  of  $20^\circ$  and wall temperature  $T_w$  of  $50^\circ\text{C}$ .

Nevertheless, the temperature profiles in Fig. 2 clearly show that the buoyancy in the air can increase the importance of the thermocapillarity especially under the heating conditions and thus influence the internal flow.

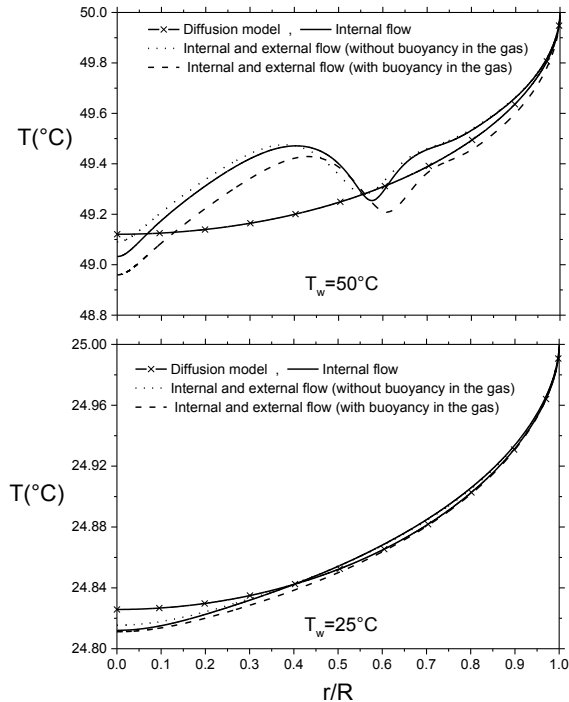


**Figure 2:** Temperature profile at drop surface for  $\theta = 20^\circ$  and  $T_w = 25$  or  $50^\circ\text{C}$ .

In comparison with the diffusion model, it can be noted that the buoyancy flow in the gas induces an increase in the evaporation rate due to the mass convective effects. This has for result a decrease in the drop surface temperature.

At the opposite, the internal flow rather implies an increase in the surface temperature at the edge of the drop, although globally the evaporation rate also increases due to thermal convective effects.

### References

Yang, K., Hong F., Cheng, P., A fully coupled numerical simulation of sessile droplet evaporation using Arbitrary Lagrangian–Eulerian formulation, *Int. J. Heat Mass Transfer* Vol. 70 pp. 409–420 (2014)

Larson R. G., Transport and deposition patterns in drying sessile droplets. *AIChE Journal*, Vol. 60 pp. 1538-1571 (2014)

Lu G., Duan Y. Y., Wang X. D., & Lee D. J., Internal flow in evaporating droplet on heated solid surface. *International Journal of Heat and Mass Transfer*, Vol. 54 pp. 4437-4447 (2011)

## Analysis of contact angles for a perfectly wetting sessile droplet evaporating into air at the evaporation stage

Alexey Rednikov<sup>1</sup>, Yannis Tsoumpas<sup>1,2</sup>, Sam Dehaeck<sup>1</sup> and Pierre Colinet<sup>1</sup>

<sup>1</sup>TIPs Laboratory, Université Libre de Bruxelles, C.P. 165/67, Brussels, Belgium

<sup>2</sup>Atomic Energy and Alternative Energies Commission, Gif-sur-Yvette, France

E-mail: aredniko@ulb.ac.be

When a droplet of a volatile liquid is deposited on a flat solid substrate, it first undergoes either a fast spreading or a fast retraction, depending on the initial conditions. The droplet volume remains practically constant at this stage, the mass loss due to evaporation being a slow process relative to the mentioned 'fast' ones. Eventually, the sessile droplet reaches a kind of quasi-steady state, whose further evolution is governed by a 'slow' evaporative volume reduction. It is this latter stage that is in the focus of the present study. The volume loss gives rise to a slowly receding contact line (slower than it could be at the initial fast-retraction stage). We note beforehand that no essential pinning is observed in the present series of experiments, and the contact line is therefore treated as freely receding.

Here we deal with droplets of perfectly wetting liquids such as various HFEs (7100, 7200 and 7500), the volatility decreasing with the number. Finite contact angles observed at the evaporation stage are principally evaporation-induced by their nature (e.g. Guéna et al. 2007, Colinet & Rednikov 2011, Tsoumpas et al. 2015, Saxton et al. 2016, Savva et al. 2017). In the present series of experiments, the droplets are deposited on a horizontal polycarbonate plate of thickness 3 mm. The initial contact radius of the sessile droplet is typically between 1 mm and 2 mm. The contact angles are of the order of 10° or below. The polycarbonate plate and the liquids being transparent, the droplet thickness profiles are measured by means of Mach-Zehnder interferometry (Dehaeck et al. 2015). A local wavelet analysis technique used by Dehaeck et al. (2015) also allows to extract the local slope profiles. A typical result for the slope profile is shown in Fig.1. A remarkable feature observed in Fig.1 is a drastic decrease of the slope in the vicinity of the contact line. This is a result of the Marangoni effect on the shape of the droplet pointed out by Tsoumpas et al. (2015). The liquid being pure (one-component) here, the Marangoni effect is of thermal nature and comes from evaporative cooling at the droplet free surface. Overall, a significant deviation from the classical steady shape (as determined by gravity and capillarity) is observed for a droplet of a given contact radius and contact angle (cf. Fig 1). In contrast, a theory appropriately taking into account the Marangoni effect succeeds in reproducing the experimental profile (see Fig. 1).

On the other hand, such a Marangoni-induced drastic decrease of the slope near the contact line makes it more difficult to precisely measure the actual contact angle (the slope at the rightmost point of the profile): the high curvature renders the wavelet analysis method not sufficiently accurate near the contact line (Dehaeck et al. 2015). In the present study, unlike Tsoumpas et al. (2015), we shall not rely upon such a direct measurement of the contact angle and proceed in a different way. This is partly motivated by the fact that we shall here be interested in finer

effects like the dependence of the contact angle on the contact radius of the droplet, hence a need to exclude such potential sources of imprecision.

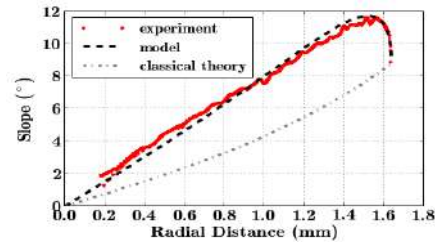


**Figure 1:** Slope profile of an HFE-7100 droplet, with the radial distance counted from the symmetry axis and the end of the profile corresponding to the contact line.

Namely, we proceed as follows. At first, with the help of a theoretical processing, we shall measure the so-called *apparent contact angle* of the sessile droplet. It is quite commonly defined as the angle required in the (theoretical) quasi-stationary droplet profile in order to have given values of the droplet's volume and contact radius. In experiment, the volume and the radius are measured from the droplet profile at each moment of the observed evolution of an evaporating droplet. Then, at each moment, the apparent contact angle is thereby inferred.

As it follows from what was already mentioned, the theoretical quasi-stationary profile, used to define the apparent contact angle, is here not merely the classical one, shaped just by gravity and capillarity, but rather the Marangoni-modified one (Tsoumpas et al. 2015). The theoretical consideration is based upon the radial distribution of the *local* evaporation rate as derived in the framework of a diffusion-limited theory (Popov 2005). Yet, the measured *global* evaporation rate (obtained by taking the time derivative of the measured droplet volume) generally turns out to somewhat deviate from the predictions of the diffusion-limited theory. On the one hand, this is attributed to neglected convective effects. On the other hand, a possible evaporative cooling of the polycarbonate plate itself is not accounted for either. To make allowance for these effects, we modify the theory by heuristically correcting the diffusion-limited local evaporation rates in proportion to the mentioned discrepancy between the measured and diffusion-limited global evaporation rates. Such an approach has proved to work well by Tsoumpas et al. (2015). Another confirmation thereof, now unlike Tsoumpas et al. (2015) not hinging upon a direct measurement of the contact angle, comes from a good agreement observed in Fig.2 in terms of the maximum slope (reliably measurable quantity within a slope profile as the one in Fig.1).

Coming back to the apparent contact angles, the results

are shown in Fig.3. Normally, for slowly receding contact lines as at the evaporation stage in question, one expects the apparent contact angles to largely coincide with the evaporation-induced ones (Saxton et al. 2016, Savva et al. 2017). Yet the comparison drawn in Fig.3 puts into evidence quite diverging tendencies for these two angles as functions of the contact radius. This compelled us to recur to asymptotic developments similar to Saxton et al. (2016) and Savva et al. (2017), looking for the velocity and other related corrections into the contact angle. However, unlike Saxton et al. (2016) and Savva et al. (2017), these developments are here applied explicitly to the evaporation stage and also take the Marangoni effect into account. The goal is to more precisely deduce the evaporation-induced angles from the apparent ones at the evaporation stage, rather than to merely assume them equal. On the other hand, an appropriate modification of the results coming from Colinet & Rednikov (2011) is also applied (see Fig.4 caption). All this turns out to work in the right sense indeed, by bringing the circles and points closer together in Fig.4 as compared to Fig.3 (a disparity of  $\sim 20\%$  now *versus*  $\sim 60\%$  before), albeit no perfect agreement is still achieved. Curiously enough, the  $\sim 20\%$  dispersion of the evaporation-induced contact angles observed in Fig.4 turns out to be roughly the same as the one obtained from the microregion model by Colinet & Rednikov (2011) as the spreading coefficient (whose value is not really known here) is varied in the range of small positive values. It is perhaps in the realm of this sensitivity to the spreading coefficient that the explanation for the remaining discrepancy and for the fact that different experimental runs result in different curves could be searched.

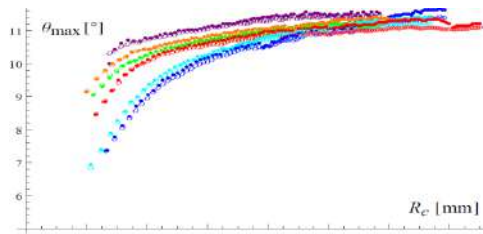


**Figure 2:** The measured (circles) and computed (points) maximum slopes of the droplet profile (cf. Fig.1) versus the droplet contact radius for HFE-7100. Different colors hereafter corresponds to different experimental runs (the same in all subsequent figures).

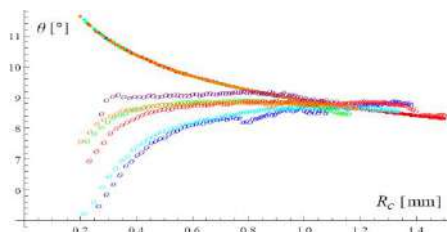


**Figure 3:** The measured apparent contact angles (circles) obtained by theoretical processing of the experimental data as described in the text, and the theoretical evaporation-induced contact angles (points, here coinciding for all runs) obtained from the de-Gennes-based contact-line microregion model described by Colinet & Rednikov (2011). Results for HFE-7100. The molecular scale value

used in the model by Colinet & Rednikov (2011) is  $a^*=1$  nm.

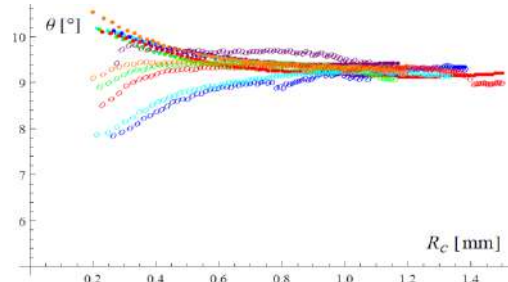


**Figure 4:** Evaporation-induced contact angles deduced from i) further theoretical processing of the measured apparent contact angles of Fig.3 as described in the text (circles), and ii) the microregion model [2] by applying the same heuristic evaporation rate modification as the one used in the context of the Marangoni effect (points). HFE-7100 with  $a^*=1$  nm.

To recapitulate, a straightforward naïve comparison between experiment and theory yields worryingly disparate tendencies for the evaporation-induced contact angle as a function of the droplet radius. However, an appropriate account for contributions and corrections due to the Marangoni effect and contact-line velocity as well as heuristic modifications, based on experiment, of diffusion-limited evaporation rates are shown to drastically reduce such a disparity. The results for other HFE liquids will also be presented.

We are grateful to the support from BELSPO & ESA PRODEX and F.N.S.-FNRS.

## References

- Colinet P. and Rednikov A., On integrable singularities and apparent contact angles within a classical paradigm, *Eur. Phys. J. Special Topics*, Vol. 197, pp. 89-113 (2011)
- Dehaeck S., Tsoumpas Y. and Colinet P., Analyzing closed-fringe images using two-dimensional Fan wavelets, *Applied Optics*, Vol. 54, pp. 2939-2952 (2015)
- Guéna G., Allançon P. and Cazabat A., Receding contact angle in the situation of complete wetting: Experimental check of a model used for evaporating droplets, *Colloids Surf. A*, Vol. 300, pp. 307-314 (2007)
- Popov Y.O., Evaporative deposition patterns: Spatial dimensions of the deposit, *Phys. Rev. E*, Vol. 71, 036313 (2005)
- Savva N., Rednikov A. and Colinet P., Asymptotic analysis of the evaporation dynamics of partially-wetting droplets, *J. Fluid Mech.*, submitted (2017)
- Saxton M.A., Whiteley J.P., Vella D. and Oliver J.M., On thin evaporating drops: When is the  $d^2$ -law valid?, *J. Fluid Mech.*, Vol. 792, pp. 134-167 (2016)
- Tsoumpas Y., Dehaeck S., Rednikov A. and Colinet P., Effect of Marangoni flows on the shape of thin sessile droplets evaporating into air, *Langmuir*, Vol. 31, pp. 13334-13340 (2015)

## An interaction of impacting droplets with superhydrophobic coatings

Nastasia Okulova<sup>1,2</sup>, Valery Okulov<sup>3,4</sup> and Rafael Taboryski<sup>1</sup>

<sup>1</sup>Department of Micro- and Nanotechnology, DTU, Ørsted Plads, Building 345C, 2800 Kgs. Lyngby, Denmark

<sup>2</sup>Danapak Flexibles A/S, Strudsbergsvej 3, 4200 Slagelse, Denmark

<sup>3</sup>Department of Wind Energy, DTU, Nils Koppels Allé, Building 404, 2800 Kgs. Lyngby, Denmark

<sup>4</sup>Institute of Thermophysics, pr. Akademika Lavrentyeva, 1, Novosibirsk, Novosibirskaya oblast', Russia, 630090  
nasok@nanotech.dtu.dk, vaok@dtu.dk, rata@nanotech.dtu.dk

A creation of new engineering materials with the super-hydrophobic properties is inspired by the nature where many water-repellent surfaces in plants and animals are caused by a complex 3D micro- or nano-structures of the hydrophobic papillae (Figure 1).

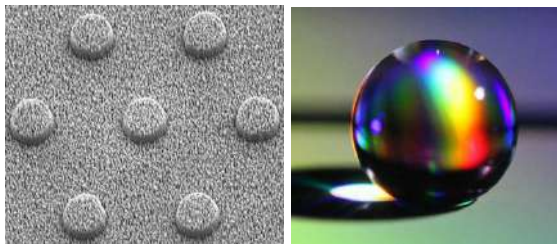


**Figure 1:** Hierarchical structure for superhydrophobic purposes and a water droplet on a superhydrophobic surface.

The main objective of this study is protection of surfaces from water and ice to prevent corrosion, improve aerodynamics or add self-cleaning properties to the material. To achieve this effect, the bulk materials are coated with hydrophobic polymer foils. To increase the hydrophobicity of the polymer surface, appropriate micro- and nanostructuring can be produced using a highly advanced nanolithographic method, which uses Roll-to-Roll Extrusion Coating (Figure 2). This high-speed and low cost lithography method is developed at DTU and Danapak Flexibles A/S (Murthy et al 2016; Telecka et al 2016, Okulova et.al. 2017). Coatings with different types of the micro- and nano-structures (Figure 3) can easily be fabricated for different scientific and industrial applications. The purpose of the current work is an experimental investigation of the water droplets impacting on the superhydrophobic coatings structured by the Roll-to-Roll Extrusion coating method.

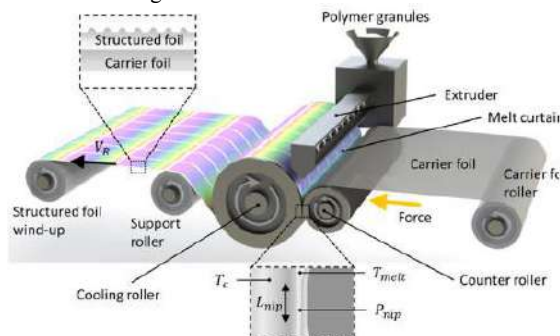


**Figure 2:** Roll-to-Roll Extrusion Coating Process. (Murthy et al 2016).

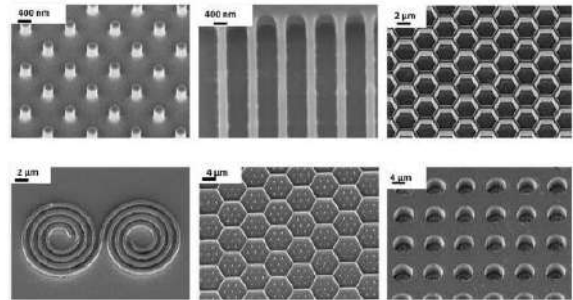


**Figure 3:** Examples of the nano-structures in polymer foils. (Murthy et al 2016)

Later-time dynamics (the contact angles and the maximum spreading ratio of the droplet diameters) of the impacting droplets are measured for different Weber numbers. The maximum spreading ratios as a function of the impact Weber number found in experiments are then compared with simple analytical estimates of the maximum spreading diameter by both momentum and energy balance approaches (Wildeman et al 2016).

### Funding

This work was supported by the Innovation Fund Denmark through the project XNano [grant number 4135-00142B].

### References

Murthy, S., et.al. Fabrication of Nanostructures by Roll-to-Roll Extrusion Coating. *Adv. Eng. Mat.*, Vol. 18, No. 4, pp. 484-489 (2016).

Telecka, A., et.al. Superhydrophobic Properties of Nanotextured Polypropylene Foils Fabricated by Roll-to-Roll Extrusion Coating. *ACS Macro Lett.*, Vol. 5, pp. 1034-1038 (2016).

Okulova, N., et. al. Replication of micro-sized pillars in polypropylene using the extrusion coating process. *MEE*, Vol. 176, pp. 54-57 (2017).

Wildeman S, et.al. On the spreading of impacting drops, *J. Fluid Mech.*, Vol. 805, pp. 636-655 (2016).

## Spreading dynamics of evaporating and perfectly wetting liquids

S Dehaeck<sup>1</sup>, A Y Rednikov<sup>1</sup>, D Seveno<sup>2</sup>, J De Coninck<sup>3</sup>, P Colinet<sup>1</sup>

<sup>1</sup> TIPS (Transfers, Interfaces and Processes), Université Libre de Bruxelles, CP 165/67, Brussels, Belgium

<sup>2</sup> Department of Materials Engineering, KU Leuven, Heverlee, Belgium

<sup>3</sup> Laboratory of Surface and Interfacial Physics, Université de Mons, Mons, Belgium

E-mail: sam.dehaeck@ulb.ac.be

When a drop of liquid first contacts a solid substrate, the theoretical initial contact angle is  $180^\circ$  with the contact region being a single point. In most practical conditions, this is however not the equilibrium situation. What typically follows is an expansion of the contact zone and a lowering of the contact angle. As the contact angle reaches the static one defined by the evaporation-induced (for volatile liquids as here) and Young's contributions, the spreading dynamics slows down, reaching it only asymptotically. In the volatile case, evaporation will eventually lead to a recession of the contact line, during which the contact angle remains roughly constant.

The initial expansion stage is known as spreading and two major theories have been developed in the past to predict the contact line velocity and contact angle evolution over time: Hydrodynamic Theory (HT) (e.g. Bonn et al. 2009) and Molecular-Kinetic Theory (MKT) (e.g. de Ruijter et al. 1999). What both theories fundamentally differ upon is how the local contact angle is modified when it is in motion, i.e. the dependency of contact angle on contact line velocity. One of the goals here is to test both models on a low viscosity (0.7cSt), low surface tension liquid (16.2 mN/m) such as 3M™ Novec™ HFE-7500.

The experiments consist in gently depositing a drop of HFE-7500 on a clean glass wafer and tracking the contact line using Mach-Zehnder interferometry. The resulting images are analyzed with the algorithms detailed in (Dehaeck, Colinet 2016; Dehaeck, Tsoumpas, Colinet 2016). From these, we extract the drop height profiles over time and in particular the contact angle and location at all points of the three-phase line. From this location, an estimate for the contact line velocity is obtained. We need to stress here that both measurements are fully local, no global fitting of the perimeter with a circle nor of the height profile with a parabola was performed. As it was shown in (Tsoumpas 2015), Marangoni effects can give rise to appreciable local curvatures near the contact line, and hence introduce significant errors in contact angle measurements when extracted from parabolic fittings. In the present context, such large local curvatures are deemed to occur due to the presence of a Cox-Voinov zone, with a logarithmic increase of the film slope, although the role of the Marangoni effect cannot be fully excluded either. Note that, due to the methodology employed for the interferometric image analysis, the measured contact angle is some kind of average over a small region near the contact line. The size of this region has not been fully quantified yet but is here expected

to be of the order of some tens of microns.

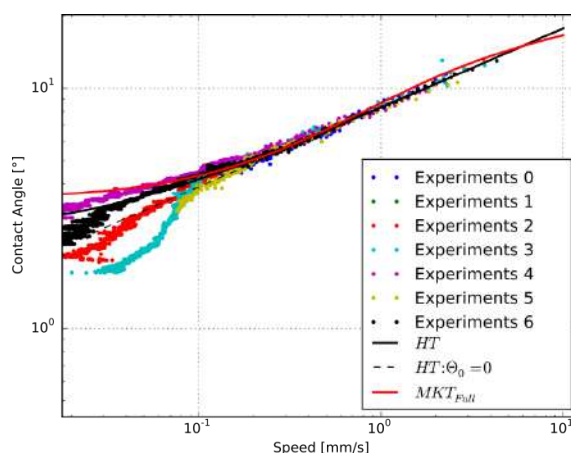


**Figure 1:** Contact angle versus contact line speed for a drop of HFE-7500 spreading on a glass substrate

In Figure 1, this measured contact angle is shown versus the contact line speed for different experiments, together with the fits for both theories. First, we notice that for speeds below 0.1mm/s a kind of transition behavior between the fast-spreading stage and the evaporation stage occurs. In this intermediate stage, the drop becomes non-axisymmetric leading to large discrepancies in the data. In the present study we discard this part and focus on the fast-spreading stage, for which we notice that all data collapse nicely and can be fitted with both theories equally well, although HT seems to catch the large speed behavior better. Two fits are shown for HT, one with the static angle  $\Theta_0$  equal to zero and one where it was fitted to the data (for speeds above 0.1mm/s) resulting in  $\Theta_0 = 2.5^\circ$ . For MKT, the full formulation was applied and this yielded the best results for  $\Theta_0 = 3.5^\circ$ . This suggests that the evaporation-induced angle, which is indeed of this order (Tsoumpas et al. 2015), can be used as a replacement for the Young's one in the present context. This has already been shown to be the case for the Gibbs' criterion for pinning in (Tsoumpas et al. 2014). Nevertheless, as the precision on the fitted static angles is quite small due to the large speeds in the fitted region, a fit with a zero contact angle is well within the uncertainty.

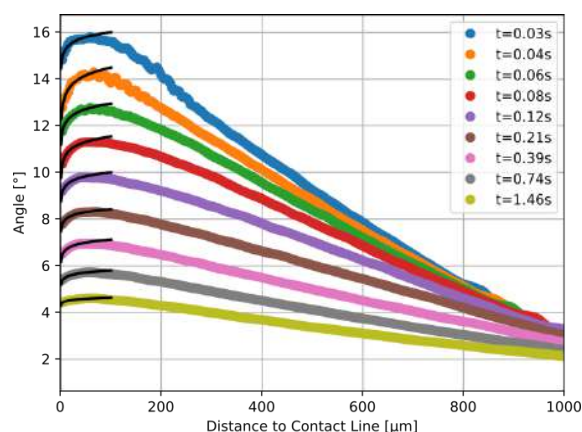


**Figure 2:** Local angle versus distance to the contact line at different times after deposition.

In Figure 2, a close-up of the local slope profile is shown versus the distance to the contact line. This profile clearly deviates from the classical static profile where the maximum angle would be obtained at the contact line itself. Here, the maximal angle is clearly seen at a distance of more or less  $60\mu\text{m}$  from the contact line. This profile is strongly reminiscent of the profiles measured by (Tanner 1979), which can perhaps be associated to viscous bending of the droplet shape. Preliminary fits of these profiles with the HT law:  $\Theta^3 = a \ln(x) + b$ , yield the full lines in the figure. As can be seen, the correspondence is rather satisfactory. To the best of our knowledge, the evaporation channel has never been combined to MKT to describe droplet spreading. In this respect, note that appropriate care must be taken when interpreting this kind of experiments, especially for liquids with low viscosity.

In the present contribution, the spreading dynamics of HFE-7500 was investigated. Both Molecular Kinetic Theory and Hydrodynamic Theory are able to predict rather well the contact angle relaxation in a range from  $15^\circ$  to  $4^\circ$ . Evidence suggests that the evaporation-induced angle can simply replace the Young's one in the adopted formulation, but this is not conclusive for the moment. We also measured the presence of a possible viscous bending zone close to the contact line, as is theoretically predicted by Hydrodynamic Theory. In the future, a more thorough theoretical analysis of the measured profile will be performed.

**Acknowledgements.** The authors gratefully acknowledge financial support from the EVAPORATION and HEAT TRANSFER projects funded by the European Space Agency and by the Belgian Science Policy Office PRODEX Programme, and from the Interuniversity Attraction Poles Programme (IAP 7/38 MicroMAST) initiated by the Belgian Science Policy Office. PC thankfully acknowledges financial support from the Fonds de la Recherche Scientifique - FNRS. This work was also performed under the umbrella of COST Action MP1106.

## References

- D. Bonn, J. Eggers, J. Indekeu, J. Meunier, E. Rolley. Wetting and spreading. *Rev. Mod. Phys.*, Vol. 81, pp. 739–805 (2009).
- M.J. de Ruijter, J. De Coninck, G. Oshanin. Droplet spreading: partial wetting regime revisited. *Langmuir*, Vol. 15, pp. 2209–2216 (1999).
- S. Dehaeck, P. Colinet. Improving speed and precision of local frequency analysis using gaussian ridge interpolation for wavelet and windowed Fourier ridge algorithms. *Optics and Lasers in Engineering*, Vol. 77, pp. 54–63 (2016).
- S. Dehaeck, Y. Tsoumpas, P. Colinet. Analyzing closed-fringe images using two-dimensional Fan wavelets. *Applied Optics*, Vol. 54, pp. 2939–2952 (2015).
- L.H. Tanner. The spreading of silicone oil drops on horizontal surfaces. *J. Phys. D: Appl. Phys.*, Vol. 12, pp. 1473–1484 (1979).
- Y. Tsoumpas, S. Dehaeck, M. Galvagno, A. Rednikov, H. Ottevaere, U. Thiele, P. Colinet. Nonequilibrium Gibbs criterion for completely wetting volatile liquids. *Langmuir*, Vol. 30, pp. 11847–11852 (2014).
- Y. Tsoumpas, S. Dehaeck, A. Rednikov, P. Colinet. Effect of Marangoni flows on the shape of thin sessile droplets evaporating into air. *Langmuir*, Vol. 31, pp. 13334–13340 (2015).

## Drying droplet deposited on poor wetting substrate: beyond the lubrication approximation

Peter Lebedev-Stepanov\*, Sergey Efimov and Alexander Kobelev

Photochemistry Center RAS (FRC Crystallography & Photonics RAS)  
Novatorov St., 7a/1, Moscow, 119421, Russia;  
National Research Nuclear University "MEPhI"  
Kashirskoe Shosse St., 31, Moscow, 115409, Russia,  
E-mail\*: petrsl@yandex.ru

Evaporating sessile droplet of aqueous solution deposited on hydrophobic surface is an urgent object both for theoretical modeling (evaporation dynamics, microfluidics inside the drop, particle dynamics in evaporating drop, etc) and applied researches (printing technologies, nanoparticle ensemble self-assembly processes, hydrophobic coatings, etc).

There are three basic problems to estimate the colloidal particles self-assembly in evaporating droplets: 1) solute evaporation from the droplet surface to surrounding air (outer problem), 2) hydrodynamic flows in droplet volume (inner problem), 3) particle dynamics into droplet with account of interparticle interactions, particle-surfaces interactions, particle-flow interactions, solvation effects (Lebedev-Stepanov et al. 2013, Lebedev-Stepanov 2015).

Although self-assembly investigation in evaporating droplet of colloidal solution on smooth surfaces with quite acute contact angles has been widely studied recently for liquids of different properties including binary solute mixtures (Deegan et al. 2000, Popov 2005, Bain et al. 2015), nanoparticles ensemble self-assembly processes in droplet deposited on hydrophobic and superhydrophobic surfaces has not received much attention up to date.

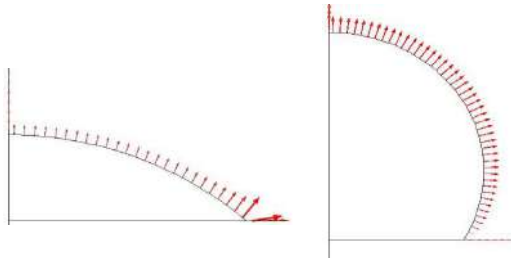


**Figure 1:** Evaporative flow density (evaporation rate) on a surface of sessile droplet with acute wetting angle (left) and with obtuse angle (right); pictures were estimated by Comsol.

The wetting angle of 'hydrophobic' droplet has a value in interval from about  $90^\circ$  to about  $180^\circ$ . In this case, evaporation flow density has no the integrable singularity at contact line, unlike a drop with an acute angle (Fig.1).

Deegan (2000), Popov (2005), Hu and Larson (2002, 2005) have elaborated the useable models of evaporation of sessile drop of single liquid based on Maxwell diffusion model.

Hu and Larson model has a good approbation for calculation of the evaporation flow for the wetting angle interval from  $0^\circ$  to  $90^\circ$ . In framework of this model, the evaporation flow density on the droplet surface is given by

$$J(r) = J_0(\phi) \left(1 - \frac{r^2}{R_d^2}\right)^{-\lambda(\phi)}, \quad \lambda(\phi) = \frac{1}{2} - \frac{\phi}{\pi}. \quad (1)$$

where  $\phi$  is a contact angle;  $R_d$  is a droplet radius (Fig. 2).

Computer modeling the self-assembly of an ensemble of nanoparticles in drying droplet requires the using of quick analytic approximation solutions for the evaporation flow, so that a good example of which are the Hu-Larson's solution given by Eq.1. But, up to date, such a solution for hydrophobic droplet is absent.

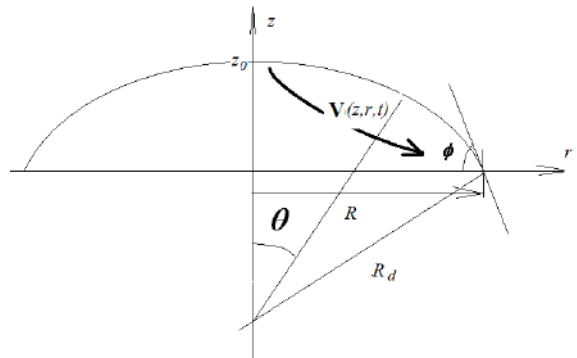


**Figure 2:** Geometry of liquid capillary-sized droplet on a flat substrate.

According to the generally accepted opinion, Popov's model can be used for whole interval of contact angles from about  $0^\circ$  to  $180^\circ$ . However, such a diffusion-only model has significant deviations from experiment for droplets on superhydrophobic surfaces with negligible contact angle hysteresis (Dash 2013).

The similar situation takes place for inner problem (hydrodynamic flows into droplet). Lubrication approximation analysis given by Oron (1997), Deegan et al (2000) can be applied only for the flow field produced by droplet evaporation under the additional approximation of a flat droplet (small contact angles). Deegan et al. (2000) have used the lubrication approximation to calculate the hydrodynamic flow into a droplet with acute angle and pinned contact line.

Hu and Larson (2002, 2005) have developed such a semianalytical approximation in their model of hydrodynamic flows in drying drop.

The kinematic boundary condition with a phase change given by Hu and Larson (2005) is

$$(\mathbf{n}, \mathbf{V}) = [n_r, n_z][0, \dot{Z}] + \frac{(\mathbf{n}, \mathbf{J})}{\rho}, \quad (2)$$

where  $(\mathbf{n}, \mathbf{J})$  is the evaporation flux along the direction normal to the free surface, where  $\mathbf{n}$  is a unit vector along the normal direction, and  $n_r$  and  $n_z$  are the  $r$  and  $z$  components of the unit normal vector  $\mathbf{n}$ , respectively.

In our work (Lebedev-Stepanov (2013)), the boundary conditions of a more general form for the rate of flow on the top of drop surface were proposed:

$$V_z(\theta, t) = \frac{J(\theta, t)}{\rho} \cos \theta - \frac{dZ(\theta, t)}{dt}, \quad (3)$$

$$V_r(\theta, t) = \frac{J(\theta, t)}{\rho} \sin \theta - \frac{dR(\theta, t)}{dt}, \quad (4)$$

where  $\rho$  is a mass density of a liquid,  $\frac{dZ(\theta, t)}{dt}$  and  $\frac{dR(\theta, t)}{dt}$  are  $z$ - and  $r$ -components of velocity of the geometrical point on a drop surface. Such a shift takes place due to the evolution of the form and size of the evaporated drop with account of the contact line movement.

These boundary conditions were successfully used to simulate the self-assembly of nanoparticles in sessile droplets with contact angles having the value smaller than right angle. However, applicability of Eqs. (3-4) for hydrophobic droplets still has not been investigated.

The boundary conditions for general case which includes the obtuse contact angles are still absent in scientific publications.

Our report includes the analysis the application of existing droplet evaporation models, the boundary conditions for the hydrodynamic flows on the drop surface, as well as the nanoparticle dynamics in the hydrophobic droplet, and the dry pattern formation processes modeling. The necessity to develop the existing models of evaporation and boundary conditions for hydrophobic sessie droplets is shown. For the first time, self-assembly model in drying droplets on hydrophobic substrate is described and estimated.

This work was financially supported by the Russian Foundation for Basic Research, project no. 15-03-08050 and by the Competitiveness Program of National Research Nuclear University "MEPhI".

## References

Lebedev-Stepanov P., Vlasov K. Simulation of self-assembly in an evaporating droplet of colloidal solution by dissipative particle dynamics. *Colloids and Surfaces A : Physicochem. Eng. Aspects*. Vol. 432, pp. 132-138 (2013).

Lebedev-Stepanov P. Introduction to self-organization and self-assembly of ensembles of nanoparticles (in Russian). Monograph. NRNU MEPhI: Moscow p. 304 (2015)

Deegan R.D., Bakajin O., Dupont T.F., Huber G., Nagel S.R., Witten T.A. Contact line deposits in an evaporating drop. *Phys. Rev. E*, Vol. 62, No. 1, pp. 756-765 (2000).

Popov Yu.O. Evaporative deposition patterns: Spatial dimensions of the deposit. *Phys. Rev. E*, Vol. 71, p. 036313 (2005).

Talbot E.L. Yow H.N., Yang L., Berson A., Biggs S.R., Bain

C.D, Printing Small Dots from Large Drops. *ACS Appl. Mater. Interfaces*. Vol. 7, No. 6, pp 3782–3790 (2015).

Hu H., Larson R.G. Evaporation of a Sessile Droplet on a Substrate. *J. Phys. Chem. B*, Vol. 106, No. 6, pp. 1334-1344 (2002).

Hu H., Larson R.G. Analysis of the Effects of Marangoni Stresses on the Microflow in an Evaporating Sessile Droplet. *Langmuir*. Vol. 21, pp. 3972-3980 (2005).

Dash S., Garimella S.V. Droplet Evaporation Dynamics on a Superhydrophobic Surface with Negligible Hysteresis. *Langmuir*. Vol. 29, pp. 10785–10795 (2013).

Oron A., Davis S.H. Bankoff S.G. Long-scale evolution of thin liquid films. *Reviews of Modern Physics*, Vol. 69, No. 3, pp. 931-980 (1997).

Hu H., Larson R.G. Analysis of the Microfluid Flow in an Evaporating Sessile Droplet. *Langmuir*. Vol. 21, pp. 3963-3971 (2005).

## Impact of a sphere onto a liquid

Evgeny Ermanyuk and Nikolay Gavrilov

Lavrentyev Institute of Hydrodynamics, Siberian Branch of Russian Academy of Sciences  
Av. Lavrentyev 15, Novosibirsk, 630090, Russia  
ermanyuk@hydro.nsc.ru

Impact of droplets on liquid layers and solids are elementary events, which occur in many applications such as surface coating by atomized paint sprays, aircraft and ship icing, etc. It is well-known that the impact dynamics is strongly affected by the presence of air cushion. The theoretical and numerical models of air cushioning based on gas-liquid lubrication-inviscid balance have been proposed by Smith, Li and Wu (2003) and Korobkin, Ellis and Smith (2008), Hicks and Purvis (2010, 2011), Mani, Mandre and Brenner (2010). There exists also a broad experimental literature on the subject: Thoroddsen, Etoh and Takehara (2003), Thoroddsen et al (2005), etc. The experimental studies of droplet impacts are significantly complicated by the necessity to capture small-scale high-speed processes. Under certain conditions the high-speed impact of small droplets can be modelled by low-speed impact of large rigid spheres, where the latter statement is much easier for experimental investigation.

In the present work we describe this approach, which helps to obtain highly reliable data on the size of the air cushion for normal impact of a sphere on the free surface. In addition, we discuss some qualitative effects of air cushioning at oblique impact, and the effect of cavitation, which occurs at collision of a rigid sphere with a rigid flat bottom. The conditions for incipient cavitation due to collision of rigid bodies immersed in a liquid are not yet fully understood, e.g. Marston et al (2011), Seddon et al (2012).

Experiments were carried out in a test tank of size  $120 \times 120 \times 30 \text{ cm}^3$ . The scheme of the experimental installation is shown in figure 1. The walls and the bottom of the test tank were made of acryl glass. Both side view and bottom view were used for visualization. For visualization we used high-speed camera MotionXtra HG-100K (Redlake) operated at the frame rate from 1000 to 4000 frames per second depending on experimental conditions.

The tank was filled with distilled water to the depth  $h$ . The present experiments were conducted with a set of acryl disks of diameter  $d = 18 \text{ cm}$  and thickness 3 cm. The bottom side of the disks was carefully machined to have a prescribed radius of curvature  $R_s$ , which took the following values: 30, 45, 60 and 80cm. The lower surface of the disks was painted white. A vertical steel rod was attached to the disks. The rod could slide free in a linear bearing serving as a guide. The mass of the disk with the rod was 2.72-kg in all experiments. The impact speed  $W$  was varied by changing the drop height  $H$ . The impact speed was measured from the side view movies and by integrating the data of the accelerometer attached to the end of the guiding rod. At low values of  $W$  the motion of the disk at constant speed was driven mechanically. Figure 1 shows the set-up adapted to the study of a normal impact. A more sophisticated version of the this set-up was used to study the

effect of air cushioning in the case of an oblique impact.

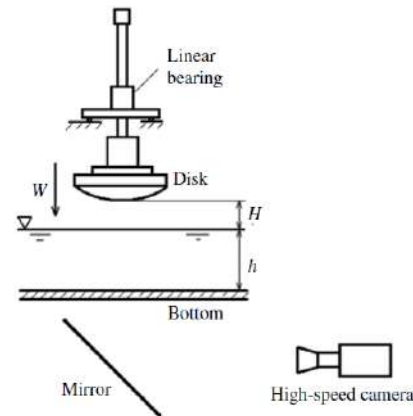


**Figure 1:** The scheme of the experimental setup

A typical sequence of video images depicting the formation of air cushion at the nozzle of the impacting sphere is shown in figure 2. It can be seen that the contact of liquid with the rigid spherical surface is localized in an annular region surrounding the central air cushion. It can be seen that the outward-propagating contact line remains smooth and circular while the inward-propagating contact line develops some fingering instability.



**Figure 2:** Development of the air pocket at disk impact onto a free surface. The data were obtained at  $R_s = 80 \text{ cm}$ ,  $W = 11.1 \text{ cm s}^{-1}$  and the frame rate 2000 fps.

The initial radius of the air pocket  $r_p$  could be reliably determined from the video records. The theory based on the lubrication-inviscid balance suggests that  $r_p$  is a linear function of  $A = [4\mu_a/(\rho_w W)]^{1/3} R_s^{2/3}$ . This dependence has been verified experimentally as shown in figure 3. For the impact of a sphere onto a water under standard atmospheric conditions we obtain  $r_p = 4A$ . More details on comparison between the numerical and experimental results and the implications to the droplet impact can be found in Hicks et al (2012). In particular, we discuss a correction to the results of Mani, Mandre and Brenner

(2010). It is interesting to note that when the angle between the velocity vector and the vertical increases (i.e. in the case of an oblique impact) the initial shape of the air pocket changes drastically. For small and moderate angles between the velocity vector and the vertical it becomes elliptical. As the velocity vector becomes closer to the horizontal the air pocket takes the form of a horse-shoe. Finally, at small angle between the velocity vector and the horizontal the effect of air-pocket formation fully disappears.

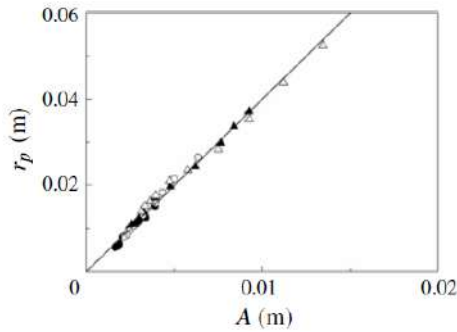


**Figure 3:** Initial radius of the air pocket  $r_p$  versus parameter  $A$ . Different symbols correspond to the following radii of curvature:  $\bullet$ , 30 cm;  $\circ$ , 45 cm;  $\blacktriangle$ , 60 cm;  $\triangle$ , 80 cm. The data obtained in the range of impact speeds between 0.02 and 1.2 m s<sup>-1</sup>.

The linear proportionality  $r_p \sim A$  suggests that at  $W \rightarrow 0$  we have  $r_p \rightarrow \infty$ , what is unphysical. In reality, at low impact the axisymmetric pattern depicted in figure 2 evolves toward non-axisymmetrical patterns. Such a behavior bears some similarity with the “frustration” phenomenon known for the drop-splash crowns (see Krechetnikov and Homsy 2009, Krechetnikov 2011).

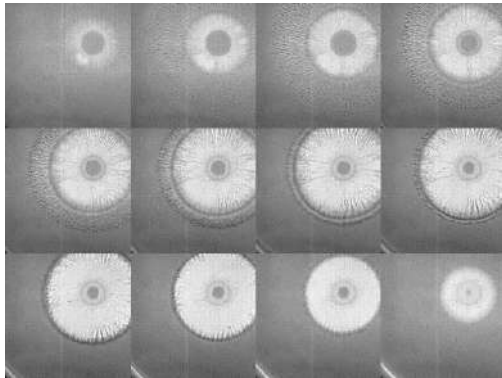


**Figure 3:** Cavitation at impact of a sphere on a flat surface

Finally, if we consider the full process of impact of a rigid sphere onto a liquid layer, the final stage of impact corresponds to a collision between the sphere and the rigid bottom. As it is shown by Brenner (1961), a collision between a sphere and a flat surface cannot occur under the action of a finite force because of high pressures in the lubrication flow in the residual liquid gap. However, under realistic conditions of unsteady flow generated by the sphere bouncing from a liquid layer, a cavitation occurs, which violates the continuity assumed in Brenner (1961) and later

works. The sequence of photos showing the stages of cavitation due to collision of a sphere with a rigid bottom is shown in figure 4. A criterion for the onset of cavitation is a subject of ongoing debate (Marston et al 2011, Seddon et al 2012).

## References

Brenner H., The slow motion of a sphere through a viscous fluid towards a plane surface, *Chem. Engng. Sci.*, Vol. 16 pp. 242-251 (1961)

Ermanyuk, E. V., Gavrilov, N. V., Experimental study of disk impact onto shallow water. *J. Appl. Mech. Tech. Phys.*, Vol. 52(6) pp. 889–895. (2011)

Hicks P.D., Purvis R., Air cushioning and bubble entrapment in three-dimensional droplet impacts, *J. Fluid Mech.*, Vol. 649 pp. 135-163 (2010)

Hicks P.D., Purvis R., Air cushioning in droplet impacts with liquid layers and other droplets, *Phys Fluids*, Vol. 23(6) paper 062104 (2011)

Hicks P.D., Ermanyuk E.V., Gavrilov N.V., Purvis R., Air trapping at impact of a rigid sphere onto a liquid, *J. Fluid Mech.*, Vol. 695 pp. 310-320 (2012)

Korobkin A.A., Ellis A.S., Smith F.T. Trapping of air in impact between a body and shallow water, *J. Fluid Mech.*, Vol. 611 pp. 365-394 (2008)

Krechetnikov R., Homsy G.M., Crown-forming instability phenomena in the drop splash problem, *J. Colloid Interface Sci.*, Vol. 331(2) pp. 555-559 (2009)

Krechetnikov R., A linear stability theory on time-invariant and time-dependent spatial domains with symmetry: the drop splash problem, *Dyn. PDE*, Vol. 8(1) pp. 47-67 (2011)

Marston J.O., Yong W., Ng W.K., Tan R.B.H., Thoroddsen S.T., Cavitation structures formed during the rebound of a sphere from a wetted surface, *Exp. Fluids*, Vol. 50 pp. 729-746 (2011).

Seddon J.R.T., Kok M.P., Linnartz E.C., Lohse D., Bubble puzzles in liquid squeeze: cavitation during compression, *Europhys. Letters*, Vol. 97 paper 24004 (2011)

Smith F.T., Li L., Wu G.X., Air cushioning with a lubrication/inviscid balance, *J. Fluid Mech.*, Vol. 482 pp. 291-318 (2003)

Thoroddsen S.T., Etoh T.G., Takehara K., Air entrapment under an impacting drop, *J. Fluid Mech.*, Vol. 478 pp. 125-134 (2003)

Thoroddsen S.T., Etoh T.G., Takehara K., Ootsuka N., Hatsuki Y., The air bubble entrapped under a drop impacting on a solid surface, *J. Fluid Mech.*, Vol. 545 pp. 203-212 (2005)

## Investigation of moist air flow near contact line using microdroplets as tracers

Vladimir S. Ajaev<sup>1,2</sup>, Dmitry V. Zaitsev<sup>1,3</sup>, Dmitry P. Kirichenko<sup>1,3</sup>, Oleg A. Kabov<sup>1,3</sup>

<sup>1</sup>Kutateladze Institute of Thermophysics,  
Novosibirsk 630090, Russia

<sup>2</sup>Southern Methodist University, Department of Mathematics  
Dallas, Texas 75275, USA  
[ajaev@smu.edu](mailto:ajaev@smu.edu)

<sup>3</sup>Novosibirsk State University,  
Novosibirsk 630090, Russia

Evaporation near contact lines is important for a number of applications such as spray cooling (Kim 2007), wickless heat pipes (Chatterjee et al. 2011) and shear-driven films (Kabov et al. 2007). It is well-known from both experimental and theoretical studies, reviewed e.g. by Ajaev and Kabov (2017), that evaporation rate increases significantly in the contact line region. Thus, it is important to obtain accurate information about the heat and mass transfer there. The objective of the present study is to obtain detailed information about the moist air velocity using microscale droplets as tracers as they move in the vicinity of the contact line.

The sketch of the experimental set-up is shown in Figure 1. The test section is a stainless steel plate 40×40×5 mm<sup>3</sup> in size with a flush-embedded 10×10 mm<sup>2</sup> copper block, electrically heated from below. The working surface of the test section was mechanically polished to the root square mean roughness (RMS) of 0.50 μm. The test section is mounted horizontally and open to the atmosphere. The surrounding air temperature is 25±2°C. The surface temperature of the copper block  $T_w$  is measured with thermocouples at three points with the accuracy of 0.1 K and frequency of 1 Hz. According to the measurements, the condition  $T_w = \text{const}$  is always met along the copper surface. In the experiments,  $T_w$  was varied from 55 to 100 °C. Ultra-pure water (Merck Millipore) is used as the working liquid. The static advancing contact angle of the working liquid on the copper surface at room temperature is 74±9°, whereas the receding contact angle is less than 10°. Optical recording is made with a high-speed camera FASTCAM SA1.1 (5400 fps with resolution of 1024x1024 pixel) coupled with a microscope objective. At the start of the experiment, a dry patch in the liquid layer is formed by a pulsed air jet.

Water microdroplets form by condensation over the liquid-vapor surface and levitate supported by the flow originated at the liquid-gas interface, as discussed e.g. in Fedorets et al. (2011). The droplets organize themselves into large arrays. When such an array is in the vicinity of the contact line, the droplet follow the trajectory shown schematically in the sketch in Figure 1, i.e. first move upward, then follow a nearly circular trajectory and end up over the dry solid substrate, where they eventually evaporate while levitating. The levitation over the solid substrate can be explained by the reflection of the flow created by the evaporating droplet off the substrate. Our main objective is to use the detailed information on the droplet trajectories to

compute the moist air velocity.

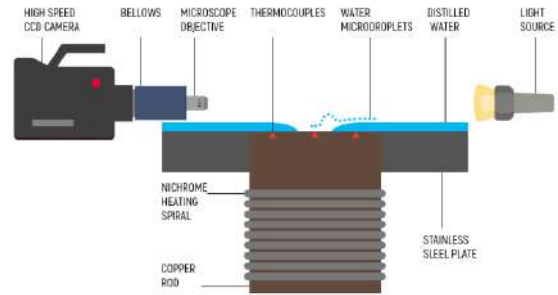


**Figure 1:** Sketch of the experimental set-up for studies of droplet motion over the contact line.

If the position of the droplet is characterized by the vector function  $\mathbf{r}(t)$ , the motion of a droplet of mass  $m$  and radius  $R$  is governed by

$$m\mathbf{r}'' = m\mathbf{g} + \mathbf{F}_b + 6\pi\mu R(\mathbf{v} - \mathbf{r}'), \quad (1)$$

where  $\mathbf{g}$  is the acceleration of gravity,  $\mu$  is the gas viscosity, and  $\mathbf{v}$  is the gas velocity. The force  $\mathbf{F}_b$  due to buoyancy is accounted for in this equation, but it is usually small, so that the main balance is between gravity and the Stokes drag force, represented by the last term on the right-hand side of Eq. (1). Expressing the volume of the spherical droplet in terms of its radius and rearranging terms in the above equation leads to the formula for the moist air velocity in the form

$$\mathbf{v} = \frac{2R^2}{9\mu} (\rho_l \mathbf{r}'' - \mathbf{g}(\rho_l - \rho_g)) + \mathbf{r}', \quad (2)$$

where  $\rho_i$ ,  $i=l,g$  are the densities of the liquid and gas, respectively. We use Eqn. (2) to obtain information about gas flow velocity distributions by analyzing trajectories of the droplets. The values of derivatives of  $\mathbf{r}(t)$  are found using the Savitzky-Golay method.

The analysis shows that for the flow near the contact line the vertical component of velocity is typically significantly higher than the horizontal one. Fig. 2 (bottom) shows the plot of the vertical component as a function of the horizontal coordinate. The corresponding trajectory is also

shown in the top part of the same figure. It is important to emphasize that the plots of moist air velocity components are only meaningful when analyzed together with the droplet trajectories since the velocity field is only probed at the locations of the droplet. In particular, when the droplet moves upward, it finds itself in a region of lower air velocity, so the value of vertical velocity drops compared to what could be expected if the droplet were moving in a horizontal direction. This explains the fact that the location of the maximum in the bottom figure is slightly shifted with respect to the contact line position. Still, it is clear that the moist air velocity is increasing as the contact line is approached. We also note that the sharp increase in the velocity in the leftmost part of trajectory has to do with the effects of reflection of the flow created by the droplet itself off the substrate and thus should not be interpreted as the true gas velocity, i.e. the velocity in the absence of droplet. Since this effect becomes significant only very close to the substrate (at a distance of the order of 10 micron), it does not affect the accuracy of the velocity profile outside of this region.

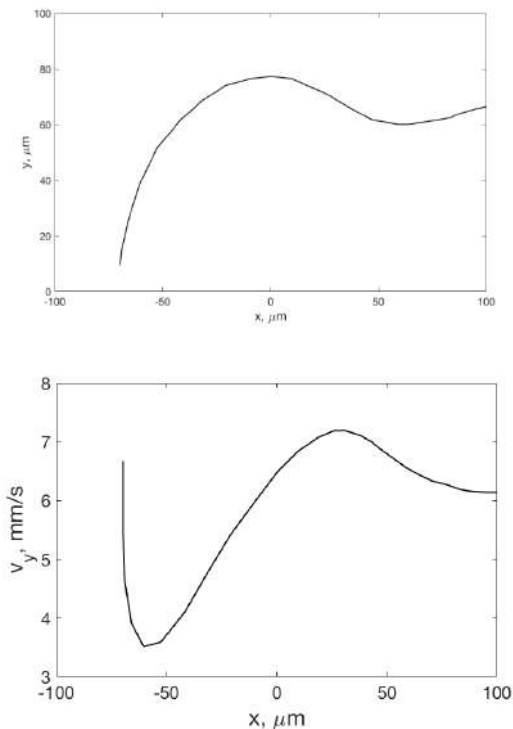


**Figure 2:** Experimental recording of a droplet trajectory (top) and the corresponding moist air vertical velocity profile (bottom).

To summarize, we study trajectories of microdrops of condensate in the vicinity of a contact line formed on a heated substrate. The contact line is the boundary of a stationary dry patch in a liquid layer on a rough copper substrate. Both velocity and acceleration of droplets from the experimental data on their positions are computed numerically using the Savitzky-Golay method. We then carried out the investigation of local flow of moist air near the contact line based on the data for droplet trajectories.

Increase in the flow velocity is observed near the contact line.

## References

Kim, J., Spray cooling heat transfer: The state of the art, *Int. Journal of Heat and Fluid Flow*, Vol. 28, pp. 753-767 (2007)

Chatterjee, A., Plawsky, J. L. and Wayner Jr., P. C., Disjoining pressure and capillarity in the constrained vapor bubble heat transfer system, *Adv. Colloid Interface Sci.*, Vol. 168, pp. 40-49 (2011)

Kabov O.A., Lyulin Yu.V., Marchuk I.V. and Zaitsev D.V., Locally heated shear-driven liquid films in microchannels and minichannels, *Int. Journal of Heat and Fluid Flow*, Vol. 28, pp. 103-112 (2007)

Ajaev, V. S. and Kabov, O. A. Heat and mass transfer near contact lines on heated surfaces, *Int. J. Heat Mass Transfer*, Vol. 108, pp. 918-932 (2017)

Fedorets, A. A., Marchuk, I. V. and Kabov, O. A., Role of vapor flow in the mechanism of levitation of a droplet-cluster dissipative structure, *Tech. Phys. Lett.* Vol. 37, pp. 116-118 (2011)

## Local heat transfer rate in the contact line area beneath vapor bubble at boiling

Anton Surtaev<sup>1</sup>, Vladimir Serdyukov<sup>1</sup>, Andrey Chernyavskiy<sup>1</sup>,  
Denis Kozlov<sup>2</sup> and Dmitry Selishchev<sup>2</sup>

<sup>1</sup> Kutateladze Institute of Thermophysics SB RAS  
Akad. Lavrentiev ave. 1, Novosibirsk, 630090, Russia

<sup>2</sup> Borekov Institute of Catalysis SB RAS  
Akad. Lavrentiev ave. 5, Novosibirsk, 630090, Russia  
surtaevas@gmail.com

An analysis of heat transfer in the vicinity of the three-phase contact line at vapor bubble base is very important for understanding physics of nucleate boiling. Since early studies (Labuntsov 1963; Cooper, Lloyd 1969), in which it has been proposed that at nucleate boiling a vapor bubble can trap a thin layer of liquid at the wall during its initial growth, a lot of questions related with the microlayer evolution, heat and mass transfer in the area of the contact line, influence of surface wettability on heat transfer are still open. Some authors explain high intensity of heat transfer at nucleate boiling with high heat transfer rate in the contact line vicinity at the stage of vapor bubble formation and growth (Yagov 2014). At the same time, in some papers, for example, in (Jung, Kim, 2014) it was experimentally shown that the contribution of heat flux by microlayer evaporation to the integral heat transfer does not exceed 20%. This shows that the physical background of microlayer evaporation is not sufficiently understood.

Due to the small area of microlayer influence and its high evaporation rate the experimental investigation of heat transfer in this area is very complicated task (Haensh 2016). However, in last decade new experimental techniques with high temporal and spatial resolution, including infrared thermometry, laser interferometry, PIV, etc., that allow to discover the boiling process on microscale are developed. For example, laser interferometric method is widely used in recent years to determine the thickness of the microlayer under single vapor bubbles at different time (Gao et al. 2013, Jung, Kim 2014). With the use of PIV technique authors (Duan et al. 2013) have analyzed the hydrodynamics of microflows at bubble appearance, growth and detachment from the surface. In recent years, a general method to study the evolution of temperature field under single vapor bubble is the high-speed infrared thermometry (IR).

But it should be noted, that exciting experimental investigations of the local heat transfer in the vicinity of contact line are usually limited by the range of low input heat fluxes and only one working liquid (water). Heat transfer in the microlayer area at boiling is still poorly investigated.

In this paper results of the experimental investigation of microlayer dynamics and temperature field evolution under single vapor bubbles at pool boiling of various liquids in a wide range of heat fluxes obtained with the use of modern techniques with high temporal and spatial resolutions will be presented. Also with the use of developed numerical algorithm and obtained experimental results of unsteady temperature field the reconstruction of local instantaneous heat flux distribution on the heater will be made.

Experiments were carried out at pool boiling of saturated ethanol and deionized water at atmospheric pressure. Detailed description of the experimental setup and measurement techniques is presented in (Surtaev et al. 2016). Thin (1  $\mu\text{m}$ ) conductive indium tin oxide (ITO) with exposed area of  $30 \times 20 \text{ mm}^2$ , vacuum deposited onto 400  $\mu\text{m}$  thick sapphire substrate was used as the heater. The main advantage of usage ITO film as a heater is its property to be opaque in the mid-IR spectrum (3-5  $\mu\text{m}$ ) and to be transparent for visible spectrum (380-750 nm). When it deposited onto thin sapphire substrates, which is transparent to both IR and visible spectrum, it became possible to investigate unsteady temperature field of ITO film by infrared recording and to observe the dynamics of vapor bubbles and contact line with the use of high-speed video camera.

Measurements of the surface temperature field were performed by high speed infrared thermographic recording (IR) with the use of FLIR Titanium HD 570M camera (spectral range 3.7 - 4.8  $\mu\text{m}$ ). Thermographic recording was made with frame rate of 1000 fps at resolution up to 13  $\mu\text{m}/\text{px}$ . High-speed visualization (HSV) was performed using Vision Research Phantom v. 7.0 camera with 2000 fps and resolution of  $640 \times 480$  (1 px  $\approx$  0.07 mm). A quick-response incandescent lamp located under the work area was used to synchronize IR and HSV recordings in time. With the use of described synchronized techniques new experimental data of heat transfer coefficients, nucleation site density, frequency and temporal characteristics of nucleation process, dynamics of vapor bubble growth and detachment were obtained. The detailed description and analysis of these data are presented in (Surtaev et al. 2016, Serdyukov, Surtaev, 2017). In this research we will focus more on local heat transfer under single vapor bubble at liquid boiling obtained by macro IR thermometry and numerical simulation.

The frames of high-speed macro IR thermography of temperature field evolution under active nucleation site at water boiling at  $q = 50 \text{ kW}/\text{m}^2$  are presented in Fig.1. As it is shown from the analysis of experimental data when vapor bubble appears on the surface, the temperature in the area of nucleation site sharply decreases. In the growth stage of vapor bubble the regions with different heat transfer mechanism (microlayer region and area of dry spot in the center of nucleation site) appear. The boundary between different heat transfer modes is the triple contact line. The area with a minimal temperature of the heater surface corresponds to microlayer region. The data analysis presented by Jung et al (2014) and Serdyukov, Surtaev (2017) shows, that after the bubble growth stage, where

microlayer evaporation plays a dominant role in heat transfer, the stage of vapor bubble detachment begins.

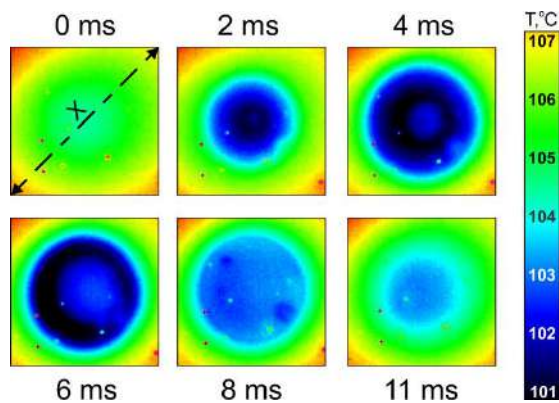


**Figure 1:** High-speed IR camera images of evolution of temperature field under single vapor bubble at water boiling ( $q = 50 \text{ kW/m}^2$ ).

At the departure stage the equivalent bubble diameter almost unchanged with a sharp reduction of the area limited by triple contact line. Experimental data of thickness of microlayer under individual vapor bubble (Jung et al. 2014) showed that on this stage the microlayer was completely depleted.

Reconstruction of the temperature fields and calculation of the heat fluxes based on experimental IR-thermometry data have been performed by cooperative solving of unsteady heat conductivity equation in the ITO film and sapphire substrate. Detailed description of the numerical simulation can be found in our previous paper (Surtaev, Serdyukov, Chernyavskiy et al. 2017).

Developed numerical algorithm has allowed to investigate evolution of local heat flux distribution on the heaters wall at boiling at input heat flux density up to  $500 \text{ kW/m}^2$  (for water). It has been shown, that at boiling of water for input heat flux  $q = 50 \text{ kW/m}^2$  the maximum heat flux density observed in microlayer reaches about  $1.2 \text{ MW/m}^2$ . With the use of obtained heat flux maps and temperature field under individual vapor bubble the microlayer thickness can be estimated. The analysis has showed, that microlayer thickness on the stage of vapor bubble growth at boiling of water and ethanol ranged from 0.5 to 5 microns, which is in good agreement with the experimental data presented in the literature and obtained using laser interferometry (Gao et al. 2014, Jung et al. 2014).

Also within the present study it is planned to carry out experimental investigation devoted to the influence of surface wettability on internal boiling characteristics, heat transfer and crisis phenomena development at nucleate boiling. Nowadays usage of various coatings and surface modification techniques is very actual and accepted way to enhance heat transfer and inhibition to fouling at boiling. However, local heat transfer characteristics, especially phenomena occur in the vicinity of the triple contact line, at boiling on modified heat exchange surfaces with different wetting properties are poorly investigated.

For this purpose in the present study various oxide ( $\text{SiO}_2$ ,  $\text{TiO}_2$ , etc.) and fluoropolymer films with wetting

contact angle varying in a range of  $20^\circ$ - $130^\circ$  on the surface of thin film heaters will be fabricated. Usage of high speed IR and video recording will allow to investigate dependence of dynamics and thermal behavior of microlayer on wetting properties for the first time.

*Reported study was funded by Russian Foundation for Basic Research (RFBR), research project No. 17-08-01342.*

## References

- Labuntsov D.A. The mechanism of vapor bubbles growth on the heating surface at boiling (in Russian), *Journal of Engineering Physics and Thermophysics*, Vol. 6, No. 4, pp. 33-40 (1963)
- Cooper M.G., Lloyd A.J.P. The microlayer in nucleate pool boiling, *International Journal of Heat and Mass Transfer*, Vol. 12, No. 8, pp. 895-913 (1969)
- Yagov V.V. Heat Transfer in Single Phase Media and Phase Transitions (in Russian), MPEI Publish, 541 p. (2014)
- Jung S., Kim H., An experimental method to simultaneously measure the dynamics and heat transfer associated with a single bubble during nucleate boiling on a horizontal surface, *International Journal of Heat and Mass Transfer*, Vol. 73, pp. 365–375 (2014)
- Hänsch S., Walker S. The hydrodynamics of microlayer formation beneath vapour bubbles, *International Journal of Heat and Mass Transfer*, Vol. 102, pp 1282-1292 (2016)
- Gao M., Zhang L., Cheng P., Quan X. An investigation of microlayer beneath nucleation bubble by laser interferometric method, *International Journal of Heat and Mass Transfer*, Vol. 57, No. 1, pp. 183-189 (2013)
- Duan X., Phillips B., McKrell T., Buongiorno J. Synchronized high-speed video, infrared thermometry, and particle image velocimetry data for validation of interface-tracking simulations of nucleate boiling phenomena, *Experimental Heat Transfer*, Vol. 26, No. 2-3, pp. 169-197 (2013)
- Surtaev A.S., Serdyukov V.S., Moiseev M.I. Application of high-speed IR thermography to study boiling of liquids, *Instruments and Experimental Techniques*, Vol. 59, No. 4, pp. 615-620 (2016)
- Serdyukov V., Surtaev A. Experimental study of multi-scale heat transfer characteristics at pool boiling, *Journal of Physics: Conference Series*, Vol. 785, p. 012007 (2017)
- Surtaev A, Serdyukov V, Chernyavskiy A. Study of thermal behavior of microlayer under vapor bubble at liquid boiling, *The European Physical Journal (EPJ)*, 5 p. (2017) (in press)

## Mathematical modeling of relief glass film formation by evaporative lithography method in combination with IR-heating

Konstantin Kolegov

Caspian Institute of Sea & River Transport the branch of the Volga State University of Water Transport  
6/14 Nikolskaya St., Astrakhan, 414000, Russian Federation  
Astrakhan State University  
20a Tatishchev St., Astrakhan, 414056, Russian Federation  
email: konstantin.kolegov@asu.edu.ru

There are applications based on the drawing of textured coatings. For example, pollution control of submerged surfaces (Efimenko et al. 2009). The method consists in using some hierarchical structures against marine microorganisms. The structure with a ribbed surface allows reducing a hydrodynamic drag of a ship (Gogte et al. 2005).

There are several approaches to create polymer coatings with topographic structure at the micro and nanoscale. The method of photolithography is widely known, but this multi-stage process is required special equipment and materials. Structured surfaces of polymers can be obtained by some moulding methods, such as nano-scale injection moulding, capillary moulding and ultraviolet nanoimprinting. These methods have several disadvantages, such as a lack of process flexibility and a need for expensive equipment.

Therefore evaporative lithography attracts more and more attention. The flow arises at a nonuniform evaporation of a colloidal film. It carries the particles to the field of an intensive evaporation. For example, the desired structure is obtained by using a mask, which is a plate with holes. It is placed above the liquid (Harris et al. 2007). The method has two restrictions. First, general time of an evaporation process increases considerably because the mask blocks the most part of a liquid surface. Second, particles of glassy polymer are not capable of film formation but yield brittle coating with cracks when their melting point is above a room temperature. This problem is solved by introducing into the system the IR-source (Georgiadis et al. 2011). Local heating creates a strong evaporation under open areas in the mask. This method is simpler, cheaper and applicable to almost any substrate without preliminary processing compared to other methods of creating textured layers.

Methods of mathematical modeling will help to understand how better operate the process. Proposed model describes mass and heat transfer at the hydrodynamic stage and the sol-glass transition. The system includes the continuity equation

$$\frac{\partial h}{\partial t} + \frac{\partial(hu)}{\partial x} = -J,$$

convection equation

$$\frac{\partial C}{\partial t} + u \frac{\partial C}{\partial x} = \frac{CJ}{h},$$

the heat conductivity equation for liquid

$$\frac{\partial T}{\partial t} + u \frac{\partial T}{\partial x} = \text{Fo}_s \frac{1}{h} \frac{\partial}{\partial x} \left( hk \frac{\partial T}{\partial x} \right) + \frac{1}{\text{Gz}} \frac{T_s - T}{h} + \text{St}_s \frac{1 - \exp(-a_\lambda h l_c)}{h} H(X_h - x) - \frac{J}{h} (\text{Bu} - T)$$

and for substrate

$$\frac{\partial T_s}{\partial t} = \text{Fo}_s \frac{\partial}{\partial x} \left( k_s \frac{\partial T_s}{\partial x} \right) + \frac{1}{\text{Gz}} \frac{T - T_s}{h_s} + \text{St}_s \frac{\exp(-a_\lambda h l_c)}{h_s} H(X_h - x).$$

The film thickness  $h$ , the lateral flow velocity  $u$ , the vapor flux  $J$ , the mass fraction of colloidal particles  $C$ , the substrate temperature  $T$ , the coefficient of thermal conductivity  $k$  and the substrate temperature  $T_s$  are functions depends on coordinate  $x$  and time  $t$ . The Fourier number  $\text{Fo}$ , the Graetz number  $\text{Gz}$ , the Stanton number  $\text{St}$  and the Bulygin number  $\text{Bu}$  are dimensionless parameters of the problem. The subscript "s" in some functions or parameters means that it related to the substrate. Dimension of a characteristic length  $l_c$  is meter. All other quantities are dimensionless. The function of Heaviside  $H$  is used for simulation of mask influence on the system. The quantity  $2X_h$  is a width of a hole in the mask. The thickness of substrate  $h_s$  is a constant. All the equations are derived from the consideration of the balance of mass and heat in an elementary volume (Kolegov and Lobanov 2012, Kolegov 2016).

The lateral flow velocity is calculated with using of lubrication approximation

$$u = \frac{1}{\text{Ca}} \frac{h^2}{3\eta} \frac{\partial^3 h}{\partial x^3},$$

where  $\text{Ca}$  is the capillary number. The viscosity  $\eta$  is a function. Empirical dependence of the viscosity on the concentration is constructed with using the experimental data (Matveyenko and Kirsanov 2011). The vapor flux is described by the model law, which takes into account dependency on concentration of solution and fluid temperature.

Consider initial and boundary conditions of the problem. The initial shape of the open surface of the film is flat,  $h(x, 0) = h_0$ . The temperatures and the concentration are uniform at the initial time,  $T(x, 0) = T_s(x, 0) = 1$ ,  $C(x, 0) = C_0$ . On the boundaries  $\partial C / \partial x = \partial T / \partial x = \partial T_s / \partial x = 0$ , because of the symmetry. The flow changes a direction at points  $x = 0$  and  $x = X$ , so the velocity is zero,  $u(0, t) = u(X, t) = 0$ .

The problem is solved by the finite difference method (implicit scheme). The resulting system of algebraic equation is solved by Newton's method. The number of grid points on the spatial coordinate equal 125 was used during computation.

The calculation results show an almost linear increase in temperature of the liquid over time (Figure 1). This is in a

good agreement with the experimental data (Georgiadis et al. 2013).

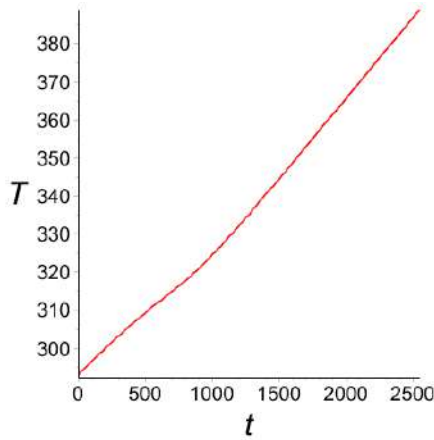


**Figure 1:** The liquid temperature (K) vs time (s) in point  $x = 0$ .

Figure 2 shows the thickness of film at different times. The liquid film is flat at the beginning of the process. The glass film with a variable thickness is formed at the final stage. The film thickness is order of magnitude greater under the hole than in the closed area. Georgiadis et al. have got similar results experimentally (2011).

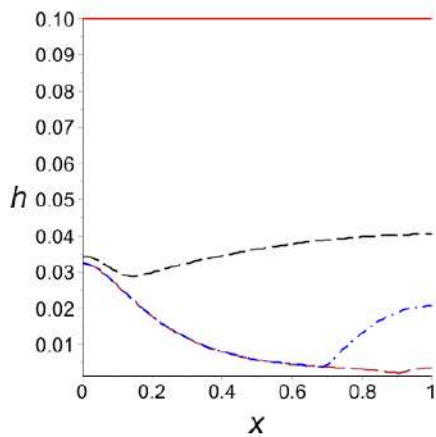


**Figure 2:** The film shape on the several serial time steps (mm).

The evolution of the mass fraction of particles is shown in Figure 3. There is almost no liquid in the film at the final stage of process.

This model takes into account only the compensation flow. The obtained result indicates that other types of flows in the studied process are of a secondary importance. The development of two-dimensional model will allow more detailed assessment of the contribution of the thermal and solutal Rayleigh-Benard-Marangoni convection.

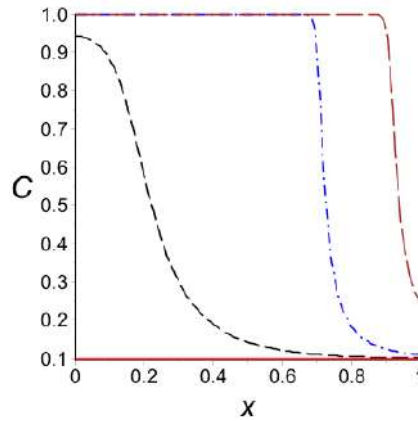


**Figure 3:** The mass fraction of particles on the several serial time steps.

The reported study was funded by RFBR according to the research project No. 16-38-00439 mol\_a.

## References

- Efimenko K., Finlay J., Callow M.E., Callow J.A. and Genzer J., Development and testing of hierarchically wrinkled coatings for marine antifouling, *Appl. Mater. & Interf.*, Vol. 1 pp. 1031-1040 (2009)
- Gogte S., Vorobieff P., Truesdell R., Mammoli A., van Swol F., Shah P. and Brinker C.J., Effective slip on textured superhydrophobic surfaces, *Phys. Fluids*, Vol. 17, pp. 051701: 1-4 (2005)
- Daniel J. Harris, Hua Hu, Jacinta C. Conrad and Jennifer A. Lewis, Patterning colloidal films via evaporative lithography, *Phys. Rev. Lett.*, Vol. 98, pp. 148301:1-4 (2007)
- Georgiadis A., Routh A.F., Murray M.W. and Keddie J.L., Bespoke periodic topography in hard polymer films by infrared radiation-assisted evaporative lithography, *Soft Matter*, Vol. 7 pp. 11098-11102 (2011)
- Kolegov K.S., Lobanov A.I., Comparing of a quasisteady and nonsteady mathematical models of fluid flow in evaporating drop, *Computer Research and Modeling*, Vol. 4 pp. 811-825 (2012)
- Kolegov K.S., Mathematical modelling of heat and mass transfer in colloidal liquid evaporating from the cell under a mask and IR radiative heating, *CASPIAN JOURNAL: Control and High Technologies*, Vol. 4 pp. 85-98 (2016)
- Matveyenko V.N., Kirsanov E.A., Viscosity and structure of disperse systems, *Bulletin of the Moscow University. Ser. 2. Chemistry*, Vol. 52 pp. 243-276 (2011)
- Georgiadis A., Muhamad F.N., Utgenannt A., Keddie J.L., Aesthetically textured, hard latex coatings by fast IR-assisted evaporative lithography, *Progress in Organic Coatings*, Vol. 76 pp. 1786-1791 (2013)

## Evaporation Local Heat Transfer Coefficients of Refrigerant HFC-245fa in a Plate Heat Exchanger

Osamu Kawanami<sup>1</sup>, Shoya Sakoda<sup>1</sup>, Naoto Sasaki<sup>2</sup>, Toshiyuki Furukawa<sup>2</sup> and Kenji Kusunoki<sup>2</sup>

1. Department of Mechanical and System Engineering, University of Hyogo  
2167 Shosha Himeji, Hyogo 671-2280, Japan  
[kawanami@eng.u-hyogo.ac.jp](mailto:kawanami@eng.u-hyogo.ac.jp)
2. Heat Exchanger Division, Hisaka Works, Ltd.  
2-1-48 Higashi-konoike-cho, Higashi-osaka City, Osaka 578-0973, Japan

Plate heat exchanger, PHE, have been widely used for chemical reaction process, food processing, dry process, power generation and many other industrial applications due to their good thermal performance, compactness, and cost effective. For geothermal power generation using low temperature heat source such as hot spring, HFC-245fa (R-245fa) is employed as a refrigerant. In the past years, few research groups reported experimental data for evaporation heat transfer using PHE. However, there are very few experimental studies discussing local heat transfer along the plate in the PHE. Djordjevic and Kabel (2008) presented experimental results on evaporation heat transfer for flow boiling of ammonia and of R134a in a chevron-pattern corrugated PHE. The evaluation of a quasi-local heat transfer coefficient along the plate was measured, and the two-phase distribution and the heat transfer mechanism during evaporation in a plate channel were discussed. F. Vakili-Farahani *et al.* (2014) and R. L. Amalfi *et al.* (2016) used high-resolution IR camera to measure local PHE wall temperature under simple PHE simulated system by using 1 refrigerant channel and electronic heatin power supply.

In this study, original PHE is made by 3D printing method and thermocouples insert from the sidewall of the each plate for better understanding of heat transfer mechanizum in the PHE. Here we report a local heat transfer coefficients in the case of 1 refrigerant HFC-245fa channel and 2 heat source channels.

Figure 1 shows the flow loop diagram used in this study. The loop mainly consists of a resourver tank, a pump,

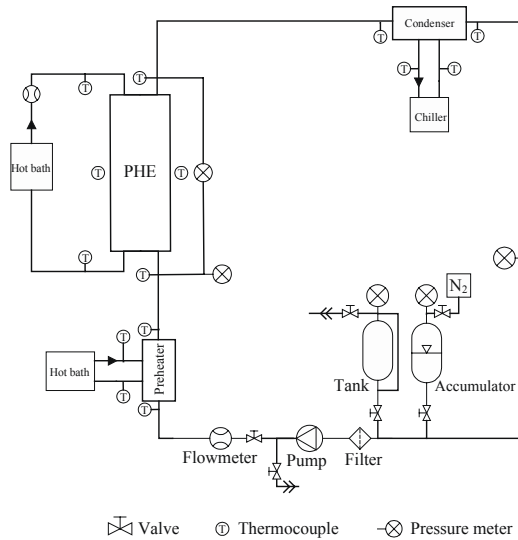


Figure 1: Flow loop diagram

an accumulator, a pre-heater, a test section and a condenser. The preheater and condenser are used a Brazed Heat Exchanger (BHE, Hisaka Works) to control inlet condition. The system pressure is controlled by the accumulator ranging from 0.4–1.2 MPa, which is corresponding to 54.9–97.8 °C. of saturated temperature. The volumetric flow

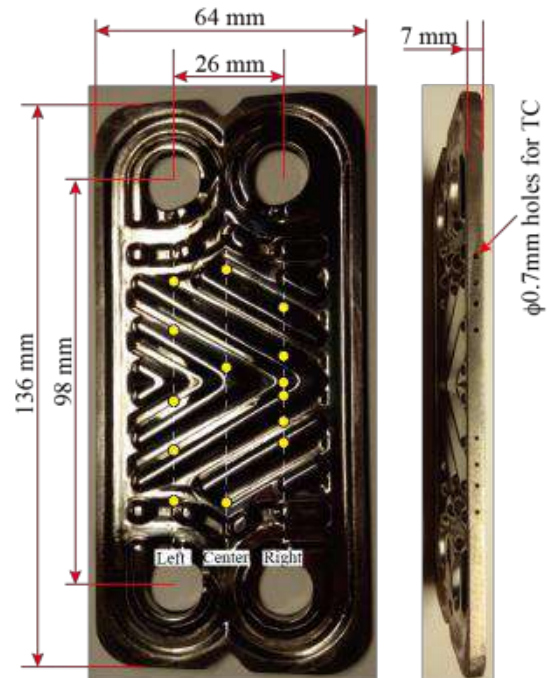


Figure 2: An image of the plate. The in-wall temperature measured at 16 locations as pointed by yellow circle.

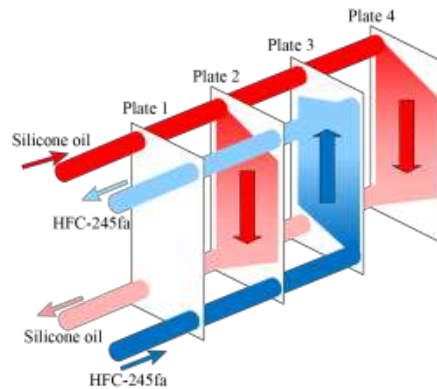
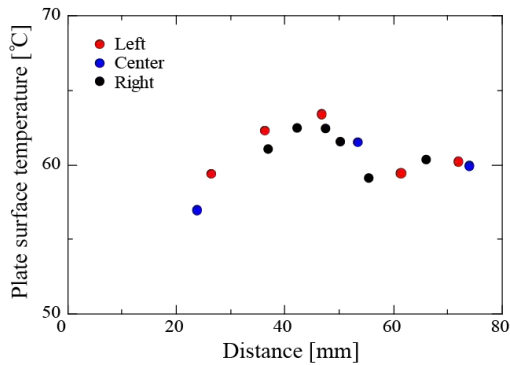


Figure 3: Fow configuration in PHE



**Figure 4:** Surface temperature of Plate 3 on the HFC-245fa side. “Left”, “Center”, “Right” are corresponding to the locations as pointed in Fig. 2.

rate set at about 30 ml/min. The subcooling temperature of HFC-245fa at the inlet of the PHE is set at 30 K. To heat HFC-245fa, hot silicone oil flows from thermostatic bath to PHE at 90-150 °C.

The PHE as a test section shows in Fig. 2. The size of heating area of the plate is 0.00406 m<sup>2</sup> (W 0.049m×L 0.08286m), and plate thickness is 1.5 mm. The hydraulic equivalent diameter,  $D_h$ , is 4 mm, and cross-section area of flow channel between plates is 117.6 mm<sup>2</sup>. The plate is made by direct metal laser-sintering system (EOSINT-M250 Xtended, EOS GmbH), and has 16 holes at the sidewall to insert  $\phi$ 0.5 mm thermocouple as shown in Fig. 2. Using those thermocouples, the local temperature in each plate can be measured. Heat flux is driven from the temperature difference and mass velocity of silicone oil. Under constant heat flux condition, local temperature of the plate surface and local heat transfer coefficient can be derived.

Figure 4 shows heated surface temperature distribution of HFC-245fa channel side on the Plate 2 and Plate 3. The horizontal axis indicates the distance from inlet of the PHE. The experimental conditions of this result are heat flux  $q = 8301 \text{ kW/m}^2$ , system pressure  $P = 0.4 \text{ MPa}$ , mass flux of HFC-245fa  $G_{\text{HFC245fa}} = 4.97 \text{ kg/m}^2\text{s}$ , Inlet subcooling of HFC-245fa  $\Delta T_{\text{sub}} = 28.75 \text{ K}$ , inlet temperature of silicone oil  $T_{\text{Silicone}} = 97.94 \text{ °C}$ . As a result, non-uniform temperature field on the plate along the width direction was not found. Recuention of temperature at 53.4 mm was clealy observed,

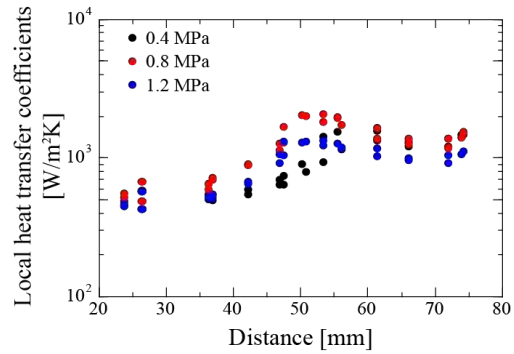


**Figure 5:** Heat transfer coefficients of Plate 2 and Plate 3 on the HFC-245fa side under various pressure conditions at  $q = 7.6\text{-}7.8 \text{ kW/m}^2$ ,  $G_{\text{HFC245fa}} = 5 \text{ kg/m}^2\text{s}$ , Inlet subcooling of HFC-245fa  $\Delta T_{\text{sub}} = 30 \text{ K}$ .

this point is defined as onset of nucleate boiling (ONB).

From the local temperature on the heated surface and HFC-245fa fluid temperature, heat transfer coefficients are calculated as a function of heat flux derived from the temperature difference between inlet and outlet of Silicone oil. The results at three difference pressures, 0.4, 0.8 and 1.2 MPa are shown in Fig. 5. The effects of pressure on the heat transfer coefficient were not observed excepting ONB. In the case of 0.4 MPa, point of ONB is moved to downstream compared with high-pressure cases under present experimental consitions.

## References

- E. Djordjevic and S. Kabelac, Flow boiling of R134a and ammonia in a plate heat exchanger, *Int. J. Heat Mass Transf.*, Vol. 51, pp. 6235-6242 (2008)
- F. Vakili-Farahani, R. L. Amalfi and J. R. Thome, Two-phase flow of R245fa in a 1 mm corrugation depth plate heat exchanger – Part 2: Flow boiling heat transfer, *Interfacial Phenomena and Heat Transfer*, Vol. 2, pp. 343-361 (2014)
- R. L. Amalfi, J. R. Thome, V. Solotych and J. Kim, High resolution local heat transfer and pressure drop infrared measurements of two-phase flow of R245fa within a compact plate heat exchanger, *Int. J. Heat Mass Transf.*, Vol. 103, pp. 791-806 (2016)

## Exact solution of the 3D problem of evaporative convection

Victoria B. Bekezhanova<sup>1</sup> and Olga N. Goncharova<sup>2,3</sup>

<sup>1</sup> Department of Differential Equations of Mechanics, Institute of Computational Modeling SB RAS  
Academgorodok, 50/44, Krasnoyarsk, 660036, Russia  
bekezhanova@mail.ru

<sup>2</sup> Institute of Thermophysics SB RAS  
Ac. Lavrentieva ave., 1, Novosibirsk, 630090, Russia

<sup>3</sup> Department of Differential Equations, Altai State University  
Lenin ave., 61, Barnaul, 656049, Russia  
gon@math.asu.ru

New physical experiments conducted in the Institute of Thermophysics SB RAS and researches performed in the frame of the ESA MAP Evaporation project allow one to investigate the structure of the flows of the evaporating liquid being under action of the co-current gas flux. The flow topology is determined by natural and thermocapillary convection, effects of the tangential stresses induced by the gas flow, thermophysical properties of used media and the mass transfer due to evaporation. The heightened interest in the problems of evaporative convection is explained not only by need of study the observed phenomena in the flow structure but also by many industrial applications of the problems of evaporative convection in development and modification of the cooling set-ups, evaporators, flash-film concentrator, rectifier equipment (Kutepov et al. 1986, Lyulin and Kabov 2014, Goncharova et al. 2015).

Mathematical modeling of the convective fluid flows with evaporation is carried out with use of the new exact solutions of the convection equations. The solution of special type of the Boussinesq approximation of the Navier-Stokes equations is a generalization in the three dimensional case of the well-known Ostroumov-Birikh solution. Let the liquid and the gas-vapor mixture fill the infinite horizontal channel and are separated by the thermocapillary interface. The exact stationary solution is characterized by dependence of the components of the liquid and gas velocity only on the transverse coordinates. The functions of temperature, pressure (deviation of pressure from the hydrostatic one) and vapor concentration in the gas-vapor phase have the terms, which also depend on the transverse coordinates. Let us note that the temperature functions in both layers and the vapor concentration function linearly depend on the longitudinal coordinate. Obtaining the exact solutions of the governing equations is very important in order to model the real fluid flows quickly and efficiently (Goncharova et al. 2012, Andreev and Bekezhanova 2013, Bekezhanova and Goncharova 2016). The exact solution allows one to describe the peculiar properties of the convective flows of evaporating liquids including the effects of thermodiffusion and diffusive thermo conductivity in the gas-vapor phase (Goncharova and Kabov 2016), to compare the analytical and experimental results and to evaluate the correctness of the mathematical model used.

On the thermocapillary interface, remaining being undeformed, the following conditions are imposed: the kinematic and dynamic conditions, the continuity conditions for the velocity and temperature, the heat transfer condition.

The last condition takes into account the diffusive mass flux due to evaporation, the mass balance equation, relation for the saturated vapor concentration and the Soret and Dufour effects. On the fixed impermeable walls of the channel the no-slip conditions for velocity fields and the conditions of thermal insulating of the lateral walls are fulfilled. Two types of boundary conditions can be used for vapor concentration function on the upper and lateral rigid walls: the conditions of absence of vapor flux or the conditions of zero vapor concentration.

The analytical approach is complemented by numerical investigations. The problem of constructing of the stationary solutions of a special type for the two-layer convective fluid flows with evaporation is reduced to sequential solving of several two-dimensional problems. The numerical procedure based on the method of alternating directions is used for approximate numerical solution of the above mentioned problems.

The flows in the liquid-gas systems (ethanol-nitrogen and HFE7100-nitrogen) with evaporation at the thermocapillary interface are computed. Influence of gravity, evaporation and values of the longitudinal temperature gradient on the structure of arising regimes is studied.

The flows are characterized as translational and progressively rotational motions and can be realized in the various forms. In figures 1-3 the topology and structure of flows and temperature distribution are presented in the case of the ethanol-nitrogen system with evaporation (fig. 1 and fig. 3 (a, c)) and without evaporation (fig. 2 and fig. 3 (b, d)) at the interface. The flow pictures are presented under conditions of micro- (fig. 1, 2) and normal (fig. 3) gravity. Values of the Grashof number  $Gr$  and longitudinal temperature gradient  $A$  are specified for all the cases.

The numerical results allow us to analyze the qualitative differences in topology of fluid flows in the liquid and in the gas-vapor phase and to develop a hierarchy of the flow regimes.

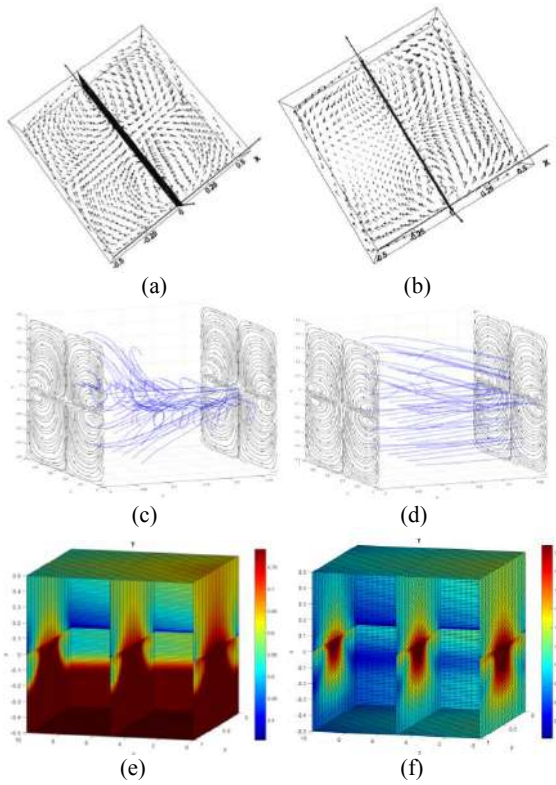


**Figure 1:** Regimes of flows with evaporation under microgravity: velocity field (a,b), trajectories and cross-section streamlines (c,d), temperature distribution (e,f);  $Gr = 470$ ;  $A = 0.01$  (a, c, e);  $A = 0.1$  (b, d, e).

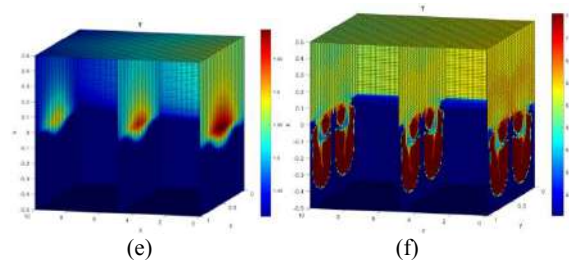
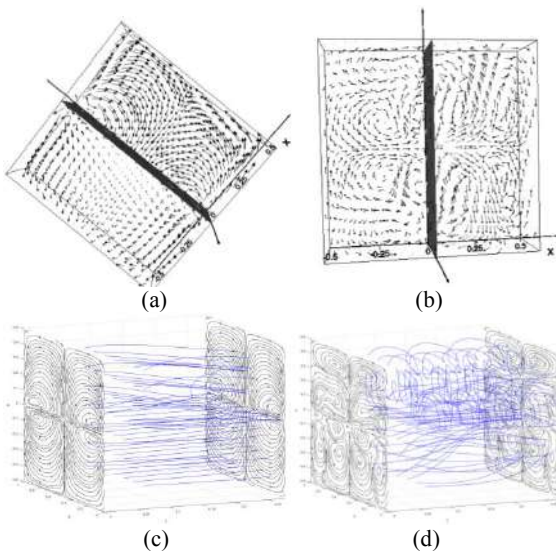


**Figure 2:** Regimes of flows without evaporation under microgravity: velocity field (a,b), trajectories and cross-section streamlines (c,d), temperature distribution (e,f);  $Gr = 470$ ;  $A = 0.1$  (a, c, e);  $A = 0.5$  (b, d, e).

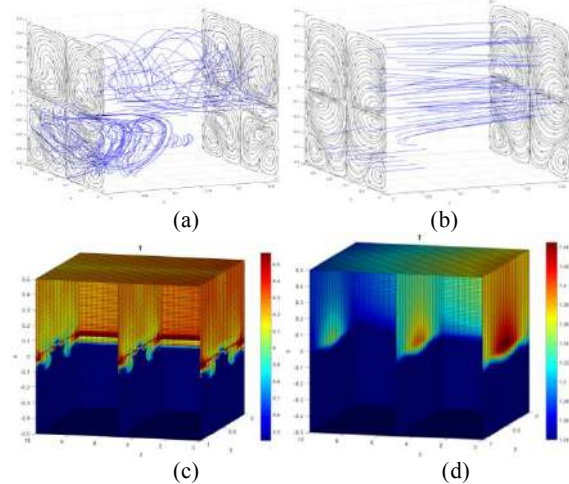


**Figure 3:** Regimes of flows under terrestrial conditions: trajectories and cross-section streamlines (a,b), temperature distribution (c,d);  $Gr = 47000$ ;  $A = 0.5$  with evaporation (a, c);  $A = 0.1$  without evaporation (b, d).

The work was supported by the Russian Science Foundation (project RSF 15-19-20049).

## References

- Kutepov A.M., Sterman L.S., Styushin N.G., Hydrodynamics and heat transfer at vaporization, Vysshaya shkola, Moscow (1986) (in Russian)
- Lyulin Y., Kabov O., Evaporative convection in a horizontal liquid layer under shear-stress gas flow, *Int. J. Heat Mass Transfer*, Vol. 70 pp. 599-609 (2014)
- Goncharova O.N., Rezanova E.V., Lyulin Yu.V., Kabov O.A., Modeling of two-layer liquid-gas flow with account for evaporation, *Thermophysics and Aeromechanics*, Vol. 22 pp. 655-661 (2015)
- Goncharova O.N., Kabov O.A., Pukhnachov V.V., Solutions of special type describing the three dimensional thermocapillary flows with an interface, *Int. J. Heat Mass Transfer*, Vol. 55 pp. 715-725 (2012)
- Andreev V.K., Bekezhanova V.B. Stability of Non-Isothermal Fluids (Review), *J. Appl. Mech. Tech. Phys.*, Vol. 2 pp. 171-184 (2013)
- Bekezhanova V.B., Goncharova O.N., *Fluid Dynamics Research*, Vol. 48(6) (2016)
- Goncharova O.N., Kabov O.A., Investigation of the two-layer fluid flows with evaporation at interface on the basis of the exact solutions of the 3D problems of convection, *Journal of Physics: Conference Series*, Vol. 754 pp. 032008 (1-6) (2016)

## Measurements of the temperature profile near liquid–gas interface during evaporation of different fluids

Elizaveta Gatapova<sup>1,2</sup>, Ekaterina Korbanova<sup>1,2</sup> and Oleg Kabov<sup>1,2</sup>

<sup>1</sup>Kutateladze Institute of Thermophysics SB RAS  
Lavrentyev Ave., 1, Novosibirsk, 630090, Russia

<sup>2</sup>Novosibirsk State University  
Pirogova Str., 2, Novosibirsk, 630090, Russia  
gatapova@itp.nsc.ru

A detailed description of molecular transport across a liquid–gas interface during evaporation/condensation process is important for many industrial applications involving the microsystems and dispersed phase systems (bubbles and microbubbles) with phase transition (Rao and Peles, 2015). The liquid–gas interface is difficult to define for microsystems, and the effects arising in the Knudsen layer become significant. A liquid–gas interface is usually far from its thermodynamic equilibrium state, which can lead to the development of different instability mechanisms.

Two most important parameters, involved in the evaporation process according to the energy balance at a liquid–gas interface, are the mass and heat fluxes in both gas and liquid directions. The investigation of the temperature profile across two different phases is an important issue for the thermal management of cooling systems, such as heat pipes, for the production of new materials as well as for design and manufacture of the microsystems with phase change. The correct definition of the boundary conditions is also an issue of fundamental importance which could be helpful for the better understanding of non-equilibrium phenomena, like for example, the Leidenfrost effect and contact line dynamics. Reliable and accurate measurements of the temperature near the liquid–gas interface and particularly in the Knudsen layer is a real challenge.

The existence of the temperature jump in the Knudsen layer during evaporation has been known in kinetic theory (Pao, 1971, Kucherov and Rikenglaz, 1960.). The approach to the description of heat and mass transfer based on the Navier–Stokes equations with temperature and pressure jumps conditions at liquid–vapor system was suggested in (Gatapova *et al.*, 2015). Analysis showed a good agreement with the temperature and pressure profiles calculated basing on the Boltzmann kinetic equations. However, most of the experimental data on the temperatures jumps at the liquid–gas interface were available only for reduced pressure conditions (Shankar and Deshpande, 1990, Rose, 1998, Fang and Ward, 1999). Recently, Gatapova *et al.* (2017) performed precise experiments on the temperature jump measurements using micro-thermocouple with the sensor thickness of 4  $\mu\text{m}$  for normal atmospheric conditions. A temperature jump at the water–air interface has been clearly detected even for small evaporation rate and the temperature jump value is found to increase with increasing the temperature difference between heater and ambient gas.

In this work we present new data on the measurement of temperature profile across the liquid–gas interface for four different fluids:  $\text{H}_2\text{O}$ ,  $\text{C}_2\text{H}_5\text{OH}$ ,  $\text{CH}_2\text{I}_2$  and HFE-7100 at normal atmospheric pressure. The different operating conditions for locally heated liquid layer are considered.

The experimental setup presented in (Gatapova *et al.*, 2017) is used. The cuvette with liquid and local heater is located inside a box, which which remains covered during the experiment to avoid external flow perturbations. Ultrapure Water (MilliQ), 99% ethanol,  $\text{CH}_2\text{I}_2$  and HFE-7100 are used as working fluid for experiments. The experiments are performed at quasi-stationary heating mode. The temperature of the heater is controlled by three thermocouples. The humidity and temperature of the ambient air inside the box are monitored by Testo device. The pressure is measured by barometer. The temperature profiles across the liquid–gas interface are measured using the specially fabricated micro-thermocouple with the sensor thickness of less than 3  $\mu\text{m}$  (Fig. 1).

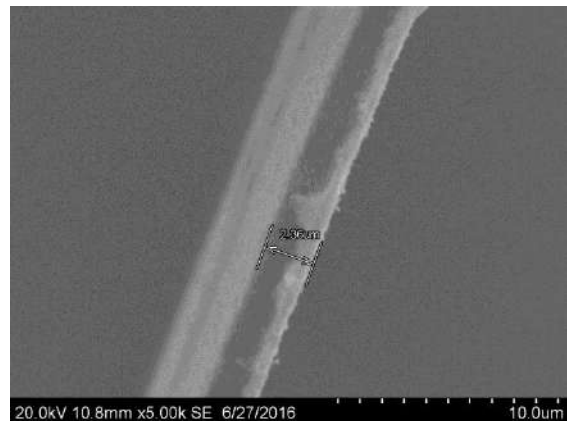
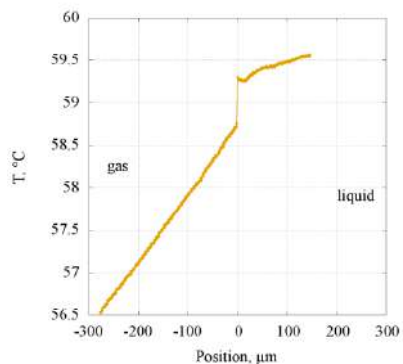


**Figure 1:** SEM image of micro-thermocouple by Hitachi S340.

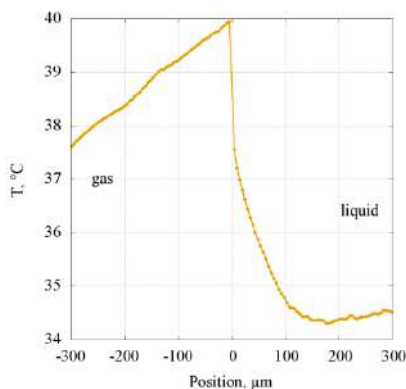
Calibrations of all thermocouples are carried out in the temperature range 5–100 °C. Data registration is carried out by means of temperature control and measurement system consisting of data collection (NI 9214) and the corresponding software. The equipment provides an accuracy of all thermocouples of 0.02 °C. The precise miniature motorized linear stage (Zaber), used as micro-positioner. It displaces the micro-thermocouple and determines its position. The range of the micro-positioner' movement is 25 mm with the minimal step of 48 nm. The micro-positioner is connected to a personal computer and it is controlled by specially developed software. The shadow technique is used for visualization with video camera providing a resolution of 3  $\mu\text{m}$  per pixel. Measurements are made for quazi-steady condition. Synchronization of the micro-thermocouple readings and its position via time is

made by specially developed software on C++. The program automatically gives the value and position of the temperature jump, provides the required graphs, and collects all necessary data.

The measurements allow us to obtain detailed information on the temperature profile across the liquid–gas layers. The existence of the temperature jump at the liquid-gas interface at atmospheric conditions has been established in (Gatapova *et al.*, 2017) for water–air system. Fig. 2a shows the temperature profile for water–air system at a heating power of 1.07 W. The temperature jump is clearly indicated. Fig. 2b presents the temperature profile for ethanol–air system at a heating power of 1.11 W. One can see a different temperature curves for water and ethanol.



a



b

**Figure 2:** Temperature profile: a) air–water system, heating power is 1.07 W, the heater temperature is 88.2 °C, air temperature is 32.3 °C, air humidity is 30.2 %; b) air–ethanol system, heating power is 1.11 W, the heater temperature is 84.7 °C, air temperature is 24 °C, air humidity is 42.5 %. Pressure is 99.5 kPa.

The temperature jump of 0.5 °C and evaporation rate of 0.215  $\mu\text{l/s}$  are detected for water-air system at experimental condition: heating power is 1.07 W, average temperature of the heater is 88.2 °C, air temperature is 32.3 °C, air humidity is 30.2 %, pressure is 99.46 kPa. The evaporation rate has the same tendency as the temperature jump: it increases with heating power increasing. This trend is in agreement with the analytical expression of the temperature jump condition.

A temperature jump at the liquid-gas interface is clearly

detected even for small evaporation rate. This jump is measured for heater temperature varying in the range 23 – 88 °C at normal atmospheric conditions. The temperature jump value is found to increase with increasing the temperature difference between heater and ambient gas, and, hence, with increasing of the evaporation rate. A specific evolution of the temperature profile with increasing of the heater temperature is obtained. Depending on the ambient condition and type of fluids, the temperature in the gas phase near the liquid-gas interface can be higher or lower than that of the liquid. The temperature profiles with negligible temperature jump at liquid-gas interface are observed for some operating conditions. The temperature jump depends not only on evaporation rate, but also on temperature gradients in liquid and gas phases near the interface. The experimental results are found to be qualitatively in agreement with the kinetic theory and quantitatively with classical energy balance on the interface.

The temperature jumps from  $-0.07$  °C to  $0.55$  °C at water–air interface and from  $-0.08$  °C to  $-2.39$  °C for ethanol–air interface are detected at the temperature difference between the air and heater from 0 to 55 °C. The results of the measurements are supported by classical energy balance equation. The reported detailed data on the phase transition phenomena for relatively high heat flux and different fluids are presented for the first time in the literature.

The work was financially supported by the Ministry of Education and Science of the Russian Federation (Agreement 14.613.21.0067, project identifier RFMEFI61317X0071).

## References

- Fang G. and Ward C.A., Temperature measured close to the interface of an evaporating liquid, *Physical Review E*, Vol. 59, pp. 417–428 (1999)
- Gatapova E.Y., Graur I.A., Sharipov F. and Kabov O.A., The temperature and pressure jumps at the vapor-liquid interface: application to a two-phase cooling system, *International Journal of Heat and Mass Transfer*, Vol 83, pp. 235 – 243 (2015)
- Gatapova E.Y., Graur I.A., Kabov O.A., Aniskin V.M., Filipenko M.A., Sharipov F. and Tadrst L., The temperature jump at water – air interface during evaporation, *International Journal of Heat and Mass Transfer*, Vol. 104, pp. 800–812 (2017)
- Kucherov R.Ya. and Rikenglaz L.E., On hydrodynamic boundary conditions for evaporation and condensation, *Journal of Experimental and Theoretical Physics*, Vol. 37, pp. 88–89 (1960)
- Pao Y.-P., Temperature and density jumps in the kinetic theory of gases and vapors, *Physics of Fluids*, Vol. 14, pp. 1340–1346 (1971)
- Rao S.R. and Peles Y., Spatiotemporally resolved heat transfer measurements for flow boiling in microchannels, *International Journal of Heat and Mass Transfer*, Vol. 89, pp. 482–493 (2015)
- Rose J.W., Interphase matter transfer, the condensation coefficient and dropwise condensation, *Proc. 11th Int. Heat Transfer Conf.* 1, pp. 89–104 (1998)
- Shankar P.N. and Deshpande M.D., On the temperature distribution in liquid-vapor phase change between plane liquid surfaces, *Physics of Fluids A*, Vol. 2, pp. 1030–1038 (1990)

## Comparison Study on the Calculation Formula of Evaporation Mass Flux through the Plane Vapour-Liquid Interface

Li Zhang, You-Rong Li, Ling-Qi Zhou and Chun-Mei Wu

Key Laboratory of Low-grade Energy Utilization Technologies and Systems of Ministry of Education,  
College of Power Engineering, Chongqing University, Chongqing 400044, China  
E-mail: liyourong@cqu.edu.cn

The evaporation phenomenon exists widely in daily life and industrial production process, such as, spray drying, electronic cooling, spray printing, DNA detection and protein chip technology and so on, in which the calculation and control of evaporation mass flux has a very important influence, and has already attracted the attention of many scholars. Many factors will affect the interfacial evaporation rate, including gas composition, temperature, pressure and flow velocity and so on; when the evaporation of liquid is in the static pure steam environment, the evaporation mass flux  $J_m$  can be calculated according to the theory of classical kinetic theory (CKT), in which linear Hertz-Knudsen-Schrage equation or Hertz-Knudsen equation (Palmer 1976) is used commonly

$$j_m = \alpha \rho_v h_{fg} \sqrt{\frac{M}{2\pi RT_v}} (T_l - T_v) \quad (1)$$

It should be noted that Eq. (1) is the calculation formulas of vapor-liquid interfacial evaporation mass flux on basis of the experiment, in which the evaporation coefficient  $\alpha$  is constant and is determined by the experiment. Therefore, Ward and Fang (1999) derived the evaporation mass flux formula according to the statistical rate theory (SRT), which was certified by a series of experimental results as follows

$$j_m = 2m_w K_c \sinh\left(\frac{\Delta s_{LV}}{k_b}\right) \quad (2)$$

where  $K_c$  is coefficient and  $\Delta s_{LV}$  is entropy variation through the vapour-liquid interface.

Compared with the traditional Hertz-Knudsen equation, the greatest merit of the SRT theory for calculating the evaporation rate on the gas-liquid interface is that it does not require any empirical constant or coefficient, and is a pure theoretical calculation formula. The comparison between the two calculation results of evaporation mass flux for water is shown in Figure 1, that is, the evaporation adaptation coefficient  $\alpha$  in equation (1) is fittingly determined according to the calculation results of the SRT. From the figure, when the steam is saturated and the evaporation temperature difference is small, the calculated results of SRT theory are very close to that of the Hertz-Knudsen equation, which is in the vicinity of the equilibrium state. As long as the suitable evaporation coefficient is selected, both calculation results are basically the same. However, when the evaporation temperature difference is larger, such as,  $\Delta T=8K$ , the difference between the calculated results is increased, and the increasing speed of the interfacial evaporation rate predicted by SRT theory with the increase of the liquid-phase temperature is slower than that of the Hertz-Knudsen equation. On the other hand, when the vapor is in an overheating state, the difference of interfacial

evaporation rate between the two indicating results increases, as shown in Figure 1 (b).

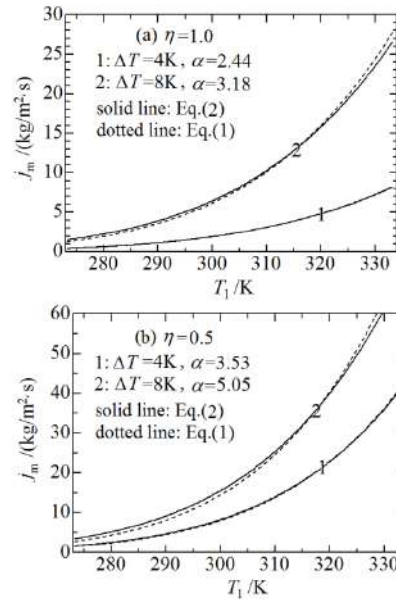


**Figure 1:** Comparison of calculating results between SRT theory and Hertz-Knudsen equation for gas-liquid interfacial evaporation mass flux of water.

Figure 2 gives the variation of interfacial evaporation flux with the liquid-phase temperature and evaporation temperature difference in superheated steam environment at  $\eta=0.5$  based on SRT theory. Overall, the change rule of vapor flux in the superheated steam is similar to that in the saturated vapor. However, the difference has three points: (1) because the steam is overheating, pressure dropped, gas-phase chemical potential decreased, the chemical potential difference between liquid phase and gas phase as the vaporing driving force increased, so the interfacial evaporation flux increased. (2) The chemical potential of the pure substance is not only related to the pressure, but also changes with the temperature; the lower the pressure is and the higher the temperature is, the lower the chemical potential is. Therefore, when the steam is in the superheated state, even if its temperature is higher than the liquid-phase temperature  $\Delta T=T_l-T_v<0$ , it also ensures that the chemical potential of the gas phase is lower than that of the liquid phase. Therefore, the evaporation process can still be carried out and interfacial evaporation flux is still positive, which have been confirmed by a large number of experimental results. (3) Due to the superheated steam, the

Clausius-Clapeyron equation is no longer applicable, and the evaporation flux no longer increases linearly with the increase of evaporation temperature difference, as shown in Figure 2 (b).

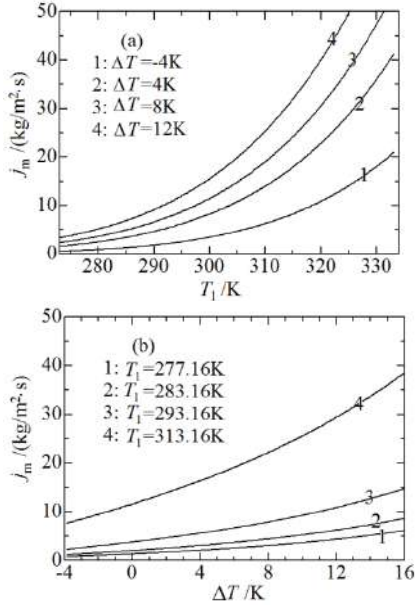


**Figure 2:** Variation of interfacial evaporation flux with the liquid- phase temperature (a) and evaporation temperature difference (b) in superheated steam environment for water at  $\eta=0.5$

When the steam is saturated, if the liquid-phase temperature is lower than the steam temperature  $\Delta T < 0$ , not the evaporation but the condensation occurs on the interface; when the steam is overheating, whether the evaporation process occurs on the interface or not depends on the two phase temperature difference and the gas-phase pressure. Obviously, when the liquid- phase temperature is low enough, the condensation process will occur on the interface. Figure 3 shows the critical conditions whether the evaporation process can occur on the interface under two typical liquid-phase temperatures. The left-upper part is the evaporation region, and the right-lower part is the condensation region. The absolute value of the critical temperature difference  $\Delta T_{\text{cri}}$  in the evaporation process decreases with the increase of the gas-phase pressure. At  $\eta=1$ , vapor is saturated steam and the gas and the liquid are in equilibrium state, therefore,  $\Delta T_{\text{cri}}=0$ .

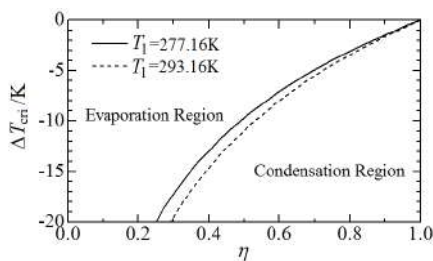


**Figure 3:** Critical conditions of interfacial evaporation.

This work is supported by National Natural Science Foundation of China (Grant No. 11532015).

## References

Palmer H.J., The hydrodynamic stability of rapidly evaporating liquids at reduced pressure, *Journal of Fluid Mechanics*, Vol. 75 pp. 487-511 (1976).

Ward C.A. and Fang G., Expression for predicting liquid evaporation flux: statistical rate theory approach, *Physical Review E*, Vol. 59 pp. 429-440 (1999).

## Modelling of liquid evaporation during gel formation

Boris Pokusaev and Dmitry Khramtsov

Moscow Polytechnic University, Faculty of Chemical and Bioengineering, Department of thermodynamics and nonequilibrium transport processes  
B. Semenovskaya, 38, Moscow, 107023, Russia  
pokusaev2005@yandex.ru

Development of additive technologies, including areas such as medicine and biotechnology requires an understanding of the dynamics of the processes of formation and aging of gels with the aim of developing optimal technological processes for bioprinting technologies (Jakab K. et al. 2010). The formation of gels is due to the complex hydrodynamic and thermo-physical processes occurring in the internal micro-structure of the gel. The processes of mass transfer in the gel involve the interaction of multiple phases on small linear scales (Pokusaev B.G. et al. 2016). In order to determine the dynamics of the process of liquid evaporation during gel formation, experimental and numerical study of measuring the rate of evaporation of the liquid phase in the course of cooling of the sample gel was performed.

Currently gels are considered a high-potential structure-forming material for formation of artificial tissues from immobilized cells using the method of additive manufacturing. Due to their rheological properties, gels refer to an intermediate state between liquid and solid. The common definition of gels is a dispersive system with liquid dispersing medium, and the dispersion phase makes up a spatial structured mesh due to intermolecular interaction in the contact areas (Arnott et al. 1974). Gels are capable of displaying both elasticity and plasticity.

The experimental setup is shown in fig. 1.

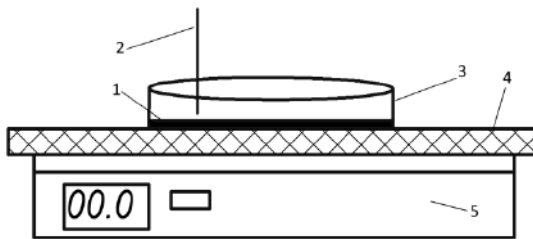


**Figure 1:** Experimental setup: 1 – layer of agarose gel, 2 – thermopair, 3 – Petri dish, 4 - heat-insulating plate, 5 – electronic scale

In the experimental study an agarose gel with concentration of 0.6 and 1% was used. At the beginning of the experiment, a prepared sample of the gel at a temperature of 60°C was applied to the surface of the Petri dish. Then Petri dish was mounted on a heat insulating plate and installed at the scale. Further thermopair was injected into the gel. Before starting the experiment a timer was set to measure time of experiment. Differences in values presented by thermopair measurements and electronic scales were recorded in the table with the corresponding time value according to the timer.

The estimated model of the process of evaporation is based on the idea of considering gel as a system of capillaries. The motion of the liquid within the gel is associated with the movement of the liquid phase in microchannels of complex configuration, where capillary force provides a supply of fluid from the inner layers of the gel to the surface during evaporation (Keita E. et al. 2014).

In this problem, in mathematical model the case of evaporation of the liquid from a surface of the gel is considered. The calculation of vapor-flow directed normal to the surface of the gel passing through the effective surface area of the capillaries in the case of stationary temperature (1).

$$F = -D \int \text{div}(n) \cdot ds \quad (1)$$

where  $F$  is the vapor flow,  $D$  is the diffusion coefficient,  $n$  – normal,  $ds$  is an elementary surface unit

The density of capillaries per unit surface area was determined using qualitative analysis of photographs of the microstructure of the gel obtained by electron microscopy (Berlin J. 2010).

Liquid evaporation from gel was observed for 2 hours and 40 minutes. This time interval allows to capture the characteristic of stage of formation and aging of the gel, including the initial stage of structure formation and polymerization. The data obtained is the dependence of change of weight of gel over the time (fig. 2).

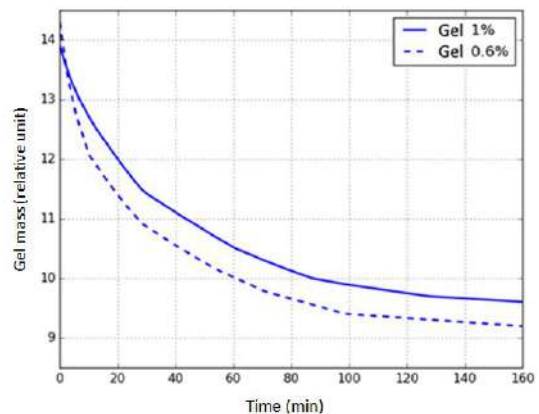


**Figure 2:** Dynamics of gel evaporation with dependence from time for different gel concentrations.

In the first 20 minutes of the experiment there is a linear dependence of change of weight of gel over the time. Dependence may be associated with the fact that in this period liquid evaporation occurs from the surface of the gel,

with the supply of fluid from the deep layers of the gel by the action of the capillary forces. In the interval from 20 minutes to 2 hours, dependency becomes nonlinear, which may occur due to the action of additional factors on the evaporation process such as the process of shrinkage of the gel. After 2 hours a stabilization of the evaporation process was observed. The cause of stabilization can be explained by the fact that the remaining liquid is not enough for the action of capillary forces to supply the liquid to the surface of the gel, which leads to the fact that the evaporation process continues within the pores, where the total surface evaporation is less in comparison with the gel surface.

Temperature measurements in time allowed to identify the mode of establishing a stationary temperature, in which case mathematical model was applied (fig. 3).

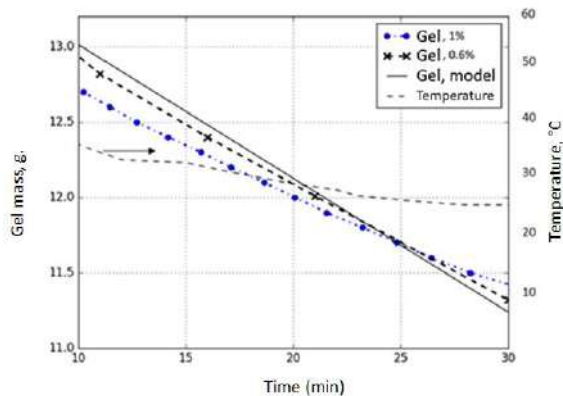


**Figure 3:** Dynamics of gel evaporation with dependence from time for different gel concentrations.

For this mode a numerical calculation of the dynamics of evaporation of the liquid was performed and a comparative analysis with experimental results for agarose gel concentrations of 0.6% and 1% was made.

The variation of the mass of the gel is of a linear nature in the area of stationary temperature. Evaporation rate for a given concentrations does not vary significantly. The similarity of the nature of evaporation for these concentrations may be related to the fact that the difference in concentration is insufficient for the occurrence of changes in the internal structure of the gel.

Three stages of evaporation of the gel were identified. These stages are: linear which corresponds to the gel formation process, nonlinear, associated with the action of capillary forces and shrinkage of the gel, and the stage of polymerization. The comparison of results of calculation and experiment shows the effectiveness of the model for the initial stage of gel formation. The character of dependencies of evaporation of the gel over the time at the stage of gel formation demonstrates a linear character, the dynamics of evaporation agarose gel with a concentration of 0.6% differs from the concentration of 1% gel insignificantly, which allows to make a conclusion about the similarity of the internal structure of the gel at these concentrations.

This work is based on the research carried out with the financial support of the grant of the Russian Scientific Foundation (project no. 15-19-00177).

## References

- Jakab K., Norotte C., Marga F., Murphy K., Vunjak-Novakovic G. and Forgacs G. Tissue engineering by self-assembly and bio-printing of living cells, *Biofabrication*. 2. pp. 20—34 (2010)
- Arnott S., Fulmer W. The Agarose Double Helix and Its Function in Agarose Gel Structure, *Journal of Molecular Biology*. vol. 90. pp. 269—284 (1974)
- Pokusaev B.G., Nekrasov D.A., Karlov S.P. and Khrantsov D.P. Experimental and numerical simulation of interphase mass transfer of gas bubble in granular backfill and gel, *Theoretical Foundations of Chemical Engineering*, Vol.50, pp. 690-696 (2016)
- Keita E., Faure P., Rodts S., Coussot P. and Weitz D. Evaporation from a capillary tube: Experiment and modelization, *5th International Conference on Porous Media and Their Applications in Science, Engineering and Industry* pp. 50-57 (2014)
- Berlin J. *Injectable Hydrogelbased Medical Devices*, Orthoworld, vol. 9, pp. 120-126 (2010)
- Jens Gerstmann, Michael E. Dreyer, The dynamic contact angle in the presence of a non-isothermal boundary condition, *Microgravity sci. technol.*, Vol. XIX-3/4 pp. 96-99 (2007)

## Experimental study of interfacial motion of a horizontal liquid layer evaporating into gas flow

Aleksei Kreta, Yuriy Lyulin and Oleg Kabov

Novosibirsk State University, 630090 Novosibirsk, Russia  
Kutateladze Institute of Thermophysics, 630090 Novosibirsk, Russia  
alexey.slav@yandex.ru

Study of heat and mass transfer through the gas-liquid interface is one of the most important problems in the present time. The intensive evaporation from the liquid surface into the gas flow induces various convective flows within the liquid. Two mechanisms have been spotted to be responsible for the convection. One of them is the gravity that acts essentially on density differences due to temperature gradients, the other one is the thermocapillarity originated by the temperature dependence of the surface tension at the liquid interface. The convective motions caused by buoyancy are known as the Rayleigh-Bénard convection. When the convection is induced by the surface tension, it is referred to as Marangoni-Bénard convection. In the most of investigations the fluid layers are steadily heated from below with a static temperature gradient and without evaporation. The evaporating fluid layers with nonlinear temperature gradient have much less been studied due to the complexity of the problem. It was found that evaporation is not only a means of cooling the layer surface, but also a driving power for the development of the convective instabilities. The problem of convection of the evaporating liquid layer under the action of the inert gas flow is much more complicated than described above, because includes also the shearstress effect induced by gas flow. The coupling between evaporation and convection caused by a shear-stress, thermocapillary and buoyancy effects in the liquid layer, has a direct effect on the evaporation flow rate, being relevant, for example, for heat-pipe grooves and thin-film evaporators. The increased interest to the problem is caused by experiments under microgravity conditions, some experiments under normal gravity and the preparation of experiments on the International Space Station in the framework of the scientific project "Convection and Interfacial Mass Exchange" (CIMEX) of the European Space Agency. These experiments are aimed to investigate the features of convective flows of a fluid in an open cavity and in an open horizontal layer under conditions of a co-current gas flow and evaporation. The processes of convection, accompanied by evaporation at the interface, are actively studied experimentally, numerically and theoretically in the present time.

The aim of this work is to experimentally study the structure of convective flows and to measure temperature distribution on the surface of horizontal liquid layer under the action of the gas flow using IR camera.

The experimental investigations were conducted on the setup shown in Fig. 1. The setup consists of the following components: test section, gas and liquid loops, data acquisition system, thermal stabilization system, and optical techniques.

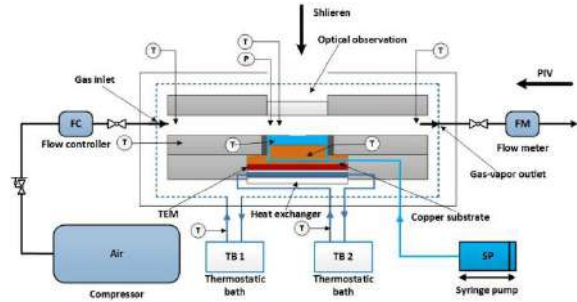


Figure 1: Scheme of the experimental setup.

Pure gas enters to the test section from the compressor. The mass flow controller sets flow rate of the gas at the inlet of the test section. The liquid is injected into the test section by a precision syringe pump. The working liquid evaporates under the gas flow and the vapor-gas mixture flows to the outlet of the gas channel in test section. The vapor-gas mixture flow at the outlet is measured by a mass flow meter. The liquid temperature in the test section is determined by the temperature of the substrate base, which controlled with the help of thermoelectric module. The position of the interface level is controlled with an accuracy of 10 micrometres using a Schlieren technique and the syringe pump.

Measurements of the temperature distribution on gas-liquid interface were conducted with the help with of Titanium 570M IR camera. An infrared wavelength region is 3-5 micrometres. Infrared imaging of liquid surface was performing through quartz optical window that implemented in the top cover of the test cell. IR camera was placed on the optical tabletop horizontally and measuring of the surface temperature of the liquid was contacted with the help of the IR mirror. The IR mirror was inclined to 45 to infrared camera and liquid surface. Optical components of the Schlieren technique and IR mirror were mounted on an optical platform of the linear actuator. Linear actuator is controlled from personal computer and by special software. The optical platform moved in the range of 50 mm and speed of 104 mm/s in horizontal direction. Initially, the platform was set in position where optical axes of Schlieren technique coincide and the interface visualized. When a flatness of interface and the stationary regime of the experiment were established the linear actuator moved the platform in position where optical axes of the IR camera and mirror also coincide and measurement of surface temperature was running.

The experiments were conducted at atmospheric pressure in a test section, and a 5 mm thick liquid layer. Ethanol liquid was used as the working liquid. The evaporation surface area was 100 mm<sup>2</sup> with the corresponding 10x10 mm cut-out in the plate. The gas flow

rate was in the range 100–1000 ml/min that corresponds to gas average velocities for 0.0138 to 0.138 m/s ( $Re=2.8-28$ ), respectively. The temperature of the "liquid-gas" system has changed from 20 °C to 40 °C. The difference between the temperature of the gas and liquid does not exceed 0.1 °C.

In Fig. 2 a typical temperature distributions of the interface in the direction of gas flow are plotted for the various temperatures. It is shown the differences in the interfacial temperature. Intensive evaporation induces temperature decreasing in initial of the evaporation surface and temperature gradient is appeared. In this case the thermocapillary effect on the gas-liquid interface takes place.

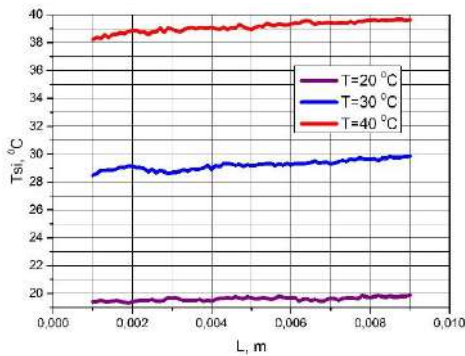


**Figure 2:** The temperature distribution on the surface of the evaporating liquid layer.

The shear stress on the liquid surface  $\tau_{sur}$  caused by the thermocapillary effect can be estimated as:

$$\tau_{sur} = \frac{\delta\sigma}{\delta T} \frac{\delta T}{\delta x}$$

where,  $\sigma_T = \frac{\delta\sigma}{\delta T}$  - temperature coefficient of surface tension is equal  $1,14 \times 10^{-4}$  N/mK.

The temperature gradient is defined as:  $\frac{\delta T}{\delta x} = \frac{T_2 - T_1}{\Delta x}$ .

Points of the temperature measuring and length  $x=0,008$  m.

Shear stresses on the liquid surface induced by gas flow can be estimated as [11]:

$$\tau_g = \eta \frac{dV}{dy} = -\frac{H}{2} \frac{\delta p}{\delta x}$$

where,  $H=0,005$  m is height of gas channel;  $\eta$  – dynamic viscosity.

Pressure gradient is calculated from the formula:  $V_g = -\frac{H^2}{12\eta} \frac{\delta p}{\delta x}$ , where average gas velocity  $V_g$ , m/c is known

value. It is assumed that in the gas channel the Poiseuille flow is realised. The gas-liquid interface is considered as a rigid surface.

Fig. 3 shows the relationship of forces shear stresses associated with the temperature gradient at the surface of the liquid layer to the forces of shear stresses caused by friction on the surface of the gas flow at different temperatures system "liquid - gas" and at different Reynolds numbers.

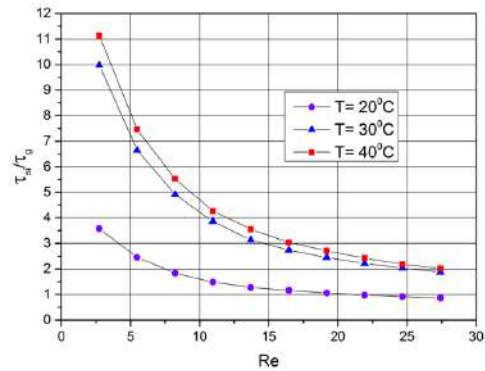


**Figure 3:** Shear stresses.

The plot show that with the increase of the gas flow relationship the thermo-capillary shear stress to the gas shear stress are decreased. It can be seen that when the small gas Reynolds the thermocapillary shear stresses are bigger than gas shear stresses in several times. This means that thermocapillary forces dominate at low gas velocities. When the maximum gas flow rate relationship the thermo-capillary shear stress to the gas shear stress are significantly decreased. However, thermocapillary forces all the same give a decisive contribution to the development of convection currents in the liquid layer.

Experiments were carried out to study the influence of the gas flow velocity and temperature system liquid-gas on the temperature distribution on the interface. Infrared study and measurements of the temperature field on the surface of horizontal liquid layer evaporating into gas flow has been performed. Temperature gradient of the gas-liquid interface has been measured with the help of Titanium 570M IR camera. Shear stresses on gas-liquid interface induced by thermocapillary effect and inert gas flow have been defined. It is shown that the main factor influencing on the development of convection in the liquid layer under the action of gas flow is thermocapillary effect.

The study was financially supported by the Russian Science Foundation (Project 15-19-20049).

## References

- Scheid B., Margerit, J., Iorio, C.S., Joannes, L., Heraud, M., Queeckers, P., Dauby, P.C., Colinet, P., Onset of thermal ripples at the interface of an evaporating liquid under a flow of inert gas, Experiments in Fluids, Vol. 52(5), pp. 1107-1119 (2012).
- Goncharova O. and Kabov O., Numerical investigation of the tangential stress effects on a fluid flow structure in a partially open cavity, J. Eng. Thermophys, Vol. 22(3), pp. 216-225, (2013).
- Lyulin Y., Kabov O., Evaporative convection in a horizontal liquid layer under shear-stress gas flow Int. J. Heat Mass Transfer Vol. 70, pp. 599-609 (2014).



2nd International School of Young Scientists  
«**Interfacial Phenomena and Heat Transfer**»

**ABSTRACTS**

## Modeling of evaporating drop of polar liquid with added surfactant

Varvara Gordeeva and Andrey Lyushnin

Perm National Research Polytechnic University, Lysva branch  
Lenina, 2, Lysva, 618910, Russia

[vanma@mail.ru](mailto:vanma@mail.ru)

Perm State Humanitarian-Pedagogical University,  
Sibirskaya, 24, Perm, 614990, Russia  
[andry@pspu.ru](mailto:andry@pspu.ru)

Polar liquids like water are important in such areas as medicine, biological investigation, and microelectronics. Experiments show that at slow evaporation a border line of an evaporating drop or thin film becomes unstable and generate a shape similar to comb. A possibility to control the shape of the comb and size of its “teeth” could be useful for producing of some microscopic devices.

Thin films of the polar liquids are interesting by the fact that they hold a stable value of thickness while evaporating (Lyushnin et al. 2002). This could be explained by disjoining pressure, introduced by Deryagin (Deryagin and Churaev 1987) and consisting of intermolecular van der Waals interaction and interaction between dipoles in the liquid (DLVO potential).

Surfactants could change evolution of the evaporating film dramatically: they could stabilize shape of the droplet, or destabilize a whole film destroying it into many little droplets. Using of effect of the surfactants to the liquids should have great practical importance. The strongest mechanism of the effect is the Marangoni effect when gradient of surface tension produces a surface velocity of the liquid. Various surfactants can increase or decrease the surface tension of the liquid, they can diffuse slow or quick along the surface, they can be soluble or non-soluble.

In this work we simulate evaporation of a droplet of some polar liquid with added surfactant. The droplet has initially semi-ellipse shape as it is in real life after setting to a substrate. A weak-soluble surfactant is added to the liquid.

During the modeling it was found that the droplet takes a well-defined shape when the film divides into parts with various thicknesses and clearly visible front between the parts (fig.1). After reaching such a form, the film saves its thickness, and liquid volume reduces in account of area of the thicker part of the film. The values of the stable film thickness are defined by the disjoining pressure. The modeling showed that the stable thickness is connected with the vapor pressure (fig. 2). So, the film thickness could be controlled by the vapor pressure.

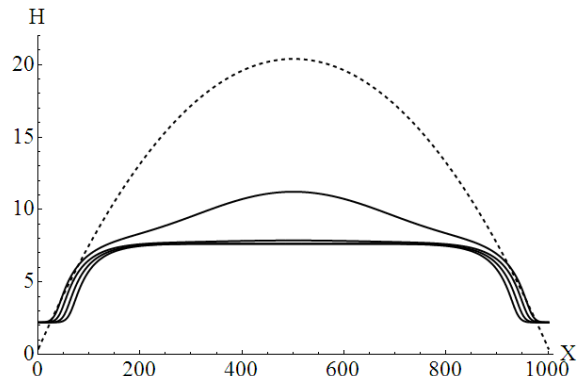


**Figure 1:** Profiles of the droplet of a polar liquid at  $S=-0.002$ . Dashed line shows initial shape of the droplet, further profiles are received after same time intervals.

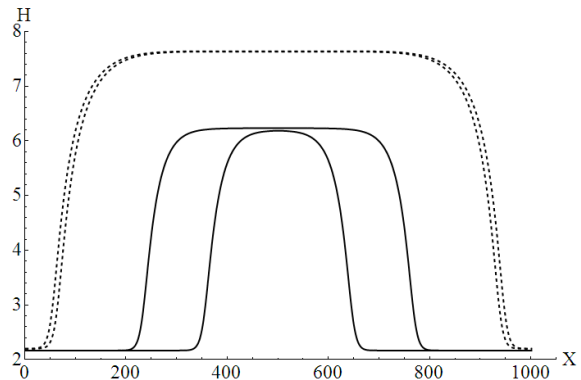


**Figure 2:** Profiles of the droplet of a polar liquid at  $S=-0.002$  (dashed line) and  $S = -0.003$  (solid line)

### References

Lyushnin A.V., Golovin A.A., Pismen L.M., Physical Review E - Statistical, Nonlinear, and Soft Matter Physics, Vol. 65, p. 021602/1 - 021602/7 (2002).

Deryagin B.V., Churaev N.V., Langmuir. 3.5, p. 607-612 (1987).

## Enhancement of heat transfer at pool boiling on small surfaces with fins and hydrophobic coating

Evgeniy N. Shatskiy, Aleksey I. Safonov, and Evgeniy A. Chinnov

Kutateladze Institute of Thermophysics SB RAS  
 Lavrentiev Avenue, 1, Novosibirsk, 630090, Russia

Recent development of technologies aimed at fabrication of the surfaces with microstructures and nanostructures makes it possible to perform experimental studies on wettability, roughness, microfinning and nanocoating effects at pool boiling heat transfer (Cheng et al. 2004).

The effect of radial microfinning and hydrophobic coatings in the form of a fluoropolymer film with different structures on heat transfer at water boiling was studied.

The working section includes the base and heating element. The heating element is copper core with a round head with diameter  $D = 5$  mm. The core tip is firmly inserted into the hole of the base and aligned in one plane. The source of heat is the nichrome ribbon, wound on the core shank. To minimize heat losses, the heating element is carefully insulated. Fiberglass wrapped in several layers around the core of the heating element is used as a thermal insulator. Thermocouples, whose beads are located along the center of symmetry, are mounted into the heaters. Thermal contact was achieved due to tight pressing of thermocouple to the heater; then, they were sealed.

Heat transfer in the evaporation zone is intensified by applying special finning to the heater, and, on the one hand, this increases the surface area of heat transfer, and on the other hand, this increases intensity of capillary suction to the heat transfer region. The finning with the number of radial fins of 16 was used.

In addition to finning, to intensify heat transfer, the fluoropolymer films with different structures were deposited on the flat surface of the heaters by the HWCVD method (Slau et al. 2001, Takachi et al. 2009, Uvarov et al. 2013). The deposition setup is described in detail in (Safonov et al. 2015). The coatings on samples “T №1” and “T №2” consist of a single fluoropolymer layer. The coating on sample “T №3” consists of two layers (the main and additional ones) with different structures.

The result of measuring the wetting angle of a water droplet on sample “T №3” is shown in Fig. 1. It can be seen that high surface hydrophobicity is achieved on the coating consisting of two fluoropolymer layers. The wetting angle is  $154.2^\circ$ . On the other samples, the wetting angles are  $110^\circ$  and  $138^\circ$ .

The dependences of the heat flux from the difference between temperature in center of the heater and saturation temperature for water pool boiling at normal pressure are presented in Fig. 2. As it can be seen, microfinning leads to significant enhancement of heat transfer in comparison with a smooth surface without coatings (the wetting angle is  $54^\circ$ ), but maximal enhancement for small temperature difference is achieved on the most hydrophobic surface with the wetting angle of  $154.2^\circ$ . This result agrees with data of [1], where it is shown that significantly less energy is spent for bubble nucleation on the hydrophobic surface.

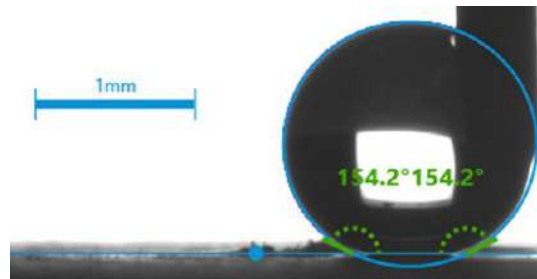


Figure1: Measurement of wetting angle on sample “T №3”.

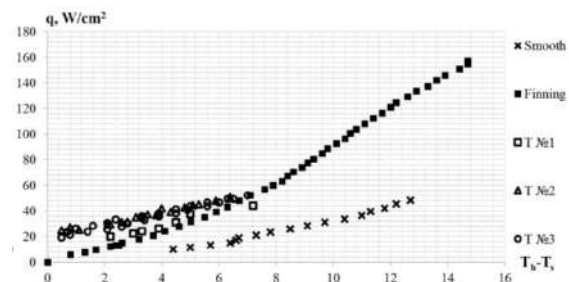


Figure2: The dependences of the heat flux from the temperature difference.

This work was supported by the grant of the Russian Science Foundation (Agreement No. 15-19-30038) and grant of the President of RF MK-5052.2016.8.

### References

- P. Cheng, X. J. Quan, S. Gong, L. N. Dong, Fangjun Hong, *Proceeding of the 15th IHTC*, pp.479-496 (2004)
- K.K.Slau, H.G. Pryce Lewis, S.J. Limb, M.C. Kwan, *Thin Solid Films*, Vol. 395, pp. 288-291 (2001)
- M. Takachi, H. Yasuoka, K. Ohdaira, T. Shimoda, H. Matsumura, *Thin Solid Films*, Vol. 517, pp. 3622-3624 (2009)
- A.A. Uvarov, S.E. Aleksandrov, *Russian journal of general chemistry*, Vol. 83, pp. 1607-1612 (2013)
- A. Safonov, V. Sulyaeva, N. Timoshenko, E. Gatapova, O. Kabov, E. Kirichenko, A. Semenov, *MATEC Web of Conferences*, Vol. 37, 01047 (2015)

## An explanation of the mechanism of heterogeneous water droplet boiling and explosive breakup using planar laser-induced fluorescence

Maxim Piskunov and Pavel Strizhak

National Research Tomsk Polytechnic University, Department of Heat and Power Process Automation, Institute of Power Engineering  
30, Lenin Avenue, Tomsk, 634050, Russia  
piskunovmv@tpu.ru

The recent years have seen the rapid development of optical methods of high-speed measurement used to obtain key parameters of gaseous, fluid and even heterogeneous media, such as temperature, speed, consumption, particle size, concentration, etc. Such contactless methods include Particle Image Velocimetry (PIV), Particle Tracking Velocimetry (PTV), Stereo Particle Image Velocimetry (Stereo PIV), Interferometric Particle Imaging (IPI), Shadow Photography (SP), Planar Laser Induced Fluorescence (PLIF), and Laser Induced Phosphorescence (LIP). PLIF is the method of choice to determine the unsteady temperature field of an evaporating heterogeneous droplet of water. Torres et al. (2013), Charogiannis et al. (2015) and Zhou et al. (2016) outline the key benefits and barriers to the use of PLIF when determining the temperature fields of liquids. The preliminary analysis has shown that using PLIF for measuring the temperature field of an evaporating droplet will provide the missing experimental information on the temperature gradient from the center to the surface of a droplet as well as from the latter to the *inclusion – liquid* interface. This information will help to substantiate or adjust the conclusions by Kuznetsov et al. (2016) on the physics of overheat, boiling, and explosive breakup of heterogeneous water droplets under high-temperature heating. Reliable experimental data will make it possible to develop adequate physical and mathematical models. These, in turn, may change the current perceptions of the optical properties of liquids (e.g., water and water-based solutions) under heat exchange with a radiating gaseous medium.

Over the recent years, the research community has taken an increasing interest in high-temperature gas-steam-droplet systems. This promotes emerging technologies in thermal or flame water cleaning from unspecified impurities. Other promising technologies include firefighting by water slurry aerosols. Their solid particles overheat in the flame and thereby intensify water evaporation or even cause the aerosol particles to break into smaller ones. This improves water use efficiency in firefighting. Almost all the water evaporates in the flaming combustion zone and reduces the temperature of the combustion source by as much as several hundreds of degrees. This is the essential condition for the effective extinguishing of fires of any complexity. Unfortunately, such firefighting technologies and thermal water cleaning have yet to become mainstream, although they have been regarded as extremely important and promising for several years already. The fact is that there are too few experimental data on the physical processes intensifying the evaporation of water slurries in hot gaseous media. The results of such experiments with temperatures over 1,000 °C are virtually impossible to find. These data are so evasive

due to fast-paced processes and difficulties in measuring the temperature in evaporating heterogeneous water droplets. The typical durations of high-temperature heating and evaporation do not usually exceed several seconds.

In this work, we conduct experiments using a heterogeneous water droplet with a single nontransparent solid inclusion to determine the unsteady temperature field of the latter. We use an optical diagnostic technique, Planar Laser Induced Fluorescence (PLIF), to study the conditions, mechanism, reasons and characteristics of water boiling leading to an explosive breakup (disintegration) of water slurry droplets. Rhodamine B acts as a fluorophore. The typical temperature gradients are determined in the depth of a droplet, near its free (outer) surface, and at the interface. The water temperature at the *water – solid inclusion* interface is shown to be higher than at the outer surface of a droplet. Furthermore, we compare the temperature fields of a homogeneous and heterogeneous water droplet under identical heating conditions. At a gas temperature over 500 °C, the presence of an inclusion in a droplet is shown to have a significant effect on the temperature field of the droplet. In this paper, we also discuss the strengths and weaknesses of using PLIF vs. thermocouple measurement. Finally, we outline the possible implications of a new approach to studying the rapid evaporation and boiling of heterogeneous liquid droplets and the PLIF technique in the research into high-temperature gas-vapor-droplet systems.

### References

- Torres L.A., Fleck B.A., Wilson D.J., Nobes D.S., Calibration of a planar laser induced fluorescence technique for use in large scale water facilities, *Measurement*, Vol. 46, pp. 2597–2607 (2013).
- Charogiannis A., An J.S., Markides C.N., A simultaneous planar laser-induced fluorescence, particle image velocimetry and particle tracking velocimetry technique for the investigation of thin liquid-film flows, *Exp. Therm. Fluid Sci.*, Vol. 68, pp. 516–536 (2015).
- Zhou X., Sun X., Liu Y., Liquid-phase turbulence measurements in air-water two-phase flows over a wide range of void fractions, *Nucl. Eng. Des.*, Vol. 310, pp. 534–543 (2016).
- Kuznetsov G.V., Piskunov M.V., Strizhak P.A., Evaporation, boiling and explosive breakup of heterogeneous droplet in a high-temperature gas, *Int. J. Heat Mass Transf.*, Vol. 92, pp. 360–369 (2016).

## Varieties of the gas driven water rivulet flow regimes in the minichannels

Olga Svetlichnaya<sup>1,2</sup> and Vyacheslav Cheverda<sup>1,2</sup>

<sup>1</sup> Novosibirsk State University, Novosibirsk, Russia

<sup>2</sup> Kutateladze Institute of Thermophysics SB RAS, Novosibirsk, Russia  
[sovatomsk.93@gmail.com](mailto:sovatomsk.93@gmail.com)

Solving of complex computing tasks requires the use of powerful electronics. Due to the large number of transistors on a limited surface, such electronic devices have a high heat dissipation, that should be compensated by cooling systems of high efficiency. Thus, it is possible to prevent the transistors from burning out and, consequently, it will help to protect electronic devices from breakdown.

Two-phase systems have a great potential for use in cooling systems. In particular, the rivulet flow, a kind of film flow, has a number of advantages useful for cooling. The main advantage of rivulet flow is the presence of two contact lines, in the area of which the heat transfer coefficient is several times greater than the average (Marchuk et al. 2015). Cheverda et al. (2016) also showed, that the maximum heat flux density takes place in the area of the contact line and exceeds the average heat flux density from the entire. The lower energy consumption for pumping the gas-liquid mixture through the channel is also an important advantage of the rivulet flow in comparison with the film flow.

To create an effective cooling system, a research of water rivulet flow regimes in minichannels at different temperatures is required. It is also important to obtain the geometric parameters of the rivulet flow and to measure the evaporation of water under different conditions.

A detailed description of the experimental stand and of the test section is given in Cheverda et al. (2012).

Employing DSA-100 system and using sessile drop method the static wetting angle is measured and it is to  $114.4 \pm 3^\circ$ . Also, we measured surface roughness of substrate. The Ra was  $0.458 \mu\text{m}$ . The surface was processed with abrasive M-40 and the roughness was measured by the TR-200 instrument.

We investigated the dependence of the regimes of rivulet flow on the substrate temperature in the range from 20 to  $60^\circ\text{C}$ .

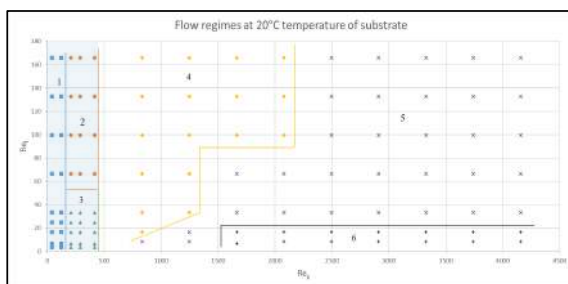


**Figure 3:** . Flow regime map representing varieties of the geometry of the nitrogen driven rivulet flow of water in the minichannel at  $20^\circ\text{C}$ . 1 – divergent rivulet bridge, 2 – straight rivulet bridge, 3 – pulsating rivulet bridge, 4 – divergent flow regime, 5 – straight flow regime, 6 – unstable flow regime. Shaded area corresponds to the rivulet bridge, the unshaded one - to the rivulet flow.

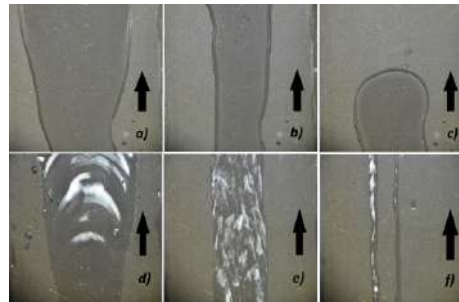


**Figure 4:** Varieties of the geometry of the nitrogen driven rivulet flow of water in the minichannel. a) - divergent rivulet bridge, b) - straight rivulet bridge, c) - pulsating rivulet bridge, d) - divergent flow regime, e) - straight flow regime, f) - unstable flow regime.

Figure 3 shows a map of regimes of stream flow, obtained at a temperature of  $20^\circ\text{C}$ . These flow regimes were revealed: divergent (Figures 4a, 4d), in which the flow width increases by more than 10% compared to the initial width; straight (Figures 4b, 4e), the width of which remains within 10% compared to the initial one; pulsating rivulet bridge (Figure 4c), in which the appearance of the drop completely filling the channel alternates with the drainage of the channel; and unstable flow regime (Figure 4f), which represents two narrow rivulets. In addition, we observed two types of flow: a normal rivulet and a “rivulet bridge” – a regime in which the liquid touches the upper wall of the channel (glass) during flow (the shaded area in Figure 3).

Depending on the temperature, the boundaries between the regimes move insignificantly, which can be explained by the intensive evaporation of water under the action of a dry gas stream with increasing temperature.

### References

Igor Marchuk, Andrey Karchevsky, Anton Surtaev, and Oleg Kabov Heat flux at the surface of metal foil heater under evaporating sessile droplets, *Int. J. Aerospace Eng.* Vol 2015 (2015)

V. V. Cheverda, I. V. Marchuk, A. L. Karchevsky, E. V. Orlik, O. A. Kabov Experimental study of heat transfer in a rivulet flow running along an inclined foil, *Thermophys. Aeromech.*, Vol. 23, No. 3 (2016)

V. V. Cheverda, A. Glushchuk, P. Queeckers, S. B. Chikov, O. A. Kabov Liquid rivulets moved by shear stress of gas flow at altered levels of gravity, *Microgravity Sci. technol.*, Vol. 25, No. 1, P. 73 (2012)

## The influence of different scale on thermocapillary convection in sessile droplet: experimental study

Xue CHEN<sup>1,2,\*</sup>, Zhiqiang ZHU<sup>2</sup>, Qiusheng LIU<sup>2</sup>

<sup>1</sup> School of Mechanical and Electrical Engineering, Guilin University of Electronic Technology, Guilin, 541004, China

<sup>2</sup> Institute of Mechanics(NML), Chinese Academy of Sciences, Beijing, 100190, China

\*E-mail: chenxue@imech.ac.cn

The evaporation of a liquid drop resting on a solid substrate is of great importance in a wide variety of industrial and scientific applications, such as evaporative self-assembly technique (DNA mapping, MEMS cooling), evaporation-induced particle deposition (thin film coating, ink-jet printing) and the design of more efficient heat transfer devices (Micro Heat Pipes and Capillary Pumped Loop). Among the mechanisms involved, the behaviour of thermo-capillary convection inside the drop induced by temperature gradient along the liquid-gas interface can significantly influence the flow instability. For this reason, understanding the flow characteristics inside the drop plays a vital role in evaporating droplet.

In the past decades, evaporating drops were attracted more and more scientific interests. Most researches concerned on the evolution of drop's contour, influence of the evaporation rate and heat transfer properties. For instance, Sobac, B. and Brutin, D. (2012) revealed the influence of the substrate temperature and substrate thermal properties on the evaporation process. However, there is rare experimental studies focusing on the influence of different scale on thermocapillary convection in sessile drop. In fact, such scale effect play a crucial role in the interfacial phenomena and heat transfer process during evaporation (Saada, M. A. et al. 2013). Therefore, the present study aims to establish the influence mechanisms of different scale on the thermocapillary convection in droplet evaporation.

To investigate the interfacial phenomena during evaporating, the infrared camera was used and the experimental apparatus was designed as shown in Figure 1. It is consisting of an enclosed test cell, injecting system, heat measurement and collection system, pressure controller and observation devises including CCD camera and IR camera (Xue, C. 2015). Experiments were performed as a preliminary work for the future space experiments on board the Chinese Space Station (CSS) to investigate the internal flow instability with free interface and phase-change process.

On the basis of this system, we conducted a series of ground experiments. The underlying mechanism of heat and mass transfer involved in the droplet evaporation with different volatile fluids was studied. Taking advantage of infrared thermal imaging technology, evidence on the various convective instabilities is then obtained, depending on the nature convection and the length scale of droplets. It is found that there are two distinct convective patterns appearing during free evaporation: one is in the form of hydrothermal waves and the other one is in the form of Rayleigh-Bernard convective cells. Owing to the scale effect, the surface-tension-driven flow may be divided into four kinds of patterns. The more detailed results will be discussed in the following article.

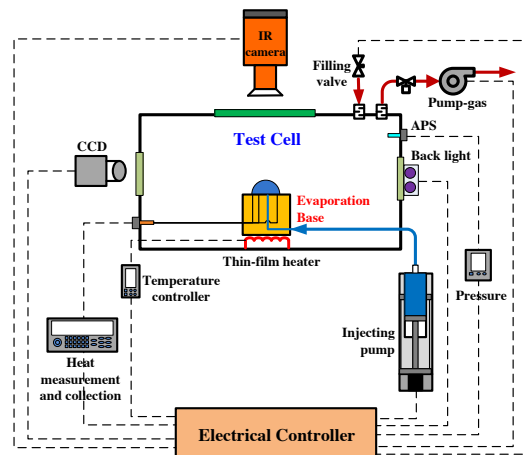


Figure 1: Schematic diagram of the experimental apparatus.

### References

- Sobac, B. and Brutin, D., Thermal effects of the substrate on water droplet evaporation. *Phys. Rev. E*, Vol.86, pp. 021602 (2012).
- Saada, M. A., Chikh, S., Tadrist, L., Evaporation of a sessile drop with pinned or receding contact line on a substrate with different thermophysical properties. *Int. J. Heat Mass Tran*, Vol.58, pp. 197-208 (2013).
- Xue, C., Z. Q. Zhu, Q. S. Liu, et al. Thermodynamic Behaviors of Macroscopic Liquid Droplets Evaporation from Heated Substrates. *Microgravity Sci. Technol.*, Vol.27, No. 5, pp.1-8 (2015).

## Measurements of the evaporation rate upon evaporation of a heated thin layer

E.G. Korbanova, E.Ya. Gatapova

Novosibirsk State University, faculty of Mechanics and Mathematics, department of Hydrodynamics  
Novosibirsk, 630090, Pirogova Street, 2  
Kutateladze Institute of Thermophysics, Siberian Branch of Russian Academy of Sciences  
Novosibirsk, 630090, Lavrentyev Avenue, 1  
E-mail: [Korbanova20@gmail.com](mailto:Korbanova20@gmail.com)

Investigation of evaporation process in a two-layer system under non-isothermal conditions is important for many applications, such as microelectronics cooling (Nasr et al. 2017). The advancement in high performance heat exchangers, vapor chambers and heat pipes with microscale passages stimulates also development of a new fundamental knowledge of the processes with phase change (Gatapova et al. 2015, Gatapova et al. 2017). Evaporative flux depends on the thermal difference at the interface (Gatapova et al. 2017), and the precise measurements of these two quantities (temperature and evaporation rate) can give information on the boundary condition at the liquid-gas interface as well as data on the evaporation/condensation coefficients.

In this work, we present the results of the evaporation rate measurements of the locally heated liquid layer.

Experiments are conducted at normal atmospheric condition. Ultrapure deionized and degassed water (MilliQ), is used as a working fluid. The liquid is injected using a syringe pump to cuvette with local heater, which is placed in microbalance system (Fig. 1). Calculation of the mass of evaporated liquid is carried out using BM-252 microbalance of accuracy class I (special), with the smallest weighing limit of 0.01 mg and control of the ambient gas humidity and temperature. Microbalance is connected to PC and measurements are controlled by special software. The experiments are performed at quasi-stationary heating mode. The temperature of the heater is controlled by three thermocouples. The pressure is measured by barometer. Calibrations of all thermocouples are carried out in the temperature range 5–100 °C. Two reference thermometers (ETS-100) are used. Data registration is carried out by means of temperature control and measurement system consisting of data collection (NI 9214) and the corresponding software.

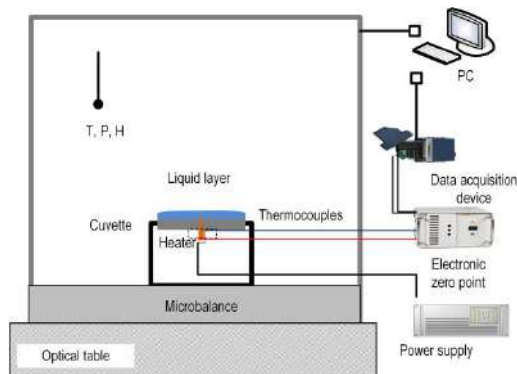


Figure 1: Scheme of the experimental setup.

Results of the evaporation rate measurements for water-air system are presented in Fig. 2. The local minimum is observed which is connected with the point of equilibrium of the liquid-gas interface. Basing on our previous temperature profile measurements [3], we can conclude that when no heat is applied to the heating element temperature in gas phase is larger than in liquid, and evaporation occurs with the rate of 0.014–0.018  $\mu\text{l/s}$ . Then evaporation rate is decreasing with increasing heater temperature until the equilibrium without temperature jump is reached at the liquid-gas interface. Further increasing of the heater temperature leads to increasing of the evaporation rate.

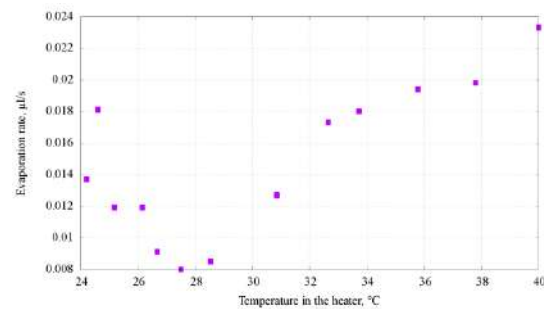


Figure 2: Evaporation rate dependence on the average temperature of the heater.

In conclusion, results of the evaporation rate measurements of a heated liquid layer are presented. It is shown that there is local minimum of evaporation at the point of equilibrium of the liquid-gas interface.

### References

- M.H. Nasr, C.E. Green, P.A. Kottke, X. Zhang, T.E. Sarvey, Y.K. Joshi, M.S. Bakir, A.G. Fedorov, Flow regimes and convective heat transfer of refrigerant flow boiling in ultra-small clearance microgaps, *Int. J. Heat Mass Transfer*, Vol. 108, pp. 1702 – 1713 (2017)
- E.Y. Gatapova, I.A. Graur, F. Sharipov, O.A. Kabov. The temperature and pressure jumps at the vapor-liquid interface: Application to a two-phase cooling system, *Int. J. Heat Mass Transfer*, Vol. 83, pp. 235 - 243, (2015).
- E.Y. Gatapova, I.A. Graur, O.A. Kabov, V.M. Aniskin, M.A. Filipenko, F. Sharipov, L. Tadrist. The temperature jump at water-air interface during evaporation, *Int. J. Heat Mass Transfer*, Vol. 104, pp. 800 – 812, (2017).

## Lattice Boltzmann simulation of bubble growth and departure during pool boiling

Mikhail Moiseev<sup>1</sup> and Maxim Shugaev<sup>2</sup>

<sup>1</sup>Institute of Thermophysics SB RAS, Novosibirsk, 630090, 1 Acad. Lavrentiev Ave., Russia  
[moisevmikhail@gmail.com](mailto:moisevmikhail@gmail.com)

<sup>2</sup>University of Virginia, Charlottesville, Virginia 22903, United States  
[mvs9t@virginia.edu](mailto:mvs9t@virginia.edu)

Boiling is one of the most effective heat transfer modes, and thus it is widely used in various technical applications. In spite of extensive study on boiling during the past century, there is no complete mathematical model of this phenomenon. Partially it's due to complicated nature of thermo- and hydrodynamical processes of bubble nucleation, growth and movement. Numerical simulation has become an important approach for such study. In the past several decades, many techniques have been developed to simulate nucleate boiling. But these techniques are often extraordinary complicated, require interface tracking, empirical correlations and assumptions which are hard to verify. In recent years Lattice Boltzmann Method, which is based on minimal lattice formulations of the kinetic Boltzmann equation, attracts attention of researchers. Its kinetic nature makes it an effective tool for numerical simulation of problems involving interfacial dynamics and curved boundaries (Q. Li et al. 2016)

In present study we adapt pseudopotential Lattice Boltzmann Method to carry out two-dimensional simulation of the life cycle of a single vapor bubble under conditions of nucleate boiling. The fluid is described by the evolution of particle distribution functions. Phase separation in this model is provided by an interparticle potential. As a result, the liquid-vapor interfaces can naturally arise, deform, and migrate without using the interface-tracking techniques. The temperature equation is solved with finite difference scheme. The LB model and the temperature equation are coupled via non-ideal equation of state.

We simulated behaviour of vapor bubbles in water under conditions of saturated pool boiling on a heater with constant temperature at the bottom boundary. Effects of gravity, contact angle and superheat on bubble departure diameter and release frequency were studied. Data on temperature and velocity fields was obtained.

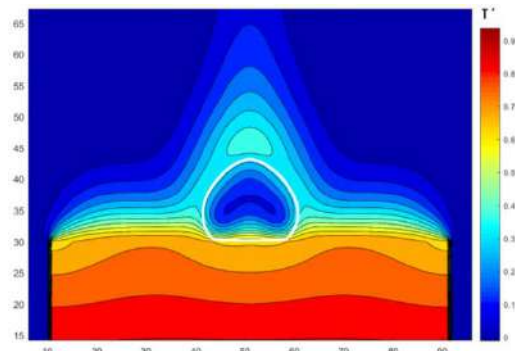


**Figure 1:** Temperature field during pool boiling on hydrophilic surface.  $Ja = 0.12$ .  $T' = (T - T_{sat}) / (T_{wall} - T_{sat})$ .

Figure 1 shows example of a temperature field during bubble growth at a hydrophilic heater (contact angle  $\theta = 60^\circ$ ). As one can see, the local temperature underneath the bubble is lower compared to the temperature at the parts of the heater covered by liquid. It means the model is able to simulate existence of evaporating microlayer under the bubble.

Figure 2 shows temporal change of the local temperature at the center of the heater surface for hydrophobic ( $\theta = 115^\circ$ ) and hydrophilic ( $\theta = 60^\circ$ ) surfaces. For the hydrophobic surface, when a bubble departs (1) there is a residual vapor at the surface, and the next bubble starts to grow immediately. Heater temperature then rises until point 2, corresponding to maximum contact area, and drops until bubble departure at point 3. For the hydrophilic surface after bubble departure 1', there is a growing period 1'-2'. With the emergence of the next bubble temperature drops non-monotonically. At point 3' temperature slightly rises, which can be interpreted as emergence of a dry spot. Then temperature drops further with bubble growth, and reaches minimum before its departure at 4'.

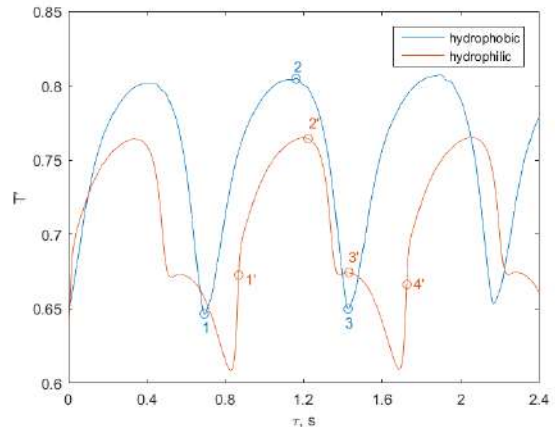


**Figure 2:** Temporal variations of temperature at the center of the heating surface.  $Ja = 0.12$ .

These simulations show that the hybrid LBM and FDM model correctly captures basic features of boiling. Also it can predict such important parameters as waiting period, which is impossible with most of other simulation techniques.

### References

Q. Li et. al. Lattice Boltzmann methods for multiphase flow and phase-change heat transfer, PECS, Vol. 52, pp. 62-105 (2016)

## Pool boiling of nanofluids on cylindrical surface

Maxim Pryazhnikov<sup>1,2</sup>, Andrey Minakov<sup>1,2</sup>, Dmitriy Guzei<sup>1,2</sup> and Alexander Lobasov<sup>1,2</sup>

<sup>1</sup> Siberian Federal University, Svobodnyi ave., 79, 660041 Krasnoyarsk, Russia

<sup>2</sup> Institute of Thermophysics SB RAS, Ac. Lavrentieva ave., 1, 630090 Novosibirsk, Russia  
arrivent@yandex.ru

Studies of the last two decades have shown that nanofluid have unusual transfer properties. In particular, small adds of nanoparticles into carrying liquid can considerably increase its heat conductivity and viscosity (Das et al. 2007). This stimulated many thermophysical applications of nanofluid, particularly, aimed at intensification of heat exchange. It has been found that nanofluid have really enhanced coefficients of heat transfer (see, for example, Terekhov et al. 2010, and literature cited therein). The further intention to increase this coefficient stimulated the study of heat transfer of nanofluid during boiling. These works have been performed quite intensely during the last decade. Nevertheless, the obtained results are rather contradictory. For example, (Kwark et al. 2009) it is noted that adding of nanoparticles does not change heat transport considerably, with an even decrease in the heat transfer coefficient during boiling been seen in (Das et al. 2008). Conversely, this coefficient rose (Shi et al. 2007).

In this work, saturated boiling of the nanofluid were prepared using distilled water and Al<sub>2</sub>O<sub>3</sub> nanoparticles was experimentally studied. The present work was aimed at studying the influence of nanoparticles on on the critical heat flux and heat transfer coefficient under boiling of nanofluid on a copper cylinder.

The study of boiling process occurred on the copper cylinder (diameter is 25 mm).

Method of procedure. The cylinder is heated in the furnace to temperature of 350 °C. After that it is immersed within studied fluid (distilled water or nanofluid) to the depth of 15 mm. Since the surface of the cylinder has a high temperature, when immersed in water formed a vapor film. The studied fluid was heated up saturation point to not spend the warm on heating fluid. Cooldown period occurs at a constant coolant temperature. The value of heat transfer coefficient is constant in the film boiling; that is the boundary condition for steady cooling regimen. Cylinder temperature is measured using thermal couple which mounted into it. The decline rate of the cylinder and the heat transfer coefficient are meant on the score of evidence from the research.

Study of boiling was drown using the distilled water, water-based nanofluid and Al<sub>2</sub>O<sub>3</sub> nanoparticles. The volume concentration of the nanoparticles in water was equal 3 %. Average particle size of Al<sub>2</sub>O<sub>3</sub> nanoparticles is 36 nm. For preparation of nanofluids we used the standard two-step process. The nanoparticles were purchased from “Advanced Powder Technologies” company LLC (APT) (Tomsk).

Figure 1 shows pool boiling curves showing heat flux as a function of wall superheat for water and Al<sub>2</sub>O<sub>3</sub>-nanofluids.

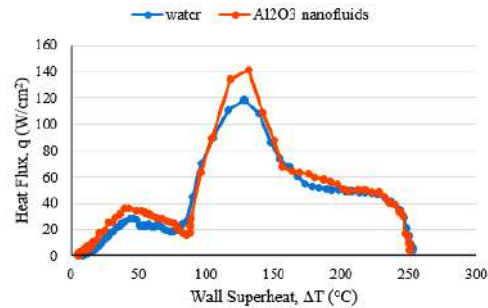


**Figure 1:** Pool boiling curves showing heat flux as a function of wall superheat for water and Al<sub>2</sub>O<sub>3</sub>-nanofluids.

As a result of experiments, it was obtained that the heat transfer coefficient of a Al<sub>2</sub>O<sub>3</sub>-nanofluid is higher by 22 % than the heat transfer coefficient of distilled water.

### Acknowledgments

The authors gratefully acknowledge the support of the projects funded by the Russian Foundation for Basic Research and Krasnoyarsk Regional Fund for Support of Scientific and Scientific-Technical Activities (Contract № 16-48-243042).

### References

- Das S. K., Choi S.U. S., Yu W., Pradeep T., Nanofluids: Science and Technology, Wiley Interscience, New Jersey (2007).
- Terekhov V.I., Kalinina S.V. and V. V. Lemanov, The mechanism of heat transfer in nanofluids: state of the art (review). Part 2. Convective heat transfer, Thermophysics and Aeromechanics, Vol. 17, pp. 157-171 (2010)
- Kwark S.M., Kumar R., Moreno G., Yoo J., You S.M., Pool boiling characteristics of low concentration nanofluids International journal of Heat Mass Transfer, Vol. 53, pp. 972-981 (2009)
- Das S.K., Narayan G.P., Baby A.K., Survey on nucleate pool boiling of nanofluids: the effect of particle size relative to roughness, Journal of Nanoparticle Research, Vol.10, pp. 1099-1108 (2008)
- Shi M.H., Shuai M.Q., Chen Z.Q., Li Q., Xuan Y., Study on pool boiling heat transfer of nano-particle suspensions on plate surface, Journal of Enhanced Heat Transfer, Vol. 14 pp. 223-231 (2007)

## Features of two-phase flow regimes in a horizontal rectangular microchannel

V.P. Fina<sup>1,2</sup>, F.V. Ronshin<sup>2,3</sup>, and V.V. Cheverda<sup>2,3</sup>

<sup>1</sup>École Nationale Supérieure d'Arts et Métiers de Bordeaux  
Esplanade des Arts et Métiers, 33405 Talence CEDEX, France

<sup>2</sup>Novosibirsk State University  
1, Pirogova str., Novosibirsk, 630090, Russia

<sup>3</sup>Kutateladze Institute of Thermophysics, Siberian Branch, Russian Academy of Sciences 1,  
Lavrentiev ave., Novosibirsk, 630090, Russia

E-mail: [valentin.fina@ensam.eu](mailto:valentin.fina@ensam.eu)

The last decades have seen the miniaturization of devices in various fields of engineering, and it is well-known that the existing cooling systems do not meet the modern requirements for heat removal from these highly heat-intense sources. It seems now probable that the next generation of cooling systems will be based on flows in mini and micro channels. Indeed, as the thickness of the channel decreases, the ratio of the channel surface to its volume increases inversely proportional to its minimal cross dimension, which leads to heat exchanges of dramatic intensity, as many studies published on this matter over the last years illustrate it. Overviews of the publications on two-phase flows in micro channels of various configurations are given in Rebrov (2010), and Chinnov et al. (2015). Research recently focused on flows within rectangular channels, however, only one study has yet to use a channel of a height of less than 100  $\mu\text{m}$  for now, and was carried by Ronshin et al. (2016) on a 50  $\mu\text{m}$   $\times$  20 mm channel. The present study comes in its wake, as flows in an even smaller channel have been investigated with the same method to better understand the behaviors previously witnessed.

The purpose of this work is thus the experimental investigation of two phase flows of distilled deionized nanofiltered water and nitrogen gas in a microchannel with the height of 50  $\mu\text{m}$  and a width of 10 mm. This study focuses mainly on two-phase flows regimes and on the boundaries between them. The scheme of the experimental setup is shown in Figure 1.

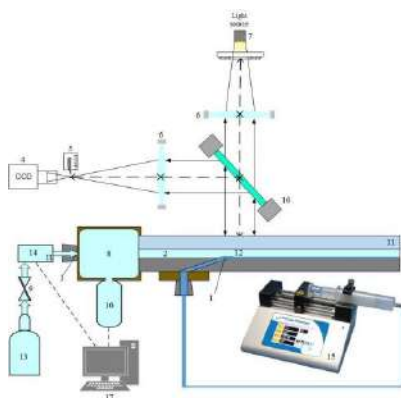


**Figure 1:** Schematic diagram of the experimental setup

The gas mixture is supplied into the central part of the microchannel from the tank (13). The gas flow rate is

adjusted from 100 to 5000 ml/min and kept constant with the aid of the flow controller El-Flow of the Bronkhorst company (14). Gas is introduced into the gas chamber (8) and enters the microchannel through a gas nozzle (2). Liquid flow rate varies from 0.5 to 50 ml/min using a high-precision syringe pump Cole-Parmer (15). The liquid is supplied into the microchannel through the liquid inlet (1). Pressure in the gas chamber (8) is measured by the pressure sensor WIKA Type P-30 (16). The data of the pressure sensor and the current gas flow rate are written in a file on a personal computer (17).

Interaction of gas and liquid in the microchannel is visualized in the area (12), using digital video cameras in the mode of schlieren photography. The schlieren method is used for registration and visualization of surface deformations of a thin liquid film. The light from the source enters the microchannel with the gas-liquid flow through a diffuser (7), lens (6), beam splitter (10) and an optical glass (11). The light reflected from the gas-liquid interface passes through a beam splitter (10), a lens (6) and a camera lens filter (4). The schlieren knife-edge shifted by a micro-screw (5) highlights the central part of the light flux. As a result, the camera captures the grayscale image, where each gray level corresponds to a certain angle of inclination of the liquid-gas interface. The following regimes of two-phase flow were detected in the microchannel: bubble, stratified, churn, jet and annular. Experimental information allows us to define the characteristics of the two-phase flow and to determine precisely the boundaries between the regimes of the two-phase flow.

The study was supported by the Russian Science Foundation (Agreement No. 15-19-30038)

### References

- Chinnov, E. A., Ron'shin, F. V., and Kabov, O. A., Regimes of two-phase flow in micro- and minichannels (review), *Thermophys Aeromech.*, Vol. 22, No. 3, pp. 265–284, (2015).
- Rebrov, E. V., Two-phase flow regimes in microchannels, *Theor. Found. Chem. Eng.*, Vol. 44, No. 4, pp. 355–367, (2010).
- Ronshin, F.V., Cheverda, V.V., Chinnov, E.A., Kabov, O.A., Features of two-phase flow regimes in a horizontal rectangular microchannel with the height of 50  $\mu\text{m}$ , *Interfacial Phenomena and Heat Transfer*, Vol. 4, No. 2-3, pp. 191-205, (2016).

## Research and development LHP for Chinese spacecrafts.

S.A. Novichkova, Y.V. Panin, M.A. Balykin, K.N. Korzhov

Lavochkin Association  
 Khimky, Moscow region, Russia  
 E-mail: [heatpipe@laspace.ru](mailto:heatpipe@laspace.ru)

In 1995 was developed and manufactured Thermal Control System (TCS) on base of Loop Heat Pipes (LHP) for Nickel-Cadmium Batteries (NCB) Cooling. This TCS was ordered by Shanghai Institute of Spacecraft Engineering for Chinese meteorological satellite of FY-1 type (Fig. 1).



**Fig. 1:** Meteorological satellite of FY-1 type.

The first Chinese satellite with LHP on board FY-1C was launched in 1999 and successfully operated 8 years in orbit. The FY-1D satellite, which has a similar system with LHP, was launched in 2002 and successfully operating on present time.

Application of LHP allowed to multiply increase the life time of Chinese satellites.

TCS of NCBs FY-1 satellites included several LHPs with ammonia that were connected in parallel with a single radiator (Fig. 2). Each LHP is equipped with a thermoelectrical cooler (TEC), which provides «start up» of the LHP circulation. The heat power transferred by each LHP was up to 40 W. TCS allowed to thermostate the NCSB in the temperature range from 10 to 30°C. The mass of the TCS, which included 3 LHPs, did not exceed 3,0 kg.

Further development of such TCSs was obtained for the thermostating of the payload of the Chinese meteorological satellites FY-3A, FY-3B, FY-3C and FY-3G. LHP for these satellites have a similar design. The body of LHP is made of stainless steel, a capillary structure is made of 1 mkm size porous nickel, a radiator is made of an aluminum alloy with a paint coating solar mirror class. The diameters of LHP transport lines and condensers are 2,0 mm. The length of transport lines is several meters long. The diameter of the evaporators is 11,0 mm.

The transferred power of LHP used on new satellites was increased to 200 W without increasing their mass and dimensions performance. Modelling and optimization of the parameters of the LHP and TCS based on them were carried out using the EASY 2.0 software package, developed by TAIS Company.

The paper presents the modelling layout and description of the TCS, the detailed description and performance of the

LHP for the FY-3 satellites, the results of calculations and thermalvacuum tests.



**Fig. 2:** The scheme of a type FY-1 meteorological satellite.

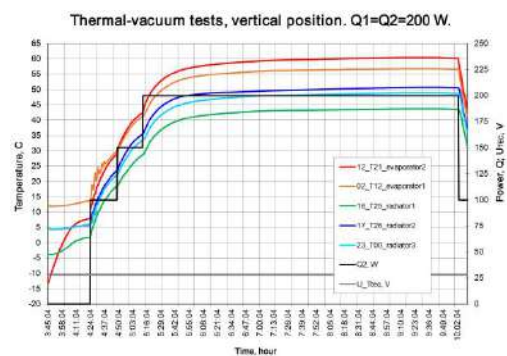


**Fig. 3:** Thermal-vacume tests.

### References

Maidanik Yu. F., Fershtater Yu.G., Pastukhov, V.G., Goncharov, K.A. Zagar, O., and Golovanov, Yu., Thermoregulation of Loops with Capillary Pumping for Space Use, SAE Paper, No. 921169 (1992).

M. Nikitkin, K. Goncharov, O. Golovin, et al., Loop Heat Pipes In Thermal Control Systems For «OBZOR» Spacecraft 4th International CPL Workshop, Baltimore, USA, September (1994).

K. Goncharov, O. Golovin, V. Kolesnikov Zhao Xiaoxiang, Development and flight operation of LHP used for cooling of storage batteries in Chinese meteorological satellites FY-1. 13 IHPC, Shanghai, China (2004)

Modeling of vapor generating in small-porous capillary structures Buz V.N., Goncharov K.A., 15th International Heat Pipe Conference (15th IHPC) Clemson, USA, April 25-30 (2010).

## Thin film evaporative cooling system for high heat flux applications

Karapet S. Eloyan and Dmitry V. Zaitsev

Institute of Thermophysics, SB RAS  
Posp. Lavrentyev 1, Novosibirsk, 630090 Russia  
[karapet8881@rambler.ru](mailto:karapet8881@rambler.ru)

One of the major problems in the field of applied thermal physics is creation of an effective cooling system for microelectronics, power chips, «green» IT. Modern cooling systems for processors are able to remove up to 150-200 W/cm<sup>2</sup>. Development of more effective and compact cooling system for electronics will lead to rapid development of powerful microelectronics. Today, in DATA centers, about 30-40% of all energy is used by cooling system. According to research [1], the heat flux in hot spots reaches up to 1kW/cm<sup>2</sup>.

One of the promising ways of removing large heat fluxes from the surface of heat-stressed elements of electronic devices is the use of evaporating thin layer of liquid film, moving under the action of the gas flow in a flat channel [2]. Recent experimental investigations conducted in works [3] proved possible removal of heat fluxes with density of up to 870 W/cm<sup>2</sup> from the heating area of 1x1 cm<sup>2</sup> using this method. The works [4,5] showed that such a system can operate stably in a wide range of the channel heights (0.17-2.00 mm) and angles of the channel inclination to the horizon (0-360°).

In this work, we present a model of evaporative cooling system for high heat flux removal with forced circulation of liquid and gas coolants, capable to remove heat flux of up to 1 kW/cm<sup>2</sup> and higher (Fig. 1).

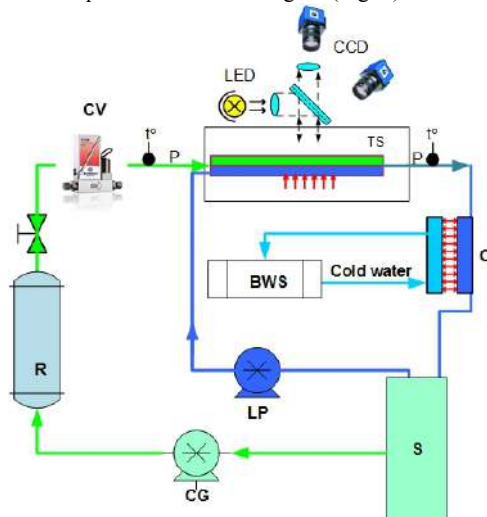
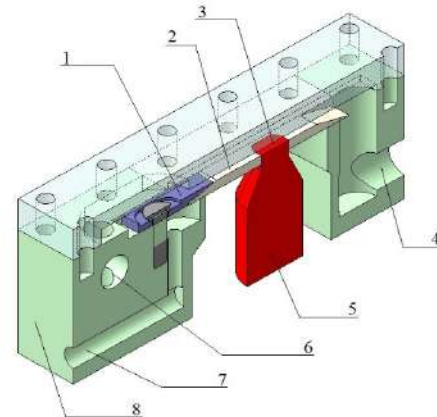


**Figure 1:** Schematic diagram of the experimental model of evaporative cooling system: TS – testing section; C – condenser; S – separator; R – receiver; CV – control valve; LP – liquid pump; CG – gas vacuum pump-compressor; BWS – building water supply.

Scheme of the test section is shown in Fig.2. The test section consists of a thin and flat stainless steel plate with a

flush-mounted cooper rod with a 1x1 cm square head, serving as a heater. The rod is heated by a nichrome spiral coiled around its bottom part (not shown in Fig. 2). The liquid film supplied from the liquid nozzle is driven by the shear stress of gas in the channel. Water and air with initial temperature of about 25 °C are used as the working liquid and gas, respectively. The channel is oriented horizontally. The channel height is 1.0 mm. The peculiarity of the test section used in the present work is that the width of the channel is equal to the width of the heating element (1 cm). It is supposed that such configuration of the test section will allow to get higher values of the heat flux compared with the case when the channel width is higher than the width of the heater (at the same Re number of liquid), since in the latter case some portion of liquid is deviating from the heater due to the thermocapillary forces.

**Figure 2:** Scheme of test section.



1- liquid nozzle, 2- stainless steel substrate, 3- 10x10 mm heater, 4 – outlet, 5- copper rod, 6- gas inlet, 7- liquid inlet, 8- textolite base.

### References

1. Bar-Cohen A, Wang P. Thermal Management of On-Chip Hot Spot // ASME. J. Heat Transfer, **134**(5), 051017, 2012.
2. O.A. Kabov, D.V. Zaitsev, V.V. Cheverda, A. Bar-Cohen, Experimental Thermal and Fluid Science, **35**, 825 (2011)
3. D. Zaitsev, E. Tkachenko, E. Orlik, O. Kabov, MATEC Web of Conferences, **92**, 01037 (2017)
4. D. Zaitsev, O. Kabov, MATEC Web of Conferences, **84**, 00043 (2016)
5. E.M. Tkachenko, D.V. Zaitsev, MATEC Web of Conferences, **72**, 01114 (2016)

## Heat and mass transfer of multiphase flow in channels with irregular geometry

Dmitry Khrantsov, Boris Pokusaev

Moscow Polytechnic University, Faculty of Chemical and Bioengineering, Department of Thermodynamics and nonstationary transfer processes  
38, B.Semenovskaya St., Moscow, 105082, Russia  
dp@khrantsov.net

One of the most common flow regimes in the pipes for energy systems, oil and gas production, as well as in microchannels is the slug flow regime of two-phase flow (Hessel et al., 2005). In such flow a large gas bubble is rising in a pipe or moving under the pressure in the capillary channels, separated by a fluid layer. Mixing of gas and liquid phases, combined with diffusion and low thermal resistance through the thin film between bubble and wall, leads to a substantial intensification of the processes of heat and mass transfer. A satisfactory theory of such flows has not yet been developed. This is due, primarily, to the complexity of such flows. Problems with the theoretical description arise even for the case of motion of a single slug in an inclined pipe and complexity increases when gas bubble flows in a channel with obstacles of arbitrary geometry and location. Such mediums occurred in pipes with granular layer and gels.

Dynamics of gas liquid flow inside irregular channels and gels are not studied enough, both experimentally and numerically. Gel is a specific two-phase system. One phase represents a relatively sparse spatial network of polymer molecules which are bonded at the intersections of intermolecular bonds. The second phase is a liquid. In the study of additive processes of application of gels in relation to problems of bioprinting, we found the effect of microchannels formation between the layers of gel, filled with gas and fluid.

In the case of the presence of microorganisms within the gel, a carbon dioxide is produced within the gel due to activity of microorganisms (Pokusaev et al., 2015). For the normal functioning of microorganisms in the gel it is required a withdrawal of produced products. In this case, the rate of drainage is influenced by the intensity of absorption and the speed of ascent of gas bubbles, which leads to the necessity of conducting experimental and theoretical studies of the process of mass transfer of gas bubbles in the gel. The relevance of such studies is also due to the active development of technologies of three-dimensional printing of living tissues and bodies (Jakab et al., 2010).

Model movement of a gas bubble in a channel with complex geometry on the process of mass and heat transfer was developed based on the smoothed particle hydrodynamics method. The method is based on representing the fluid as a set of particles, which are located at some distance from each other, the distance called smoothing (Liu and Liu, 2003). The influence of each particle on the properties of nearby particles is calculated on the basis of its density and the distance from the particle for which parameters.

For the calculation we introduce the notion of kernel functions. As a kernel function, typically uses a Gaussian function. In the case of motion of a gas bubble of carbon

dioxide in the channel with obstacles (Figure 1). For verification of the developed model was used for calculation of test problem on simulation of freely rising gas bubble in a pure liquid at various angles of inclination of the tube for the purpose of comparison with previously obtained experimental data.

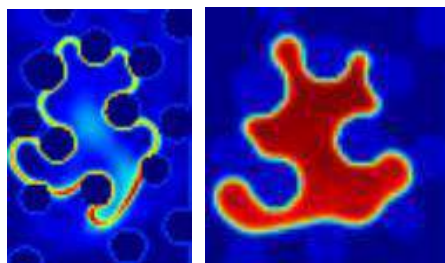


**Figure 1:** Computer modeling of two-phase flow in liquid filled with obstacles.

The maximum value of the effective mass transfer coefficient corresponds to the angle of inclination at which the speed of ascent of the bubble maximum. If you increase the speed of ascent of the gas bubble passes the work area in less time, respectively, the interaction time between phases decreases. The obtained dependence allows to conclude that the time of interfacial contact is the defining characteristic of the intensity of the process of mass transfer.

### References

- Hessel V., Lowe H., Muller A., Kolb G., Chemical Micro Process Engineering. Wiley VCH, Weinheim, Germany (2005)
- Pokusaev B.G., Karlov S.P., Vyazmin A.V., Nekrasov D.A., Diffusion phenomena in gels, Chemical Engineering Transactions, Vol. 43, pp. 1681-1686 (2015)
- Jakab K., Norotte C., Marga F., Murphy K., Vunjak-Novakovic G., Forgacs G., Tissue engineering by self-assembly and bio-printing of living cells, Biofabrication, Vol. 2, pp. 20-34 (2010)
- Liu G.R., Liu M.B., Smoothed Particle Hydrodynamics: A Meshfree Particle Method. World Scientific, Singapore (2003)

## THE INTERACTION OF A IMPINGING WATER DROP WITH A HEATED SURFACE

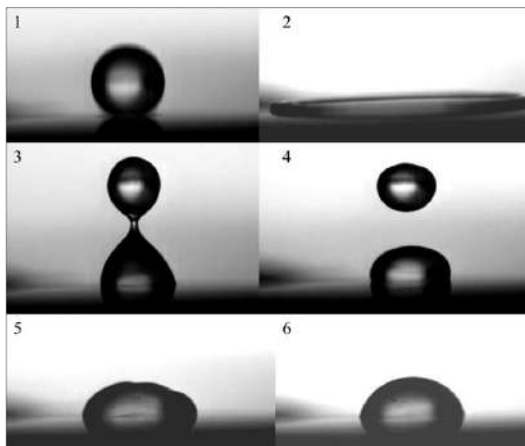
E.O. Kirichenko<sup>1,2</sup>, E.Ya. Gatapova<sup>1,2</sup>

<sup>1</sup>Kutateladze Institute of Thermophysics, Siberian Branch, Russian Academy of Sciences  
 1, Lavrentyev ave., Novosibirsk, 630090, Russia

<sup>2</sup>Novosibirsk State University, 1, Pirogova str., Novosibirsk, 630090, Russia  
 E-mail: [kirichenko\\_ekaterina@outlook.com](mailto:kirichenko_ekaterina@outlook.com)

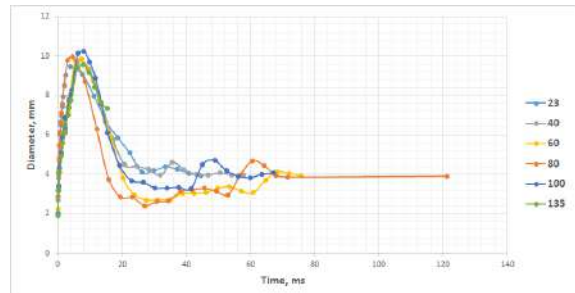
The purpose of this work is the investigation of the main stages of the interaction of a falling water droplet with a heated substrate at various temperatures and inclines of the surface. Characteristic stages of the drop interaction with a substrate at various temperatures are revealed: impact, spreading, rollback, separation of microdroplets, formation, stabilization. The effect of the temperature on the characteristic time of these stages and the droplet diameter was studied. A drop of 25-30  $\mu\text{l}$  is dosed to the surface using a syringe pump. Ultrapure deionized water (MilliQ) is used as a working fluid. Sapphire round plate with Polyimide Thermofoil Heater is used as a substrate. The range of the investigated temperatures is from 23 to 135°C. Substrate surface temperature was controlled by thermocouple. The distance from the needle to the sapphire substrate is 14.5 cm. A high-speed camera Fastcam SA 1.1 Photron with a resolution of 1024x1024 pixels and rate of 5400 fps records the interaction process.

It is shown that the spreading time of the droplet is the same 4.1-4.8 ms in the entire temperature range for a horizontal substrate. The microdroplets detachment from the droplet surface are observed before formation for substrate temperature of 60 °C. The drop is divided into several drops after the spreading for 130 °C. Figure 1 shows the main stages of the drop interaction with the surface at temperature of 60 °C.



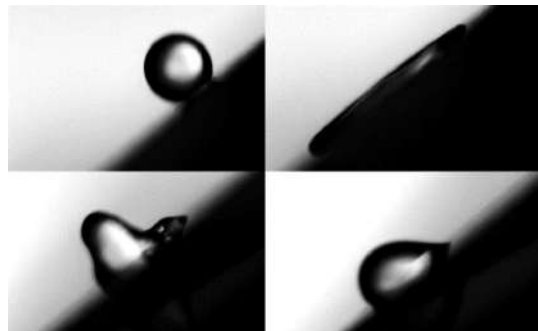
**Figure 1:** The main stages of the drop interaction with a heated substrate.  $T=60^{\circ}\text{C}$ .

Figure 2 shows the dependence of the droplet diameter on time. The characteristic spreading time of the drop is the same for all temperature regimes and is of 4.0-4.8 ms. The temperature rise leads to decrease of the diameter during the rollback phase.



**Figure 2:** Changing the droplet diameter in the interaction with the surface at different temperatures.

When the drop of water interacts with the inclined surface (38° to horizon), the following stages can also be distinguished as for a horizontal surface: 1 - impact, 2 - spreading, 3 - rollback, 4 - formation. A continuous sliding of the drop on the surface follows all of the main stages.



**Figure 3:** The main stages of the drop interaction with an inclined surface.

The stage of separation of microdroplets from the main droplet is completely absent when the substrate is heated, which was observed for a horizontal surface at substrate temperatures of 60 °C and higher. The stabilization stage is also absent, since after the stage of formation the drop continues to slide gradually on the surface under the action of the gravity.

The work was financially supported by the Ministry of Education and Science of the Russian Federation (Agreement 14.613.21.0067, project identifier RFMEFI61317X0071).

## Numerical simulation of turbulent scalar transport in a confined plane jet

Andrey Bazhenov, Michael Hrebtov and Boris Ilyushin

Institute of Thermophysics SB RAS  
Lavrentiev ave. 1, Novosibirsk, 630090, Russia  
weexov@yandex.ru

Turbulent jets are of great importance in industrial applications dealing with heat and mass transfer. The processes inside the jet are affected to a large degree by inflow conditions (the shape of the nozzle, swirl rate, harmonic forcing) and by the geometry of the flow. Such a big influence is caused by the high sensitivity of the shear layer to the small flow perturbations that may lead to the change of dominant instability mode.

The confined or slot jets (where the flow is bounded by two closely placed parallel walls) are especially interesting because of interaction of the jet shear layer with the wall. In that case the instabilities generated at the wall interact with the main Kelvin-Helmholtz type vortices in the shear layer. For different aspect ratios between the jet width and the distance between the walls the flow develops large-scale meandering oscillations and quasi-two-dimensional checkerboard pattern of vortices resembling von Karman's vortex street. For large (~10) aspect ratios these features are more pronounced in a turbulent regime for large enough Reynolds numbers (~ $10^4$ ).

This meandering behavior of the flow must affect the turbulent diffusion of passive scalars enhancing the transport of the scalar in transversal direction (Rowland et al. 2009). The present work was aimed to investigate this process.

For present numerical simulation we consider a wall-bounded shallow jet flow in the rectangular domain of the size  $L \times H \times W$ , where  $L = 200H$  and  $W = 150H$ .  $L$  and  $W$  are much larger than  $H$  (see Fig. 1). The size of the domain is taken in accord with the experimental studies (Shestakov et al. 2015).

The inflow channel is a short duct of the length  $5H$  (and the cross-section  $B \times H$  with  $B = 9.6H$ ). The inflow velocity profiles are taken from a precursor simulation of a fully developed turbulent duct flow. The Reynolds number of the flow was  $2 \times 10^4$  based on the distance between the walls ( $H$ ).

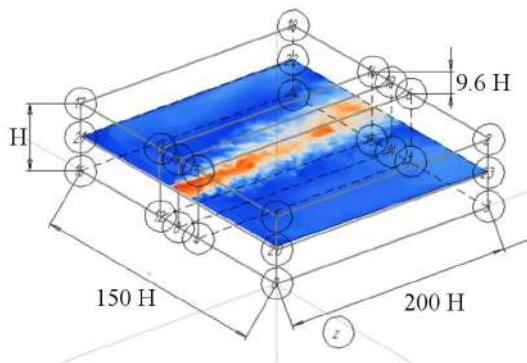


**Figure 1:** The schematics of the computational domain.

The numerical grid consisted of  $20 \times 10^6$  cells with the adjacent gridcell width ( $h_0^+$ ) was about 0.2 in wall units. Such grid resolution was chosen based on preliminary simulations with a set of grids with different number of cells.

The momentum and scalar transport equations were discretized using finite volume scheme with second order accuracy in time and space (the modified solver from OpenFoam package was used). We use large eddy simulation approach with dynamic Smagorinsky model, where the model constant is averaged over lagrangian trajectories (Meneveau et al. 1996).

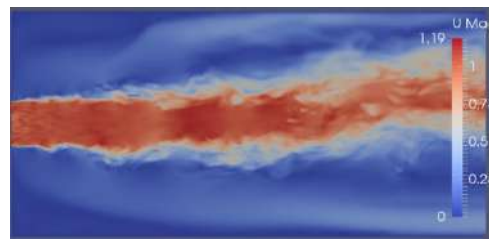


**Figure 2:** The instantaneous velocity magnitude in the central cross-section.

The results show that the long-wave sinusoidal oscillations are developed in the far region of the jet affecting the mean velocity and scalar distributions. The turbulent energy and scalar concentration spectra were computed in different parts of the flow showing two distinct slopes: steep slope (about -3 for turbulent energy) at low frequencies and milder slope at higher frequencies (close to -5/3 for turbulent energy). This behavior could be attributed to the dominance of two-dimensional effects at scales larger than the distance between the plates and Kolmogorov's behavior at smaller scales.

### References

- Meneveau C., Lund T. and Cabot W., A Lagrangian dynamic subgrid-scale model of turbulence. *J. Fluid Mech*, Vol. 319, pp. 353-385 (1996)
- Rowland, J.C., Stacey M.T., and Dietrich W.E. Turbulent characteristics of a shallow wall-bounded plane jet: experimental implications for river mouth hydrodynamics. *Journal of Fluid Mechanics*, Vol. 627, pp. 423-449 (2009)
- Shestakov M.V., Dulin V.M., Tokarev M.P., Sikovsky D.P., Markovich D.M. Piv study of large-scale flow organisation in slot jets, *Int. J. Heat Fluid Flow*, Vol. 51, pp. 335-352 (2015)

## Gas jet deposition of diamond from high velocity gas flows

Alexey Rebrov

Kutateladse Institute of Thermophysics  
Prosp. Lavrentieva 1, 630090, Novosibirsk, Russia  
rebrov@itp.nsc.ru

At the moment, diamond is one of the most promising functional materials rather than a precious jewel. This material is in high demand in various fields of industry, including production of electronic devices, cutting and drilling tools, optics, high-pressure engineering, etc. If diamond is obtained by means of chemical vapor deposition (CVD), its mineral properties are retained and its extreme properties can be also used, whereas the overall cost of the material is decreased. In terms of types of activation precursor gases necessary for growth of diamond structures, the CVD technology is implemented by several different methods: activation in radio frequency and microwave plasmas, activation in the arc discharge plasma, and thermocatalytic activation on hot wires made of refractory metals (W, Mo, Ta, or Re). All these methods have certain advantages and, correspondingly, disadvantages.

The main goal of activation is to decompose the gases to active fragments. The kinetic features of the formation and transportation of particles are different in plasma and thermocatalytic methods [15] of activation. In electric arc plasmotrons, activation occurs in the electric arc column. In the case of deposition on hot wires, activation occurs due to thermocatalytic reactions. It is known that atomic hydrogen plays a key role in obtaining diamond structures by the CVD method, because it assists in methane decomposition to methyl CH<sub>3</sub>, which serves as a source of diamond growth, activates the diamond surface, prevents graphitization of the substrate surface, and saturates broken bonds on the diamond surface. In CVD methods with thermal activation on hot wires, there is a problem to ensure a sufficiently high concentration of atomic hydrogen in the H<sub>2</sub> flow and also to prevent carbidization of activating surfaces.

The present presentation describes the results of using the CVD method with thermocatalytic activation in the case of interaction with extended heated metal surfaces. An important feature of this approach is a higher degree of dissociation of hydrogen molecules. The CVD process can be organized both under the condition of a frozen composition of the mixture after gas decomposition in the reactor and in a completely equilibrium state. The main goal of optimization of diamond-like film deposition is to identify parameters that produce the most important effects on the growth process. These are the pattern of injection of the mixture into the regions of activation and heating, the temperature of the activation surface, the gas flow intensity, the pressure in the test section, the substrate material, the methane concentration in the H<sub>2</sub>+CH<sub>4</sub> mixture, and the substrate temperature. A novel source of the activated gas mixture was used in the present study, which ensured a possibility of changing test parameters within wide limits.

Specific features of hydrogen dissociation in channels were numerically studied, and possibility of reaching a high

degree of hydrogen dissociation at the channel exit owing to multiple collisions with the surface was demonstrated. This fact gave grounds for using a special reactor whose design allows one to combine the advantages of different activation methods, thus, expanding the parameter adjustment options.

The results of diamond structures deposition will be presented in the lecture in the range of examples.

This work was supported by Russian Scientific Foundation 15-19-00061.

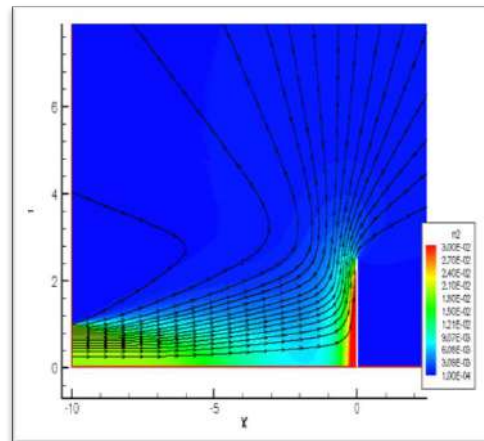


Figure 1: Conception of deposition.

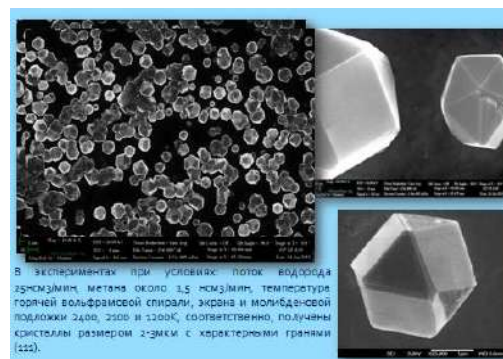


Figure 2: Example of deposition.

## Hydrodynamics and heat transfer in two-phase gas-liquid flows

Oleg N. Kashinsky<sup>1</sup>, Vyacheslav V. Randin<sup>1, 2</sup>

<sup>1</sup>Institute of Thermophysics SB RAS, Lavrentyev ave., 1, Novosibirsk, 630090, Russia

<sup>2</sup>Novosibirsk State University, Pirogova str., 2, Novosibirsk, 630090, Russia  
kashinsky@itp.nsc.ru, randin@itp.nsc.ru

The structure of gas-liquid flows is not determined only by channel Reynolds number but depends significantly on channel orientation and flow direction. The variety of flow regimes makes it necessary detailed experimental studies of the hydrodynamical flow structure and heat transfer.

Local characteristics of downward bubbly flow in a 42.3 mm i.d. vertical pipe were investigated. An electrochemical technique was used to measure flow parameters. A gas-liquid mixer was used permitting the change in size of gas bubbles for the same gas and liquid flow rates. Special attention was paid to measurements close to the pipe wall. Wall shear stress in downward bubbly flow is higher than in a single-phase flow with the same liquid velocity. The value of the wall shear stress ratio depends strongly on the mean bubble size increasing with larger bubbles. A good correlation with the prediction of Clark and Flemmer was observed. Liquid velocity measurements demonstrated the validity of the single-phase “law-of-the-wall” for two-phase velocity profiles. Turbulence suppression phenomena were observed for downward bubbly flow both for wall shear stress and liquid velocity fluctuations.

Experimental study of downward bubbly flow in a 20 mm i.d. vertical pipe was carried out. Experiments were performed at superficial liquid velocities of 0.2 to 1 m/s. Both mean and fluctuating liquid velocity and wall shear stress were obtained. A strong deformation of liquid velocity distribution takes place even at very low gas flow rate ratios. A significant decrease of liquid velocity fluctuations close to the wall compared to those in single-phase flow was observed.

A study of the local structure of the turbulent gas-liquid bubble flow in a tube with an inner diameter of 20 mm was conducted. A special feature of this research is the relatively small (up to 5% of the volume) quantities of gas added to the flow. It was shown that adding even small quantities of gas into the flow leads to a change in the liquid velocity profile in comparison with the one-phase flow and rearrangement of the turbulent structure of the flow. It is shown that it is on the turbulent structure of the flow that the gas addition exerts the maximum influence. Increasing of the gas bubble size leads to a complex increase of the turbulent pulsations of the flow. As the liquid flow rate decreases, the influence of the gas addition on the liquid velocity profile increases.

An experimental study of laminar downward bubbly flow in a 20 mm i.d. vertical pipe was performed. Water-glycerine solution with the viscosity five times higher than that of water was used as the test liquid. Experiments were made for subcritical pipe Reynolds numbers,  $Re = 500, 1000$  and  $1500$ . The experiments demonstrated the strong effect of gas phase on the flow structure resulting in the

increase of wall shear stress and flattening of the velocity profile in the central part of the pipe. Effect of the gas phase on the flow parameters was observed even at very low gas flow rate ratios. A significant deviation from the single-phase flow occurs even at gas flow rate ratios of 0.005 to 0.01. The main feature of downward flow is the concentration of the bubbles in the central part of the flow and the flattening of the liquid velocity profile in the central part of the pipe. The development of wall-induced turbulence was indicated. This behaviour correlates with the previous measurements in the turbulent flow regime (Kashinsky, Lobanov, & Randin, 2008).

Experimental investigation of a bubbly gas-liquid flow in an inclined flat channel was performed. The measurements were carried out in the range of superficial liquid velocities of 0.3-1.1 m/s and with different values of the volumetric gas flow rate ratio. Values of average shear stress and heat transfer coefficient for different orientation of the channel were found. It is shown that in a bubbly gas-liquid flow the shear stress and heat transfer depend substantially on the channel inclination angle. The wall shear stress and the heat transfer in a two-phase bubbly flow in a rectangular channel with variable orientation were experimentally investigated. It has been shown that in a gas-liquid flow the channel inclination angle relative to horizon has substantial effect on shear stress and heat transfer. The greatest values of shear stress and heat transfer correspond to intermediate channel inclination angles. Qualitative similarity of the behavior of shear stress and heat transfer with changing channel inclination angle was noted. It has been shown that the influence of the gas phase on the shear stress and heat transfer decreases with an increase of superficial liquid velocity. A good correlation with the prediction (Gorelikova, Kashinskii, Pakhomov, Randin, Terekhov, & Chinak, 2017) was observed.

The experiments performed provide a complete set of detailed experimental data on the structure of bubbly flows in different channels and flow regimes. These data are useful for the development and testing of analytical and numerical models for gas-liquid flow predictions.

### References

- Gorelikova, A. E., Kashinskii, O. N., Pakhomov, M. A., Randin, V. V., Terekhov, V. I., & Chinak, A. V. (2017). Turbulent flow structure and heat transfer in an inclined bubbly flow. Experimental and numerical investigation. *Fluid Dynamics*, 52, 115-127.
- Kashinsky, O. N., Lobanov, P. D., & Randin, V. V. (2008). The influence of a small gas addition to the structure of gas-liquid downward flow in a tube. *Journal of Engineering Thermophysics*, 17, 120-125.

## Investigation of influence of high frequency external perturbation on flow in a T-shape microchannel by $\mu$ LIF and $\mu$ PIV methods

Aleksandra Kravtsova and Yury Meshalkin

Kutateladze Institute of Thermophysics, Siberian Branch of the Russian Academy of Sciences  
Lavrentyev Ave. 1, Novosibirsk, 630090, Russia  
E-mail: Kravtsova.Alya@gmail.com

External perturbation effect on flow inside various systems operating with liquids, such as microreactors and micromixers is known to be one of the major sources of changing mixing efficiency of streams. The growth of mixing efficiency due to transition from steady to unsteady flow regimes leads to increase in device performance. However, a few authors investigated an influence of external perturbation on structures and hydrodynamic characteristics of flow inside microchannels. The influence of a piezoelectric transducer on the flow in different Y-shape microchannels with sidewall sharp-edge structures was studied by N. Nama et al. (2014). These authors investigated multiple device parameters such a tip angle, oscillation amplitude and channel dimensions. Their results indicate that, due to the inherent nonlinearity of acoustic streaming propagating from transducer, the channel dimensions could significantly impact the flow patterns and device performance. Claudio P. Fonte et al. (2016) using Computational Fluid Dynamics (CFD) model have studied the effect of the pulsation of the opposed jets flow rate modulation on the vortex formation and mixing efficiency in a T-jet microchannel. Out-of-phase pulsations were performed with various amplitudes and frequencies. Authors have shown the imposed oscillation values close to the natural frequency generated by developed vortices can make the move of vortex more orderly. An energy of the flow oscillations is increased for resonance frequency. However, an experimental confirmation has still not been obtained. Thus, in this paper, the influence of high frequency external pulsation on flow in a T-shape microchannel is considered. We report a visual analysis of flow regimes and spatial distributions of velocity and turbulent fluctuation inside microchannels here.

Experimental setup consists of a syringe pump KD Scientific company with two outputs, an excitation system of the flow based on the piezoelectric actuator integrated in loop, microscope Carl Zeiss Axio Observer.Z1 and a T-shaped microchannel made of optically transparent material SU-8 with dimensions of  $120 \times 120 \times 240 \mu\text{m}$  (height, width of the input channel and the width of the output channel) mounted on the microscope stage. To obtain the characteristics of the flow the method of laser induced fluorescence (micro-LIF) and particle image velocimetry (micro-PIV) was used. The resulting images are operated via a computer using "ActualFlow" software.

The experiments were carried out for Reynolds numbers  $Re = 120, 186, 300, 400$ . The high frequency external perturbation of jets flow rate was generated in the same phase on both inputs of the microchannel with the frequency  $f$  range from 0 Hz to 1000 Hz with step 100 Hz. The sampling frequency of measurements was increased

four times (step of the measurements was 25 Hz) in region of greatest change of the mixing efficiency (400 Hz to 800 Hz).

A significant change of the structures of the flow and the mixing efficiency was obtained in case of stationary flow regimes. For the vortex stationary regime ( $Re = 120$ ), increase of frequency of jets flow rate to  $f = 650$  Hz leads to a growth of interface width by 10%, up to 1000 Hz by 50% of the width of the output channel. The vortex structures move from the center of the channel to its sidewalls. The vortex length decreases. For a stationary asymmetric flow regime ( $Re = 186$ ), the S-shape structure inside microchannel has constriction by inlet of mixing channel for the increase of imposed oscillation up to  $f = 800$  Hz. When the frequency of external perturbation is  $f = 500$  Hz and 800 Hz the flow regime become unsteady and happen the sharply increase of mixing efficiency. Also, the decrease of longitudinal component of mean flow velocity and the increase of turbulent pulsation velocity within vortexes was shown.

In the case of an unsteady asymmetric regime ( $Re = 300$ ), the vortex structures have the same  $Re = 186$  constriction by inlet of mixing channel and its length become smaller. However, the mixing efficiency change insignificantly. For a quasiperiodic unsteady regime ( $Re = 400$ ), in case of the increase of frequency of external perturbation the mean and turbulent pulsations flow velocity growth over a length of the mixing channel was shown. The mixing efficiency is slowly growing. Thus, the change in the flow structure has been studied, and it is also shown that the efficiency of mixing in the T-microchannel can be substantially changed by imposing a certain frequency on the flow of external perturbations.

### References

- Nama N., Huang P.-H., Huang T.J., Costanzo F. Investigation of acoustic streaming patterns around oscillating sharp edges, *Lab on a Chip*, Vol. 14, pp. 2824-2836 (2014).
- Erko E., Fonte C.P., Dias M.M., Lopes J.C.B., Santos R.J. Numerical study of active mixing over a dynamic flow field in a T-jets mixer—Induction of resonance, *Chemical Engineering Research and Design*, Vol. 106, pp. 74-91 (2016).

## Experimental investigation of heat transfer in the region of contact line of the liquid rivulet

Tatyana Ponomarenko<sup>1,2</sup> and Vyacheslav Cheverda<sup>2,3</sup>

<sup>1</sup>Novosibirsk State Technical University, 630073, K. Marx Ave., 20, Novosibirsk, Russia,  
<sup>2</sup>Kutateladze Institute of Thermophysics SB RAS, 630090, Lavrentyev Str., 1, Novosibirsk, Russia,  
<sup>3</sup>National Research Novosibirsk State University, 630090, ул. Pirogov Str., 2, Novosibirsk, Russia

Email: [t.evans2010@yandex.kz](mailto:t.evans2010@yandex.kz)

The using of high evaporative thin liquid film, drop and rivulet modes of flow, which provides the most effective heat transfer processes, has prospects for rejection of high heat flux.

During the rivulet flow of liquid the high heat transfer coefficient is observed in the small field of three-phase contact line [1]. Physical processes in the region of the contact line "solid – liquid – gas" determine the nature of the flow in time of heating, and is investigated not completely in the present day. Though creating a perspective cooling system is one of the major objectives for today.

The earlier studies of the rivulet flow are focused on the liquid flow over the inclined plane and the impact of surface tension and viscosity on the emergency of varieties of rivulet flows; the maps of modes of rivulet flows are plotted [2,3].

The study aims to determine heat flux density in the region of contact line of the liquid rivulets of FC-72 and water flowing down over the heated surface.

The experimental investigation are performed using the vertical foil with the length ( $l$ ) of 80 mm, the width ( $w$ ) 35 mm and the thickness ( $h$ ) 25 microns, which is connected to the DC power source through the brass electrode holders (Fig. 1). Foil heating is carried out by the power source and heat power on the foil is regulated in the range from 0.09 to 1.47W. The liquid is supplied with the flow rate from 0.1-5 mL/min to the foil through the pipe with a special nozzle using the syringe pump. The foil is coated with black graphite paint with the emissivity factor of about one.

The photcamera and the infrared (IR) scanner are used to make the observations. The width of the FC-72 liquid rivulet is measured with using the photographs and it was from 1.4 to 25 mm. Also the width of the water liquid rivulet was measured.

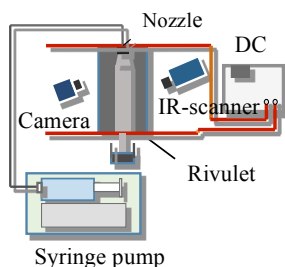


Figure 1: The scheme of the experimental setup.

An infrared scanner is used to measure distributions of temperature on the bottom side of foil surface from the rivulet flowing down over the heated foil. The thermograms from the side opposite to the rivulet of FC-72 and water received with the help IR-scanner are compared with among themselves.

The calculation of heat flux from the foil is performed with using the images of the IR-scanner without consideration of the heat fluxes in foil and by means of solving the Cauchy problem, which described heat conductivity inside the foil. It is shown that the heat flux density across the water rivulet flow considerably changed: maximum heat flux density is observed near the contact line in [4] (Fig. 2). Such results are expected in this experiment with the rivulet of FC-72.

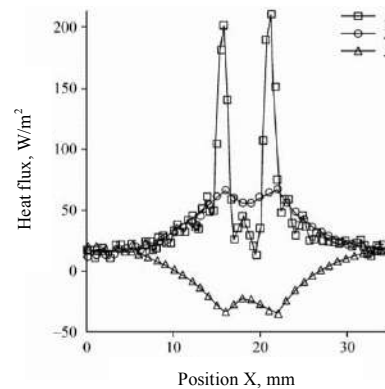


Figure 2: Heat flux density in the middle cross-section; solution to Cauchy problem (1), calculation without consideration of heat flux redistribution in foil (2) and on the bottom side of foil (3) [4].

The heat production in the field of the contact line can be explained by the heat influx from the foil periphery to the rivulet due to high evaporation rate in the region of the contact line and high value of heat conducting coefficient of the foil.

### References

- Stephan P., Brandt C. Advanced capillary structures for high performance heat pipes // *Heat Transfer Engng.* Vol. **25**, No. 3. P. 78–85 (2004)
- Schmuki P., Laso M. On the stability of rivulet flow // *J. Fluid Mechanics.* Vol. **215**. P. 125–143 (1990)
- Hirt C.W. Simulating the wetting and drying of shallow flows // *Los Alamos: Flow Sci.*, 7 p (1998)
- Cheverda V.V., Marchuk I.V., Karchevsky A.L., Orlik E.V., Kabov O.A. Experimental investigation of heat transfer in a rivulet on the inclined foil // *Thermophysics and Aerodynamics*, Vol. **23**, No. 3 (2016)

## Experimental-calculated study of the forced convection magnetic nanofluids

Dmitriy Guzei<sup>1,2</sup>, Andrey Minakov<sup>1,2</sup>, Maxim Pryazhnikov<sup>1,2</sup> and Konstantin Meshkov<sup>1</sup>

<sup>1</sup>Siberian Federal University, 79 Svobodny pr., Krasnoyarsk, 660041, Russia

<sup>2</sup>Institute of Thermophysics SB RAS, 1 Acad. Lavrentiev pr., Novosibirsk, 630090, Russia  
gudimas@yandex.ru

Experimental study and numerical simulation of the magnetic nanofluids forced convection in a constant magnetic field was carried out. Iron oxide nanoparticles Fe<sub>3</sub>O<sub>4</sub> were used for preparation of the nanofluid. The average particle size is 100 nm. Distilled water was used as the base fluid.

Three permanent neodymium magnets 50×30×10 mm of size were used for creation of the magnetic field. The maximum value of the magnetic induction near the magnet is up to 0.3 T. In experiments the magnets were located in the immediate vicinity of the heated section at the same distance from each other. Nanoparticles volume concentration varied in the range from 0.25 to 0.75 %. The Reynolds number ranged from 2000 to 6000. Experiments on the study of nanofluid forced convection were carried out at the experimental stand of the Department of Thermophysics of the Siberian Federal University.

The average and local values of the heat transfer coefficient on the channel walls were measured as a result of experiments. The dependencies of the heat transfer coefficient on the Reynolds number and volume density under magnetic field and without it are obtained.

Experiments proved that local and average heat transfer coefficient of the magnetic nanofluids is increasing under magnetic field influence. The influence of the magnetic field makes it possible to intensify the local heat transfer coefficient near the magnet to 1.8 times against the magnetic nanofluid without the magnetic field. The average heat transfer coefficient of the nanofluid under magnetic field at the constant Reynolds number is 1.55 times higher than the average heat transfer coefficient of the base fluid. It is established that the local and average heat transfer coefficients of magnetic nanofluids are increasing if the Fe<sub>3</sub>O<sub>4</sub> particles concentration is rising as well. The effect of the heat transfer coefficient increasing takes place by fixed value of the Reynolds number and the coolant flow too. However, the turbulent heat exchange of nonmagnetic nanofluids or nanofluids without the magnetic field influence, with a fixed value of the coolant flow rate, the heat transfer coefficient can decrease with increasing particle concentration, investigated earlier by Minakov (2016).

The dependencies of the pressure drop on the Reynolds number and volume density under magnetic field and without it are obtained. Experiments proved that the magnetic field has a significant effect on the pressure drop in the working section. It is established that the effect of the magnetic field weakens by the decrease of the nanoparticles concentration. In the experiments it was shown that three magnets located along the tube increase the pressure drop in the channel with the nanofluid with the volume density of Fe<sub>3</sub>O<sub>4</sub> particles 0.75 % to 2.96 times compared to the pressure drop without the field.

In the experiments it was shown that three magnets located along the tube increase the pressure drop in the channel with the nanofluid with the volume density of Fe<sub>3</sub>O<sub>4</sub> particles 0.25 % to 21 % compared to the pressure drop without the field. The pressure drop magnitude of the nanofluid with the particles volume density of 0.25 % without magnetic field at the constant Reynolds number is 30 % higher than the pressure drop of the base fluid.

Numerical simulation of transport of nanoparticles in the constant magnetic field was conducted. To simulate the transport of nanoparticles in the magnetic field we used a novel Euler-Lagrange combined two-component approach. As part of the Lagrange approach for the base fluid the equations of continuity, momentum and energy were being solved and the movement of the particles was modeled on the basis of Newton's second law by solving an ODE. Euler two-component model describes nanoparticles in a liquid as a binary mixture, where nanoparticles are one of its components. Statement of the problem completely repeats the experimental study. The verification and adaptation of mathematical models of magnetic nanoparticles transport under the influence of external electromagnetic fields based on the experimental data was performed. The numerical results were compared with experimental data. Numerical simulation of nanoparticles transport in the constant magnetic field are carried out for various Reynolds numbers. Good qualitative and quantitative agreement is obtained between numerical simulation and experiment.

The reported study was funded by Russian Foundation for Basic Research, Government of Krasnoyarsk Territory, Krasnoyarsk Region Science and Technology Support Fund to the research project №16-48-243061.

### References

Minakov A.V., Guzei D.V., Pryazhnikov M.I., Zhigarev V.A., Rudyak V.Ya., Study of turbulent heat transfer of the nanofluids in a cylindrical channel, *Int. Journal Heat and Mass Transfer*, Vol. 102, pp. 745-755 (2016)

## Experimental study of the effect of the substrate roughness on the thermocapillary rupture of a horizontal liquid film

Dmitry Kochkin and Dmitry Zaitsev

Kutateladze Institute of Thermophysics SB RAS  
 1, Ac. Lavrentieva ave., Novosibirsk, 630090, Russia  
[kochkin1995@mail.ru](mailto:kochkin1995@mail.ru)

The modern industry often uses apparatus with liquid film flow. Thin liquid film is a promising approach for developing of cooling of devices with high local heat release, in particular, for high-end electronic chips. The industry creates a need for cooling of high local heat fluxes from electronics components like computer chips, and power electronics (transistors and thyristors).

Film-based cooling systems are highly efficient since they provide a high rate of heat transfer at moderate flow rates of the coolant. The reduction in the film thickness enhances heat transfer; however, thin films are prone to film breaking and this increases drastically the temperature of the cooled element and may cause failure.

The papers (Zaitsev et al. 2015, Zaitsev et al. 2007) demonstrated that the critical heat flux for the case of horizontal liquid films is by several times higher than the critical level for gravity-driven liquid films. This explains the relevance of presented study.

The key object of this study is the effect of substrate roughness on the threshold heat flux which causes film breakdown and also the dynamics of this breakdown.

Experiments were conducted with locally heated substrates with different size of roughness made of stainless steel with the diameter of 50.8 mm and thickness of 1 mm. The substrate was mounted on a textolite basement with an embedded copper rod with the diameter of 12.7 mm (Fig. 1), and thermal paste was applied for improvement of heat contact between the substrate and basement. The copper rod has a thermal contact with a ceramic heater. The heat flux was calculated from the temperature drop over the copper rod for the situation of steady process. It was also controlled by the known electric power consumed by the heater. The working liquid was distilled super-pure Milli-Q water with the initial temperature of 25°C. The proper volume of water was fed to the substrate via a syringe pump. The substrate perimeter has cooling arrangement. The water temperature in the cooling circuit was sustained at 5°C.

The using of removable substrate in this setup ensures study of breaking a horizontal liquid layer on substrates with different roughness. The different scale of roughness was achieved by surface polishing.

The liquid film thickness was measured with a probe moved with a motor-driven microdisplacement tool. As the film surface is touched by the probe tip, this creates a liquid meniscus recorded with a CCD camera. The total film thickness was controlled by the known volume of liquid fed using the syringe pump. Experiments were carried out for films with the initial thickness 350 μm (+/- 5 μm).

The tests demonstrated that the substrate roughness has almost no impact on the critical heat flux needed for breakdown of a locally heated liquid film. However,

roughness is significant for breakdown dynamics (Fig. 2) and the final size of the dry spot. For a higher roughness of substrate, the contact line velocity and the final size of dry spot become lower.

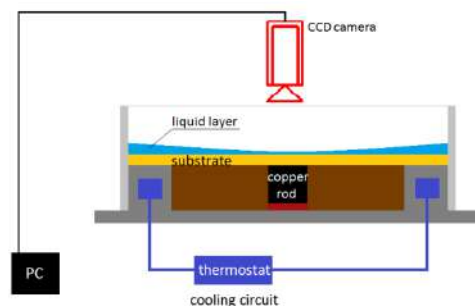


**Figure 1:** Scheme of the experimental setup.

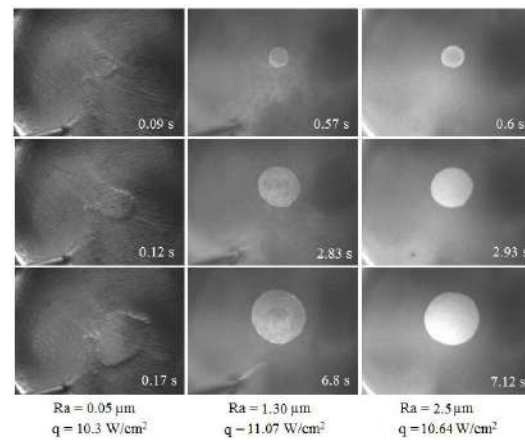


**Figure 2:** The dynamics for dry spot expansion on the stainless steel substrate with the thickness of 1 mm at different scales of roughness (for initial film thickness 350 μm). The time is measured since the breakdown startup.

The research was supported by the Russian Science Foundation, Project No. 1419-01755.

### References

- D. V. Zaitsev, D. P. Kirichenko, and O. A. Kabov, *Technical Physics Letters*, Vol. 41, p. 551 (2015)
- D.V. Zaitsev, O.A. Kabov, *Microgravity science and technology*, Vol. 19, No. 3/4, p. 174 (2007)

## Rivulets deflection on surface of heated liquid films

Vitaliy V. Semionov, Evgeniy N. Shatskiy, and Evgeniy A. Chinnov

Kutateladze Institute of Thermophysics SB RAS  
 Lavrentiev Avenue, 1, Novosibirsk, 630090, Russia  
 vitalik.semionov@gmail.com

The film flows are widely used in various industrial devices and apparatus. Understanding the processes occurring in the heated liquid films is very important for the design and implementation of such apparatus.

When the liquid films flow along the heated surfaces, not only hydrodynamic instabilities develop, leading to transformation of a two-dimensional flow into the three-dimensional waves, but also the thermocapillary structures of various types arise (Chinnov et al. 2003). The aim of this work is to study the influence of interaction of three-dimensional waves with thermocapillary structures on characteristics of the film flow at Reynolds numbers from 15 to 50 and initial liquid temperature from 15 to 70 °C.

The experimental setup was a closed circulation circuit, including working section, pipelines, thermostat with a pump, stop valve, and rotameter. The working section consisted of a textolite plate with film former, thermostabilizer and heater located on this plate. A flat heat exchanger 100 mm long and 150 mm wide, where heated water was pumped through the channels, was used as a heater. Distilled water with addition of a dye was used as the working liquid. The more detailed description of setup is presented in (Chinnov 2017).

Due to wave interaction with thermocapillary structures, the rivulets are formed on the liquid film surface and move across the flow, Fig.1. The maximal amplitude of deflection was defined as the distance between the extreme right and extreme left positions of the rivulet crest during thermal imaging (600 frames).

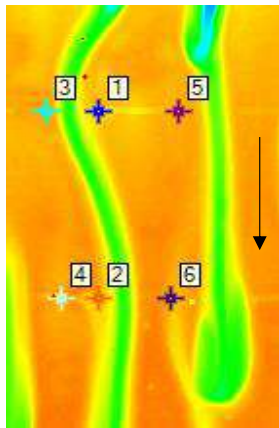


**Figure 1:** Thermogram of the film surface with a rivulet. Points 1, 3, 5 are at the distance of 50 mm from the upper edge of the heater. 2, 4, 6 – 75 mm.  $Re=33$ ,  $T_0=23$  °C,  $q=4.25$  W/cm<sup>2</sup>. The arrow indicates flow direction.

In more detail, the procedure for calculating the amplitude is illustrated in Fig.1. Points 1 and 2 correspond to the rivulet crest position in the figure averaged by 600 frames. Points 3 and 4 correspond to the extreme left positions of the rivulet crest at distances of 50 and 75 mm from the upper edge of the heater, respectively, points 5 and 6 correspond to the extreme right positions. The maximal amplitude of rivulet deflection for 50 mm is equal to the distance between points 5 and 3 and, respectively, for 75 mm – between points 6 and 4.

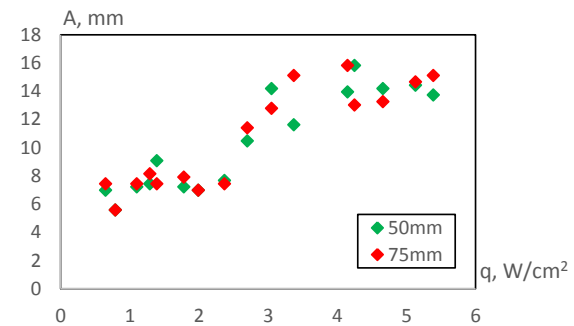


**Figure 2:** Dependence of maximal amplitude of rivulet deflection in the center of the heater on the heat flux.  $Re=33$ ,  $T_0=23$  °C.

Dependence of the maximal amplitude of deflection on the heat flux is shown in Fig. 2. According to the diagrams, at low heat fluxes, the deflection amplitude is small. When the threshold value of the heat flux (corresponding to formation of thermocapillary structures of type A [2]) is achieved, maximal amplitude of deflection increases substantially, reaching the values equal to the distance between the rivulets, and this leads to rivulet interaction and merging.

Rivulet motion in the horizontal direction prevents formation of dry spots on the heater surface and leads to repeated irrigation of dry zones and, ultimately, an increase of the critical heat flux corresponding to the liquid film breakdown.

This work was supported by the grant of the Russian Science Foundation (Agreement No. 15-19-30038).

### References

- E.A. Chinnov, O.A. Kabov, Jet formation in gravitational flow of a heated wavy liquid film, *J.Appl.Mech. Tech. Phys.*, Vol. 44, No. 5, pp. 708–715 (2003).
- E.A. Chinnov, Formation of the unsteady thermocapillary structures in the residual layer of three-dimensional waves, *Int. J. Heat Mass Transfer*, Vol. 108, pp. 2053–2059 (2017).

## Thermography of flame during diesel fuel combustion with steam gasification

Igor Anufriev<sup>1</sup>, Sergey Arsenyev<sup>1,2</sup>, Mikhail Agafontsev<sup>3</sup>, Evgeny Kopyev<sup>1</sup>,  
Egor Loboda<sup>3</sup>, Evgeniy Shadrin<sup>1</sup>, Oleg Sharypov<sup>1</sup>

<sup>1</sup> Kutateladze Institute of Thermophysics SB RAS  
1 Ac. Lavrentieva ave., Novosibirsk, 630090 Russia

<sup>2</sup> Novosibirsk State University  
1 Pirogova str., Novosibirsk, 630090 Russia

<sup>3</sup> Tomsk State University  
36 Lenin Ave., Tomsk, 630090 Russia  
E-mail: kopyev.evgeniy@mail.ru

At the Institute of Thermophysics SB RAS a new method for fuel combustion with the use of steam when the gasification of carbon-containing particles during the incomplete combustion of liquid hydrocarbons occurs is proposed (Vigriyanov et al. 2003). It was shown that the supply of overheated steam to the liquid hydrocarbon combustion zone sharply intensifies combustion (Alekseenko et al. 2016). This combustion method provides stable ignition, high completeness of fuel combustion and a low level of toxic components in combustion products. This method is promising for utilization of low-grade liquid hydrocarbon fuels and combustible industrial wastes with producing of heat energy. To study the influence of steam parameters on the main characteristics of the liquid hydrocarbons combustion process (the composition of combustion products and the specific heat release capacity) it is necessary to obtain the data for different combustion regimes.

In analogy with the procedure applied in previous work (Alekseenko et al. 2014), the thermal imaging measurements were conducted for the outer flame during combustion of liquid hydrocarbon fuel (diesel fuel) in a perspective burner device with the controlled forced supply of overheated steam into the combustion zone. A thermal imaging camera (FLIR, JADE J530SB) was used in the experiments. This device has a high temporal resolution: the frame rate up to 177 Hz with a maximum resolution of 320x240 pixels and up to 18 kHz with a resolution of 320x4 pixels. The minimum time of frame exposure is 6  $\mu$ s. The operating range of the thermal imager is in the middle infrared range of 2.5-5.0 microns. Temperature measurement range is determined by the thermal imager calibration and equals 583-1773 K (for the selected narrowband F0616 dispersion optical filter with a bandwidth of 2.5-2.7 microns).

The studies were conducted at the firing stand equipped with a new burner device (power up to 10 kW), an electric steam generator (average consumed power 1.5 kW), a plunger metering pump (flow rate up to 1.6 l/h), an automatic steam generator control system, a fuel supply system, electronic scales to control the flow of water and fuel and necessary control and measuring equipment (see in figure 1). In the experiments the direct-flow evaporative type burner device was used. Measurements were carried out in a wide range of regime parameters (fuel consumption at a constant 0.8 kg/h): steam flow rate 0.25-1.0 kg/h, superheated steam temperature 150-550 °C at a pressure of 8 atm.).

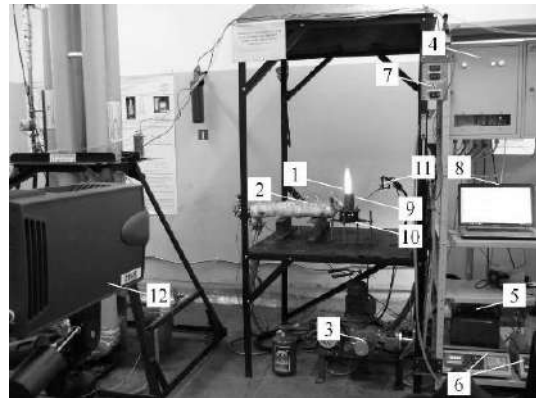


**Figure 1:** Firing stand for the study of liquid hydrocarbon combustion with steam gasification: 1 – burner device, 2 – electric steam generator, 3 – plunger metering pump, 4 – automatic steam generator control system, 5 – fuel supply system, 6 – electronic balance, 7 – indicators of control and measurement instruments, 8 – computer, 9 – gas-generation chamber of the furnace unit, 10 – combustion chamber of the furnace unit, 11 – fuel pipe, 12 – thermal imager (FLIR JADE J530SB with optical filter 2.5-2.7  $\mu$ m)

The dependence of effective emissivity coefficient of the flame from the steam flow rate has been obtained. The steam parameters have been found to influence the temperature in the outer flame of the burner device.

### References

Vigriyanov M.S., Salomatov V.V., Alekseenko S.V., Russian Federation Patent No. 2219435 (2003)

Alekseenko S.V., Anufriev I.S., Vigriyanov M.S., Kopyev E.P., Sharypov O.V., Characteristics of diesel fuel combustion in a burner with injection of a superheated steam jet, *Combustion, Explosion, and Shock Waves* Vol. 52 pp. 286-293 (2016)

Anufriev I.S., Kopyev E.P., Loboda E.L., Study of flame characteristics during liquid hydrocarbons combustion with steam gasification, *Proceedings of SPIE - The International Society for Optical Engineering*, 9292, 929226 (2014)

## Interdroplet distance in a structured monolayer of levitating liquid microdroplets

A.I. Shatekova and D.V. Zaitsev

Kutateladze Institute of Thermophysics SB RAS, Novosibirsk, Russia;  
 Novosibirsk State University, Novosibirsk, Russia  
 Email: [zaitsev@itp.nsc.ru](mailto:zaitsev@itp.nsc.ru)

Structured monolayer of levitating liquid microdroplets can form over the surface of liquid heated from below. The monolayer consists of several hundreds or thousands of drops packed into one layer, forming a hexagonal structure. The mechanism of levitation is the Stokes force acting onto a drop from the flow originated at the interface, as discussed in Fedorets et al. (2011) and Zaitsev et al. (2017).

Here we study the distance between adjacent droplets in the monolayer, depending on the parameters of experiment. The scheme of the experimental setup is shown in Fig. 1. The test section is a stainless-steel plate with a flush-mounted copper block of working area  $1 \times 1 \text{ cm}^2$ . The block is electrically heated from below. The block surface temperature ( $T_w$ ) is measured by thermocouples. The heating power  $P$  is determined by the electric power released at the heater and is kept at 25 W. Degassed distilled water with the initial temperature of  $25^\circ\text{C}$  is used as the working liquid. The test section is kept in the box with transparent walls; the temperature of ambient air is  $23 \pm 2^\circ\text{C}$ . Before conducting experiment, a given volume of liquid is put onto the working surface by means of a syringe. The initial thickness of the liquid layer  $h_0$  varies from 0.3 to 0.9 mm. To register monolayer formation, a high-speed camera coupled with Schlieren optical system is used.

Increase of the substrate temperature induces formation of the monolayer of microdroplets levitating over the liquid surface. Usually, the monolayer is of an elliptical shape, Fig. 2, having size growing in time from 1 to 5 mm. Figures 3 and 4 represent variation of the interdroplet distance with time and with the distance from the center of monolayer, respectively. From Figs. 3-4 it is seen, that the distance between the drops increases with time (temperature) and with the distance from the center of monolayer; but decreases with the increase of the liquid layer thickness.

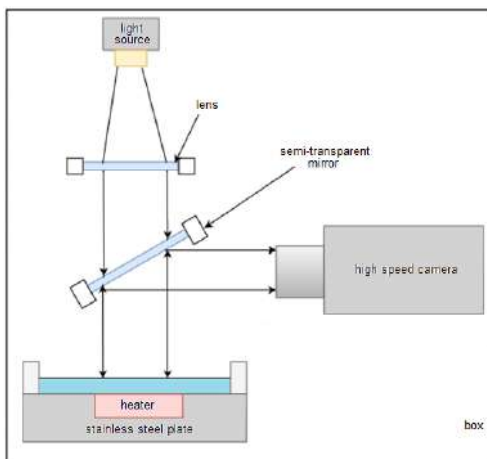


Figure 1: The scheme of the experimental setup.

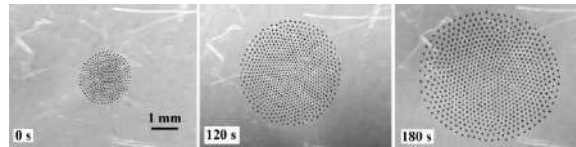


Figure 2: Growth of monolayer with time (top view).

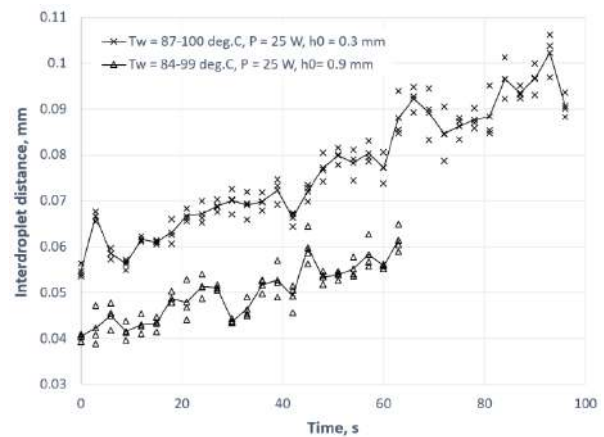


Figure 3: Interdroplet distance vs. time (temperature).

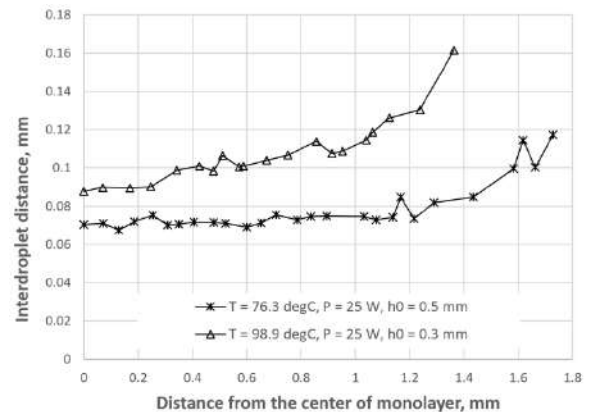


Figure 4: Interdroplet distance vs. distance from the center of monolayer.

### References

- Fedorets A. A., Marchuk I. V. and Kabov O. A., *Technical Physics Letters*, Vol. 37, pp. 116-118 (2011)  
 Zaitsev D.V., Kirichenko D.P., Ajaev V.S., Kabov O.A., *Physical Review Letters* (to appear in 2017)

## Experimental investigation of pikoliter liquid drops evaporation on a heated solid surface

D.P. Kirichenko<sup>1,2</sup>, D.V. Zaitsev<sup>1,2</sup>, and O.A. Kabov<sup>1,2</sup>

<sup>1</sup>Kutateladze Institute of Thermophysics, Siberian Branch, Russian Academy of Sciences  
 1, Lavrentiev ave., Novosibirsk, 630090, Russia

<sup>2</sup>Novosibirsk State University, 1, Pirogova str., Novosibirsk, 630090, Russia  
 E-mail: [Dmitriy\\_Kirichenko@mail.ru](mailto:Dmitriy_Kirichenko@mail.ru)

The process of liquid drop evaporation, which takes place in a variety of technological systems in power engineering, medicine, agriculture, chemical and other industries, has been actively investigated during the last decade. Most experimental and theoretical studies deal with evaporation of isothermal water drops. There are many publications studying evaporation of drops with volume from 1 to 1000  $\mu\text{l}$ , but studies of nonisothermal evaporation of liquid drops of pikoliter volume are almost absent in the literature.

The purpose of this work is to experimentally investigate the evaporation of sessile pikoliter liquid drops on a heated substrate. The substrate is a copper block heated from below with the root mean square surface roughness of 0.50  $\mu\text{m}$ . The advancing static contact angle measured at different points over the surface of the copper heater was  $74 \pm 9^\circ$ , whereas the receding contact angle was close to zero (less than  $10^\circ$ ). Substrate surface temperature was measured by thermocouples embedded in the copper block and was kept at 134  $^\circ\text{C}$ . Liquid droplets (with initial size of 20-50  $\mu\text{m}$ ) were applied on the working surface by a spray device placed a few centimeters above the heating area. Room-temperature degassed ultra-pure water (Merck Millipore) was used as the working liquid. Optical recording was made at 5400 frames per second using a high-speed CCD camera equipped with a microscope objective of high resolving power (spatial resolution of up to 0.8  $\mu\text{m}$  per pixel).

During evaporation diameter of the drop is almost constant (the contact line is pinned) and start to decrease only at the final moment of drop life, Figs. 1, 2. Figure 3 shows the volume of an evaporating droplet versus time for different initial droplet sizes. Figure 4 shows the specific evaporation rate of a droplet (droplet weight loss per unit time per unit droplet surface area) versus time. It is seen that the specific evaporation rate is not constant over time: it gradually grows with time up to a maximum, but at the final stage, when the height of the drop becomes on the order of 1  $\mu\text{m}$ , it decreases rapidly.

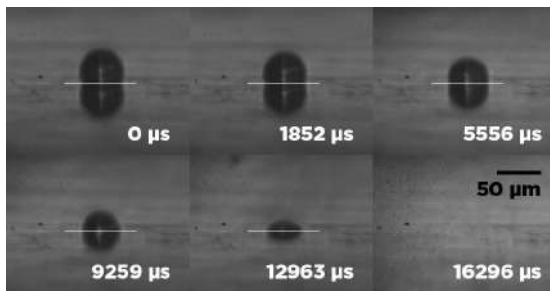


Figure 1: Change of drop shape (side view) during sessile

droplet evaporation on a heated substrate,  $T_w=134^\circ\text{C}$ .

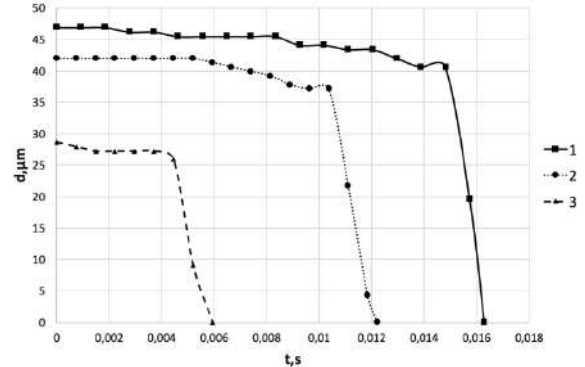


Figure 2: Diameter of wetted area versus time for three different sessile drops,  $T_w=134^\circ\text{C}$ .

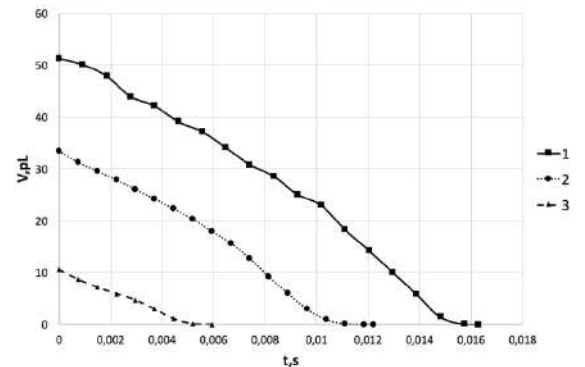


Figure 3: Volume versus time for three different sessile drops,  $T_w=134^\circ\text{C}$ .

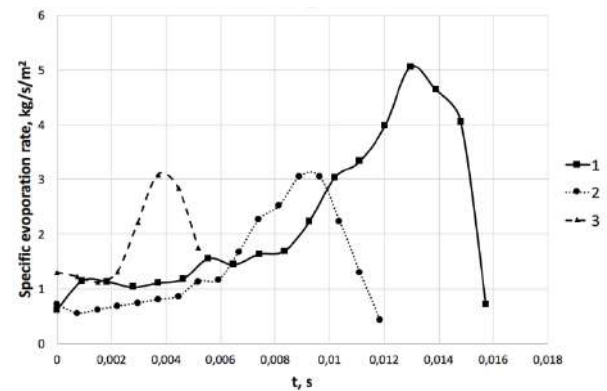


Figure 4: Specific evaporation rate versus time for three different sessile drops,  $T_w=134^\circ\text{C}$ .

## Suspended nanofluid droplet evaporation

Aleksandr Borisov<sup>1</sup>, Aleksandr Nazarov<sup>1,2</sup>, Elena Bochkareva<sup>1</sup>, Nikolay. Miskiv<sup>1</sup>

<sup>1</sup>Kutateladze Institute of Thermophysics SB RAS, Novosibirsk, Russia

<sup>2</sup>Novosibirsk State University, Russia

It is necessary to understand the heat-and-mass exchange mechanisms during complex and nanofluid evaporation for flows with phase changes studying. There are a significant number of articles concerning complex droplet evaporation problem (Talbot et al., 2016), with no universal complex mixture droplet evaporation theory having been made which could compose all principles experimentally obtained. The aim of experiments was to obtain the data regarding solid admixture concentration impact on liquid carrier evaporation rate from the droplet surface in heated air flow.

The experimental equipment consisted of vertical cylindrical air channel with a stainless steel confuser ( $l = 0,5$  m,  $d = 50$  mm, outlet nozzle  $d = 10$  mm) and heat exchanger covered with thermal insulation; electrical heater was distributed along the entire air channel with thyristor power regulator (Bochkareva et al., 2016). The air flow was regulated with reducing gearbox at the start of the heating system within the range from 0.1 m/sec up to 5 m/sec. After heating section (within the range from 20 °C) up to 150 °C) the air flow passed through initial linearization assisted by honeycomb, secondary linearization was performed with a grid in front of the confuser. A nanofluid droplet ( $2 \pm 0.3$  mm diameter) was suspended on a carrier at a distance of 20 mm from the centre of confuser outlet. Droplet liquid was prepared using distilled water (DW) and SiO<sub>2</sub> nanoparticles ~ 200 nm size with mass fraction  $m_{\text{SiO}_2}/m_{\text{H}_2\text{O}}$  2%, 3%, 4%, 5%, 6%, and 7%. Droplet diameter was captured during the evaporation process using Digi Scope II v3 microscope and was determined after the experiment processing digital images. Droplet surface temperature acquired with Thermo Tracer thermoimager was determined on the thermal images with special software.

Experiments had been conducted to estimate air flow rate and temperature influence on suspended nanofluid droplet evaporation rate. Nanofluid droplet evaporation dynamics was detected for DW+ SiO<sub>2</sub> in comparison with DW droplet evaporation (initial conditions: air flow rate  $u_0 = 0.2$  m/sec and 1.5 m/sec, ambient and air flow temperature  $t_{0g} = t_{0s} = 23.4$  °C, air flow relative humidity  $\phi = 1\%$ , ambient pressure  $P = 1$  atm). Water evaporation time for the nanofluid mixtures was significantly different from that for the DW ( $t_{\text{H}_2\text{O}}$ ) prior to checkpoint ( $d/d_0 = 0.6$ ). It can be noted, that air flow rate increase (1.5 m/sec) significantly reduced nanofluid droplet evaporation time, with evaporation rate difference

keeping ( $\Delta t \sim 40\%$ ). When air flow temperature was raised up to  $t_{0g} = 100$  °C ( $u_0 = 1$  m/sec), overrun flow temperature raise accelerated droplet evaporation, whereas nanoparticle concentration in liquid increased. Experimental data demonstrate, that nanofluid droplet evaporation dynamics has an interval of accelerated evaporation when overrun flow rate increases.

The dependance of relative nanofluid evaporation time to base liquid evaporation time ratio (60% of initial diameter) from nanofluid concentrations is shown in Figure 1, where  $f = (t_n - t_{\text{H}_2\text{O}}) / t_{\text{H}_2\text{O}}$ ,  $t_n$  – nanofluid evaporation time. It can be noted, that air flow with temperature lower than 100 °C affected evaporation intensity when admixture concentration ranged from 3% up to 7%. With the air flow temperature being ~ 100 °C, the opposite effects can be detected, so that droplet evaporation rate increase was observed within all admixture concentrations range (Figure 1). The results obtained show, that there is an opportunity to use the effect of more effective mixture dividing (up to 30%) in manufacturing processes of distillation.

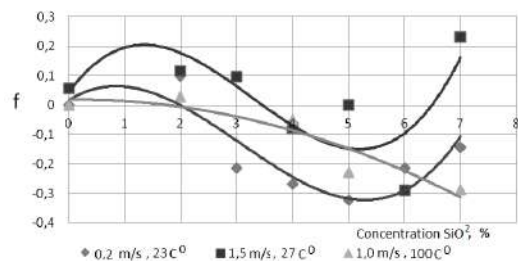


Figure 1: Nanofluid droplet evaporation dynamics.

The work was conducted with the financial support of Russian Federation President Grant **SS-8780.2016.8**.

### References

Talbot P., Sobac B., Rednikov A., Colinet P., Haut B. Int. J Heat Mass Transfer, Vol. 97, p. 803, (2016)

E. M. Bochkareva, V. V. Terekhov, A. D. Nazarov, A. A. Borisov, V International Seminar with elements of scientific school for young scientists (ISHM-V) “Topical issues of heat and mass transfer at phase transitions and multiphase flows in modern chemical technology and energy equipment”, 1, (2016)

## The effect of dry spots on heat transfer in a locally heated liquid film moving under the action of gas flow in a channel

Egor Tkachenko\*, Dmitry Zaitsev, Oleg Kabov

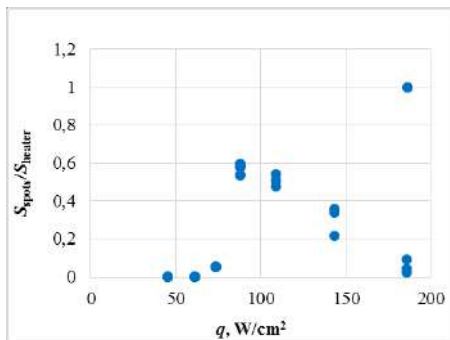
Kutateladze Institute of Thermophysics, Siberian Branch, Russian Academy of Sciences  
Lavrentiev ave. 1, Novosibirsk, 630090, Russia  
Novosibirsk State University, Pirogova st. 2, Novosibirsk, 630090, Russia  
E-mail: [egor.tkachenko@mail.ru](mailto:egor.tkachenko@mail.ru)

The authors propose a new method of effective cooling, in which heat removal is due to intensive evaporation of a thin liquid film, moving in a flat micro-, minichannel under the action of gas flow. Our paper deals with systematic experimental studies of the flow and destruction of a water film, shear-driven in the channel, under heating from a local heat source with size of  $1 \times 1 \text{ cm}^2$ . The influence of dry spots, liquid (distilled water with initial temperature of  $25^\circ\text{C}$ ) and gas (Air with temperature of  $24\text{-}27^\circ\text{C}$  and relative humidity of  $15\text{-}30\%$ ) flow rates, on the heat transfer and crisis have been investigated.

With the help of high-speed imaging, it was found that the maximum intensity of heat removal from the heater is achieved in the mode, when the film flow continuity is broken. The heater is covered with small (of about 100 microns) dry spots with the lifetime of about  $1/100 - 1/1000 \text{ s}$ . The number of spots can reach several hundred.

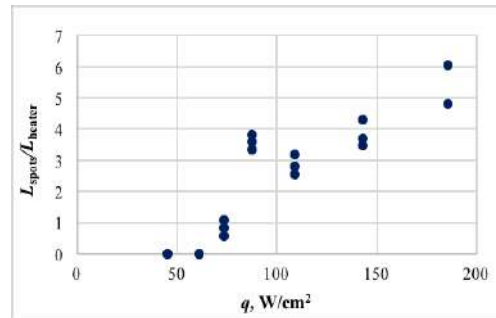
Also, there is another interesting phenomenon connected with total area of dry spots on the heater surface. During the experiment the total area of dry spots increases with increasing heat flow and heater temperature, but when the heater reaches a certain temperature ( $\approx 100^\circ\text{C}$ ), the total area begins to decrease.

Figure 1 shows the photo processing results (photo were processed using ImageJ application). The dependence of the total area of dry spots, divided by the area of heater, on the heat flux is shown on the graph for  $Re_1 = 45$  and  $U_{Sg} = 7.4 \text{ m/s}$ .



**Figure 1.** The dependence of the total area of dry spots, divided by the area of heater, on the heat flux at  $Re_1 = 45$  and  $U_{Sg} = 7.4 \text{ m/s}$ .

The dependence of the total contact line, divided by length of the heater, on the heat flux at  $Re_1 = 45$  and  $U_{Sg} = 7.4 \text{ m/s}$  is shown in Fig. 2. In contrast to the area of dry spots, the length of contact line increases with increasing heat flux and reaches a maximum in the pre-crisis regime. Intensive evaporation in the region of the contact line can explain the achievement of such high heat fluxes using a thin liquid film.



**Figure 2.** The dependence of the total contact line, divided by the length of the heater, on the heat flux at  $Re_1 = 45$  and  $U_{Sg} = 7.4 \text{ m/s}$ .

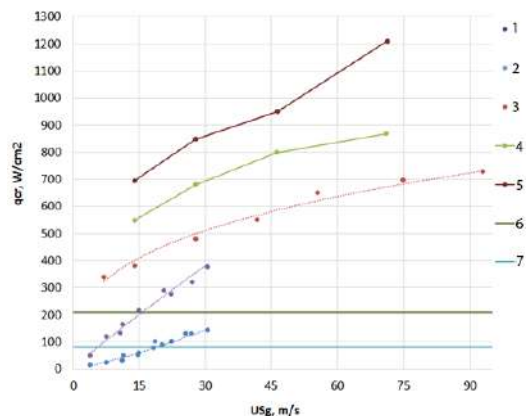


**Figure 3.** The dependence of the critical heat flux on the superficial gas velocity,  $U_{Sg}$ , the Reynolds number of the liquid,  $Re_1$ , and the channel height,  $H$ . 1 –  $Re_1 = 8.5$ ,  $H = 1.2 \text{ mm}$ ; 2 –  $Re_1 = 30$ ,  $H = 1.2 \text{ mm}$ ; 3 –  $Re_1 = 62$ ,  $H = 1 \text{ mm}$ ; 4 –  $Re_1 = 113$ ,  $H = 1 \text{ mm}$ ; 5 –  $Re_1 = 193$ ,  $H = 1 \text{ mm}$ ; 6 – boiling water in the channel  $Re_1 = 62$ ; 7 – falling water films  $Re_1 = 62$ .

Figure 3 shows the dependence of critical heat flux on  $U_{Sg}$  and  $Re$  number of liquid. Experiments have resulted in the values of heat flux and heat transfer coefficient, which are a record for a thin liquid film ( $1200 \text{ W/cm}^2$  and  $300\,000 \text{ W/m}^2\text{K}$ , respectively). The values of the critical heat flux are by an order higher than the corresponding values in falling water films and by free times higher than in the forced flow of boiling water in the channel for the same fluid flow rates ( $Re_1 = 62$ ,  $G = 105 \text{ ml/min}$ ). This confirms the prospects of using thin liquid films, moving under the influence of the gas flow friction in modern systems of equipment cooling with high local heat release.

## The drop evaporation on a heated substrate with single wall nanotubes coating

Andrey Semenov<sup>1,2</sup>, Dmitry Zaitsev<sup>1,2</sup>

<sup>1</sup>Institute of Thermophysics, SB RAS  
Lavrentyev ave. 1, Novosibirsk, 630090 Russia

<sup>2</sup>Novosibirsk State University, Pirogova str. 2, Novosibirsk, 630090 Russia  
[semenov.itp@gmail.com](mailto:semenov.itp@gmail.com)

The phenomenon of liquid drop evaporation, which takes place in a variety of technological systems in power engineering, agriculture, medicine, cooling systems, chemical and other industries, has been actively investigated during the last few years, e.g. Sobac and Brutin (2011), Gatapova et al. (2014).

The main objective of the present work is to study the effect of nanotubes coating on the dynamics and evaporation of the sessile liquid drop in quasistationary conditions when it is heated from the substrate. It is assumed that due to the multifarious influence (variable wettability, thermal conductivity of wall layer, surface structure at the micro- and nanoscale) the use of the nanotubes coating allows to substantially intensify the evaporation process.

In this paper, we study evaporation of a liquid drop into the open atmosphere. The initial drop volume was less than 1  $\mu\text{l}$ . A drop of liquid is placed on a surface with controlled wettability. Further, a drop is heated until quasi-stationary heat transfer between the solid substrate and liquid drop. Distilled deionized nano-filtered water of Milli-Q Company is used as the working fluid. The use of water with relatively high boiling point as a working fluid allows us to study in detail the influence of temperature difference between the solid surface and surrounding atmosphere on the rate of evaporation and heat transfer. The temperature difference between the solid and external atmosphere varies from 30 to 50  $^{\circ}\text{C}$ .

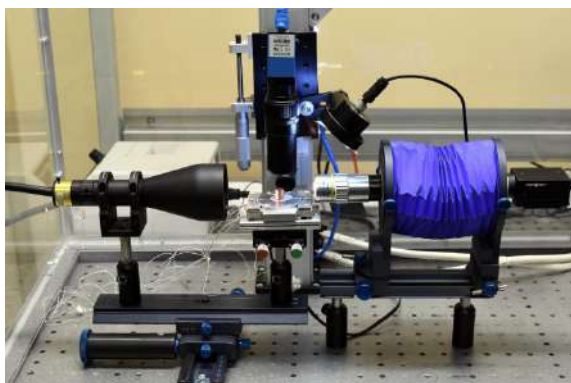


**Figure 1:** The photo of the experimental setup.

Two optical methods were used in the work. The first one is the shadow method consisting of a halogen light source Edmunds Optics MI-150 connected by a fiber optic lightguide with a lens system that produces a beam of parallel light of 50 mm in diameter on one side of the

working area and a PointGray fast speed camera with a 10X Mitutoyo microscope lens, which was connected through Novoflex focusing bellows on the other side. The spatial resolution of such a system was 0.5  $\mu\text{m}$  / pixel, and the shooting frequency was up to 500 frames per second. Obtained shadow photos of the liquid drop profile were processed by the KRUSS Drop Shape Analysis software.

The second optical technique used 5 megapixels Imaging Source camera with 20X Mitutoyo microscope lens, which was placed above the liquid drop and allows visualization of evaporation process from the top and control the drop symmetry. If the drop lost its symmetry, the experiment was repeated.

Two substrates made of copper were investigated. One of them had no coating and was polished to the root mean square roughness of 0.50  $\mu\text{m}$ . Another one was coated with single wall nanotubes. The morphology of the working surface was analyzed using a scanning electron microscope (HITACHI S3400N) and atomic force microscope (Solver Pro NT MDT). Photograph from the scanning electron microscope of the coated substrate is shown in Fig.2.

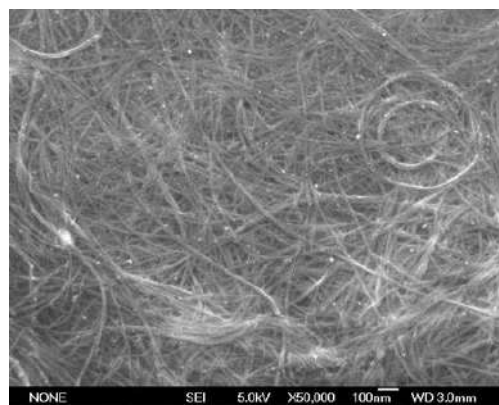


**Figure 2:** SEM image of coating of single wall carbon nanotubes with orientation along copper substrate.

### References

- B. Sobac and D. Brutin, *Langmuir*, Vol. 27, pp. 14999-15007 (2011).
- E.Ya. Gatapova, A.A. Semenov, D.V. Zaitsev, and O.A. Kabov, *Colloids and Surfaces A: Physicochemical and Engng Aspects*, Vol. 441, pp. 776–785 (2014).

## Evaporation of a thin liquid film sheared by gas in a mini/microchannel in the presence of an area of intensive heating moving toward the gas flow

Tatiana Korbanova, Oleg Kabov

Kutateladze Institute of Thermophysics SB RAS  
Ac. Lavrentiev ave. 1, 630090, Novosibirsk, Russia  
Novosibirsk State University  
Pirogova str. 2, 630090, Novosibirsk, Russia  
[Korbanova.tanya@rambler.ru](mailto:Korbanova.tanya@rambler.ru)

Variation or controlling of thermocapillary forces to induce a controlled temperature field at the gas–liquid interface is mainly based on modification of substrate or on modification of thermal boundary conditions at the wall see for example (Webb and Kim, 2005) and (Kabova et al. 2014). Theoretical analysis of a moving local heater effect on the deformations and pattern of a thin liquid layer flow down the horizontal substrate was performed in (Kuibin, Sharypov, 2008). The heat source was assumed to be placed inside the substrate and moves along it without dragging the liquid. In other words, the authors consider the case of planar “thermal wave” propagating along a liquid layer. The moving local heat source in the work simulates some exothermal process like, for example, combustion wave spreading along the substrate. If such wave propagates in the substrate, then thermal boundary layer appears in the liquid. It reaches the free surface and causes a non-homogeneous temperature distribution at the surface of liquid. Thermocapillary force induces the flow of the liquid in the direction of thermal wave propagation and leads to free surface deformation. In the same way it is possible to control and change the temperature field at a free surface by affecting directly the gas-liquid interface. In (Basu and Gianchandani, 2007) the hot spots at the gas-liquid interface are generated by placing the tip of a thin resistance-heated cantilever at a distance of less than 400  $\mu\text{m}$  from the film surface. These hot spots cause toroidal-shaped flow patterns when the liquid flow is directed outwards from the hotter areas near the free interface and directed inwards to the deeper layers of the film. In (Wedershoven et al. 2014) the film deformations and rupture caused by infrared laser irradiation of the gas-liquid interface were studied. It was shown that the rupture time increases with increasing beam radius at a constant laser power that can be explained by the reduction of the temperature gradients responsible for Marangoni forces. It should be noted that controlling thermocapillary force by heating the gas-liquid interface is very promising. Optimization of this technique requires detailed studies. It is important to study the heat transfer between the heat source and the film surface and to take into account the spectral radiative properties of the medium and the description of the hydrodynamics. Choosing of the appropriate method for controlling the Marangoni force depends on a specific application. For example, using the condition that the temperature difference at the gas-liquid interface is caused by the radiation exposure does not fit for applications associated with cooling.

The tendency to decrease the characteristic scales of the devices in various fields of technology set down the main tendencies in hydrodynamics and heat mass transfer research in mini- and microchannel. For example, many

works devoted to the combustion of gaseous fuels in narrow channels of various configurations have been appeared recently. This is due to the great practical interest in miniature power sources, heat sources and mechanical energy sources (Maruta, 2011), caused by the high energy density of hydrocarbon fuels in comparison with traditional energy accumulators. Reducing the height of the flat channels leads to decreasing of heat exchange in microsystems.

The main goals of this work are to understand the evaporation mechanism and to study the heat and mass transfer process taking place at joint motion of thin viscous liquid film and gas in a horizontal rectangular mini/microchannel in presence of an area of intensive heating (thermal wave) moving in the gas phase directly related to the vapor concentration in the gas. And as a first step authors attempts to model the processes that take place in this case in the liquid and the gas. Model is two-dimensional with non-deformable gas-liquid interface. It takes into account the processes of evaporation and condensation, heat release in gas, interphase heat exchange, thermocapillary effect, as well as convective and conductive heat transfer in gas and liquid. Numerically it is shown that velocity of the area of intensive heating moving toward the gas flow depends on the basic parameters of the problem, in addition velocities in the liquid and gas phases were calculated taking into account the thermocapillary effect.

The study was financially supported by the Russian Science Foundation (Project 14-19-01755).

### References

- R.L. Webb, N.H. Kim, Taylor & Francis, Boca Raton, Florida (2005)
- Yu.O. Kabova, V.V. Kuznetsov, O.A. Kabov, T. Gambaryan-Roisman, P. Stephan, *Int J Heat Mass Transf*, Vol.68, pp. 527-541 (2014)
- A.S. Basu, Y.B. Gianchandani, *Appl Phys Lett*, 90, pp. 34102 (2007)
- H.M.J.M. Wedershoven, C.W.J. Berendsen, J.C.H. Zeegers, A.A. Darhuber, *Appl Phys Lett*, 104, pp. 54101 (2014)
- Sharypov O.V., Kuibin P.A., *Microgravity Sci. Technol* pp. 321-3324 (2008)
- Maruta K., *Proc. of the Combustion Institute*, Vol. 33, No. 1, pp. 125–150 (2011)

## Time domain analysis of pressure drop characteristics in parallel multiple microchannels

Run-gang Yan<sup>1,2</sup>, Liang-ming Pan<sup>2,\*</sup>, Hui He<sup>2</sup>, Hao-jie Huang<sup>2</sup>

1. Factory 7304, China Aerospace Science and Technology Corporation, Chengdu, 610100, China

2. School of Power Engineering of Chongqing University, Chongqing, 400044, China

\*Corresponding Author: Liang-ming Pan, +86-23-65102280, cneng@cqu.edu.cn

With the increasing application of Microelectro Mechanical Systems (MEMS) in aerospace field etc., flow boiling heat transfer in microchannels is widely applied due to their compact sizes and effective heat transfer by utilizing the latent heat of phase change. As a result of the large ratio of surface area to volume in micro/minichannels, a higher heat transfer performance is expected comparing to the conventional ones (Wu and Sundén. 2014).

The state-of-art study on the pressure drop characteristics of parallel multiple microchannels are mainly focused on the total pressure drop characteristics (Qu and Mudawar. 2004, Wang et al. 2008, Law and Lee. 2015). With the exception of that Mosyak et al. (2012) measured the upstream and downstream pressure inside few individual channels of the parallel multiple microchannels which were connected through needle tip. However, they did not clarify the relationship between total pressure drop and single-channels pressure drop characteristics. To address this issue, both the total pressure drop between plenums of the test section and that of individual single-channel are studied based on the experimental loop system shown as Fig. 1. In addition, there are 6 parallel rectangular channels in the test section. The distance between the upstream and downstream two pressure measuring tips inside the second and fourth single-channels are 42 mm. In this paper, the pressure drop between two measuring tips inside the second and fourth single-channels are expressed as  $\Delta p_2$  and  $\Delta p_4$ , respectively. And the pressure drop between plenums of the test section is  $\Delta p_{exp}$ . The flow boiling experiment is carried out by using high purity deionized water as the working fluid. And the main results in terms of frequency domain analysis of pressure drop are shown in Fig. 3-4.

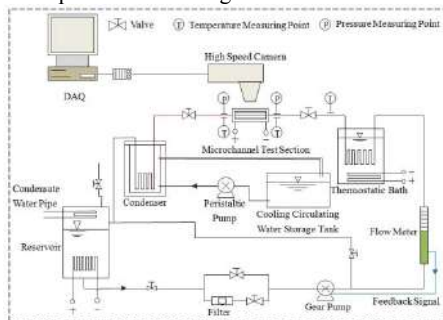


Figure 1: Schematic diagram of the flow loop.

The results show that the amplitude of pressure drop oscillation in single phase is small. For the condition of boiling two-phase flow, when keeping the mass flux and inlet temperature constant, with the increase of heat flux, the pressure drop oscillation increases, and its oscillation period change longer. The trend of the pressure drop oscillation in two individual single-channels is consistent with that of total

pressure drop, but there is a great difference in the amplitude of the pressure drop oscillation. Especially, the difference is that the pressure drop inside the single channel has a negative value.

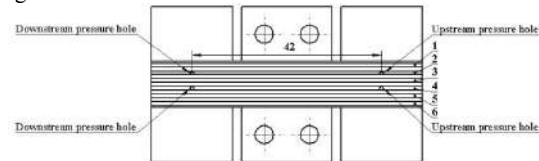


Figure 2: Schematic diagram of the local pressure measuring point and distribution

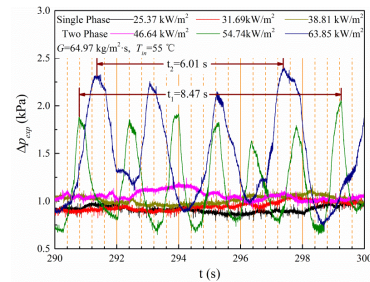


Figure 3: Time domain characteristics of the total pressure drop under different heat flux.

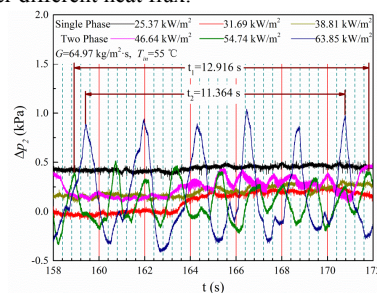


Figure 4: Time domain characteristics of the pressure drop inside the second channel under different heat flux.

### References

- Z. Wu, B. Sundén, *Renew Sust Energ Rev*, 40:11-27 (2014).  
 W. Qu, I. Mudawar, *Int. J. Heat Mass Transfer*, Vol. 47, pp. 2045-2059 (2004).  
 G. Wang, P. Cheng, A.E. Bergles, *Int. J. Heat Mass Transfer*, Vol. 51, pp. 2267-2281 (2008).  
 M. Law, P.-S. Lee, *Int. J. Heat Mass Transfer*, Vol. 85, pp. 797-810 (2015).  
 A. Mosyak, L. Rodes, G. Hetsroni, Vol. 47, pp. 150-159 (2012).

## Heat Transfer Enhancement at Boiling and Evaporation on Microstructured Surfaces

Aleksandr N. Pavlenko

Kutateladze Institute of Thermophysics, Siberian Branch, Russian Academy of Sciences  
 1, Lavrentyev Avenue, 630090, Novosibirsk, Russia  
 pavl@itp.nsc.ru

To intensify the heat and mass transfer processes in industrial heat exchangers the developed surfaces of different geometry are widely used. The report presents the results of experimental studies of heat transfer and crisis phenomena at pool boiling and boiling and evaporation in the film flows on the microstructured surfaces.

In the first part of the report, there is the comparative analysis of heat transfer efficiency and critical heat flux in the film flows of refrigerants R21 and Freon mixture R21/R114 over a vertical cylinder with the horizontal microtexture, diamond-shaped cut, and mesh covers of various forms. The schematic diagram of the experimental setup designed to study heat transfer, crisis phenomena and wave characteristics at the film flow of binary Freon mixtures of various compositions were described in detail in Pecherkin et al. (2015). The mechanisms of heat transfer enhancement at evaporation and boiling at different irrigation degrees are discussed for the used methods of modification of the heat transfer surface. These results are compared with data of other authors obtained for different microstructured surfaces and well-known calculation dependences for the coefficients of heat transfer and critical heat flux. The estimate of the value of heat transfer enhancement on different structured surfaces is shown in Fig. 1. On the surface with rhomb-shaped texture at heat fluxes of  $\sim 1 \cdot 10^4 \text{ W/m}^2$ , a slight increase in the heat transfer coefficient in comparison with a smooth surface is observed at evaporation. Installation of the mesh coating led to heat transfer enhancement by 40–60% as compared with the smooth surface at heat fluxes of up to  $1.5 \cdot 10^4 \text{ W/m}^2$ , and by 15–20% at higher heat fluxes. At high Reynolds numbers, Fig. 1(b), the relative heat transfer coefficients on all surfaces increase with an increase in the heat flux and reach the twofold value for the heat fluxes of about  $1 \cdot 10^4 \text{ W/m}^2$ , then, they reduce to one. At evaporation, the maximal heat transfer enhancement is achieved on the surface with horizontal ribbing. In the area of nucleate boiling, the maximal heat transfer enhancement is observed on the surface with the mesh coating. At intense nucleate boiling,  $q \geq 2.5 \cdot 10^4 \text{ W/m}^2$ , the heat transfer coefficients on the structured surfaces almost coincide with the heat transfer coefficients on the smooth surface. It is found out that a change in the character of the wave film flow on the surface with horizontal ribbing at film Reynolds numbers  $Re > 400$  leads to heat transfer intensification at evaporation compared with the smooth and rhombshaped surfaces. At evaporation and development of nucleate boiling, the heat transfer coefficient on the surface with mesh coating is higher than for the smooth and textured surfaces. It is shown that the influence of the initial composition of a mixture with close saturation temperatures on the heat transfer coefficient at evaporation and boiling is insignificant.

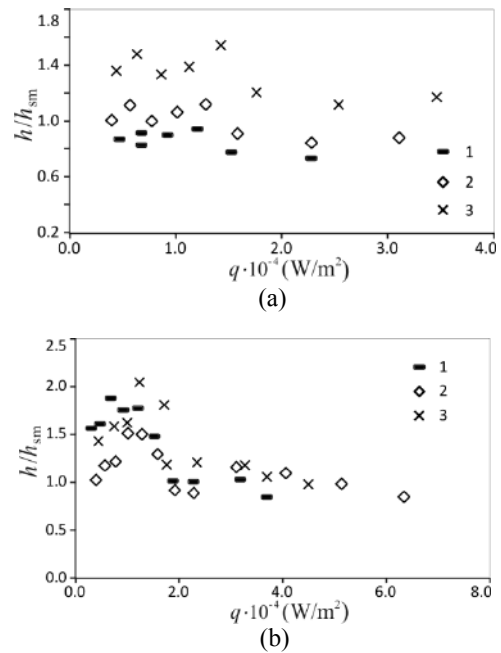


**Figure 1:** Relative heat transfer coefficient on the structured surfaces: (a) –  $Re = 200$ ; (b) –  $Re = 640$ ; 1 – ribbed surface; 2 – rhomb-shaped texture; 3 – mesh coating.

It is shown that the development of crisis phenomena on the studied structured surfaces is determined by the regularities of dry spot formation, characteristic to evaporation of the wave liquid film. Experimental studies of heat transfer and crisis phenomena in the regime of evaporation and nucleate boiling on the surface with mesh coating having the characteristic cell size, comparable in scale with the length of large waves were also conducted. The mesh covering was made of mesh with wire diameter of 0.7 mm and a cell size of  $6 \times 6$  mm. Generalization of the obtained experimental data showed that heat transfer coefficients in the evaporation regime with the large gauze are close in magnitude to the values of heat transfer for mesh coatings with a smaller cell size and also approximately twice more the values obtained for the smooth surface.

The second part of the report highlights the new experimental data on heat transfer and critical heat flux obtained at pool boiling with different laws of heat generation in different liquids on new structured capillary-porous coatings produced by directed plasma spraying. The experimental study of heat transfer at pool boiling of a liquid was carried out in an experimental setup described in detail elsewhere Surtaev, Pavlenko et al. (2017).

The working liquids were nitrogen, water and Freon R21 (CHCl<sub>2</sub>F) occurring on the saturation line. The experiments were performed with heaters representing an uncoated tube and five tubes with coatings. Six base cylindrical stainless steel tubes had a length of 47 mm, an external diameter of 3 mm, and a wall thickness of 0.5 mm. These coatings were formed on the initial steel surface by the method of plasma deposition. The coating appears as crests and narrow troughs almost uniformly distributed over the substrate surface and predominantly oriented in one direction. It should be noted that, in the transverse direction, the crests have less steep faces on one side and steeper faces (with negative slope) on the other side. In the given case, the widths of crests, as well as troughs between them, vary within 400–2600 μm and the minimum pore size on the structured surface is several microns. The main characteristics of coatings used in the experiments are shown in the Table, where λ<sub>m</sub> is the average distance between adjacent ridges (the modulation wavelength of the structure). Figure 2 shows the boiling curves of nitrogen and water on heaters without and with plasma-deposited coatings. As can be seen from Fig. 2, the heat transfer coefficient for the heaters with coatings in the regime of nucleate boiling several times greater compared to uncoated tube.

Table

№	Particle size, μm	δ, μm	Porosity, %	λ <sub>m</sub> , μm
1	20-32	400	71	530
2	71-100	500	74	1360
3	20-32	540	80	820
4	71-100	800	72	1800
5	71-100	1390	68	2600

In this series of experiments, we have also studied the influence of plasma coatings on heat transfer and critical heat fluxes at pool boiling of nitrogen, water and Freon R21 at different laws of heat release. It is shown that the critical heat flux at liquid nitrogen boiling under the stationary heat release on the surface with a capillary-porous coating is 20% higher than the critical heat flux values obtained for a smooth sample. It is also shown that at the step-wise heat release on the coated heater, fast transition to the regime of film boiling without nucleate boiling stage is not observed until heat loads, exceeding the critical heat flux at stationary heat release by the factor of 2.5. According to processing of experimental data obtained by high-speed video recording, the presence of a capillary-porous coating at fast heat loading leads to a drastic decrease in the temperature differences, when liquid boils up. Under these conditions, liquid boiling has a smoother character without development of the self-sustained evaporation fronts, propagating fast over the heated surface. Development of nucleate boiling on the capillary-porous surfaces at lower temperature differences prevents heat accumulation in the boundary layer near the heat-releasing surface and, respectively, excludes the possibility of developing the self-sustained evaporation fronts. This leads to the fact that the critical heat flux at the stepped heat release on the heaters with capillary-porous coatings is almost identical to the critical heat flux under the stationary heat release.

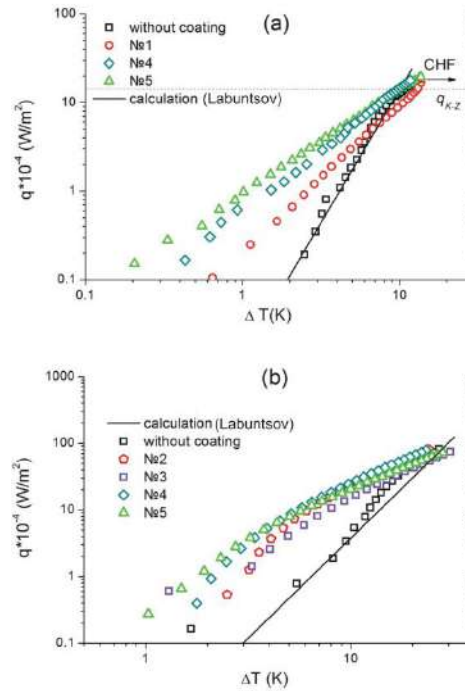


Figure 2: (a) – nitrogen, (b) – water.

In the third part of the report, we compare the experimental and simulation results on rewetting of significantly superheated bodies by the falling liquid films, when the cooled surface is covered by the new structured capillary-porous or low heat-conducting coatings.

The study was performed at Kutateladze Institute of Thermophysics SB RAS and was financially supported by the grant of the Russian Science Foundation (project No. 14-49-00010: blocks of investigations on heat transfer enhancement at evaporation and boiling in the film flows with the use of the mesh covers and the other microstructures of various forms on the heat-transfer surface) and the Russian Foundation for Basic Research Grant (project No. 15-08-03221: blocks of investigations on heat transfer enhancement at boiling with the use of new structured capillary-porous or low heat-conducting coatings of various form).

### References

- Pecherkin N.I., Pavlenko A.N. and Volodin O.A., Heat transfer and critical heat flux at evaporation and boiling in refrigerant mixture films falling down the tube with structured surfaces, Intern. J. Heat Mass Transfer, Vol. 90 pp. 149-158 (2015)
- Surtaev A.S., Pavlenko A.N., Kuznetsov D.V., Kalita V.I., Komlev D.I., Ivannikov A.Yu., Radyuk A.A., 2017, Heat transfer and crisis phenomena at pool boiling of liquid nitrogen on the surfaces with capillary-porous coatings, Intern. J. Heat Mass Transfer, Vol. 108 pp. 146-155. (2017) Science Direct

## Boiling Heat Transfer Enhancement by Using Micro-pin-finned Surfaces and Its Application in a Novel Loop Heat Pipe.

Jin-Jia Wei

Xi'an Jiaotong University  
 Xianning West Road 28, Xi'an 710049, CHINA

With rapidly increasing power dissipation rate for electronic components, sophisticated electronic cooling technology is required to maintain relatively constant component temperature below the junction temperature, approximately 85 °C for most mainframe memory and logic chips. Boiling heat transfer with latent heat release in the phase change process is considered as the promising scheme for cooling high heat flux electronics. Experiments were conducted to study the boiling heat transfer performance of FC-72 over square silicon chips with the dimensions of  $10 \times 10 \times 0.5$  mm<sup>3</sup>. For enhancing boiling heat transfer, four kinds of micro-pin-fins with the dimensions of  $30 \times 60$  (PF30-60),  $30 \times 120$  (PF30-120),  $50 \times 60$  (PF50-60),  $50 \times 120$  (PF50-120)  $\mu\text{m}^2$  (thickness,  $t \times$  height,  $h$ ) were fabricated on the chip surfaces by the dry etching technique. A smooth surface was also tested for comparison. All micro-pin-finned surfaces have considerable heat transfer enhancement compared to a smooth surface, and the boiling heat transfer can be enhanced by increasing total surface area. It was found that the capillary force generated at the vapor-liquid interface of a large bubble sitting on the micro-pin-fins could drive a plenty of bulk liquid to access the heater surface easily for evaporation through the regular interconnected structures formed by the micro-pin-fins, leading to high boiling heat transfer performance. The micro-pin-finned surfaces were also tested in microgravity provided by Drop Tower Beijing, and the boiling heat transfer enhancement is still obvious. The boiling heat transfer performance is closely related to bubble dynamics, and a new bubble detachment model was proposed to predict the bubble departure diameter on the micro-pin-finned surfaces in microgravity by considering the additional drag force of small bubble groups underneath the large departing bubble, and the prediction agrees well with the experimental data. The micro-pin-finned structures were further applied in a novel loop heat pipe (NLHP), in which the evaporator was only used for generating capillary force to drive the fluid circulation in the loop, and an additional boiling pool was used for main heat dissipation. It was found that the micro-pin-finned structures can enhance the boiling heat transfer in the boiling pool, and thus reduce the thermal resistance of the entire loop heat pipe greatly.

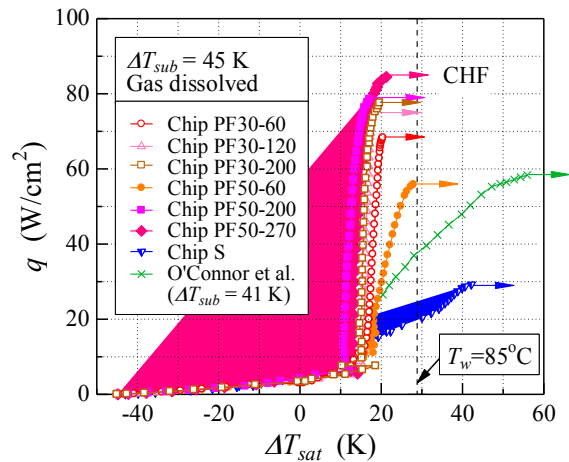


Figure 1: Boiling curves of micro-pin-finned chips

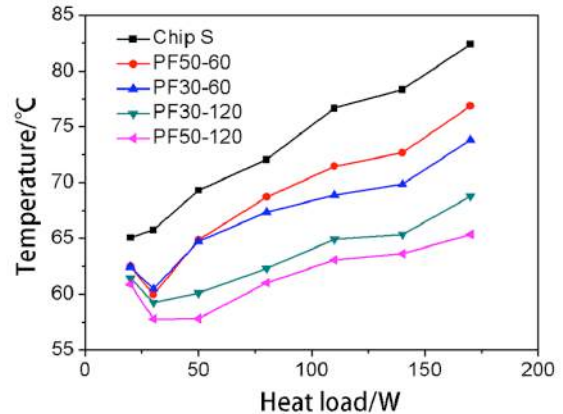


Figure 2: Temperature decreases by using micro-pin-fins in NLHP

## Huge Wave and Droplet Entrainment in Churn Flow

Bofeng Bai<sup>1</sup> and Ke Wang<sup>1,2</sup>

1. Xi'an Jiaotong University, State Key Laboratory of Multiphase Flow in Power Engineering  
 No.28, Xianning West Road, Xi'an, 710049, China
2. China University of Petroleum, Beijing Key Laboratory of Process Fluid Filtration and Separation  
 No.18, Fuxue Road, Changping, Beijing, 102249, China  
 E-mail: bfbai@mail.xjtu.edu.cn

Churn flow is one of the least understood gas-liquid flow regimes due to its complexity and there have been enduring efforts to define it. Generally, churn flow is considered as an intermediate flow regime between slug flow and annular flow and occurs after the break-down of slug flow as its velocity increases. As it frequently occurs in power plants, chemical engineering, petroleum and other industrial applications, churn flow has a significant influence on the safety and management control.

Churn flow appears a highly-disturbed flow of gas and liquid and is generally characterized by the presence of a very thick and unstable liquid film with the liquid frequently oscillating up and down. It normally occurs in vertical or nearly vertical pipes and features interfacial waves, termed as huge waves, over a liquid film which are larger in amplitude, wavelength and velocity than disturbance waves. Profound knowledge on the huge wave properties, mechanisms of entrainment and entrained droplets in churn flow is crucial to provide better understanding of churn flow. Due to the complexity of churn flow, these issues are not well documented in the existing literature.

The existence of huge waves (or called flooding-type wave or large wave) formed on the thin falling liquid film is one of the most important features of churn flow. The liquid is transported upwards in the huge wave which intakes the liquid from a foregoing falling film and sheds the liquid to a falling film behind them. The wave reversal is found to be the most significant feature during the whole process and believed to be the reason for the liquid oscillation under the churn flow condition: the huge wave periodically forms and grows in both the radial and axial direction, as shown in Figure 1.

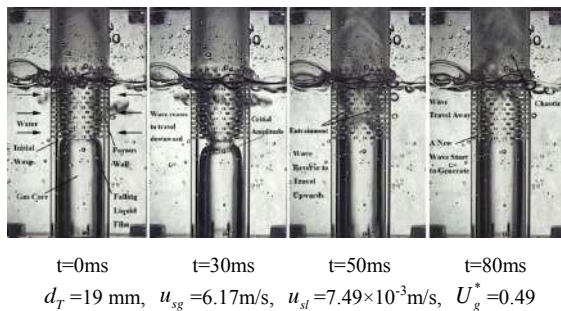
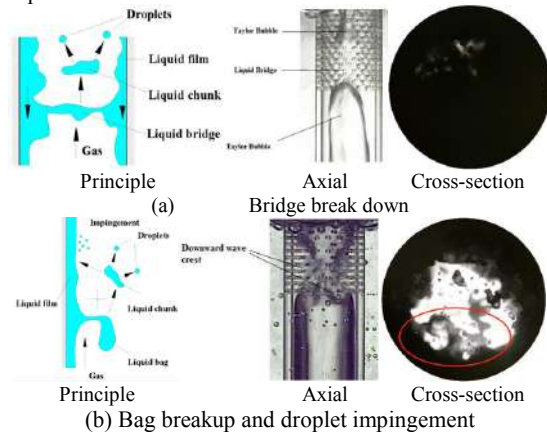


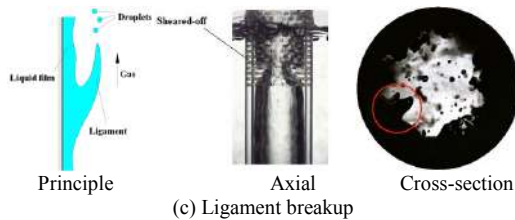
**Figure 1:** Evolution of huge waves in churn flow

The oscillation of the falling liquid film shows different features during the transition from churn flow to annular flow, i.e. it experiences four states: from the unstable to the stable and then to the unstable again, and finally disappearing when entering annular flow. The effect of the

interfacial shear stress varies during the transition from churn flow to annular flow, and combines with other factors (gravity, inertia and viscosity, and surface tension included), resulting in the oscillation of the falling liquid film under two conditions: at the lower gas superficial velocity or near the churn-to-annular transition.

During the upward moving process, part of the liquid is entrained into the gas core, and eventually breaks up into droplets of various sizes. Three main mechanisms for droplet generation are found in churn flow, as illustrated in Figure 2. In the slug-churn flow transition, with an increase in gas flow rate, the Taylor bubble becomes seriously distorted. The liquid slug shrinks and finally collapses into liquid chunks. This breakdown of liquid slug results in a sudden acceleration and impels the chunks to break up into small droplets (see Figure 2a). Subsequently, the falling liquid accumulates, forming the so-called huge wave, and is again broken up by the gas. Thus, the bag breakup (undercut) plays a dominant role at low gas superficial velocity (see Figure 2b), whereas the ligament breakup (sheared-off) comes to gain greater importance with the increase of gas flow rate (see Figure 2c). In the case of ligament breakup, the wave crest is "stretched" into the gas core (see the protrusion in Figure 2c) and then sheared off by the coming gas flow. The filament subsequently breaks up into small droplets. Comparably, small droplets tend to stay in the core for much longer due to the turbulent eddy interactions within the gas core. In the case of bag breakup mechanism, an open-ended bubble is formed with a thick filament rim and the part of the wave is undercut to form a liquid chunk. Subsequently, the chunk breaks up into smaller droplets or deposits instantly on the liquid film to cause a secondary entrainment (impingement) to generate smaller droplets.





(c) Ligament breakup  
**Figure 2:** The mechanisms of droplet generation.

We analyzed the effects of gas and liquid phases on the wave behavior and found that flooding of the film was a characteristic of the churn flow through out of the regime. Falling film was observed to go through a process from unstable to stable and unstable again from churn flow to annular flow, depending on the comparison among gravity, surface tension and countercurrent or cocurrent shear stress. Therefore, Orr-sommerfeld equations were solved to investigate the effect of gas and liquid flow on the film stability and two thresholds of shear stress were obtained and discussed in detailed. According to the analysis of the initial condition of huge wave movement, it can be inferred that the huge wave disappears as the sign for the transition from the churn flow to the annular flow.

Bag break-up mechanism and ligament break-up mechanism were found coexistent in churn flow. At lower gas velocity, larger drops are generated from the huge waves through the bag break-up mechanism. As the gas flow rate increased and this under-cutting mechanism subsided, leading to decrease entrainment. With further increasing of the gas flow rate, the ligament breakup gained greater importance and generated relative smaller drops. In the cross-section of the pipe, the amount of liquid entrained is high in churn flow and decreases with increasing gas velocity, reaches the minimum around the churn-annular flow transition.

The underlying physical behavior for the drop entrainment is believed to be the Kelvin-Helmholtz instability. We established an analytical model based on this theory to study the drop entrainment under churn flow condition. The proposed model was verified qualitatively and quantitatively and we analyzed in detail the impact of the gas and liquid flow rate, pipe diameter and pressure on the drop entrainment rate. Thus, we proposed a more accurate formula for the entrainment rate in churn flow based on the comparative analysis with entrainment rate in annular flow. The new formula was then compared with existing prediction equation, and the results obtained have been discussed and believed to be more well in agreement with the real entrainment process.

Since entrained drops in churn flow have “memory effect” on the flow in annular flow, a developed film flow model was established to predict the critical heat flux in churn flow regime. By analyzing the impact of the entrainment fraction at the onset of annular flow on the prediction of the critical heat flux and referring to our experimental results, we pointed out that the commonly used approaches about the onset entrainment fraction of annular flow was lack of theoretical basis. Thus, we considered the drop “memory effect” and proposed that it should be carried out the integration process in film flow model from the onset of churn flow rather than annular flow and provided a more

reasonable assumption of the entrainment fraction at the onset of churn flow. The results indicated that the developed model ensure an accuracy of prediction and reflect a more realistic influence of flow pattern on the critical heat flux.

## References

- Azzopardi, B.J., Drops in annular two-phase flow, *Int. Journal of multiphase flow*, Vol. 23 pp. 1-53 (1997)
- Azzopardi, B.J., Wren, E., What is entrainment in vertical two-phase churn flow? *Int. Journal of Multiphase Flow*, Vol. 30 pp 89-103 (2004)
- Barbosa, J.R., Govan, A.H. and Hewitt, G.F., Visualization and modeling studies of churn flow in a vertical pipe, *Int. Journal of multiphase flow*, Vol. 27 pp. 2105-2127 (2001)
- Barbosa, J.R., Hewitt, G.F., König, G., Richardson, S.M., Liquid entrainment, droplet concentration and pressure gradient at the onset of annular flow in a vertical pipe, *Int. Journal of multiphase flow*, Vol. 28 pp. 943-961 (2002)
- Hewitt, G.F. Churn and Wispy Annular Flow Regimes in Vertical Gas-Liquid Flows. *Energy & Fuels*, Vol. 26 pp. 4067-4077 (2012)
- Wang, K., Ye, J., Bai, B. F. Entrained Droplets in Two-phase Churn Flow. *Chemical Engineering Science*, 2017, 164: 270-278.
- Wang, K., Ye, J., Bai, B.F. Profile of huge wave in gas-liquid churn flow. *Chem. Eng. Sci.*, Vol. 163 pp. 137-144 (2017)
- Wang, K., Bai, B.F., Ma, W.M. An improved liquid film model to predict the CHF based on the influence of churn flow. *Appl. Therm. Eng.*, Vol. 64 pp. 422-429 (2014)
- Wang, K., Ma, W.M., Bai, B.F. A model for droplet entrainment in churn flow. *Chem. Eng. Sci.*, Vol. 104 pp. 1045-1055 (2013)
- Wang, K., Ma, W.M., Bai, B.F. Huge wave and drop entrainment mechanism in gas-liquid churn flow. *Chem. Eng. Sci.*, Vol. 104 pp. 638-646 (2013)
- Wang, K., Ma, W.M., Bai, B.F., Cui, J.H. A physical model for huge wave movement in gas-liquid churn flow. *Chem. Eng. Sci.*, Vol. 79 pp. 19-28 (2012)

## Models of evaporation near contact lines

Vladimir Ajaev<sup>1,2</sup>

<sup>1</sup>Department of Mathematics, Southern Methodist University,  
 Dallas TX 75275, USA

<sup>2</sup>Kutateladze Institute of Thermophysics, SB RAS, Novosibirsk 630090, Russia  
 ajaev@smu.edu

In heat transfer applications, liquid-gas interfaces can come into contact with heated solid substrates. The gas phase can be pure vapor or moist air, leading to different limiting mechanisms for local evaporation rates near contact lines. Several mathematical models of evaporation process from the liquid-gas interface in the contact line region, schematically illustrated in Fig. 1 (top), have been developed over the past decades in order to describe coupling of evaporation and a number of other relevant physical phenomena such as capillarity, viscous liquid flow, London-van der Waals disjoining pressure, Marangoni stresses, diffusion and fluid flow in the gas phase, electrostatic interactions of interfaces, and vapor recoil. These studies address static and dynamic configurations for both triple lines, i.e. lines of contact of liquid, gas, and solid phases, and the so-called apparent contact lines, which are transition regions between macroscopic liquid-gas interfaces and ultra-thin films covering the solid substrate (Wayner 1999). A useful mathematical framework for all these studies is provided by the so-called lubrication-type models (Craster and Matar 2009), which are based on the assumption of length scales along the substrate being much larger than the length scale in the direction normal to it.

The advantage of lubrication-type models is that the description of evaporation, viscous flow, and other relevant physical effects discussed above can be reduced to a single partial differential equation for the scaled liquid layer thickness,  $h$ . The nondimensional evaporative flux  $J$  can also be expressed in terms of this quantity; a commonly used expression is of the form

$$J = \frac{(h_{xx} + \Pi) + T_0}{K + h} \quad (1)$$

where  $T_0$  is the substrate temperature,  $\Pi$  is the disjoining pressure due to physical effects such as unbalanced London- van der Waals interactions at very small layer thickness (Wayner 1999); nondimensional parameters  $\Pi$  and  $K$  describe shifts in the interfacial temperature due to changes in the liquid pressure and non-equilibrium effects, respectively. Once the partial differential equation for thickness is solved numerically, the flux profile can be recovered from Eq. (1). Typical result for the spatial flux variation is shown in Fig. 1 (bottom). Here the  $x$ -coordinate is along the substrate. Note that the region of highest evaporation rate is near the contact line due to small thermal resistance in the thinner part of the liquid layer. However, evaporation is suppressed by disjoining pressure in the ultra-thin film, resulting in the sharp drop of the flux there.

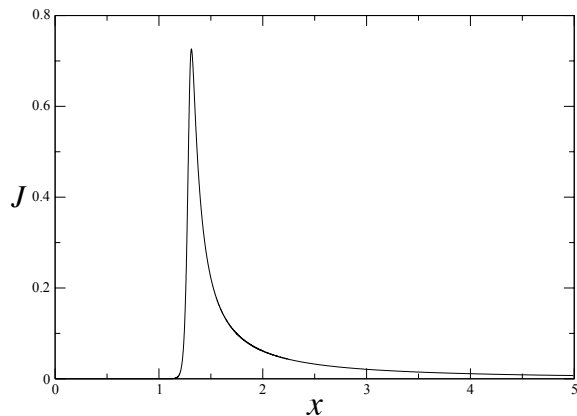
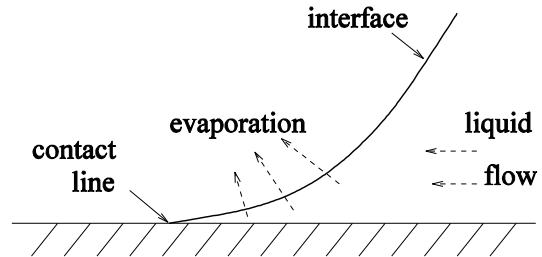


**Figure 1:** (top) Geometric configuration considered in models of contact lines; (bottom) Typical scaled evaporative mass flux profiles obtained from the model.

Several more recent developments in the field focused on contact line motion over chemically patterned and structured surfaces, as discussed e.g. in Ajaev et al. (2016).

### References

- Wayner P. C., Intermolecular forces in phase-change heat transfer: 1998 Kern award review, *AIChE J.*, Vol. 45, pp. 2055-2068 (1999)
- Craster R.V., Matar O.K. Dynamics and stability of thin liquid films, *Rev. Mod. Phys.*, Vol. 81, pp. 1131-1198 (2009)
- Ajaev V.S., Gatapova E.Ya., Kabov O.A., Stability and break-up of thin liquid films on patterned and structured surfaces, *Adv. Colloid Interface Sci.*, Vol. 228, pp. 92-104 (2016)

## **Buoyancy and thermocapillary induced convection and its influence on crystal growth**

Vladimir Berdnikov

Kutateladze Institute of Thermophysics SB RAS  
Lavrentyev ave., 1, Novosibirsk, 630090, Russia  
berdnikov@itp.nsc.ru

It is known for a long time that interfacial tension of liquids and melts depend on temperature. It is also known that temperature gradient on the liquid surface results in the occurrence of the tangential force. But a little attention is paid to solving of the heat convection problem. Heat exchange processes at dropwise condensation [1] are a rare exception, for example. V. Isachenko introduced the parametre considering influence of thermocapillary on growth and convective heat exchange of a condensed phase [1]. It can be treated as the ratio of thermocapillary forces to forces of viscosity. The situation is similar to when the buoyancy force is considered as the small insignificant additive in heat convection problem. But at development of technologies of reception of especially pure materials and high-quality crystals it has appeared, that a buoyancy force and thermogravitational convection makes essential impact on a course of technological processes even in regimes of the mixed convection [2,3]. Under ground conditions badly controllabled thermogravitational convection is inevitable in the basic methods of crystal growth: in a Czochralski method, in floating zone growth and horizontal oriented crystallization. In all these methods of the directed crystallisation there exist sections of nonisothermal free surfaces of melts.

With development of flights in space and the beginning of researches of behaviour of a liquid in microgravity conditions researches of convective and complicated heat exchange, including phase changes have begun: boiling, crystallization, behaviour of substance to a critical state (or near to critical temperature). History of development of an early stage of researches of features of behaviour of liquids in zero gravities and the basic received results are systematised in [4-6]. In the same place statements of problems and results of technological researches are presented. One of directions is a check of possibility to exclude forces of buoyancy in the conditions of microgravitation and to organise onboard space vehicles crystal growth of high quality and other technological processes. As all experimental researches in the microgravity conditions were duplicated on similar installations in ground conditions it has been especially clearly realised, that thermocapillary convection has essential influence on hydrodynamics of liquids and melts.

The first main effects:

1. The strong influence of capillary phenomena and first of all thermocapillary effect. And at studying of thermocapillary convection and crystallisation processes the essential role of processes of adhesion and wetting of the rigid surfaces by liquids and melts was clarified. These processes are important from the point of view of guidance of behaviour of liquid mediums in weightlessness and at attempts of creation of composite materials.

2. Have found out a high level of vibrations onboard orbital stations and their strong influence on investigated processes. The new scientific direction - vibrational hydrodynamics has been as a result developed. The new scientific direction - vibrating hydrodynamics has been as a result developed. Monitoring systems of parametres of vibrations, systems of suppression or exclusion of vibrations have been created. Within the limits of this scientific direction have been executed extensive theoretical and experimental researches of influence of vibrations parametres on hydrodynamics and heat exchange. Vibrations make essential influence on hydrodynamic processes and on a convective heat transfer in the conditions of microgravitation and in ground conditions. They are practically omnipresent.

Comprehension of importance of the account of thermocapillary effect and in ground conditions at single-crystal growth by various methods in the presence of a free surface became one of effects of researches in space. The reason is obvious. At crystal growing from the melt system is nonisothermal. Along the free boundary and on a normal line to it necessarily there are temperature gradients. In a Czochralski method [2,3], floating zone growth [5,6], in a method of a horizontal directional crystallization (in horizontal Bridgman crystal growth) [6-9] longitudinal temperature gradients significant owing to the principle of crystal growing in the presence of nonisothermal free boundaries. Thermocapillary convection in these methods develops against thermogravitational convection or against the mixed convection. Even in a vertical Bridgman method (in vertical Bridgman configurations) at crystallization of a melt from a bottom of a crucible upwards there are the radial temperature gradients [10]. Because of presence of longitudinal temperature gradients on solidified fronts hot melts in all listed methods of reception of crystals accumulate. As a result of it in the field of a leaking of a hot melt growth rate and a solidified front drops has major curvature. In crystals in these areas there are big local temperature gradients and heat stresses.

Less visible effect on development of convective current of a temperature gradient perpendicular to a fluid free surface. As from free surfaces of melts as a rule there is an intensive convective heat exchange in surrounding gas environment except longitudinal temperature gradients on a demarcation a melt-gas there are temperature gradients in boundary layer of melts on a normal line to the free surface. As a result there are conditions for development of instability and formation of the secondary small-scale currents of Rayleigh-Benard nature [11-18].

In ground conditions it is a question on influence of thermocapillary effect and on its relative role in Rayleigh-Benard convection. The interfacial tension role in formation of Benard cells in fluid shallow layers is shown

for the first time experimentally in work [11]. Theoretical researches of Benard convection without a buoyancy force have been fulfilled in [12]. Experiments on thermocapillary convection in space [13] have been made. In [14] influence of a buoyancy force and thermocapillary effect has been investigated. In case of the former the system is absolutely unstable, and in the second case there is a threshold of stability and critical values of Marangoni and Rayleigh numbers. Generalisation of results in of this area of researches is presented in [15].

Researches in microgravity conditions and on the Earth have forced to study more penetrating a role of thermocapillary convection and in ground technologies [6-18]. Therefore now it is a question not of uncontrollable thermogravitational convection, and about buoyancy and thermocapillary driven convection in problems of the conjugate heat exchange in technological processes [18,19]. In all modern researches of processes of crystal growth by methods of the directed crystallization one of the important problems is a finding-out of the relative role of a buoyancy force, thermocapillary effect and centrifugal forces. For creation of operated technological processes it is necessary to have basic fundamental knowledge of thermal gravity-capillary convection, and then and of the mixed convection in Czochralski method and floating zone growth [2-10].

The mixed convection grows out of joint influence of a buoyancy force and centrifugal forces at rotation of crystals and crucibles. These methods now the cores at reception большей parts of single crystals for microelectronics, the laser technics and other ranges of application. The conjugate heat transfer in vicinities of front of crystallization and the complicated conjugate heat exchange of crystals with a surrounding medium define thermal history of crystals [2,3,19]. Fields of temperature and heat stresses depend on features of these processes, the shape of front of crystallization and on the properties of the grown crystal.

## References

1. V. Isachenko, V. Osipova, A Sukomel, Heat Transfer (Revised from the 1965 Russian edition), Mir Publishers, Moscow, 1969. – 552 p.
2. Berdnikov V.S., Vinokurov V.V., Panchenko V.I., Solovov S.V., Heat exchange in the classical Czochralski method, Journal of Engineering Physics and Thermophysics. 2001. T. 74. № 4. C. 1007-1014.
3. Berdnikov V.S., Prostomolotov A.I., Verezub N.A., The phenomenon of "cold plume" instability in Czochralski hydrodynamic model: physical and numerical simulation, Journal of Crystal Growth. 2014. T. 401. C. 106-110.
4. Materials Sciences in Space With Application to Space Processing. Edited by Leo Steg. Vol. 52. Progress in Astronautics and Aeronautics. Princeton University. Princeton. New Jersey. 1977
5. Materials Sciences in Space. A Contribution to the Scientific Basis of Space Progressing. Edited by d. Feuerbacher, H. Hamacher, R.J. Naumann, Springer-Verlag, Berlin, Heidelberg, New York, Tokyo (1986)
6. Fluid Dynamics, Vol. 29 (5) (1994)
7. Birich R.V. Thermocapillary convection in a horizontal layer of fluid, Journal of Applied Mechanics and Technical Physics, Vol.7, pp. 69-72, (1966)
8. Berdnikov V.S., Gaponov V.A., Kovrizhnykh L.S., Thermal gravitational-capillary convection in a cavity with a longitudinal temperature gradient, Journal of Engineering Physics and Thermophysics. 2001. Vol. 74. № 4. pp. 999-1006.
9. Zabrodin A.G., Berdnikov V.S., Thermal convection and instability mechanisms in liquid with capillary effects, Journal of Engineering Thermophysics. 1991. Vol. 1. № 3. pp. 245-257.
10. Antonov P.V., Berdnikov V.S., Dependences of the shape of the crystallization front and growth rate of a silicon ingot on the heat transfer mode in the bridgman-stockbarger method, Journal of Applied Mechanics and Technical Physics. 2012. Vol. 53. № 6. pp. 860-870.
11. Block M.J., Surface tension as the cause of Benard cells and surface deformation in a liquid film, Nature, Vol. 178 (4334) pp. 650-651 (1956)
12. Pearson J.R.A., On convection cells induced by surface tension, J. Fluid Meech., Vol. 4 (5) pp. 489-500 (1958)
13. Grodzka P.G., Bannister T.C., Heat flow and convection demonstration experiments aboard Apollo 14, Science, Vol. 176 (4034) pp. 506-508 (1972); Heat flow and convection experiments aboard Apollo 17, Science, Vol. 187 (4172) pp. 165-167 (1975)
14. Nield D.A. Surface tension and buoyancy effects in cellular convection, J. Fluid Meech., Vol. 19 (3) pp. 341-352 (1964)
15. Koschmieder E.L., Benard Cells and Taylor Vortices, Cambridge Monographs on Mechanics and Mathematics (Cambridge Univ. Press, Cambridge, 1993)
16. Berdnikov V.S., Structure of free convection liquid flow at a free heat - exchange surface // Heat transfer, Soviet Research, Vol.11, N3 pp. 13-24 (1978).
17. Berdnikov V.S., Grishkov V.A., Kovalevskii K.Y., Markov V.A., Thermal imaging studies of the laminar-turbulent transition in the Rayleigh-Benard convection, Optoelectronics, Instrumentation and Data Processing, Vol. 48, № 3, pp. 311-318 (2012).
18. Berdnikov V.S., Gaponov V.A., Grishkov V.A., Markov V.A., Likhansky P.M., Effect of nonstationary thermal gravitation-capillary convection on temperature distribution in a thin vertical wall, Thermophysics and Aeromechanics, Vol. 17, № 2, C. 181-191 (2010).
19. Berdnikov V.S., Mitin K.A., Effect of heat transfer mode on the temperature and thermal stress fields in single crystals, Bulletin of the Russian Academy of Sciences: Physics, Vol. 80, № 1, pp. 68-73 (2016).

## Contact line movement over polished and laser processed metal surfaces

Evgeniya Orlova, Dmitry Feoktistov and Anastasya Islamova

National Research Tomsk Polytechnic University, Power Engineering Institute, Theoretical and Industrial Heat System Engineering  
Department, 30, Lenin Avenue, Tomsk, 634050, Russia  
lafleur@tpu.ru

There are several theories describing spreading (Blake et al. 1969, Voinov 1976) establishing the dependences of two droplet parameters: the dynamic contact angle (DCA) and the contact line (CL) speed. They can be classified according to the different energy dissipation mechanisms near the contact line: molecular-kinetic (MKT) and hydrodynamic (HDT). According to the MKT the dependence of the dynamic contact angle on the contact line speed is the result of molecular adsorption and desorption on the three-phase CL. From the HDT, it is known that the bulk viscous friction prevents the contact line motion. In addition, there is a theory based on the integration of the MKT and HDT dependencies (Petrov and Petrov 1992). Despite the fact that these theories satisfactorily describe the spreading of liquid droplets over solid substrates, it has not been established that they can be used to describe spreading on rough substrates.

The purpose of this paper is to analyze the application of spreading theories to the description of wetting and dewetting of polished and specially structured aluminum surfaces by distilled water.

The studies were conducted on the experimental setup with implementation of shadow method (Kuznetsov et al. 2016). Two substrates made of aluminum were used. The surface of the first substrate was polished, the second surface was processed by laser radiation. For each surfaces the contact angle hysteresis was calculated as the difference between the advancing ( $\theta_A$ ) and receding ( $\theta_R$ ) DCA.

The contact angle hysteresis (CAH) on the polished surface reaches 5°. It confirms the relative smoothness and homogeneity of the surface. For laser-processed surface, the CAH does not exceed 2°. This value is small and lies within the confidence interval, so there is no reason for the statement about the CAH on such a surface.

Fig. 1 shows the dependences DCA on the CL speed on the polished surface. All theories are found to agree well with the results of experimental studies. The combined model is in better agreement with the experimental data in comparison with MKT and HDT. This is explained by the fact that this theory takes into account the friction of the contact line as well as the viscosity force in the volume of the liquid.

The fitting of experimental data with the theories obtained on the laser-processed surface is shown in Fig. 2. It was found that the dependencies of the advancing/receding DCA on the CL speed on the laser-processed surface fit better with the theories compared with the polished ones. It can be assumed that this is due to an insignificant hysteresis value on such a surface (2°). Hence, it can be concluded that the theoretical dependences do not take into account the CAH resulting from the chemical surface heterogeneity or roughness.

The reported study was supported by the grant of President of Russian Federation for the government support of young Russian scientists (MK-6810.2016.8).

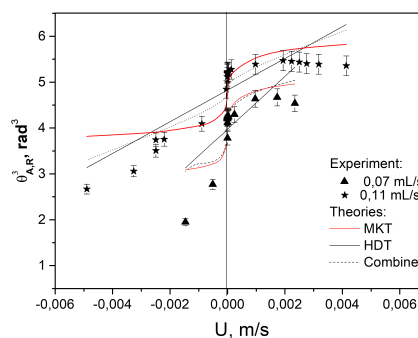


**Figure 1:** Dependencies of the advancing/receding DCA on the CL speed on polished surface. Symbols corresponds to the experimental data, lines – theories.

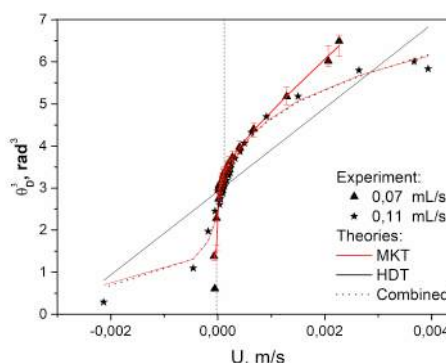


**Figure 2:** Dependencies of the advancing/receding DCA on the CL speed on the laser-processed surface. Symbols corresponds to the experimental data, lines – theories.

### References

- Blake T. D., Haynes J. M. Kinetics of liquid liquid displacement, *J. Colloid Interface Sci.*, Vol. 30 pp. 421-423 (1969)
- Voinov O. V. Hydrodynamics of wetting, *J. Fluid Dyn.*, Vol. 11 pp. 714-721 (1976)
- Petrov P.G., Petrov J.G. A combined molecular-hydrodynamic approach to wetting kinetics, *Langmuir*, Vol. 8 pp. 1762-1767 (1992)
- Kuznetsov G.V., Feoktistov D.V., Orlova E.G. Regimes of Spreading of a Water Droplet Over Substrates with Varying Wettability, *J. Eng. Phys. Thermophys.* Vol. 89 pp 317-322 (2016)

## Author index

<b><u>A</u></b>		De Smet L.	27
Aitsaada M.	139	Dehaeck S.	141, 144
Agafontsev M.	189	Dementyev Yu.	67
Ajaev V.	35, 150, 202	Demin V.	113
Aktershev S.	55	Deng Yu.	31
Alava M.	21	Denoyel R.	59
Alekseenko S.	17	Di Marco P.	25
Alexandre V.	29	Didier B.	29
Antoni M.	59	Ding Z.	53
Anufriev I.	189	Du C	93
Arsentyev S.	189		
Asano H.	13	<b><u>E</u></b>	
Ayel V.	65, 69, 86	Efimov S.	146
		Elkes A.	121
<b><u>B</u></b>		Eloyan K.	178
Bai B.	23, 200	Ermanyuk E.	148
Balykin M.	177		
Barakhovskaia E.	129	<b><u>F</u></b>	
Baranov E.	38, 104	Fina V.	176
Barskii A.	81	Franz B.	119
Bartkus G.	71	Furukawa T.	156
Bazhenov A.	181		
Bekezhanova V.	158	<b><u>G</u></b>	
Berdnikov V.		Gatapova E.	160, 173, 180
Bertin Y.	65, 69, 86	Gavrilov N.	148
Bilsky A.	33	Gerasimov Yu.	103
Bochkareva E.	192	Gibbons M.	25
Bondarenko D.	19	Gobyzov O.	33
Borisov A.	192	Goncharov K.	82, 136
Boronin S.	88	Goncharova O.	158
Bouchenna C.	139	Gordeeva V.	111, 168
Buz V.	82	Graur I.	84
		Guo H.	15, 73
<b><u>C</u></b>		Guzei D.	175, 186
Cao Z.	31		
Chauris N.	69	<b><u>H</u></b>	
Chen N.	79	Hammer C.	9
Chen Xi.	93	Haquet J.	59
Chen Xu.	53, 172	He Z.	62
Chen Z.	77	Hrebtov M.	181
Cherdantsev A.	17	Huang H.	117, 196
Cherdantsev M.	17		
Chernyavskiy A.	57, 152	<b><u>I</u></b>	
Chevalier T.	21	Ilyushin B.	181
Cheverda V.	3, 61, 67, 171, 176, 185	Inzhevatkin K.	33
Chikh S.	139	Isaenkov S.	17
Chinnov E.	48, 55, 67, 104, 134, 188	Ivanova N.	123
Colin C.	9		
Colinet P.	141, 144	<b><u>J</u></b> Jia Yi.	97
Coninck J.	144		
Chongfang M.	115	<b><u>K</u></b>	
		Kabov O.	3, 35, 46, 61, 67, 104, 105, 127 164, 150, 160, 166, 191, 193, 195
<b><u>D</u></b>		Kabova Yu.	3, 46, 134
Dávalos-Orozco L.	51	Karelin V.	137
De Simone A.	27		

Karlov S.	42	Matthieu R.	29
Kashinsky O.	183	Meshalkin Yu.	184
Kawanami O.	156	Meshkov K.	186
Khmel S.	38, 104	Minakov A.	175, 186
Khramtsov D.	42, 164, 179	Miskiv N.	192
Kim J.	9	Miyawaki S.	13
Kirichenko D.	35, 150, 191	Mizev A.	113
Kirichenko E.	107, 180	Mohamed F.	7
Kitanin E.	19	Moiseev M.	174
Kitanina E.	19	Montrone L.	27
Klyuev D.	123	Murata Yu.	13
Kobelev A.	146		
Kochkin D.	187	<b>N</b>	
Koivisto J.	21	Nazarov A.	129
Kolegov K.	154	Nekrasov D.	42
Kong X.	31	Novichkova S.	177
Kopyev E.	189		
Korbanova E.	160, 173	<b>O</b>	
Korbanova T.	195	Obreschkow D.	7
Korzhov K.	177	Ohta H.	11
Kozlov D.	152	Okayama S.	11
Kozulin I.	63	Okulov V.	143
Krasinsky D.	133	Okulova N.	143
Kravtsov P.	19	O'Shaughnessy S.	25
Kravtsova A.	184	Osiptsov A.	88
Kreta A.	166		
Kuznetsov V.	46, 63, 71, 134	<b>P</b>	
		Pagnoni F.	86
<b>L</b>		Pan L.	117, 196
Lebedev-Stepanov P.	146	Panin Y.	177
Li H.	5, 99	Pavlenko A.	57, 197
Li K.	5, 99	Peganova M.	19
Li Yon.	79	Pervunin K.	109
Li You-R.	36, 162	Petukhov M.	113
Li Z.	36, 162	Philippe A.	29
Liang R.	95	Piluso P.	59
Lili S.	115	Piralishvili S.	121
Liu B.	31	Piskunov M.	170
Liu Li	23	Podzharov Yu.	127
Liu Li-N.	36	Pokusaev B.	42, 164, 179
Liu P.	5	Poletaev I.	109
Liu Q.	172	Polikarpov A.	84
Liu R.	53	Ponomarenko T.	185
Lyubimova T.		Prikhodko V.	103
Lyulin Yu.	81, 105, 125, 166	Pryazhnikov M.	175, 186
Lyushnin A.	111, 168	Puisto A.	21
Liu X.	15, 73		
Lobasov A.	175	<b>Q</b>	
Luc B.	29	Qiu H.	
<b>M</b>		<b>R</b>	
Ma C.	15, 73, 93	Randin V.	183
Maltsev L.	127	Ranebo H.	27
Manukov A.	44	Raufaste C.	121
Marchuk I.	81, 105, 129	Rebrov A.	182
Marengo M.	65	Rednikov A.	141, 144
Marcovich D.	17	Renaud L.	29
		Rezanova E.	125

Reznik V.	42	Tolmacheva K.	88
Robinson A.	25	Tóth B.	27
Romestant C.	65, 69	Trejo E.	9
Ronshin F.	67, 176	Tsoumpas Ya.	141
Rouzes M.	25		
Ryabov M.	33	<b>U</b>	
Robinson A.	25	Ukena R.	13
Romestant C.	65, 69	Umirzakov I.	131
Ronshin F.	67, 176		
Rouzes M.	25	<b>V</b>	
Ryabov M.	33	Veretennikov S.	121
		Vigoureux F.	65
		Vyazmin A.	42
<b>S</b>			
Saccone G.	25		
Safonov A.	107, 169	<b>W</b>	
Sakoda S.	156	Wang J.	79
Salomatov V.	137	Wang K.	201
Santucci S.	21	Wang T.	97
Sasaki N.	156	Wei J.	31, 199
Savchenkova N.	44	Wei W.	115
Selishchev D.	152	Wen Q.	93
Semenov A.	194	Wu C.	36, 162
Semenov S.	59	Wu K.	5, 99
Semionov V.	104, 188	Wu Y.	93
Serdyukov V.	152		
Seveno D.	144	<b>X</b>	
Sharypov O.	133, 189	Xia K.	79
Shatekova A.	192	Xiao S.	95
Shatskiy E.	38, 104, 169, 188		
Shefer I.	40	<b>Y</b>	
Shelukhin V.	101	Yan J.	79
Shi J.	77	Yan R.	117, 196
Shi W.	97	Yarygin I.	103
Shinmoto Ya.	11	Yarygin V.	103
Shmakova N.	21	Ye F.	15, 73
Shugaev M.	174	Yevdokimov O.	121
Skladnev D.	42	Yuting W.	115
Skorovarov A.	103	Yves G.	29
Solé-Agostinelli T.	65		
Son E.	1	<b>Z</b>	
Spesivtsev S.	105	Zaitsev D.	3, 35, 150, 178, 187, 190, 191, 193, 194
Stepanov S.	19		
Stephan P.	119	Zakharov N.	42
Strizhak P.	170	Zamaschikov V.	48, 134
Sulyaeva V.	107	Zamchiy A.	38, 104
Supponen O.	7	Zhang D.	93
Surtaev A.	152	Zhang G.	27
Svetlichnaya O.	171	Zhang L.	77
		Zhang Li	36, 162
		Zhang Lia.	99
<b>T</b>		Zhang Yo.	31
Taboryski R.	143	Zhao J.	5, 15, 31, 73, 99
Tadrist L.	139	Zhao L.	23
Tianhao R.	11	Zherebzo V.	19
Timoshenko N.	107	Zhou L.	162
Timoshevskiy M.	109	Zhu J.	97
Tkachenko E.	193	Zhu Z.	172
Tokarev M.	109		

## \* NSU IN FACTS & FIGURES

**6000**  
STUDENTS

**1400**

FOREIGN  
STUDENTS  
from 50 countries



**6**

departments

**3**

institutes

**2000**

UNIVERSITY STAFF MEMBERS

**880** ASSOCIATE  
PROFESSORS

**570** FULL PROFESSORS  
with doctoral degrees

**73** MEMBERS  
OF THE RAS

MORE THAN **80**

COUNTRIES  
REPRESENTED BY MOOCs STUDENTS

**119**

PARTNER  
UNIVERSITIES  
in 24 countries

**JOINT PROGRAMS  
WITH COMPANIES:**

Baker Hughes, OCSiL, Intel,  
Yandex, ZGS, Academpark,  
Biotechnopark, Sberbank  
Technologies

**35**

PARTNER  
INSTITUTES  
in Akademgorodok

**139**

LEADING  
RESEARCHERS

**H>20**



**138**

LABORATORIES

**6** MIRROR LABORATORIES

**5-100** LEADER OF TOP 5-100  
PROJECT –

the project oriented at making leading Russian  
universities competitive on world market of  
education services

**TOP-50** IN PHYSICS

QS University Rankings

**TOP-500** ACADEMIC RANKING  
OF WORLD  
UNIVERSITIES

3rd position among  
Russian universities

**20<sup>th</sup> POSITION**

QS UNIVERSITY RANKINGS BRICS

RESEARCH GROUPS ARE  
INVOLVED IN NSU

**21**

INTERNATIONAL  
COLLABORATIONS  
in the field of elementary  
particle physics and life  
sciences



**2<sup>nd</sup> POSITION**

QS UNIVERSITY RANKINGS EMERGING  
EUROPE AND CENTRAL ASIA

**107<sup>th</sup> POSITION** **190<sup>th</sup> POSITION**

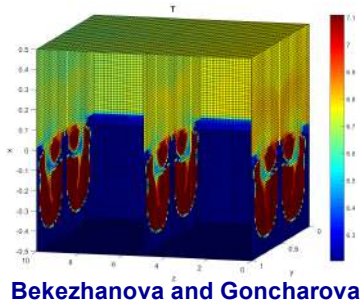
QS UNIVERSITY  
RANKINGS  
NATURAL SCIENCES

GOOGLE SCHOLAR  
CITATIONS

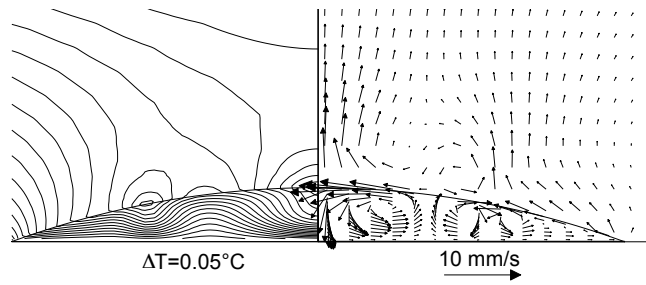
**291<sup>st</sup> POSITION**

QS UNIVERSITY RANKINGS  
among 20 000 world universities

**N\***



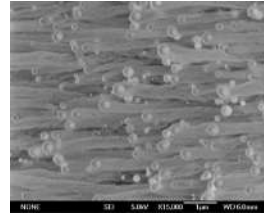
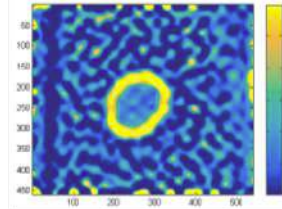
Bekezhanova and Goncharova



Tadrist et al.



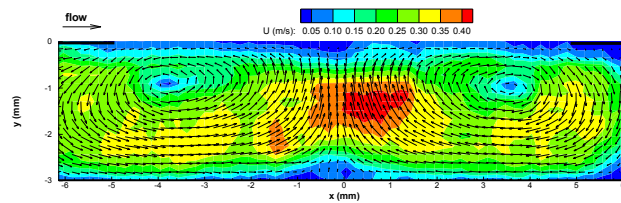
Paolo Di Marco



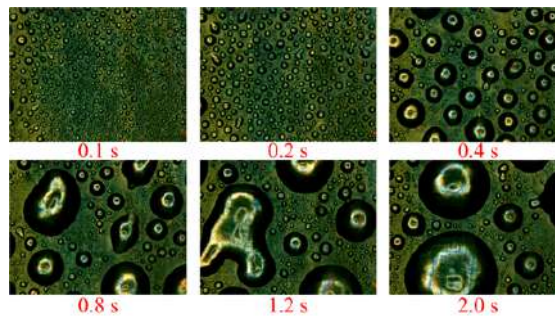
Baranov et al.



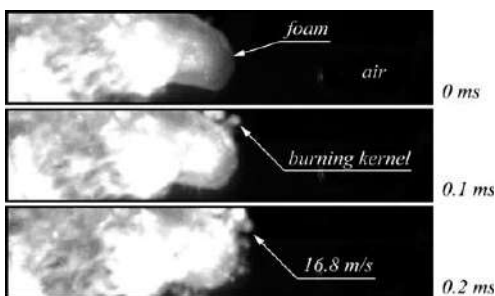
Toth



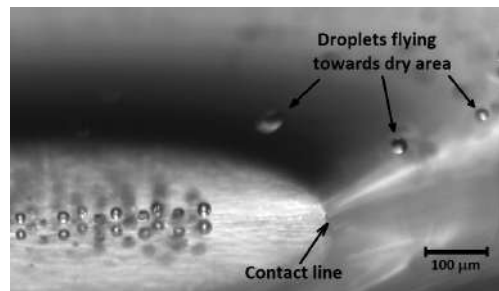
Lyulin et al.



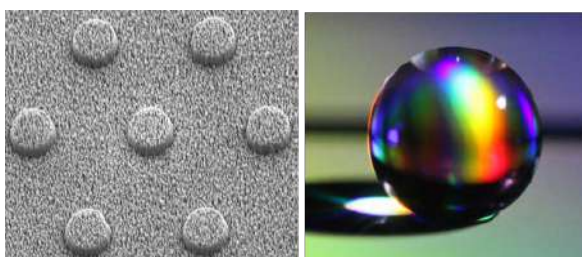
Yong Li et al.



Son



Zaitsev et al.



Okulova et al.



Ke Wu et al.